THE UNIVERSITY OF HULL

Electroluminescence and Inorganic Phosphor Science

Being a Thesis submitted for the degree of Doctor of Philosophy
in the University of Hull

by

Ioannis Metsios, BEng, Msc

April 2007

I would like to dedicate this work to my parents. They have taught me critical thought and perseverance at a young age. The two qualities have proved my most valuable in my studies, research and life.

A few words of inspiration

When Vincenzo Casciarolo had found the Bolognia stone, and Henning Brand separated the element phosphorous in the 17th century, they were both considering the application of their new discoveries in resolving the alchemist's problem of converting matter to gold. Three centuries later it appears that they were on the right track, as the impact expected by GaN (a formerly known phosphor material) blue laser diodes in the electronics industry of today will make wide bandgap semiconductor, phosphor materials, much more valuable than gold.

Acknowledgements

These few words are devoted to the people that have helped me in this research, in one way or another.

First of all I would like to thank my two supervisors, Dr. David Sands and Dr. Nigel Young, that have guided me with their great knowledge and experience, in every step of the PhD, and yet encouraged me to develop my own initiative.

Then I would like to state how grateful I am to a very good, wise and important man, the late Paul Monk. I believe that most of the students in their twenties, that worked in the laser physics labs, would agree with me in that Paul have always dealt with our queries as a loving father, rather than a lab technician. He has shared his knowledge and experience with us openly and always with a friendly smile, while his help and technical solutions were invaluable. Though he has left us for a better place, his spirit is what keeps everything he ever touched in the laser labs, in a working order, and his advice will be valuable for life.

I would also like to thane the following people, for the advice and help they provided with my experimental work. The friend and fellow researcher Martin Schlaf. Veronica Hewer for her help with the XRD experiments, Gordon Sowersby, Antony Sinclair and Michael Bailey from the staff of the physical sciences department.

Abstract

The research is focussed on wide bandgap II-VI semiconductors, and more specifically on ZnS and CdS, with applications as thin film electroluminescent displays in the expanding display device market. The science of electroluminescent semiconductors and inorganic salt precipitation is combined with a unique, thin film laser processing technique known as laser induced forward transfer or direct writing (the later terminology used mostly in the case of metal films).

Zinc sulfide and cadmium zinc sulfide films with a thickness ranging between 70 and 400 nm have been prepared in an aqueous chemical bath, on optically smooth, silica, or silica based, substrates. The chemical bath contained zinc and cadmium chlorides, thioacetamide, and urea, and the most successful combination of concentrations was found to be 2.6 mM, 56.36 mM and 167.71 mM, respectively. The solution was only slightly acidic, with a pH between 5 and 6.5, and a bath temperature of 90 to 92 ^{o}C (as measured at 1 cm from the water surface of the bath) was found to be the most efficient. The films were doped with impurities, such as Cu, Ag and Mn in order to achieve specific luminescent characteristics.

A KrF excimer laser at 248 nm was used to transfer the films from their original substrate to a new one. The laser pulse was focussed on the chemically deposited films through the back of the transparent silica substrate. The detached film was transported across a gap of 15 μm and attached to the new substrate. A fluence between 0.5 and 0.7 Jcm^{-2} was found to give the best transfers, and also able to achieve multiple layer transfers over the same area of the target substrate. The transfers were performed in an argon atmosphere of 4 x10^{-2} mbar pressure.

Ellipsometry and film reflectivity measurements were used to model and determine the film thickness of the chemically deposited films and the values obtained were confirmed by scanning electron microscopy. The latter, together with optical microscopy, atomic force microscopy and interferometry were exploited to investigate the structure of the chemically deposited and laser transferred films. It was found that a very thin ZnO film initially adhered to the substrate in the bath, on which the ZnS or CdZnS main film was attached as homogenously grown cluster beads or grown via ion by ion deposition. The homogeneously grown beads had a phase separation, containing the sulfide with the lowest K_{sp} in the centre, enclosed by highest K_{sp} sulfides, with the highest one as a shell. The phase separation between CuS and ZnS was also confirmed by extended X-ray absorption fine structure. The elemental composition of the chemically-prepared and laser-transferred films was investigated by energy dispersive X-ray analysis (EDX), inductively coupled plasma mass spectrometry and Raman microspectrometry, while the EDX and Raman methods also helped to confirm the phase separation between CdS and ZnS. Cathodoluminescence and photoluminescence measurements were employed to investigate the luminescence properties of the films, and the Mn doped films that were annealed at 700 ^{o}C were found to be the most efficient cathode ray excited phosphors, while the Cu doped phosphors came next in efficiency, performing equally well under an electron or a UV laser beam (from a HeCd laser at 325 nm). Smaller luminescence peaks were also detected in Ag doped films. Transferred films showed similar luminescent properties to their original films, but with lower intensity. Thus the chemical bath deposition and laser transferring were successful, but the methods can be further improved.

Table of contents

Chapter 1.

Introduction

Chapter 1. Introduction

1.1 Introduction

A certain class of semiconductor materials with abilities to phosphoresce when excited by energetic photons or electrons form the igniting core of interest in this research. These materials have offered means of converting electricity into light in a general or selective manner for more than a century. The gradual spread of their applications as a result of advances in the science of semiconductors is going to be laid out in the first part of this chapter. A description of the scientific background and understanding that evolved around their luminescent attributes will follow. The interest is then focused more specifically on II-VI compounds and their modern applications of high interest with a portrayal of the established methods for their fabrication and processing. The objectives of this work and the reasons for choosing the specific methods of production and processing of these materials are then put forward, followed by an outline of this written work.

From Phosphorescence to Electroluminescence

The first historical observations regarding phosphorescence were recorded during the 17th century. Barium sulfate called the "Bolognian Stone" was noted for its phosphorescent properties in 1602 by Vincenzo Casciarolo. Approximately seventy years later, an alchemist called Henning Brand was the first to use the word Phosphor, which he used for a rather pure form of the now homonymous element that he obtained for the first time in history. Unlike today's use of the term phosphor, the light emitting properties of the elemental phosphor in air that Henning observed would now be characterised as chemiluminescent. It wasn't until two hundred years later that electroluminescence was observed as a distinct phenomenon. Science was at the time evolving an interest in the effects of electric and magnetic fields. The response of many types of materials inserted in such fields was investigated and the first material ever to be observed exhibiting electroluminescence was silicon carbide by Henry Joseph Round in 1907.[1] He found that SiC would emit a yellow light when electric current was passed through it, but he did not perform any further research to explain this phenomenon. Thirteen years later, what came to be known as the Gudden-Pohl[2] and later on the Dechence[3] effects, from the names of their

researchers, concerned the emission of light by copper-doped zinc sulfide, when subjected to an electric field. The term "electroluminescence" was first used to describe the phenomenon by Georges Destriau in 1936 [4, 5] who experimented with electric current passing through a suspension of ZnS:Cu and other phosphors. He established the uniqueness of the phenomenon and distinguished it from the emission of light from junction diodes. It was thus discovered that materials such as zinc sulfide had the ability to immediately convert the energy provided by an electric field into light, unlike, the most common, incandescent sources that convert electricity to light through heat.[6] Various cells enclosing phosphors were constructed in order to take advantage of the phenomenon, where continuous output of light could only be achieved by a field of alternating polarity, as the application of a constant field generated a rapidly decaying emission only on its initiation and termination. Even under these conditions, the lifetime of the constructed devices was too short for commercialisation.[7]

The interest in electroluminescence had almost disappeared in the next 30 years, with only small progress taking place, mostly concerning ZnS:Mn powders in an attempt to construct light sources. In the 1960s an interest in display devices pushed the research in the field a few steps further and combined with the progress made in thin film technology it yielded the first electroluminescent (commonly abbreviated as EL) displays. Sigmatron Corporation produced the first a.c. thin film dot matrix displays in 1965,[8] and in 1968 A. Vecht demonstrated a d.c. driven EL display.[9] The reliability and lifetime of these devices, though had yet to be improved and no commercial device was ever produced from these efforts. In 1978 Sharp Corporation produced an a.c. thin film EL planar monochrome television display,[8] incorporating a three layer arrangement of ZnS:Mn sandwiched in two insulating sheets, suggested by Russ and Kennedy in 1967.[10] Later on (1994) Planar systems constructed a prototype flat panel, full colour ACTFEL (alternating current thin film electro-luminescent) display.[11] In 1997 EL flat panel displays managed to gain 8% of the flat panel display market, demonstrating a lifetime of over 50 000 h (< 10% change in luminescence) and a greater shock, vibration and temperature resistance than any other flat panel display.[12, 13] The increase in lifetime was a result of manufacturing in a controlled humidity environment, as it had been observed that moisture was a great degradation factor for the phosphors. This has also enabled the development of thin

EL green and blue lamps (with phosphors such as ZnS:TbOF and SrS:Ce), replacing the common (and mostly red) light emitting diodes in some of their applications.

1.1.a. Photoluminescence in materials

The materials that have been used in electroluminescent devices and the studies that have been conducted on them have always been related to the phenomenon of photoluminescence. Photoluminescence is a term employed in this field of science to describe the emission of light by matter, following a photonic excitation procedure of one form or another. The phenomenon is then subdivided to phosphorescence and fluorescence. An account of the current understanding of these two phenomena is given here since the related concepts are exploited throughout this work.

Phosphorescence and Fluorescence – General Principles

The discrimination between fluorescence and phosphorescence was initially based upon the duration of luminescence after the excitation ceases. This belief slowly faded away when each phenomenon was associated with a more precise scientific explanation and later on with the increase in observations upon materials featuring both types of photoluminescence. If the Lorentz-Drude model is used to describe an excited electron, emitting a photon on its de-excitation transition, the average transition lifetime can be calculated as follows:

$$\tau = \frac{3}{8\pi^2} \cdot \frac{m_q c}{e_q{}^2 v^2} \qquad 1.1$$

τ = transition duration, m_q = mass of electron, 9.1066×10^{-31}kg, e_q = charge of electron = 1.602×10^{-19} Q, c = speed of light $3 \times 10^8 ms^{-1}$ and v = frequency of oscillation in s^{-1}. For emission of a photon in the middle of the visible spectrum with a wavelength of 550 nm, equation 1.1 yields a transition time in the order of 10^{-8} s.[14] Hence it was slowly derived that fluorescence was taking place within timescales of 10^{-9} to 10^{-6}, while phosphorescence durations would begin at 10^{-5} s and reach up to several seconds. The longer lifetimes observed for phosphorescence were attributed to transitions from a metastable state, following a three level scheme. The difference in polarisation and temperature dependence between the emissions of the two

phenomena was found to be suggestive of an improbable transition between an excited singlet and an excited triplet state from where a radiative transition back to the ground state would return a delayed photon of lower energy than that emitted by a fluorescence procedure and certainly lower than the excitation energy. Transitions between singlet and triplet states involve a change in spin of the electron and therefore are considered kinetically unfavourable.[15, 16] The energy of an excited triplet state is found at a slightly lower level to that of the excited singlet state, thus a backwards transition is even more improbable as it requires extra energy given to the system (Figure 1.1) [17, 18].

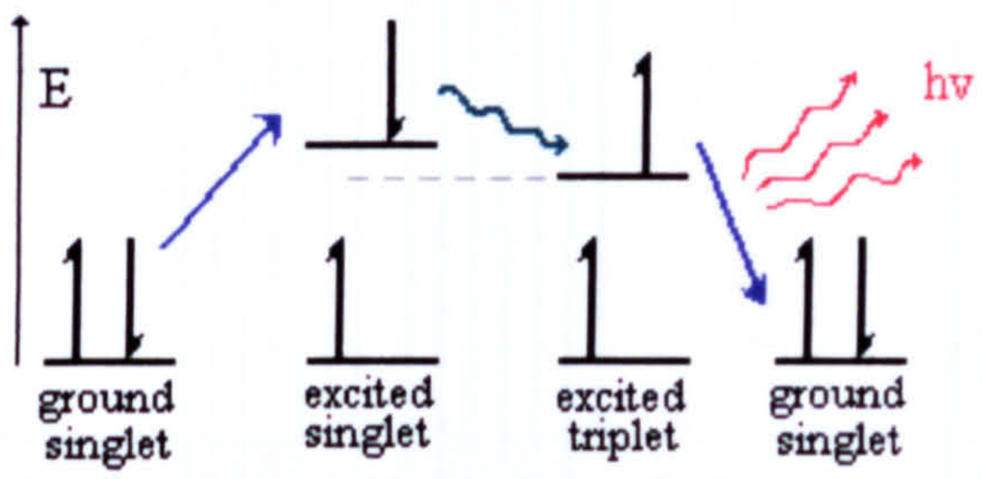

Figure 1.1 Three level procedure of phosphorescence involving a change in the electron spin multiplicity

A more detailed schematic of the transitions between the various states resulting in either fluorescence or phosphorescence is depicted in figure 1.2. Assuming that the initial state of the electron lies in the lowest level of the ground singlet state S_0, transitions can take place only towards the excited singlet states S_1 and S_2. Transitions from the ground to the excited triplet states are considered forbidden as they involve a change in multiplicity and a jump over a large energy gap. Apart from the direct $S_2 \leftarrow S_0$ and $S_1 \leftarrow S_0$ transitions, excitation can result in any of the overlying associated vibrational level if the photon caries the right amount of energy. Hence, absorption is observed for wavelengths that reside around λ_1 and λ_2 instead of being strictly monochromatic. Relaxation between the vibrational levels is a very fast and efficient process, which distributes each of the small quantities of energy difference between them as temperature vibrations or phonons in the material. Such vibrational relaxation processes are expected to last between 10^{-12} to 10^{-14} seconds. As a result, the radiative transitions are almost always observed between the lowest vibrational level of an excited state and any of the ground vibrational levels. The

process also gives rise to emission of wavelengths around λ_3 and λ_4 for fluorescence and phosphorescence respectively.[18]

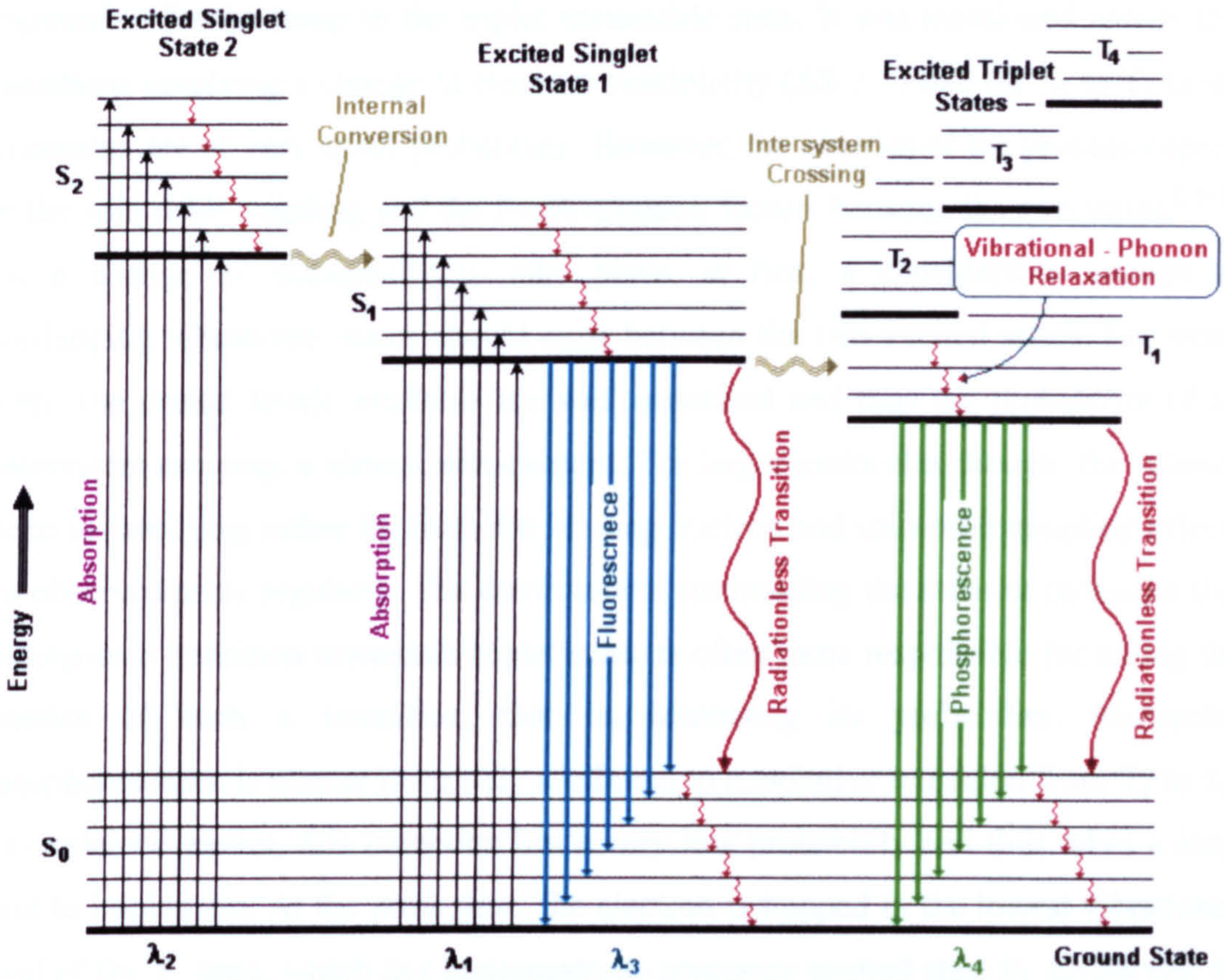

Figure 1.2 Energy levels and transitions related to photoluminescent processes. Schematic adapted from reference 18 and reference 19. [18, 19]

Three other processes are also taking place in the system, leading eventually to either fluorescence with a longer wavelength than the absorbed that of the absorbed photon, phosphorescence or non-radiative transitions. Internal conversion takes place when the excitation state changes from higher to lower energy excited singlet states. The vibrational levels of the lower state should be overlapping with at least the lower level of the higher energy state from which the conversion will arise. A system like that would present a continuous absorption spectrum over the two wavelengths λ_1 and λ_2 and possibly more, if other states of even higher energy were available. Moreover internal conversion between the various excited singlet states would result in a fluorescent emission centred on the lower wavelength λ_3, as it is often a faster procedure than a radiative transition from the lowest vibrational level of any exited state to the ground.

Intersystem crossing is a process transitioning between electronic states of different energies and different multiplicity at the same time. It is the process responsible for the jump to the triplet metastable state. It was mentioned earlier that transitions involving a change in electron multiplicity ($\Delta S \geq 1$) like the S_1 to T_1 in the schematic, are of very small probability. However, the kinetics of the process depend on the spin-orbit coupling and the Frank-Condon factors between the two states.[20-23] For a change in multiplicity to take place, at first, a considerable amount of overlapping vibrational states should exist between the two excited states. For small atoms the orbital levels available are well quantised and thus the probability of an intersystem crossing is almost non-existent. For larger molecules though, the valance electrons are lying rather far from the binding nucleus and spin-orbit coupling effects are observed more regularly. The environment surrounding the atom or molecule that undergoes a transition towards a triplet state, is often more responsible for aiding the kinetics of such a transition, that is, increasing its probability. Molecular phosphorescence is almost invariably attributed to a radiative transition from T_1 to S_0. As explained earlier, this transition has a very low probability and thus takes a long time to implement. At the same time, the electron is trapped in the lowest vibrational level of the T_1 state, which lies underneath its precursor excited state S_1, giving rise to a metastable state. Therefore, the electron will stay in that state until it performs a radiative transition to the ground, emitting a wavelength of λ_4 as mentioned before, or undergo a, perhaps more probable, radiationless transition. The highly improbable path that the emitting electron has to follow in order to result in phosphorescence is responsible for the frequently observed low yield in comparison with fluorescence.

The last type of transition of interest that often competes with the emission yields of both the fluorescence and phosphorescence processes is the radiationless transition from the excited states to the ground state. There are many possible routes leading to a de-excitation of the atom/molecule from either a singlet or triplet state. Two main classifications of them are internal conversion, mentioned earlier and external conversion. For an internal conversion to occur, the excited and ground state energies should preferably have a small energy difference, so that vibrational levels of the ground state could reach up to the energy level of the excited state. The external conversion process features more possibilities. Most usually though it is brought about by distributing the energy to the surrounding molecules vibrationally, or in a similar manner, generating phonons in the crystal lattice for the case of solids. For the

case of solid semiconductors, the electron could also migrate further down in the lattice where it can loose its energy in impurity atoms of different electronic structure attributing more favourable kinetics.

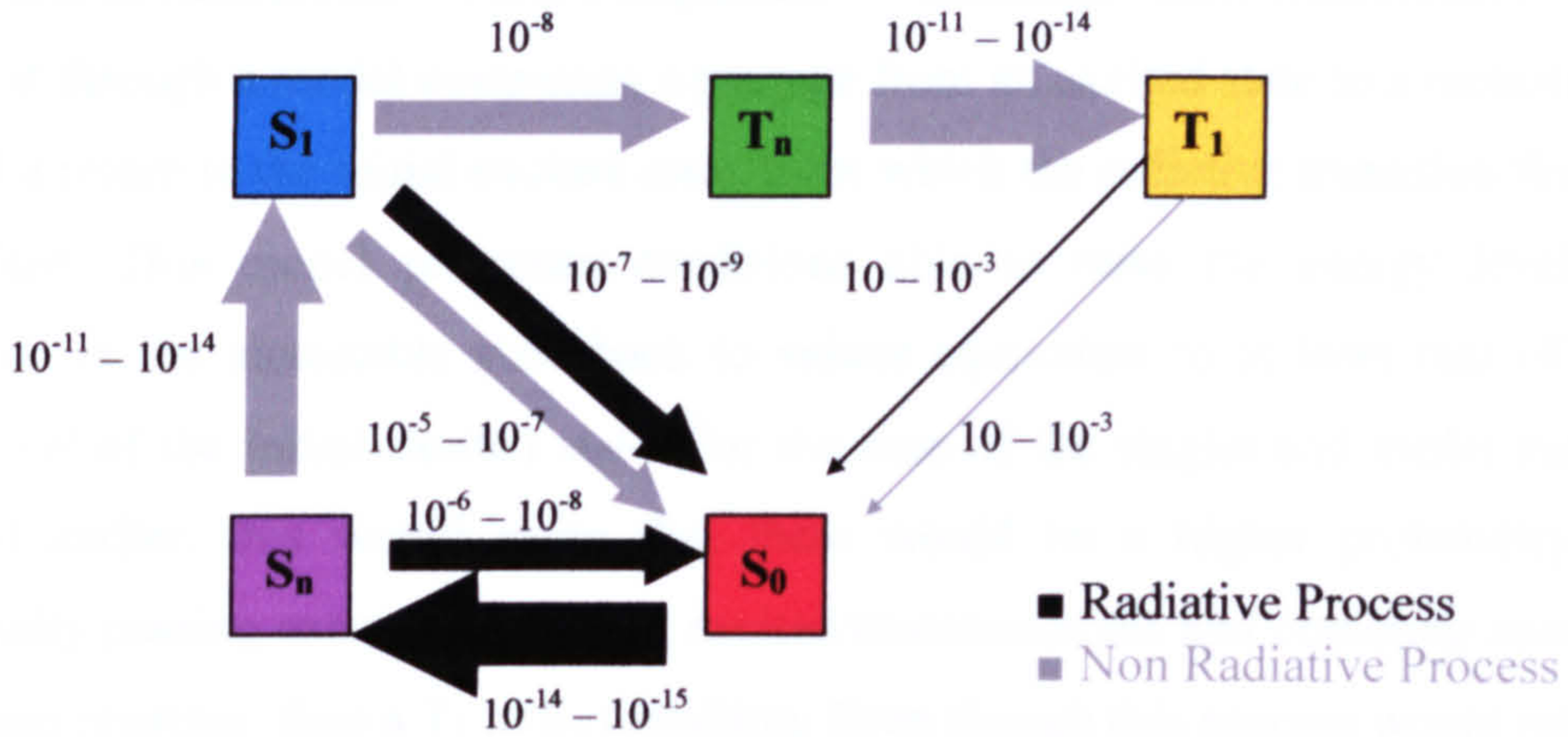

Figure 1.3 Time duration of different processes involved in photoluminescence. The arrow thickness is proportional to the probability of each transition or inversely proportional to its expected duration. The numbers next to the arrows represent this duration in seconds. Schematic adapted from reference 19.[19]

The schematic in Figure 1.3 illustrates the five main energy states described earlier and the transitions between them, in accordance with estimated values for each transition.[18, 19, 24] Processes that either involve the exchange of a photon or not, are shown. It becomes quite evident, how easy it is to follow a clockwise rotation route of the states as depicted, reaching the metastable state T_1 and how small is the probability of escaping from it. Moreover, a critical point appears when depopulating the S_1 state, where the radiative de-excitation probability can either exceed or be deficient to that of intersystem crossing towards T_n. That is also where a comparison between the efficiencies of the two processes can be determined. For materials that do not present photoluminescent effects, the radiationless process from S_n to S_0 becomes highly probable and thus inhibiting progress to further steps.

When all this is taken into consideration, it becomes apparent that the notion presented by early researchers in the field of photoluminescence, about discriminating between phosphorescence and fluorescence on the basis of time delay of the emission, is not consistent with today's scientific concepts related to the field. The two processes are now defined according to the state from which the radiative transition occurs instead of the time taken until realisation of such a transition. Consequently,

this method of discrimination is also inherently related to the emitted wavelength of the photoluminescent process in question. Modern research has proven that the time scale of singlet-to-singlet radiative transitions can exceed by far what was established as the limits of fluorescence. Peter Pringsheim [14] mentions "slow fluorescence" and explains it through a model containing a passage from an excited state to a metastable state and a return to the initial excited state, from which the radiative transition finally takes place. This model presumes conditions able to raise the energy level of theelectron in the metastable state back to values equivalent to at least that of the lowest level of the initial excited state. For the case of the singlet and triplet model described earlier, this would mean that there would be a higher probability of vibrationally passing energy back to the excited atom/molecule and obtaining another intersystem crossing, than a T_1 to S_0 transition. Even though this process would return a photon similar in energy to that expected from the typical fluorescent emission, the delay of the emission reaches timescales corresponding to phosphorescence. Two good recent examples of phenomena of this type were examined as temperature-activated delayed fluorescence by Lam et al. for the case of erythrosine B and eisin Y in sol-gel glasses[25] and by Kaputskaya et al. for acriflavine in dried polyvinylalcohol films[26] with delayed fluorescence recorded at $2 \cdot 10^{-6}$ s in the first case and approximately 1s after excitation respectively. This method of discrimination between the two emission processes proves versatile for scientific purposes, but lacks agreement with common sense, defining fluorescent materials as those that shine a different colour of light than that projected at them and phosphors as materials that charge up and retain their glow.

Photoluminescence of semiconductors

The description of the photoluminescence phenomenon that has been laid out up to this point was developed for molecular photoluminescence which was usually observed in dispersions (mostly fluid ones) of luminescent molecules. Nonetheless, it is a useful basis for the theoretical models that apply in the case of photoluminescent and electroluminescent semiconductors. Up to now, the exchange of energy was centred on a molecule or atom featuring certain interactions with its surrounding environment. This exchange of energy mainly between photons and electrons, the variations of it arising from transitions and the concept of photoluminescence being

based on dominant kinetic scenarios will also be applied extensively throughout the rest of this work.

It was mentioned earlier that electrons move between orbitals of different energy. It is now well established that the orbitals and in extension the energy states of individual atoms, are combining in the formation of a crystal lattice, displacing each other by a small amount due to the Pauli exclusion principle and form energy bands that run throughout the solid body. For semiconductors and insulators, the valance electrons of each atom are used to form covalent bonds with its neighbouring atoms. The excited states of the covalent bonds are grouped together, in a higher energy band called the conduction band, as any electron promoted to such an energy state would have the ability to travel through the solid body and thus contribute to conductivity. The covalent bonds are holding the electrons around the two atoms participating in the bond and together form the valance band.[27, 28] The energy difference between the bands is the bandgap and is equal to the amount of energy needed to be exchanged with an electron for the achievement of its transition from one band to the other. Metals contain atoms with the same number of valance electrons that are equally shared between all atoms in the solid. The valance electrons of the atoms in a metal body can move freely over the atoms within the solid and through the wide energy band that is formed by the metallic bonding type.

The occupation of the various energy levels forming the bands in metals and semiconductors is defined by a probability. This probability is related to temperature and can be described with Fermi-Dirac statistics by use of the following equation [29]:

$$p(E) = \frac{1}{1 + \exp(\frac{E - E_f}{kT})} \qquad 1.2$$

where *p(E)* is the probability of occupation of a state at an energy *E*, *k* is the Boltzmann's constant ($8.617339 \cdot 10^{-5}$ $eV \cdot K^{-1}$), T is the absolute temperature in degrees Kelvin and *Ef* is the Fermi energy level. The Fermi energy level is characteristic for each material at its ground state and is the point where the probability of occupation for a state of energy $E=E_f$ is 50%. From equation 1.2 it becomes clear that the probability of occupation of a state depends on absolute temperature. As the temperature rises, more and more electrons will acquire energy and advance to higher energy states. The distribution of probabilities over the energy of states is illustrated in figure 1.4. So, at temperatures approaching absolute zero, all the energy levels

below E_f will be occupied and all above it will be empty, which is another way of defining the Fermi energy level. In semiconductors where the unoccupied conduction band levels are equal in density to those occupied lying in the valance band, the Fermi energy level at a state of thermal equilibrium is found in the middle of the bandgap. Application of an electric field or doping of a semiconductor can also alter the position of the Fermi energy level with respect to the band edges.

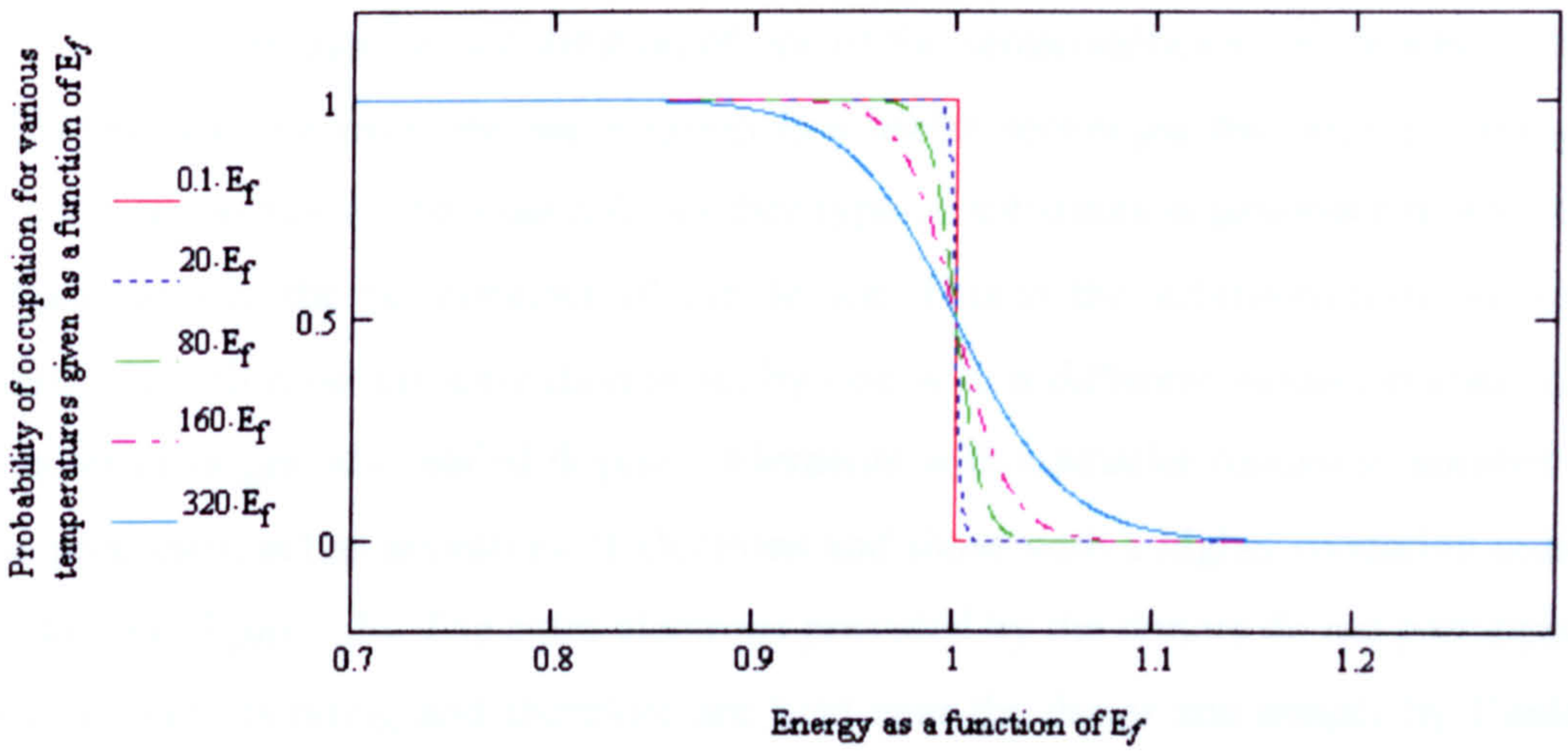

Figure 1.4 Probability distribution regarding the occupation of states with energy E.

Indeed the first efforts to control the electronic, optical and thermal properties of semiconductors were focused around alloying or mixing diverse elements in the lattice. Though two of the most important semiconductrors are formed by Si or Ge atoms, all the materials that are of interest for electroluminescent applications combine two different species of atoms, an electropositive and an electronegative one, coming from the II, III and VI, V groups of the periodic table respectively. Taking the case of ZnS, being a typical II-VI phosphor, one could easily imagine the replacement of zinc by other elements of the II_b group such as cadmium and mercury and that of sulfur by elements of the VI group such as oxygen, selenium and tellurium. Almost all possible combinations of the elements mentioned from the two groups have yielded useful and important semiconductor lattices for a number of applications, especially in optoelectronics. Now if a zinc atom in the ZnS lattice was replaced by cadmium, apart from the slight lattice distortion due to the change of the element's size, the electrons participating in the covalent bonds with the cadmium atom would need less energy in

order to become excited. That is because the valance electrons of cadmium are further away from its core and are exposed to a weaker attraction from the cadmium core than for the former case of zinc. Thus, states that belong to the conduction band would have to approach the valance band in a local context. If the concentration of cadmium in the lattice increased to magnitudes comparable with those of the zinc atoms, a general shrinking of the semiconductor bandgap would have to be considered. Similar effects can be expected for the replacement of sulfur by the group VI elements, depending on their electronegativity.

Even though the substitution of one of the semiconductor constituent elements with another one from the same group is a useful technique that aids in tuning the general properties of the material, another type of substitution generates more intense adjustments to the performance of the device. This is the substitution of one of the elements with a certain oxidation state, by one with a different oxidation state, either smaller or larger, also called doping. Elements with a smaller oxidation number than the precursor, act as acceptors of electrons and those with a higher oxidation number, as donors (figure 1.5). The extra electrons provided by the donors do not participate in any covalent bonding and therefore are held near the donor site simply by Coulomb attraction to its core. Very little energy is needed, in comparison to the semiconductor gap, in order for the electron to become promoted to the conduction band. In a similar manner, an acceptor will absorb any electron from a nearby atom, which has gained some small amount of energy, hence creating a free travelling hole in the valance band. The introduced donor and acceptor levels are also found locally when they exist in small concentrations in the lattice. Nonetheless, they can be accessed by free moving electrons or holes from theoretically the whole solid body. At larger concentrations they form extra states within the bandgap. And as the concentration of the dopants reaches comparable levels to those of the original element, the states extend to small bands that eventually merge with either the valance or conduction band, similar to the case of substitution with elements of the same oxidation state.

III	IV	V
13 Al	14 Si	15 P
31 Ga	32 Ge	33 As
49 In	50 Sn	

I_b	II_b	III
29 Cu	30 Zn	31 Ga
47 Ag	48 Cd	49 In
79 Au	80 Hg	

V	VI	VII
7 N	8 O	9 F
15 P	16 S	17 Cl
33 As	34 Se	35 Br
51 Sb	52 Te	53 I

Acceptor Substituent Donor

Figure 1.5 Substitution of elements in II-VI semiconductor materials by donors and acceptors of a single electron, in adjacent groups. Examples for group IV semiconductors are also given as a reference.

Considering all this, it is understood that photoluminescence in semiconductors is a result of transitions that involve the various energy bands of the material rather than specific energy levels of single molecules. When an energetic enough photon or electron interacts with the semiconductor lattice it will excite electrons across the bandgap, leaving a hole in the valance band behind it. Both the electron and hole are free to travel through the material as long as the energy bands are continuous. An electron and a hole can then recombine over the bandgap to return a photon of energy equal to that of the bandgap. Even though an excitation might have included a photon of greater energy than the bandgap, the maximum that can be expected in return will normally be equal to the bandgap. Doping can provide more states to and from where an electron can de-excite radiatively. The typical possibilities are from the conduction band to an acceptor level, from a donor level to the valance band and from a donor to an acceptor level (Figure 1.6).[14, 17, 24, 30, 31] Usually in semiconductors, acceptors are expected to receive electrons from the valance band, as mentioned earlier, in the form of a hole's propagation. But since their inherent attribute is to lack an electron and its level is lying closer to the conduction band, compared with the top of the valance band, it makes an ideal site for recombination.

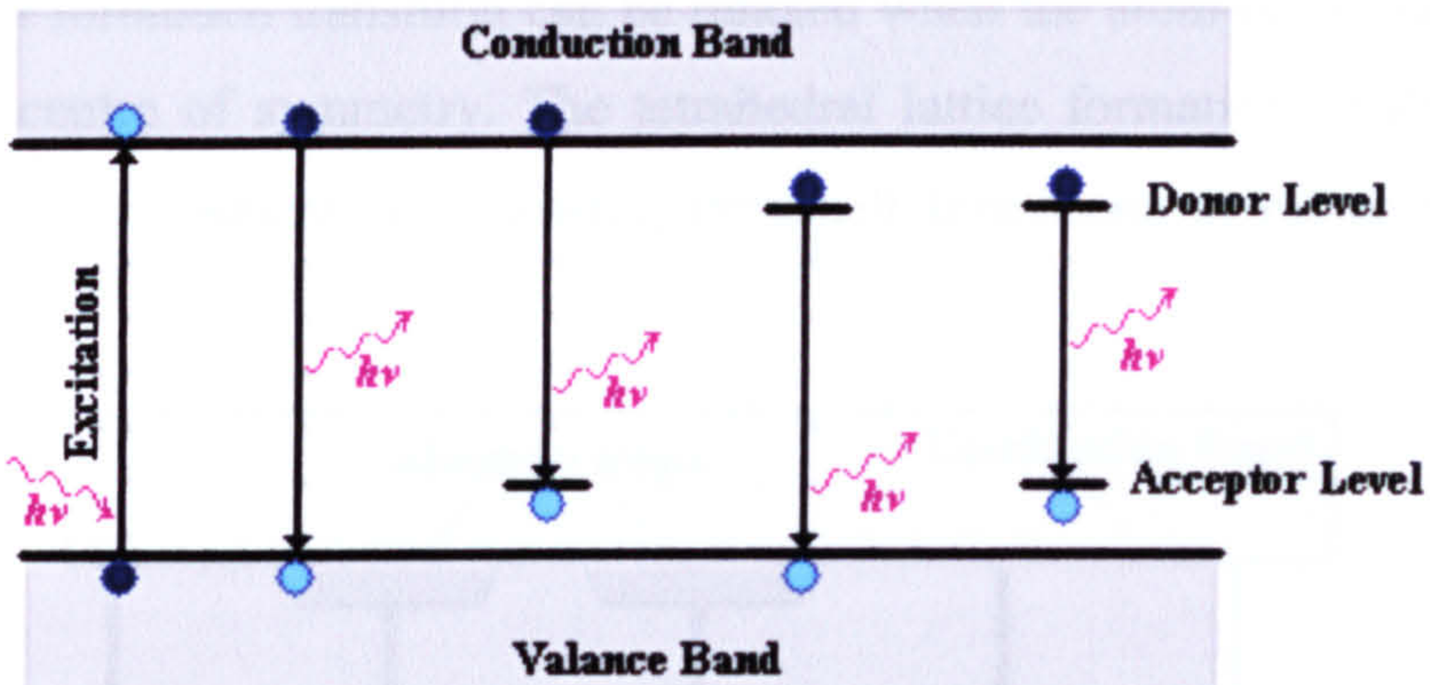

Figure 1.6 Transitions involving absorption and emission of radiation in a semiconductor.

Bands or levels within the bandgap can be generated by absence or excess of one of the intrinsic lattice constituents apart from the donor and acceptor dopants. For example, if a zinc atom is missing from its site in a zinc sulfide lattice, a vacancy of two electrons will appear. In a similar way, an extra zinc atom residing in an interstitial space of the lattice would provide two extra electrons with small excitation energy. Lattice mismatches and cluster edges of the crystal would also provide similar effects, as there will be a shortage of valance bonds for some of the atoms on the interfaces. Pure zinc sulfide is found to be self activated in such a way by zinc vacancies. Similar effects would be observed by vacancies or excess of the electronegative species e.g. sulfur. [28, 30]

By the analysis of kinetics for fluorescence and photoluminescence above, it became apparent that transitions from states with a slower rate would result in either type of photoluminescence. One of the factors discussed, that determines a slow transition process was the involvement of a forbidden change in electron spin. When considering semiconductor transitions, another factor should be considered. The Laporte selection rule states that an electronic dipole optical transition is allowed only when the angular momentum quantum number changes by 1, i.e. $\Delta l = \pm 1$. The rule applies for atoms that here act as activators in the semiconductor, which have symmetrical outer shell orbitals. Therefore, intrashell transitions like p-p, d-d and f-f are forbidden and intershell transitions like s-p, p-d and d-f are allowed. As the electron spin forbidden transition was relaxed by a large spin-orbit coupling there are certain conditions that relax the Laporte selection rule.[32-34] Vibrations in the lattice can result in vibronic transitions with non-zero oscillator strength. More importantly

though, a Laporte forbidden transition can be relaxed when the atom or ion resides in a site without a centre of symmetry. The tetrahedral lattice formation of ZnS does provide the right environment for allowing intrashell transitions at rather efficient rates.[24, 30, 35, 36]

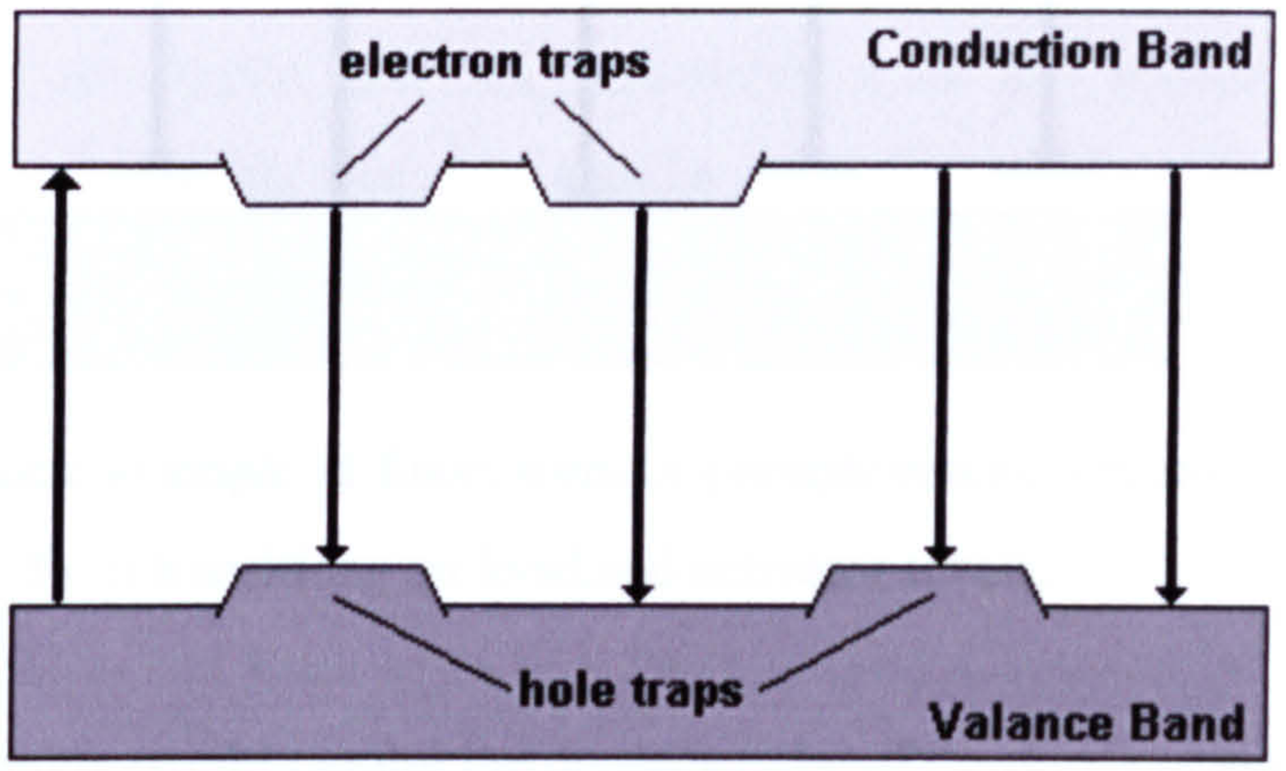

Figure 1.7 Schematic example of fluorescent or phosphorescent emission resulting from transitions at bandgap disturbances or over the whole bandgap.

To sum up, there are three main routes leading to either fluorescence or phosphorescence that can be distinguished in semiconductors. Their distinction is mostly dependent upon the type of activators and co-activators used. The simpler one includes an excitation from the valance band to the conduction band, thus creating a free travelling exciton pair. A radiative recombination of them over the whole bandgap would return the largest possible energy in a photon for a specific semiconductor, though such a condition is rarely observed. The only reason for it to occur would be some discontinuity in the crystal lattice and thus in the special structure of the energy bands. Materials constituted by small-sized grains, do have a tendency to emit in wavelengths related to the whole bandgap. This is accomplished by taking advantage of bandgap discontinuities, induced by doping with small concentrations of species with the same oxidation number as the anion or cation constituents of the lattice. As explained earlier, these sites in the lattice would act as localised discontinuities being able to trap electrons or holes and aid their radiative transition over a smaller energy gap (figure 1.7).[30, 37-41] Under such circumstances we observe one of the most efficient phosphor systems, the ZnS:Mn crystals (see section 1.2).

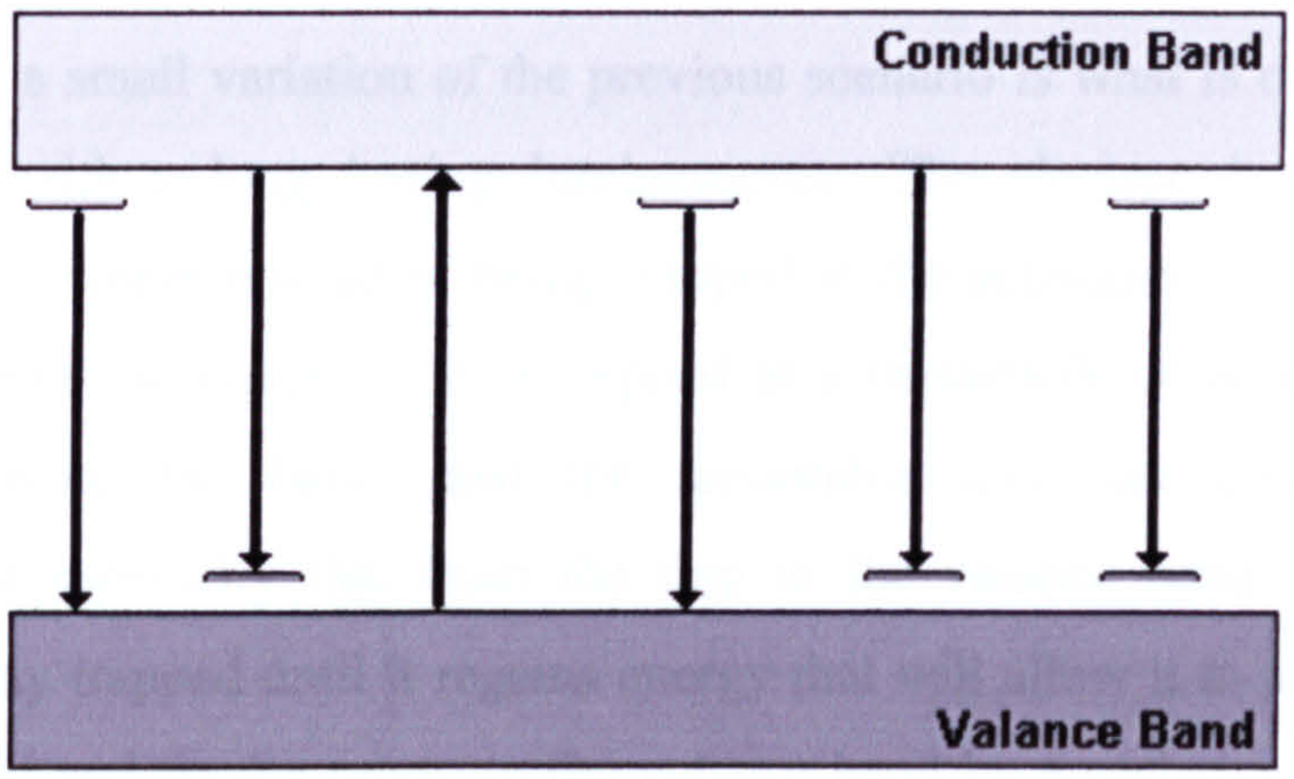

Figure 1.8 Schematic example of fluorescent or phosphorescent emission resulting from transitions on localised activator levels.

The second route would require the dopants to be of the donor or acceptor type for the host material. The excitation can be achieved over the bandgap as before, or with a lower energy photon between the valance band and an empty donor energy level, or a populated acceptor energy level and the conduction band in higher temperature environments. Thermal energy is required in both cases to transfer the electron from the localised donor or acceptor level to or from the band respectively. The electron whole pair can then be trapped locally at activator sites consisting of either donors (electron traps), acceptors (hole traps) or both, which also results in the most efficient luminescence pathway (figure 1.8). Depending on the implementation of any kinetic selection rules on the activator's system, the transition to the valance band can either result in fluorescence for allowed transitions and phosphorescence for forbidden transitions.[42-44]

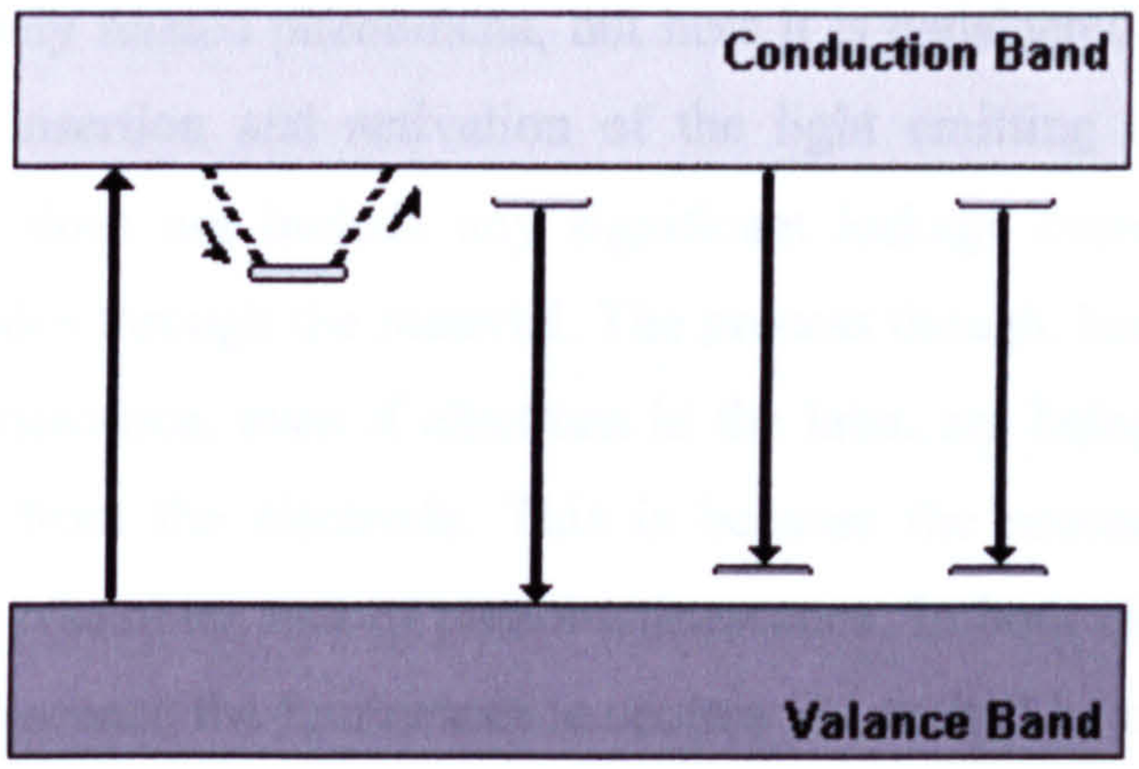

Figure 1.9 Schematic example of phosphorescent emission including a precursor metastable donor trap.

Finally, a small variation of the previous scenario is what is often considered for phosphors with a long lasting luminescence. The electron is excited to the conduction band where instead of being trapped at the activation centre, which will then cause a photonic emission, it is trapped at a metastable co-activator site. The transitions between the bands and the metastable level are considered rather improbable and especially that from the trap to the valance band. Therefore, the electron will stay trapped until it regains energy that will allow it to pass back to the conduction band and finally return to the valance band by a radiative transition of a much higher probability offered on an activator site. The activator featuring the radiative transition can be a donor, acceptor or both, as in the previous scenario (figure 1.9). The duration of luminescence in such a system depends mostly on the kinetics governing the escape from the metastable co-activator traps and their saturation.[14, 17, 24, 42, 43, 45, 46] The amplitude of luminescence features an exponential decay with time and a half-life reaching the scale of minutes.

1.1.b. Electroluminescence in materials

Electroluminescence is a phenomenon very closely related to photoluminescence as described above. Most importantly it is often exhibited efficiently by the same inorganic materials that present phosphorescent characteristics when submerged in intense, high-energy lighting. After all, its observation started as an interest in the effects of high electric fields upon these scientifically intriguing materials. As it turned out, the terminology is sometimes used to describe two different, but closely related phenomena, but here it is considered to be the one that results from the insertion and activation of the light emitting material within an electric field and does not include any significant leakage current from the field generating electrodes through the material. The process though, has more in common with cathodoluminescence, even if electrons in the later, are being sent towards the material, straight from the electrode. This is because the procedure, taking place within the lattice, resembles that of photoluminescence. In both electroluminescence and cathodoluminescence the luminescence centres are excited by travelling electrons instead of photons. The emission of light is then in close resemblance to that

described for phosphors earlier. Both phenomena have been utilised for the generation of successful light emitting and display devices.

Electroluminescence from minority carrier injection over a diode junction

One method of direct, non-incandescent conversion of electrical energy into light is by injecting minority charge carriers, either at an electrode contact or a p-n junction. At such a junction in the absence of an applied voltage there is a state of dynamic equilibrium between processes of thermal conduction and subsequent recombination of electron hole pairs. Some of the recombinations occur with the emission of radiation which contributes to normal thermal (black-body) radiation of the material.

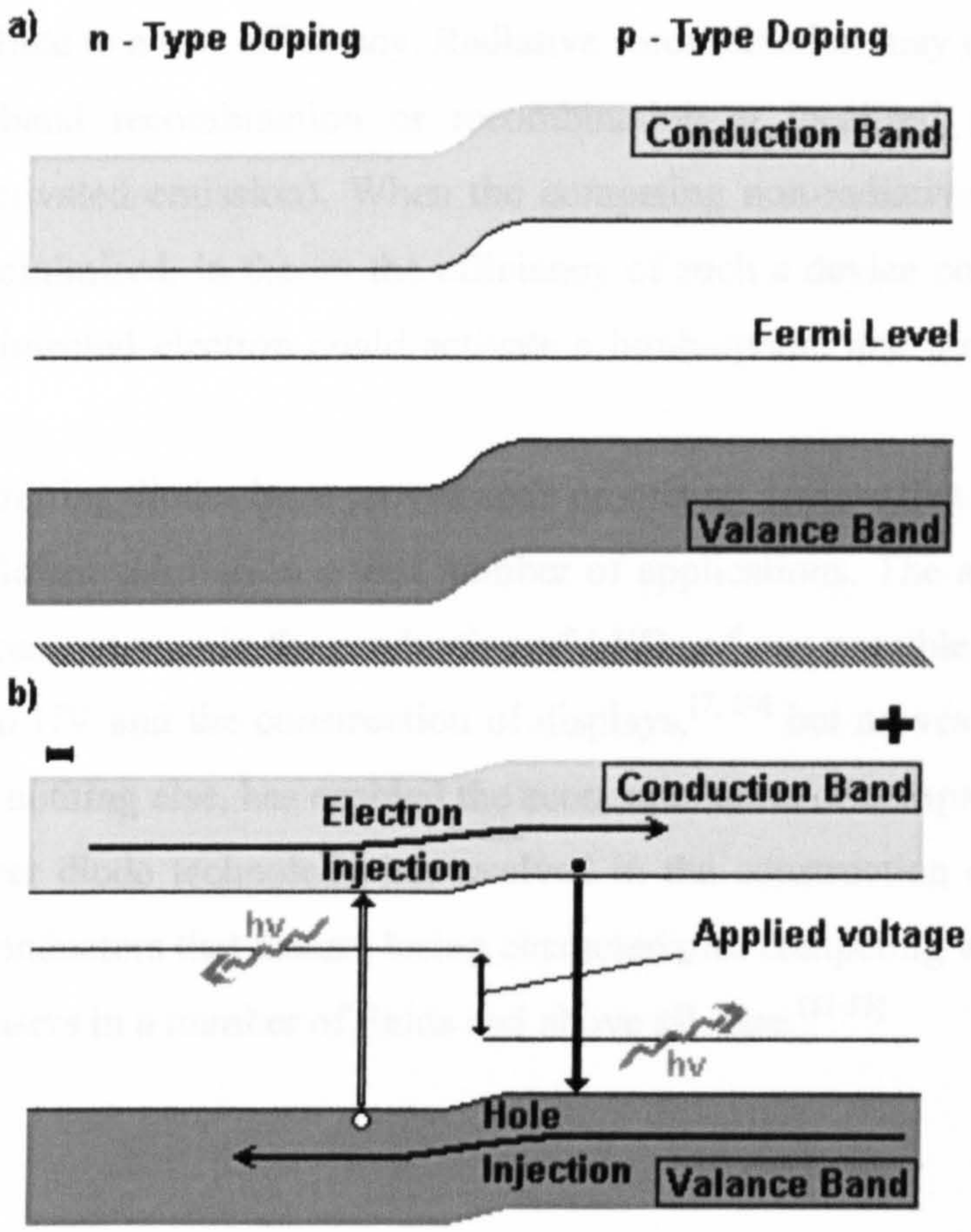

Figure 1.10 Schematic of energy band structure of a light emitting diode, (a) unbiased and (b) forward biased with minority carrier injection and resulting luminescence due to recombination.[47]

When a voltage is applied in the forward direction and additional carriers are injected, however, this equilibrium is upset and the rate of recombination increased (figure 1.10). If some of these recombinations occur with the emission of radiation the result is the phenomenon that may be called injection electroluminescence. This is the basis of operation of one of the most common light emitting devices used in electronics today, called the Light Emitting Diode, since the device has the structure of a p-n homojunction. It was actually observed and developed upon the diode technology used as rectifying crystals in the 1920s. Lossew who observed it in SiC crystals,[48] also investigated of the reverse, photovoltaic operation of the device.[49] It may be noted that no high electric field is required in this case, since the junction is biased in the forward direction, the junction field is actually lower when the voltage is applied than in its absence. Once the minority carriers are injected, a variety of recombination mechanisms are possible. Some of these do not lead to luminescence and thus contribute to a low efficiency. Radiative recombination may occur either as a result of interband recombination or recombination at localised activator levels (extrinsic or activated emission). When the competing non-radiative recombination processes are minimised, in theory the efficiency of such a device could reach up to 100% as each injected electron could activate a luminophore and result in a photon emission.

Light emitting diodes have proved such promising devices that were employed as the most efficient solution in a vast number of applications. The achievements in their domain does not stop in the production of LEDs of any possible colour ranging from infrared to UV and the construction of displays,[7, 50] but moves on to the laser diode, which if nothing else, has enabled the economic boom of compact discs. In just a few years laser diode technology has evolved in the construction of multilayered complex semiconductors that feature lasing characteristics competing with most of the other types of lasers in a number of fields and above all, size.[51-53]

Electroluminescence induced by an electric field over an insulator encapsulated phosphor

Though light emitting diodes have proved very successful, the name electroluminescence was initially reserved for the phenomenon observed by Destriau, where the field-applying electrodes did not conduct electricity with the luminescent layer. The layer luminesces solely because of its existence inside the field. Theoretically luminescence could be induced upon the material remotely, if such a high density field could be applied over it from a distance. The first devices ever built, utilised a dispersion of the phosphor material in a transparent polymer or even a liquid. Soon, the bulky electroluminescent lamps progressed into thin layers of the dispersion and then an encapsulated crystal layer between insulators, leading to the thin film electroluminescent devices of today.

It is still interesting to briefly review the operation of a dispersion device before moving on to the well-engineered thin films. The observations concluded that luminescence was occurring close to the electrodes, at the edges of the phosphor particles, decaying fast in intensity with time and presenting maximum performance with an alternating current. Moreover, the existence of small amounts of impurities surrounding each phosphor cluster was proven beneficial in polymer dispersions. Production of layered structure devices made more sense, not only because of achieving a larger electric field over the small electrode distance, but also because more material was closer to the electrodes than in a bulky structure. The explanation of all these observations is offered by the tunnelling effect induced by an electric field.

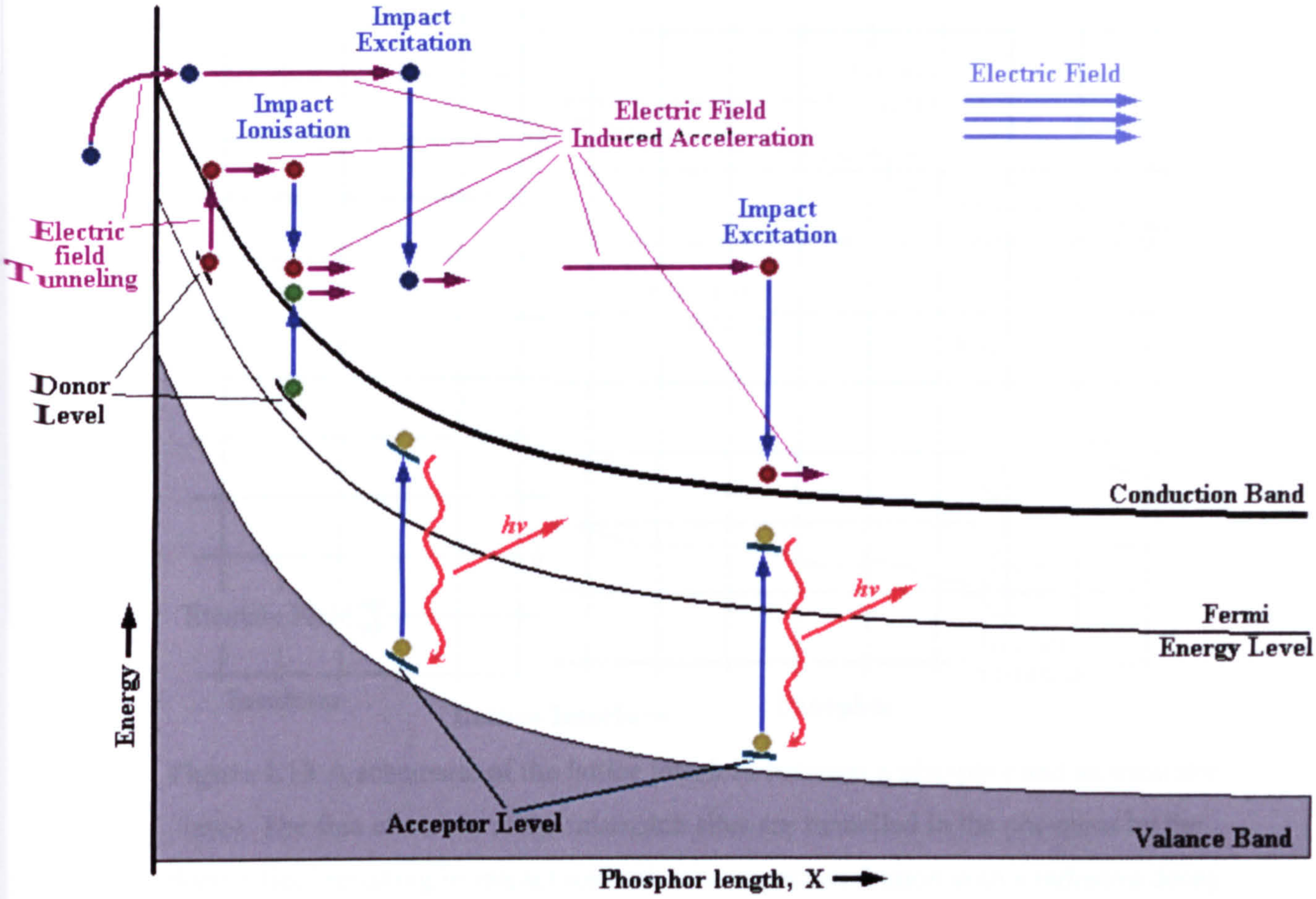

Figure 1.11 Electron tunnelling at an interface and from donor levels, in a strong electric field. Subsequent impact excitation and impact ionisation of filled acceptor luminescent centres and donor levels respectively.

In the schematic above, the energy band structure of an electroluminescent material being bent in an electric field is considered, close to the interface of a cluster or a semiconductor film. The areas closer to the interface are subjected to a higher field strength than the insides of the material. The energy bands are thus bent steeper. It is assumed that at the interface another semiconductor exists. The interface between the two semiconductors is an electron trap, as there are different energy levels offered from the two sides of the interface. As the bands of the phosphor material are bent by the electric field, the conduction band reaches close to those electron trap levels or near the conduction band of the insulating semiconductor, allowing the electrons to tunnel over to it and start moving away from the interface. For a dispersion of the phosphor, it is often found that the formation of phosphors like ZnS by chemical methods often yields clusters of similar materials on its sides, such as CuS for example. The interface between the two was aids the tunnelling process significantly.

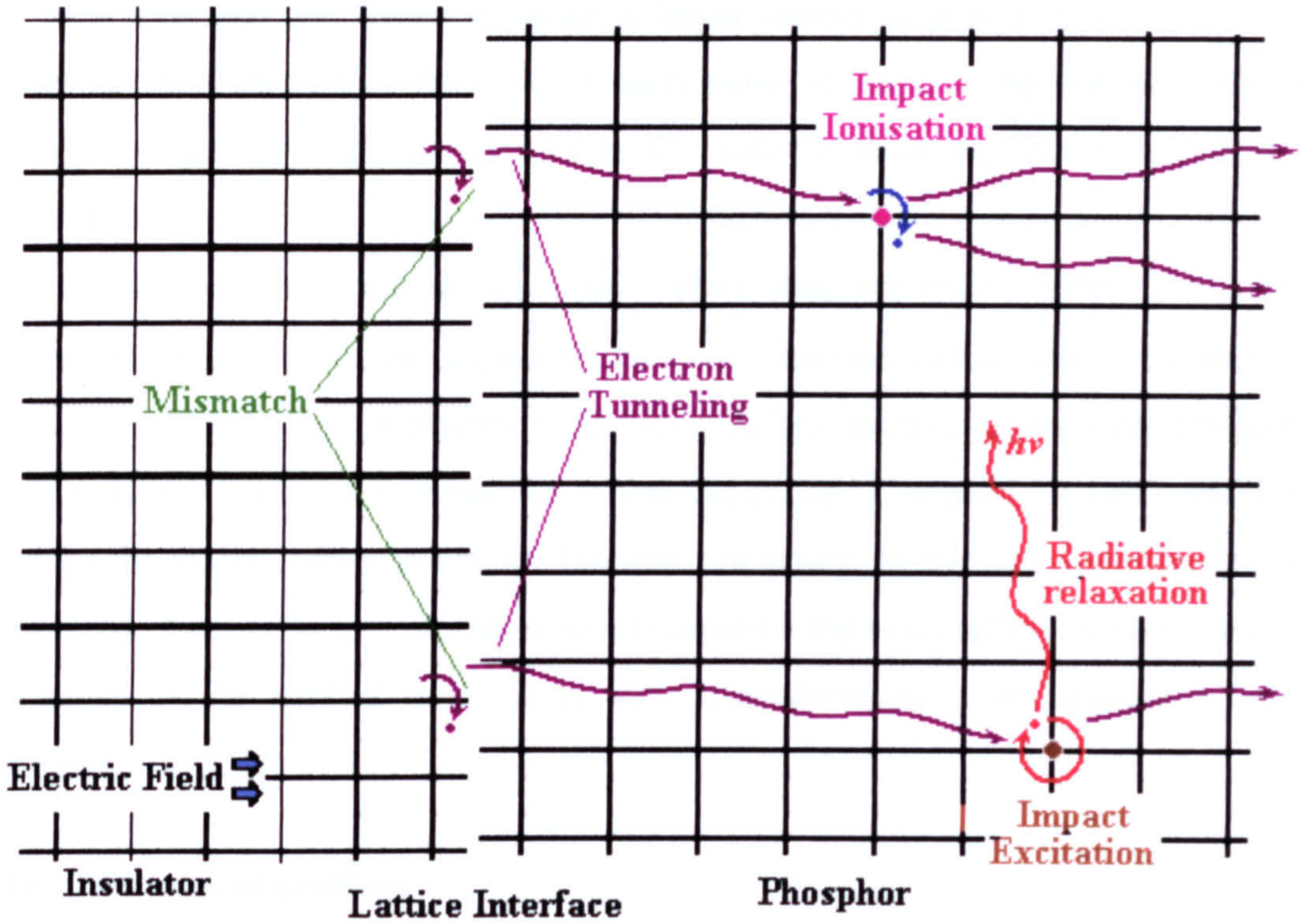

Figure 1.12 A schematic of the lattice interface between a phosphor and an insulator layer. The free electrons at the mismatch sites are tunnelled in the phosphor by the electric field resulting in impact ionisation or impact excitation with a radiative decay of the excited site.

A careful choice of layers in a thin film device is critical when engineering a successful tunnelling process. Efficient tunnelling provides high enough currents for excitation of the luminescent centres. Certain co-activators of the donor type, incorporated in the prepared phosphor materials could also assist in tunnelling, by introducing shallow localised levels, ready to offer their spare electrons to the bent conduction band. A dimensional restriction of the material only within the high field density region is what guarantees the occurrence of only useful excitation, which will either lead to a localised radiative transition, or a tunnelling ionisation and re-acceleration.

Once the interface closer to the negative electrode is depleted of electrons (figure 1.12), the material will cease to luminesce. If the field is removed, the electrons will slowly start drifting back to their original positions, so as to maintain equilibrium. The drift current is very slow and therefore, a new application of a homodirectional field would now generate a smaller pulse in luminescence intensity. An application of a reversed field though will meet most of the displaced electrons at

the new interface and hence generate a larger carrier migration than the first. So, reversing the direction of the field at each pulse is found to be the most efficient method of driving such devices even for today's most advanced thin film EL structures.

As it is understood, the electroluminescence effect resembles cathodoluminescence in the aspect of exciting localised luminophores by energetic electrons accelerated in an electric field. Nevertheless, cathodoluminescence follows a pattern similar to photoluminescence, where the excited electron-hole pair recombines through the closer energy levels of a luminescent centre. In an electroluminescent cell, the electric field is so intense that it would separate the two carriers instantly towards the poles of the applied field. Thus their recombination is not considered at all probable.

Electron acceleration

Another important aspect that determines the efficiency of an electroluminescent device is the electron acceleration, which is mostly influenced by the strength of the applied electric field. Hence in the early devices and those used primarily for lighting purposes, it can be easily pushed to the required levels by adjusting the voltage between the electrodes. For electronically-controlled thin film devices such as display screens, this may pose some difficulties. Most of the electronic devices today use 5 volts maximum and for high-speed complex integrated circuits, switching voltages are pushed down to approximately 1 volt, in order to improve the switching speed and reduce interference between the multiple layers of conductors and semiconductors. A display screen is a matrix with numerous conducting lines running on the back in order to provide switching drive for every pixel. The construction of a large area display operating at voltages of the order of a few hundred volts would be difficult to construct and control efficiently without interferences, wearing of insulators and rising of temperature on the conductor network.

Thus efforts are put forward by the various manufacturers, in order to achieve the highest possible fields over the thin insulator-phosphor-insulator structure, with application of the smallest possible voltages. The field should have to be strong enough to accelerate the tunnelled electrons at kinetic energies reaching the levels

equal or larger to the excitation energy of the luminescent centres. Construction of films with thickness in scales of a few hundred nanometers seem as an adequate solution, when considering the large electric fields, in the vicinity of $MV \cdot cm^{-1}$, calculated for thin film capacitors. Under such strong fields an electron travelling in vacuum would acquire excitation energy within a space corresponding to a few tenths of atoms arranged in a lattice. Unfortunately, electrons actually travelling through the phosphor lattice have to overcome a number of possible scattering mechanisms before reaching appropriate speeds. Examples of such mechanisms are intervalley scattering, polar optical phonon scattering, acoustic phonon scattering, ionised impurity scattering, band-to-band impact ionisation and impact excitation. These scattering mechanisms depend on the energy band properties of the host phosphor.[54] Very complex calculations are performed by some researchers using Monte Carlo modelling, allowing them to calculate scattering and final kinetic energies of electrons in thin phosphor films.[55-58] The effects of impurities can also be investigated.

Impact Excitation/Ionisation and Intrashell localised transitions

Once the electron is tunnelled in the phosphor layer and accelerated by the electric field it could be carrying enough energy to trigger luminescence from one of the activation centres. An electron of the activation centre is promoted to an excited state or to the host material's conduction band by the energy provided from the accelerated electron. The two processes are called impact excitation and impact ionisation respectively.[59, 60] On impact ionisation the new electron becomes free and starts moving towards the positive side of the electric field. The process causes an avalanche effect, as each new electron can also be accelerated to an ionising energy. The ionised centre can now only emit a photon by capturing another of the moving free electrons. This, however, requires the existence of low energy free electrons, which is a rather unlikely situation in a thin film EL device. There may be occurences of such electrons arising from nearby similarly ionised activation centres, or at parts of the device where the density of free moving electrons has become very large. Nonetheless, the direct contribution of the impact ionisation process to the luminescence of the device is very small compared to that of impact excitation.

If the luminescent centre is brought to an excited atomic state, then the processes described earlier for photoluminescence in semiconductor materials would

apply. The excited electron can return to the ground state radiatively or non-radiatively, obeying any selection rules relating to spin or angular momentum. The two processes compete against each other. The radiative decay is governed by factors relating to probability of spontaneous emission. A rough calculation of the emission within a time interval *t* can be based on Eq. 1.3 below:

$$N(t) = N(0) \cdot \exp(- P_{em} \cdot t) \qquad (1.3)$$

N(t) is the number of emissions in time *t*, N(0) is the number of excited luminescence centres at time 0 and P_{em} is the probability of spontaneous emission. If the probability P is related to the radiative decay time d as an inverse proportion, then the equation becomes:

$$N(t) = N(0) \cdot \exp(- t / d) \qquad (1.4)$$

So, if we assume conditions of fast re-excitation of the luminescent centres, which can be achieved by the high intensity field of the EL device, then the efficiency of the device is proportional to the number of luminescence centres and inversely proportional to their decay time, as this would result in fast emissions and recharging on the luminescent centre sites.[24] A high current of free electrons is assisted by heat, as seen above for the effect of tunnelling. But, a high temperature is found to hinder the efficiency of radiative emissions, by promoting the non-radiative ones. This arises from the fact that an excited electron can easily lose parts of its energy to a more rigorously vibrating environment. Hence, tunnelling and vibrational relaxation of activators have to compete against each other on an increase of temperature and in most cases, it is found that the efficiency of the device is reduced, thus the latter process eventually dominates. Moreover, excitation of lattice defects such as interstitial atoms, vacancies, undesired impurities, linear misalignments and crystal cluster formation are another important factor impeding the luminescence efficiency of the crystal.[61-63]

1.2 Materials for Electroluminescent Devices

It is in the interest of the experiments described in this thesis to develop new methods for processing electroluminescent phosphor materials, so a small description of the properties of materials already incorporated in the fabrication of EL devices is laid out in this section. A basic idea of the positive and negative physical properties of the materials, affecting the operation of the possible final device is portrayed, hence enabling a clearer view of the results of this work discussed in chapters 4, 6 and 7. First the phosphor host lattices considered to provide the best performance characteristics are introduced, then their possible activators. A small reference to materials used as electrodes, regarding the construction of EL devices, is also included. And finally a small review of typical processing methods commonly employed for II-VI materials

1.2.a. Phosphors

Many materials can be found to luminesce under a strong electric field, both organic and inorganic. The philosophy behind electroluminescent devices is such that requires special electro-optical characteristics from active host material, due to the nature of induced luminescence and the required emitted radiation. One of the most important aspect of the semiconductor host lattices is their bandgap. Wide bandgap semiconductors (like the II-VI ones) are ideal for building such devices, because of their very defining property, the wide bandgap, which permits photons of high energy to transmit through the lattice, without causing excitation of the lattice itself. Photon energies up to 3.0~3.1 eV would have to be accommodated in order to allow for blue light transmission. Another important property is a high dielectric strength. Since large electric fields (> 1 $MVcm^{-1}$) are going to be applied to them in order to accelerate tunnelling electrons at small distances, breakdown within the crystal should be avoided. A high density of interface states would also provide high tunnelling currents thus increasing the activation efficiency. And finally, the lattice defines the bonding environment of the luminescent centres, thus creating possibilities for intrashell transitions, or interaction with unshielded excited states of the luminescent centre, affecting the emitted photon wavelength.

Zinc sulfide is by far the most studied electroluminescent phosphor material of the II-VI group, followed by it's close variants, zinc oxide and cadmium sulfide. The bandgap of ZnS conveniently lies just above the highest visible energy photon, at 3.7-3.8 eV, with plenty of space for incorporation of luminescent centres that emit even at the near UV levels. Its breakdown strength is above 1 $MVcm^{-1}$ and is known to promote a high density of interface states for most insulator materials.[64] Its lattice structure is tetrahedral and therefore can ease the Laporte selection rule for metals performing intrastate transitions. ZnO presents almost the exact same characteristics, with a slightly smaller bandgap at 3.35 eV. ZnSe filters out only about 50 nm from the blue part of the spectrum and CdS cuts off at the edge of green at 2.42 eV. Calcium sulfide and strontium sulfide have very large bandgaps at 4.5 and 4.32 eV respectively and an octahedral symmetry. They are usually doped with lanthanide rear earths, like Ce, Eu and Sm and make very efficient phosphor lattices, much like ZnS.[65, 66]

1.2.b. Luminescent centres

As luminescence centres, a selection of transition metals or rare earth lanthanides are the most common choices. Manganese forms the strongest luminescent agent when mixed with zinc sulfide performing an intrashell 3d-3d transition, which is rendered possible by the tetrahedral asymmetrical structure of the lattice.[38, 41, 62, 67] The peak emission of ZnS:Mn is perceived as yellow/orange and is quite reminiscent of old monochromatic computer displays. Copper is perhaps the second most efficient activator for ZnS. In the tetrahedral crystal field of the four S^{2-} ligands the $3d^9$ ground-state splits into higher lying t_2 levels and lower lying e levels. It is often included with chlorine as a donor coactivator. Transitions between shallow delocalised donors and the t_2 level are believed to be the source of the familiar green emission, while a transition from the conduction band to the t_2 level would generate blue light. It is also used as a red phosphor where the transition happens from a deep localised donor level to the t_2 higher level.[68, 69] Silver also acts in a similar manner to copper, as it can accept transitions from shallow donor levels or more often from the bandgap itself, therefore in the case of $Zn_xCd_{1-x}S$:Ag, the emitted wavelength can be altered by the zinc and cadmium proportions of the alloy, achieving emission over the whole visible spectrum.[70, 71] Terbium can also be introduced in a ZnS lattice with fluorine or fluorine and oxygen as lattice mismatch and charge compensators.

Terbium is another material performing a 4f-4f intrashell transition with relaxed Laporte selection rule characteristics, also being enhanced further by the oxygen incorporation. Its emission spectrum is centred at 545 nm.[72-74] Europium is used as a rare earth dopant in CaS, performing 5d-4f transitions and emitting in the 650 nm red area.[24, 75-78] A similar action is observed in cerium when doped in a SrS host lattice, emitting at 515 nm in the green-towards-blue region. Other colours achieved by rare earths in a SrS lattice include samarium and neodymium at red, terbium, erbium and dysprosium at green and praseodymium and holmium at purple (blue and red).[65] The list is quite large, but only a few important examples have been given here. This research deals only with ZnS and ZnCdS doped with Mn, Cu and Ag and also a couple of non-luminescent elements cobalt and nickel, for possible investigation of their local geometry of substitution in the matrix.

1.2.c. Electrodes

Materials used for electrodes in making EL cells or ACTFEL pixels for displays (see section 1.3) are mostly typical electrodes used for other similar devices, for example liquid crystal based. It is essential for the electrodes to have low resistivity, especially when it is intended to drive the device at fast speeds. The response speed is inversely proportional to the product of electrode resistance and electrostatic capacitance of the cell, therefore, it is an advantage to control the resistance of the electrodes by a right choice of materials. It is found necessary to employ a transparent electrode at the top of the cell, letting out the light emitted by the phosphor. A typical first choice is indium tin oxide (NESA glass), which is widely used in the industry in a variety of applications, e.g. solar cells. Its conductivity arises from either oxygen vacancies or Sn^{+4} substituting for In^{+3}, thus presenting shallow donor levels that can easily provide electrons to the conduction band.[79, 80] ZnO is also known for its transparent conductive properties, with oxygen vacancies being again the source of shallow donor levels for the pure substance, or dopings of Al or In can also be introduced for increased conductivity. Electron mobilities for thin films have been measured at 115-155 $cm^{2}\cdot V^{-1}\cdot s^{-1}$ [81] and hole mobilities at 10 to 15 $cm^{2}\cdot V^{-1}\cdot s^{-1}$,[82] both values given for undoped ZnO. The counter-electrode is usually a metal, with aluminium being the most typical choice due to its high conductance and ease of processing.

1.2.d. Typical deposition methods of II-VI materials

Electroluminescent thin film devices have been constructed for the past 30 years, at least. The methods that have been followed are those that were developed for building integrated semiconductors. Some of the most common ones are laid out here.

Radio frequency sputtering is a technique with a very high deposition rate, used to grow various types of films. Sputtering is a physical process whereby atoms in a solid target material are ejected into the gas phase due to bombardment of the material by energetic ions. Sputtering is largely driven by momentum exchange between the ions and atoms in the material, due to collisions. The process can be thought of as atomic billiards, with the ion (cue ball) striking a large cluster of close-packed atoms (billiard balls). Although the first collision pushes atoms deeper into the cluster, subsequent collisions between the atoms can result in some of the atoms near the surface being ejected away from the cluster. The number of atoms ejected from the surface per incident ion is called the *sputter yield* and is an important measure of the efficiency of the sputtering process. Other things that the sputter yield depends on, are the energy of the incident ions, the masses of the ions and target atoms and the binding energy of atoms in the solid.

The ions for the sputtering process are supplied by a plasma that is induced in the sputtering equipment. In practice a variety of techniques are used to modify the plasma properties, especially ion density, to achieve the optimum sputtering conditions, including usage of RF (radio frequency) alternating current, utilization of magnetic fields and application of a bias voltage to the target. Films grown by it often need to be annealed in order to obtain a good crystal structure. In addition, it is rather hard to maintain the desired stoichiometry of the film. Examples of ZnS film deposition are a 50 nm layer of distinct crystalline structure and orientation of both a cubic and a hexagonal form,[83] and a successive layer deposition of ZnS:Mn upon a SrS:Ce layer.[84]

Vapour deposition has been attempted, which requires a temperature above 1200 °C, even though it produced some very good crystals of ZnS.[85]

Metalorganic vapour phase epitaxy (MOVPE) is a chemical vapour deposition method of epitaxial growth of materials, especially semiconductors from the pyrolysis of organic compounds containing the required chemical elements. Today low temperature deposition methods have been made possible for the deposition of

zinc sulfides and selenides. Both these two materials have been deposited by P. Prete et al.[86] on GaAs substrates, at a temperature range of 300 to 500 °C, using diethyldisulfide and dimethyldiselenide to provide for S and Se and dimethyly-zinc-triethylamine (DMZn-TEN) for Zn. Diethyldisulfide decomposes via the loss of ethylene molecules, while the decomposition of dimethyldiselenide is dominated by sequential loss of methyl radicals, both processes allowing for growth of S and Se based compounds in temperatures below 400 °C. Moreover, crystals with dimensions that can pose quantum confinement for applications in lasers have been achieved for the II-VI group. DMZn-TEN, dimethyl-cadmium (DMCd) and ditertiarybutylsulfide (DtBS), at 350 °C have been used for growing sulfide films with such characteristics, by C. Meyne et al. Selenides where grown by I. Suemune et al., with DtBSe and DMCd at 350 °C and diethyl-zinc (DEZn) at 450 °C for CdSe and ZnSe respectively.[87, 88]

Molecular beam epitaxy (MBE) is also a common solution to the semiconductor growth problem. It achieves good crystallinities of the films and provides a good control of the stoichiometry.[89] It also requires a rather high temperature of the substrate (400 °C). The growth rate of the films is moderate, approximately 400 nm in two hours. In solid-source MBE, ultra-pure elements such as zinc and sulfur would be heated in separate quasi-Knudsen effusion cells until they each slowly begin to evaporate. The evaporated elements then condense on the wafer, where they react with each other, forming, in this case, single-crystal zinc sulfide. The process takes place in high vacuum or ultra high vacuum. The term "beam" simply means that evaporated atoms do not interact with each other or any other vacuum chamber gases until they reach the wafer, due to the large mean free path lengths of the beams. During operation, RHEED (Reflection High Energy Electron Diffraction) is often used for monitoring the growth of the crystal layers. The wafers on which the crystals are grown are mounted on a rotating platter, which can be heated to several hundred degrees Celsius during operation. Examples include ZnSSeTe films grown on GaAs[90] substrates and on ITO substrates[91] and the growth of ZnCdS/ZnMgS on a GaP substrate.[92]

Atomic layer epitaxy (ALE) is a specialized form of epitaxy, with a similar approach to MBE, that typically deposits alternating monolayers of two elements onto a substrate. The crystal lattice structure achieved is thin, uniform and aligned with the structure of the substrate. The reactants are brought to the substrate as alternating

pulses with "dead" times in between. ALE makes use of the fact that the incoming material is bound strongly until all sites available for chemisorption are occupied. It is a similar approach to MBE. The method presents a good thermal compatibility with glass and can be performed in lower temperatures than MBE. Moreover, it can be used for the deposition of the whole insulator, phosphor, insulator structure deposition and achieve the desired compositions to a high precision. The greatest drawback is its very low growth rate. It is clearly expected for such a technique to achieve any desired form of crystal structure[93] or orientation and of course strained lattice quantum wells.[94, 95]

Almost all of the procedures described, including CBD, require post processing of the grown films by chemical etching or laser ablation, in order to generate the appropriate patterns necessary for the EL device structure. A few methods exist where the deposition takes place in small (micron-scale) selected areas and most of them include the use of one or even more laser beams. A common technique that is based on the use of lasers is laser ablation deposition,[96] which can be performed in a variety of ways, generating films under many different conditions. It is also commonly known as **pulsed laser deposition.** It uses a pulsed laser beam to carry out a process of ablation in order to deposit materials as thin films. Examples of its use to materials related in this work are laser deposition of 330 nm thick ZnS layer on quartz, using 5 ns pulses of a tripled YAG laser frequency at 355 nm, a fluence of 0.3 Jcm^{-2} and an ablation chamber pressure of 5×10^{-2} Pa, while the substrate was heated at 400 °C.[97] Also, 200 nm thick ZnS films were deposited on yttrium stabilised zirconia heated substrates at 500 °C with a KrF laser at $2Jcm^{-2}$ in a H_2S/Ar atmosphere.[98] Similar conditions were followed in this work for the laser induced forward transfer procedure on ZnS and ZnCdS that is described further down.

1.3 Uses and typical processing methods of II-VI materials

1.3.a. EL Lighting

As mentioned in section 1.1 above, when the phenomenon of electroluminescence was discovered, it was immediately attempted to construct lighting devices that made use of the direct conversion of electricity into light. A

number of shapes and configurations were devised, but none of the conventional ideas of generating light from a point source seemed to extract great efficiency levels from an EL device. Instead, designs that exploited the use of EL phosphors as wide area sources were more successful, as it was being observed that most of the light was being emitted from the volume of the phosphor that resided closer to the electrodes. Soon flat electroluminescent panels were constructed, with a structure that sandwiched the phosphor dispersion between the electrodes. Yet, the incandescent or later fluorescent lamps were still stronger emitters. So no one ever considered EL lamps to be very promising for common lighting purposes, but instead some emergency low consumption signs (or as tritium excited phosphorescent signs) were produced. When electroluminescence as in direct conversion of electricity into light took the road of light emitting diodes, they also became the best choice for small emitter indicators in the electronics industry. The layer structure of the EL lamps though remained a promising design that would later find use in the construction of flat panel display devices.[7,8,13,14] What follows is a description of the main aspects regarding today's technology in electroluminescent display devices with a small reference on other possible used of similar materials, such as solar cells and semiconductor lasers.

1.3.b. EL Display Devices

The greatest portion of today's electronic display device market until recently was dominated by cathode ray tube screens and their largest application is in television and computer screens. Their technology has been hugely improved since their discovery and they are now compatible with any existing picture signal generator. Their two biggest disadvantages though, have always been their size (and weight) and their large power consumption. Both of these arise from their most fundamental element, the cathode ray tube, which needs a certain length in order to accelerate and coordinate the cathode rays and the energy needed to generate them in the first place. In the 1990s the progress in integrated circuits made it possible for the whole driving circuit of a television or a display device to fit in a pocket, thus the use of a CRT as means of displaying a picture was no longer convenient. Also the increasing demand for reduced volume, portable electronic appliances that have

existed for years in homes and businesses, established the trend for flat panel displays to replace the large in volume televisions and computers screens.

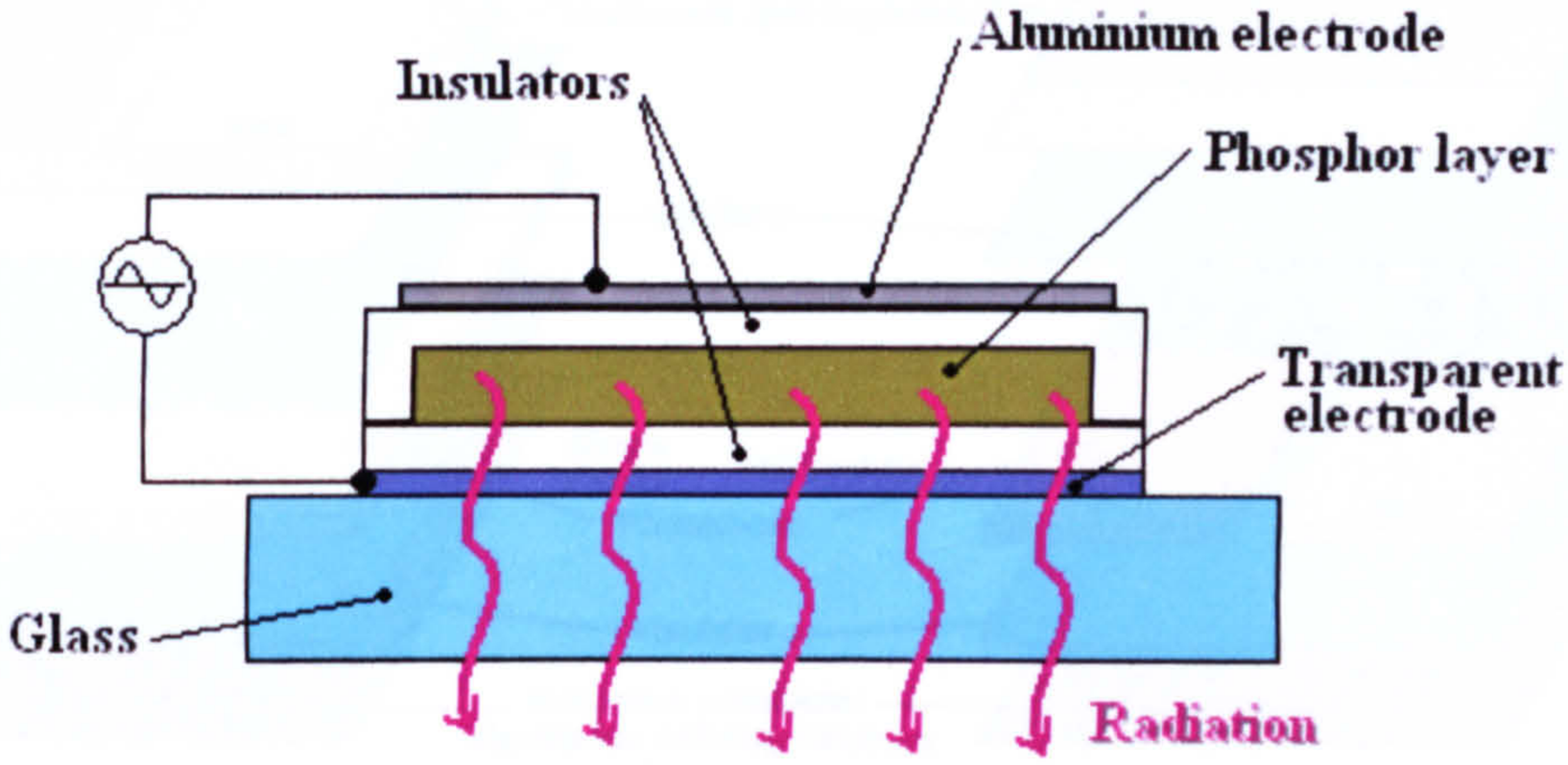

Figure 1.13 Schematic of electroluminescent cell. The yellow active layer can be either a dispersion of phosphor particles, where the encapsulating insulators are used only as hermetic sealing, or it can be the phosphor layer itself, where the insulators are also providing the tunnelling interfaces.[7]

Liquid crystal display technology has proven more than adequate for most of the display needs in watches, calculators, TV and computer screens, etc up until today, but the growth of the market has allowed a reinvestigation of many older proposals for the construction of innovative display devices. Amongst others the EL technology was one of them. A thin film EL display device makes use of a phosphor encapsulating cell comprised of a three layer sandwich of the film between two insulators and a second set of electrodes, one reflective and one transparent, that are applying the necessary field (Figure 1.13). A display screen makes use of a matrix of such cells that are multiplexed in order to generate the large number of picture elements (pixels). Different combinations of phosphors are also used to produce the three basic colours. In order to accelerate the electrons sufficiently in such a small distance, high electric fields are essential, therefore large voltage differences (50[11] to 250 Volts) need to be established across the two electrodes, introducing, in this way, a compatibility problem with the rest of the low voltage (1.5 to 12 Volts) diving circuitry.

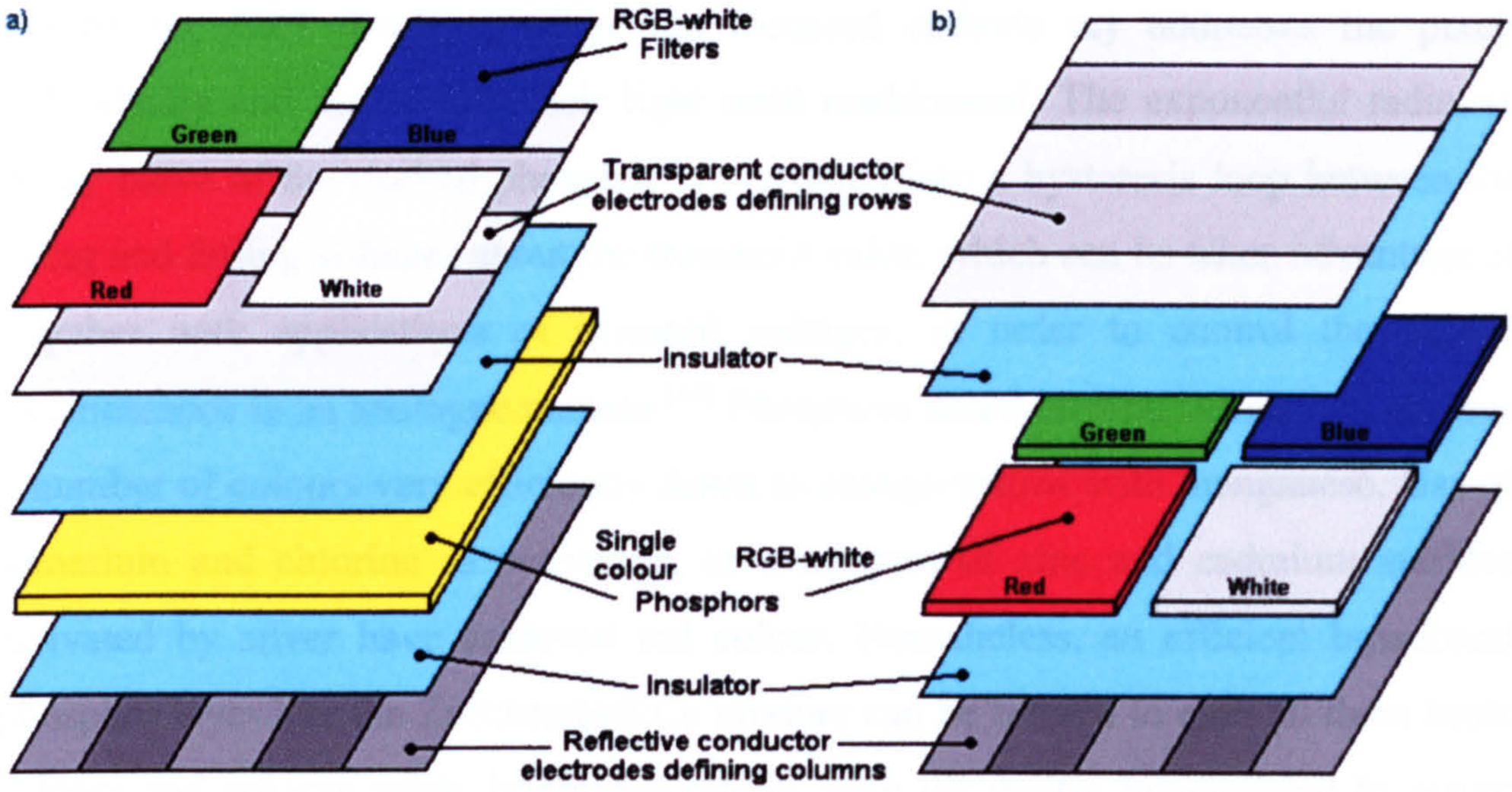

Figure 1.14 Pixel structure of an AC Thin Film Electroluminescent display device, with (a) a monochromatic active phosphor layer and filters and (b) with red, green, blue and white active phosphor elements.[24]

As technology has been advancing in efficiently fabricating thin films for the semiconductor technology, soon it made sense to incorporate EL phosphor layers in thin film devices for the construction of displays. The same basic structure of the initial EL cells is used, but in thin films, which also raises the advantage of even higher electric fields being achieved over the small thickness of the films. The structure contains a metal conductor at the bottom usually chosen to be a reflective one, redirecting any emitted light upwards, an insulator-phosphor-insulator sandwich which is designed for efficient tunnelling and also with transparent insulators and appropriate dielectric constants of all three layers and finally an upper transparent conductor that allows the emitted light towards the viewer. A matrix of rows and columns of conducting lines is exploited on the two conducting layers that applies the threshold voltage and hence electric field across any part of the phosphor, thus defining the lit picture element. For example, to light the pixel with coordinates 32, 176, power is applied on the equivalent column and row conducting lines and the threshold voltage would thus be applied across that part of the phosphor, causing it to luminesce (figure 1.14.a).

With the active layer actually being a phosphor, that is it continues to emit light for at least a short time after its excitation has ceased, it means that it will retain its assigned luminescence until readdressed by the matrix. This idea was already in

use by the CRT displays, where the focussed cathode ray addresses the pixels individually and they retain their light until readdressed. The exponential radiative decay curve of the excited phosphor is translated into a hysteresis loop between the rising and falling voltages about the threshold value, which can be taken advantage of together with applications of inverted voltages, in order to control the pixel's luminescence in an analogue manner.[50] Phosphors based on zinc sulfide can achieve a number of colours very efficiently down to orange-yellow with manganese. Use of samarium and chlorine as activators, or a mixture of zinc and cadmium sulfides activated by silver have achieved red colour. Nonetheless, an efficient broadband phosphor layer like the ZnS:Mn/SrS:Ce mixture can be filtered to emit all three basic colours and achieve white brightness tuning, with the matrix manipulated to assign different brightness values on the phosphor underneath each filter element. Phosphor elements of different colours is the other solution, for which every colour element would have to be processed differently with a writing technique when depositing the phosphor compound film (figure 1.14.b). The filter elements situated at the top of a white phosphor thin film device can acquire their colour filtering attributes by localised impurity injection.

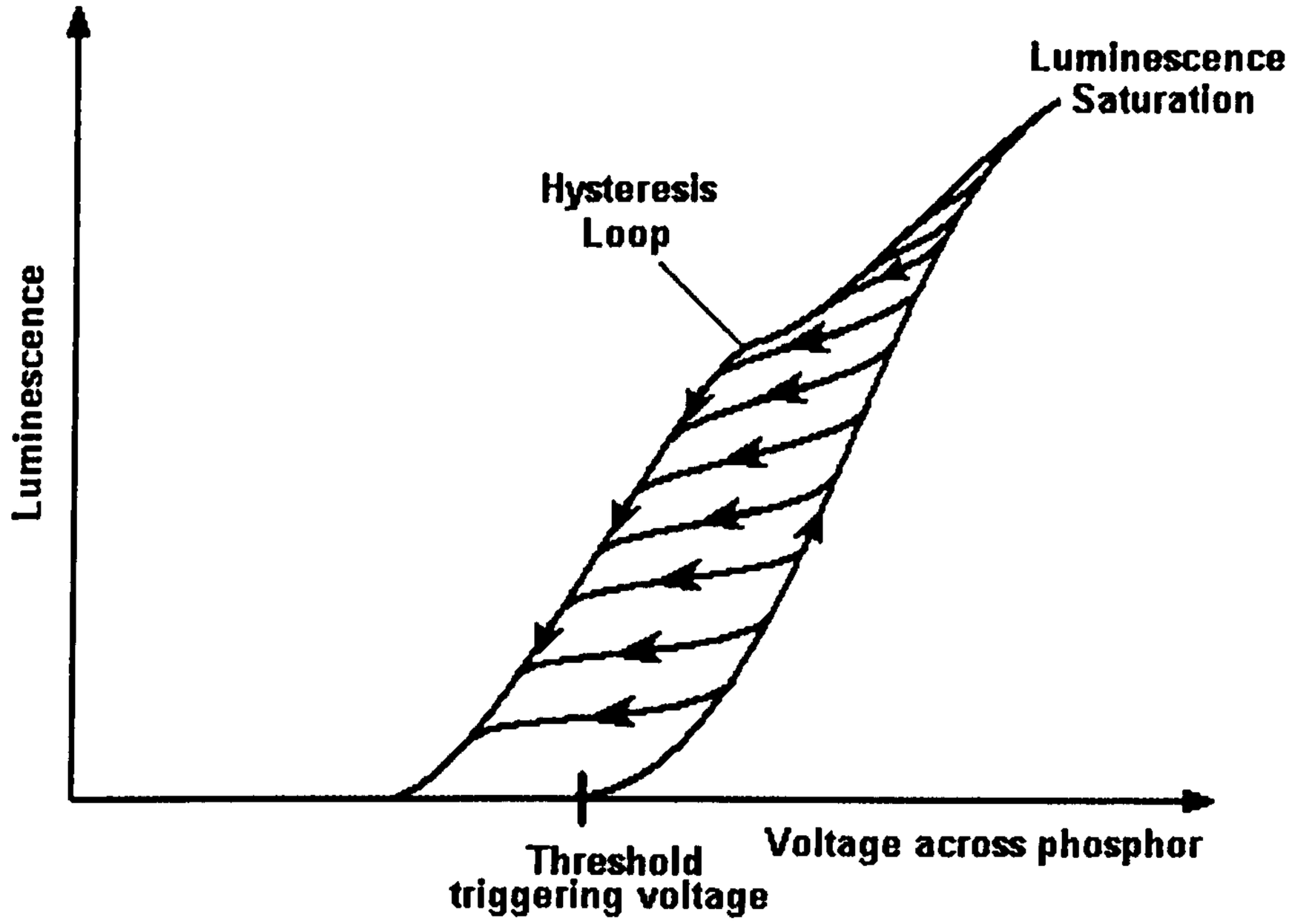

Figure 1.15 Voltage-Luminescence diagram indicating the curve above the threshold voltage for lighting of the phosphor and the hysteresis loop exploited by the driving electronics for achievement of analogue luminance.[24, 50]

The main substrate upon which the layers are built is usually the thick screen glass. The structure can be built on top of the substrate, with a rather thin protective transparent layer situated on top of all other layers, in which case, the substrate could also be a reflecting conductor or semiconductor. Another approach would have the thick transparent screen glass on top of the surface, with the rest of the layers deposited underneath it and the driving electronics under the device. A readjustment of the transparent insulator carrying the rows or columns conductor lines for the display is to have the whole transparent electrode at a set voltage, therefore a homogeneous layer is employed and two layers of vertically oriented conducting lines underneath the phosphor-insulator sandwich. The two adjacent conductor layers forming the matrix in this case are separated by another insulating film. The voltage values assigned at either the rows or the columns is half the desired voltage difference between the bottom of the phosphor sandwich and the top conducting transparent layer. The phosphor picture element will not be excited unless the threshold voltage levels are reached by applying voltage to both its row and column conductor lines (figure 1.15). The semiconductor driving electronics underneath the thin film EL structure is called an active matrix and the whole device structure is often referred to as AMEL.[99]

1.3.c. Solar cell windows.

The wide bandgap of II-VI materials is not only an advantage in fabricating phosphors and phosphor layers for light emitting devices. It is also of great use in the construction of solar cells. Apart from the fact that some of the first and still most efficient photoconductors built for detection of IR radiation were based on cadmium sulfides and tellurides, II-VI crystals are employed as suitable windows for solar cells. The wide bandgap can permit most of the visible light to pass through towards the active layer. Similar materials can be used for both the windows and the active material, thus avoiding lattice mismatches. The active material is appropriately doped in order to generate electrons from excited atoms, hence inducing a voltage difference between the device layers.[100-102] When used as window materials, they can provide good transmission properties, together with the virtues of a transparent conductor, with the most promising material being ZnO doped with boron,[103] indium, gallium

and aluminium.[104] Moreover, oxides such as ZnO are as inert as SiO_2, thus being a perfect material for windowing applications.

1.3.d. Considerations on crystal size.

The optical properties of the II-VI materials is what makes them interesting for applications in electroluminescence and they mainly relate to the bandgap defining their semiconductor properties and applications in general. Their ionic structure permits for fabrication methods that are promising in achieving crystal sizes of the nanometer scale, mostly being implemented as quantum dots. This effect had been undesirable until the beginning of 1980s as it meant that the attempted fabrication methods of bulk crystals were failing, therefore generating products of low crystallinity. Moreover, non-radiative absorption, scattering or recombination at the nanocrystal interfaces are also undesired effects. On the other hand though, size reduction of such crystals has offered some unique capabilities of controlling the band structure of materials and taking advantage of the new structure in conjunction with other semiconductors.

As explained earlier, a wide bandgap allows for transmission of visible light and can accommodate doping levels within the bandgap, for generation of light at any wavelength within the visible range. The available states in a semiconductor of extremely reduced dimensions, become less and less in number and thus do not form energy bands any more, but rather discrete energy levels. Hence transitions can only take place between those energy specific levels. Furthermore, the distance between filled and empty levels is now increased significantly, often observed as an emission colour change towards the blue. This change is clearly observed as a displacement of the absorption threshold in transmission spectra. The other effect occurring by the reduction of the size of semiconductors to that equivalent to a few tenths of sequential atoms in the lattice, is that it reaches a state where quantum confinement occurs. That is, charge carriers in the material are trapped within dimensions close to their de Broglie wavelength.

Examples of manipulation of the II-VI semiconductor properties by quantum dot implementation, has been reviewed for the fabrication of solar cells,[105] electroluminescent cells,[106] and laser gain medium.[107, 108] Quantum confinement is a phenomenon of greater interest in the fabrication of laser semiconductors. The ability

to control the availability of energy levels and induce specific energy transitions between them is of unique importance to the construction of such devices, moreover, the confinement of excited carriers in the gain medium is another advantage.[52, 109]

1.4 Objective and presentation of the research work

Research Objective

The primary objective of this research was to deposit materials of the II-VI group described as phosphors or electroluminescent materials with a chemical method onto appropriate substrates and then transfer them to new substrates with the use of a technique called Laser Induced Forward Transfer. The chemical deposition method was chosen as a way to generate the materials (phosphor crystals) in the first place, before applying the second step of laser processing and more specifically laser transferring. Chemical bath deposition has been researched for depositing thin films of inorganic salts before.[41,69,71,100,107,110] The method has also been used for generating thin films[102,110] or nanosized rods and particles[100,105-108] of II-VI phosphor materials. It was considered advantageous in comparison with other techniques due to the low cost of execution, ease to perform and repeat and effectiveness in generating thin films over comparably large surfaces of the candidate substrates. The low temperature (less than 100 °C) nature of the process was also a very attractive aspect. The chemical bath deposition method was optimised in terms of generated film adherence and film thickness and also chemical composition and luminescence of the films. The idea was to produce continuous phosphor films with know properties, on transparent substrates, that can be used for the laser transferring step.

The materials chosen were the most widely accepted ZnS and CdS for which a chemical deposition method was already developed by O' Brien et al.[110] but had to be optimised for the purposes of the current research. The films were formed on sodium-doped microscope slides and later on quartz microscope slides for the purposes of laser transferring. The deposited films were analysed by various methods for the purposes of determining thickness, composition, optical and luminescence qualities. Annealing steps were also attempted with the aim to improve these qualities.

The laser induced forward transfer method was considered ideal for the purposes of depositing the electroluminescent films onto new substrates. As the chemical deposition method applies the film over the whole exposed area of the substrate, the LIFT process can selectively redeposit small areas of the initial film on a substrate with minimal effects on it. The technique becomes very useful when depositing films for the purposes of constructing multilayer microelectronic devices, including thin film electroluminescent devices that are of interest here. Such devices often require a sequence of films consisting of different materials that can be sensitive to high temperatures or gas and liquid chemical environments that are involved in other methods of film deposition. The method can used for printing various shapes or lines made of sequential adjacent transfers, in which case it is usually referred to as direct writting, or for controlling the thickness of the final phosphor layer by placing successive layers on top of each other.[111,112] Finally, by careful control of the transfer parameters (and mostly that of the laser beam energy) there are possibilities of improving the crystalline and therefore the luminescent characteristics of the transferred films.[113,114] When this research was started the method had not been applied before in transferring zinc or cadmium sulfides.

The chemically deposited films were then transferred on new substrates, either silica or standard microscope slides with the aid of a krypton fluoride laser. Its characteristic lasing frequency at 248 nm lies well within the absorption region of ZnS, therefore ensuring photon absorption, heating and ablation of at least part of the films residing close to the interface. The substrate is still transparent to the laser energy to a great extent, thus allowing a forward transfer configuration where it faces the laser source having the film facing away from it and opposing the new substrate. Melting conditions must be achieved on the film, but complete ablation proves destructive. Careful control and tuning of the laser's output power is hence required for a successful transfer. Optimisation of other parameters such as ambient chamber pressure, atmosphere and distance from the target substrate was another necessary task. The resulting transferred films should be investigated once more and ideally they should retain composition and any luminescent properties. Thin transferred films and improvement of the luminescent properties through the laser-processing step would also be considered an advantage. The LIFT process has been performed before on semiconductors, but not specifically for chemically deposited ZnS or CdS up to the date that this research was initiated.

Thesis Presentation

The theoretical basis and a small review of the literature in applications of phosphors and electroluminescent materials were concluded in this chapter. In the following chapter some of the main principles and procedures for analysis of the results are laid out. The chapter is meant to give a summary of the principles of these techniques and will not go into great details of their supporting science. After that the work is divided in three sections, the first is concerned with the chemical formation and deposition of the film in question. The second one with the laser transferring of the chemically deposited films. Both of these large sections are separated in appropriate chapters regarding either some supporting theory for the method followed and the reasons that it was chosen as the most appropriate. Then follows a description of the experimental details of each method and how the optimisation has progressed through observation. And finally the analysis of the yielded films is presented.

The last section elaborates on the total achievement of sequentially applying the two deposition methods for depositing films segments of zinc and cadmium sulfides, doped or undoped on the decided target substrates. A more composite analysis of the results is thus performed. The thesis has been sectioned in such a way, aiming to help the readers of any discipline, in concentrating towards that part of their greatest interest. This work like many others in its field is a unique composition of three fields of science, those of inorganic chemical synthesis, laser processing of materials and optoelectronics semiconductor characterisation and evaluation.

1.5 References

1. H. J. Round, *Electr. World*, 1907, **19**, p 309.
2. B. Gudden and R. Pohl, Enhancement of Phosphorescence by Electric Fields, J. Phys., 1920, **2**, p 192.
3. G. Dechene, Influence of an Electric Current on Phosphorescence in Zinc Sulphide, C.R. Acad. Sci., 1935, **201**, p 139.
4. G. Destriau, Scintillation of Zinc Sulphide With a-rays, *J. Chim. Phys.*, 1936, **33**, p 587.
5. G. Destriau, Analytical Study of the Conditions of Excitation of the Phenomena of Electroluminescence, J. Chim. Phys., 1937, **34**, p 462.
6. G. Destriau, New Phenomenon of Electro-Photoluminescence and its Possibilities for Investigation of Crystal Lattice, Phil. Mag., 1947, **38**, p 700.
7. J. I. Pankove, Topics in Applied Physics: Display Devices, Springer Verlag, 1980.
8. J. A. Castellano, Handbook of Display Technology, Hartcourt Brace Jovanovich, New York, 1992.
9. A. Vecht, J. Appl. Phys. I, 1968, p 134.
10. M. J. Russ and D. I. Kennedy, J. Electrochem. Soc., 1967, p 1066.
11. W. A. Barrow, R. C. Coovert, E. Dickey, C. N. King, C. Laakso, S. S. Sun and R. T. Tuenge, SID Dst., 1993, p 761.
12. C. N. King, EL 96, 1996, p 375.
13. P. D. Rack, A. Naman, P. H. Holloway, S. S. Sun and R. T. Tuenge, MRS Bulletin, 1996, **49**, p 21.
14. P. Pringsheim, Fluorescence and Phosphorescence, Interscience Publishers Ltd., 1961.
15. D. M. Grimes, Electromagnetism and Quantum Theory, 1969
16. A. Hinchliffe and R. W. Munn, Molecular Electromagnetism, John Wiley & Sons Ltd., Surrey, 1985.
17. M. D. Galanin, Luminescence of Molecules and Crystals, Cambridge International Science Publishing, 1996.
18. H. H. Willard, L. L. Merritt, J. A. Dean and F. A. Settle, Fluorescence and Phosphorescence Spectrophotometry, in Instrumental Methods of Analysis, Wadsworth Publishing Company, 1988, p 197.
19. R. S. Becker, Theory and Interpretation of Fluorescence and Phosphorescence, Wiley Interscience, 1969.
20. V. G. Plotnikov, Theoretical Basis of Spectral-luminescent Systematics of Molecules, Ups. Khimii, 1980, **49**, p 327.
21. J. F. Endicott, Y. J. Chen and P. Xie, Electron-transfer Spectroscopy: Donor-Acceptor Electronic Coupling, Reorganizational Energies, Reaction Pathways and Dynamics, Coord. Chem. Rev., 2005, p 343.
22. S. S. Skourtis and A. Teklos, Electron Transfer Through Time Dependent Bridges: Differences between Franck-Condon and Born-Oppenheimer Breakdown, Chem. Phys., 2005, **319**, p 52.
23. K. Fink, Ab initio Cluster Calculations of the Magnetic Properties of ZnO Doped with Transition Metal Ions, Chem. Phys., 2006, **326**, p 297.
24. P. D. Rack and P. H. Holloway, The Structure, Device Physics and Material Properties of Thin Film Electroluminescent Displays, Mater. Sci. Eng., 1998, **R21**, p 171.

25. S. K. Lam and D. Lo, Time-resolved Spectroscopic Study of Phosphorescence and Delayed Fluorescence of Dyes in Silica-gel Glasses Chem. Phys. Lett., **281**, p 35.
26. I. A. Kaputskaya, E. A. Ermilovb, S. Tannertb, B. Röderb and S. K. Gorbatsevicha, The Influence of Förster Energy Transfer on Spectral and Kinetic Characteristics of Phosphorescence and Thermally Activated Delayed Fluorescence of Acriflavine in A Polyvinylalcohol Matrix, J. Lumin., 2005, **121**, p 75.
27. M. Balkanski and R. F. Wallis, Series on Semiconductor Science and Technology: Semiconductor Physics and Applications, Oxford University Press, Oxford, 2000.
28. R. A. Smith, Semiconductors, 2nd Edition, Cambridge University Press, 1978.
29. D. A. Fraser, The Physics of Semiconductor Devices, 3rd Edition, Oxford University Press, 1983.
30. W. V. Gool, Fluorescence Centres in ZnS, Philips Research Reports Supplements, University of Amsterdam, Amsterdam, 1961.
31. H. E. Ruda, Electronic Materials: Widegap II-VI Compunds for Opto-electronic Applications, Chapman & Hall, London, 1992.
32. D. P. Graddon, An introduction to Co-ordination Chemistry, Pergamon Press, Oxford, 1961.
33. G. Rogers, Introduction to Coordination, Solid State and Descriptive Inorganic Chemistry, McGraw, New York, 1994.
34. F. A. Sidney, Physical Inorganic Chemistry: A Coordination Chemistry Approach, Spektrum Academic, Oxford, 1996.
35. M. Aven and J. S. Prener, Physics and Chemistry of II-VI Compounds, North-Holland Publishing CO., Amsterdam, 1967.
36. M. Ladd, Crystal Structures, Lattices and Solids in Stereoview, Horwood Publishing Ltd., Sussex, 1999.
37. A. K. Arora and A. Mansingh, The Influence of Manganese Doping on the Optical Properties of Zinc Sulphide Films, J. Phys. D: Appl. Phys., 1991, **24**, p 1462.
38. W. Chen, G. Li, J. O. Malm, Y. Huang, R. Wallenberg, H. Han, Z. Wang and J. O. Bovin, Pressure Dependence of Mn^{2+} Fluorescence in ZnS : Mn^{2+} Nanoparticles, J. Lumin., 2000, **91**, p 139.
39. V. Swaminathan and L. C. Green, Low Temperature Photoluminescence in Ag-Doped ZnSe, J. Lumin., 1976, **14**, p 357.
40. T. D. Thompson and J. W. Allen, Electroluminescence from Minority Carrier Injection Produced by Deep-Level Impact-Ionisation, J. Cryst. Growth, 1990, **101**, p 981.
41. H. Yang, J. Zhao, L. Song, L. Shen, Z. Wang, L. Wang and D. Zhang, Photoluminescent Properties of ZnS:Mn Nanocrystals Prepared in Inhomogeneous System, Mater. Lett., 2003, **57**, p 2287.
42. R. N. Bhargava, Doped Nanocrystalline Materials - Physics and Applications, J. Lumin., 1996, **70**, p 85.
43. G. F. J. Garlick, Luminescent Materials, Oxford University Press, London, 1949.
44. I. Szczurek and H. Lozykowski, Electroluminescence of ZnSe Thin Films Doped with the Rare-Earth Fluorides, J. Lumin., 1976, **14**, p 389.
45. R. Evrard, E. Kartheuser and F. Williams, Polaron Formalism Applied to Donor-Acceptor Pairs in Semiconductors, J. Lumin., 1976, **14**, p 81.

46. E. Grillot, M. Bancie-Grillot, M. Egee, G. M. Ary, J. C. DeVos and M. Rousseau, Spectral Distribution of the Emission Probability in the Broad Fluorescence Bands of the II-VI Luminophores, J. Lumin., 1976, **14**, p 219.
47. H. F. Ivey, Advances in Electronics and Electron Physics: Electroluminescence and Related Effects, Academic Press Inc., New York, 1963.
48. O. W. Lossew, Wireless World, 1924, **15**, p 93.
49. O. W. Lossew, C. R. l'Academie. Sci., URSS, 1940, p 360.
50. S. Matsumoto, I. Ohta, T. Kamegaya, M. Tamura, T. Beppu and H. Morita, Electronic Display Devices, English Edition, John Wiley & Sons, Tokyo, 1984.
51. S. Nakamura, The Blue Laser Diode : GaN Based Light Emitters and Lasers, Springer, Berlin, 1997.
52. D. Sands, Series in Optics and Optoelectronics: Diode Lasers, Institute of Physics Publishing Ltd., Bristol, 2005.
53. D. Wood, Prentice Hall International Series in Optoelectronics: Optoelectronic Semiconductor Devices, Prentice Hall International Ltd., Hemel Hempstead, 1994.
54. K. Bhattacharyya, S. M. Goodnick and J. F. Wager, Monte Carlo Simulation of Electron Transport in Alternating-Current Thin-Film Electroluminescent Devices, J. Appl. Phys., 1992, **73**, p 3390.
55. S. H. Chen, A. P. Greeff and H. C. Swart, A Comparative Study Between the Simulated and Measured Cathodoluminescence Generated in ZnS:Cu, Al, Au Phosphor Powder, J. Lumin., 2005, **113**, p 191.
56. Q. F. He, Z. Xu, D.A. Liu and X. R. Xu, An Analytical Model of Monte Carlo Electron Scattering in ZnS, Solid-State Electron., 2006, **50**, p 456.
57. M. Reigrotzki, J. R. Madureira, A. Kuligk, N. Fitzer, R. Redmer, S. M. Goodnick, M. Dür and W. Schattke, Impact Ionization and High-Field Effects in Wide-Band-Gap Semiconductors, Physica B, 2002, **314**, p 52.
58. E. Schreiber and H. J. Fitting, Ballistic Electrons in GaAs and ZnS, Physica B, 2003, **131-132**, p 87.
59. E. Bringuier, Electron Multiplication in ZnS-type Electroluminescent Devices, J. Appl. Phys., 1990, **67**, p 7040.
60. E. Bringuier, Impact Excitation in ZnS-type Electroluminescence, J. Appl. Phys., 1991, **70**, p 4505.
61. J. Benoit, P. Benalloul, A. Geoffroy, N. Balbo, C. Barthou, J. P. Denis and B. Blanzat, Study of Highly Concentrated ZnS : Mn ACTFEL Devices, Phys. Status Solidi A, 1984, **83**, p 709.
62. J. Benoit, P. Benaloul, C. Barthou, S. Casette and J. C. Soret, De-Excitation Processes and Efficiency in ALE ZnS : Mn Thin Film Electrolumninescent Devices, Phys. Status Solidi A, 1990, **122**, p 427.
63. H. Xian, P. Benalloul, C. Barthou and J. Benoit, Quantitative Analyses and Crystallographic Studies of ZnS:Mn Thin Films Prepared by R.F. Magnetron Reactive Sputtering, Thin Solid Films, 1994, **248**, p 193.
64. E. Bringuier, Tentative Anatomy of ZnS-type Electroluminescence, J. Appl. Phys., 1994, **75**, p 4291.
65. I. Tanaka, Y. Izumi, K. Tanaka, Y. Inoue and S. Okamoto, Electroluminescence Properties of Rare-Earth-Activated SrS Thin Films Under Light Rrradiation, J. Lumin., 2000, **87-89**, p 1189.

66. D. Jia, R. S. Meltzer and W. M. Yen, Ce^{3+} Energy Levels Relative to the Bandstructure in CaS: Evidence from Photoionisation and Electron Trapping, J. Lumin., 2002, **99**, p 1.
67. M. Frackowiak, E. Chimczak, M. Kozielski, J.Kruszyna and A. Kuleczka, Luminescent Thin ZnS : Mn Films, J. Lumin., 1975, **14**, p 243.
68. A. A. Bol, J. Ferwerda, J. A. Bergwerff and A. Meijerink, Luminescence of Nanocrystalline ZnS:Cu^{2+}, J. Lumin., 2002, **99**, p 325.
69. W. Sang, Y. Qiana, J. Mina, D. Lia, L. Wanga, W. Shia and L. Yinfengb, Microstructural and Optical Properties of ZnS:Cu Nanocrystals Prepared by an Ion Complex Transformation Method, Solid State Commun.,2002, **121**, p 475.
70. M. S. Waite, D - A recombination Luminescence in (Zn, Cd)S DCEL Powder Cells, J. Lumin., 1981, **24-25**, p 921.
71. L. Chen, L. Wang, T. Luo and Y. Qian, A Hydrothermal Method to Prepare the Spherical ZnS and Flower-Like CdS Microcrystallites, Mater. Lett., 2006, **60**, p 3627.
72. T. Toyama, K. Yoshimura, M. Fujii, H. Haze and H. Okamoto, Novel Green Thin-Film Electroluminescent Devices Utilizing ZnS Nanocrystals Doped with Tb Compounds, Appl. Surf. Sci., 2005, **224**, p 524.
73. M. Leskelä, Rare Earths in Electroluminescent and Field Emission Display Phosphors, J. Alloys Compd., 1998, **275-277**, p 702.
74. J. P. Kim, M. R. Davidson, M. Puga Lambers, E. Lambers. and P. H. Holloway, Oxygen Codoping of ZnS:Tb,F Electroluminescent Thin Film J. Lumin., 2004, **109**, p 75.
75. C. Guo, D. Huanga and Q. Sub, Methods to Improve the Fluorescence Intensity of CaS:Eu^{2+} Red-Emitting Phosphor for White LED Mater. Sci. Eng., B, 2006, **130**, p 189.
76. D. Poelman, R. Vercaemst, R. L. V. Meirhaeghe, W. H. Laflère and F. Cardon, The Influence of Se-Coevaporation on the Emission Spectra of CaS:Eu and SrS:Ce Thin Film Electroluminescent Devices J. Lumin., 1995, **65**, p 7.
77. A. Choa, S. Y. Kima, M. Leea, S. J. Kim, C. H. Kimb and C. H. Pyunb, Fast Luminescence Decay Processes of Photoexcited Eu^{3+} in CaS : Eu,La, J. Lumin., 2000, **91**, p 215.
78. N. Yamashita, O. Harada and K. Nakamura, Jpn. J. Appl. Phys., 1995, **34**, p 5539.
79. Y. Yanga, X. W. Suna, B. J. Chena, C. X. Xua, T. P. Chena, C. Q. Suna, B. K. Taya and Z. Sun, Refractive Indices of Textured Indium Tin Oxide and Zinc Oxide Thin Films, Thin Solid Films, 2006, **510**, p 95.
80. S. Li, X. Qiao and J. Chen, Effects of Oxygen Flow on the Properties of Indium Tin Oxide Films, Mater. Chem. Phys., 2006, **98**, p 144.
81. E. Kaidashev, M. Lorenz, H. v. Wenckstern, A. Rahm, H. C. Semmelhack, K. H. Han, G. Benndorf, C. Bundesmann, H. Hochmuth and M. Grundmann, High Electron Mobility of Epitaxial ZnO Thin Films on c-plane Sapphire Grown by Multistep Pulsed-Laser Deposition. Appl. Phys. Lett., 2003, **82**, p 3901.
82. K. Minegishi, Y. Koiwai, Y. Kikuchi, K. Yano, M. Kasuga and A. Shimizu, Growth of p-Type Zinc Oxide Films by Chemical Vapor Deposition, Jpn. J. Appl. Phys., Part 2, 1997, **36**, p 1453.

83. L. X. Shaoa, K. H. Changa and H. L. Hwang, Zinc Sulfide Thin Films Deposited by RF Reactive Sputtering for Photovoltaic Applications, Appl. Surf. Sci., 2003, **212-213**, p 305.
84. J. A. Ruffner, R. T. Tuenge, S. S. Sun, P. D. Grandon and P. F. Hlava, Sputter Deposition of ZnS:Mn/SrS:Ce Multilayered Thin Film White Phosphor, Thin Solid Films, 1997, **310**, p 123.
85. H. K. Hennisch, Electroluminescence, Pergamon Press Ltd, 1962.
86. P. Prete, N. Lovergineb, S. Petronib, G. Meleb, A. M. Mancinib and G. Vasapollob, Functional Validation of Novel Se and S Alkyl Precursors for the Low Temperature Pyrolytic MOVPE Growth of ZnSe, ZnS and ZnSSe, Mater. Chem. Phys., 2000, **66**, p 253.
87. C. Meyne, U. W. Pohl, W. Richter, M. Straßburg, A. Hoffmann, V. Türck, S. Rodt, D. Bimberg and D. Gerthsen, Quantum Island Formation in CdS/ZnS Heterostructures Grown by MOVPE, J. Cryst. Growth, 2000, **214**, p 722.
88. I. Suemune, K. Yoshida, H. Kumano, T. Tawara, A. Ueta and S. Tanaka, II–VI Quantum Dots Grown by MOVPE, J. Cryst. Growth, 2003, **248**, p 301.
89. K. Tanaka, Y. Inoue, S. Okamoto and K. Kobayashi, Blue Luminescent SrGa2S4:Ce Thin Films Grown by Molecular Beam Epitaxy, J. Cryst. Growth, 1995, **150**, p 1211.
90. W. R. Chen, High-Quality ZnSSeTe Epitaxial Layers Grown by MBE, J. Cryst. Growth, 2004, **256**, p 525.
91. D. Shen, S. Y. Au, G. Han, D. Que and I. K. Sou, MBE-Grown ZnSSe Thin Films on ITO Substrates for Liquid-Crystal Light Valve Applications, Mater. Sci. Semicond. Processing, 2001, **4**, p 611.
92. K. Ichino, H. Kariya, N. Suzuki, K. Ueyama, M. Kitagawa and H. Kobayashi, Molecular Beam Epitaxy and Optical Properties of ZnCdS/ZnMgS Quantum Wells on GaP, J. Cryst. Growth, 2000, **214-215**, p 135.
93. A. Szczerbakow, E. Dynowska, K. Witek and M. Godlewski, Monocrystalline Films of Sphalerite-type ZnSe Grown by Atomic Layer Epitaxy in a Gas Flow System, J. Cryst. Growth, 1999, **207**, p 148.
94. C. T. Hsu, Epitaxial Growth of II–VI Compound Semiconductors by Atomic Layer Epitaxy, Thin Solid Films, 1998, **335**, p 284.
95. M. Yokoyama and N.-T. Chen, ALE Growth and Optical Characterization of ZnSe/ZnS Strained Quantum Well Structures on Si Substrate, J. Cryst. Growth, 2003, **223**, p 369.
96. A. Piqué, R. C. Y. Auyeung, S. B. Qadri, H. Kim, B. L. Justus and A. L. Huston, Growth of Epitaxial Doped Strondium Sulfide Thin Films by Pulsed Laser Deposition, Thin Solid Films, 2000, **377-378**, p 803.
97. S. Yano, R. Schroeder, B. Ullrich and H. Sakai, Absorption and Potocurrent Poperties of Thin ZnS Films Formed by Pulsed-Laser Deposition on Quartz, Thin Solid Films, 2003, **423**, p 273.
98. H. Hiramatsu, H. Ohta, M. Hirano and H. Hosono, Heteroepitaxial Growth of Single-Phase Zinc Blende ZnS Films on Transparent Substrates by Pulsed Laser Deposition Under H2S Atmosphere, Solid State Commun., 2002, **124**, p 411.
99. PalanarSystems, Active Matrix Electroluminescence, http://www.planar.com/Advantages/WhitePapers/docs/overview.pdf, 1996, www.planar.com.
100. R. M. Pérez, G. S. Rodríguez, J. S. Hernández, A. M. Acevedo, A. A. Carbajal, O. V. Galan, J. C. Alonso and G. C. Puente, Effects of Thiourea

Concentration on CdS Thin Films Grown by Chemical Bath Deposition for CdTe Solar Cells, Thin Solid Films, 2005, **480-481**, p 173.
101. A. Strohm, L. Eisenmann, R. K. Gebhardt, A. Harding, T. Schlötzer, D. Abou-Ras and H. W. Schock, ZnO/InxSy/Cu(In,Ga)Se2 Solar Cells Fabricated by Coherent Heterojunction Formation, Thin Solid Films, 2005, **480-481**, p 162.
102. J. V. Gheluwe, J. Versluys, D. Poelman and P. Clauws, Photoluminescence Study of Polycrystalline CdS/CdTe Thin Film Solar Cells, Thin Solid Films, 2005, **480-481**, p 264.
103. S. Faÿ, U. Kroll, C. Bucher, E. Vallat-Sauvain and A. Shah, Low Pressure Chemical Vapour Deposition of ZnO Layers for Thin-Film Solar Cells: Temperature-Induced Morphological Changes, Sol. Energy Mater., 2005, **86**, p 385.
104. E. G. Fu, D. M. Zhuang, G. Zhang, Z. Ming, W. F. Yang and J. J. Liu, Properties of Transparent Conductive ZnO:Al Thin Films Prepared by Magnetron Sputtering, Microelectr. J., 2004, **35**, p 383.
105. W. U. Huynh, J. J. Dittmer and A. P. Alivisatos, Hybrid Nanorod-Polymer Solar Cells, Science Magazine, 2002, p 2425.
106. L. Qian, T. Zhang, F. Teng, Z. Xu and S. Quan, Luminescent Properties and Excitation Mechanism of ZnSe Quantum Dots Embedded in ZnS Matrix, Mater. Chem. Phys., 2006, p 337.
107. G. Hodes, Chemical Solution Deposition of Semiconductor Films, Marcel Dekker, New York, 2003.
108. K. Kyhm, S. M. Kim, J. H. Kim, B. J. Kim, H. H. Lim, K. S. Hong, M. S. Cha and H. S. Yang, Optical Gain in CdSe Nanocrystals, J. Lumin., 2006, p 808.
109. D. Bimberg, M. Grundmann and N. N. Ledentsov, Quantum Dot Heterostructures, John Wiley and Sons, Ltd., Sussex, 1999.
110. P. O'Brien, D. J. Otway and D. S. Boyle, The Importance of Ternary Complexes in Defining Basic Conditions for the Deposition of ZnS by Aqueous Chemical Bath Deposition, Thin Solid Films, 2000, **361-362**, p 17.
111. A. Piqué, D. B. Chrisey, R. C. Y. Auyeung, J. Fitz-Gerald, H. D. Wu, R. A. McGill, S. Lakeou, P. K. Wu, V. Nguyen and M. Duignan, A Novel Laser Transfer Process for Direct Writing of Electronic and Sensor Materials, Appl. Phys. A, 1999, **69 [Suppl.]**, p S279.
112. F. J. Adrian, J. Bohandy, B. F. Kim, A. N. Jette and P. Thompson, A Study of the Mechanism of Metal Deposition by the Laser-Induced Forward Transfer Process, J. Vac. Sci. Technol., 1987, **B5**, p 1490.
113. E. A. Mastio, E. Fogarassy, W. M. Cranton and C. B. Thomas, Ablation Study on Pulsed KrF Laser Annealed Electroluminescent ZnS:Mn/Y2O3 Multilayers Deposited on Si, Appl. Surf. Sci., 2000, **154-155**, p 35.
114. E. A. Mastio, C. B. Thomas, W. M. Cranton and E. Fogarassy, The Effects of Multiple KrF Laser Irradiations on the Electroluminescence and Photoluminescence of RF-Sputtered ZnS:Mn-Based Electroluminescent Thin Film Devices, Appl. Surf. Sci., 2000, **157**, p 74.

Chapter 2.

Description of analysis techniques

Chapter 2. Description of analysis techniques

2.1 Introduction

A range of techniques was used to analyse the chemically prepared or laser processed phosphor films discussed in this work. As the discussion of the analysed results is carried forward in chapters 4 and 6, there are various references to the techniques used and how their features and setup parameters might have influenced the observed results. The references to each technique occur at many points throughout the text therefore it makes sense to compile the descriptions of the analysis techniques in this chapter, before presenting the experimental procedures for the preparation of the samples.

Not all of the analysis techniques used during this research are presented here, as some were so basic, or typical in their operation (e.g. optical microscopy, transmission spectroscopy, etc), that it was not necessary to say anything further about them. Of those that are presented, a small digest of the supporting theoretical background is given for each one, so as to point out the little aspects that become important when applying a technique to the current materials of interest. The descriptions vary; some require an extended account of their experimental execution which was performed in a rather unique way. Others need only a small overview, since they were used in the most typical and commonly understood mode of operation.

2.2 Optical techniques for determination of film thickness

2.2.a. Ellipsometry

Background theory

Ellipsometry is a sensitive optical technique which enables the measurement of the refractive index and the thickness of semi-transparent thin films. Ellipsometry relies on the fact that the reflection at a dielectric interface depends on the polarization of light while the transmission of light through a transparent layer changes the phase of the wave according to the refractive index of the material. Polarization changes are very sensitive to the presence of a thin film or a layer of adsorbed molecules.[1]

Ellipsometry can be applied to surface films throughout the thickness range from partial monatomic coverage (0.1 nm) up to several hundred microns.[2] The most important applications of this technique are the accurate thickness and refractive index measurement of thin films, the identification of materials and thin layers and the characterisation of surfaces.

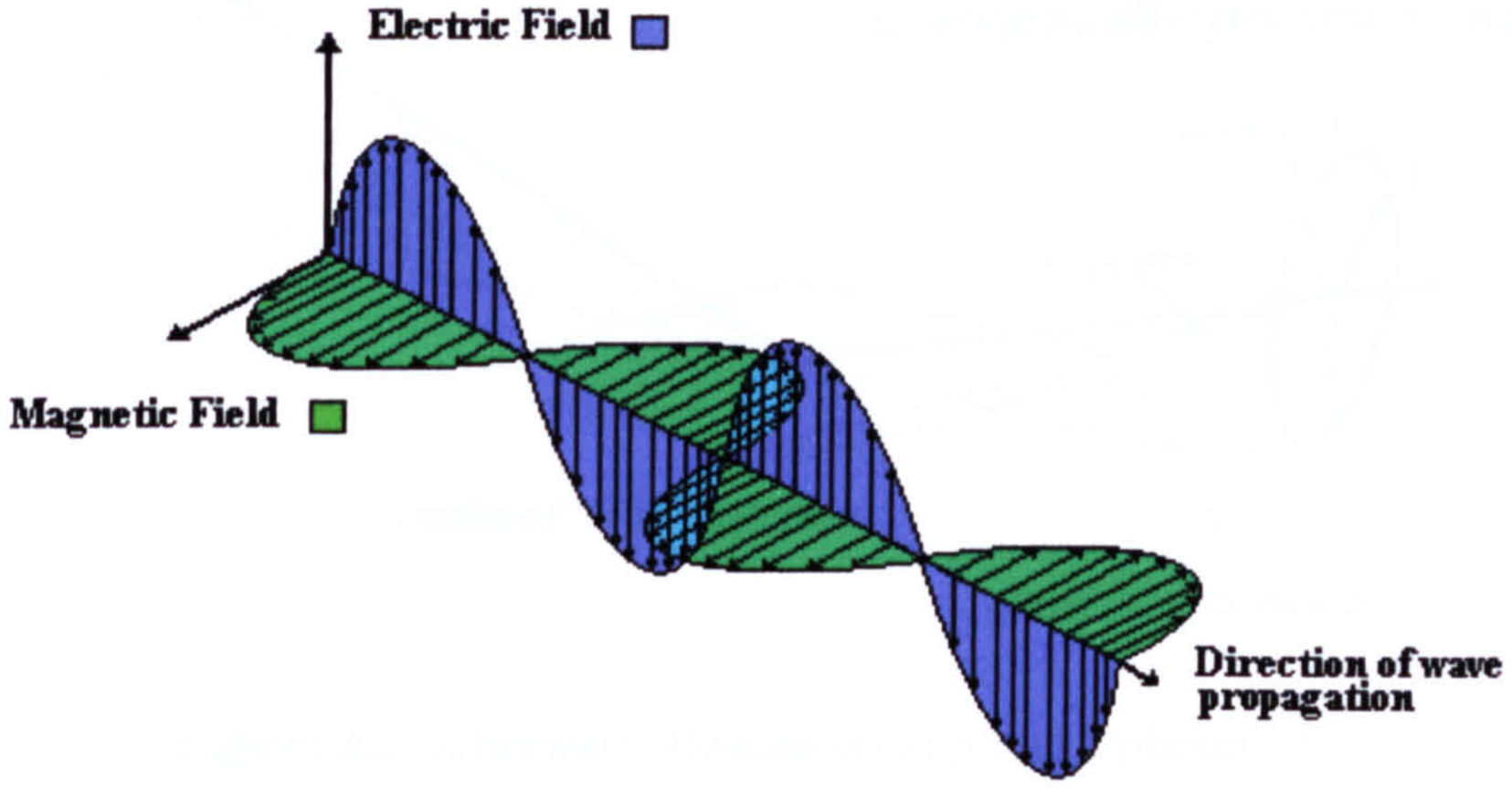

Figure 2.1 The two components of the electromagnetic wave

A plane electromagnetic wave consists of an alternating electric field and a magnetic field at 90° to each other, which are both orthogonal to the direction of the beam propagation axis, as illustrated in Figure 2.1. The state of polarisation is defined by the phase and amplitude relationships between the two component plane waves into which the electric field oscillation can be resolved. One component, designated *p*, is in the plane of incidence and is normal to the surface, whereas the *s* component lies parallel to the surface and is normal to the plane of incidence, as shown in Figure 2.2. The state of polarisation depends on the phase difference between the two rays. If the *s* and *p* rays propagate in the same direction that the photon is propagating through space and in phase with each other, then the light is called linearly polarised. If the two component waves are equal in amplitude and 90° out of phase (one reaches a maximum as the other is at a minimum), then the light is called circularly polarised. Finally when *s* and *p* waves take on arbitrary phases and amplitudes then we have elliptically polarised light. Reflection causes a change in the relative phases of the *p* and *s* waves and a change in the ratio of their amplitudes. The effect of reflection is characterised by the angle Δ, defined as the change in phase and the angle Ψ, whose tangent is the ratio of the magnitudes of the total reflection coefficients.

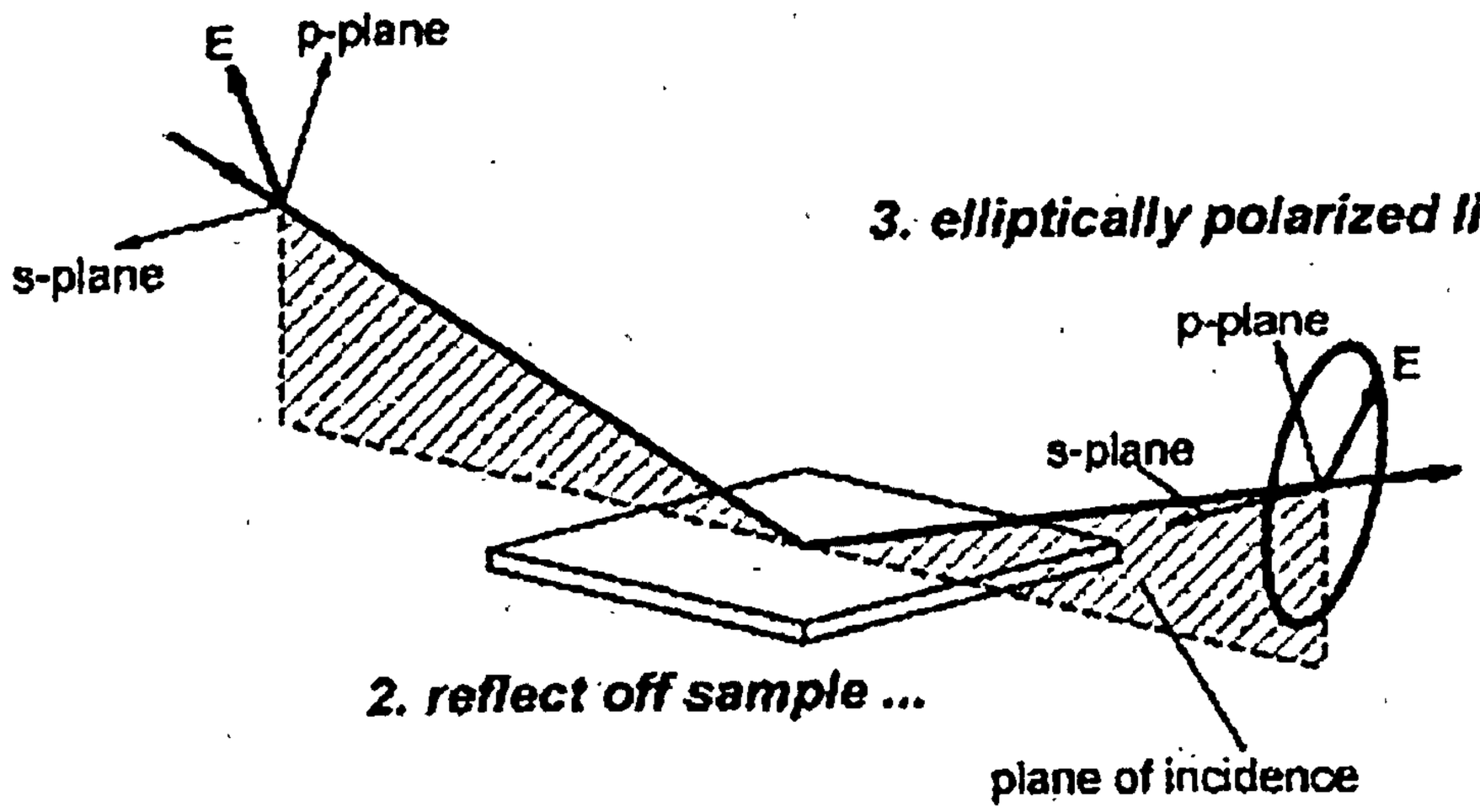

Figure 2.2 Schematic illustration of *p* and *s* planes.[3]

The angle Δ is given by the equation:

$$\Delta = \delta_1 - \delta_2 \tag{2.1}$$

where δ_1 is the phase difference between the parallel and the perpendicular component of the incoming wave and δ_2 is the phase difference between the parallel and perpendicular component of the outgoing wave. The angle Ψ is given by equation:

$$\tan\Psi = \frac{|R_p|}{|R_s|} \tag{2.2}$$

The amplitude of both perpendicular and parallel components may change upon reflection. $|R_p|$ and $|R_s|$ are the ratios of the outgoing wave amplitude to the incoming wave amplitude for the parallel and perpendicular components, respectively.

Ellipsometry measures the Ψ and Δ values that are related to the ratio of Fresnel reflection coefficients R_p and R_s, as represented in equation 2.3 below.[4, 5]

$$\rho = \frac{|R_p|}{|R_s|} = \tan(\Psi)e^{i\Delta} \tag{2.3}$$

where ρ is referred to as the 'ellipticity'.

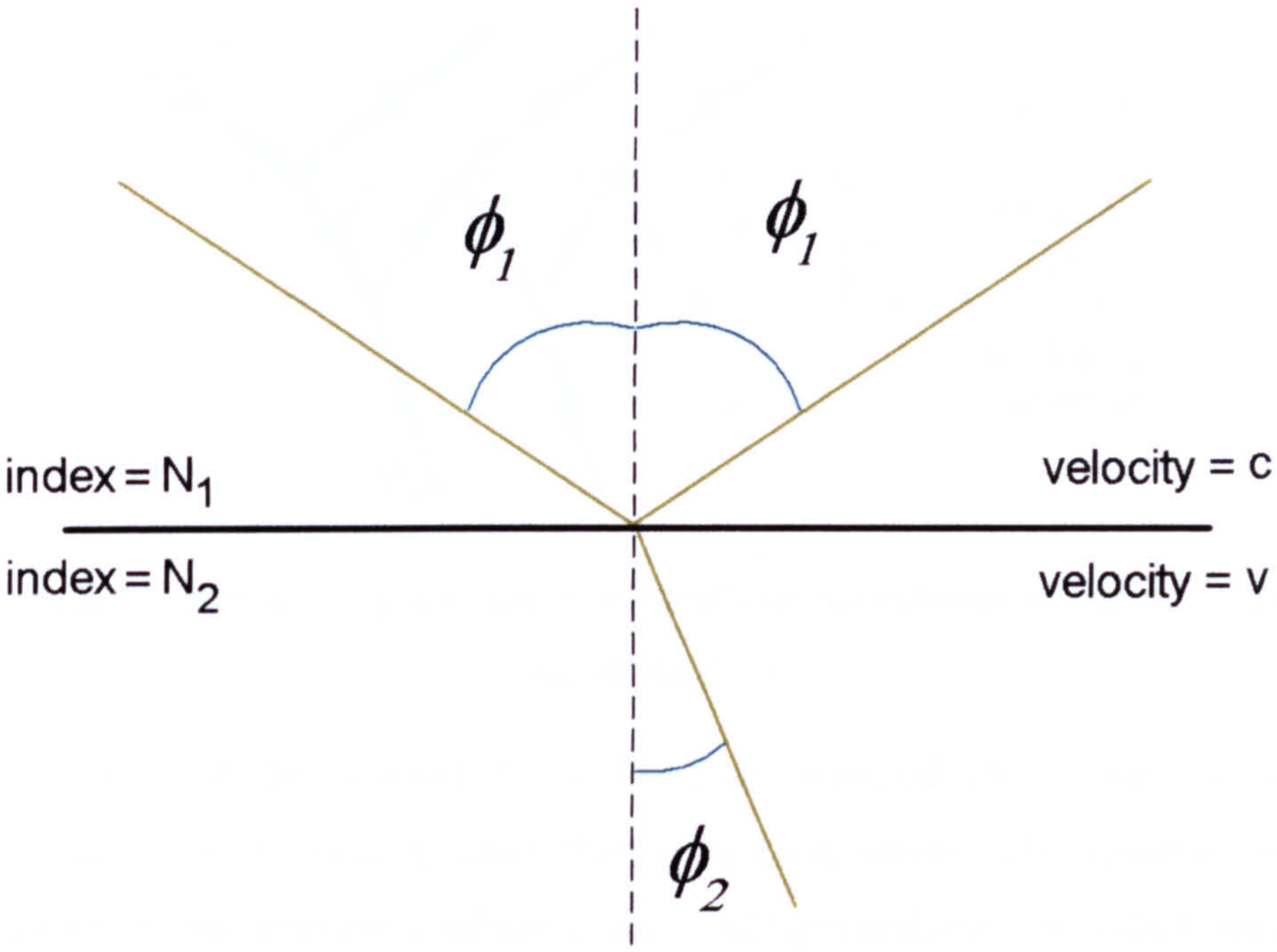

Figure 2.3 Schematic illustration of reflection and transmission of light at the interface between two semi-infinite media.

The Fresnel reflection coefficients are derived from the transmission and reflection of a monochromatic light beam (practically being a laser beam) at the interface between two semi-infinite media as illustrated in Figure 2.3, where the reflection coefficients are given by:

$$r_{p12} = \frac{(N_2 \cos\phi_1 - N_1 \cos\phi_2)}{(N_2 \cos\phi_1 + N_1 \cos\phi_2)} \tag{2.4}$$

and

$$r_{s12} = \frac{(N_1 \cos\phi_1 - N_2 \cos\phi_2)}{(N_1 \cos\phi_1 + N_2 \cos\phi_2)} \tag{2.5}$$

Light will be reflected at an angle equal to that of its incidence, hence:

$$\phi_{\text{incidence}} = \phi_{\text{reflection}} = \phi_1 \tag{2.6}$$

Also according to Snell's law

$$N_1 \sin\phi_1 = N_2 \sin\phi_2 \tag{2.7}$$

With N being the complex refractive index:

$$N = n - ik \tag{2.8}$$

where n is the index of refraction, k the extinction coefficient and i the imaginary square root of -1.[6]

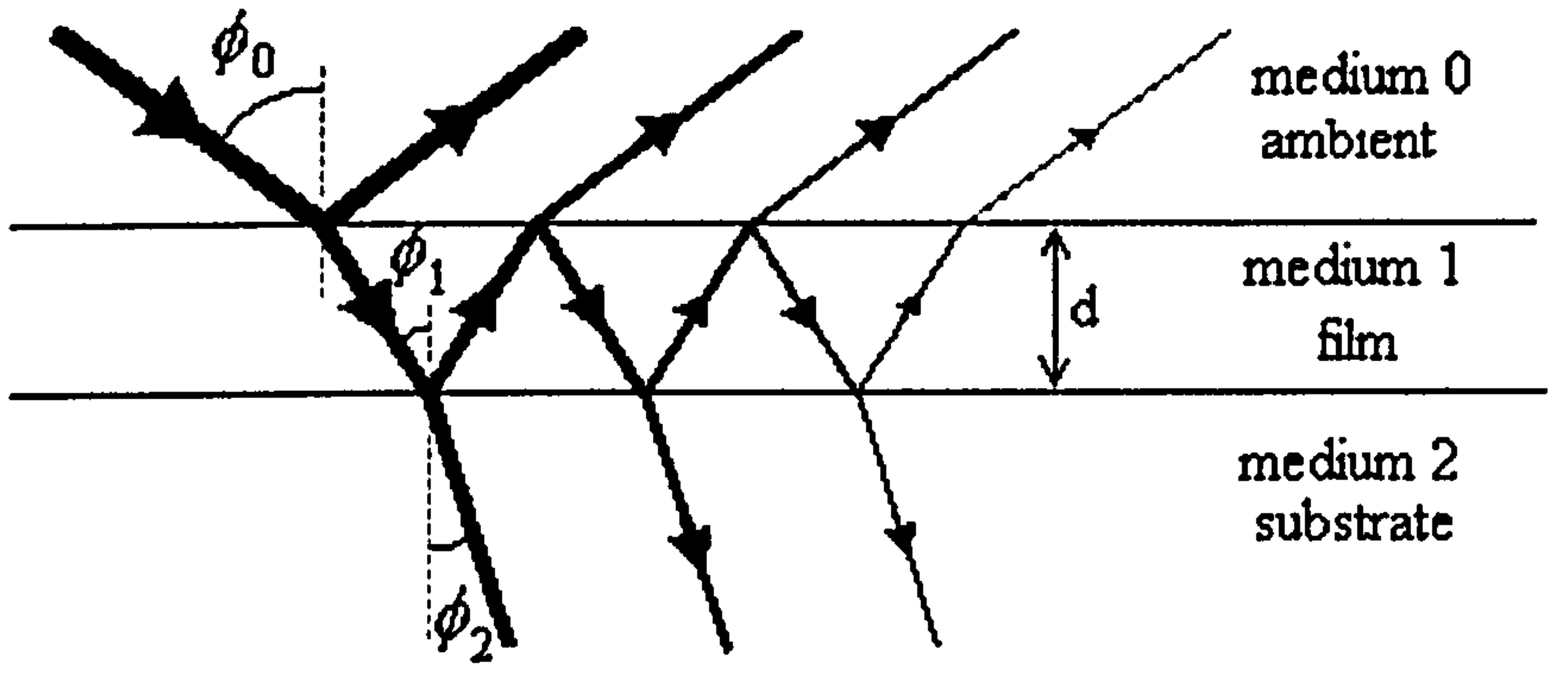

Figure 2.4 Schematic representation of multiple reflections occurring in a film covered surface.

For a substrate covered by a film, as depicted in Figure 2.4, multiple reflections occur each with its own change in polarisation. The resultant reflected light returning to the ambient medium consists of light reflected directly from the first interface plus all transmissions from light approaching the interface from the film. Due to the film having a thickness many orders of magnitude smaller than the diameter of the laser spot, the reflected beam is in fact the sum of all these reflections. The ratio of the reflection coefficients for the *p* and *s* wave is given by:

$$\frac{R_p}{R_s} = \tan\psi . e^{i\Delta} = \frac{r_{01}^p + r_{12}^p e^{-2i\delta}}{1 + r_{01}^p r_{12}^p e^{-2i\delta}} \cdot \frac{1 + r_{01}^s r_{12}^s e^{-2i\delta}}{r_{01}^s + r_{12}^s e^{-2i\delta}} \qquad (2.9)$$

where the r values on the right hand side of the equation are for the individual interfaces (01 or 12) and δ is the phase difference introduced by traversing the film at an angle of φ_1 and is a function of the film thickness and refractive index. The ellipsometer measures the parameters Ψ and Δ and it then carries out a complex computation to calculate from these the thickness and the refractive index of the thin film. These calculations can be performed by fixing the refractive index to the known value for the material of the film or by floating (varying) the refractive index and determining the thickness and the refractive index together. This 3-layer model (Figure 2.4) uses a method of computation based on the procedure of McCrackin.[7] Though, all of the systems used in this work were conventionally regarded as 3-layer model, the method can be extended to a 4-layer model as in equations 2.10 and 2.11.

$$r_{p34} = \frac{(N_4 \cos\phi_3 - N_3 \cos\phi_4)}{(N_4 \cos\phi_3 + N_3 \cos\phi_4)} \qquad (2.10)$$

$$r_{s34} = \frac{\left(\mathrm{N}_3 \cos\phi_3 - \mathrm{N}_4 \cos\phi_4\right)}{\left(\mathrm{N}_3 \cos\phi_3 + \mathrm{N}_4 \cos\phi_4\right)} \tag{2.11}$$

The 4-layer model can be used for modelling film roughness. As the chemically deposited films have a bead-like composition (see analysis in chapter 4), their top surface is never flat and parallel to that of the substrate. This can only be verified only when observed under large magnification, otherwise, they appear as totally flat to the naked eye. The film can thus be separated in two layers (Figure 2.5). The lower layer, closer to the substrate is composed of the pure material only. The upper layer starts from the appearance of the first exposed surface bits of the film to air, as we move away from the substrate. The upper layer basically includes the roughness features of the film. When modelled by ellipsometry or other optical techniques, its refractive index is taken as an effective one, varying between the values of the film's material and air. Thus, the four layer model can be used to find the thickness of the pure film layer, that of the mixed, roughness layer and also the refractive index of the roughness layer, which is directly proportional to the percentages of its constituents.

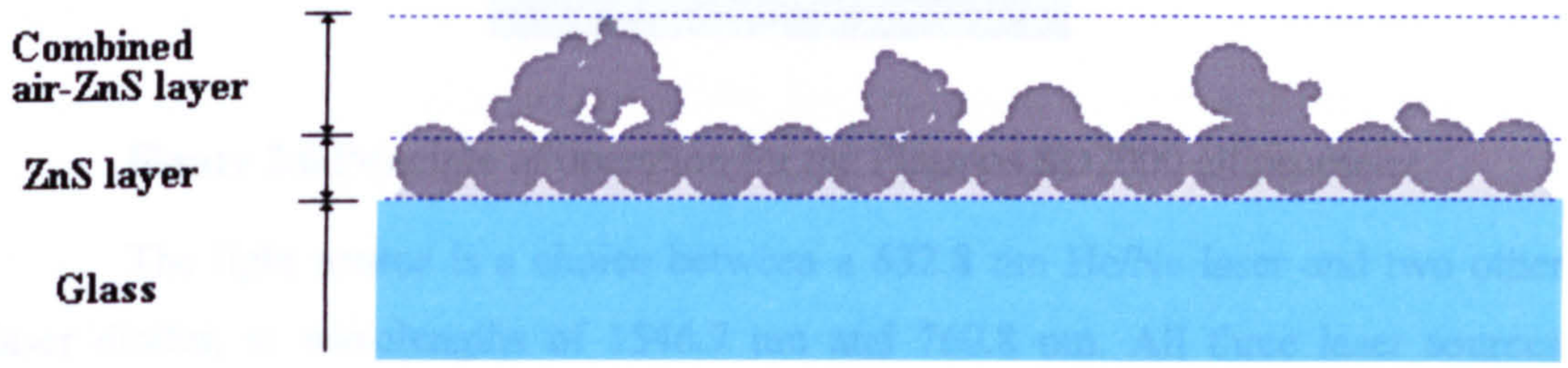

Figure 2.5 Splitting of chemically deposited film in two layers, when using the four layer model, accounting for a mixed composition of a roughness layer.

Experimental

The ellipsometer used was an SD2000 Ellipsometer manufactured by Plasmos and marketed by Philips. The schematic drawing shown in Figure 2.6 shows the principle of operation of an ellipsometer. An unpolarised and monochromatic light beam, generated by a laser, is directed through a polariser to produce linearly polarised light and then through a quarter wave plate (compensator) to obtain

circularly polarised light [6] by varying the angle of the polariser. An ideal compensator is an optical retarder that has a retardation of exactly 90^0 between the perpendicular components of the electric field of the light beam. Retarders are generally constructed from thin plates of a birefringent material or from polished crystal rhombi. The laser beam finally hits the sample surface at a well-defined angle of incidence. The beam is reflected off the layer of interest and then analysed with the analyser. In simple ellipsometers, the operator changes the angle of the polariser and analyser until a minimum signal is detected. This signal is detected if the light reflected by the sample is linearly polarised, while the analyser is set so that only light with a polarisation which is perpendicular to the plane of reflection polarisation is allowed to pass.

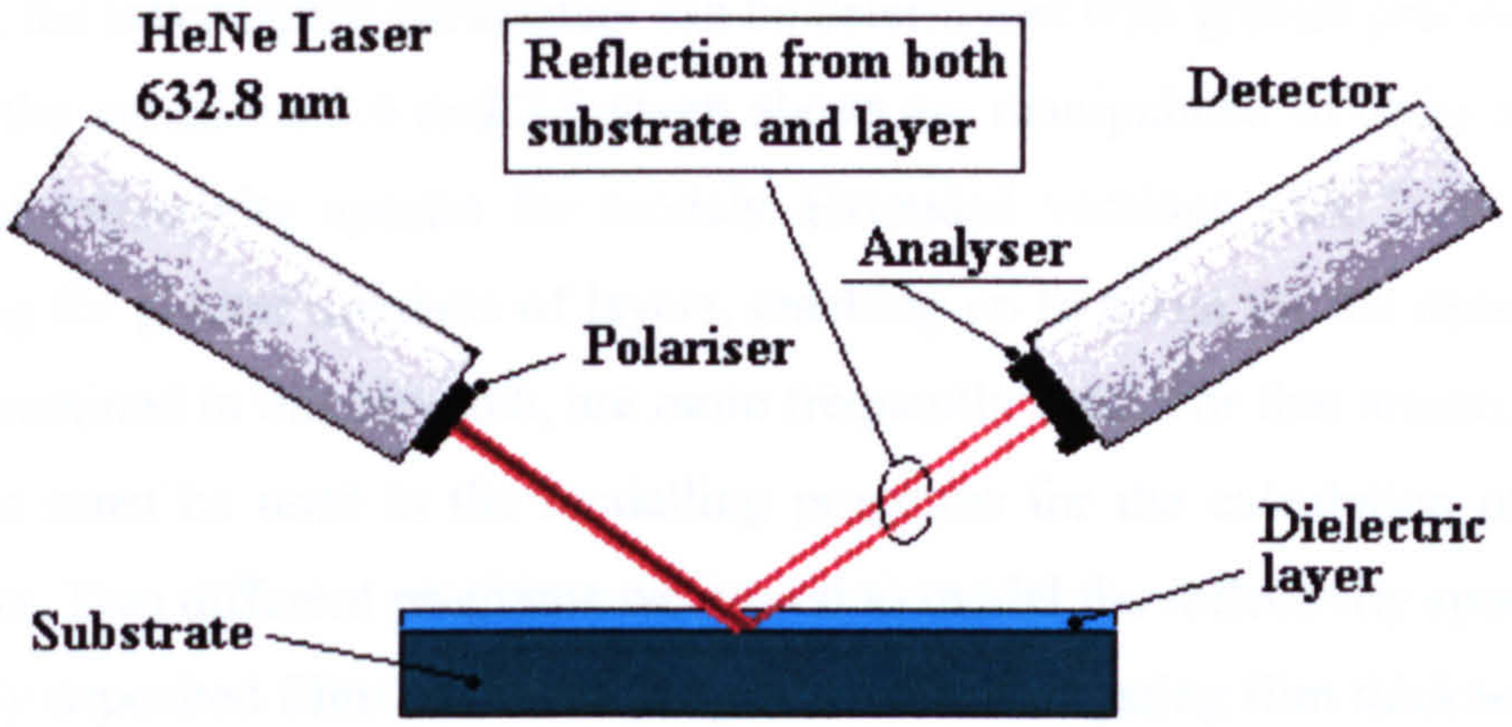

Figure 2.6 Principle of operation for the Plasmos SD2000 ellipsometer.

The light source is a choice between a 632.8 nm He/Ne laser and two other laser diodes, at wavelengths of 1546.7 nm and 760.8 nm. All three laser sources project a beam with microspot diameter 50 μm and power 1 milliwatt max/cw. The polariser is kept at a fixed azimuth angle of 45^0 to the horizontal plane. The analysis of the status of polarisation is made by a permanently rotating analyser followed by a photodetector whose sinusoidal output signal is sent to the system's computer for the calculation of the film thickness and refractive index. The polariser and analyser, of Glan-Thompson type, are made of calcite, which is a birefringent [6] material. A camera and an electrically moving stage were used to adjust the level and the sharpest image of the sample for achieving maximum intensity.

2.2.b. Fitting of reflectivity spectra in the UV-Vis

In ellipsometry, the electromagnetic wave equations are manipulated in terms of their *s* and *p* components, for a static wavelength. The reflectivity value for a static wavelength can be deduced from thickness and refractive index parameters of a film coated substrate, but the reverse is impossible, unless ellipsicity is considered. However, the reflectivity of a film covered substrate system over a range of wavelengths, forming a spectrum, is almost uniquely associated with the examined system. Thus, models of the examined system can be constructed, in which the parameters under investigation are varied. A best match is then obtained between the model generated spectrum and the experimentally acquired spectrum. Especially when spectral features related to bandgap cut-offs are included in the analysed spectrum, the investigated parameters can be determined with greater precision.

So the equations 2.4 and 2.5 given above are manipulated in order to produce theoretical reflectivity spectra for models. Extended versions (like 2.10 and 2.11) accounting for greater numbers of layers, reaching up to seven for the most complex models examined in this research, are more frequently used. For that reason, powerful algorithms must be used in the modelling programs for the calculation of required parameters. Two different programs were used to model the reflectivity spectra of the chemically deposited films. Both the programs are investigating film thickness, or two layer film thickness and refractive index for the upper, roughness layer. One uses existing data, defining the refractive index spectra of the materials included in the model and the Runge-Kutta algorithm which generates reflectivity spectra based on the differential equation of refractive index and layer thickness data, through a series of repetitive iterations.[8-11] The theoretical and experimental spectra of reflectivity are then compared on a least square of sums basis. As the refractive index spectrum of the roughness layer is not readily available, a combination of the refractive indices of the film and air is calculated and the percentage of participation of each substance is modelled for. The Runge-Kutta based, modelling program was written in Fortran and runs in a UNIX environment supported by a SUN network server.

A more powerful optimisation algorithm called simulated annealing is able to handle variations of a larger number of modelling parameters.[12] Therefore, the experimentally recorded spectra can be modelled for both film thickness and refractive index. The algorithm is much more demanding in terms of computer

processing power, but the evolution in PC, main processor technology allows for relatively fast execution of such an algorithm. The program runs in an MS-DOS environment of a modern PC system. A simulated annealing optimisation method will accept variable changes that reduce the sum of squares, or satisfy a probability criterion, in a similar manner to the rearrangement of atoms in a crystal during annealing. The technique is hence designed to avoid local minima in a multidimensional (holding a multitude of variables) optimisation process.

The reflectivity of the deposited films in the visible spectrum was measured for all the samples of the temperature and acidity variation tests. An Ocean Optics s2000 spectrometer was used for the measurements. A configuration like the one illustrated in Figure 2.7 was employed. A tungsten or deuterium lamp generated Visible or UV light respectively. The lamps were enclosed in metal cases that restricted any interference by ambient light. The UV or visible light was passed from the lamps to the surface of the samples via multiple optical fibres. The reflected light was collected by another optical fibre and directed to the spectrometer, which is controlled by computer software. The software was responsible for processing, storing and displaying the spectrum taken.

Another software program written in Fortran and running under a UNIX environment was used for the calculation of reflectivity. It was based on the reflection of light from the same source, by a polished smooth surface of a silicon wafer. The samples are modelled by either of the optimisation techniques as 3 layer or 5 layer systems (or 5 and 7 layer systems respectively when the surrounding air is taken into account), depending on whether film covers one or both sides of the glass slide. Shell batch command scripts were also written, feeding a large number of reflectivity spectra, data files automatically in the model-fitting programs and organising the output data. Any file that produced incomprehensible data was handled alone, manually, by changing the generalised modelling parameters of the data file batch to more appropriate ones for the specific sample.

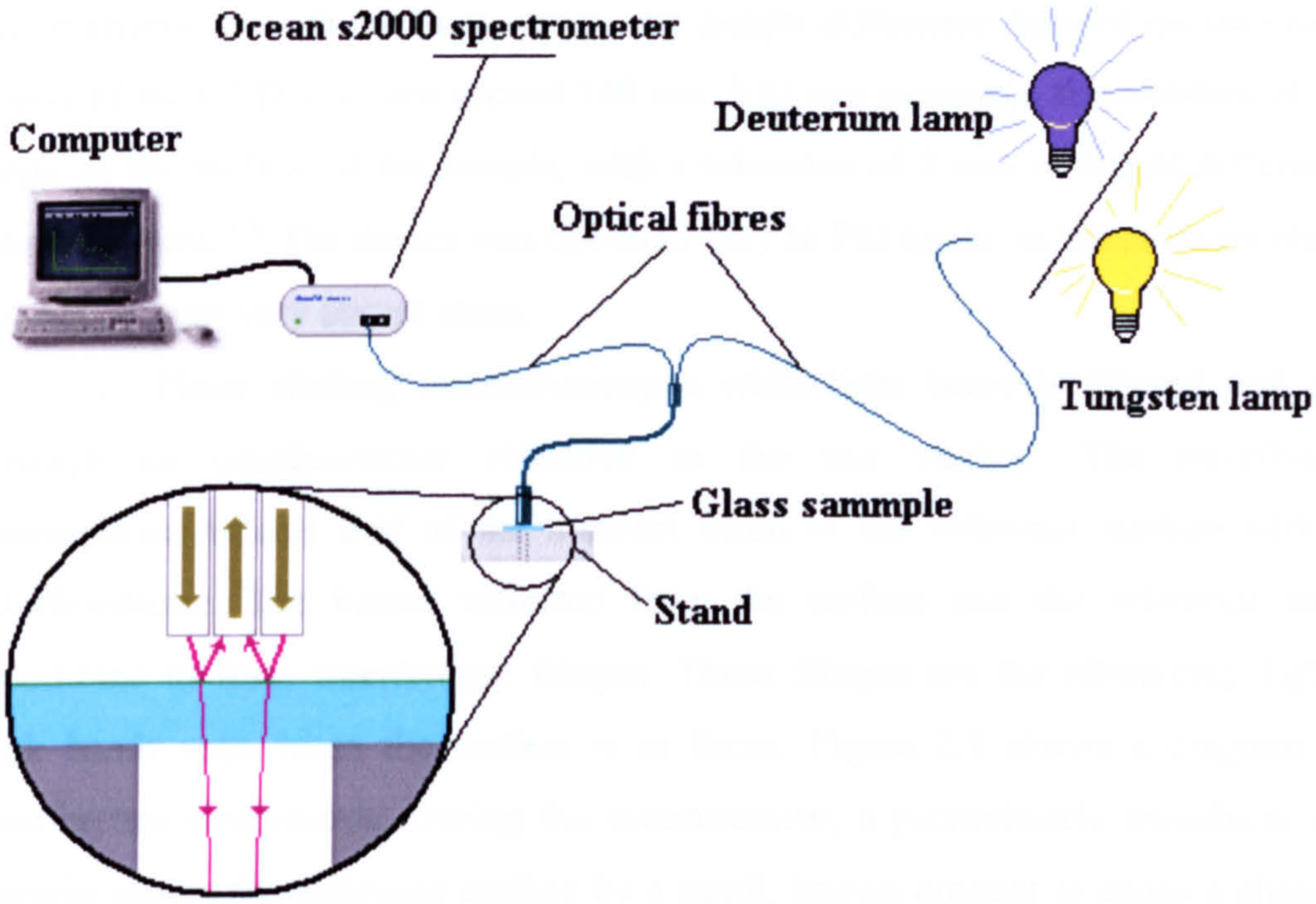

Figure 2.7 Apparatus configuration for obtaining reflectivity data.

2.3 Surface profiling by Interference Microscopy (Interferometry surface profiling)

Interference microscopy combines an interferometer affected by surface formations of the sample under inspection with focussing optics.[13] An interferometer works on the principle that two waves that coincide with the same phase will add to each other while two waves that have opposite phases will cancel each other out, assuming both have the same amplitude. A typical interference pattern can be obtained by splitting a beam of light in two, passing each component through different length optical paths and then recombining them. The interference pattern can be analysed in terms of the phase difference between the two components and thus the difference in the optical paths can be found.[14] The most common type of interferometer used in conjunction with micrometry is a Mirau interferometer.[15] Due to the very small wavelength of visible light, interference patterns can be obtained from changes of the optical path in the scale of nanometers.[16]

A WYKO NT1100 surface profiler by Veeco Metrology Group was used to obtain the surface profiles examined in this work. It operates in two modes, Phase-shifting interferometry (PSI) and vertical scanning interferometry (VSI). PSI is used

for relatively smooth surfaces, where the height difference imaged on two adjacent points of the CCD does not exceed 160 nm. VSI can overcome the problem of abrupt steps on the surface of the sample, with a tolerance of 2 mm of height difference on adjacent point.[17] The device was operated only in PSI mode, as the surfaces observed did not contain very abrupt steps.

In Phase shifting interferometry a white-light beam is filtered and passed through an interferometer objective to the test surface. The interferometer beamsplitter reflects half of the incident beam to the reference surface within the interferometer. The beams reflected from the surface and the reference surface, recombine to form interference fringes. These fringes are the alternating light and dark bands seen when the surface is in focus. Figure 2.8 shows a diagram of an interference microscope. During the measurement, a piezoelectric transducer (PZT) linearly moves the reference surface by a small, known amount to cause a phase shift between the test and the reference beam. The system records the intensity of the resulting interference pattern at many different relative phase shifts and then converts the intensity to wavefront (phase) data by integrating the intensity data. The phase data are processed to remove phase ambiguities between adjacent pixels and the relative surface height can be calculated from the phase data by the following equation:

$$h(x,y) = \lambda \cdot \varphi(x,y) / 4\pi \qquad (2.10)$$

where λ is the wavelength of the source beam and $\varphi(x,y)$ is the phase data.[15, 17]

This technique for resolving surface heights is reliable when the fringe pattern is sufficiently sampled. When the surface-height difference between adjacent measurement points is greater than $\lambda/4$, height errors in multiples of $\lambda/2$ may be introduced and the wavefront cannot be reliably reconstructed. Thus, conventional phase-shifting interferometry is limited to fairly smooth, continuous surfaces. The light for both techniques originates from a white-light source. In the PSI mode, however, it is filtered to produce red light at a nominal wavelength of 632 nm and thus the tolerance of 160 nm abrupt height differences is obtained.[18]

Moreover, the detector depends on the light intensity difference between the pixels in order to find the phase difference. Materials with large reflectivity in the visible part of the spectrum and most importantly around 632 nm for PSI, are easier to examine. Also, surfaces that include two materials with a large difference in their

refractive index over the red part of the spectrum, will most likely give erroneous readings. The difference in refractive index will manifest as a difference in the reflectivity of the two materials. Hence, even if the surface is completely flat, the increase or decrease of reflected light intensity due to the equivalent change of refractive index between the two materials, will be interpreted as a phase difference and therefore a height difference between them. Even if there is a height difference between the two different reflectivity surfaces, the height difference can be misinterpreted due to this effect.[14, 19]

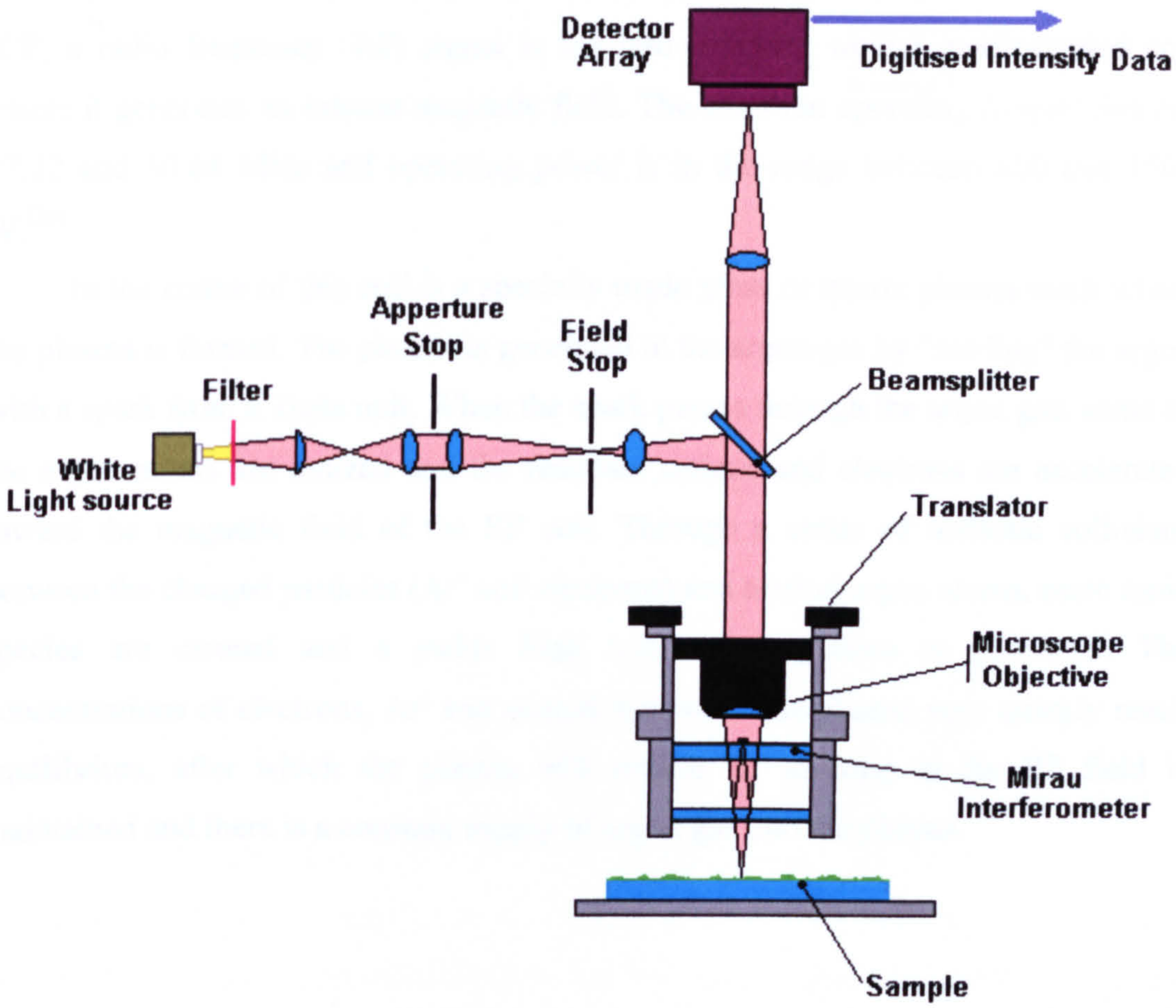

Figure 2.8 Schematic of interference microscope.[17]

2.4 Inductively Coupled Plasma based spectroscopic methods

2.4.a. Theory

Inductively coupled plasma is a high temperature plasma sustained with a radiofrequency electric current, which acts to produce ions in a stream of fast flowing gas. It is a very efficient method of producing ions and at the same time a very aggressive one.[20, 21] Because the source operates at temperatures of 5000 to 10000 K, virtually all molecules in a sample are broken up into their component atoms.[22] In ICP, a radio frequency (RF) signal is fed into a tightly wound, water-cooled coil where it generates an intense magnetic field. The common operating frequencies are 27.12 and 40.68 MHz and operating power is in the range between 800 and 1500 W.[23]

In the centre of this coil is a specially made glass or quartz plasma torch where the plasma is formed. The plasma is generated in the argon gas by "seeding" the argon with a spark from a Tesla unit. When the spark passes through the argon gas, some of the argon atoms are ionized and the resultant cations and electrons are accelerated toward the magnetic field of the RF coil. Through a series of inelastic collisions between the charged particles (Ar^+ and electrons) and neutral argon atoms, more ionic species are created and a stable high temperature plasma is generated. The concentrations of electrons, Ar^+ and neutral species in the plasma very quickly reach equilibrium, after which the plasma will remain 'lit' as long as the RF field is maintained and there is a constant supply of argon gas into the plasma.

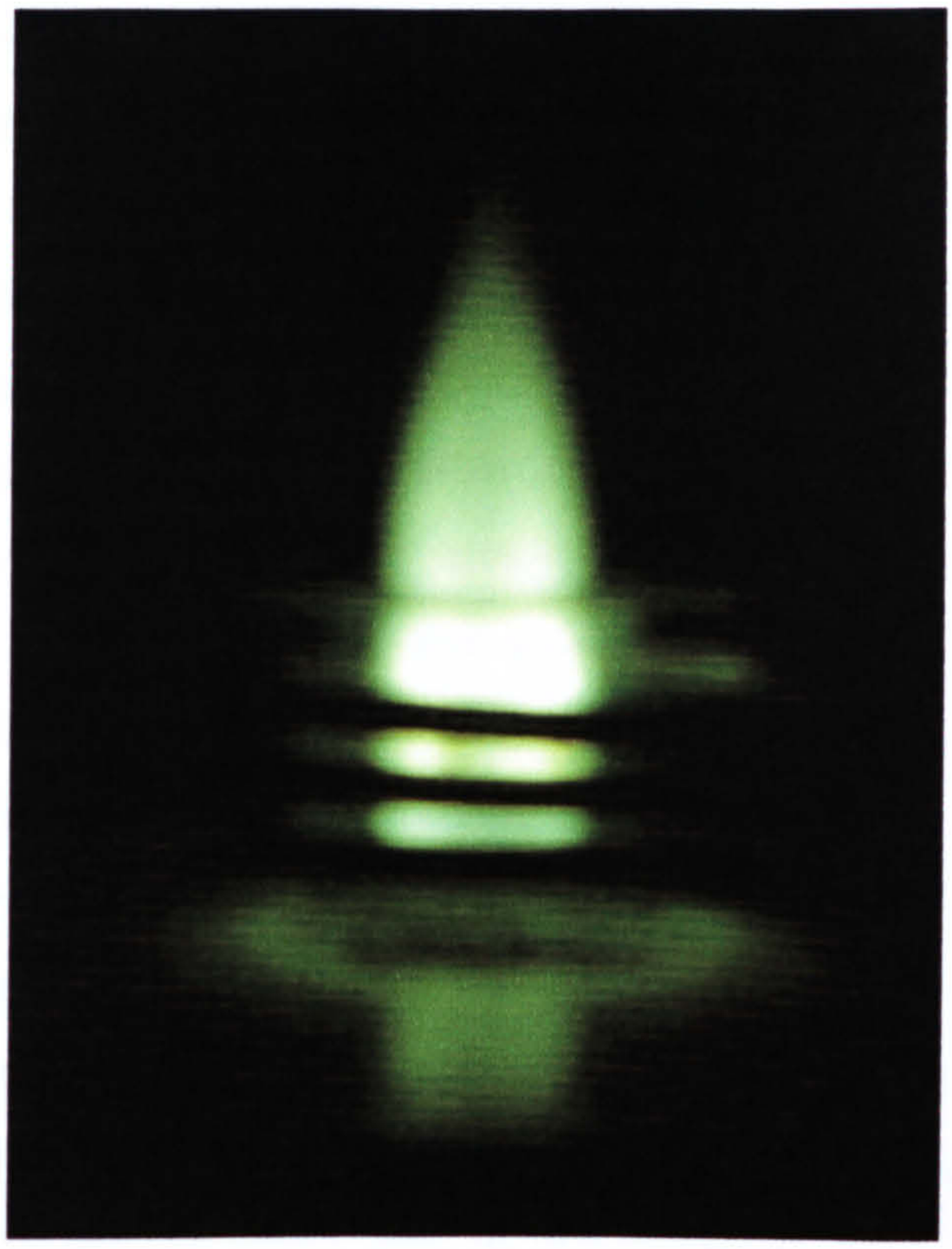

Figure 2.9 Photograph of a green inductively couple plasma. The rf coil is visible as shadows in front of the plasma.

To prevent melting of the torch a high flow rate of argon is used in the outermost tubing. The total gas consumption of a typical analytical ICP is in the range of 14 - 18 L/min. In order to reduce capacititive coupling between the coil and plasma, some designs employ an additional metal sheet between the torch body and the induction coil. Also, the plasma torch is designed in such a way as to allow a sample to be injected directly into the heart of the plasma. The sample consists of a fine aerosol, which can come from any number of sources including, but not limited to, nebulized liquids and ablated solids. As the sample aerosol passes through the plasma, it collides with free electrons, argon cations and neutral argon atoms. The result is that any molecules initially present in the aerosol are quickly and completely broken down to charged atoms. These are usually in the M^+ state although a few M^{++} are also formed. Some of these charged atoms will recombine with other species in the plasma to create both stable and meta-stable molecular species (e.g. MAr^+, M_2^+, MO^+, etc.). Many of these molecular species will be positively charged and will also be transmitted into the mass analyzer along with the charged atoms (M^+ and M^{++}).[23]

After creating the ions, there are two main roots of sample analysis that can be followed. One is Atomic Emission Spectrometry (or Optical Emission Spectrometry) and the other is Mass Spectrometry.[24] In atomic emission spectrometry (abbreviated as ICP-AES or ICP-OES), the emitted radiation from the plasma is analysed in terms of emitted photon energy by a diffraction grating and photomultiplier arrangement. The photomultiplier is also comparing between different amounts of energy emitted over the spectrum. As specific spectra correspond to specific ionised element recombinations, it is possible to detect and quantify the elements present in the injected sample solution. For the case of mass spectrometry (abbreviated as ICP-MS), the ions are passed through a series of depressurising cones, into a mass spectrometer. The mass spectrometer types that are often used are the quadrupole analyser and the electrostatic and magnetic combination of analysers. Both types of mass spectrometers will analyse the species based on their mass to electric charge ratio.[24] The mass spectrometry technique is a much more sensitive quantitative and qualitative analytical technique, being able to detect certain species at a part per quadrillion level.[23]

2.4.b. Experimental

The experimental procedures described below were carried out by Bob Knight, who then composed a summarising report of the results and analysis.

Main component element analysis by ICP-AES

The sample was the chemically deposited film on the surface of a quartz substrate. The weight was recorded, then 1 ml nitric acid (Romil SpA grade) was added and flushed across both sides of the glass and the film was dissolved. There were no apparent bubbles of gas evolved, which would have been SO_2. The acid was then diluted to 10ml in a volumetric flask, making sure all the glassware was efficiently rinsed. The dry glass plate was weighed dry to enable the film weight to be determined.

The elements of interest were S, Zn, Cd, Ag. Their concentrations were measure on the Perkin Elmer Optima 5300DV emission ICP instrument. After an initial experiment to determine the analysis conditions, the Zn, Cd and S were analysed in radial view while the silver was measured in the more sensitive axial view

mode. The elements were calibrated to 20 ppm and the 8 point calibration lines were acceptably linear and a 10 ppm calibration check solution gave acceptable values. Each measurement was made in 3 replicates to enable a 3σ detection limit to be determined. Each element was measured at two emission wavelengths which agreed well in all cases, which indicates that the wavelengths used were nearly interference free.

Trace metal element analysis by ICP-MS

The 10 ml digest of the film was analysed for all metals in a qualitative way on the Perkin Elmer Elan DRCII ICPMS instrument. The totalquant method was calibrated using 1 ppb Mg, In, Ce, 10 ppb Ba and a blank to calibrate the mass response and 10 ppb Ga, Rh, Ho, Bi, as the internal standard. The results presented later on in chapter 3, are for the elements which showed significant amounts of metals above the blank 2% nitric acid. There is a discrepancy between these results and the emission ICP values for the major metals. The ICP-MS is more sensitive to trace metal constitution, so the major metal concentrations are most likely detected in error here, mainly because of counting statistics at high intensity and the elements were not quantitatively calibrated. Therefore, the emission ICP result should be used for the major elements, while the ICP-MS for trace elements. Any elements not listed or mentioned in Chapter 3 were not present.

2.5 Extended X-ray Absorption Fine Structure (EXAFS)

Apart from defining which atoms constitute an investigated material, it is also of great importance to determine the position of those atoms with respect to each other in the material's structure. X-rays can be exploited in order to extract such information from a sample and one such technique with a wide range of applications is known as Extended X-ray Absorption Fine Structure (abbreviated as EXAFS). The technique is a type of X-Ray Absorption Spectroscopy (XAS), as a spectrum of photon energies is examined. The idea behind EXAFS lies in the ability of X-ray photons to interact with core electrons in an atom and force their ejection from the atom. This interaction comprises the main process of X-ray absorption in the energy range between 0.2 to 35 keV.[25] The technique can return element specific

information for almost every material of interest. However, a greater emphasis is given on the investigation of heavier elements in a material.[26, 27]

A beam of X-rays is directed towards the sample. The wavelength of the beam is controlled by monochromating crystals. The photon energy of the beam is gradually increased, traversing an absorption edge of the element under investigation. Below the absorption edge, the photons cannot excite the electrons of the relevant atomic level in the element and thus absorption is low. However, when the photon energy is just sufficient to promote the electrons to the continuum, then a large increase in absorption occurs appearing as an abrupt edge on the absorption spectrum, hence it is called the absorption edge. The energy of the ejected photoelectron is that of the impinging photon minus its binding energy as a core electron. At the part of the spectrum that lies just after the absorption edge, the photoelectron will be of rather low energy and thus it can be backscattered by the atoms surrounding the emitting atom.[25, 28, 29] The photoelectron is emitted radially in a wavelike manner (Figure 2.10) and hence its energy and therefore the energy of the absorbed X-ray photon, will affect its phase and amplitude when backscattered from the surrounding atoms to the origin atom. The emitted and backscattered photoelectrons will interfere at the origin point and so this interference modulates the absorption cross section, thus creating an oscillating trail on the recorded absorption spectrum following the absorption edge. As the phase and amplitude of the backscattered photoelectron will also be affected by the distance of the surrounding atoms from the emitting one and also their elemental characteristics, so will the oscillations in the spectrum. These oscillations can be used to determine the atomic number, distance and coordination number of the atoms surrounding the element whose absorption edge is being examined.[26, 27, 30]

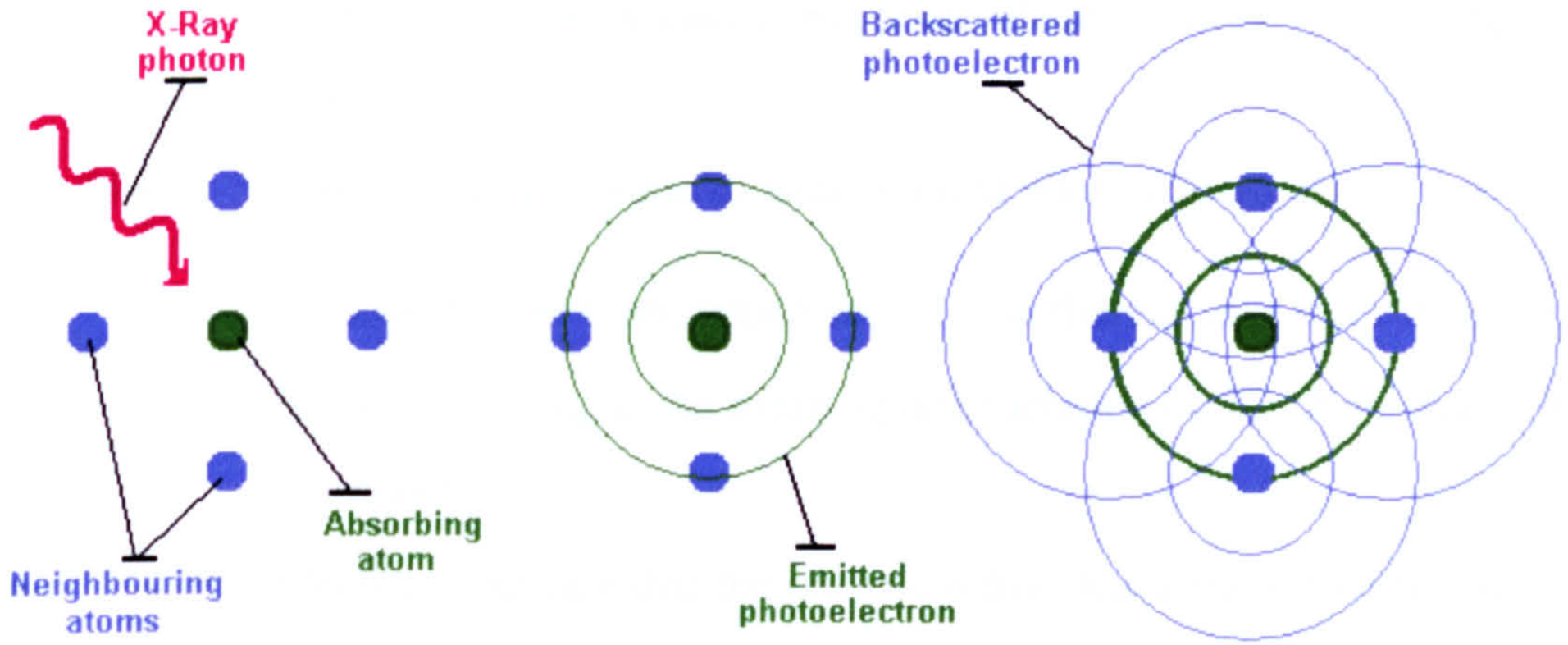

Figure 2.10 Schematic of absorption of X-ray photon by core electron in the absorbing atom, resulting radial emission of photoelectron and backscattering of photoelectron by neighbouring atoms.[27, 31]

A simplified model of the backscattered photoelectron as it appears in the post-edge part of the spectrum is given by equation 2.11 below.[32] The spectrum is recorded with respect to the photoelectron wave vector *k*. This equation was developed to express the backscattering in two dimensions only, as a plane wave approximation. However, it gives a good idea of the parameters involved in the EXAFS analysis. In practice, a spherical wave equation[33] is manipulated by computer software to deduce the parameters of interest with greater accuracy.

$$\chi(k) = -S_o^2 \sum_s \left[\left(\frac{N_s}{kR_{as}^2} \right) \cdot \left| F_s(\pi, k) \right| \cdot \exp^{\left(-2k^2\sigma_{as}^2\right)} \cdot \exp^{\left(-2R_{as}/\lambda(k)\right)} \cdot \sin\left(2kR_{as} + 2\delta_a + \alpha_s\right) \right] \tag{2.11}$$

Where:

N_s = Number of equivalent scatterers (ie same atom types at same distance)

k = photo-electron wavevector = $\sqrt{\left[\left(2m_e/\hbar^2\right)\left(E - E_0\right)\right]}$

R_{as} = distance between the absorbing and backscattering atoms.

$2\delta_a$ = phaseshift experienced by photo-electron on leaving and re-entering the absorbing atom a.

α_s = phaseshift experienced by photo-electron when backscattered by scattering atom s.

$|F_s(\pi,k)|$ = amplitude and phase of back scatterd photo-electron at given k.

$\exp^{(-2k^2\sigma_{as}^2)}$ = Debye-Waller term, which models the thermal and static disorder in the system, ie σ_{as} is the mean square variation of R_{as}. Note that it is k dependent.

$\exp^{(-2R_{as}/\lambda(k))}$ = Reflects the fact that the photo-electron has a finite lifetime, ie $\lambda(k)$ is the electron mean free path, which is typically 10 Å at 100-1000 eV.

S_o^2 = This is known as the shake up and shake off factor and is used to take account of the fact that not all the photoelectrons participate in the EXAFS. Usually set at 70-80%.

The ripples and oscillations that occur after the absorption edge can also be observed as a fluorescence spectrum. If the surface of the sample is turned at an angle (in the current experiments 45^0) to the X-ray beam, a fluorescence spectrum with similar characteristics can be recorded. This variation of the technique is mostly employed when the experiment focuses on the surface of the sample. Samples comprised of thin films on a substrate as in the case of the present research, are ideally investigated under fluorescence mode, as the signal reflected towards the detector contains information more relevant to the reflecting/fluorescing surface, than the carrying thick substrate. The method is also very useful for dilute systems, where the absorption edge step would be very small to be observed or analysed when monitoring the transmitted beam, while it is possible to discriminate between the fluorescence and unwanted, scattered signal from the background.[27]

As the photon energy in the X-ray beam needs to be swept along the absorption edge, an ideal source of radiation is a synchrotron ring.[30] The synchrotron facilities at Daresbury Laboratories were used to conduct the EXAFS experiments in this research. More specifically, station 7.1 was considered the most suitable for the investigation of manganese, copper, cobalt, nickel and zinc K-edges, residing between the 4 to 12 keV spectroscopic range of the station. The station obtains its beam from a 1.2 Tesla bending magnet. The beam then is collimated vertically by a platinum coated plane mirror. A servo driven, water cooled, double crystal Si(111)

monochromator is then used for harmonic rejection. Sagittal horizontal focussing is possible by a second monochromating crystal. Focussing achieves a high flux of radiation through the sample, enabling the investigation of dilute systems.[34]

Though measurements in transmission mode were attempted, acquisition in fluorescence mode gave more reliable results, as the samples were thin films. For acquisition of fluorescence spectra, the beam strength was measured using an ion chamber before interacting with the sample and the fluorescence signal was collected by a 9 element, liquid nitrogen cooled, monolithic germanium detector. The ion chamber consists of two metallic plates with a potential difference of 600 V induced between them by an Ortec 456 HT supply. The chamber is filled with Ar as the active gas, which is ionized by the X-ray photons and and is then attracted by the plates. The current between the plates is amplified by a Keithley 427 current amplifier. This amplified signal is fed to a voltage-to-frequency converter, whose digital output is sent to a scalar counter read by the station computer. The solid state detector is coupled with computer controlled XPRESS electronics which help to synchronise the signal detection and distinguish the fluorescence signal from the total scattered radiation.[34]

The absorption edge spectra were passed through a series of specialised software in order to be brought to an acceptable form and be analysed. The program PAXAS is used to calibrate the spectrum by converting the millidegree units defining the monochromator's position to energy units and dividing the signal reading by the reference one for obtaining the fluorescence spectrum (essentially generating an I_f/I_o graph against energy in eV). Subtraction of the background curves in the pre- and post-edge parts of the spectrum is performed again with the aid of the PAXAS program using quadratic and high order polynomials respectively. Finally the remaining EXAFS oscillations are fitted and analysed by the EXCURV98 program, using tabulated values for the first maximum and the first derivative spectra of the appropriate metal foil. All software is operating in a UNIX environment and was accessed on a network server computer XRSSERV1, devoted for handling data for X-ray spectroscopy experiments performed at Daresbury Laboratories. The data collected, were processed and analysed by Dr. Nigel Young, being one of the two supervisors of this research and an expert in the field of EXAFS.

2.6 X-ray Diffraction (XRD)

The orientation of atoms in a crystalline sample can also be determined by another X-ray related method, called X-ray diffraction (often abbreviated as XRD). In XRD, a diffraction pattern is examined, rather than a spectroscopic pattern. The method is not element specific like EXAFS, in addition it is sensitive to a relatively long range order within the material,[35] while EXAFS only requires a repeatable orientation in short range, around the targeted element. Moreover, X-ray diffraction is generally performed on materials in their solid phase, either as monocrystaline or polycrystalline and also as ground powder diffraction.[36, 37]

The material characterisation and analysis is based on Bragg's law of diffraction, which was developed to explain why the cleavage faces of crystals appear to reflect X-ray beams at certain angles of incidence. The basic idea was developed to describe two parallel and coherent beams travelling close to each other and being reflected by two parallel planes with a distance d between them (Figure 2.11). The beam that meets the first plane is deflected at an angle θ (theta), from the normal axis to the plane, which is equal to the angle of incidence, again measured from the normal to the plane. The beam deflected from the second plane will have to travel a further distance equal to $\sin\theta \cdot d$ and will combine in constructive interference with the first beam, only if that extra distance is an integral multiple of the wavelength of the beams.[35] In crystals, the atoms are arranged in a repetitive manner and the smallest repeated block is called a cell, with atoms situated on its edges. As the X-ray photons will interact and deflect from the electron cloud around the atoms, the planes defined by the atoms on the cells are equivalent to the ones in the simple model described earlier. So every crystalline material, based on the distances between the atoms in its lattice and their orientation in the cell, will diffract a certain wavelength of X-rays at specific angles.[38]

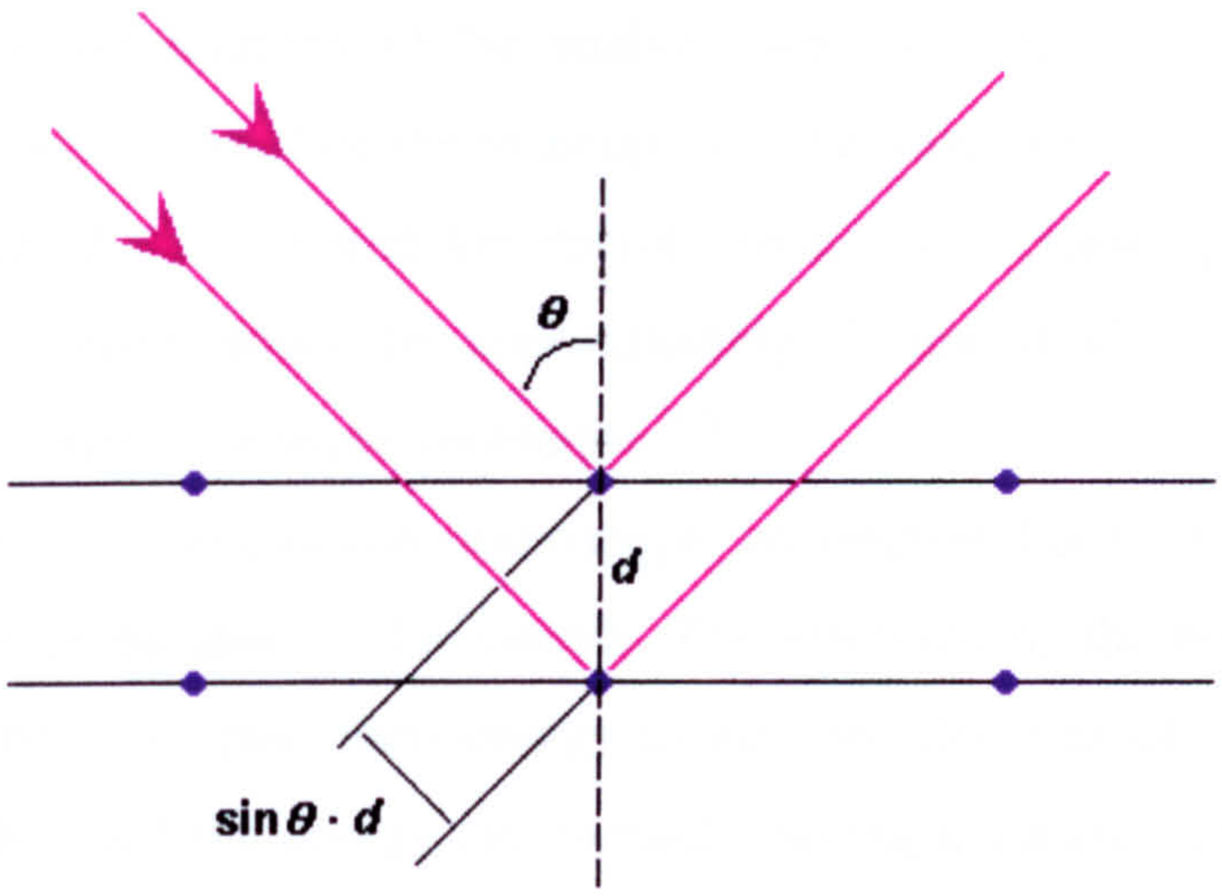

Figure 2.11 Rays of coherent radiation being deflected by atoms on two planes, defined by the crystal lattice cells.[35]

The device employed to determine at which angles a sample diffracts X-rays is called an X-ray diffractometer and the design is based on a goniometer. A source producing a coherent, monochromatic beam of X-ray photons is kept stable, directing the beam towards the sample, which is situated at the centre of the device. The sample is then tilted at an angle θ and the detector at $2\cdot\theta$, both with respect to the incident beam. Thus, the diffractogram recorded, contains characteristic peaks of the structure of the material, while their heights depend on the elements included in the crystal lattice and the alignment uniformity of the crystallites in the examined sample.[39, 40] The detector used to record the diffractograms in this work was a Siemens D500 X-ray diffractometer, which was operated by Veronica Hewer.

2.7 Energy Dispersive X-ray analysis (EDX)

Another spectroscopic analysis technique that was used in this work and is based on X-rays is Energy Dispersive X-ray analysis (abbreviated as EDX analysis and sometimes as EDS standing for Energy Dispersive Spectroscopy). EDX is an elemental analysis technique, i.e. it is used to identify the elements that comprise the sample.[41] It uses the ability of an X-ray or electron beam to interact with the core electrons of an atom and identifies the atom by the element specific radiation that is emitted from this interaction. Its relation with the electron beam excitation has

conveniently allowed coupling of the analyser with an electron microscope of the SEM or TEM type.[42] Therefore the technique can be used over a relatively wide area or an easily selected small area in the micron scale. The increased penetration depth of the electron beam down to approximately 2 μm hinders the technique's classification as a surface analysis technique.[43]

When used with an electron microscope, an electron beam of 10 to 20 keV is focussed on a selected area of the sample. The electrons of the beam collide with atoms in the sample and pass their energy to the core electrons of those atoms. The electrons that absorbed the energy are ejected, leaving a vacancy in the electronics structure of the atom. An electron from an outer, higher energy shell drops to fill the vacancy and the energy difference is emitted as an X-ray photon (Figure 2.12). The energy carried by the emitted photons is characteristic of the electronic transitions happening in an element due to its excitation by the electron beam.[25] Thus the elements contained in the selected area can be identified by careful analysis of the detected X-ray photon energies. The spectrum analysed ranges from photon energies of 0.1 to 20 keV, but more typically lies between 0.5 and 10 keV.[42]

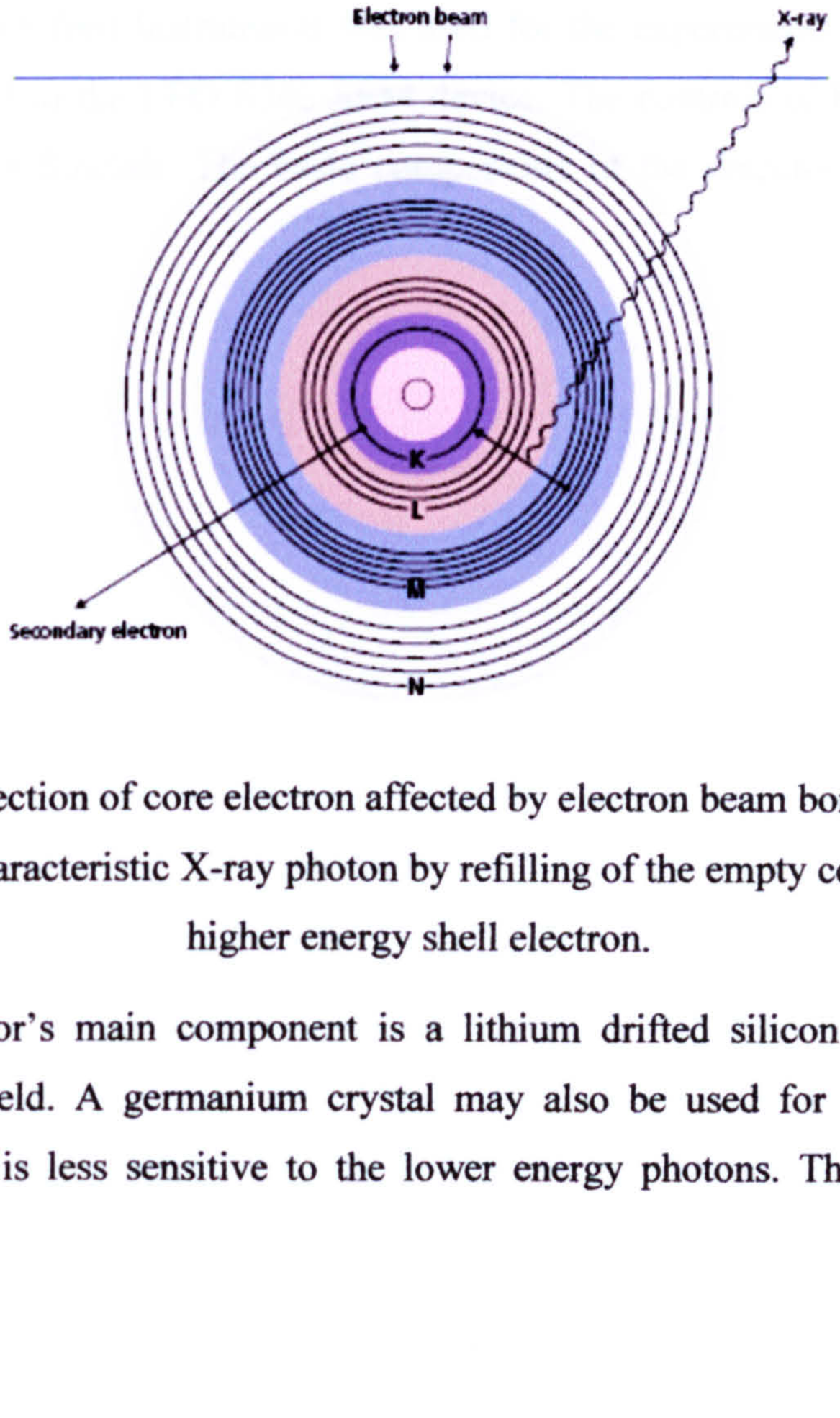

Figure 2.12 Ejection of core electron affected by electron beam bombardment and emission of characteristic X-ray photon by refilling of the empty core orbit with a higher energy shell electron.

The detector's main component is a lithium drifted silicon crystal inside a strong electric field. A germanium crystal may also be used for its higher purity attributes, but it is less sensitive to the lower energy photons. The X-ray photons

promote electrons of the silicon semiconductor to the conduction band, which are accelerated by the strong electric field towards the positive electrode and depending on their initial energy, acquired by the X-ray photon, they will inflict excitation of even more electrons in the semiconductor. Therefore, the number of electrons reaching the positive electrode will correspond to the energy of the detected photon. The charge raised at the electrode is then converted into voltage difference by a field effect transistor. Both the transistor and the crystal detector are operated at very low temperatures, usually achieved by mounting them on a liquid nitrogen cooled finger. The reason for low temperature operation arises from the need to avoid thermal noise on the semiconductor devices. The devices are also kept in ultra high vacuum, with a beryllium or thin polymer window standing between the detector crystal and the sample chamber. A strong magnetic ring is often employed before the window as an electron trap, diffracting any scattered electrons that are travelling towards the detector and will undoubtedly affect its reading. The aperture allowed by the magnet or its holder also imposes an area targeting effect, thus forbidding any X-rays emitted by the surroundings of the sample to enter the detector.[44] An OX200 EDX spectrometer by Oxford Instruments was used for the experiments performed in this research, attached to the LEO S360 SEM device. The controls of both devices were operated by Tony Sinclair. The basic components of the detector are illustrated in Figure 2.13.

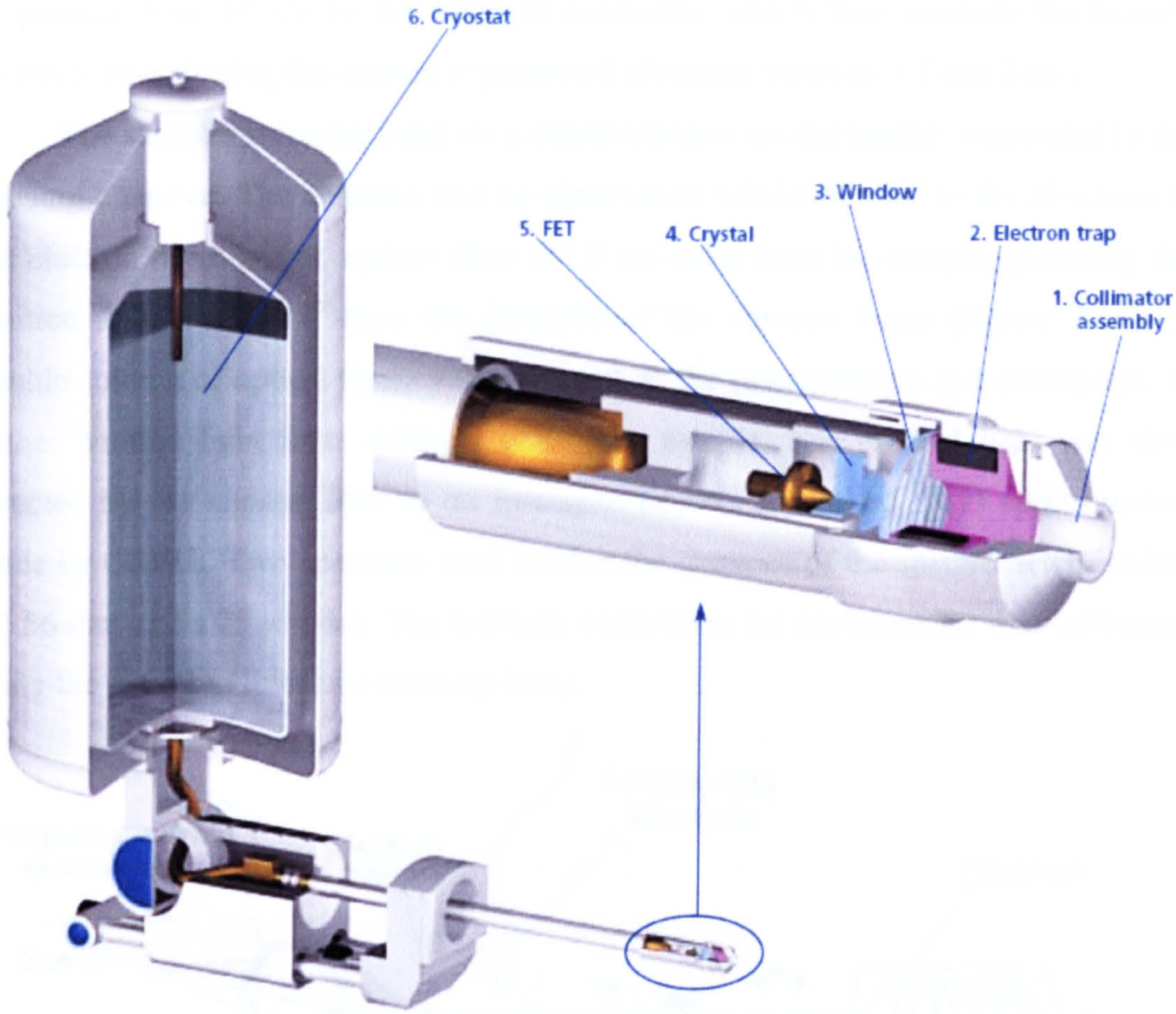

Figure 2.13 Oxford Instruments EDX analyses detector, cut-out schematic of it's main components. [44]

2.8 Experimental investigation of Cathodo-luminescence

As it was mentioned in section 1.1.a and 1.1.b, phosphor materials, whether in layer or in bulk, can be excited by a cathodic ray (otherwise referred to as an electron beam) and emit in their characteristic bands.[45] The process is called cathodoluminescence and it is equivalent in principle to a cathode ray tube (or Brown tube) used in CRT display devices.[46-48] A heated filament is used to produce the electrons, which are accelerated, focused and guided by electric and magnetic fields. The electron beam travels from the filament to the samples through vacuum. The vacuum is sustained between 2 $x10^{-5}$ to 8 $x10^{-5}$ torr by a liquid nitrogen cooled Edwards Vapour Trap. An Alpha Series, Brandenburg, high voltage supply was used

to provide 8 to 10 kV to the filament controller, which then controls the beam's intensity by adjusting the current of projected electrons between 0.5 and 2 mA.

The samples were mounted on a liquid nitrogen cooled holder, suspended in the vacuum chamber. The chamber had an observation window at 90° to the direction of the electron beam and an optical fiber at 1.5 cm away from the sample, gathering the emitted radiation at 45° from the direction of the electron beam (Figure 2.14). A double column of optical fibers was also used, at the same position and orientation, to gather emitted light from different parts of a sample. The emitted light was then directed by the chosen fiber to an Instaspec IV, PC controlled CCD spectrometer, made by ORIEL. Two apertures were used at the entrance of the spectrometer device, a 1.56 mm and a 25 μm one. The software controlling the spectrometer was calibrated using the emission lines of a mercury lamp.

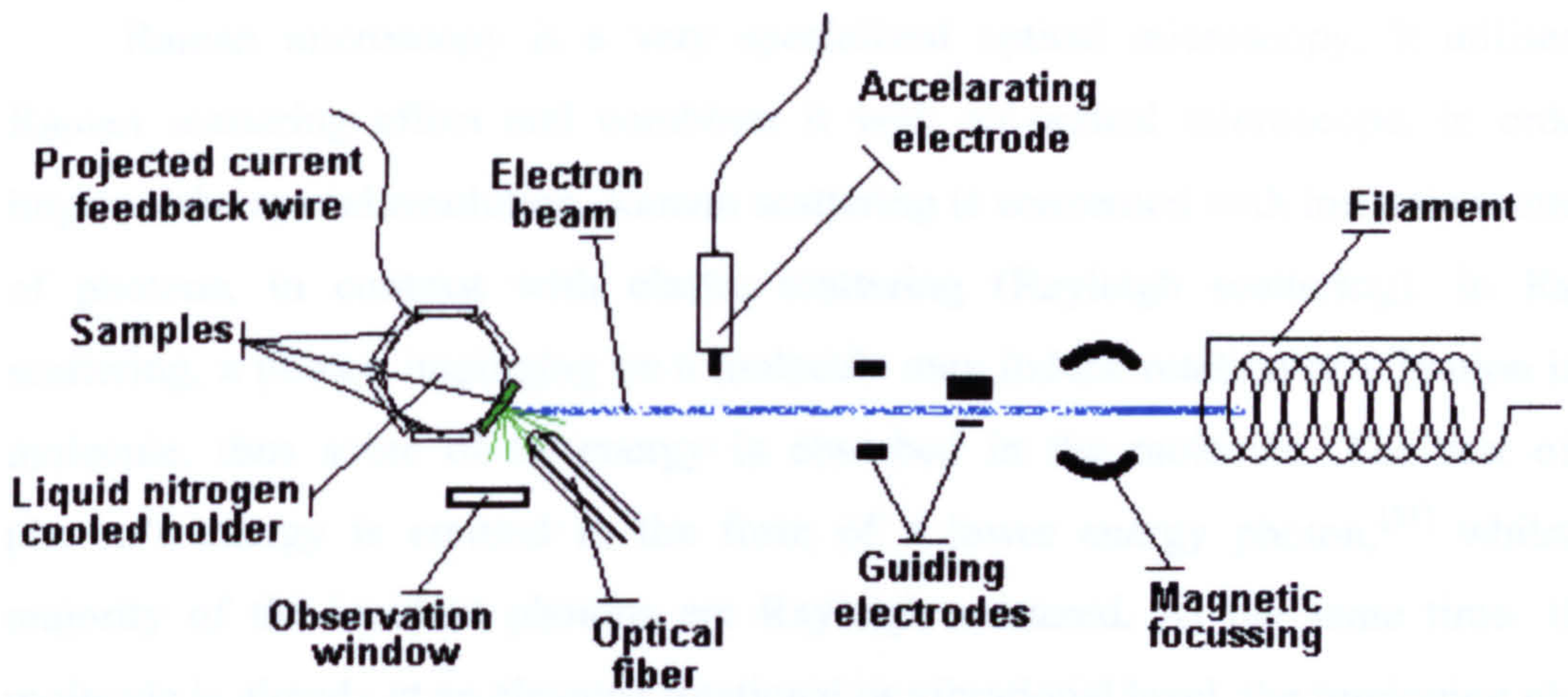

Figure 2.14 Cathodoluminescence of samples inflicted by a focussed electron beam in vacuum.

2.9 Experimental investigation of Photoluminescence

Photoluminescence is a method of phosphor luminescence analysis, equivalent to cathodoluminescence, where the phosphor is excited by high energy photons instead of electrons. The photon energy needed in this case had to exceed the bandgap energy of ZnS, being the host lattice material with the largest bandgap in this work.[47-50] A HeCd laser tuned at 325 nm can provide photons of sufficient energy for the excitation of ZnS and of course CdS, or a ternary complex of the two. A KIMON helium cadmium laser, tuned at 325 nm was thus used for this purpose.

The laser beam was directed in a dark chamber. The samples were held in front of the beam for ambient temperature investigation. For investigation of photoluminescence at the liquid nitrogen temperature, the beam had to be deflected into a dewar. The dewar had the sample lying on its base and it was filled with liquid nitrogen. An optical fibre was used in both occasions to collect the light emitted from the sample and guide it to an OCEAN S2000 computer controlled spectrometer. The fibre was set at an angle, against the sample, in ambient temperature acquisition and inside the dewar, as close to the sample as possible, during liquid nitrogen temperature acquisition.

2.10 Raman Microscopy

Raman microscopy is a very specialized optical microscopy. It utilises the Raman scattering effect and combines it with an optical microscope, in order to improve the spatial resolution. Raman scattering is concerned with inelastic scattering of photons, in contrast with elastic scattering (Rayleigh scattering). In Raman scattering, a photon impinging on a molecule may induce rotation or vibration in the molecule, thus some of its energy is absorbed in the molecule. The rest of the photon's energy is emitted in the form of a lower energy photon,[51] whilst the majority of the incident photons are Rayleigh scattered. At the same time, if the molecule is already at an elevated rotational or vibrational level, the impinging photon may acquire this energy and scatter away with more energy than what it arrived with. When scattered photons have lost energy due to their interaction with the scattering molecules the process is called Stokes scattering, while if they gained energy, it is called anti-Stokes. Stokes scattering is more intense than anti-Stokes scattering due to the different relative populations of ground and exited states.[52, 53]

When a monochromatic light source is used to excite molecules of a sample under investigation, the Rayleigh scattered photons can be filtered out, so as to observe the weaker Raman scattered radiation. Information regarding molecular bonds and orientation can be deduced from this radiation. A spectrum is constructed from the energy difference of the scattered photons with the excitation radiation photons. Raman active materials have characteristic Raman spectra.[54] Consequently the method is used for chemical analysis and the identification of different

crystallographic types. A laser is often used to provide the excitation monochromatic light.[55,56] When combined with a microscope (becoming Raman Microspectroscopy) the laser beam is focussed down on the sample's surface and the light reflected from the sample is passed through the optics of the microscope to a monochromator and then a photomultiplier tube or a charge coupled diode array, which analyse the amount of photons scattered over the different areas of the spectrum.

Here an MKI Renishaw Raman imaging microscope was used to investigate the films deposited on the glass or silica substrates, by either the chemical deposition method or laser transferring. The excitation light was produced by a diode laser at 780 nm, as a continuous beam of accordingly varied power between 0.2 and 9.2 mW. The focal spot of the laser and thus the examined area is 1 to 2 μm in diameter. The scattered light acquired and used for analysis is therefore emitted from a volume of somewhat cylindrical shape around the focal spot and its vertical (depth associated) dimension is 2 μm. So, with deposited films featuring a mean thickness well below 400 nm, it was almost impossible to obtain a meaningful spectrum from a 2 μm deep cylinder, as it is also explained in chapters 4 and 6. However, when the technique of multiple layer LIFT was used, films of greater thickness, reaching 1 μm or more, were deposited and it was possible to acquire some interesting spectra from the now dominating volume of the phosphor material. Acquisition times of 60 to 300 seconds were used, with accumulations of 50 to 100 acquired spectra. Understandably, more than three hours were usually needed in order to conclude an experiment. A cosmic ray extractor, built in as a software component, was also employed removing sharp peaks that can be generated by cosmic noise.

2.11 Surface topography acquisition by Atomic Force Microscopy

A Picoscan, atomic force microscope (AFM), manufactured by Molecular Imaging (part of Agilent Technologies Ltd.), was used to obtain surface topography images of chemically deposited and laser transferred films. The samples were mounted on a piezoelectric tube controlled stage. In contact mode,[57] the feedback loop maintained the atomic force between the tip and the sample constant by adjusting

the height of the piezoelectric tube stage, so that the tube and thus the controlling voltage, follows the contour of the sample surface exactly. The movement was recorded in the computer controlling the microscope device and was processed to produce the 3-D topography of the sample surfaces. As the tip scanned the surface of the sample, moving up and down with the contour of the surface, the laser beam was deflected off the attached cantilever into a dual element photodiode. The photodetector measured the difference in light intensities between the upper and lower diodes and then this difference was converted to an equivalent voltage difference. Feedback from the photodiode signal difference, passed through appropriate controlling software in a computer system, enables the tip to maintain either a constant force or a constant height above the sample. The AFM tips are typically made from Si_3N_4 or Si and are extended down from the end of a resonance vibrating cantilever.[58] The AFM head employs an optical detection system, which focuses on the edge of the cantilever where the tip is attached. A diode laser is used to produce the focussing beam on the cantilever.

2.12 Evaluation of analysis techniques

A small evaluation of the benefits and limitations of the above techniques, as they were applied in this research, is brought forward here. In terms of performing composition analysis on the films, EDX is considered the most simple, efficient, versatile and plausible method, with the greatest limitation being the carbon coating process before the analysis. The availability of modern SEM-EDX machines that do not require coating for insulators and semiconductors will help to overcome this problem. With appropriate calibration, it can also become a powerful quantitative method with accuracy between 1 to 0.1 % (element dependent). ICPMS was the most accurate method, with detection limits down to parts per billion, but poses several problems, like dissolution of the films and sample volume requirements. Raman microspectroscopy becomes area specific and is a non-destructive process, but loses on accuracy. When calibrating with good reference samples, its detection limits are expected down to 0.5 %. Optical transmission measurements in the UV-Vis range, does provide an easily accessible, non destructive method, especially when combined with reflectivity measurements and material bandgap determination. CL is very

specific to impurities and can be very sensitive to small quantities of them, occasionally reaching down to 0.01 ‰. EXAFS does give element specific information, but is not recommended for composition analysis, since other X-ray techniques are more appropriate like EDX and XPS.

Optical microscopy was the first step in analysing surface morphology, due to the ease of accessibility and a great number of features were identified by it, before investigating further by higher magnification techniques. Surface analysis in 3 dimensions is also possible in the micrometer scale by focussing and filtering in digital and analogue. Interferometry can be incredibly precise in one dimension, while offering all the advantages of optical microscopy in 3 dimensions. However it is limited by changes in refractive index over the investigated area. SEM is very efficient both in applicability and magnification, but still requires a sample preparation step. AFM would have proved a most potent surface analysis technique if it was coupled with an optical microscope to aid targeting on the samples surface, or if the sample surface was continuous. Ellipsometry and reflectivity measurements have been used to deduce surface morphology parameters such as roughness of surface, but were mostly used to determine film thickness for which they have been ideal, as they posed errors between 10-20 nm. An insight to film thickness was also given by SEM, by obtaining images at angles of grazing incidence. Thickness could have been determined with greater precision (down to a few Å) by interferometry if the difference in refractive index between film and substrate was absent.

XRD, EXAFS and Raman spectrometry are used to determine crystal structure, with the later being the most accessible. However, there was a certain lack of sample volume on the prepared films and thus it has been possible to apply it only on selected films. EXAFS was by far the most precise, while XRD needs a rather continuous crystal structure. Transmission spectroscopy can help to distinguish between hexagonal and cubic form of crystallisation and so can cathodoluminescence and photoluminescence when all other parameters are known. However, the last two methods are used efficiently to find the luminescence properties of the films, with cathodoluminescence being more related to the materials' end application, electroluminescence. Photoluminescence can be more surface sensitive when examining luminescence properties, however, the lack of an acceleration field implies totally different excitation and radiative recombination routes to those present in an electroluminescent cell.

2.13 References

1. L. Ödberg, S. Sandberg, S. W. Klintström, and H. Arwin, Thickness of Adsorbed Layers of High Molecular Weight Polyelectrolytes Studied with Ellipsometry, Langmuir, 1995, **11**, p 2621.
2. R. J. Archer, Ellipsomtry, Palo Alto, California, 1996.
3. S. D. G. Sharma, Investigation of the Surface Interactions of Polymers and Surfactants in Non-Polar Media, PhD University of Bristol, Bristol, 2002.
4. A. Rothen, The Ellipsometer, an Apparatus to Measure Thicknesses of Thin Surface Films, Rev. Sci. Instrum., 1945, **16**, p 26.
5. J. C. Cigal, A Novel Spectroscopic Ellipsometer in the Infrared, PhD Technical University of Eindhoven, Eindhoven, 2002.
6. E. Hecht, Optics, 4th Edition, Addison Wesley Longman, Inc., 2002.
7. F. L. McCrackin,E. Passaglia, R. R. Stromberg and H. L. Steinberg, Measurement of the Thickness and Refractive Index of Very Thin Films and the Optical Properties of Sunfaces by Ellipsometry, J. Res. Natl. Bur. Std. 1963, **67A**, p 363.
8. C. Runge, Über die numerische Auflösung von Differentialgleichungen, Math. Ann., 1895, **46**, p 167.
9. M. W. Z. Kutta, Beitrag zur näherungsweisen Integration totaler Differentialgleichungen, Z. Math. Phys. 1901, **46**, p 435.
10. J. D. Lambert and D. Lambert, Ch. 5 in Numerical Methods for Ordinary Differential Systems: The Initial Value Problem., in Numerical Methods for Ordinary Differential Systems, Wiley, New York, 1991.
11. W. H. Press, B. P. Flannery, S. A. Teukolsky and W. T. Vetterling, Numerical Recipes in FORTRAN: The Art of Scientific Computing: Method and Adaptive Step Size Control for Runge-Kutta, 2nd Edition, Cambridege University Press., Cambridge, 1992.
12. P. J. M. V. Laarhoven and E. H. L. Aarts, Simulated Annealing: Theory and Applications, R.Reider Publishing Company, Dordrecht, Holland, 1987.
13. S. Tolansky, Multi-Beam Interference Microscopy of Metals, Academic Press Inc., London, 1970.
14. W. H. Steel, Interferometry, 2nd Edition, Cambridge University Press, Cambridge, 1983.
15. S. Tolansky, An Introduction to Interferometry, 2nd Edition, Longman Group Ltd., London, 1973.
16. M. Francon, Optical Interferometry, Academic Press Inc., London, 1966.
17. C. Lamb and M. Zecchino, WYKO Surface Profilers Technical Reference Manual, Veeco Metrology Group, Edition 2.2.1, Tuscon, Arizona, 1999.
18. S. Tolansky, Multi-Beam Interferometry of Surfaces and Metals, Oxford University Press, London, 1949.
19. C. Lamb and M. Zecchino, WYKO Surface Profilers Technical Reference Manual, Edition 2.2.1, Veeco Metrology Group, 1999.
20. M. A. Kettani and M. F. Hoyaux, Plasma Engineering, Butterworth & Co, London, 1973.
21. D. Montgomery, Strongly Magnetised Classical Plasma Models: Plasma Physics, Gordon and Breach, Science Publishers Ltd, London, 1975.
22. E. W. Laing, Plasma Physics, Chatto & Windus, London, 1976.

23. H. H. Willard, L. L. Merritt, J. A. Dean and F. A. Settle, Atomic Emission Spectroscopy with Plasma and Electrical Discharge Sources, in Instrumental Methods of Analysis, 1988, Wadsworth Publishing Company, p. 197.
24. A. N. Eaton, Applications of Plasma Source Mass Spectrometry, The Royal Society of Chemistry, Bath, 1991.
25. J. G. Brown, X-Rays and their Applications, Iliffe Books Ltd., London, 1966.
26. Y. Iwasawa, X-Ray Absorption Fine Structure for Catalysts and Surfaces, World Scientific Co. Pte. Ltd., Singapore, 1996.
27. J. F. W. Mosselmans, Introduction and a Simple Picture of EXAFS, http://srs.dl.ac.uk/xrs/index.html, CCLRC Daresbury Laboratories, 1999.
28. K. L. Williams, Introduction to X-Ray Spectrometry: X-ray Fluorescence and Electron Microprobe Analysis, Allen & Unwin Ltd., London, 1987.
29. R. Tertian and F. Claisse, Principles of Quantitative X-Ray Fluorescence Analysis, Heyden & Son Ltd., London, 1982.
30. B. K. Teo, EXAFS: Basic Principles and Data Analysis, Springer-Verlag, Berlin, 1986.
31. J. F. Rooms, A Matrix Isolation Investigation of Tellurium Cryochemistry Using Hydrogen Telluride and Tellurium Dimers as Precursors, PhD University of Hull, Hull, 2005.
32. D. E. Sayers, E. A. Stern and F. W. Lytle, New Technique for Investigating Noncrystalline Structures: Fourier Analysis of the Extended X-Ray - Absorption Fine Structure, Phys. Rev Lett., 1971, **27**, p 1204.
33. S. J. Gurman, N.Binsted and I.Ross, A Rapid, Exact, Curved-Wave Theory for EXAFS Calculations. II. The Multiple-Scattering Contributions, J. Phys. C, 1984, **19**, p 143.
34. L. M. Murphy, K. C. Cheung, R. L. Bilsborrow and J.F.W.Mosselmans, Station 7.1 Manual (of the SRS at CCLRC Daresbury Laboratories), CCLRC Daresbury Laboratories, Daresbury, 1999.
35. P. Luger, Modern X-ray Analysis on Single Crystals, De Gruyter, Berlin, 1980.
36. A. Guinier, X-ray Diffraction in Crystals, Imperfect Crystals and Amorphous Bodies, Freeman, San Francisco (Cal), 1963.
37. H. S. Peiser, H. P. Rooksby and A. J. C. Wilson, X-ray Diffraction by Pollycrystalline Materials, The Institute of Physics, London, 1955.
38. W. Clegg, Crystal Structure Analysis : Principles and Practice, Oxford University Press, Oxford, 2001.
39. F. D. Bloss, Crystallography and Crystal Chemistry : an Introduction, Holt, Rinehart and Winston, New York, 1971.
40. E. W. Nuffield, X-ray Diffraction Methods, John Wiley & Sons, New York, 1966.
41. C. Whiston, X-ray Methods, Wiley, Chichester, 1987.
42. D. B. Williams, J. I. Goldstein and D. E. Newbury, X-ray Spectrometry in Electron Beam Instruments, Plenum Press, New York, 1995.
43. P. J. Goodhew, Electron Microscopy and Analysis, Wykeham, London, 1975.
44. Oxford Instruments Analytical - Technical Briefing: Energy Dispersive X-ray Microanalysis Hardware Explained, Oxford Instruments Analytical Ltd.
45. L. Ozawa, Cathodoluminescence: Theory and Applications, John Wiley & Sons Inc, 1990.
46. G. Parr and O. H. Daive, The Cathode-Ray Tube and its Applications, 3rd Edition, Chapman and Hall, London, 1959.

47. P. Goldberg, Luminescence of Inorganic Solids, Academic Press, New York, 1966.
48. D. Curie, Luminescence in Crystals, Methuen, London, 1963.
49. Goldberg and J. W. Nickerson, D.C. Electroluminescence in Thin Films of ZnS : P, J. Appl. Phys., 1963, **34**, p 1601.
50. L. Ozawa, Cathodoluminescence and Photoluminescence, CRC, 2007.
51. A. Anderson, The Raman Effect, Dekker, New York, 1971.
52. J. R. Ferraro and K. Nakamoto, Introductory Raman Spectroscopy, Academic Press, Boston, Mass, 1994.
53. W. T. Silfvast, Laser Fundamentals, 2nd Edition, Cambridge University Press, Cambridge, 2004.
54. B. S. Galabov and T. Dudev, Vibrational Intensities, Elsevier, Amsterdam, 1996.
55. M. C. Tobin, Laser Raman Spectroscopy, Wiley-Interscience, New York, 1971.
56. J. Loader, Basic Laser Raman Spectroscopy, Heyden, London, 1970.
57. R. Wiesendanger, Scanning Probe Microscopy and Spectroscopy, Cambridge University Press, Cambridge, 1994.
58. D.Sarid, Oxford Series in Optical and Imaging Sciences: Scanning Force Microscopy, Oxford University Press, New York, 1991.

Chapter 3.

Chemical Bath Deposition of ZnS and CdZnS

Chapter 3. Chemical Bath Deposition of ZnS and CdZnS

3.1 Introduction to chemical bath deposition of wide bandgap semiconductors

3.1.a. Chemical precipitation of inorganic salts

Chemical precipitation of ionic salts is a very common phenomenon in nature. It is the process of obtaining an amount of salt at the bottom or on the walls of a container in which a solution of this salt exists (or existed). There are two main routes for obtaining a precipitate. The most common one is when the solvent in which the salt is dissolved in, evaporates or in a more general way, its volume in the common container is reduced, e.g. by osmosis, or by transformation through a chemical reaction. The second route involves the coexistence of two compounds of which the ionic component of the one can be combined with the oppositely charged ionic component of the other and thus give the salt in question (Figure 2.1). In both scenarios the precipitated salt must be partially or entirely insoluble in the present solution in order to obtain it as a solid precipitate.

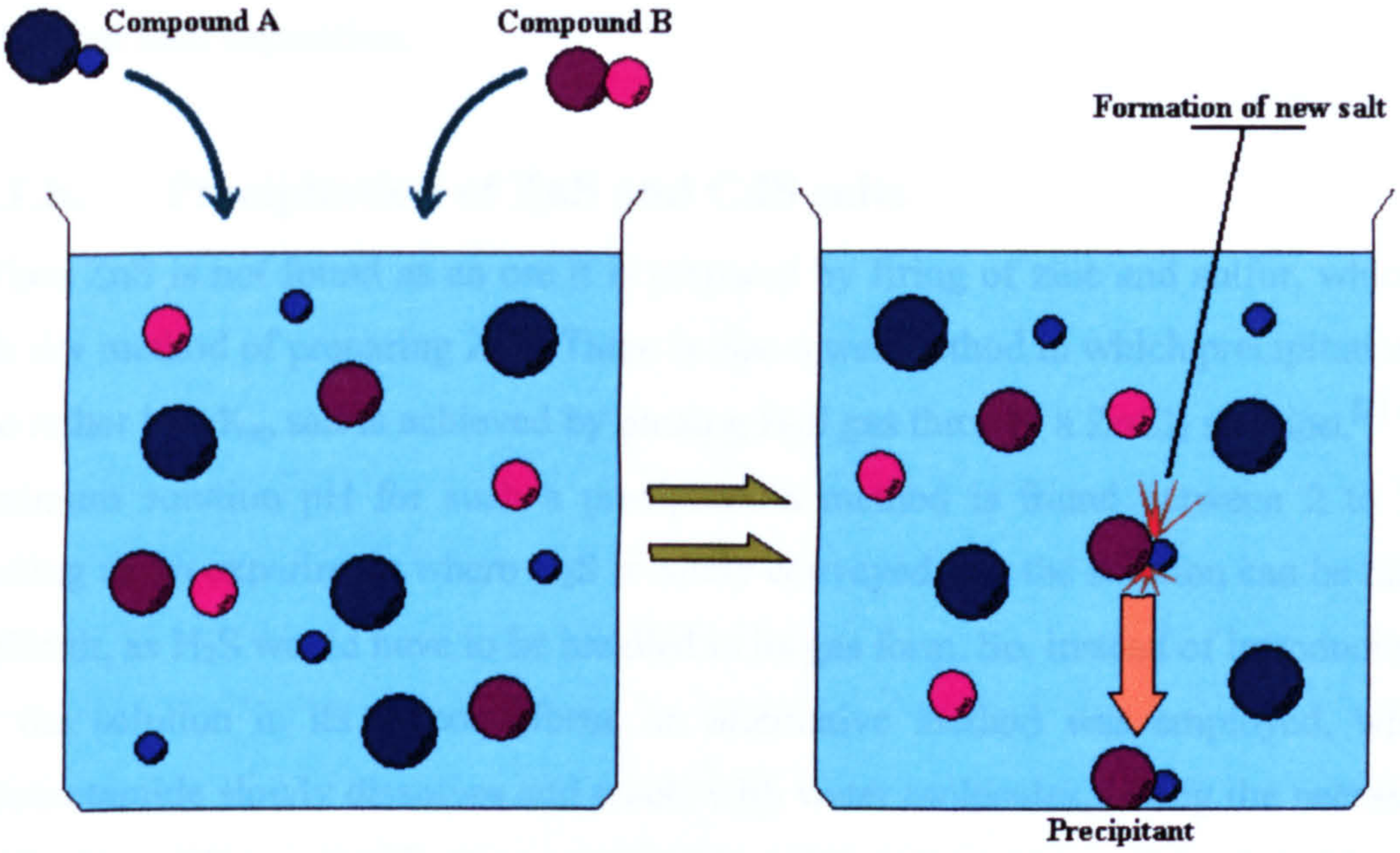

Figure 3.1 Chemical precipitation by reaction of two species.

A salt is termed partially insoluble when only a certain amount of it can be ionically dissolved in a defined volume of solvent (in most cases water). This is because a solvent can only withstand a limited amount of the salt in question, being dissolved in it. Thus there is always an attempt to keep the concentrations of the salt's ions below a specific level. This level is defined by the solubility product (K_{sp}) of the salt.[1] The solubility product is equal to the product of the concentrations of the salt's ions that are permitted in the solution:

$$M_aX_{b\,(s)} \leftrightarrow aM^{n+} + bX^{m-} \qquad (3.1)$$

$$K_{sp} = [M^{n+}]^a [X^{m-}]^b \qquad (3.2)$$

$$\ln K_{sp} = -\Delta G^0 \cdot R^{-1} \cdot T^{-1} \qquad (3.3)$$

The greater the solubility of the product, the larger is the value of K_{sp}. This means that even the strongest electrolytes will precipitate in very large concentrations (or very small amounts of solvent) and salts that are often termed as insoluble, can be dissolved in great volumes of solvent, as every salt is dissolved even in very small amounts. The solubility product is also a thermodynamic constant, thus it is dependent upon temperature (eq. 2.3).[1] In principle, it is possible to precipitate a salt with a rather small K_{sp} by mixing two other salts containing its two ionic components that have higher K_{sp} value. This type of salt precipitation / deposition is often called a chemical bath deposition.

3.1.b. Precipitation of ZnS and CdS salts

When ZnS is not found as an ore it is prepared by firing of zinc and sulfur, which is the dry method of preparing ZnS. There is also a wet method in which precipitation of the rather low K_{sp} salt is achieved by passing H_2S gas through a $ZnCl_2$ solution.[2] The optimum solution pH for such a precipitation method is found between 2 to 3.[2] Setting up an experiment where H_2S is safely conveyed into the solution can be rather difficult, as H_2S would have to be handled in its gas form. So, instead of introducing it in the solution in its gaseous form, an alternative method was employed, where thioacetamide slowly dissolves and reacts with water molecules, giving the necessary sulfur ions. Thioacetamide is an organic substance commonly used in chemistry for generation of hydrogen sulfide. Its structure can be seen in Figure 3.2.a. Borges, Lincot and Vedel,[3] used it in 1992 as part of a chemical bath method that precipitates

ZnS thin films. Others have followed their example, using either water or ethanol as solvent. Boyle et. al. have used a very similar method for the precipitation of cadmium zinc sulfide films.[4] In their experiments, urea was also introduced in the solution, partially playing the role of complexant, controlling the release of Zn ions and partially as dispersant of the embryo clusters of material grown in the solution.

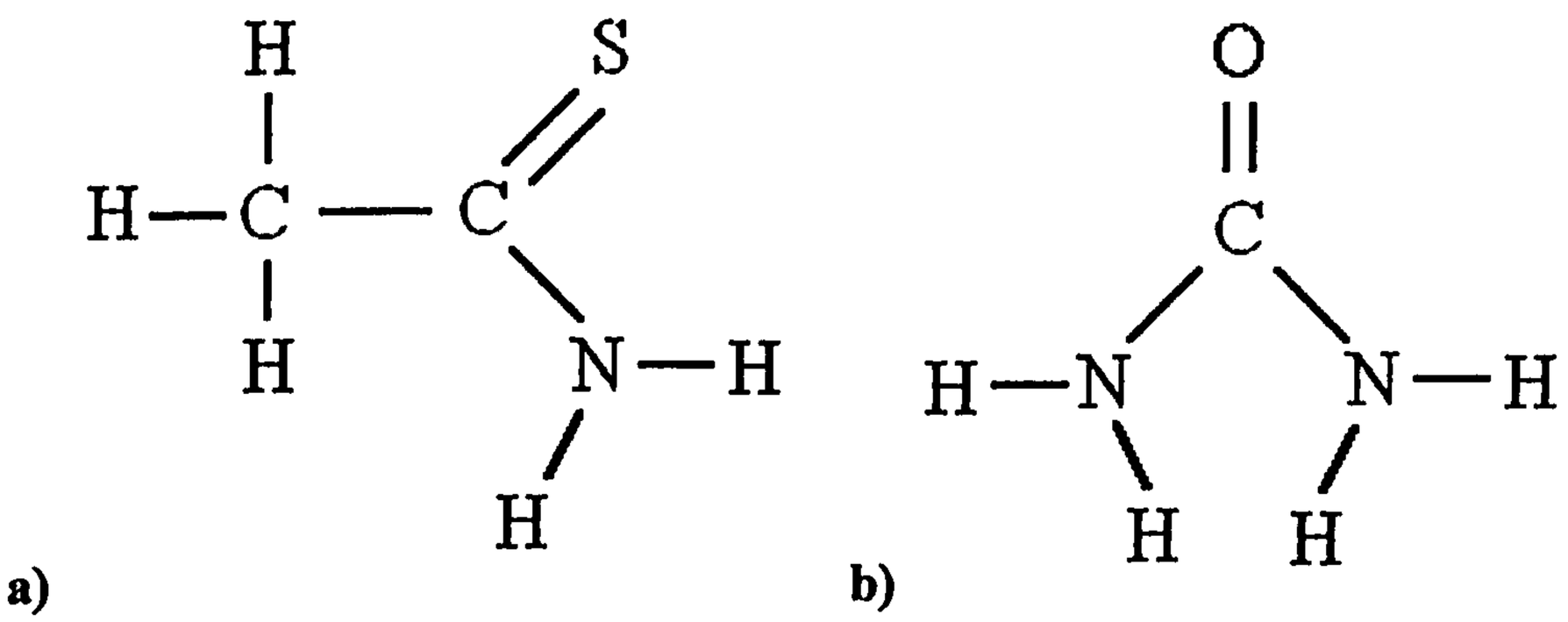

Figure 3.2 Molecular structures of a) thioacetamide and b) urea.

This method is also adopted in this research, where thioacetamide provides the sulfur ions in the solution, forming dissolved sulfuric acid, zinc or cadmium chloride salts provide the metal ions. The use of urea is also adopted and though it is not a very strongly binding complexant, the reaction is controlled also by the slow release of sulfur from thioacetamide. The chemical reactions are given below.

$$2\,H_2O + CH_3CSNH_2 \rightarrow CH_3CONH_2 + H_2S \qquad (3.4)$$

$$H_2S \xrightarrow{(H_2O)} 2\,H^+ + S^{2-} \qquad (3.5)$$

$$ZnCl_2 \xrightarrow{(H_2O)} Zn^{2+} + 2\,Cl^- \quad , \quad CdCl_2 \xrightarrow{(H_2O)} Cd^{2+} + 2\,Cl^- \qquad (3.6)$$

$$Zn^{2+} + S^{2-} \rightarrow ZnS\downarrow \quad , \quad Cd^{2+} + S^{2-} \rightarrow CdS\downarrow \qquad (3.7)$$

Here the difference between homogeneous and inhomogeneous growth of films and clusters of the sulfide material should be clarified. Normally, it is expected for the positive and negative ions to meet somewhere in the solution, form an ionic bond and slowly coagulate with other molecules of the same material due to Coulomb attraction between the dipole molecule and the surrounding ions or previously formed molecules. Small coagulations of molecules composed of a few molecules only are often called embryo clusters. Larger ones can be termed as nuclei clusters when they form the bases for growth of a slightly different material. When the clusters acquire a

certain size, they will be too heavy to be suspended in the solution and thus will fall as a precipitant at the bottom of the vessel. This type of material growth is called homogenous,[1] because the clusters are formed within a homogenous medium. Surfactants are often employed in the growth of such clusters, by means of a colloidal suspension, a method that gives advanced control over the size and shape of the precipitated particles. It is very common to obtain rods and spheres of very specific dimensions, when using such a method.[5-12]

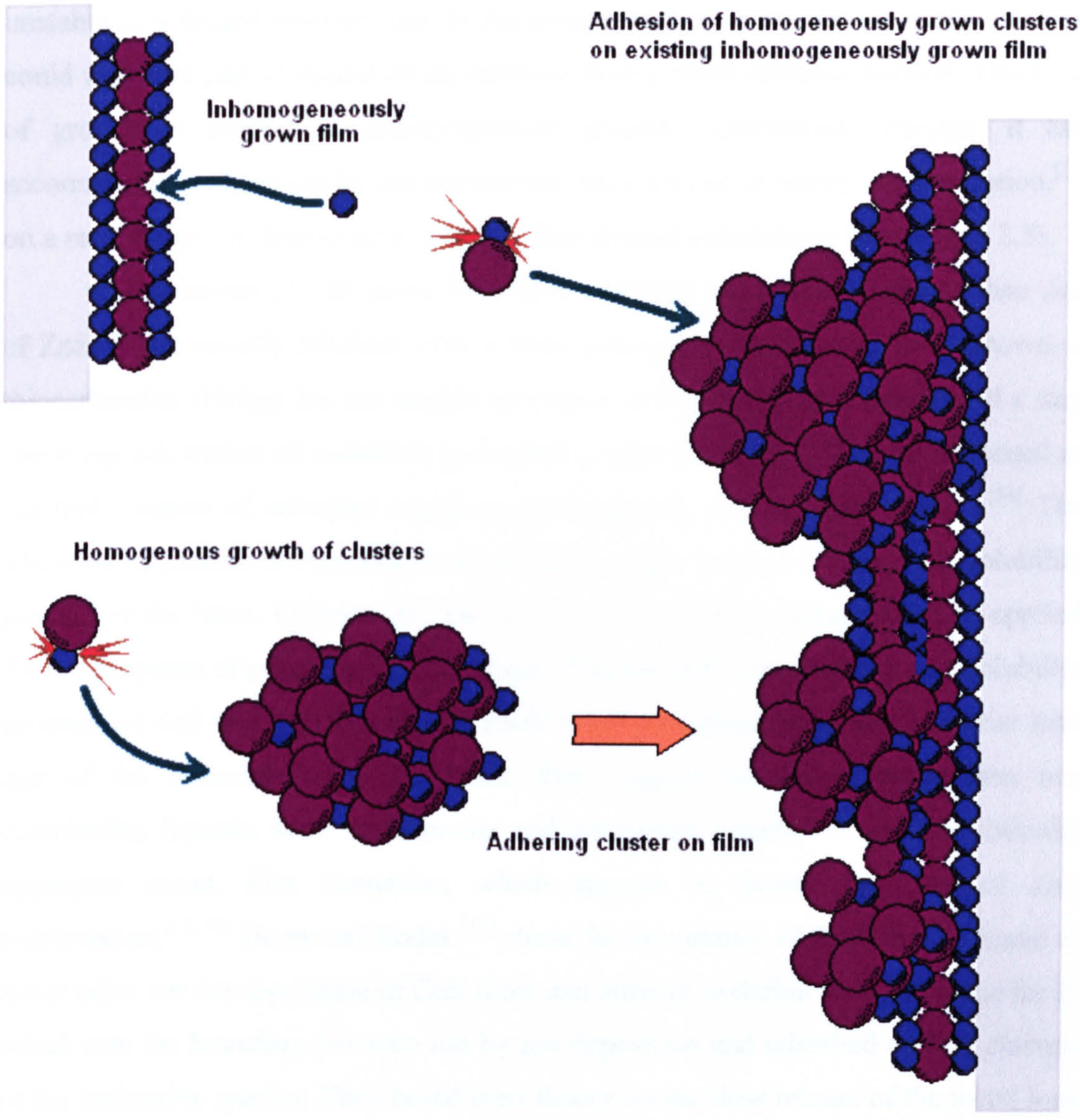

Figure 3.3 Schematic of homogeneous, inhomogeneous and mixed precipitation of a binary salt.

On the other hand, the existence of an interface between the solution and a substrate, for example glass, may conveniently support the formation of material in a film-like manner. This situation is accommodated mainly for three reasons. One is the possible enhanced adsorption of one of the ionic species on the substrate surface, which will then cause the interface to act as a catalytic agent for the formation of the film. The second is the existence of firm nucleation sites on the substrate, such as scratches, pores and other anomalies of the surface, able to trap ions, molecules or clusters. And the third reason is that the homogeneously grown embryo clusters are unstable in a heated solution, due to the kinetic energy of the solvent molecules and could thus find partial shelter on an interface with a solid substrate surface. This type of growth is termed as inhomogeneous growth. Interestingly enough, it can accommodate both an ion by ion mechanism and a cluster or embryo incorporation,[13] on a recently grown film or an expanding film around a nucleating site (Figure 3.3).

Precipitation of CdS alone by similar methods was practised longer than that of ZnS. It was usually obtained from a basic solution, where thiourea (also known as thiocarbamide $(NH_2)_2CS$) was mainly used as a sulfur supplying chemical and a step involving adsorption of cadmium hydroxide on the substrate surface is presumed as the main reason of selective inhomogeneous growth (see reactions below).[14] The adsorbed hydroxide is eventually converted to sulfide because of the lower solubility product of the latter. O'Brien and McAleese note that this process cannot be applied for the purposes of precipitating ZnS films,[13] as the difference between the solubility products of ZnS and $Zn(OH)_2$ is very small in basic environments, much smaller than that of the cadmium salts. Therefore, they suggest the use of more than one complexing ligands, such as ammonia and hydrazine, which will aid the colloidal aggregate based, film formation, which appears to favour the case of ZnS precipitation.[15, 16] Gorer and Hodes [17] stress the importance of the complex ligand to metal ratio, for the deposition of CdS films and attempt to define a critical value for it, which sets the boundary between ion by ion deposition and adsorbed colloid clusters of the hydroxide species. They based their theory on the slow release of the metal ions in the solution, which prohibits their fast reaction with the abundant hydroxide ionic species originating from the solvent. For CdS, it is expected that a certain volume of the adsorbed hydroxide clusters would still be converted to the sulfide species, as long as the sulfinating agents become available around the clusters.[1] Doña and Herrero[18] suggest that the slow release of zinc ions would also favour the precipitation of ZnS

against $Zn(OH)_2$ which is more critical in obtaining ZnS films instead of oxide and hydroxide ones. However, the formation of zinc sulfide against that of the hydroxide can also become favourable in a neutral or slightly acidic bath, as the difference between their solubility products becomes much greater in such environments.[13, 19] Thus, such a route is followed in the preparation of ZnS and CdZnS films here. The film's attachment to the substrate's surface is accomplished by condensation of ionic species on the surface[18] which will not be consisting strictly of ZnS, but a possible oxide or hydroxide precursor film that will act as a basis for the mixed (homogeneous and inhomogneous) growth of the sulfide film, a scenario analysed in chapter 4 of this work.

$$Cd^{2+}_{aq} + 2\,OH^{-} \xrightarrow{(nucl.site)} Cd(OH)_{2,ads} \qquad (3.8)$$

$$(NH_2)CS + Cd(OH)_{2,ads} \xrightarrow{(nucl.site)} CdS + (NH_2)CO + H_2O \qquad (3.9)$$

3.2 Materials and Apparatus

A detailed description of the characteristics of materials used for the purposes of the chemical bath deposition experiments, such as reactants and substrates, is given here for purposes of reference. Model details of the various apparatus of significance are also provided in order to enable comparison between their performance during the execution of the experimental procedures described in this work and other documented similar attempts. Glassware and other common apparatus used during the experiments are described in the following text, explaining the experimental procedure. The reactants of the chemical bath depositions are tabulated in Table 3.1. They have been purchased from different suppliers and the product number assigned for each chemical by its supplier is listed, so as to be used for any possible inquiry regarding impurity composition and other material production details.

Table 3.1 Chemical reactants used in the chemical bath deposition process.

Name	Formula	Supplier	Purity %	Product Number
Urea	$NH_2.CO.NH_2$	Prime Chemicals	-	CU 4504-56
Zinc Chloride	$ZnCl_2$	Prolabo	98	Code: 29 144.230
Thioacetamide	CH_3CSNH_2	Aldrich	99+	Lot 01227MI-312
Copper II chloride	$CuCl_2.\,2H_2O$	Analar	99.0	Prod. 100884E
Cadmium chloride	$CdCl_2.\,2.5H_2O$	Acros	99.7	c.a.s. 7790-78-5
Manganous chloride	$MnCl_2$	Analar	98	2181 B214038

The substrates used initially to hold the precipitated ZnS or CdZnS films were cut pieces of microscope slides, with approximate dimensions 2 x 2.5 x 0.2 cm. They are commonly called window or sodalime glasses, because of their sodalime substance additive (approx 75 % $Ca(OH)_2$, 20 % H_2O, 3 % NaOH and 1-2 % KOH) and the characteristic green colour, observed in thick samples. These were changed to fused silica slides, with better transmission characteristics in the UV, but with a non-optically polished surface. The increased transmission in the UV band is necessary for allowing the excimer laser beam through the substrate, in order to achieve laser induced forward transfer in the next stage of the experiments. The laser beam used here has a distinctive wavelength at 248 nm. The fused silica samples had varying dimensions, usually according to the sample batch. Optically polished silica substrates, cut from silica microscope slides, were then used with dimensions of 2 x 2.5 x 0.1 cm. These last two batches, named S5 and S6 sillica substrate sample batch, featured even more improved transmission characteristics and helped standardising the deposition and transfer process, mostly in terms of the apparatus used. The transmission spectra of all three types of substrates are shown in Figure 3.4.

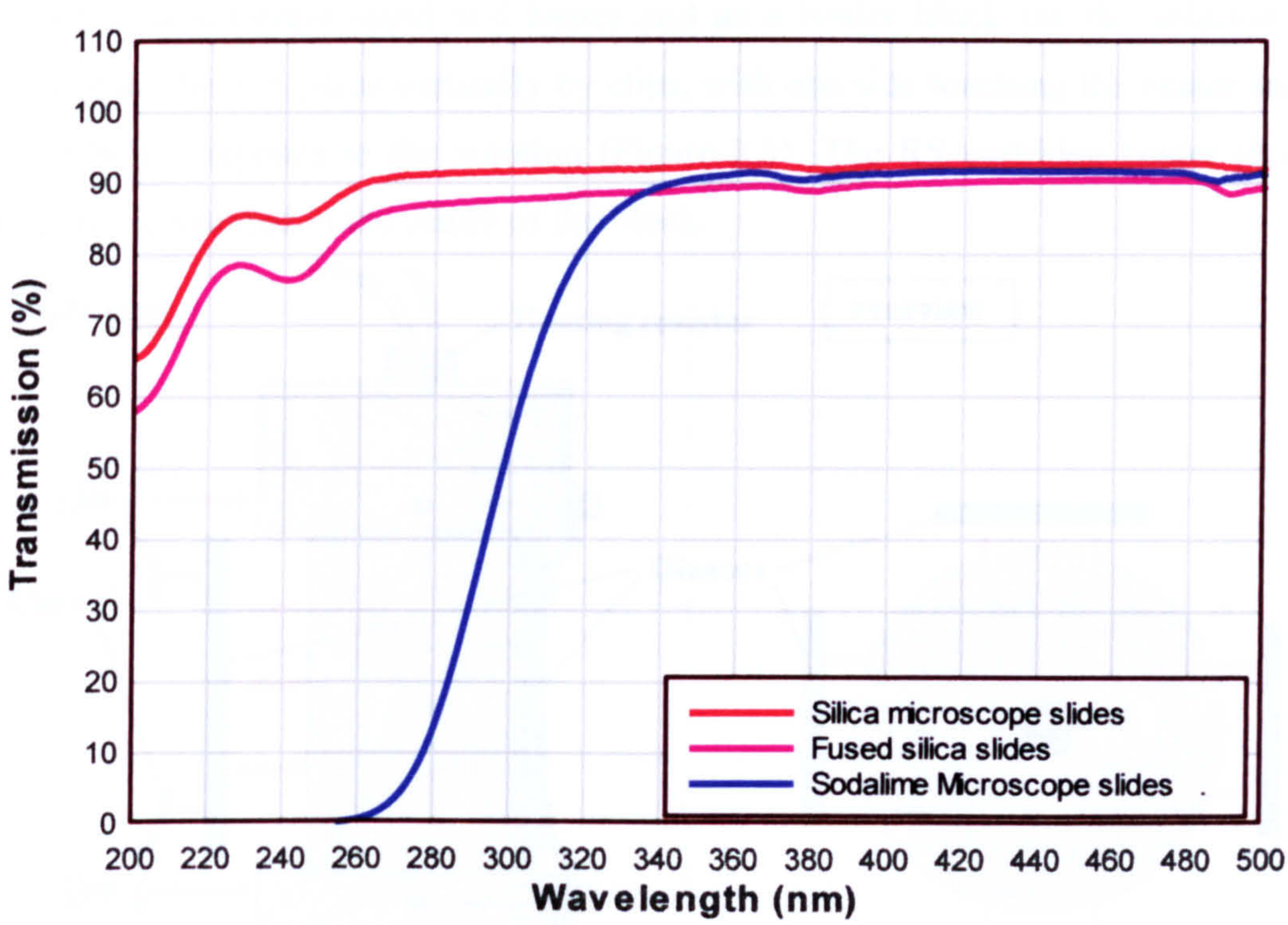

Figure 3.4 Transmission spectra of the three types of substrate glasses used. The faint trough features observed around 380 nm and between 480 and 500 nm are known spectrometer errors.

The apparatus used in chemical bath depositions that should be specified are the PID controller which was employed after a certain point, for regulating the bath temperature and the heating element. The PID (Proportional, Integral, Differential) controller is a CAL 9900, twin SSR, automatic temperature controller. The P, I and D parameters have been set by the device itself by an automatic calibration session. The target temperature is set at 92 °C permanently and the voltage feed at the thyristor was usually kept constant at 180 V. The controller regulates the temperature by turning on and off the heating element.

The heating element is a 300 W cartridge heater with a maximum operating voltage of 240 V. It is an RS component with part number HS37-2.5. Its dimensions are 2.5 inches in length and 3/8 of an inch in diameter. The heater is essentially a resistor, enclosed in a stainless steel capsule. The element is installed in a stainless steel heater block, which enables heating of the solution and the substrates. It was observed by earlier researchers that better results in terms of film adherence, are obtained by applying heat directly on the glass substrates than generally to the bath. Therefore, a stainless steel block with four faces accepting glass substrates was built to act as a substrate stand and heater and as a heater block for the solution. The glasses are held in place vertically by clips, with one side touching the heater and the other being exposed to the solution (Figure 3.5). The RS cartridge heater (heating resistor) is inserted in the centre of the block.

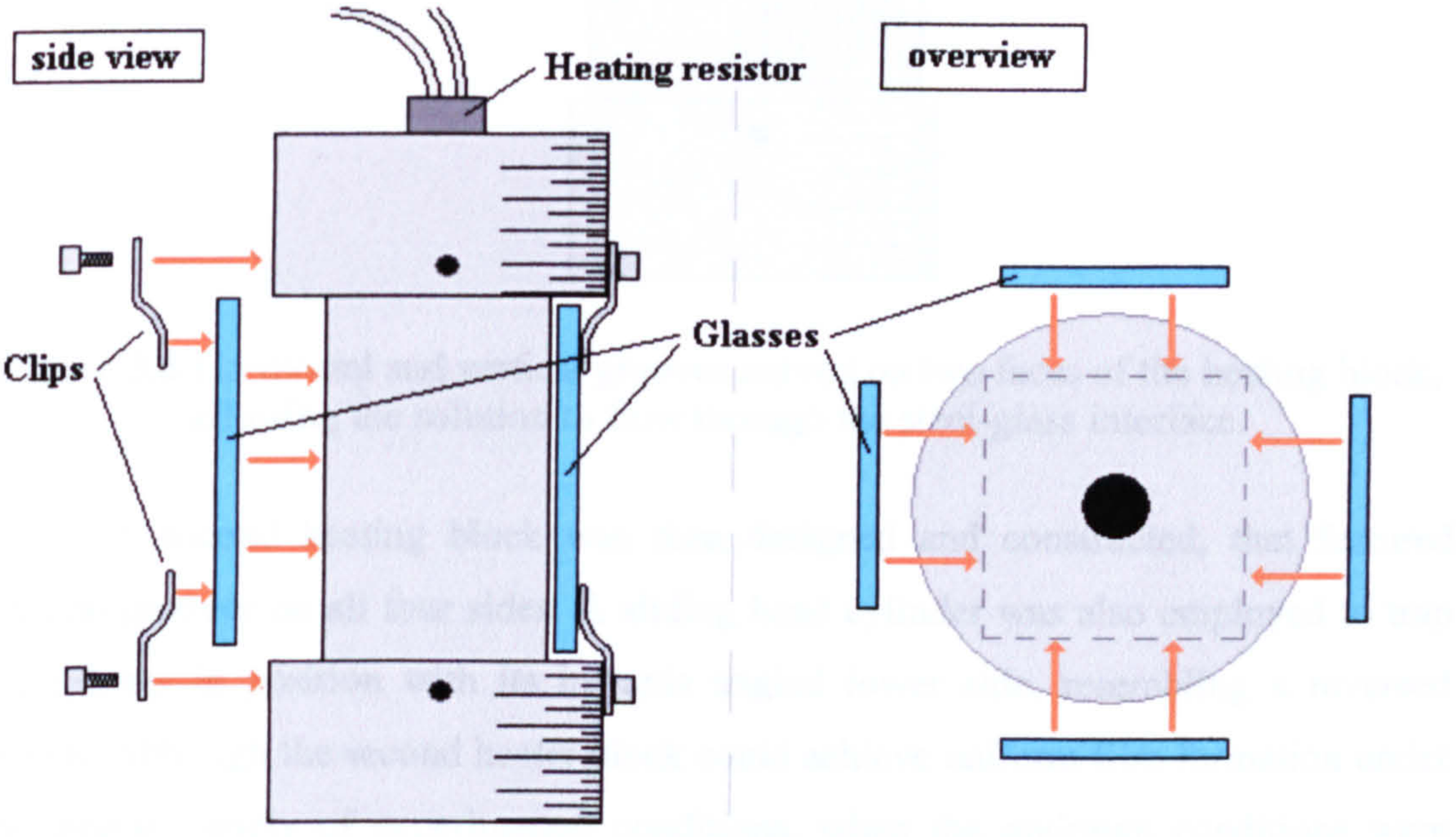

Figure 3.5 Heating device and arrangement of glass samples.

Another observation by previous users of the heating device was that the solution was intruding at the inner side of the glass samples set against the heater's side, through small scratches on the steel surface. The solution was forming films of better quality there than the exposed outer side of the samples, possibly because of the higher temperature or a provided shielding from disturbing turbulences. These films were restricted to areas that were accessible by the solution through the scratches. Therefore, horizontal and vertical grooves were curved on two of the four sides of the first heater block (Figure 3.6), to test the accessibility of the solution over the inner side of the glasses. The vertically oriented groves gave more homogeneous and intact films due to a more constant flow, governed by convection flow.

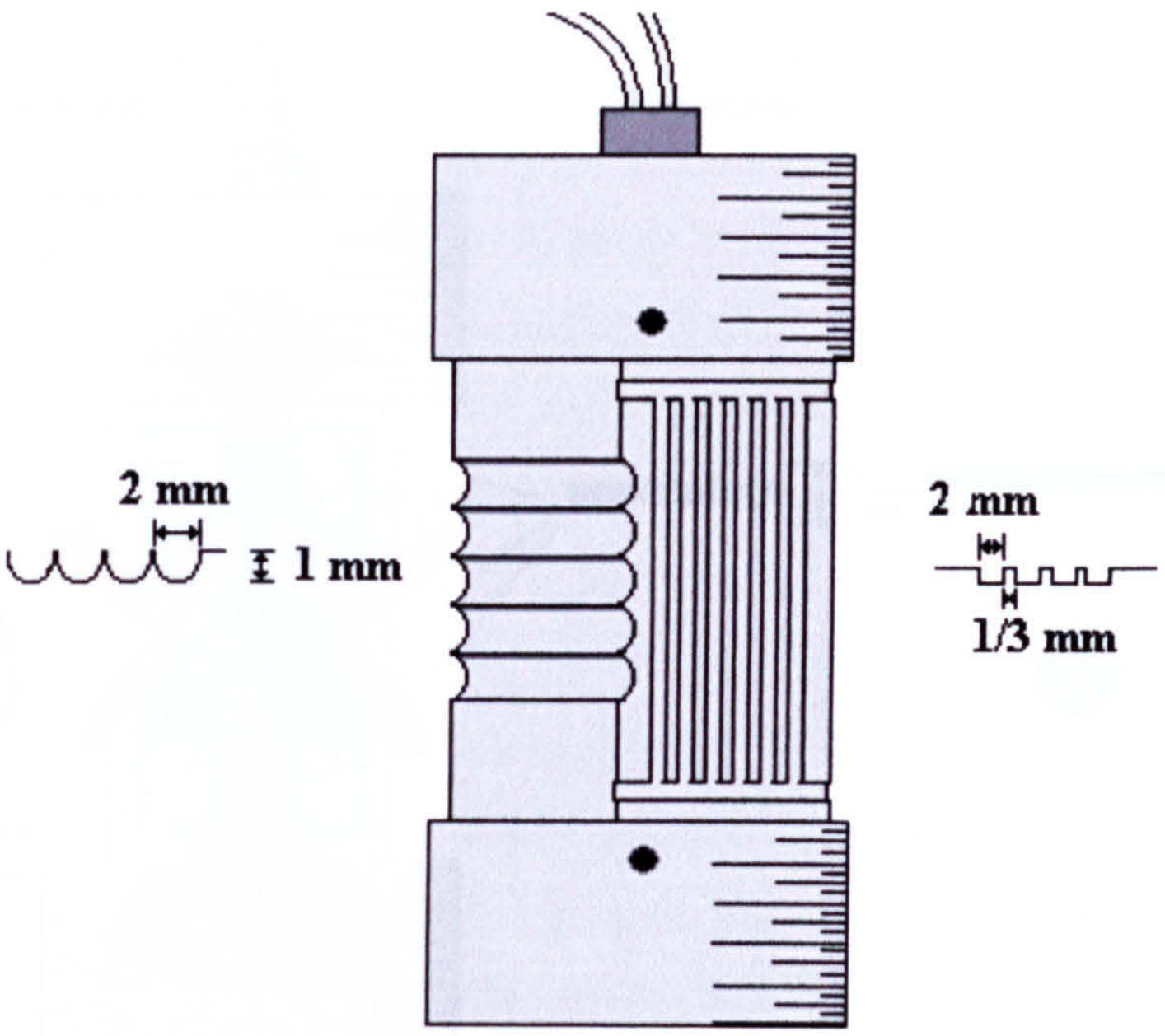

Figure 3.6 Horizontal and vertical grooves curved on two faces of the heating block, allowing the solution to flow through the steel-glass interface.

A second heating block was then designed and constructed, that featured vertical grooves on all four sides. A sliding head cylinder was also employed to trap the glasses in position with its inwards angled lower side, resembling a reversed crown. Although the second heater block could achieve uniform film formation under the largest variety of experimental conditions, when the optimum conditions were used, the best quality film was grown on the outer side of the glasses. These outer side

films had full coverage of the glass surface and a greater degree of homogeneity, as there is nothing in contact with the outer side of the glass apart from the heated liquid solution. A rather good homogeneity of the inner side film was also achieved by introducing thin glass separators between the metal heater surface and the glass. The liquid was again circulated due to convection, as it is shown in Figure 3.7, but areas of the glass surface were left uncovered because of their contact with the glass separators. Hence, the optimum film growth conditions, analysed in the following chapter, were used to produce films intended for the laser transfer process. The second heater block was used under those conditions, while the inner side film was cleaned with 2 to 3 M hydrochloric acid, so as to provide a clean path for the laser beam, before it meets the film of interest.

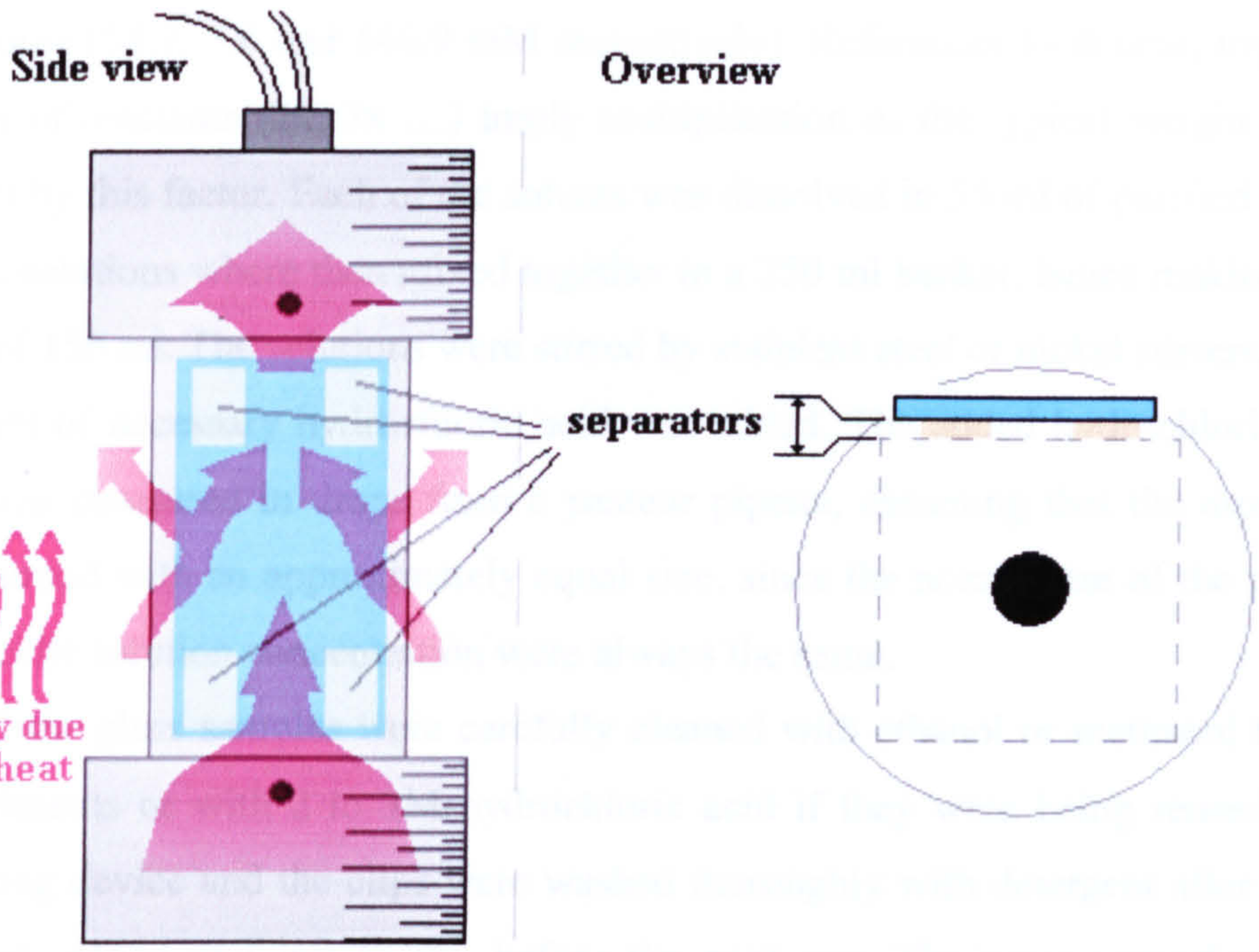

Figure 3.7 Position of separators and flow of solution beneath the surface of the glass substrate. Suggested separators are glass cover slips, with a thickness of 0.25 mm.

3.3 Experimental methods

The reactant concentrations suggested by Paul O'Brien et al [4] for precipitation of CdZnS films were used as a reference. According to the recipe, the bath should contain 0.02 M zinc chloride (or metal chloride salt in general), 0.2 M thioacetamide (TAA) and 0.5 M urea at a pH 5.5 to 4.9, which is controlled by the addition of 2 M hydrochloric acid. In the experiments described in this work, the typical mix contained a third of these concentrations for each substance. All experiments were conducted with exactly the same amount of initial solvent (water) volume, being equal to 150 ml. Consequently, the concentrations are directly equivalent to the weight of each additive and so, the amount of participating reactants is mentioned in the analyses of the various cases in chapter 4, instead of the concentration. Therefore, a typical CBD solution contained 0.75 g of thioacetamide, 0.13 g of zinc chloride and 1.5 g of urea (58.7, 5.6 and 146.9 mM respectively). References to double, triple etc quantities of reactants (2x, 3x ...) imply multiplication of the typical weight of the ingredient by this factor. Each of the solutes was dissolved in 50 ml of purified water. The three solutions where then mixed together in a 250 ml beaker, hence making up a solution of 150 ml. The solutions were stirred by stainless steel or nickel stirrers. Then the amount of necessary hydrochloric acid was added. The added hydrochloric acid volume was measured in drops from a pasteur pipette, assuming that the drops are always formed with an approximately equal size, since the nozzle size of the pipette and the acidic solution concentration were always the same.

All the glass samples were carefully cleaned with ethanol or methanol before the experiments or with 2 to 3M hydrochloric acid if they were being reused. The steel heating device and the clips were washed thoroughly with detergent after every experiment, wiped and left to dry before the next use. The same procedure was followed for all the other appliances taking part in the experiments. Once the glasses were attached firmly on the heater block, the assembly was inserted in the beaker containing the solution. The solution at this point covers the glasses completely. As the experiment progresses, the solution is meant to lose volume due to evaporation, since the temperature is almost always kept above 70 °C and at the optimum conditions around 92 °C. Initially, to avoid the effects of increasing reactant concentrations and exposure of the glasses to air, volumes of 25 to 50 ml were added at set times. This resulted in significant temperature changes of the solution, which

demanded careful control of the bath temperature, by rather temperamental adjustments of the voltage fed into the cartridge heater.

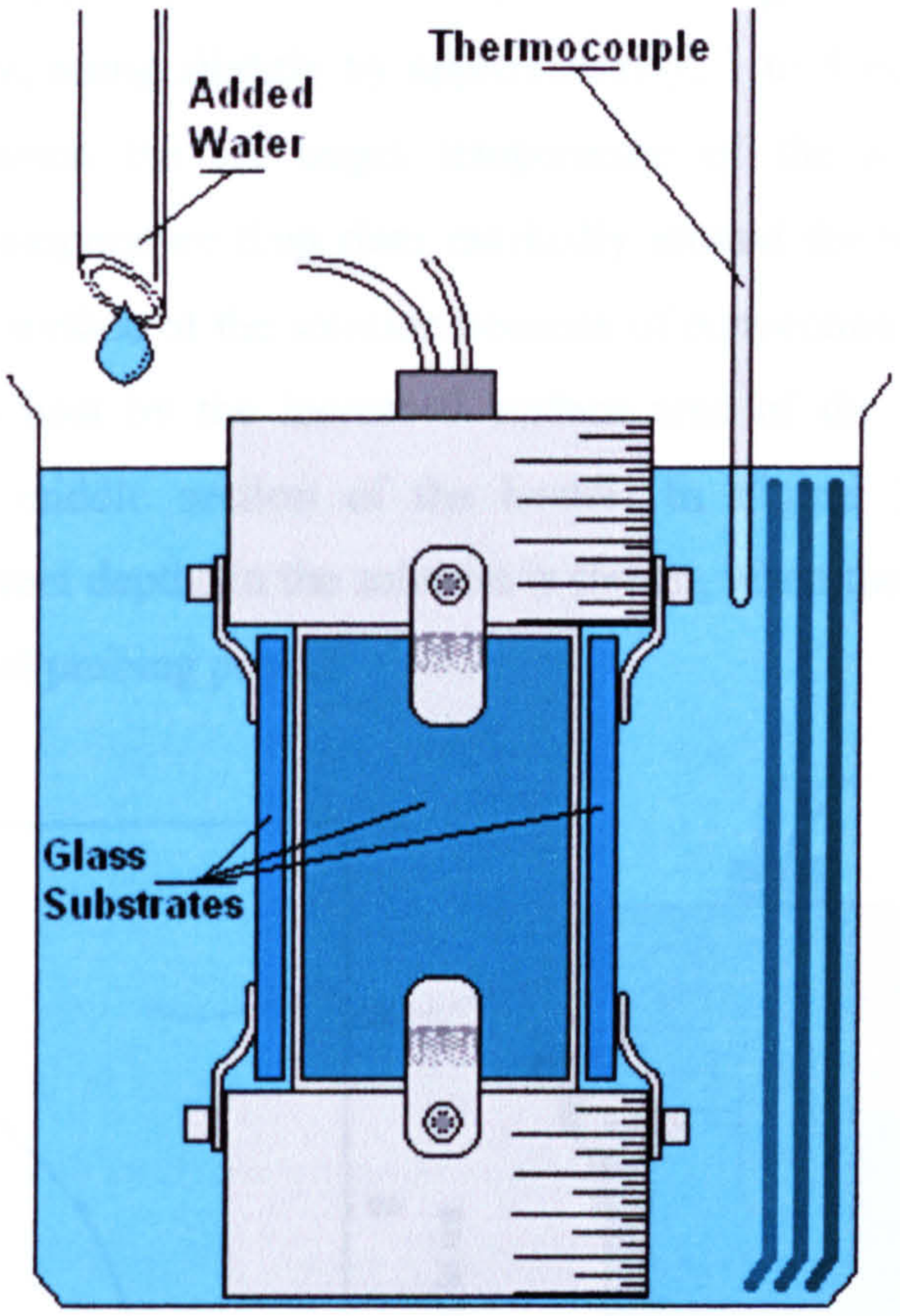

Figure 3.8 Schematic of chemical deposition experiment.

In order to avoid the large temperature fluctuations a separating funnel was used to replenish the lost water in a dropwise manner, as seen in Figure 3.8. A drop-rate of approximately 1 drop every 2.5 seconds was found to adequately stabilise the solution level above the glass substrates, for monitored temperatures above 80 °C. Here it is assumed that only water is being evaporated, while all other reactants are expected to remain in the liquid solution. It is very likely that hydrochloric acid will also evaporate, but very small amounts are used and at the optimum conditions, no acid is added.

The solution temperature is monitored close to the surface of the solution by a type K thermocouple. There is a temperature gradient in the solution also analysed in section 4.4.b., with respect to its influence by ambient temperature. The temperature gradient observed at different depths in the solution arises from the structure of the metallic holder and the position of the heating element. The rod-like heating element

reaches down to the beginning of the lower cylinder of the heater block. Therefore, the lower part is rapidly losing its temperature to the environment and the cold floor where the beaker stands. The mid section, where the glasses stand, has a rather uniform temperature, rising slightly by approximately, 1 to 4 degrees, depending on the difference between the set target temperature of the solution and ambient temperature. The temperature then rises markedly around the top cylinder reaching its maximum at the surface of the solution because of convection flow and the greater amount of radiated heat by the increased surface area of the top cylinder and its interface with the middle section of the heater. In Figure 3.9, the gradient of temperature at different depths in the solution is shown, when the temperature was set at 81 °C at the typical probing point.

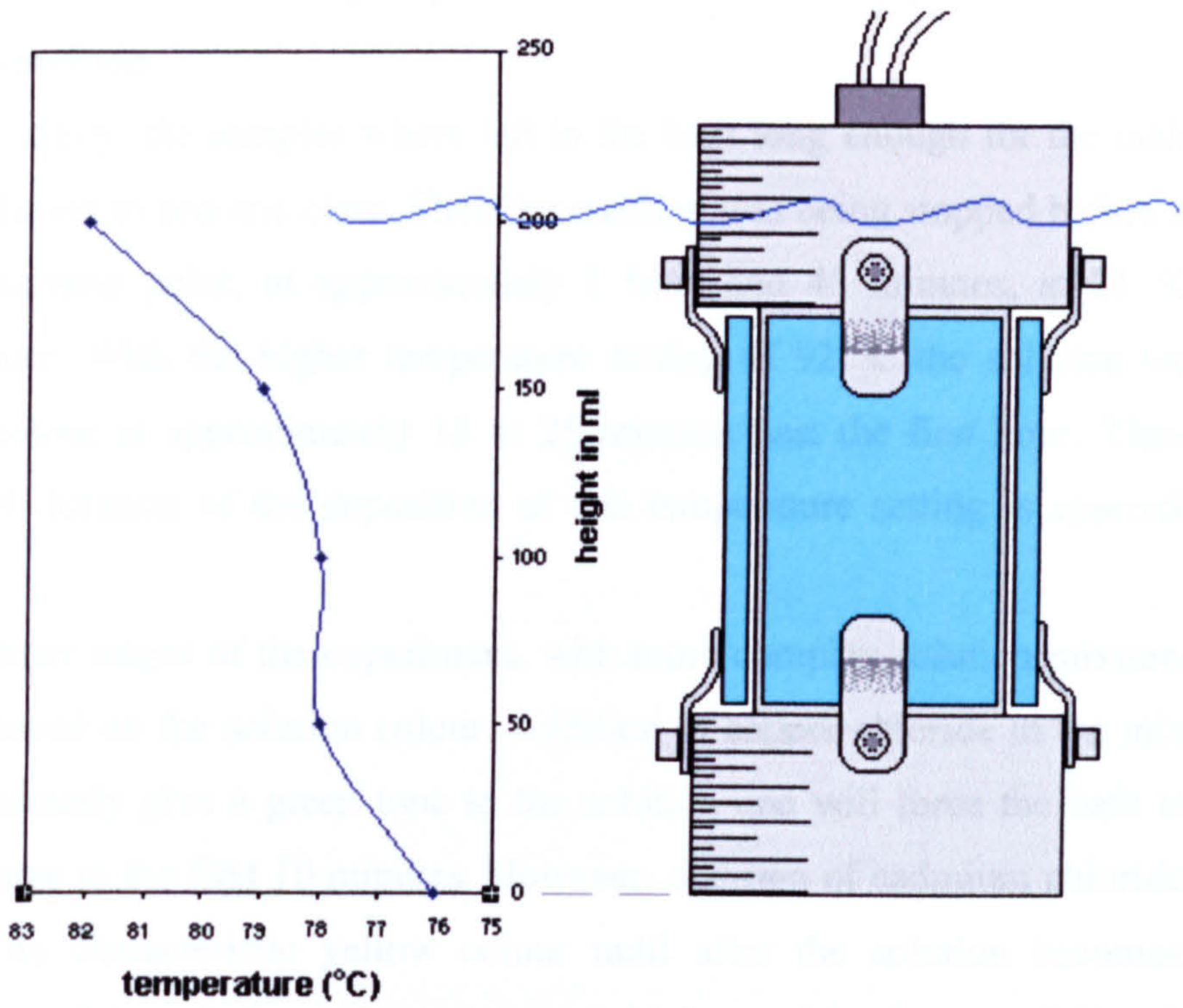

Figure 3.9 Heater block and temperature gradient in the solution, relative to depth, measured at a target temperature of 81 °C when the temperature is monitored at the usual level.

3.3.a. Duration and timeline of deposition

The duration of each chemical bath defined by the reference recipe was 3 hours. Theoretically the substrates can remain in the bath until the reactants are depleted. After a certain point, the grown films lose their adherence to the substrate,

but first they will lose their smoothness and uniform thickness. Therefore, the bath process is stopped much earlier than the depletion of reactants. Changes in colour and clarity of the solution, do signify different parts of the reaction. In the beginning of the experiment, at room temperature, the solution is often clear and colourless unless an additive with very low solubility product is introduced in the bath, intended usually for doping of the films. At the simplest type of deposition, that of undoped ZnS film deposition, the solution becomes cloudy white when the reaction starts, because of the homogeneous formation of suspended ZnS particles. This condition is observed in the first 20 to 30 minutes, with a surface temperature target above 85 °C. The solution will then become white and opaque and it will stay in this condition until the depletion of reactants, towards which it will start obtaining a grey tint and then it will separate between the heavy precipitant and the clear water solvent with the dissolved reaction products.

Initially, the samples where left in the bath long enough for the main volume of the solution to become clear. Then the reaction was being stopped before the colour defined turning point, at approximately 1 hour and 45 minutes, at 81 °C surface temperature. With the higher temperature setting of 92 °C the solution would start turning colour at approximately 15 to 25 minutes past the first hour. Therefore the suggested duration of the deposition at this temperature setting is approximately 1 hour.

Other stages of the experiment, with more complex solution mixtures, can be defined based on the solution colour. Addition of copper chloride in the mixture will almost instantly give a green tone to the solution and will force the bath to reach a cloudy stage in the first 10 minutes. However, addition of cadmium chloride will not produce its characteristic yellow colour until after the solution becomes cloudy. Regardless of the solution colour, the precipitation and beginning of film growth on the substrates is related to the point in time where the cloudiness appears. At 92 °C, it takes approximately 45 to 50 minutes for a good quality film to form, fully covering the outer surface of the samples. Observations concerning the colour and opacity of the chemical bath, helped to determine the optimum duration of precipitation. The experimental timeline has evolved through three main stages that were partially discussed above. The first was that of varied voltage settings attempting to accommodate the temperature changes caused by the occasional addition of water. In the second stage, the whole bath procedure was performed with one voltage setting

and a constant rate of water replenishment in a drop-wise manner. The experimental process followed in this second stage of development is often called CT140 process, which is an abbreviation of constant temperature (pursued by a stable voltage setting) at 140 Volts. At the third stage of development the PID controller is used to control the temperature, while the water is again added in drops at a constant rate. A certain amount of time is required for the solution to reach a temperature of high rate of evaporation, approximately 10 minutes for a temperature of 80 ^{o}C with a voltage feed of 180V at the PID controller. The timelines of the three stages are given in charts 3.1, 3.2 and 3.3 below.

Chart 3.1 A typical 1st stage of development, deposition timeline, taken from deposition 4A

Timeline	Action	Comments
-	Solution's preparation	The substrates and reactants are in the solution.
-	2 drops of acid	The appropriate amount of acid is added.
0:00'	200 Volt	The experiments begins, initial setting 200 Volt.
0:03'	150 Volt	Change of heater setting.
0:12'	110 Volt	-‖-
0:30'	+ 60 ml water	The volume of water decreased, more is added.
0:34'	150 Volt	Change of heater setting.
0:43'	120 Volt	-‖-
0:52'	+ 15 ml water	The volume of water decreased, more is added.
0:56'	110 Volt	Change of heater setting.
2:00'	120 Volt	-‖-
2:02'	+ 50 ml water	The volume of water decreased, more is added.
2:05'	140 Volt	Change of heater setting.
2:18'	100 Volt	-‖-
2:26'	+ 2 drops acid	pH has increased, more acid is added.
2:55'	Turn off heater	The heating resistor is removed from the device.
23:00'	Samples are removed	The samples are taken out of the solution.

Chart 3.2 A 2nd stage of development, deposition timeline - CT140

Timeline	Action	Comments
-	Solution's preparation	The substrates and reactants are in the solution.
-	Addition of acid	The appropriate amount of acid is added, if needed.
0:00'	140 Volt	A constant voltage at 140 V is set.
0:17'	Water addition initiated	The stopper is opened allowing 0.4 drops per second
1:10'	Turn off heater	The heating element is removed from the block.
1:10'	Removal & Cooling	The heater block with the samples is removed from the solution and is introduced in a cold, purified water bath for fast cooling.
1:20'	Sample wash	The samples are detached from the heating block and washed with purified water.

Chart 3.3 A 3rd stage of development, deposition timeline		
Timeline	Action	Comments
-	Solution's preparation	The substrates and reactants are in the solution.
-	Addition of acid	The appropriate amount of acid is added, if needed.
0:00'	180 Volt	A voltage feed of 180 V is given to the PID controller and a target temperature is set to 92 °C.
0:17'	Water addition initiated	The stopper is opened allowing 0.25 drops per second
1:10'	Turn off heater and temperature controller	The heating element is removed from the block.
1:10'	Removal & Cooling	The heater block with the samples is removed from the solution and is introduced in a cold, purified water bath for fast cooling.
1:20'	Sample wash	The samples are detached from the heating block and washed with purified water.

The rate of drops added to replenish the water lost from the bath by evaporation was decided based on experiments performed to determine the amount of water lost at different bath temperatures. A calibration plot was put together from the collected data (Figure 3.10). The lost volume was measured for thirty minutes of keeping a constant temperature in the bath. It proved to be a quite accurate guide in calculating the amount of water that will be lost during an experiment. Again the plot does not apply for temperatures lower than 30 °C. The curve fitted on the data of the plot does not represent an actual equivalence in such low temperatures. It is extrapolated only to show the exponential nature of the data points. The equation describing the fitted curve is $V = 0.3869 \cdot \exp(0.0405 \cdot T)$, where V is the volume of water that was evaporated and T is the temperature of the bath. According to the equation, at 92 °C there are approximately 15.7 ml of water lost every half an hour. With drops of around 0.2 ml each, being added every 2.5 seconds, it works out that approximately 14.4 ml are added back to the solution every half an hour. But it should also be noted here, that the solution's evaporation rate is expected to be lower than that of clean water,[20] which was used for obtaining the calibration plot data.

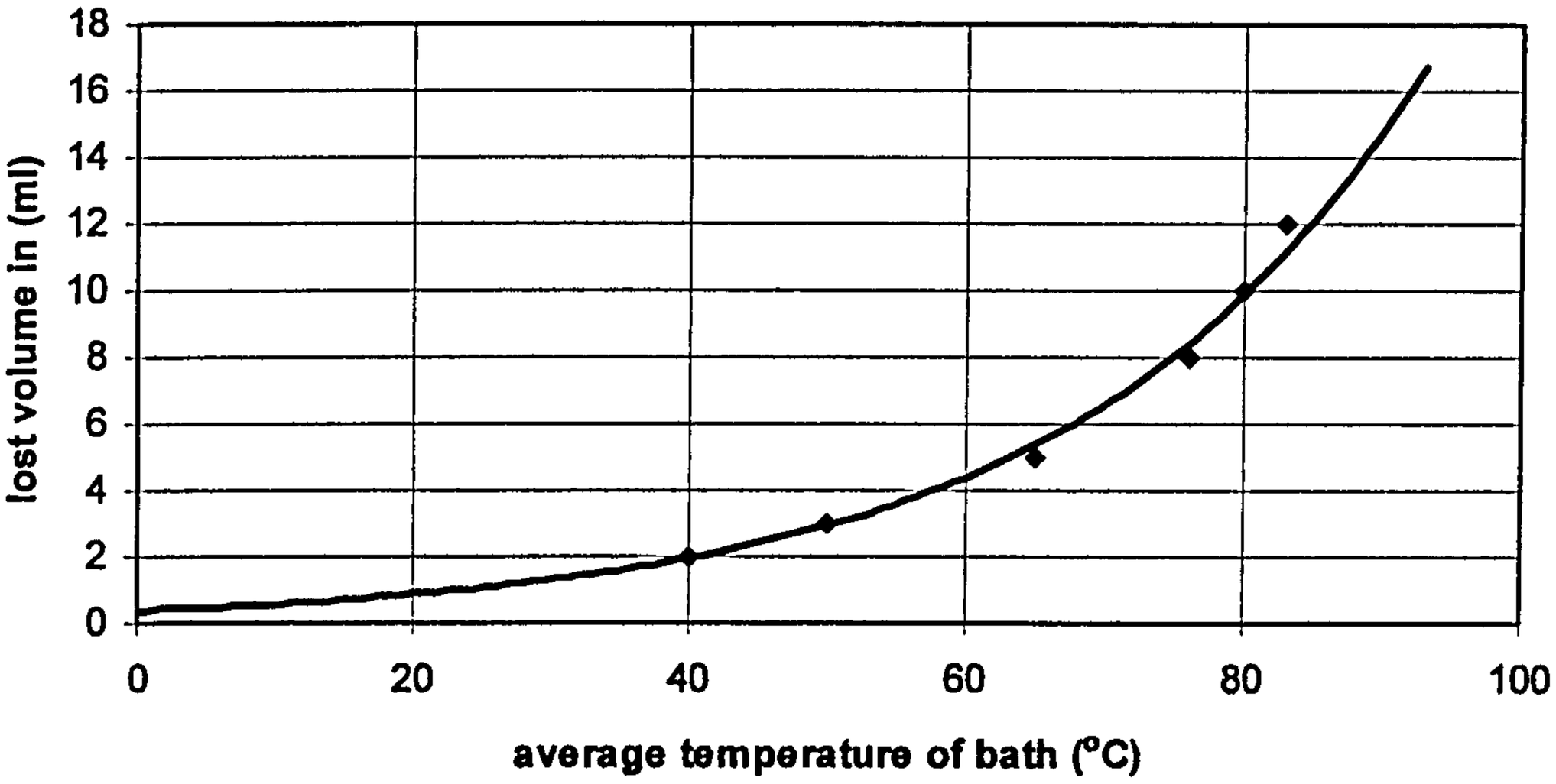

Figure 3.10 Lost volume of water from the bath, over a 30 minutes period at a constant temperature setting.

3.3.b. Variation of acidity, temperature and distance

It was already mentioned above that the acidity of the solution is controlled by addition of drops of hydrochloric acid. The acid was added at the beginning of the bath, right after mixing the reactants. Moreover, it was also added at approximately 2/3 of the duration of the bath, when a larger quantity was needed. Drops of acid may have also been added in the solution at the end of the bath, if the glass samples were intended to remain in the solution overnight after the experiment. The reason that the acid was added in two or maybe three doses was that the acidity of the bath was reducing during the course of the reaction. The same will happen if the samples are left in the bath to cool down overnight.

The first experiments were conducted with a pH of 3.5, achieved by addition of 4 drops of acid solution (the HCl concentration of the drops as mentioned above was 2 M). An investigation of the effects of the bath's acidity on the deposited films was performed in conjunction with a variable temperature deposition procedure. The deposition procedure lasted 3 hours and the samples were each time left in the solution to cool off overnight. Addition of acid was done in two doses, one at turn on and one after 2 hours and 26 minutes. By rule, more drops were included in the first dose, than the second, as their purpose was to reduce the solution pH and then perform the deposition. The second dose only had to measure up to the lost amount of

acid. The acidity was measured after each addition, by an electronic pH checker (Hanna Instruments Checker1 with a HI-1270 electrode) when the solution was cold and with pH indicator papers when the solution was hot. Table 3.2 shows the amount of drops used in the acidity investigation series of experiments, together with the measure pH of the solution for each occasion. In the CT140 and the PID temperature controlled depositions there were no drops of acid added and the pH of the solution remained at 6 to 6.5 for the duration of the deposition.

Table 3.2 Acid drops and measured pH at the acidity investigation experiment series

No of drops at turn on	Measured pH	Number of drops at 2:26'	Measured pH
0	6.0	0	5.6
1	5.5	0	5.5
2	5.0	0	5.5
3	5.0	0	5.0
7	4.0	3	4.5
18	1.5	6	4.0

The temperature was usually monitored close to the surface of the solution, approximately one centimetre below it. This point coincided with the top of the glass samples. As it was discussed earlier in Figure 3.9, the temperature reduces towards the bottom of the beaker. Nonetheless, the temperature measured close to the surface is used as a reference for the description of all the experiments; it is also the reading that was fed into the PID controller device. The temperature is monitored by a type K thermocouple.

As different voltage feeds are given to the heating element, the solution temperature becomes stabilised at different points. Hence, the voltage setting can be used to define the solution temperature, when a constant voltage setting is used without the aid of the PID controller. A calibration plot of the applied voltage against the temperature of the bath was obtained after one hour at each voltage setting (Figure 3.11). The plot seems to be linear, with a rate of change approximately equal to 0.7. Although the linearity is not valid for temperatures close to 100 ^{o}C or close to the ambient temperature.

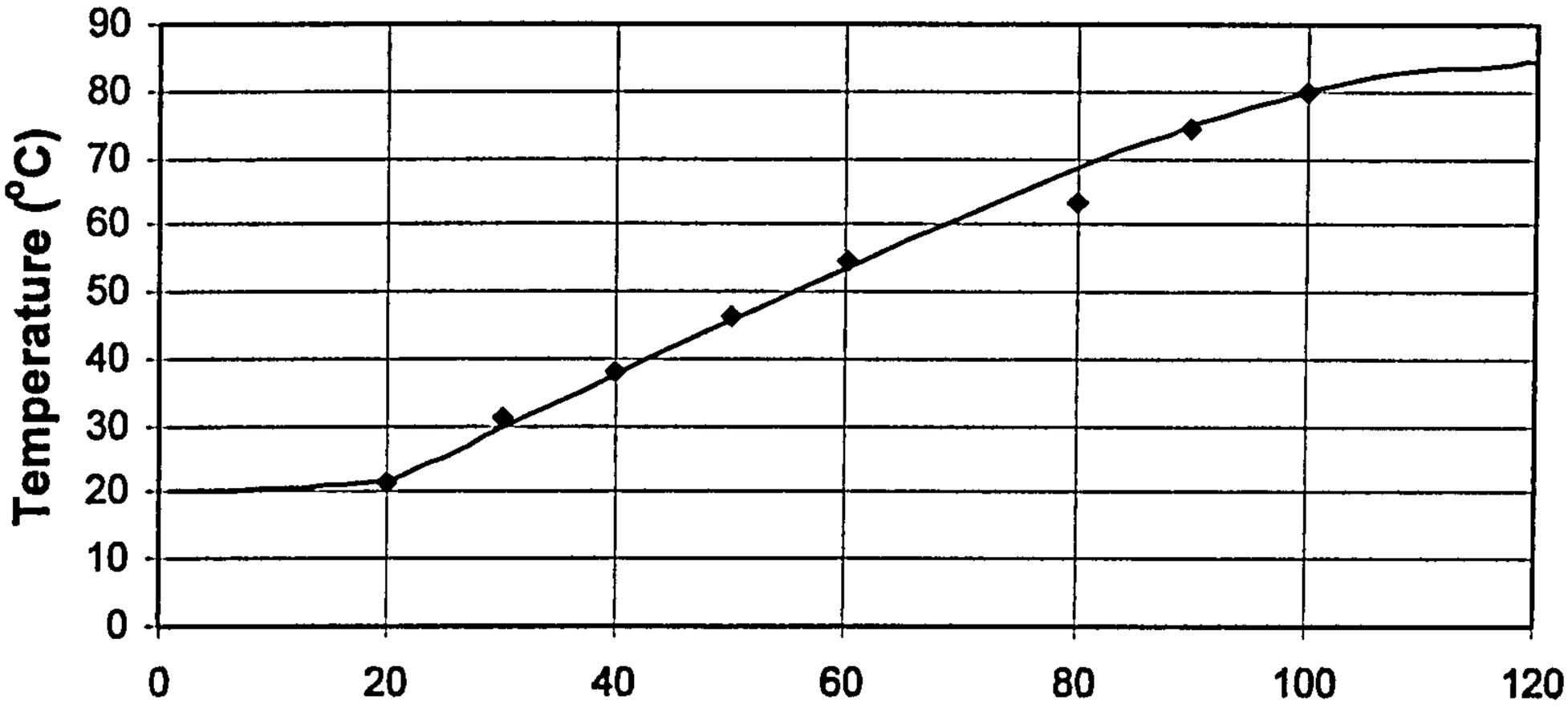

Figure 3.11 Calibration plot of the bath temperature against voltage applied to the cartridge heater.

In chemical bath depositions where the PID temperature controller was used, the only temperature settings ever applied were of 92 and 94 °C. The controller monitors the current temperature of the bath via the thermocouple and turns on or off the voltage feed to the cartridge heater, using thyristors. The voltage feed used with the controller was 180 V for all experiments, which will give the ability to raise the temperature of the solution at a rather fast pace. The controller was automatically calibrated for the heater-bath system using the same voltage feed. With the automatic calibration, the controller obtains the optimum proportional, integral and differential parameters by the characteristics of the system. When available, the PID controller is the best method of setting the temperature of the bath, as it is immune to instabilities caused by the environment.

The distance of the glass substrates from the metallic heater was controlled by the use of separators, as it is displayed in the schematic of Figure 3.7. The groves curved on the heater's surface are of course another way of introducing some spacing between the heater's surface and the inner side of the glasses. The separation between the heater and the substrate is meaningful only when the useful film is intended to be deposited on the inner side of the sample. Apart from two types of glasses that were used as separators, it was also attempted to create the necessary separation by the use of aluminium foil sheets. The thickness of each type of separator is given in Table 3.3. The aluminium foil separators were only used in three experiments, as they were

found to affect the uniformity of the deposited films, since the foil moulds into the microscratches of the heater's surface thus not achieving the separator effect.

Table 3.3 Types of heater-substrate separators

Thickness	Material	Origin
1mm	Sodium doped glass	Microscope slides
0.25mm	Sodium doped glass	Glass cover slips
0.015mm	Aluminium	Ordinary aluminium foil

3.3.c. Tube annealing in argon and H_2S

Certain samples were put through an annealing process after the chemical bath deposition has taken place. Some of the laser transferred films have also been annealed in a similar way. Temperatures between 500 and 750 °C were used for annealing of the samples. Thus, the films had to be deposited onto silica glass substrates in order to withstand such high temperatures. The melting point of silica is at 1710 °C.[21] Silica was also used to build the tube vessel where the samples are kept during the annealing process (Figure 3.12). They were annealed under a nitrogen or argon atmosphere in order to avoid oxidation of the sulfide films. The tube was filled with the inert gas before raising the temperature. The gas flow was maintained at 2.5 cc/min all the way through the experiment, entering one end of the cylinder and channelled out through the other end into tubing leading to the flow gauge. The glass samples were set on a silica tray and were separated from it with silica stands. The tube was then inserted in a furnace built to accommodate it. The temperature was monitored by a thermocouple, inserted in the gap between the glass tube and the inner side of the furnace's curvature. The tip of the thermocouple was reaching the middle of the tube. Up to four samples can be situated on the silica tray. A variable voltage transformer is also used here to control the power applied to the furnace. It takes 3 to 6 hours for the furnace/tube system to reach the desired temperature and almost double that time for it to cool down. The amount of annealing time at a certain temperature stated for each sample is the amount of time that the sample has remained in such a temperature and does not include the heating up and cooling down periods.

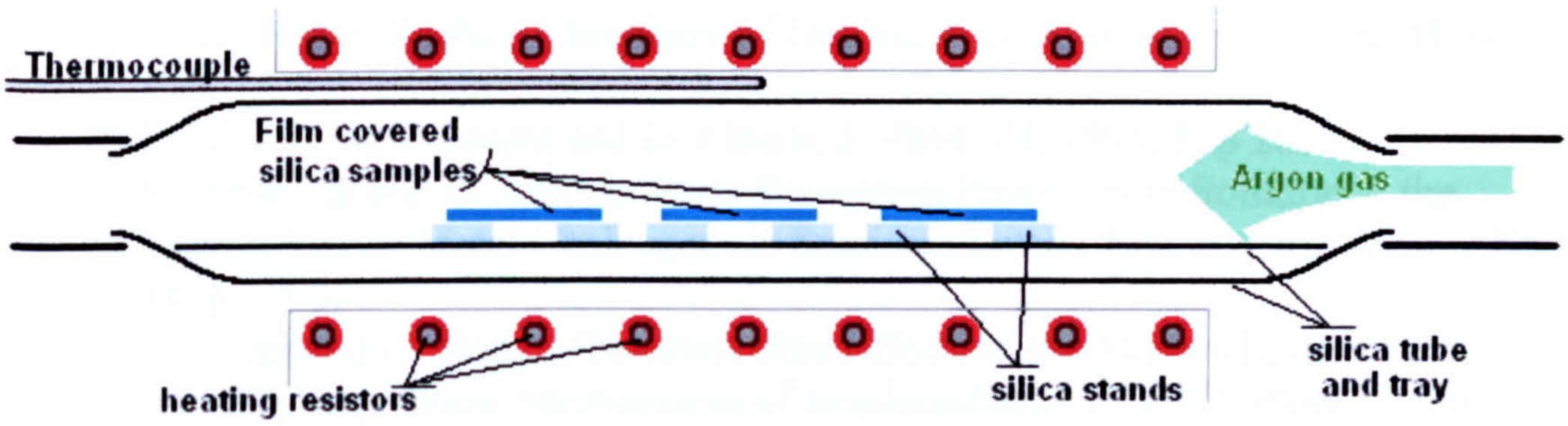

Figure 3.12 Annealing of films deposited on silica substrates. A cylindrical tube is inserted in a furnace, while the samples are sitting on a tray inside the tube. Argon gas is used to provide an inert atmosphere, flowing from one side of the tube to the other.

3.4 References

1. G. Hodes, Chemical Solution Deposition of Semiconductor Films, Marcel Dekker, New York, 2003.
2. M. Farnsworth, Zinc Chemicals, Zinc Development Association, London, 1973.
3. R. O. Borges, D. Lincot and J. Vedel, Chemical Bath Deposition of Zinc Sulfide Thin Films, 11th E.C. Photovoltaic Solar Energy Conference, Montreux, Switzerland, 12-16 October, 1992, p 862.
4. D. S. Boyle, O. Robbe, D. P. Halliday, M. R. Heinrich, A. Bayer, P. O'Brien, D. J. Otway and M. D. G. Potter, A Novel Method for Synthesis of the Ternary Thin Film Semiconductor, Cadmium Zinc Sulphide, from Acidic Chemical Baths, J. Mater. Chem., 2000, **10**, p 2439.
5. K. Manzoor, V. Aditya, S. R. Vadera, N. Kumar and T. R. N. Kutty, Enhanced Electroluminescence Properties of Doped ZnS Nanorods Formed by the Self-Assembly of Colloidal Nanocrystals, Solid State Commun., 2005, **135**, p 16.
6. Q. Zhao, L. Hou and R. Huang, Synthesis of ZnS Nanorods by a Surfactant-Assisted Soft Chemistry Method, Inorg. Chem. Comms., 2003, **6**, p 971.
7. J. Xu and Y. Li, Formation of Zinc Sulfide Nanorods and Nanoparticles in Ternary W/O Microemulsions, J. Colloid Interface Sci., 2003, **259**, p 275.
8. L. Wang, X.-T. Tao, J.-X. Yang, Y. Ren, Z. Liu and M.-H. Jiang, Preparation and Characterization of the ZnS Nanospheres with Narrow Size Distribution Opt. Mater., 2006, **28**, p 1080.
9. M. Kostoglou, N. Andritsos and A. J. Karabelas, Incipient CdS Thin Film Formation, J. Colloid Interface Sci., 2003, **263**, p 177.
10. X. Liu, J. Cui, L. Zhang, W. Yu, F. Guo and Y. Qian, A Solvothermal Route to Semiconductor ZnS Micrometer Hollow Spheres with Strong Photoluminescence Properties, Mater. Lett., 2006, **60**, p 2465.
11. L. Chen, L. Wang, T. Luo and Y. Qian, A Hydrothermal Method to Prepare the Spherical ZnS and Flower-Like CdS Microcrystallites, Mater. Lett., 2006, **60**, p 3627.
12. H. Deng, C. Chen, Q. Peng and Y. Li, Formation of Transition-Metal Sulfide Microspheres or Microtubes, Mater. Chem. Phys., 2006, **100**, p 224.
13. P. O'Brien and J. McAleese, Developing an Understanding of the Processes Controlling the Chemical Bath Deposition of ZnS and CdS, J. Mater. Chem., 1998, **8**, p 2309.

14. G. D. Parfitt, Surface Chemistry of Oxides, Pure Appl. Chem., 1976, **48**, p 415.
15. B. Mokili, M. Froment and D. Lincot, J. Phys. III, 1995, **5**, p 261.
16. M. Froment and D. Lincot, Phase Formation Processes in Solution at the Atomic Level: Metal Chalcogenide Semiconductors, Electrochim. Acta, 1995, **40**, p 1293.
17. S. Gorer and G. Hodes, Quantum Size Effects in the Study of Chemical Solution Deposition Mechanisms of Semiconductor Films, J. Phys. Chem., 1994, **98**, p 5338.
18. J. M. Doña and J. Herrero, Process and Film Characterisation of Chemical-Bath-Deposition ZnS Thin Films, J. Electrochem. Soc., 1994, **141**, p 205.
19. P. O'Brien, D. J. Otway and D. S. Boyle, The Importance of Ternary Complexes in Defining Basic Conditions for the Deposition of ZnS by Aqueous Chemical Bath Deposition, Thin Solid Films, 2000, **361-362**, p 17.
20. J. C. Kotz and P. Treichel, Chemistry and Chemical Reactivity, 4th Edition, Saunders Colledge Publishing, 1999.
21. A. Goldsmith, H. J. Hirschhorn and T. E. Waterman, Handbook of Thermophysical Properties of Solid Materials, Revised Edition Vol. 2 & 5, Pergamon Press, Oxford, 1961.

Chapter 4.

Analysis of Deposited films

Chapter 4. Analysis of Deposited films

4.1 Introduction

Depositing thin phosphor material films by chemical precipitation was the first step of this research. Before moving on to the laser transferring step, the films precipitated were evaluated. This evaluation aimed at improving the deposition method in terms of efficiency and the quality of the films. It is expected that the laser transfer process would require melting of the film and an abrupt loss of momentum at the instance the film is travelling across the gap between the two substrates. Therefore, it can be argued here that just those two intense mechanical and physical phenomena would be enough to diminish any quality of the chemically prepared films. Nonetheless, it remains a challenge to accomplish a successful transfer of a luminescent film. Additionally some film properties sought here, would aid the transferring process. A continuous film, both in constitution and structure, will provide for a good basis of comparison between the precipitated and transferred film and will later on support possible requirements of area selective transfers used as a semiconductor writing technique.

The concept of a continuous structure also extends over film thickness, thus including roughness and isolated features. Finally, the size of the film is a delicate property when it comes to forward transferring. A very thick film will be forced away from the primary (source) substrate with great difficulty and will probably never reach a high enough temperature in order to adhere to the new (target) substrate. The most possible result would be a cracked layer on the source and small-scattered pieces on the target. Some of the material is meant to evaporate and diffuse into the surrounding atmosphere, due to the high pressure of the gases formed. Hence a very thin precipitated film, could easily vanish under the laser radiation, or could form scattered droplets on the target substrate, which may be of interest for further investigation, but removes the ability to transfer coherent layers of the material.

Thickness and roughness are investigated as the main mechanical properties, luminescence and composition as the physical and chemical properties. Surface morphology and crystal lattice structure were also considered very interesting fields of research, as they can help establish the capabilities of the chemical bath process

used here, as a means of depositing thin semiconductor films. There is already a large amount of literature on the deposition of II-VI materials by similar chemical methods, some claiming the formation of very high quality crystals, or nanosized crystals. Thus, information on these aspects of the films would also permit for comparison between the different documented methods.

In this chapter, a collection of the results obtained by each analysis technique is put forward in an attempt to define the various properties of the chemically prepared films. The results obtained from the techniques are categorised by the type of information they provide about the films. The categories are: composition; morphology; film size; crystal structure and luminescence. Some of them may participate in two categories, as for example optical microscopy, as it is a technique of rather general observations. Others are confined within one category even if they have the ability to define a wider variety of film properties, such as EXAFS, yet their predominant focus in that field dictates their discrete participation in a single category. A conclusion over the observations on the chemically prepared films combines all the discussed results hence presenting a comprehensive evaluation of the films.

For investigation of composition, as in qualitative and quantitative elemental analysis, the main technique used was Energy Dispersive X-ray Analysis and Inductively Coupled Plasma Mass Spectroscopy was applied on a single sample to detect for trace metal elements. EDXA offers reliable recognition of the various elements expected to be found in the films, down to approximately 1% in concentration. ICPMS is very precise in detecting metal composition at concentrations of parts per billion.

The surface morphology of the films was observed by Optical and Scanning Electron Microscopy. Optical microscopy is probably the best observation technique for micrometer-sized features. For smaller features, approaching a few tenths of nanometers, SEM is perhaps the most reliable observation technique, even when in the case of semiconductors, the surface has to be covered by a very thin film (~5 nm) of carbon or gold. The ability to turn the sample holder at different angles permits observation of features in three dimensions.

The thickness of the films was determined by four different methods. Two of them were based on reflectivity spectra and have used innovative algorithms to model the thickness and roughness of the films in terms of layers of materials with different

refractive indices. In a similar manner, a more established technique, Ellipsometry was employed to model for film thickness and roughness, based on the polarisation of light reflected from the sample. SEM is again used here to measure the thickness of the films, as electron micrographs of the edges of various films were available at an angle small enough to sanction examination of the height difference between the substrate's and the film's surface. Measurement of film thickness by SEM is the straightforward method, but to perform it with increased accuracy, precise cutting, smoothing and polishing of the cut edge had to be performed and then viewing it at a vertical angle to the plane of the film. Unfortunately the appropriate apparatus to perform these tasks were not available.

The phase of crystallisation is usually determined for semiconductors, which is also expected to affect the material's bandgap by a small amount. This can be defined by X-ray Diffractometry, while Raman spectroscopy can also differentiate between the two phases. X-ray diffraction patterns have been used for determination of the dominating crystal phase at various annealing temperatures, but it was impossible to apply Raman spectroscopy to the chemically deposited films, as they were very thin for the probing abilities of the technique. X-ray techniques are more reliable in characterising crystals as by definition they employ small wavelengths, able to return information directly related to atoms. The positions, distances and coordination of atoms around a specific element can be determined by EXAFS, information that can then be extrapolated in determining the structure of the crystal lattices. But the position of activation elements within the lattice is closely related with the luminescent properties of the films and of course with the film formation procedure. A macroscopic view of large crystalline formations seen through the optical microscope is also considered.

Finally the luminescence and optical properties of the films are contemplated, based on cathodoluminescent, photoluminescent and UV-Visible transmission spectra. Cathodic rays and high energy UV laser light can be used to excite electrons over the phosphor's bandgap, which will then recombine through the various activation centres. Thus, the luminescent characteristics and efficiency of the films can be defined. Transmission spectra can define more properties of the films, but the results are mostly related to the optical, luminescent and composition properties. The most significant of the optical properties is the bandgap of the films, which was here exclusively determined from the transmission spectra.

The theory and performance of the techniques was analysed in chapters 1 and 2. Chapter 6 will also follow route in the analysis of results obtained after the laser transferring step. This will enable for direct comparison between the chemically deposited films and the laser transferred films. After this comparison, a more integral outlook of the chemical deposition procedure is assembled which is found in the conclusions chapter (chapter 7).

4.2 Element Composition of Films

4.2.a. EDX

It was already explained in section 2.7 of this thesis, that energy depressive x-ray analysis (EDX-A) can be used for qualitative elemental analysis of a specimen's surface. The method is also able to provide quantitative information as a percentage within the probed area, when it is accordingly calibrated. The OX200 EDX system bundled with the LEO-S360 SEM at the university campus was not calibrated for the elements of interest to this research; therefore no exact figures of percent participation were made available by the analysis. Nonetheless, there can be a comparison between spectra and for a material with the same proportions of each element, similar ratios between the peak heights would be expected. EDX is a standard, fast and reliable technique for performing elemental analysis on any surface, without inflicting changes to the sample. It is also very conveniently combined with a scanning electron microscope, which permits both a morphology investigation and a composition analysis of any solid sample surface and at a very small scale, reaching down to nanometre levels. The sensitivity of the technique reaches to about 1-2 %, so it can be used to detect dopants at their largest acceptable concentrations.

EDX analysis was initially employed to verify the existence of zinc and sulfur in the films. It can be considered as a sign of successful precipitation of zinc sulfide when combined with results from other techniques. In Figure 4.1 the zinc L_a and L_b emission at around 1 keV is seen at a comparable height to the sulfur K_a emission peak at 2.3 keV. The zinc K emissions have a difference of approximately 30 eV, hence being difficult to distinguish between the two in the spectrum. The K_a and K_b peaks of zinc are also slightly visible at 8.63 and 9.57 keV respectively, but at significantly lower levels. The Si peak at about 1.8 keV corresponding to either a K_a

or a K_b transition has a strong presence in the spectrum, arising from the silicon content of the substrate, since the technique reaches a probing depth of approximately 1 to 2 μm[1] depending on the material and the as deposited films hardly ever reach a thickness of 400nm.

Impurities of the microscope slide like calcium, magnesium, aluminium and potassium all of them likely to be incorporated in an oxide or other salt-like form, are observed too on the spectrum. Calcium comes from the limestone ($CaCO_3$) component element of sodalime glass. Sodium would be expected to present its K_a line at around 1 keV, though this coincides with the zinc L emissions, therefore it is not easily observable. The resulting peak at 1 keV though, could be a composite of emissions from both elements. In Figure 4.2 for example the spectrum of a similar film deposited on silica, shows a smaller peak for the zinc L emissions, comparable to its K_a peak and being approximately half the height of the sulfur peak. At the same time, the zinc K_a peaks remains at a height reaching approximately a third of that belonging to sulfur.

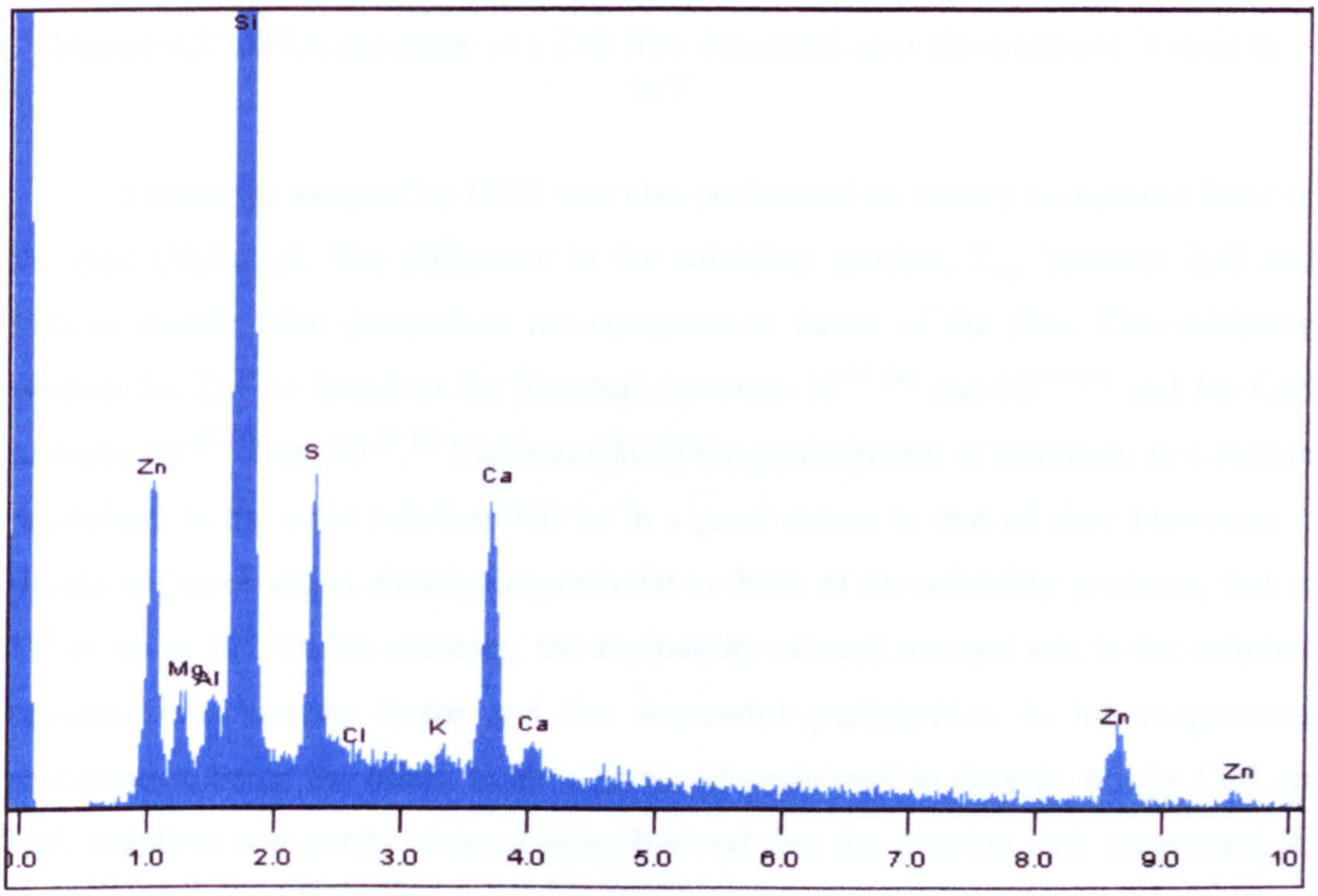

Figure 4.1 EDXA spectrum of a ZnS film deposited on a sodalime glass microscope slide. X-axis in keV.

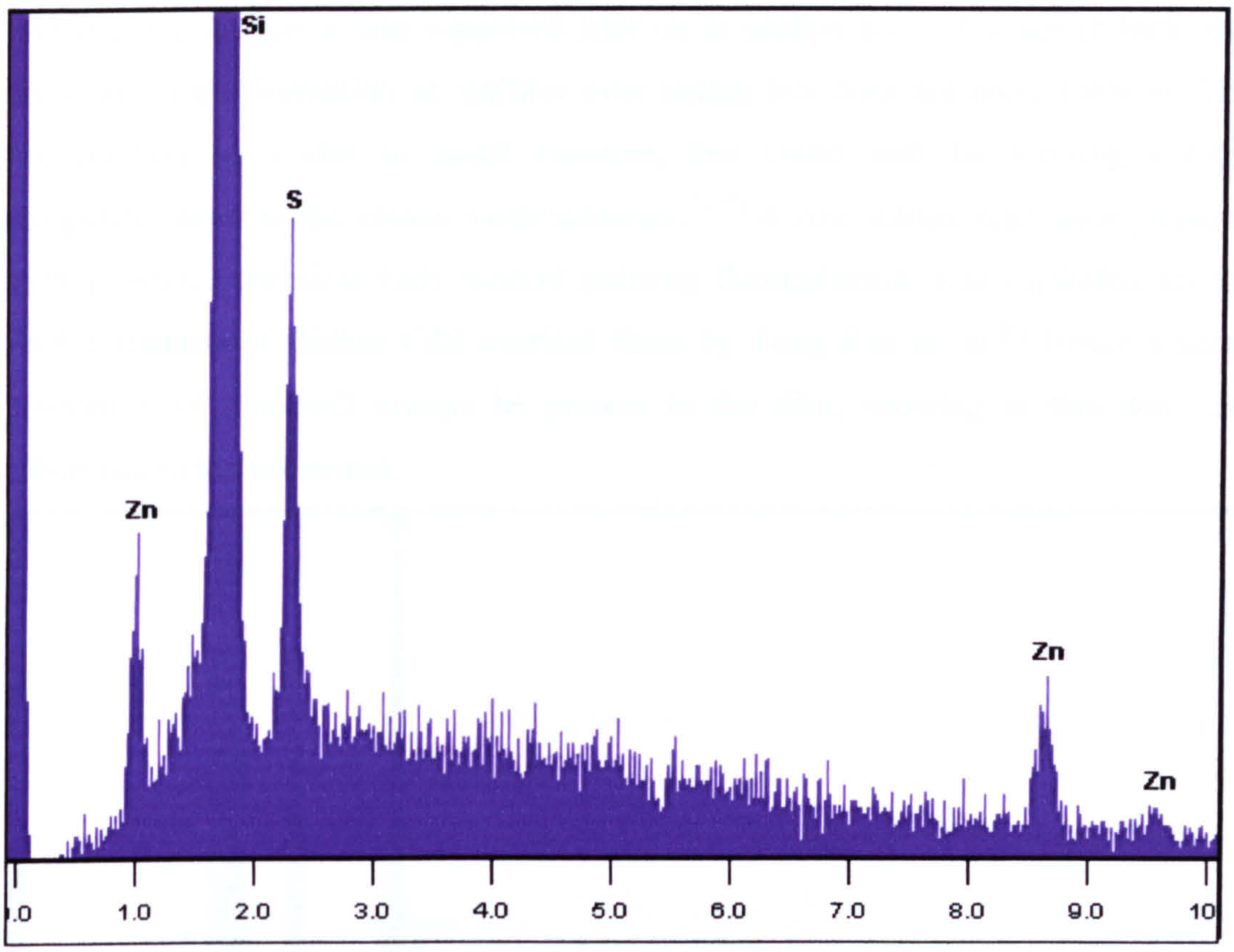

Figure 4.2 EDXA spectrum of a ZnS film deposited on a silica sample. X-axis in keV.

Elemental analysis by EDX was also performed on ternary compound films of the type $Cd_xZn_{1-x}S$. The difference in the solubility product, K_{sp}, between ZnS and CdS is mainly what determines the composition factor of the film. The solubility product for ZnS is found in the literature between 10^{-25} [2] and 10^{-21} [3] and for CdS between 10^{-28} [2] and 10^{-29}.[3] Understandably the participation of cadmium as a sulfide precipitant in the solid solution will be in a great excess to that of zinc. However, it should not reach ratios directly proportional to those of the solubility products, that is 10^3 or up to 10^8. On the contrary, the availability of each reactant salt in the solution becomes one limiting factor and the successful participation in inhomogeneous precipitation being the other. In an experiment performed to deposit strictly CdS on both sodalime and quartz slides it was observed that the reaction bath progressed in the same way as that of ternary precipitations, but there was no adherent films obtained on the glasses and least of all on the quartz. As a consequence, a thin layer of zinc sulfide or possibly zinc oxide is required to form at the glass solution interface, before any other homogeneously grown particles adhere on the glass in order to form the film (see 4.3.a). The assumption of a ZnO or ZnS thin film, binding the particles

on the glass surface is also supported later on in section 6.1.c. The acidic bath used does favour the formation of sulfides over oxides but does not completely exclude precipitation of oxides in small amounts, that could well be forming a more compatible layer to the silicon oxide substrate.[4, 5] A zinc sulfide seed layer prepared with a similar chemical bath method utilising thioacetamide was exploited for the final formation of thicker CdS overlaid films by Tong Ren et. al.[6] Hence a small proportion of zinc will always be present in the film, securing in this way film adherence to the substrates.

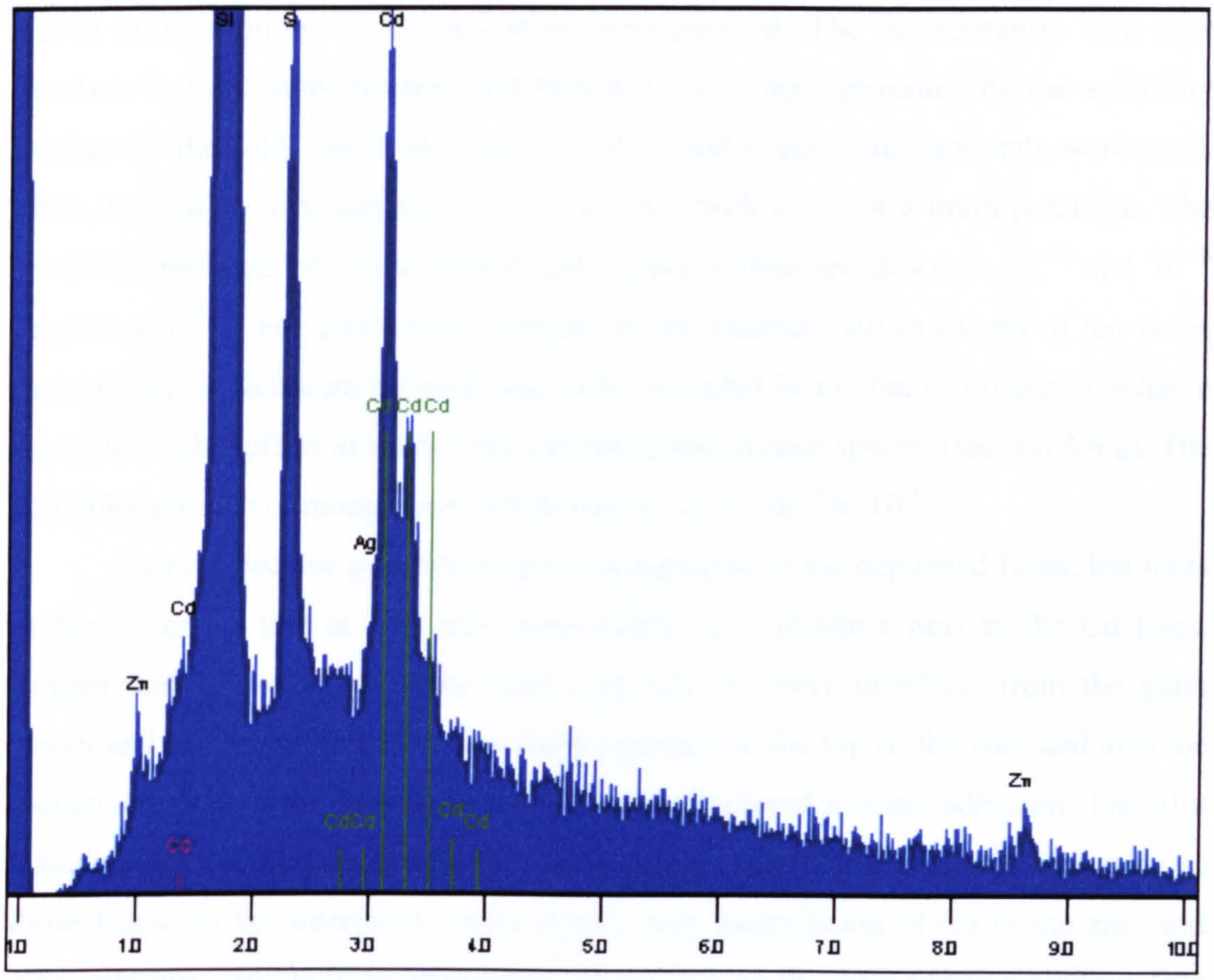

Figure 4.3 EDXA spectrum of a ternary $Cd_xZn_{1-x}S$ film, doped with Ag and deposited on quartz. X-axis in keV.

In the figure above, a spectrum of a ternary film is depicted. Lines corresponding to the theoretically calculated emissions of Cd are also given in dark green with the three taller lines standing for L_{a1} L_{b1} and L_{b2}. They are well distinguishable in the spectrum, with the first one reaching to similar levels to the sulfur peak. Zinc peaks are also distinguished on either side of the spectrum, with the zinc L lines being significantly smaller when compared against sulfur than what was

found for the zinc sulfide film on quartz in Figure 4.2. The zinc to sulfur peak height ratios are approximately ½ for the ZnS film and 1/6 to 1/7 for the ternary film.

Silver or any other dopant used should be detectable when it reaches high enough concentrations in the film, close to 1 or 2 percent.[7] Such high concentrations of dopants might not prove very efficient in a phosphor, since zinc and cadmium based phosphors are usually doped at levels between 0.01 to 1 percent maximum. However, at an experimental level, in an attempt to prove the possibility of incorporation of appropriate activators in the film by the same chemical method, higher concentrations of the activators were pursued. The incorporation here only involves in very small fraction and thus it is even more governed by the solubility product of the salts. So in the cases of silver and copper, tiny amounts were used, often impossible to weigh on a typical balance with a 1% of a gram precision. The solubility products of silver sulfide and copper sulfide are down to 10^{-50} and 10^{-48} respectively.[2, 3] For manganese, weights of the chloride salt in excess of ten times that of zinc or cadmium chloride had to be included in the bath in order to achieve some detectable effect at least in the cathodoluminescence spectra (section 4.6.a). The solubility product of manganese sulfide reaches up to 10^{-15} to 10^{-13}.

It never became possible to detect manganese in the deposited films, but hints of the silver L_{a1} line at 2.98 keV were visible as a shoulder next to the Cd lines. Copper sulfide seemed to form films very fast on every interface, from the glass vessel and glass samples, to the air water interface at the top of the bath and also the metallic surface of the heating device, where it displayed a better adhesion. The film adhesion of CuS on glasses was very poor. On the other hand, the early formation of those films, on the interfaces, could signify easy assimilation of Cu in the zinc and zinc cadmium, sulfide films and perhaps even more on the early forming binding ZnO and ZnS layers discussed earlier. The introduction of silver chloride in the bath, aiming at silver doping of the films, gave a slower change in colour than that of copper and sustained its homogeneity at better levels throughout the reaction. This could be taken as an indication of silver participating in the formation of both the inhomogeneously grown bonding films and the homogeneously grown cluster particles adhering to the film later.

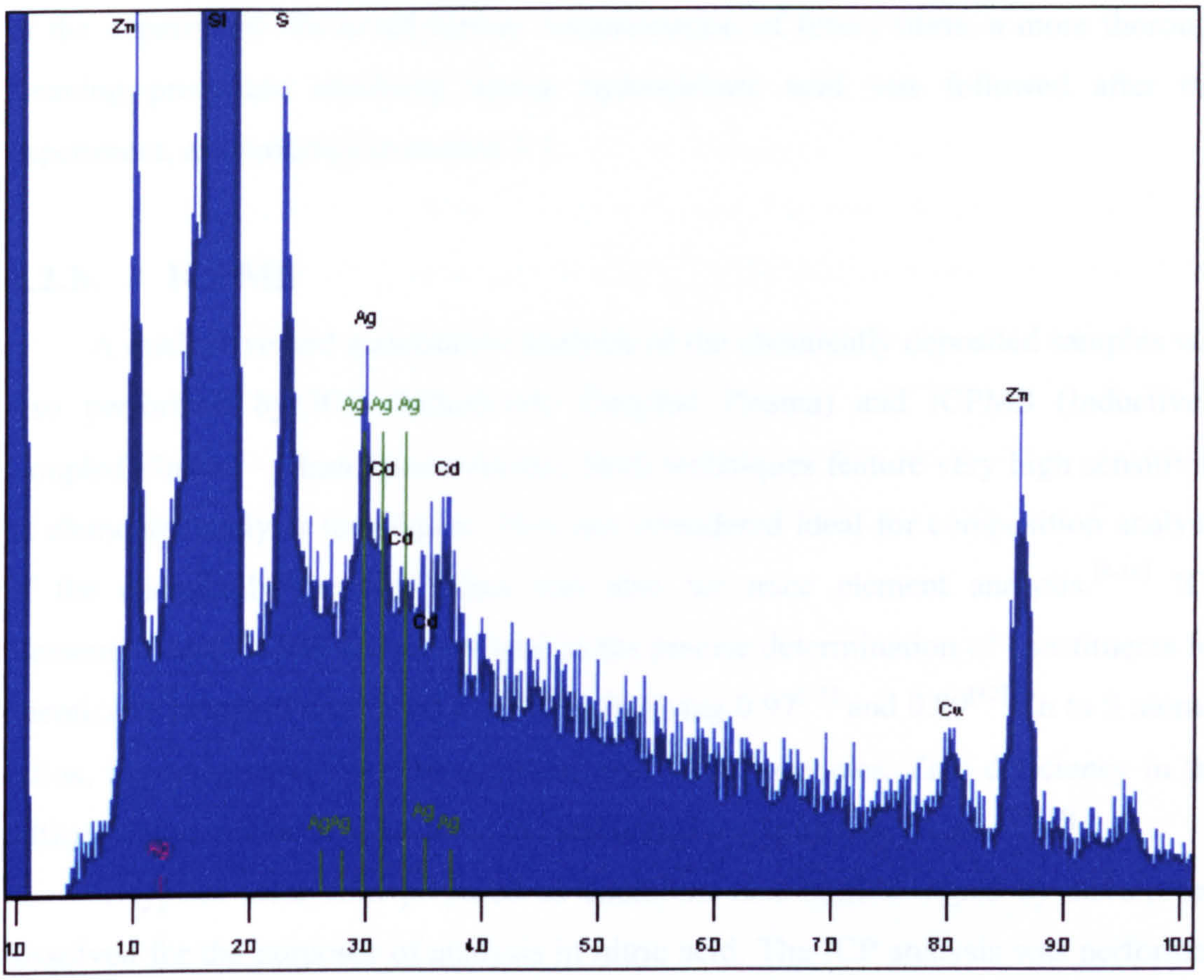

Figure 4.4 EDXA spectrum of the remaining film on the source sample (glass substrate that participated in the chemical bath). The substrate was a quartz slide. Large peaks of Zn, Ag and Cu are distinguished, compared to those for sulfur and cadmium. X-axis in keV.

A clear detection of silver and copper was achieved on a thin film remaining on the substrate used in the chemical bath, called the source sample, after ablation and redepostion of the upper part of the film on a new substrate by the LIFT method (as explained in Chapter 5). In Figure 4.4 the silver L_{a1} line is now highly pronounced above those expected for Cd and also the copper K_a line at 8 keV is now visible. The high peak corresponding to zinc at 1 keV (compared to that of sulfur) denotes again that the part of the film closer to the substrate has a higher concentration of zinc, as explained earlier. The Cd lines are now very weak and allow for those of silver to become visible. Silver chloride was included in the bath for doping, but copper is also visible because large concentrations of copper chloride in previous experiments had contaminated the metallic heater. The existence of Cu_2S in the bath was verified by

the fast change of bath colour to dark green and its equally fast fading, from the start of the experiment. To avoid further contamination of future films, a more thorough cleaning procedure involving strong hydrochloric acid was followed after this experiment, as explained in section 3.3.

4.2.b. ICPMS

A qualitative and quantitative analysis of the chemically deposited samples was also performed by ICP (Inductively Coupled Plasma) and ICPMS (Inductively Coupled Plasma – Mass Spectrometry). Both techniques feature very high sensitivity as elemental analysis techniques. They are considered ideal for composition analysis of the chemically prepared films and also for trace element analysis.[8-10] ICP elemental analysis has been employed in the precise determination of constituents for chemically prepared nanosized ZnS crystals giving 0.97[11] and 0.89[12] Zn to S atomic ratios, implying small concentrations of zinc atom vacancies. Zinc deficiency in the lattice of zinc sulfide is considered the self activation inflicting factor. [13, 14]

A typical clear film prepared as cadmium zinc sulfide doped by silver, was dissolved for the purposes of analysis in nitric acid. The ICP analysis was performed on the basis of zinc, cadmium, sulfur and silver that were already expected to be present in the sample and the more sensitive ICPMS analysis was used for trace metal element analysis of a large variety of metals that can typically be detected by the technique. ICPMS did detect quantities of zinc and cadmium in conjunction with the rest of the metals, but their high concentration saturated the detector, which had been set up for small quantities of each metal. Thus, the readings from the ICP method are used for the main constituent elements zinc, cadmium and sulfur, while the ICPMS results are considered more reliable for resolving the impurity concentrations. ICPMS was also considered a more reliable route for determining the concentration of silver, even though the percentage participation values from both techniques were in close agreement, 0.074 % for ICPMS and 0.092 % for ICP.

All participation ratios or concentrations were converted to molar percentages of the total substance that resulted from dissolution of the film. The film weight was found by precisely weighing the sample before and after removing the film and was found to have a total mass of 0.0004 g. Summation of all percentages of detected elements does not reach a concluding 100 %. A remaining 4.48 % was attributed to

oxygen as zinc oxide or possibly cadmium oxide compounds can be expected to form in the solution or inhomogeneously on the substrate surface. The oxygen would have escaped during dissolution of the film, or in any case would not be detected by any of the two methods. The molar participation percentage of oxygen was derived by presuming that the missing weight ratio percentage corresponds to oxygen and thus applying its molecular weight to the calculations. There is an expectancy of chlorine incorporation in the films but at much smaller levels than oxygen, so its occurrence was neglected in the calculations. The percentage sum of impurity metals, excluding that of silver, was also subtracted from the total undetectable elements percentage of the ICP method. When silver is included in the total impurity percentage, it rises up to 1.64 %.

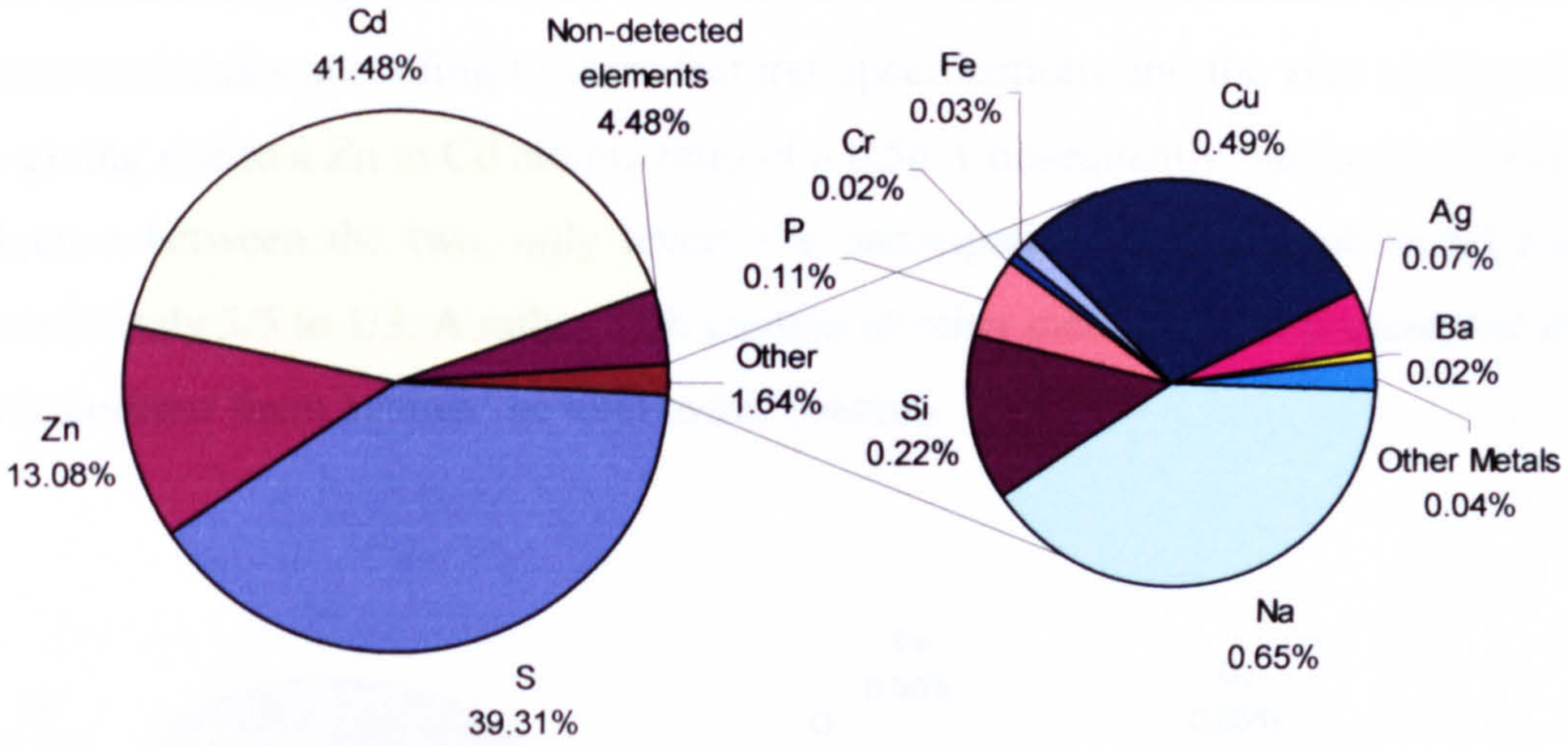

Figure 4.5 Combined ICP and ICPMS elemental analysis of a CdZnS:Ag film. Molar percentages of each element are given.

Examination of the percentage of occurrence for each element in Figure 4.5 above, suggests a high metal content in the film. A ratio between the metal atoms (mainly Zn and Cd) and the anions (here being S and possibly O or small quantities of Se) calculated to 1.28 / 1. The non-detected elements proportion is considered to be due to oxygen as it was explained earlier. So there would be an extra atom of a metal (Cd or Zn) for every three of them participating in bonds. Either bonding or

interstitially residing metal atoms included in the sulfide crystals are 69.94 % of the total metal atom content and in the oxide crystals, a 7.97%.

The cadmium and sulfur proportions are similar but it cannot be assumed that only cadmium participates in sulfide formation. On the other hand, most of the assumed oxygen content could be attributed to zinc oxide formation on the substrate interface. Under this condition, only about a third of the total zinc metal is bonded with oxygen. The rest soon reverts to the sulfide form. A zinc to sulfur ratio is also observed at approximately 31 %. Remarkably, the weight ratios of the two chloride salts, cadmium chloride and zinc chloride were usually kept between 1:3 and 2:3, though for the specific experiment it was recorded at 1:3. However, the molecular weight of zinc chloride was much smaller of that of cadmium chloride, not only because of the atomic weight difference between the two elements, but also because of the molecular weight difference between their hydrates. The cadmium salt includes 7 water molecules according to manufacturer specifications and the zinc salt has 2.5, thus giving rise to a Zn to Cd atomic ratio of a 0.56. Consequently, the large solubility difference between the two, only levers the participation ratio of each metal from approximately 3/5 to 1/3. A rather high content of other metals is also present, but it is best to contrast them against the total metal content.

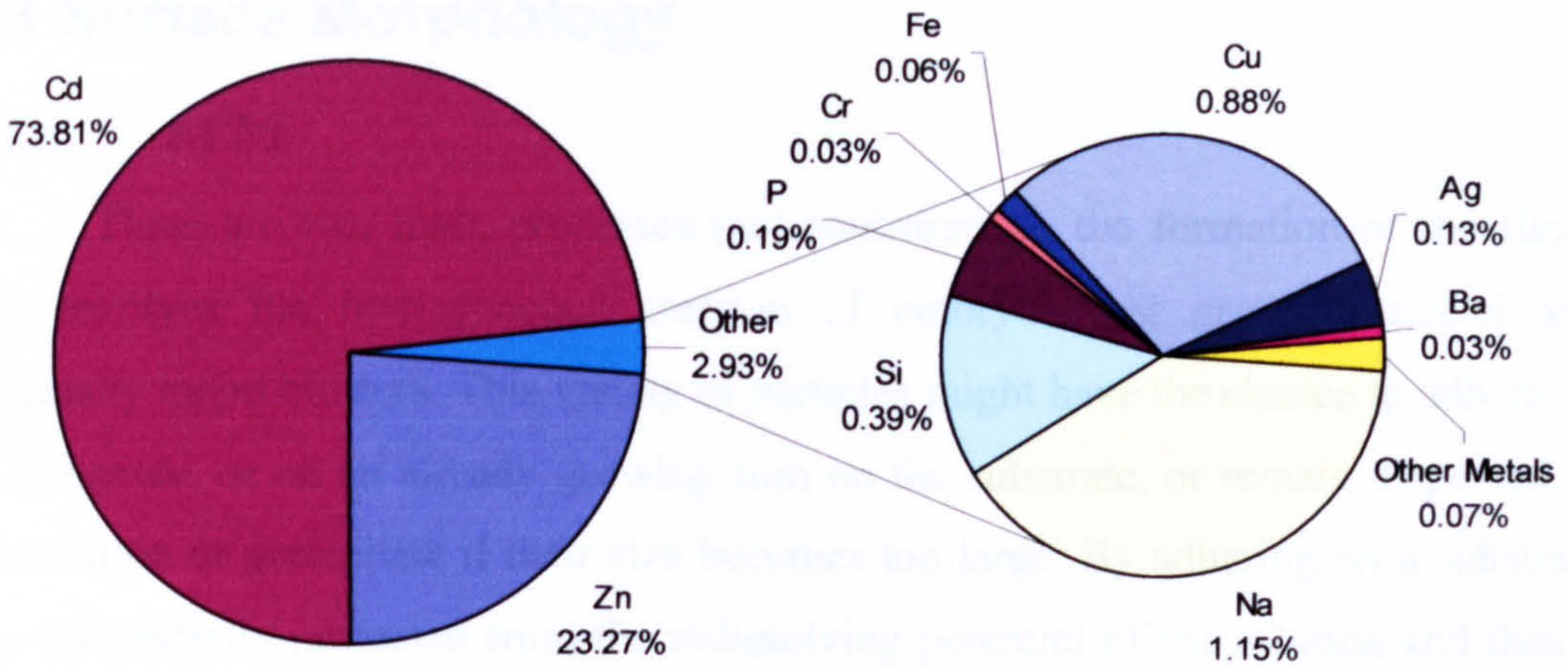

Figure 4.6 Combined ICP and ICPMS elemental analysis restricted to metal content. Molar percentages of each element are given.

An almost 3% of the metal content of the film was composed of impurities. Silver was intentionally introduced, but reaches only a small level, 0.13 %, which nonetheless is considered ideal for doping of sulfide phosphors. [13-18] Interestingly, a higher proportion of Cu was found, as a remainder from previous baths that included high concentrations of copper chloride salt (see also section 4.2.a). A high concentration of sodium was also found. This is more than 1 % of the total metal content in the film. High concentrations of activator atoms (1% or more) often appear to distort significantly the luminescence spectrum of a phosphor and often reduce its luminescent efficiency as the concentration keeps on increasing.[19-21] When the same conditions take place for non-activator atoms such as sodium in this case, many possibilities are presenting for non-radiative transitions, thus quenching any expected luminescence, especially when the concentration of the metal exceeds those of the activators. A high concentration of the element phosphor will also affect the luminescent properties of the material, both by prohibiting ionisation of silver or by acting as an activator itself.[22, 23] Finally the silicon content most likely comes from the glass substrate and has low possibilities of posing as a contaminant from any other source. Efforts towards a cleaner environment of preparation and higher purity of reactant salts should help tackle this contamination problem.

4.3 Surface Morphology

4.3.a. SEM

There are two main processes that contribute to the formation of the films. One involves the homogeneous creation of embryos that grow to nuclei and eventually larger clusters. This variety of particles might have the chance to adhere on the substrate, or on an already growing film on the substrate, or remain dispersed in the solution or precipitate if their size becomes too large. By adhering on a substrate they are partially protected from the redissolving potential of the solution and thus a more stabilised growth process is attained. The other process is an ion by ion deposition on the substrate, or on the already grown film. This process results in a fusion effect of the successive ion layers and the adhered clusters. The combination of the two processes is evident in the scanning electron microscope images of the grown films. Certain conditions favour one or the other process, but both have taken part in

all of the observed films. The effect of the various growth conditions attempted in the chemical bath experiments is analysed in greater detail in Section 4.4 concerning also the size of the deposited films. A most remarkable effect is that the homogenously grown clusters can grow in random shapes or in the shape of almost perfect spheres, of different or indifferent sizes.

The spheres can arrange in a single layer array, forming a film of almost continuous height, as in Figures 4.7, 4.8 and 4.9. Such layers have been observed for both ZnS and CdZnS films. Chemically formed spheres of ZnS and CdS are commonly found in the literature, with sizes ranging from 100 nm[24] or less[25] to 4 μm,[26] but most of them have a radius of 1 to 2 μm.[27-29]

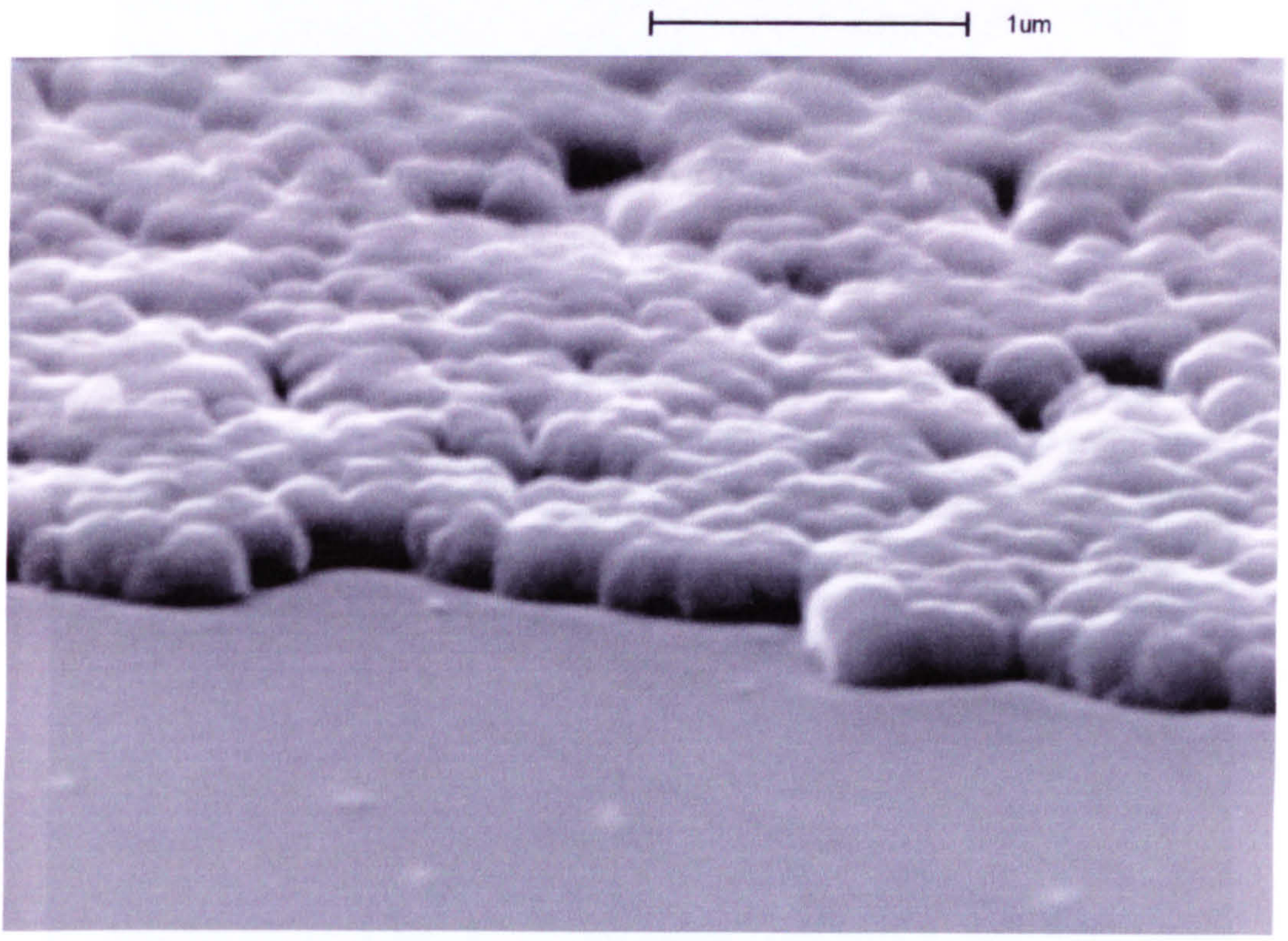

Figure 4.7 SEM image of the edge of a ZnS film composed by an array of spherical beads.

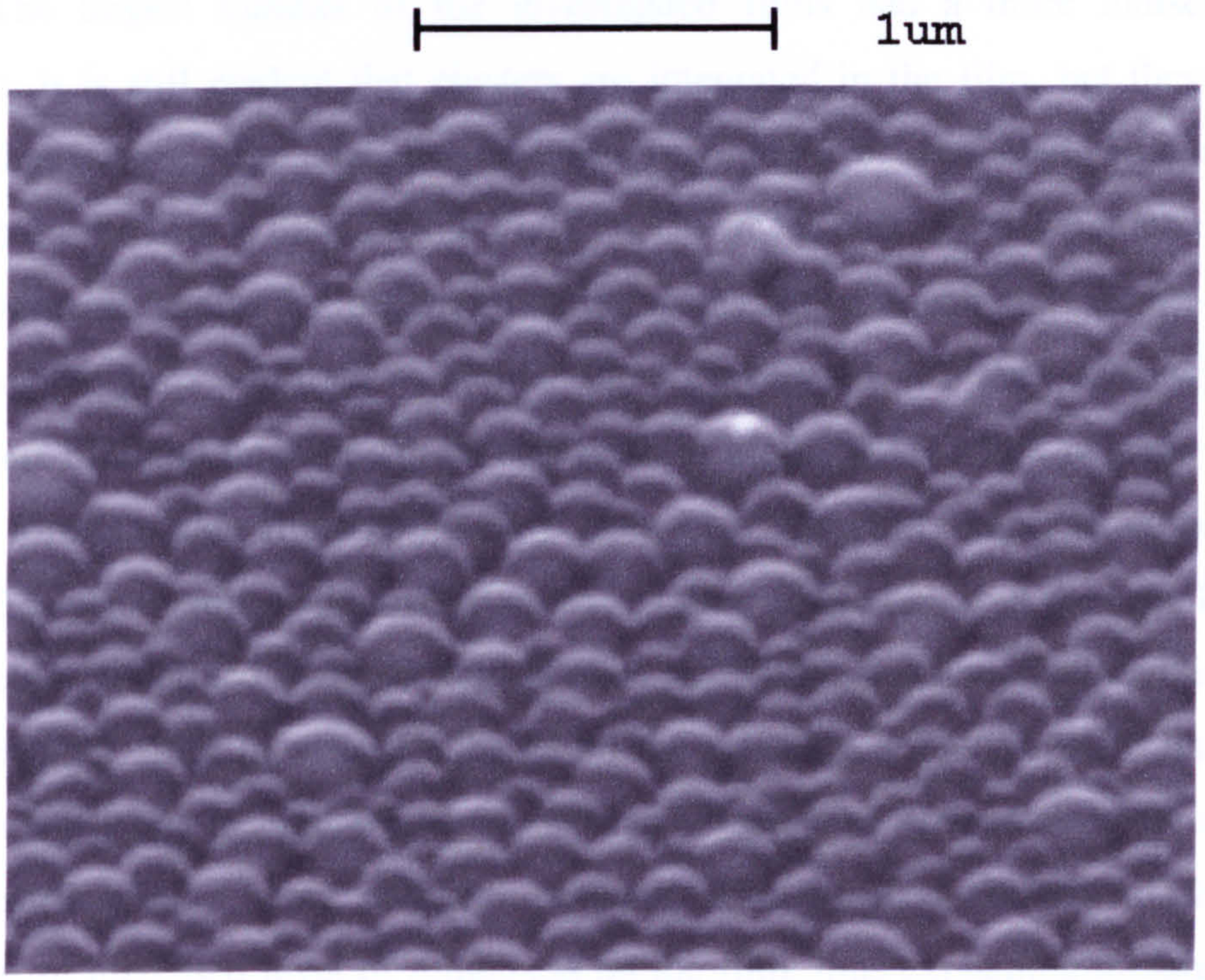

Figure 4.8 An SEM image of a CdZnS:Ag film, composed by spherical beads.

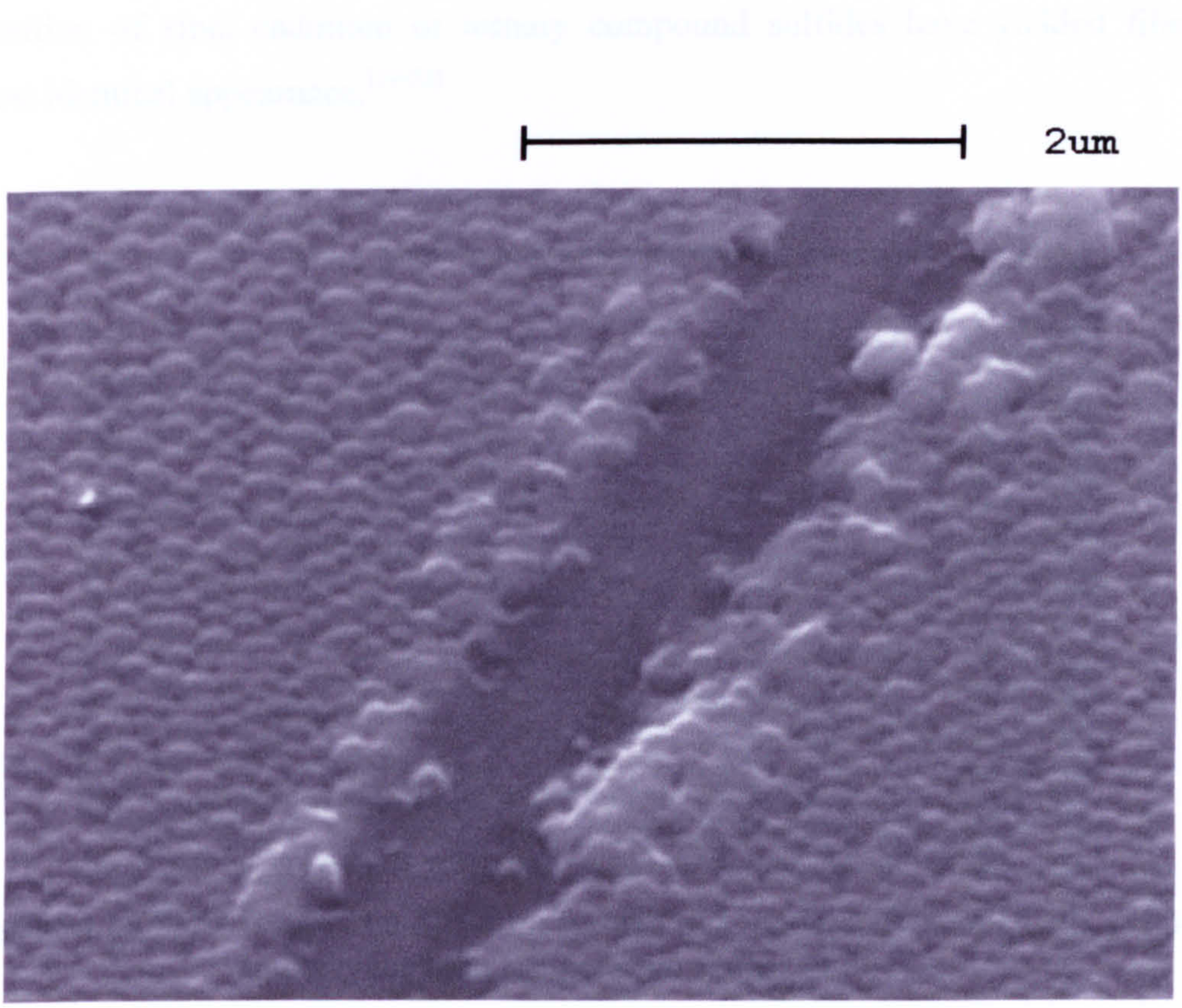

Figure 4.9 An SEM image of a CdZnS:Ag film composed of spherical beads, featuring a thin scratch where the beads have been displaced on either side of the scratch trench. Film deposited under a constant temperature of 92 ^{o}C and no added acid.

The largest number of the investigated films had a more indiscriminate structure. It is still evident that clusters are integrated in the film, but they are not spherical any more. The edge of such a film spanning over what could be considered a scratch on the film is displayed in Figure 4.10, where clusters of different sizes and shapes seem to be fused together, constituting the rather rough film on the smooth surface of the glass substrate. A similar film is presented in Figure 4.20, where the continuous film and its edge can be observed. In Figure 4.11, a hint is given that the clusters forming such films could have been of a spherical shape, as some of the spherical cups are still distinguished on the surface of the film, but they are likely to loose their well defined shape as soon as more material is deposited on them, in an ion by ion manner, after they have adhered on the substrate. Finally a more interesting structure is the one in Figure 4.12 where many clusters of various sizes are attached on the surface of a more coherent sublayer. The attached clusters of this type introduce an increased level of roughness on the film, thus explaining measurements of roughness factors way beyond 4 in Section 4.4.b. Similar methods of chemical deposition of zinc, cadmium or ternary compound sulfides have yielded films of almost identical appearance.[30-32]

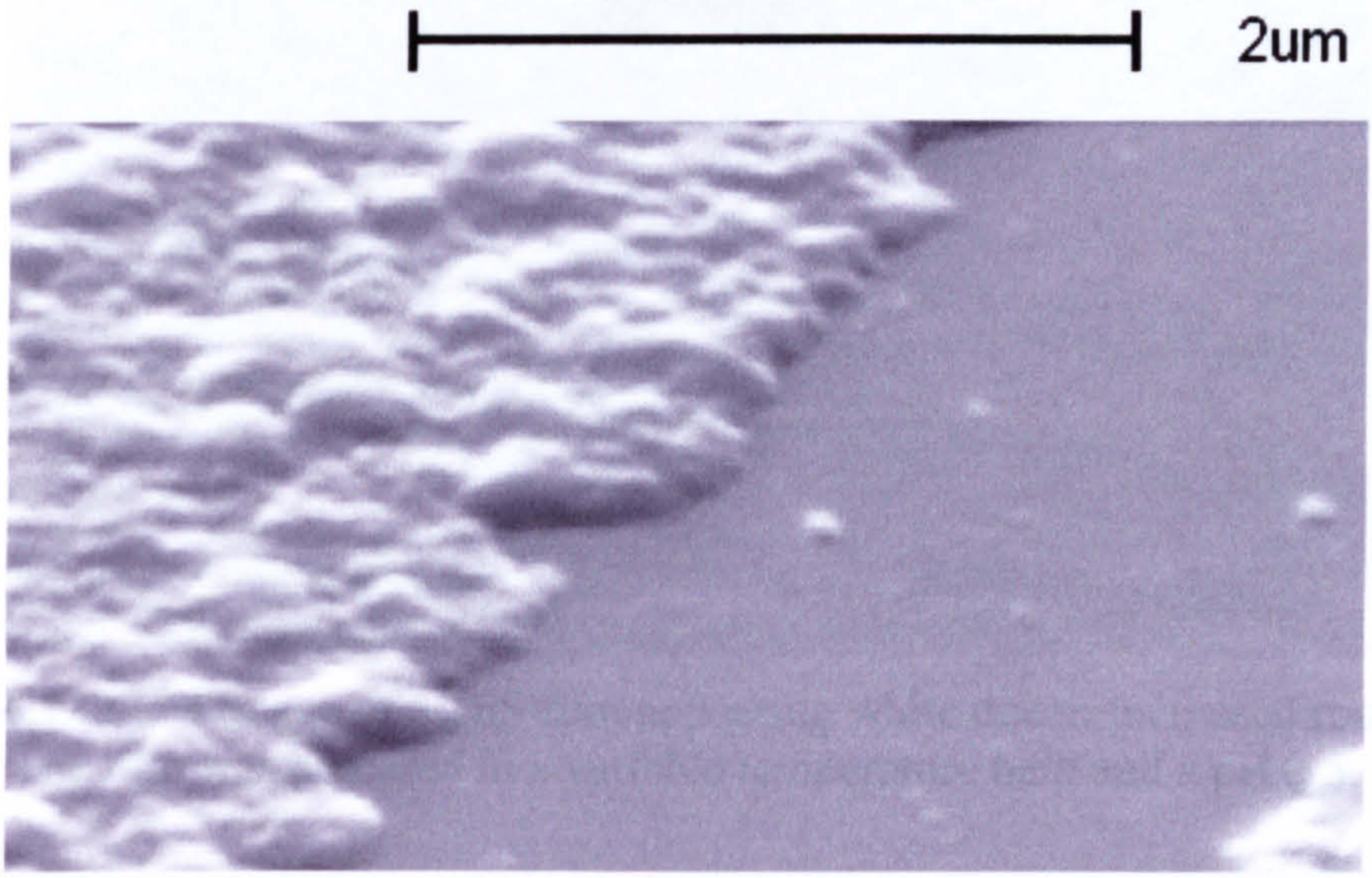

Figure 4.10 SEM image of a ZnS film formed in a moderately acidic bath, pH 3.5, under a constant temperature setting at 88 °C.

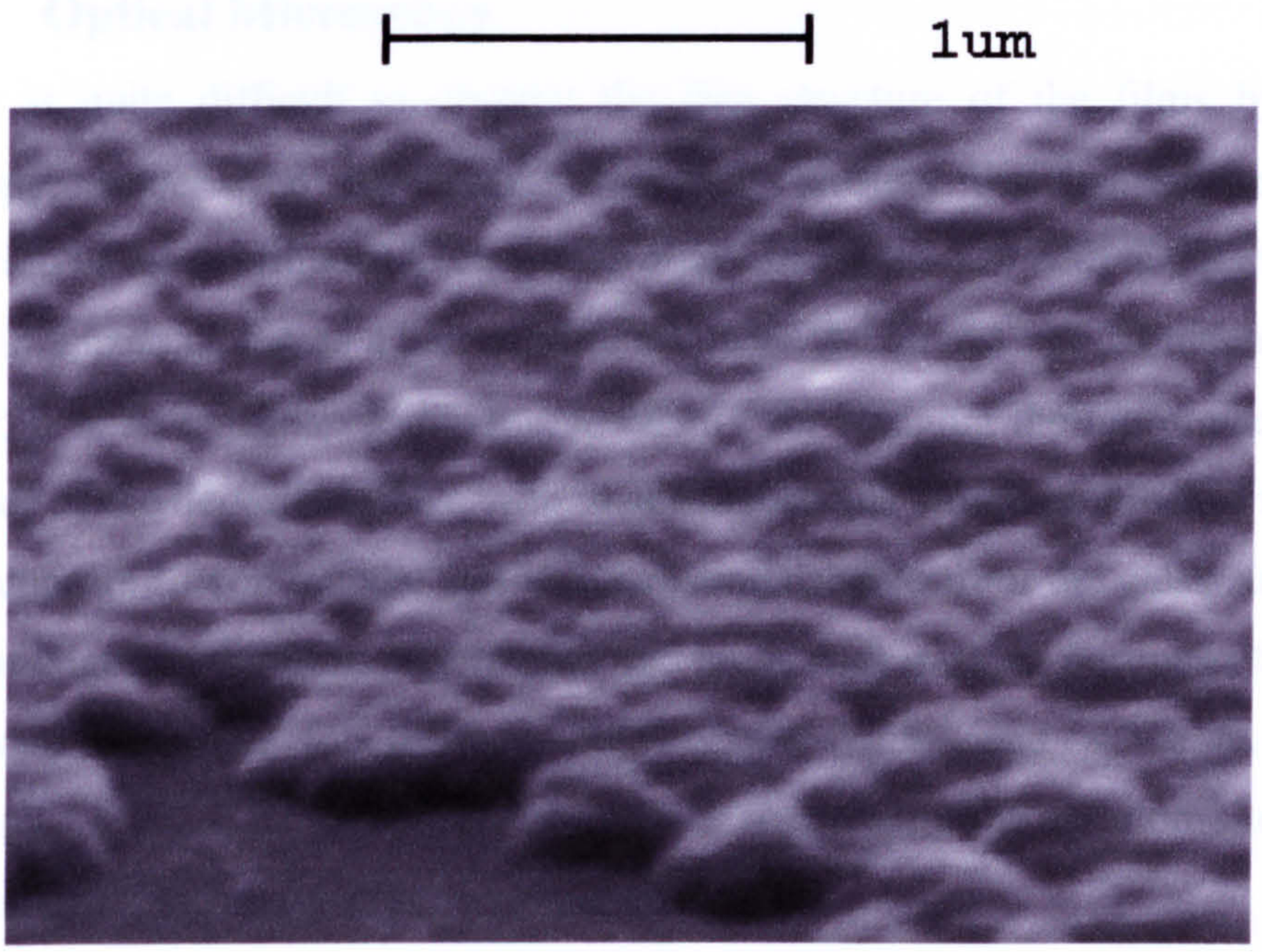

Figure 4.11 An SEM image of a ZnS film from a bath with constant temperature bath (90 °C), with no acid.

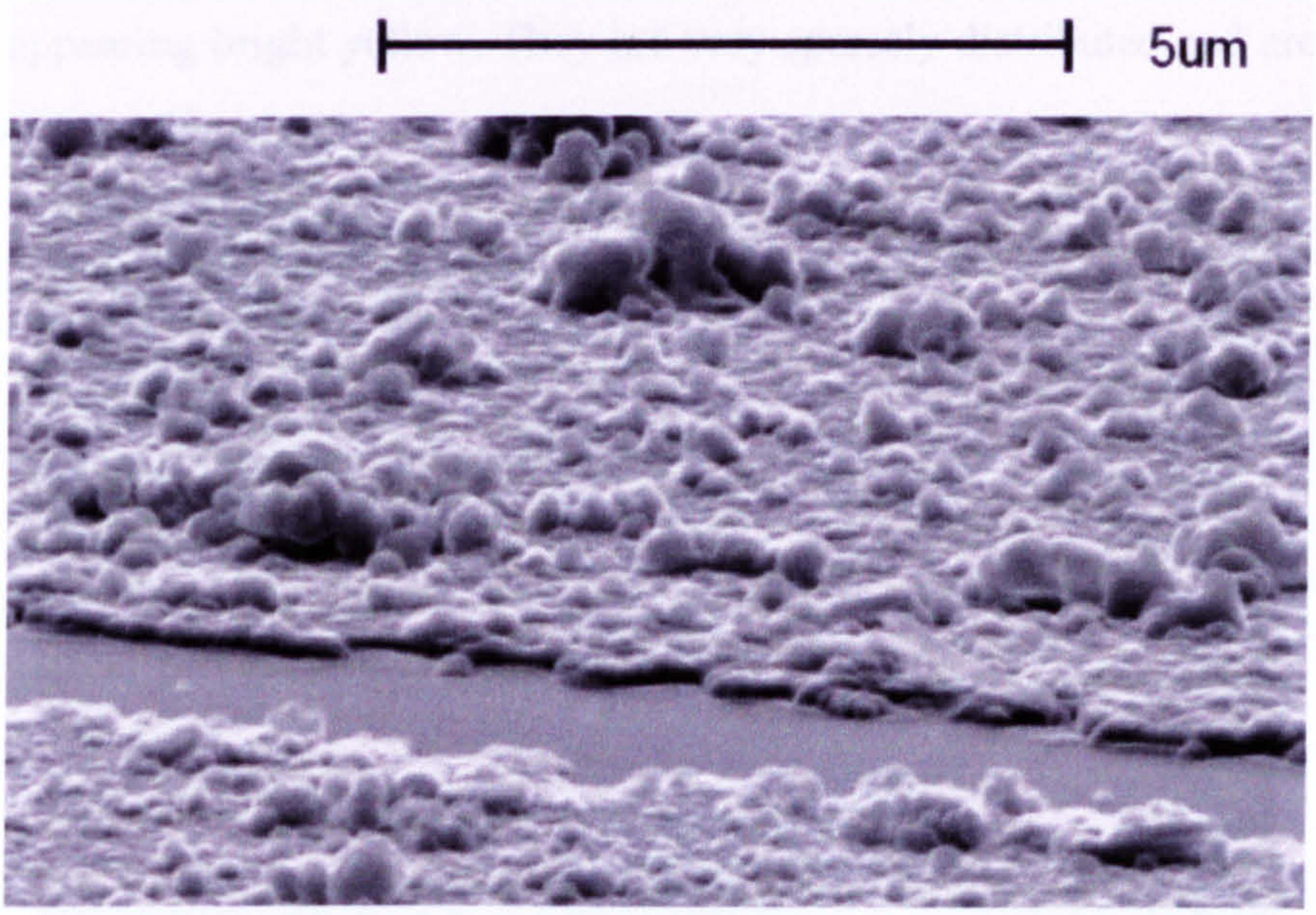

Figure 4.12 SEM image of a ZnS film appearing white due to increased roughness. The film was prepared in a variable temperature bath and a pH 2.5.

4.3.b. Optical Microscopy

It is quite difficult to observe the fine structure of the films by optical microscopy, since even the largest spherical clusters that participate in the construction of the continuous films shown above in Figure 4.8, with diameters of 500 nm, would appear as big as a half millimetre under the largest optical magnification. However, it is an objective technique, necessary for bridging the more macroscopic appearance of the deposited films, with their microscopic structure. Most of the times the film appears so continuous, that it is indistinguishable from the glass surface, so looking at edges of the film, or scratches and areas with missing portions of the film are a good approach for differentiation between film and substrate. Optical microscopy becomes far more interesting in characterising the ablation sites of the laser transferring technique described in chapter 6.

In Figure 4.13 the edge of a CdZnS:Mn film is illustrated, against a small uncovered area. One can marginally observe that the edge is analogous to those in the SEM pictures in Figure 4.10 and Figure 4.20. Some large particles seem to exist over the film, appearing bright yellow. They are very sparsely distributed and are found in almost every sample.

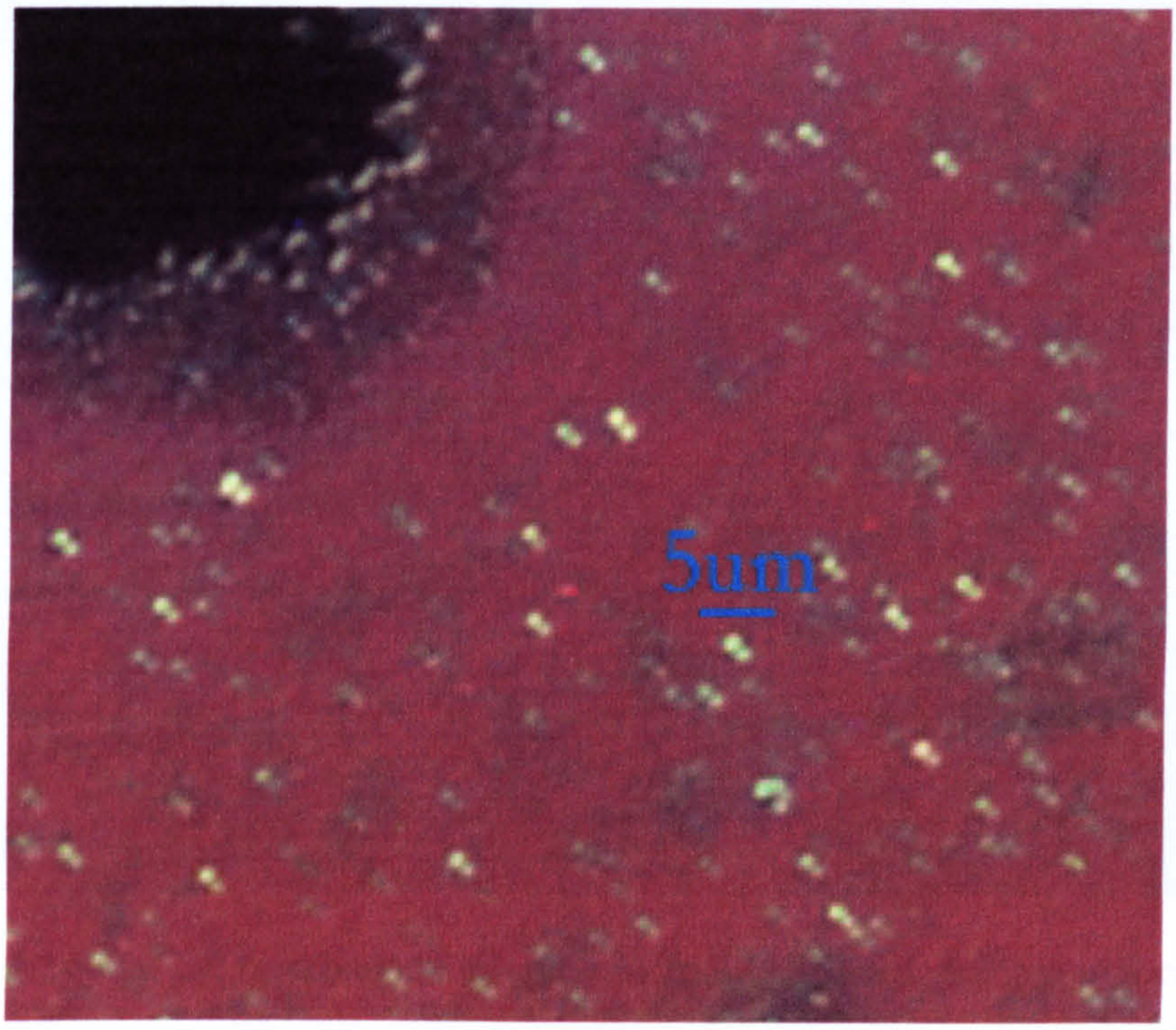

Figure 4.13 Optical microscope image of a CdZnS:Mn film and a missing portion of it. The film was grown in a constant temperature bath with no added acid and 1:1:10 proportions of zinc, cadmium and manganese chloride salts.

A transition from a fairly smooth and continuous film to a thinner film with sparsely deposited roughness features is depicted in Figure 4.14. A scratch renders apparent the existence of film on both the dark and the brighter (thicker film) areas. It is established by a series of experiments, that material precipitated in absence of any zinc chloride, are characterised by very low adherence. Therefore, a very thin layer, possibly of zinc oxide is expected to deposit first on the surface of the glasses, accommodating further growth of zinc or cadmium sulfide, or the attachment of equivalent particles. The film observed here in darker shade seems to be of greater thickness though, as it is only observed under an optical microscope.

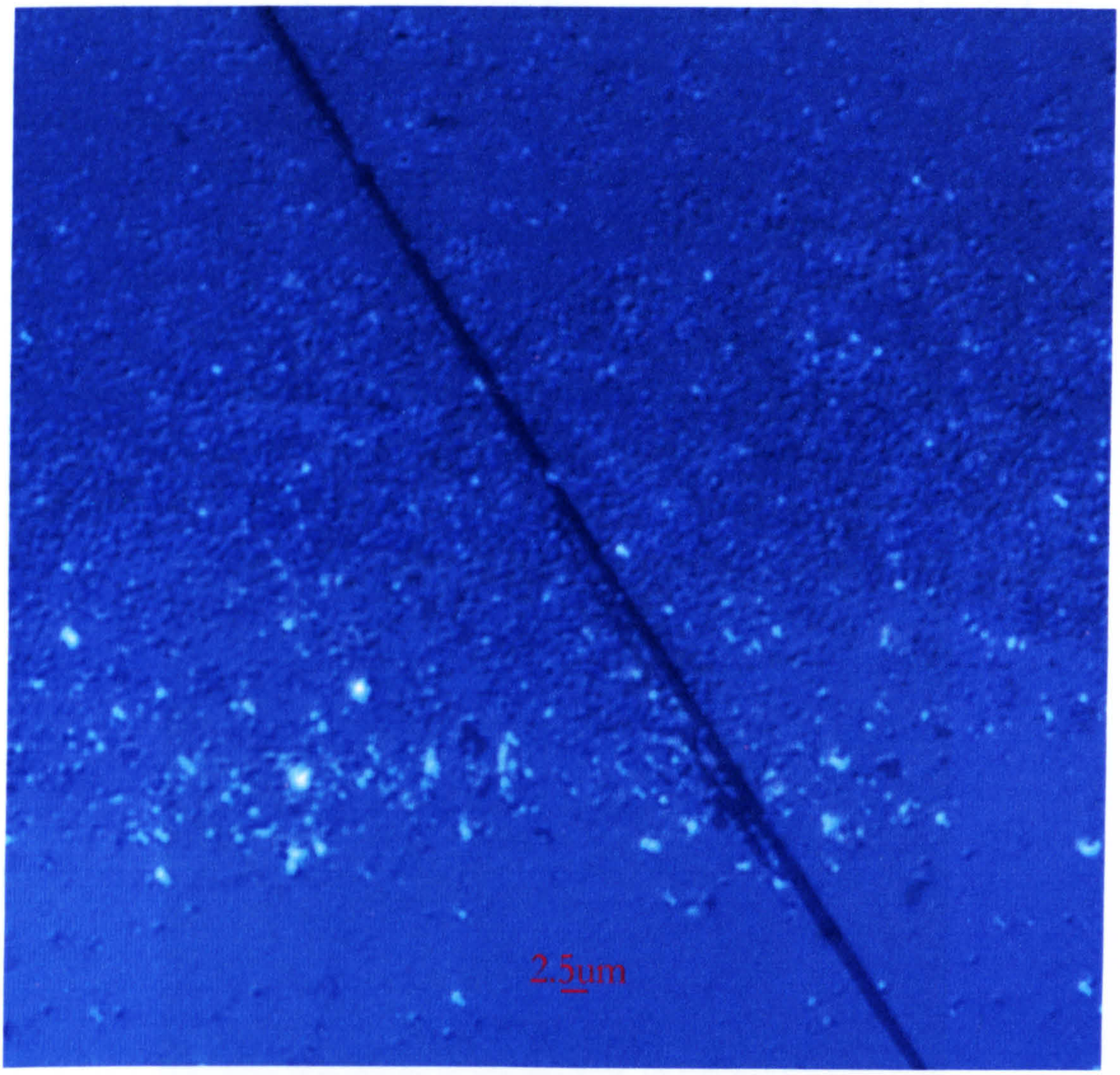

Figure 4.14 Optical microscope image of a ZnS:Cu film deposited in a constant temperature bath at 86 °C with no added acid. A thicker (lighter) and thinner (darker) are of the film is observed in large magnification as a transition to a lightly covered area on the substrate.

The two levels then are believed to arise from the existence of a moderately thin layer, with sparsely attached particles on its surface and a thicker layer composed mainly of such particles. When these particles are deposited in a more condensed manner, they are fused together, hence increasing significantly the observed thickness of the film. This process reduces the roughness of the film, as the next level of large deposited particles is of much greater size. Dense adherence of very large clusters would induce instability of the film, as it grows on an optically flat surface, with decreased adsorption capabilities.

A selection of different colours is often found on optical microscope pictures, exchanging between them rapidly over large areas covered by the deposited films. This variety of colours is quite vibrant, even without the use of colour enhancement optical filters. It is more noticeable in ternary films or doped ZnS films, possibly confirming difference in elemental composition between areas of different colour. This assumption is investigated in greater depth in chapter 6 by Raman microscopy being performed in spots of different colour. An example of such a film, composed of CdZnS:Ag, is given in Figure 4.15 below at a large magnification. The green areas are expected to be richer in ZnS and the red/yellow ones in CdS. This means that there largely exists a phase separation between the two metal sulfides, at least at a micrometer range, as seen in this picture.

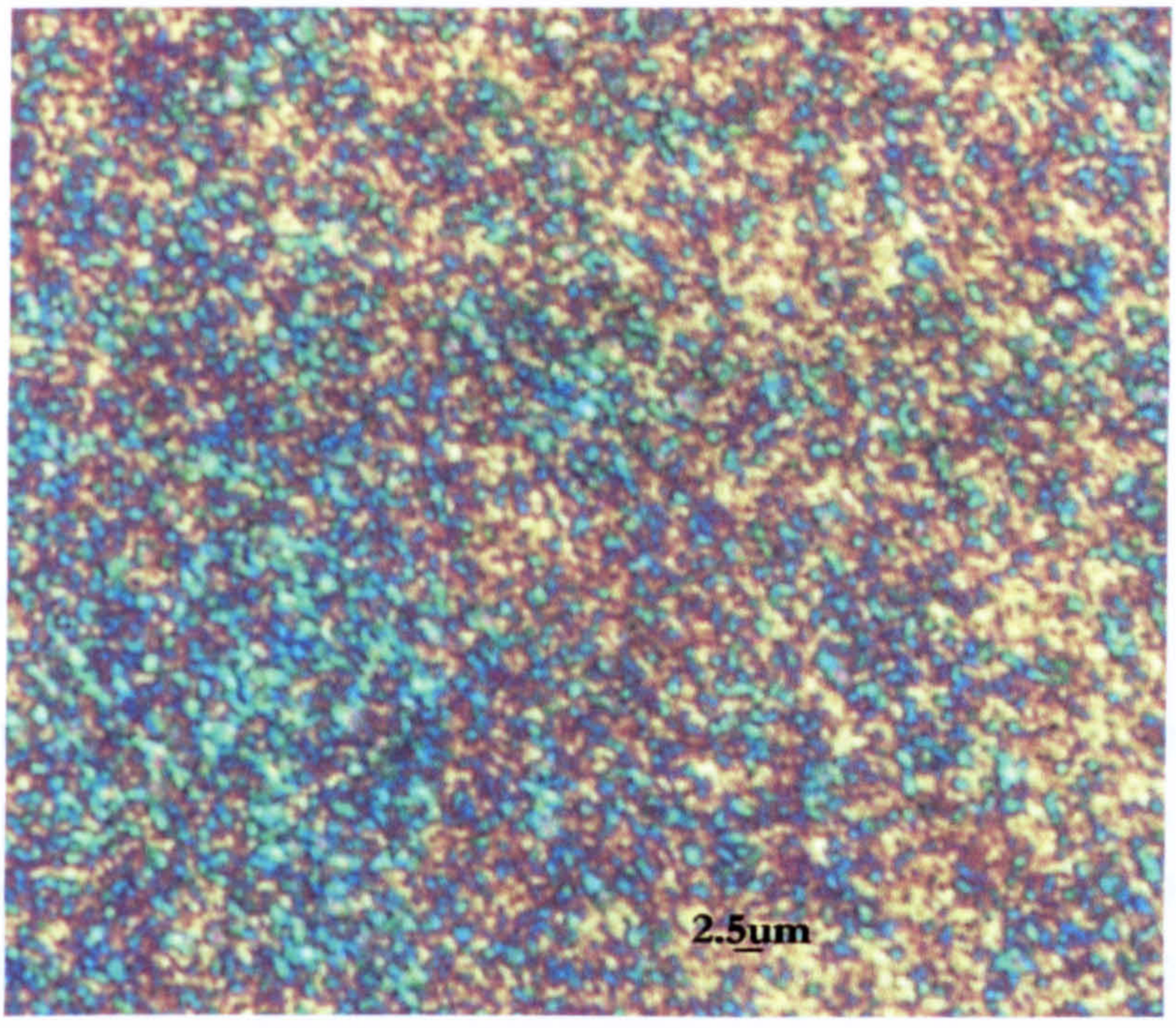

Figure 4.15 Optical microscope image of a CdZnS:Ag film prepared in a bath with a 2:1 weight ratio of Cd to zinc chloride, at a constant temperature of 92 °C.

4.4 Film Thickness

4.4.a. SEM

A rather conceptually simple method of measuring the thickness of the produced films was based on SEM microscopy. Pictures of the films can be taken at an angle below 90° from the surface plane, focussing at an edge of the film. If the edge is close to the edge of the substrate, the layers can also be viewed sideways, which can be one of the most accurate methods of film thickness measurement, but it is also very subjective with respect to the small area of the sample being examined by the microscope. The films were divided in two layers for ease of investigation, because of the roughness features observed on the films surface, as explained in sections 2.3 and 2.3. The lower layer is pure compact solid material and the upper layer contains the materials roughness features, like protrusions, or extra deposited particles, and air. Even though this method is more compatible with the next two analysis techniques, which are both based on the refractive index of each layer, the division is also adopted in the SEM analysis of film thickness at certain points, for the purposes of result comparison between the methods. SEM imaging also gives a unique insight in the relationship between measured film thickness and observed morphology of the films.

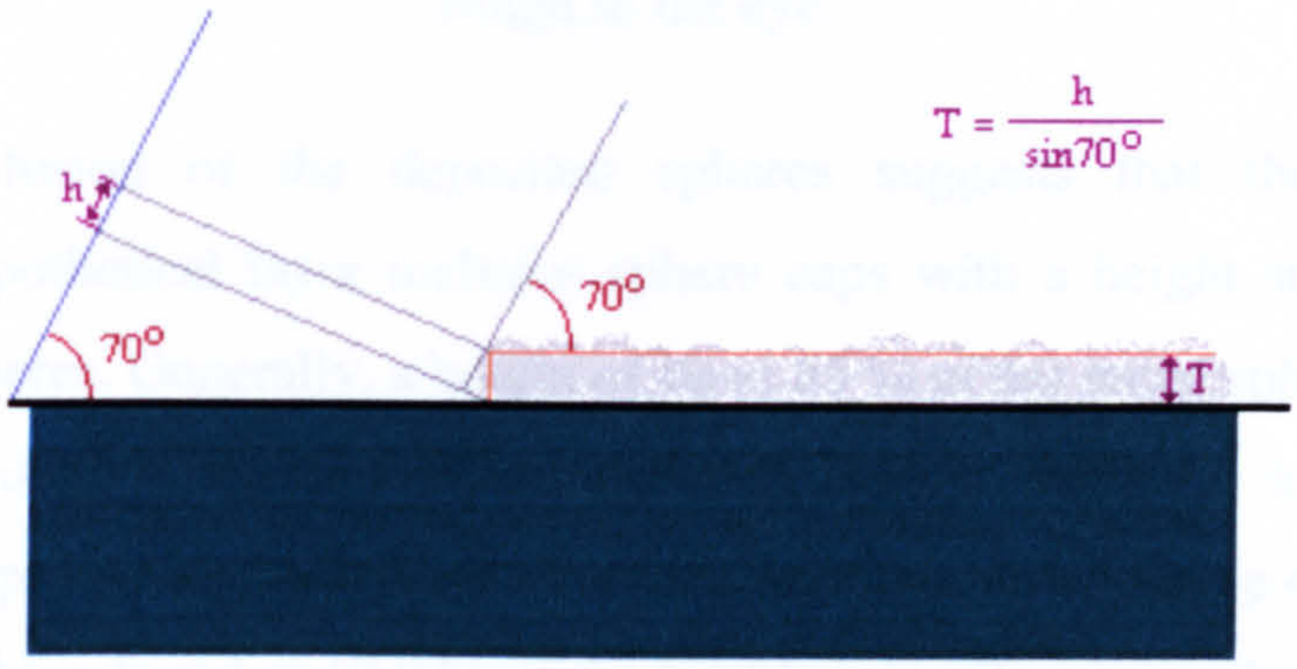

Figure 4.16 Measurement of film thickness T of a film observed by SEM at an angle of 70 degrees.

Most of the films are composed of spherical-like cluster building blocks, a situation that reduces the accuracy of the measurements to a certain level. The schematic in Figure 4.16 explains the deduction of film thickness from the observed height difference between the film and substrate surfaces, at an angle of 70° from the substrate, which was used for the specific SEM imaging. Measurement of the upper, roughness layer and the air percentage in it is much more devious. It is only possible

for films with a rather clear spherical cluster composition, where the top caps of the spheres are the ones contributing to the largest amount of the film's roughness. The spheres are fused together on the sides presumably as the ion-by-ion precipitation takes over when the homogeneously grown spherical clusters have adhered on the glass substrate. Good examples of the spherical cluster composition of the films are shown in Figure 4.17, for what is perceived as clear smooth film by the naked eye and a white, rough film. The roughness layer calculations are performed only on films resembling the single layer structure.

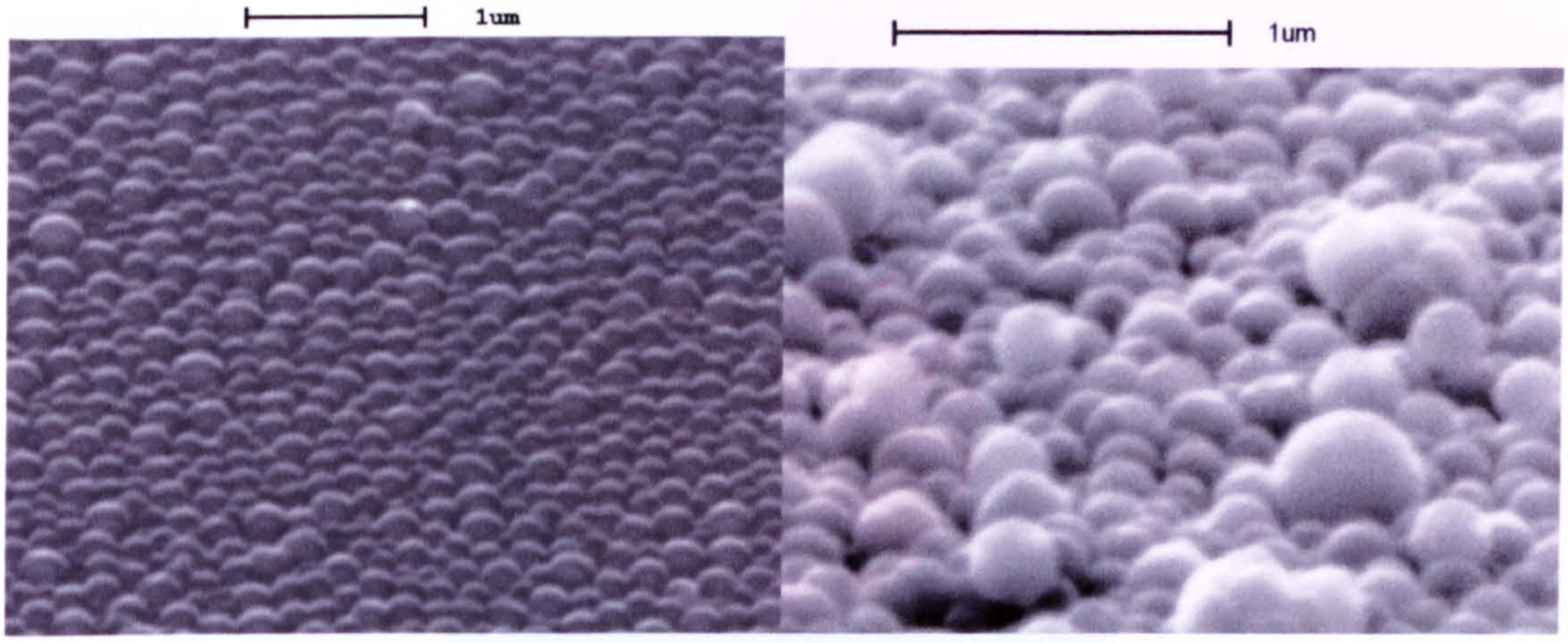

Figure 4.17 Structure of films composed by spherical clusters. On the left, a film with a single layer of spheres appearing smooth and clear to the eye. On the right, a film with different sizes of clusters, deposited at different levels, appearing white and rough to the eye.

Partial fusion of the deposited spheres suggests that the air-phosphor combination hypothetical layer includes sphere caps with a height smaller than the radius of the spheres. Generally, a height of 80 to 85 % of the mean sphere diameter is assumed to belong to the first hypothetical layer and only the top 20 to 15% constitutes the upper, roughness layer. This is demonstrated in Figure 4.18, where the upper layer height is found at 17.8 % of the total height. The picture has been zoomed in accordingly, to allow for more precise measurement.

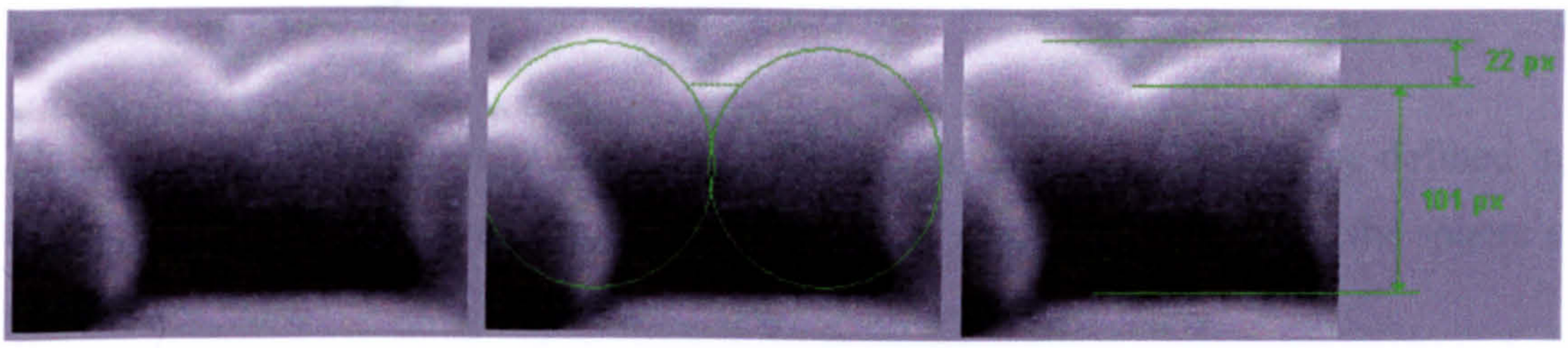

Figure 4.18 Fused deposited spheres and measurement of the height ratio between the two modelled hypothetical layers. Total height is 123 pixels, with the upper layer being only 22 pixels, working out as 17.8 % of the total height. 1 pixel = 1.86 nm.

In order to calculate the air percentage in the upper, modelled roughness layer, the spherical building blocks were modelled in terms of volume, enclosed in a cube of air. The cube has a side equal to the diameter of a sphere and is filled up to a level with deposited material, either included in the sphere, or grown around the sphere, fusing it with the substrate and any adjacent spheres. The top of the cube is filled with air, apart from the volume occupied by the sphere. The volume ratio of the sphere cap and the cube section, or that of the remaining air volume and the cube section, can be calculated to give the phosphor material or air percentage in the roughness layer respectively.

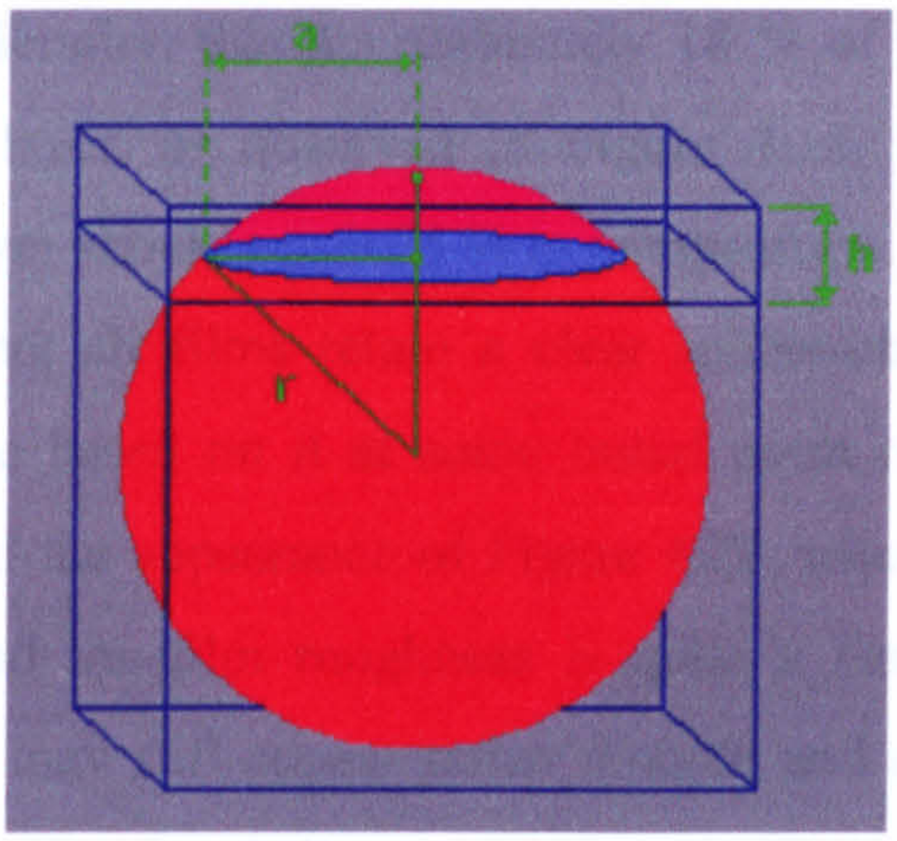

Figure 4.19 Modelled spherical building block of deposited films, enclosed in a cube. It is assumed that a sphere cap is exposed over the compact film mass, thus constituting the hypothetical air-phosphor mixed layer. The cap has a height h and a base radius a.

The volume of a sphere cap, V_{cap}, is given by:

Eq. 4.4.1 $$V_{cap} = \frac{1}{6}\pi h\left(3a^2 + h^2\right)$$

Where h is the height of the sphere cap and a is its radius. The ratio between the sphere cap height and the sphere diameter, or the side of the cube can be defined as m:

Eq. 4.4.2 $$m = \frac{2r}{h}$$

Thus, the volume of the upper section of the ensnaring cube, V_{cbs}, can be defined in terms of m and the total volume of the cube, which is defined in terms of the sphere's radius r.

Eq. 4.4.3 $$V_{cbs} = m \cdot V_{cb} = m \cdot 8r^3$$

The radius of the cap base is related to r and m by trigonometry as follows:

Eq. 4.4.4 $$a = r \cdot \sin(\arccos(\frac{r-h}{r})) = r \cdot \sin(\arccos(1-2m))$$

Therefore, the air percentage in the upper cube layer and hence in the upper layer of the film is found in terms of the height ratio between the layer and the sphere diameter, or the full film height alike.

Eq. 4.4.5 $$Air_p = \frac{V_{cbs} - V_{cap}}{V_{cbs}} \cdot 100 = 100 \cdot \left[1 - \frac{1}{24}\pi(3\sin^2(\arccos(1-2m)) + 4m^2)\right]$$

Now taking into consideration that approximately 18 % of the sphere's diameter is exposed in the upper layer, as observed in Figure 4.18, it is found that the air percentage in the top layer should reach 75 % in composition.

Unfortunately, not all films retain a clear sphere-cluster composition, even though they seem to be based on it at some initial point of their growth. A large number of the films had the appearance of Figure 4.20, where spherical features are hardly distinguished and the film roughness is quite a random effect of multiple factors. Yet such films may still appear rather smooth and clear to the eye. On the other hand, films with a clear bead-like structure, as in Figure 4.17 may appear white (rough) because of multiple layer packing of the spheres, or highly inhomogeneous sphere radii distribution. Nonetheless, the aforementioned calculations are in good agreement with the results obtained by the reflectivity modelling method 1 (Section 4.4.b), for growth conditions residing in temperature levels ranging between 86 to 94°C at pH 6 and at temperatures 78 and 90°C at pH values of 4 and 3, respectively. The SEM images where the modelled double layer film thickness was measured indeed correspond to samples prepared in similar bath conditions, mostly in the 88 to 92°C temperature range and at a pH of 5 to 6. At those conditions, embryos are developing fast into stable nuclei under the partial protection of the substrate against thermal redissolution. It is also possible that their transition to stable nuclei on the substrate, is allowed only up to a certain point, therefore, a single layer of beads is only possible, with a large number of them at similar radii magnitudes as no further stable nuclei are produced in the solution homogeneously. Further analysis of the film growth scenarios is given in section 4.8 taking into consideration all investigated parameters.

A more typical measurement of the film thickness on an SEM image taken at 70 ° is shown in Figure 4.20 below. Here the roughness features are neglected and the film thickness is measured at the edge of the film, assuming a wall-like vertical edge of the film. The thickness is measured in pixels, then converted into nanometres, using the scaling bar and then correcting in terms of the tilt angle. The final thickness of the film is found to be 135 nm. Four more films were examined by SEM, with similar deposited film thickness of around 140 nm and similar structure. In all such cases, the film roughness was neglected.

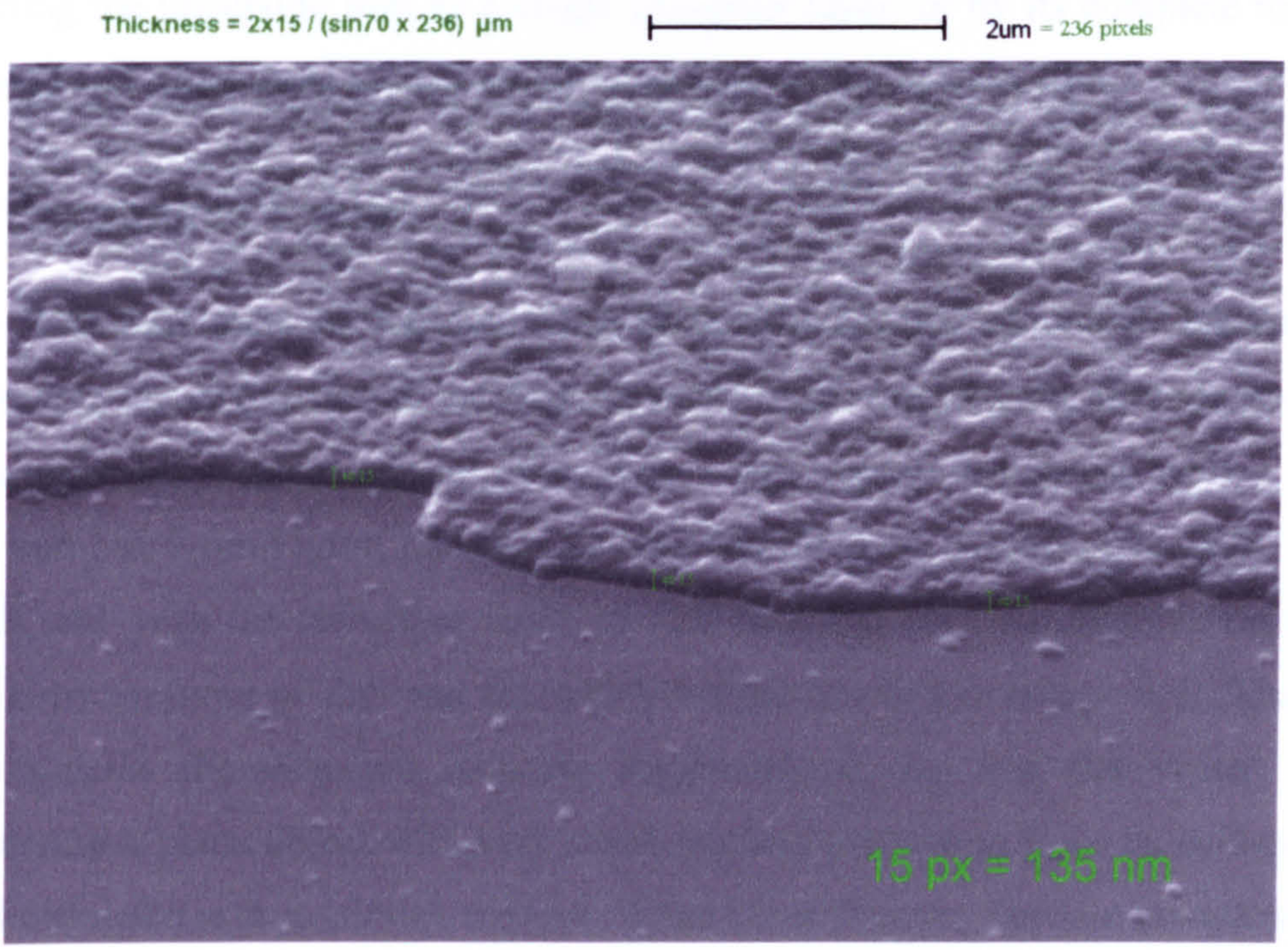

Figure 4.20 Film thickness measurement on an SEM image.

4.4.b. Reflectivity fitting

Two methods based on the refractive index and consequently on the reflectivity of modelled material layers were also used to aid the film thickness investigation of the chemically deposited films. One employs the runge-kutta algorithm in predicting a layer's refractive index spectrum, according to its derivative. The other is applying simulated annealing for adjusting the parameters (including thickness) that would generate a spectrum similar to the recorded one. The two methods have been described in greater detail in Section 2.2. They both model the films as composites of two layers, the compact phosphor layer and the upper, mixed air-phosphor layer inducing any film roughness, as it was also explained in 4.4.a.

Above the film, an infinite layer of air is presumed. Beneath the film, the modelled material layer was either glass (silicon oxide) reaching to infinity, since its known thickness was by far greater than that of the film. The comparison yields a four orders of magnitude difference that arises between the 1 to 3 mm thick glass slides and the approximately 100 to 500 nm thick films. Despite this, modelling of a 7 layer system was also attempted in some cases, comprising of air, air-phosphor blend, phosphor, glass substrate, phosphor, air phosphor and air again. Better results (as in better agreement between modelled and recorded spectra) were though obtained by modelling the underside film as a single phosphor layer, or by its complete removal with acid and subsequent modelling of the sample with an absent film.

The Roughness Factor

The roughness of the deposited films was considered one of the quality-determining-characteristics of the film. In order to characterise the films in terms of their roughness, a factor can be devised that will express roughness with a single scalar number. From Figure 2.5 it can be seen that there are two layers included in the models, one with the refractive index of ZnS and one with an effective refractive index between those of ZnS and air, which defines the air percentage in it. Thus this layer contains the elements inducing roughness on the first flat virtual layer. Considering a plane object with very small features protruding from its surface, one would characterise it as almost smooth. When these features become comparable in size to the thickness of the object, then the object's surface is characterised as rough. Therefore the ratio between the two layers is an indication of roughness.

These features are often formed by almost spherical particles and other times by more complex formations based on spherical nuclei. Therefore, when the surface concentration of those spheres (roughness features) is very small, then quite a large amount of air is separating them. Thus the combined layer would contain a large amount of air and it would most probably look rather smooth to the eye. On the other hand when their area concentration is too large, then they would be closely packed with each other, generating in this way another flat layer with small gaps of air in it. Consequently, the percentage of air in this layer is a second indication of roughness, which at a value of ~50% would signify a very rough surface. Therefore, the function employed to give the roughness factor of the deposited film was:

Eq. 4.4.6 $$F_r = (ULT / LLT) \times ((AP^2 - 100 \cdot AP) / 1250)^2$$

F_r is the roughness factor, LLT and ULT are the lower and upper layer thicknesses respectively and AP is the air percentage in the upper layer. A few typical examples of roughness factors can be laid out here for the purposes of familiarising with the notion of the roughness factor. A value of 4 as a roughness factor represents a film with upper and lower layers of equal thickness and an air percentage of 50 %. Films with higher roughness factor than 4 are only possible when the upper layer is of greater thickness than the lower. If the air percentage increases to 75 % or drops to 25 %, the film would then be characterised by a roughness factor of 1. A value of 0 for roughness factor would mean that the air percentage is either 100 % or 0 %, where the upper layer can either be considered part of the lower layer, or it is inexistent. When the roughness factor reaches very high levels, the lower level is very small compared to the roughness features, thus the deposited film is mainly characterised as random deposits, instead of a continuous film. A film comprising of quasi-dimensional spheres arrayed in a single layer, with sphere caps exposed at a height of 18 % of the sphere diameter, in the upper layer, as described in section 4.4.a, above, would carry a roughness factor of approximately 0.5. For highly ordered surfaces with even a 50 % air concentration, a roughness factor may loose its eloquentness of visible roughness, as the surface may no longer feature visible irregularities, yet they are considered as mechanically coarse surfaces.

It is interesting to observe the changes in thickness and roughness of the films over a spectrum of deposition parameters. Sample distance from the heater was varied by employing farrows on the heater's surface, or separators between the heater and the substrates. The variation of distance was found to affect the deposition results in an abrupt way, differentiating mainly between acceptable deposition conditions or not, mostly in terms of substrate coverage and adherence of the films. Ultimately, deposition of good quality films was achieved on the outer face of the substrates; therefore any further investigation in substrate distance from the heater was abolished.

Two important parameters were the bath temperature and acidity of the solution. A number of samples were produced in the middle ranges of the attempted values for each parameter. The number of samples generated towards the more extreme case was significantly lower, as they were only of investigative interest and could not contribute significantly to the rest of the research and most of all to laser

transferring. The more ideal deposition conditions were found between temperatures of 88 to 94 °C and a pH 4.5 to 6.

The values obtained for thickness of both modelled layers are depicted here as surface plots over a variation of temperature and bath acidity (Figure 4.21 and Figure 4.22). Most of the points represent averages of measurements taken from a number of samples (10 to 30) grown under the same conditions. Conditions at the edges of the surface plots were attempted less (<5) often and hence a greater disagreement is observed between the graphs belonging to the two methods, over those areas, especially the low pH band region. Over the central regions, representing the more frequently attempted conditions considered as more ideal for the deposition, a larger agreement between the two modelling methods is observed. This indicates that the two methods can produce consistent results over a certain average. The roughness factor is also plotted instead of air or zinc sulfide content of the upper film, as it gives a better idea of the roughness of the upper layer (Figure 4.23).

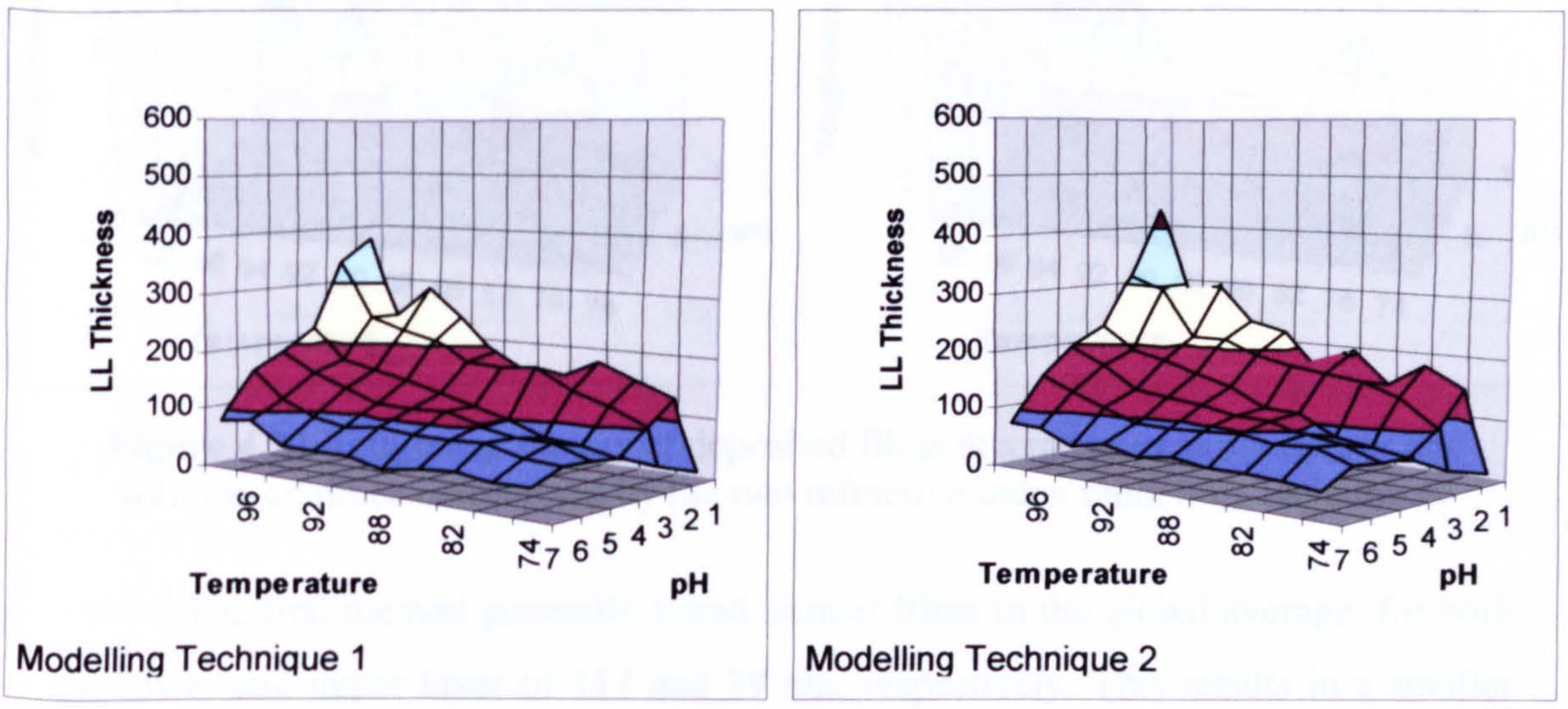

Figure 4.21 Lower layer thickness of deposited films at a range of temperatures and solution acidities determined by the two refractive index modelling techniques.

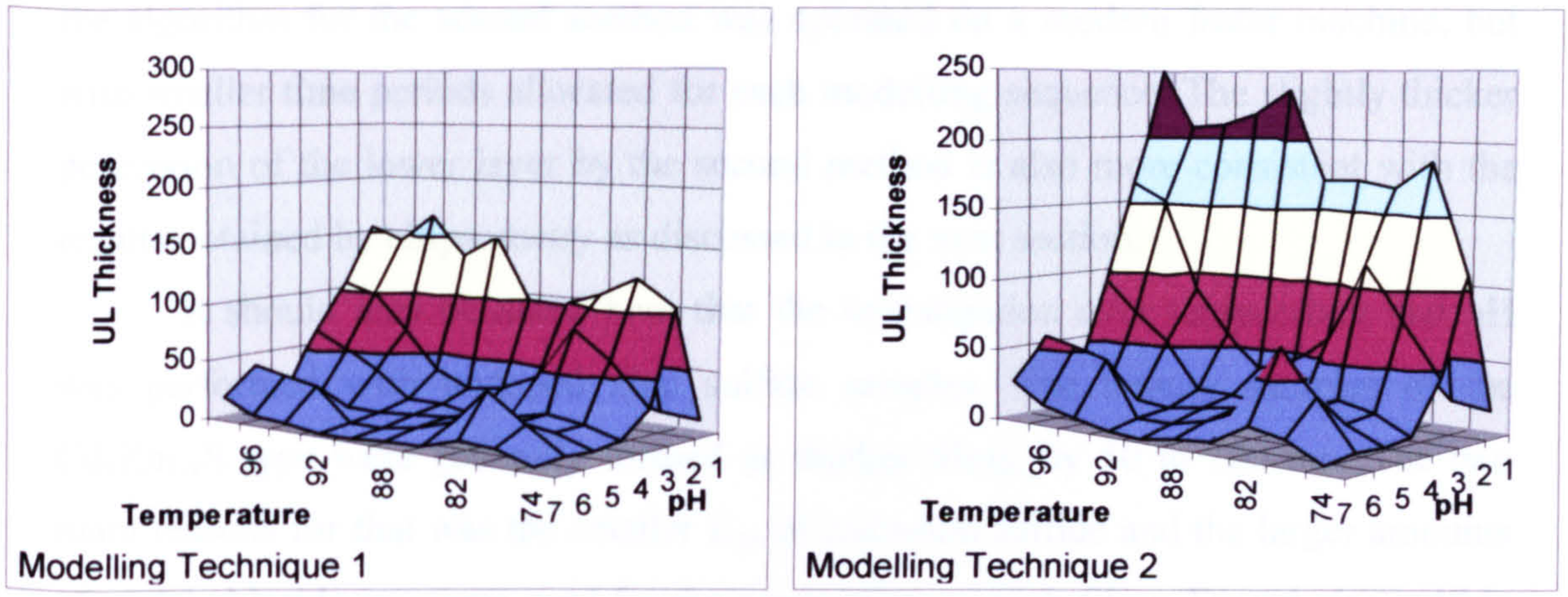

Figure 4.22 Upper layer thickness of deposited films at a range of temperatures and solution acidities determined by the two refractive index modelling techniques.

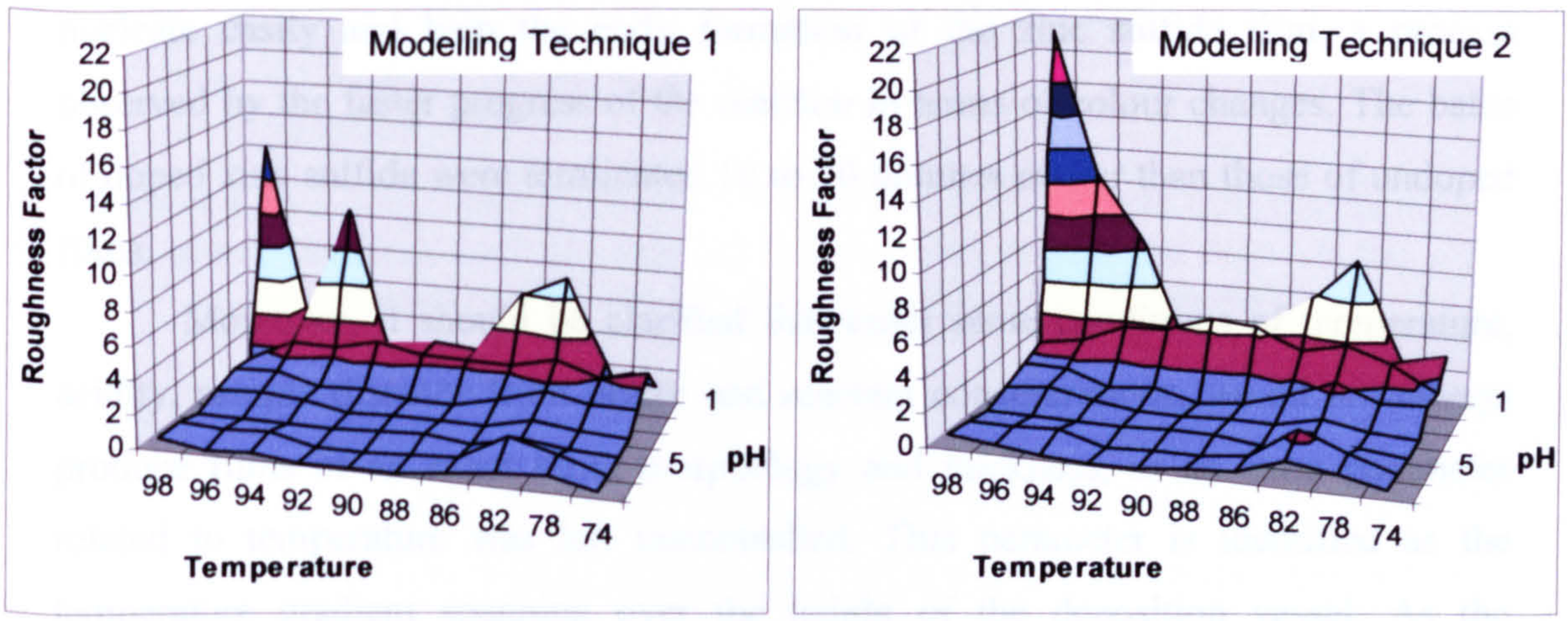

Figure 4.23 Roughness factors of deposited films at a range of temperatures and solution acidities determined by the two refractive index modelling techniques.

The first method generally found thinner films in the global average, for both the lower and upper layer of 117 and 39 nm, respectively. This results in a smaller averaged roughness factor, at 1.66, even if the air percentage approaches more towards 50 %, averaging at 41 % air in the upper layers. The equivalent values for the method employing the simulated annealing algorithm are 125 and 58 nm as lower and upper layer thicknesses and 36.5 % air percentage in the upper layer, reaching a roughness factor of 1.99. The difference between the two methods most likely inheres in how each method perceives and models the upper layer containing the roughness features. The second reflectivity fitting method gave fits with a better least squares value (R^2) than those of the first and therefore it is considered more reliable in modelling the rough layer. On the other hand though, one would have to consider that

the algorithm for the second method was operated on a modern faster machine, but with smaller time periods allocated for each modelling sequence. The slightly thicker perception of the lower layer by the second method is also more consistent with the results obtained by ellipsometry as discussed in the next section.

It should also be noted here that the investigation over temperature and pH was performed with undoped zinc sulfide samples. The ternary samples of the $Cd_xZn_{1-x}S$ type were generally formed as thicker films, by 50 to 100 nm. The two main reasons for that was the smaller K_{sp} of cadmium sulfide and the larger amounts of metal chloride reactants used for the preparation of such films. Doped zinc sulfide films were again of the same thickness and with silver and copper as activators, films were of the thinnest variety. It is believed that the low K_{sp} silver and copper sulfides nucleate easily and help the early formation of the zinc sulfide film, a process observed by the faster progress of the reaction in terms of colour changes. The baths of doped zinc sulfide were terminated 10 to 30 minutes earlier than those of undoped films.

Moreover, it should be clarified that exact same conditions of temperature, acidity, sample distance from heater and reactant concentrations, would not always produce films of an exact same morphology and thickness, as an extra parameter related to temperature was left uncontrolled. This parameter is identified as the temperature gradient spanning over the height of the deposition vessel. As the temperature was monitored near the top of the glass samples by a thermocouple, the remaining volume of the solution underneath that spot, could attain any temperature gradient depending mostly on the environmental temperature and even more on the heat diffusion at the bottom of the vessel which is also related to environmental temperature. The temperature gradients in the vessel were recorded at different days, with different ambient temperatures, for a stabilised 81 ^{o}C condition towards the top of the heater and are illustrated in Figure 4.24, in parallel to the glass slide heater module. A remedy for this deviation of environmental parameters could be achieved by monitoring the temperature closer to the middle of the glass slides and setting the PID controller to 3 or 4 degrees lower accordingly.

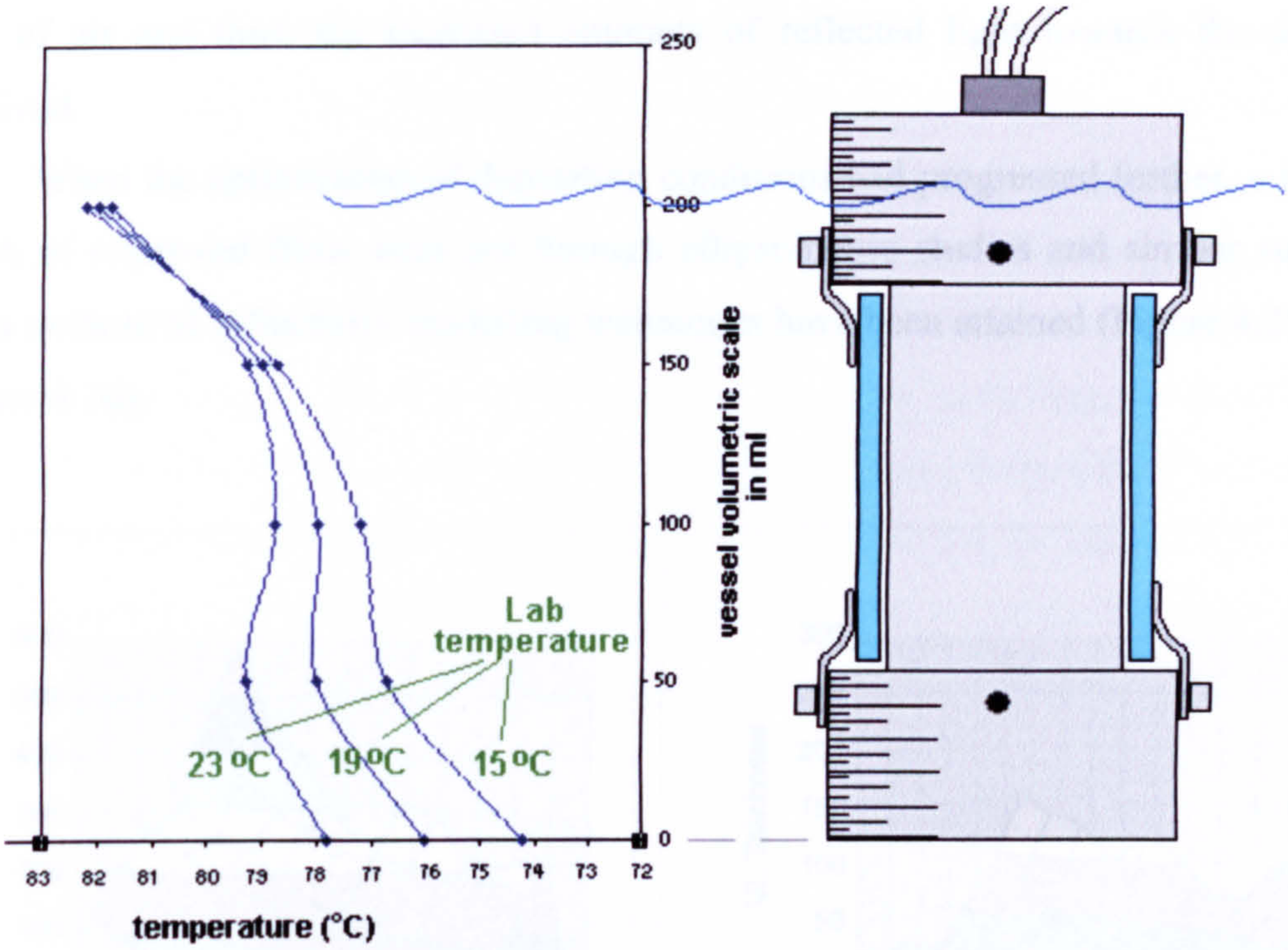

Figure 4.24 Temperature gradients measured at different depths (volumetric scale lines of beaker). Each gradient line was recorded at different days and the corresponding laboratory ambient temperature is indicated.

4.4.c. Ellipsometry

A number of the chemically deposited ZnS samples where investigated by ellipsometry in terms of their thickness and roughness in a very similar manner to that of fitting reflectivity spectra. The total number of samples investigated by ellipsometry was less than a third, but all possible combinations of the two controllable deposition parameters, temperature and acidity were examined. Ellipsometry has been used to investigate the thickness of ZnS films grown by low energy thermal evaporation[33] and surface sol–gel reactions,[34] at scales of 40-50 nm and 2 to 10 nm, respectively. Four main layers are taken again into account here, as explained in section 2.3, the top being air and the bottom being the glass substrate. The middle two are again separated in a layer containing zinc sulfide only and another being composed of a mixture of air and zinc sulfide protrusions from the first layer. An initial batch of deposited films that was investigated gave a variety of film thicknesses and roughness factors. That batch was mostly composed of rather thick films with moderate roughness, measuring up to 300 nm or more for the lower layer and 150 to 200 nm for the upper layer. Regardless, the films were found ideal for ellipsometric measurements, due to their rather high refractive index difference from

that of air and thus, the increased amounts of reflected light towards the angled received.

When the optimisation of deposition conditions had progressed further, a larger batch of improved films were put through ellipsometric studies and similar surface plots to those of reflectivity modelling techniques have been attained (Figure 4.25 and Figure 4.26).

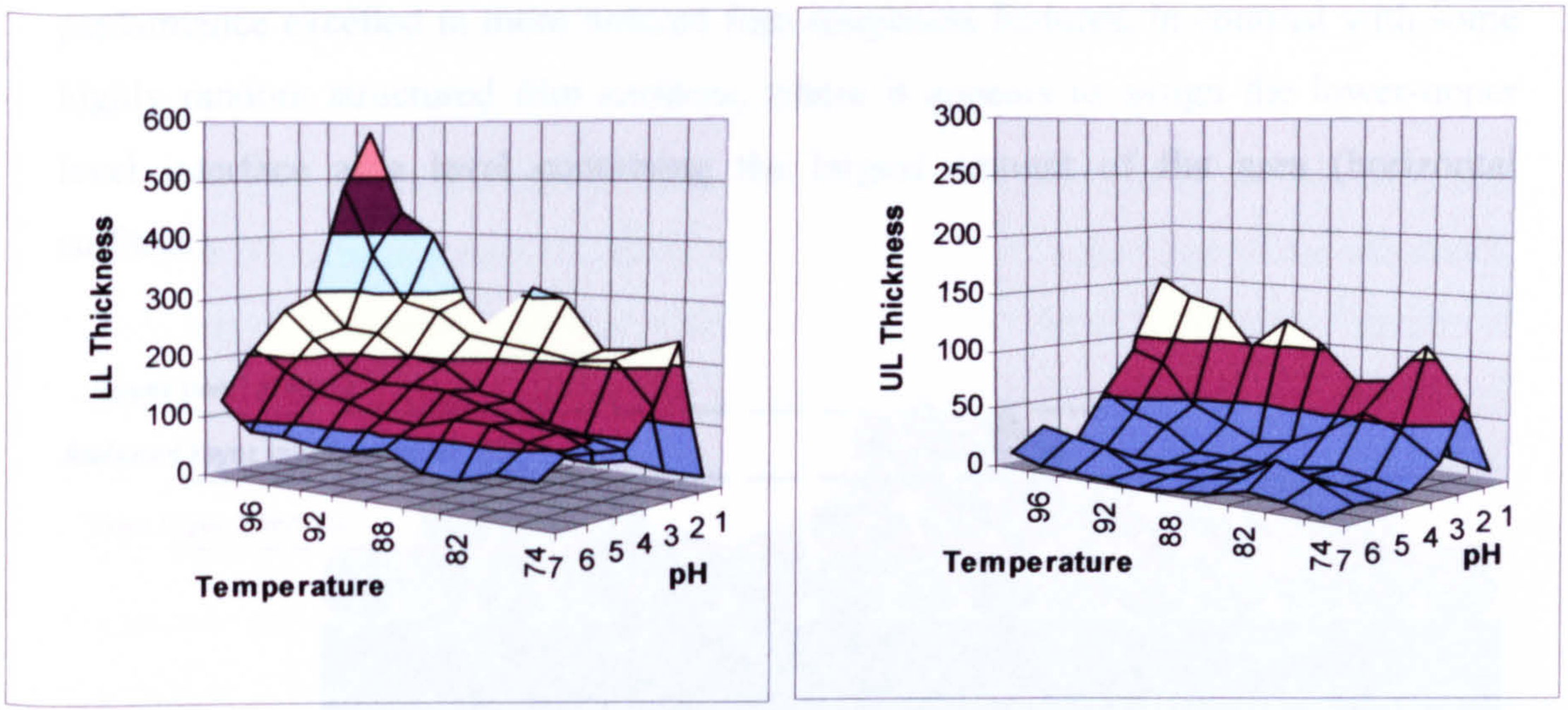

Figure 4.25 Lower and upper layer thickness of films precipitated under different temperature and acidity conditions, as modelled by ellipsometry.

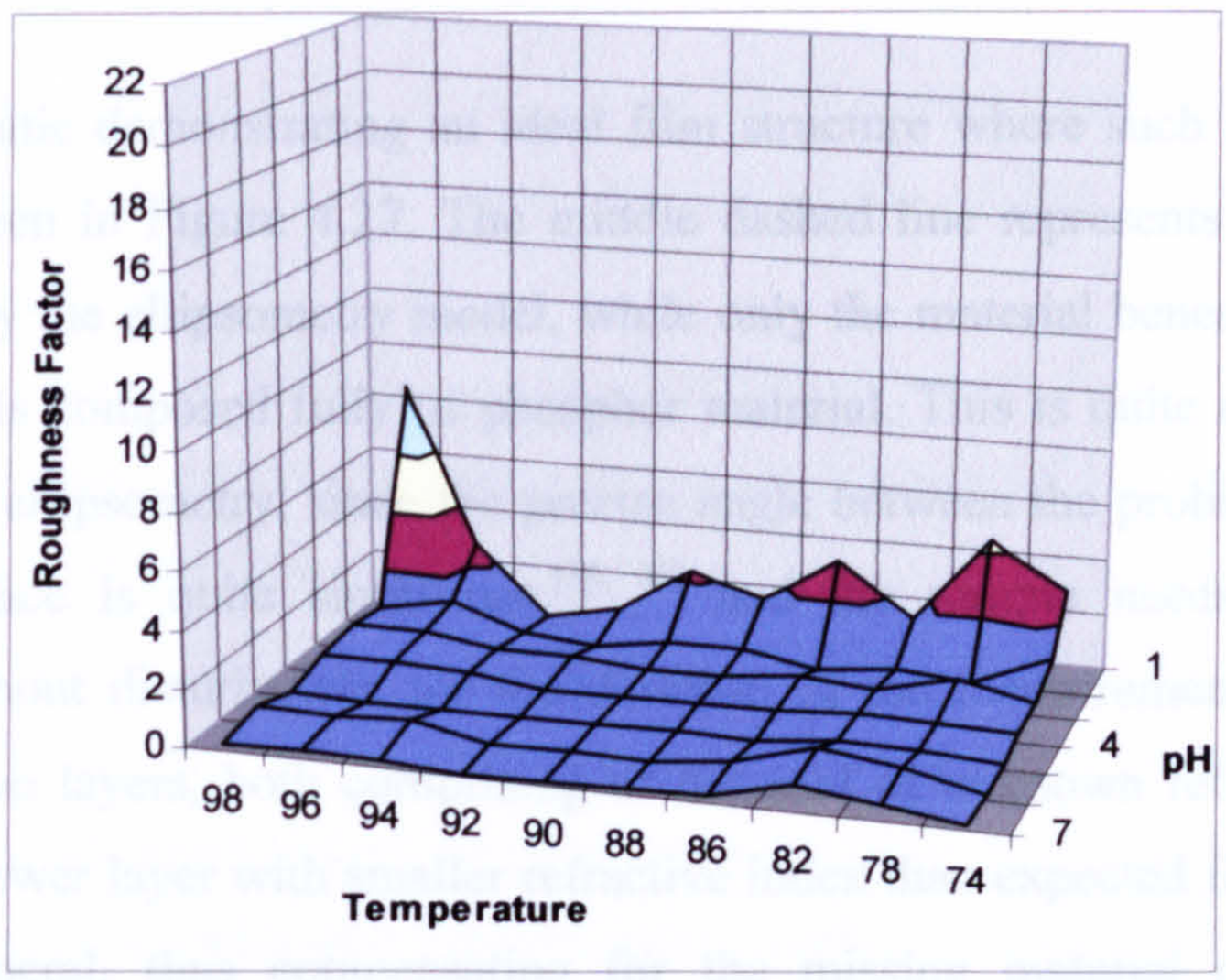

Figure 4.26 Roughness factor calculated for films precipitated under various temperatures and solution acidities. Calculations are based on modelling of the film thickness and layer compositions by ellipsometry.

The surface plots highly resemble those produced by the reflectivity fitting methods. Especially at the central area of interest, ellipsometry seems to detect thicker lower layers of films, with a mean value around 162 nm and thinner upper layers at an average of 30 nm, with a small air percentage, approximately 42 %. This suggests that ellipsometry has a tendency to attribute the largest part of the films' volumes to ZnS, when compared to the previous two methods of thickness modelling. Comparison of the results of ellipsometric measurements with SEM images, showed that the methods performance excelled in more ordered film roughness features, in contrast with some highly random structured film surfaces, where it appears to assign the lower-upper level interface at a level containing the largest amount of flat area (horizontal surfaces).

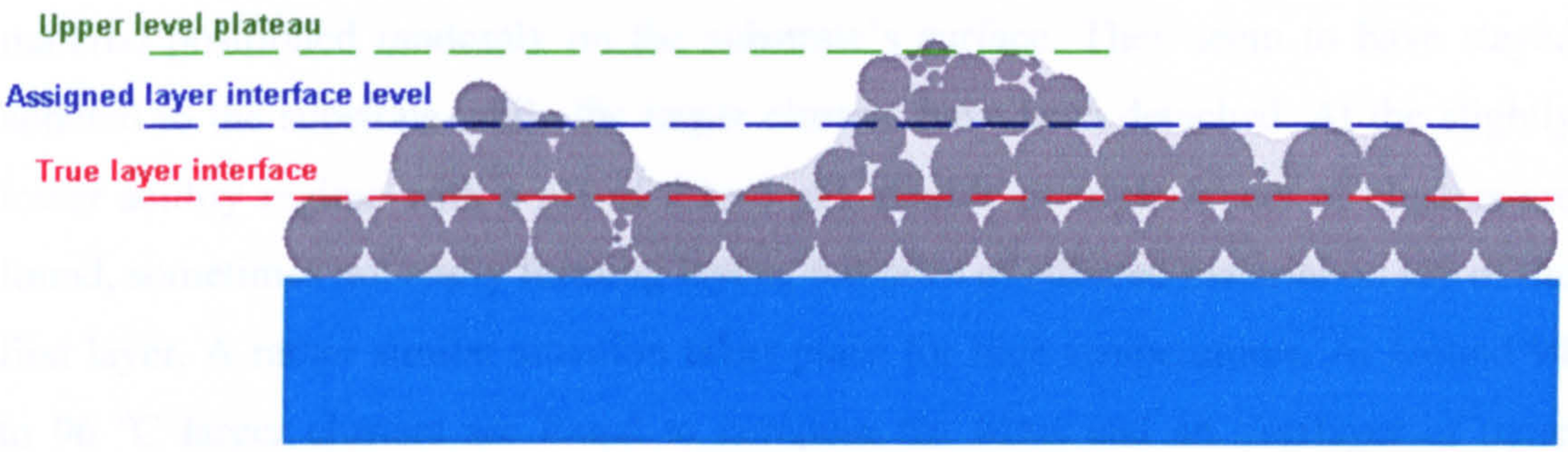

Figure 4.27 False layer interface assignment by ellipsometry, when a larger flat area is detected at a different level.

A schematic demonstrating an ideal film structure where such a case would apply, can be seen in Figure 4.27. The middle dashed line represents the assigned layer interface by the ellipsometry model, while only the material beneath the lower, red dashed line is composed fully of phosphor material. This is quite an acceptable presumption for ellipsometry, since the precise angle between the probing beam and the probed surface is quite significant,[35, 36] and the sample needs to be held horizontally without disturbances for the duration of the measurement.[37] Perhaps modelling for two layers, both comprising of material of unknown refractive index would return a lower layer with smaller refractive index than expected for ZnS or the phosphor in general, thus compensating for the missing material of the lower modelled layers in highly disordered film surfaces.

4.4.d. Concluding remarks on film thickness and roughness

It is interesting at this point to try and frame the effect the two main parameters discussed above, being the bath temperature and solution acidity, would have on the thickness of the deposited films and how this relates to the morphology of the films and in extent, to their growth mechanism. Even though the complete growth mechanism will be summarised in the last part of this chapter, its observed effects can be laid out here. Figure 4.28 provides a schematic summarising those effects. It is assumed that one parameter is set at the optimum value when the other is varied. The two optimum values are as discussed above 92 ^{o}C and 5.5 for pH.

At high acidities, large clusters are found on the film and in the solution, until a pH of 1 is reached, where the films severely loose their adherence to the substrates. Under those conditions, one can some times discover small remaining features of material positioned randomly on the substrate's surface. They seem to have stayed adhered to the substrate while the larger clusters have been detached. At the slightly lower acidity regime with a pH of 2 to 3 pH, double or triple layers of clusters are found, sometimes not really forming layers, but piles of adhered material on top of the first layer. A rather similar situation takes place for high temperatures. At around 94 to 96 ^{o}C larger clusters are found to compose the films and an overlayer of more deposits and piles of those clusters is formed. The upper layer contains or evolves upon such, spherical or non spherical clusters, of a larger variety of shapes and sizes than those constituting the lower layer. At very high temperatures, the film hardly adheres to the substrate any more, unless the substrate's surface has some form of small inherent roughness.

At lower acidities (pH 4 - 6), a smoother layer is found, with smaller nucleating clusters and eventually only a sparse distribution of very small beads is seen on the surface of the film or partially plunged into it. At pH values approaching those of pure water, the film becomes extremely thin, between 50 to 70 nm. The exact same situation exists for lower temperatures, with an even smaller apparent participation of beads and clusters in the formation of the film. The film may also reach such a small thickness and perhaps even smaller, if lower temperatures are attempted. So a film thickness of approximately 70 to 250 nm can be developed by spanning across the range of temperatures and acidities and a certain amount of control is also given upon the structural features included in the film.

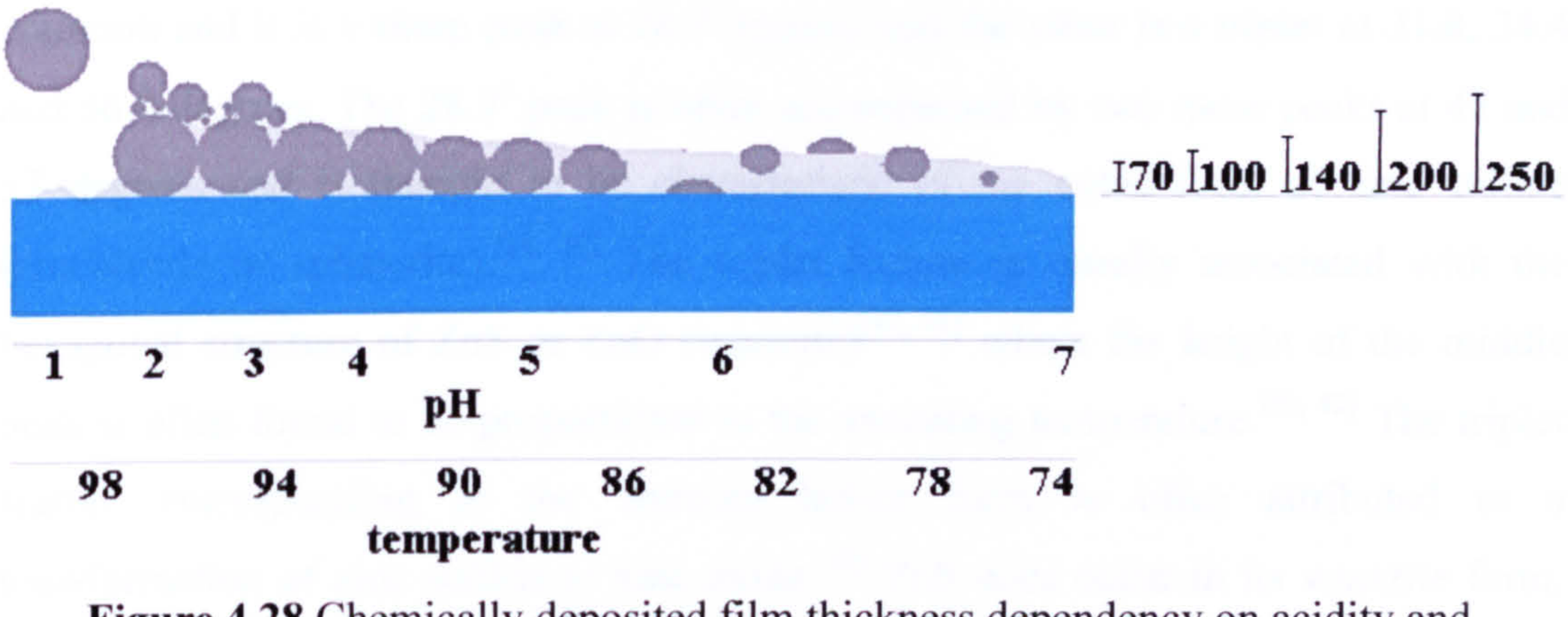

Figure 4.28 Chemically deposited film thickness dependency on acidity and temperature.

Finally the ideal deposition conditions were determined to be at a 92 °C constant temperature setting, with a pH between 5.5 and 6, a drop rate of 0.4 drops per second and films grown on the outer side of the slide substrates. A three times larger amount of metal chloride reactant, than the initial recipe, proved to ensure film adherence and better luminescent characteristics as will be pointed out later on. The thickness of the films (lower layer) at those conditions was 156 nm with a standard deviation of 12 nm. This average of thickness measurements acquired mostly from CdZnS samples, as the conditions were finally optimised in the stages of production of ternary compound films. The value does not change much for ZnS samples, as long as the quantity of the metal chloride reactant is kept at the same levels as those of cadmium and zinc together in the ternary compound precipitation procedure. The upper layer is kept at rather insignificant dimensions, with an average thickness of 20 nm and a standard deviation of approximately 3.2 nm. A roughness factor from the average values is calculated, reaching 0.45.

4.5 Crystal structure

4.5.a. XRD

The analysis technique of X-ray diffraction was performed on a very small selection of prepared samples, using a Siemens S5000 X-Ray diffractometer with a Cu K_α 1.5404 Å wavelength at a 2θ angle coupled scan arrangement. The films were analysed as prepared and after annealing at 500 °C and 700 °C. According to the literature, there are two features expected from a ZnS crystalline sample. One is more

common and it is a sharp peak at 28.7 degrees and the other is a triplet at 31.8, 34.4 and 36.2 degrees. The 28.7° peak is often accompanied by two more peaks at 47 and 57 degrees and is thought to be characteristic of the cubic form of zinc sulfide (zincblende or sphalerite).[38, 39] The triplet feature is usually associated with the hexagonal structure of ZnS or ZnO (wurtzite)[40, 41] where the height of the middle peak is often found to be proportional to the annealing temperature.[40, 42] The triplet feature corresponding to the wurtzite lattice form is often attributed to a transformation of zinc sulfide to zinc oxide.[43] ZnS does occur in its wurtzite form, but it is often required to anneal it at a temperature above 1000 °C.[14] Alongside the 28.7 ° peak, a weaker peak or shoulder is often observed and those who take notice of it, report it as a hexagonal phase ZnO feature.[38, 44] Unlike ZnS, the oxide attains the hexagonal form almost as a rule. Sometimes, the 27° feature, occurs as a very intense sharp peak on its own, or with also sharp accompanying peaks, at further away places, for example at 35, or 48 degrees and it is then again attributed to a hexagonal orientation.[32, 45]

Clearly the technique of X-ray diffraction is powerful in identifying the crystallinity of the samples in question. Moreover, the amount of crystalline material found in a specific phase will be proportional to the amount of diffracted light detected, relating to the material's orientation. The examined films have a thickness of the order of 100 to 200 nm, a large proportion of their volume was generated inhomogeneously and then adhered on the substrates surface. Therefore the XRD signals presented here carry significant noise, making it difficult to distinguish features. Even when annealed, the lack of active mass prevents any straightforward identification of patterns. The results were corrected against the substrates recorded signal and were then processed with averaging Gaussian distributed proportion filters (average of a moving sample of datapoints, weighted by a Gaussian distribution function applied over the central point of the sample), in order to eliminate excess noise. Figure 4.29 demonstrates the results of filtering.

A well-adhered, clear film prepared on a quartz substrate was investigated and produced the pattern in Figure 4.30. Even though the graph is still very noisy, one can observe a peak rising above the others at 28.7°, exactly were the diffraction signal from the cubic form of ZnS is expected. Some more features are observed at 31.6, 34.5, 36.7 and 50.4°, reported as being associated with the wurtzite orientation [9]. It is questionable whether one can assume the remaining smaller peaks as real signal or

noise. Yet, some of them do occur in either the wurtzite or cubic related angle positions.

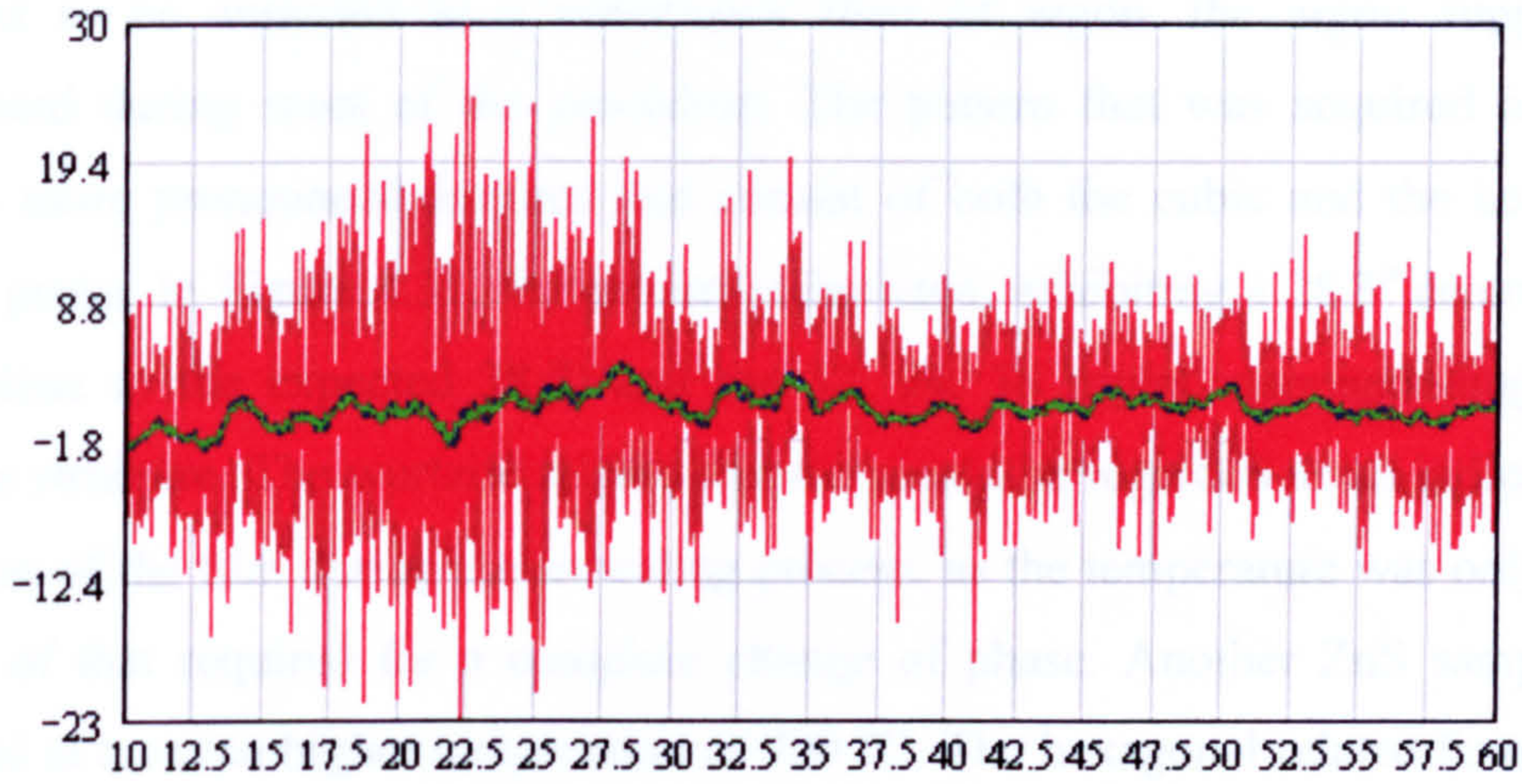

Figure 4.29 Results of filtering a noisy XRD pattern. With red colour is the unfiltered corrected pattern; with green and blue (overlapping lines) are the corrected, filtered signals with median and averaging filters respectively.

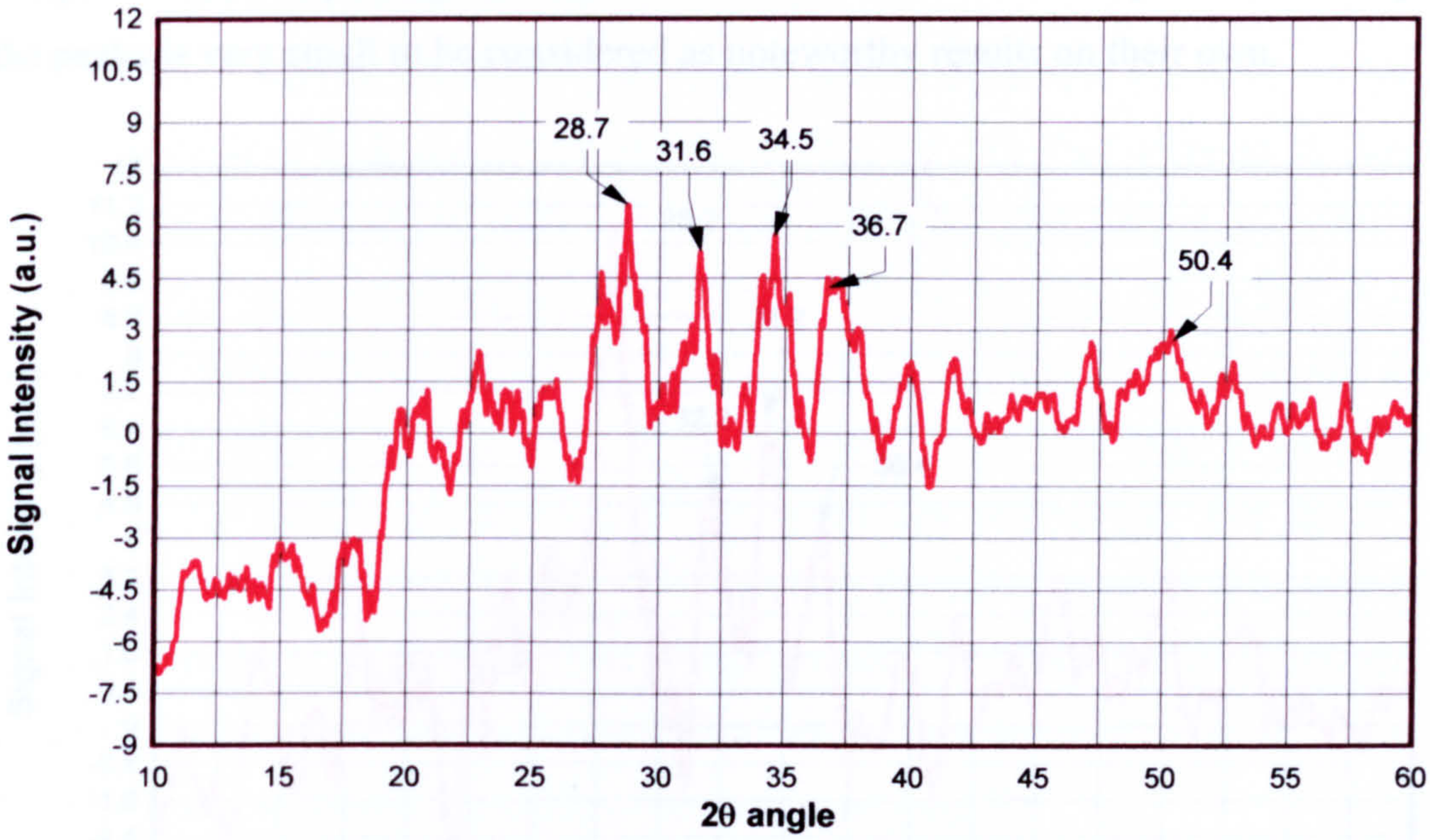

Figure 4.30 Corrected and filtered pattern of an as deposited, clear, adherent film, grown on quartz.

In order to increase the crystallisation of the film, the aforementioned sample was annealed overnight (24h) at 500 °C. Unfortunately, even though the sample was intended to be annealed in a continuous flow of argon, the argon supply was interrupted during most of the procedure. The pattern that was acquired now had slightly more pronounced features that consist of both the cubic and the hexagonal related peaks. In Figure 4.31, the pattern is depicted, exhibiting a 28.3° centred peak (very close to the expected 28.7) and the 32, 34, 36 triplet, corresponding to the wurtzite structure. The wurtzite related features could be regarded as an indication of oxidation of the film during the annealing process, as the temperature was only raised to half of that required for a complete change of phase. Another ZnS sample was annealed at an even higher temperature of 700 °C. The hexagonal related features are now even more pronounced (Figure 4.32), suggesting that as the temperature is approaches the phase change temperature boundary of 1000 °C, the film is slowly acquires its hexagonal form. The generally more pronounced features also indicate an increased crystallinity with increasing temperature of annealing, as expected. Nonetheless, it should be noted here that these observations were done on single samples without repeating the XRD measurements on more samples. The clarity of the peaks is very small to be considered as noteworthy results on their own.

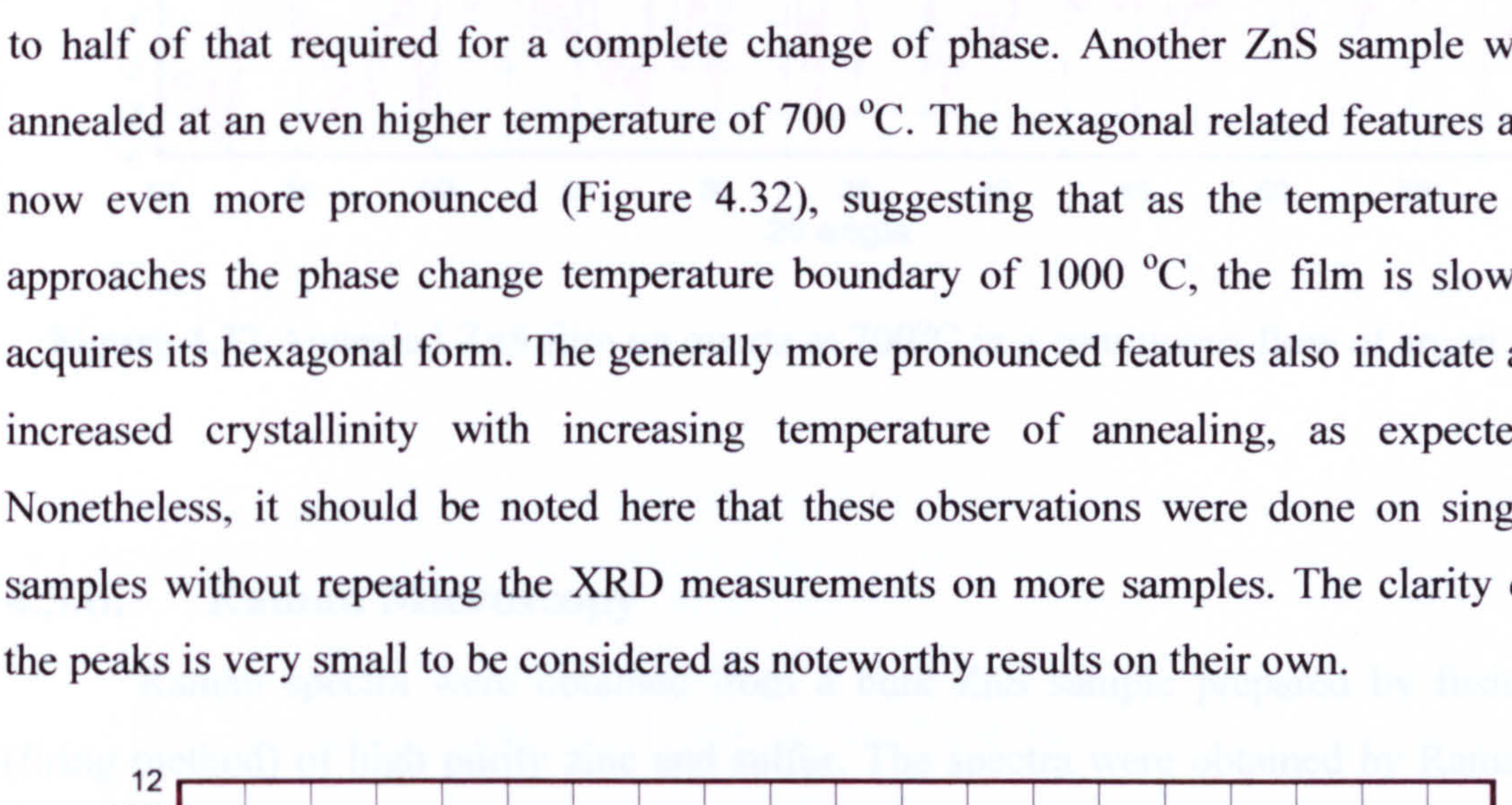

Figure 4.31 Annealed ZnS film on quartz, at 500°C under a non-continuous flow of argon.

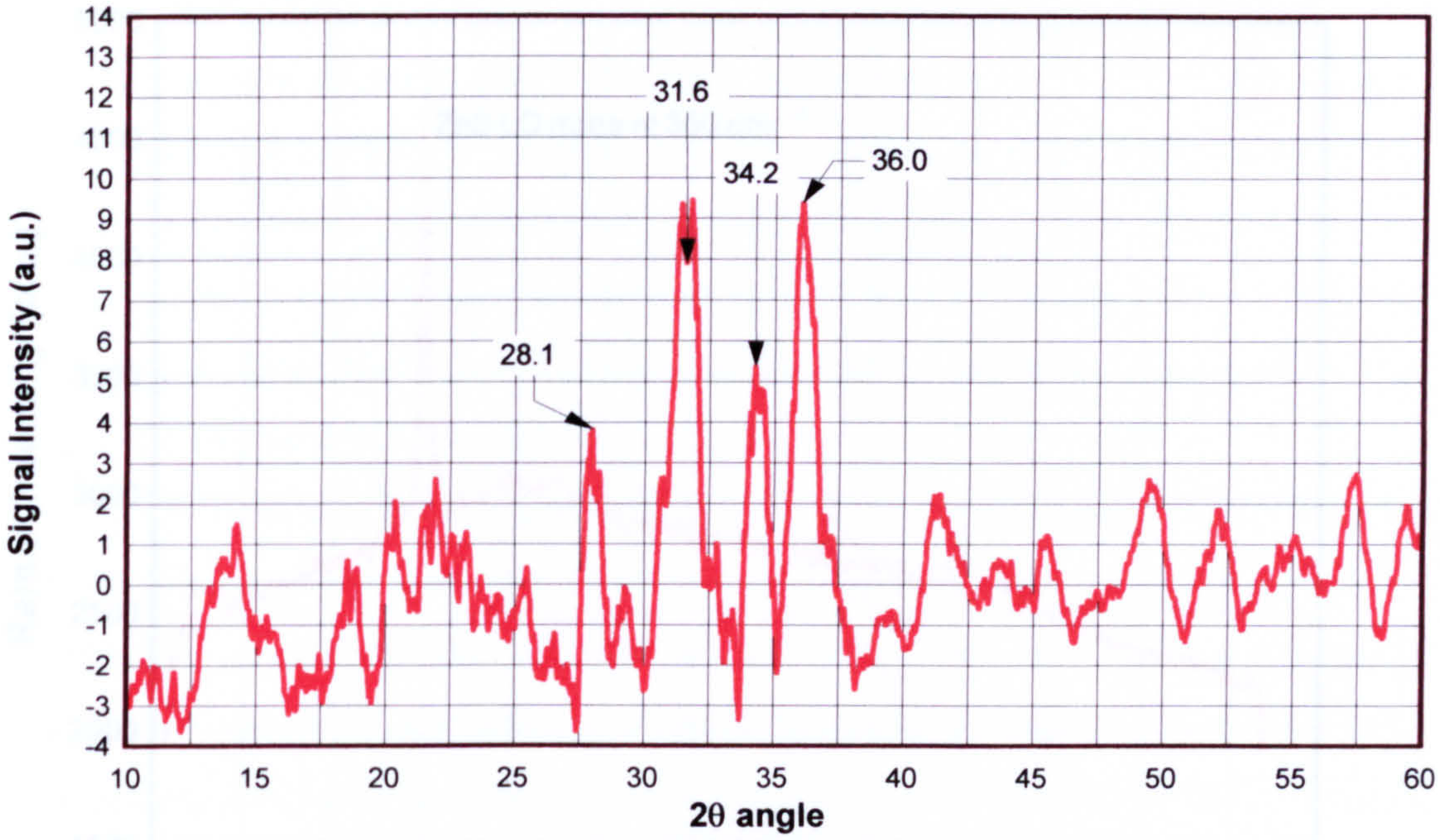

Figure 4.32 Annealed ZnS film on quartz at 700°C in a continuous flow of argon.

4.5.b. Raman Microscopy

Raman spectra were obtained from a bulk ZnS sample prepared by fusion (firing method) of high purity zinc and sulfur. The spectra were obtained by Raman microscopy as discussed in section 2.10. Due to the fact that Raman microscopy is acquiring spectra by interrogating very small areas, for the bulk zinc sulfide sample rather representative spots were chosen as the basis of investigation. A spectrum from such a representative spot is given in Figure 4.33 below. The longitudinal optical phonon at 350 cm^{-1} is clearly visible.[46] No scattering is observed from transverse optical phonons though, at 284 cm^{-1}.[47] Therefore, the cubic structure is assumed for this bulk sample of zinc sulfide. Zinc sulfide prepared by firing is indeed expected to crystallise in the cubic form, because of the rather lower temperature of the reaction than that expected for the formation of its hexagonal form.[14]

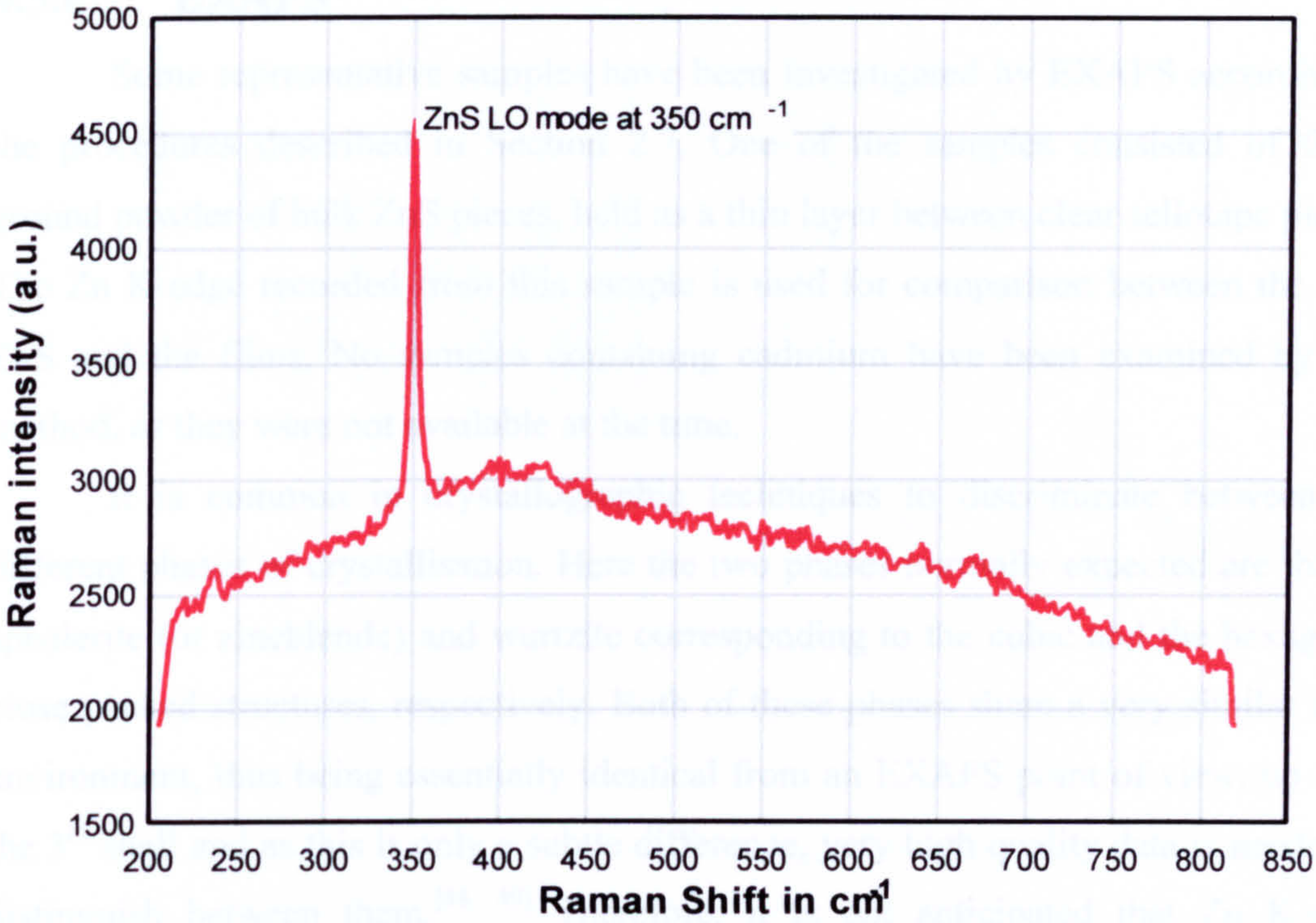

Figure 4.33 Raman spectra of a bulk zinc sulfide sample. Aperture open cycle, 150 sec, at 60 cycles, excitation wavelength 532 nm, 100x objective lens and 2.4 mJcm^{-2} beam power.

The maximum thickness of any of the films produced by chemical bath deposition has never exceeded 500 nm. On the other hand, the Raman microscope at its best focused configuration, using the 100x objective lens acquires its spectrum from a volume that can be approximated as a cylinder of 2 μm height and 1μm diameter (as mentioned in section 2.10). Therefore, acquisition of a decent spectrum from the chemically grown films was unsuccessful. The spectra did not allow discerning of any peaks within the expected boundaries of 200 to 500 cm^{-1}. All the spectra taken from chemically grown films were significantly covered in noise. Attempting to focus the microscope at a slightly higher level in order to probe only air and possibly the top layer of deposited film, for a longer time, was also unsuccessful. The technique though has yielded interesting results for the films that were produced by multiple transfers over the same target area (section 6.1.a). Those films reached a thickness of up to 1 μm, which is half of the Raman probing depth and approximately 5 times greater than the average precipitated film.

4.5.c. EXAFS

Some representative samples have been investigated by EXAFS according to the procedures described in Section 2.7. One of the samples consisted of finely ground powder of bulk ZnS pieces, held as a thin layer between clear sellotape pieces. The Zn K-edge recorded from this sample is used for comparison between the bulk ZnS and the films. No samples containing cadmium have been examined by this method, as they were not available at the time.

It is common in crystallographic techniques to discriminate between the different phases of crystallisation. Here the two phases normally expected are that of sphalerite (or zincblende) and wurtzite corresponding to the cubic and the hexagonal close packed structures, respectively. Both of these phases share a very similar local environment, thus being essentially identical from an EXAFS point of view, up until the 3rd shell and as this is only a subtle difference, very high quality data is needed to distinguish between them.[48, 49] Therefore, it is not anticipated that Zn K-edge EXAFS will be able to identify whether sphalerite or wurtzite is formed in the chemical bath deposition. The Zn K-edge EXAFS and FT for a sample of ZnS mounted on sellotape are shown in Figure 4.34. The difference between the sphalerite and wurtzite structures, manifests itself as a weak shoulder in the FT at about 5 Å and due to the noise in the data, it has been fitted to the sphalerite structure, which is normally expected for samples created by the firing process.[14, 50] The first Zn-S shell bond length refines to 2.35(2) Å which is in very close agreement with the structure determined by diffraction techniques.[51] The more outlying shells are also in good agreement with the literature values, indicating that the accuracy of the data analysis is very good as regards the distances. The intensity of the oscillations and hence the coordination numbers are slightly problematic, in as much the first coordination shell refines to about 2, rather than 4. This is most likely to be due to collection of data in fluorescence mode from a neat sample mounted on sellotape. In such a case, what is known as self-absorption can occur, where the fluorescence from one atom is absorbed by others surrounding it. Although this is also likely to be a problem for the thin film samples, it should be less problematic.

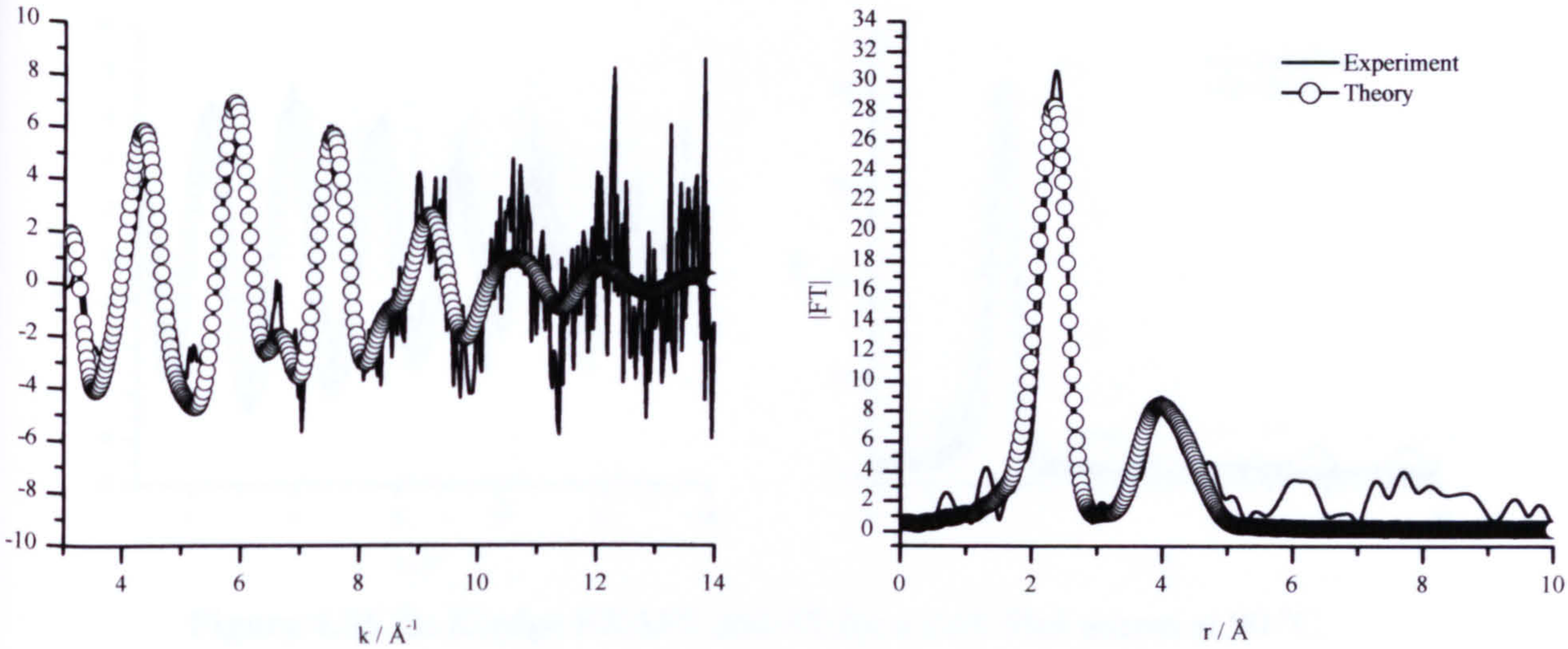

Figure 4.34 Zn K-edge EXAFS and its Fourier Transform for powdered bulk ZnS.

The Zn K-edge EXAFS data for the various ZnS thin films investigated were very similar (see Table 4.1 and Figures 4.35, 4.36 and 4.37). Only the first Zn-S shell was included in the data analysis, as the other outlying features were too weak to be used for reliable fitting. The Zn-S distance is reproducibly shorter in the thin films than the bulk by about 0.01-0.02 Å. Whilst this is within the accepted errors of *ca* ±1%, it does appear to be consistent and whilst observed previously, was not commented upon.[52] In all cases the Zn-S coordination number of this first shell refines very close to 4. For the majority of the films there is no problem identifying the local Zn environment as ZnS_4. For one of the samples though, (see Figure 4.38) the EXAFS and FT are very different, but fit very well to ZnO (see also Table 4.2). This sample was prepared in a bath 3 times more concentrated in all of the three main reactants than normally and then it was annealed in air at 540 °C, for 16 hours. Therefore, the annealing process was expected to have transformed the film into mostly ZnO. The appearance of the film to the naked eye has also changed significantly, as from a mostly white and rather thick film, it has turned to an almost totally clear thinner film. So all other samples were consistent with the ZnS structure.

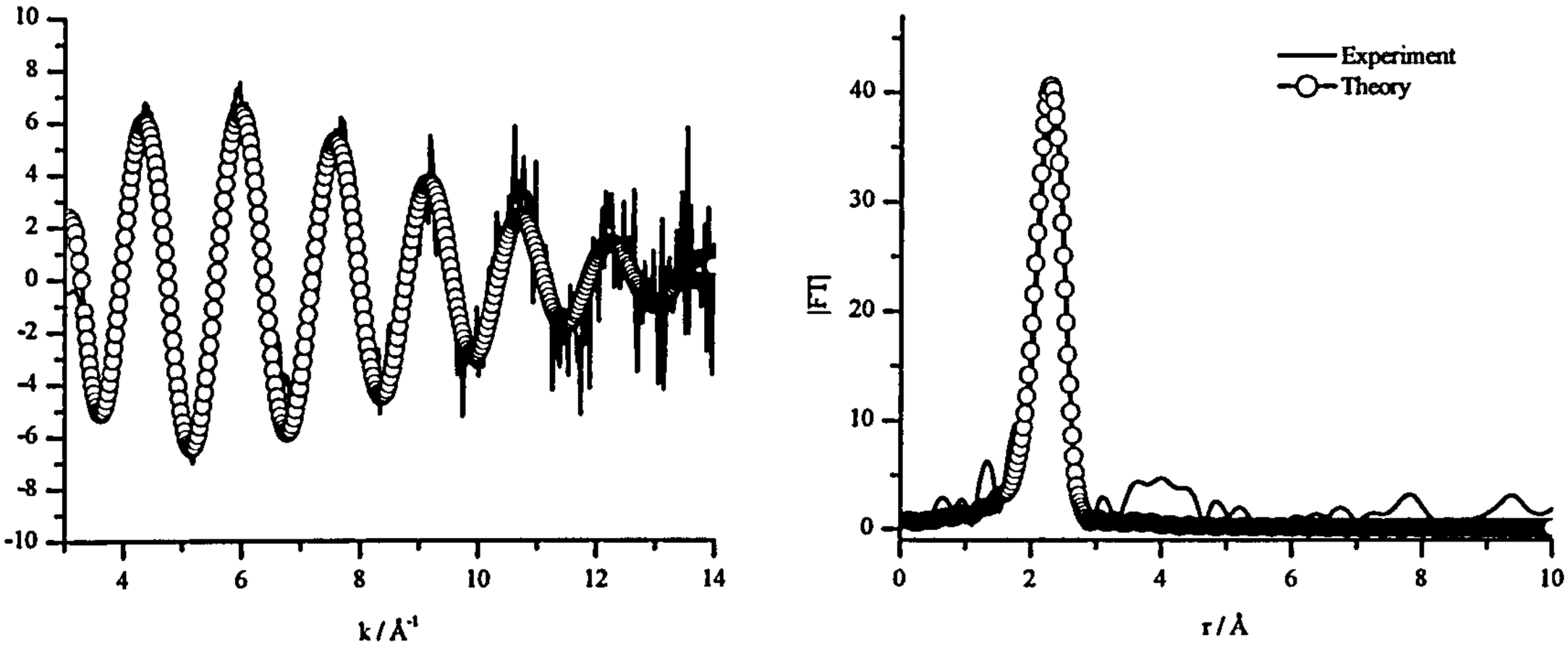

Figure 4.35 Zn K-edge EXAFS and FT for a ZnS film grown at 90 °C.

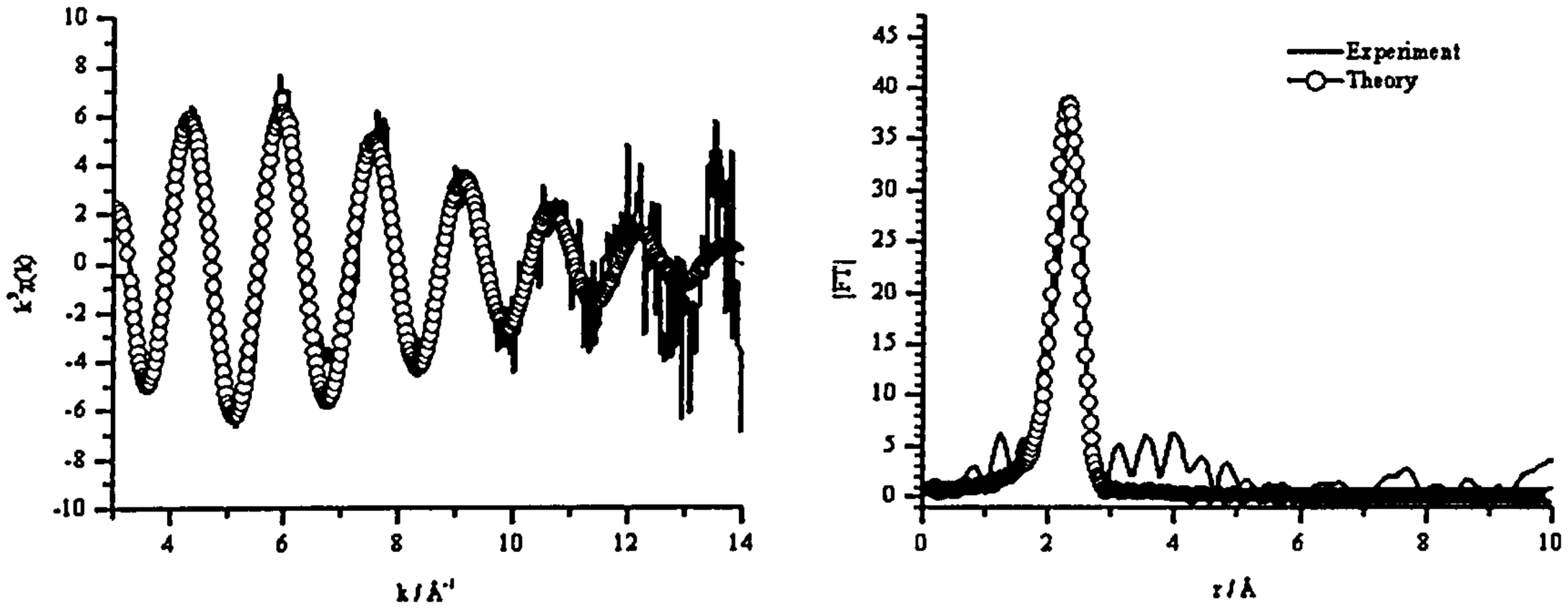

Figure 4.36 Zn K-edge EXAFS and FT for a ZnS film grown in a bath with 0.4 g of $ZnCl_2$ salt (3xZn, 17.3 mM) at 95 °C, constant temperature setting.

Figure 4.37 Zn K-edge EXAFS and FT for another ZnS film grown at 90 °C.

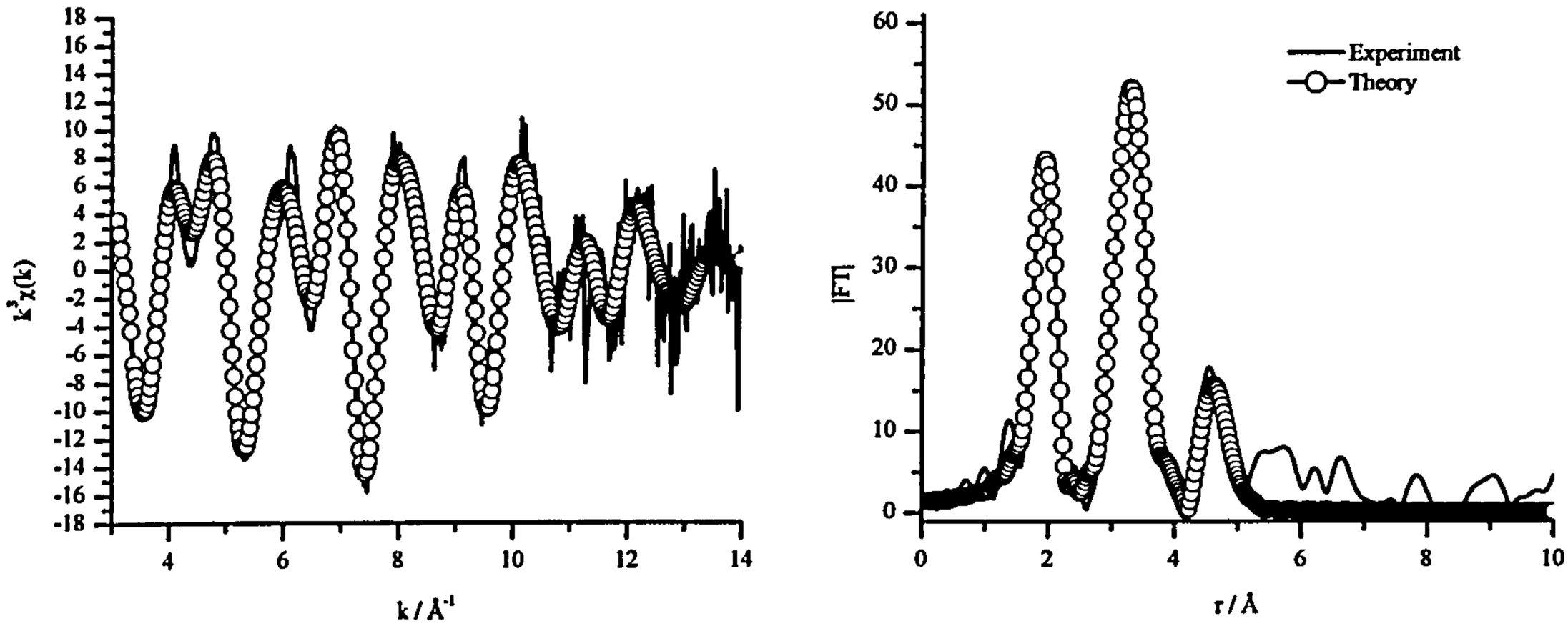

Figure 4.38 Zn K-edge EXAFS and FT of a ZnS sample prepared from a bath with tripled reactant quantities and annealed in air at 540 °C for 16 hours.

Samples doped with copper, manganese, cobalt and nickel were also examined by EXAFS, but only the Cu doped films gave analysable data. The signal for the other three was very weak or too noisy to resolve. The Zn K-edge data for the Cu doped films was very similar to that from the undoped films,[53] but the Cu K-edge data can be used to determine if Cu is occupying substitutional sites, or if it has phase separated into ZnS and CuS rich areas. If the Cu is occupying substitional sites within the sphalerite lattice, then the Cu-S bonds would be expected to have very similar lengths to those of Zn and S in the parent ZnS lattice. If Cu has phase separated in forming its own sulfide, then bond lengths similar to those of bulk CuS should be detected to the greatest extent.

Previous work on copper sulfide precipitates has shown that there is a primitive copper sulfide formed initially which has a second Cu-S shell at distances slightly longer than the main Cu-S distance.[54] Fitting of this 2nd Cu-S shell as observed in the primitive copper sulfide precipitates does not work in this case. The observed 2.27 Å, Cu-S distance is considerably shorter than what would be expected for a ZnS lattice, hinting that Cu is not occupying substitutional sites (see **Figure 4.39** and Table 4.3). In addition it is very similar to that observed in covellite (CuS).[54] Covellite is not isostructural with the ZnS phases, as it has 4 tetrahedral Cu with a Cu-S distance of 2.31 Å and 2 triangular Cu with 2.19 Å, thus the Cu K-edge Cu-S distances average to 2.27 Å. Although it is possible to try to fit the Cu-Cu outlying shell, it is not really statistically significant. Hence a single Cu-S shell was used throughout (Figure 4.41). The Cu K-edge XANES (see Figure 4.40)of the sample

with the smallest expectancy of copper incorporation (originating from a solution with 0.4g / 17.3 mM of $ZnCl_2$ and 0.0007g of $CuCl_2.2H_2O$ / 0.02 mM of $CuCl_2$) contains a shoulder on the edge at 8986.5 eV that is characteristic of covellite.[54] Therefore, the fact that both EXAFS and XANES fit very well to covellite implies that the vast majority of the copper is present as a CuS, covellite phase, rather than being substituted into the ZnS lattice.

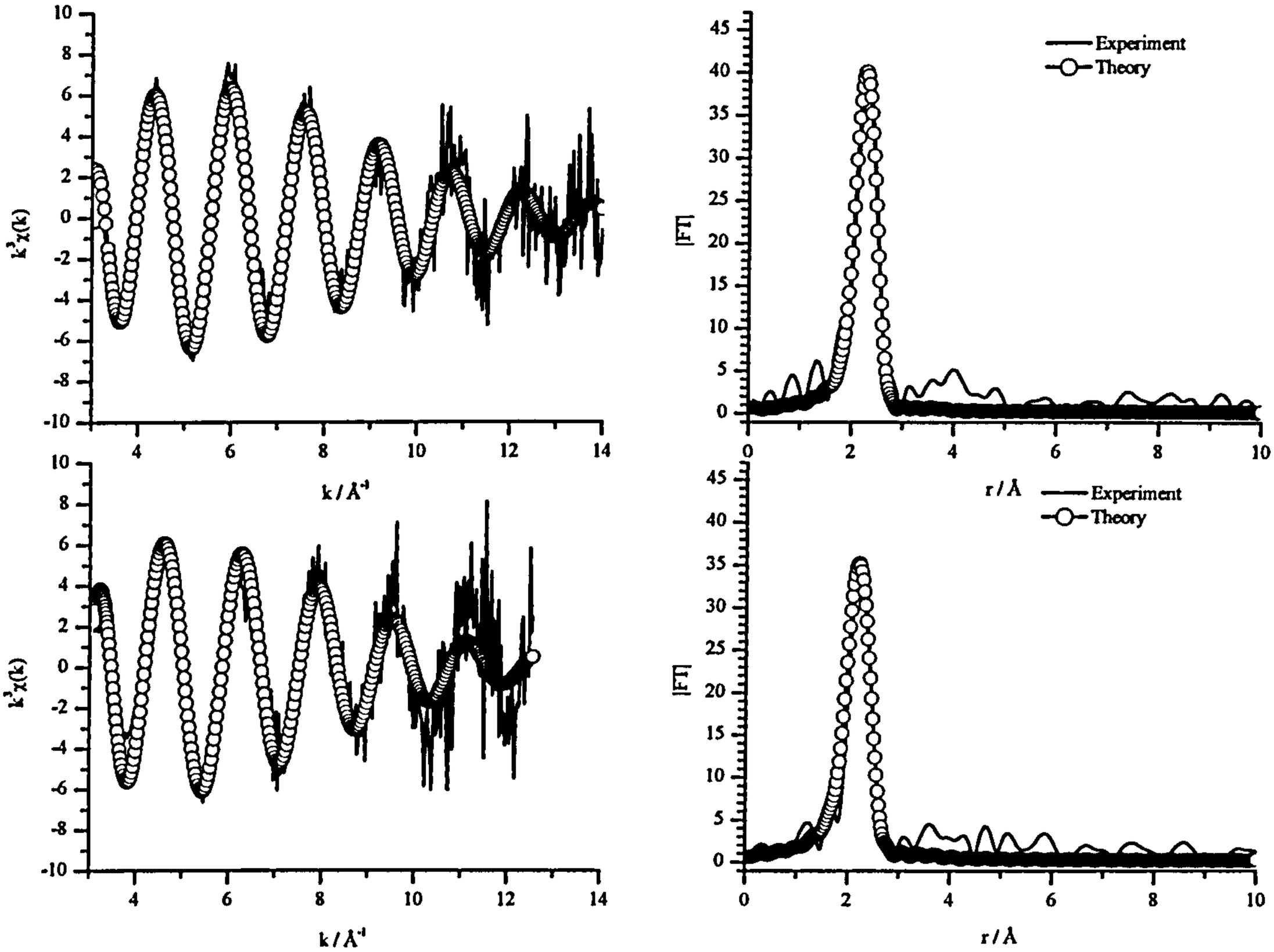

Figure 4.39 EXAFS and FTs for a ZnS sample doped with Cu, prepared at 95 °C with 0.4g and 0.0007g of Zn and Cu chloride salts respectively. Presented for comparison between the Zn K-edge (top) and the Cu K-edge (bottom).

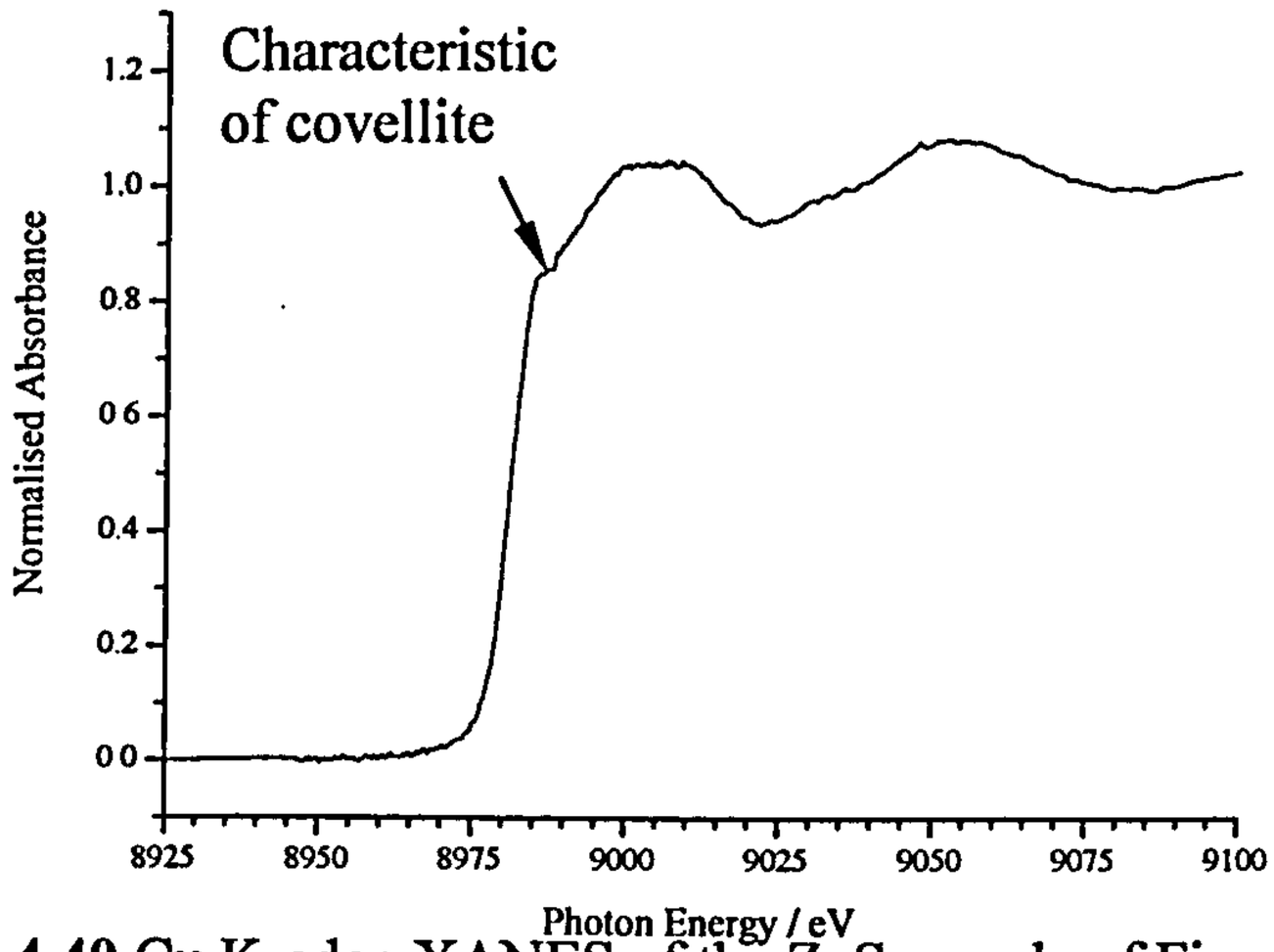

Figure 4.40 Cu K-edge XANES of the ZnS sample of Figure 4.39.

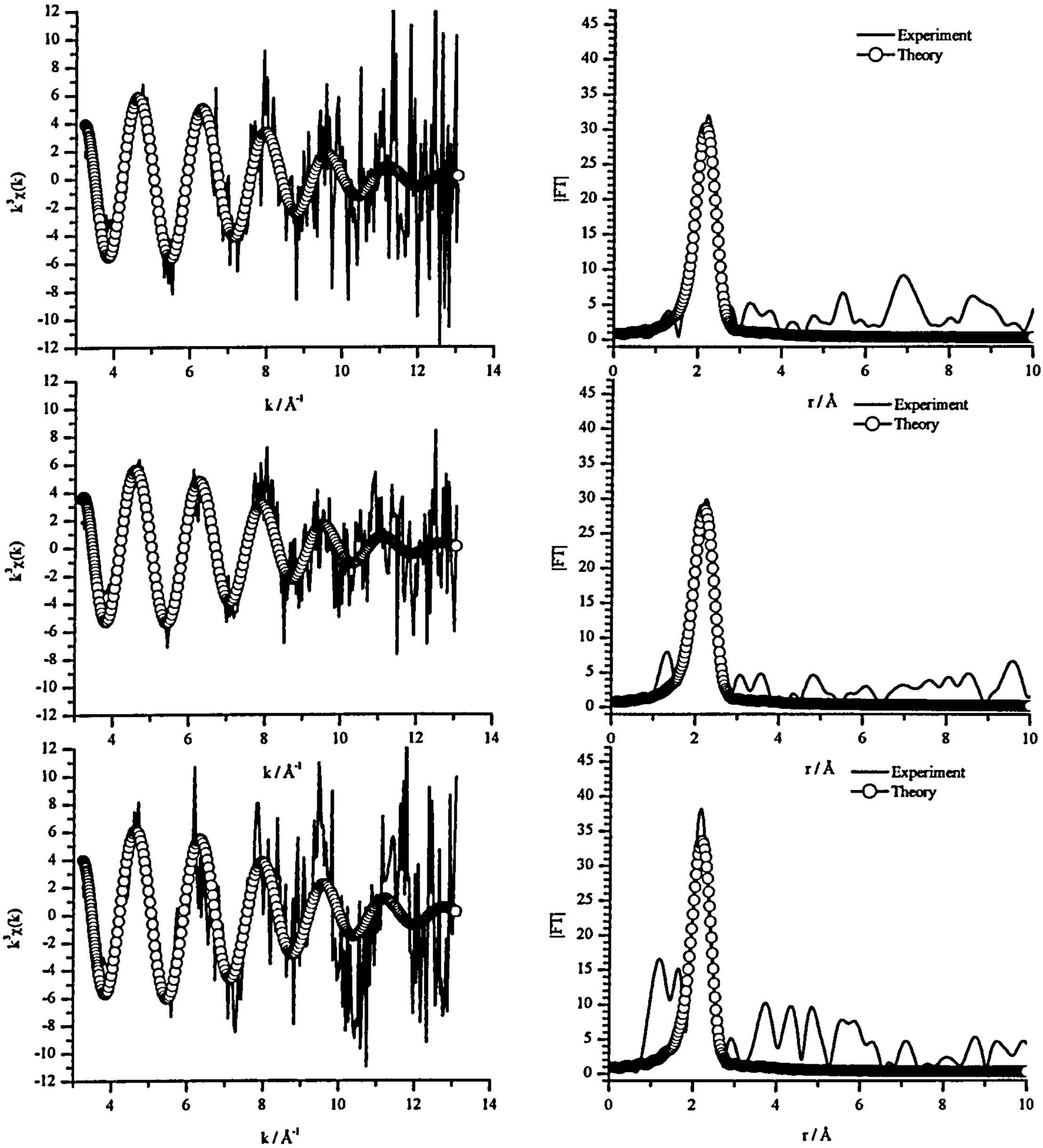

Figure 4.41 Cu K-edge EXAFS and FTs for ZnS films doped with Cu, prepared in baths containing 0.1g / 3.5 mM (top), 0.01g / 0.4 mM (middle) and 0.005g / 0.2 mM (bottom) of copper chloride salt.

Table 4.1 Refined Zn K-edge EXAFS parameters for ZnS (bulk) and ZnS thin films.

	r_{Zn-S} /Å (x4)	$2\sigma^2_{Zn-S}$ / Å^2	r_{Zn-Zn} /Å (x 12)	$2\sigma^2_{Zn-S}$ / Å^2	r_{Zn-S} /Å (x 12)	$2\sigma^2_{Zn-S}$ / Å^2	E_f /V	R	FI
ZnS (EXAFS)	2.346(12)	0.0210(18)	3.838(23) x 12	0.0411(56)	4.443(53)	0.0557(201)	- 8.4(14)	61.1	1.67
ZnS (XRD)[51]	2.345		3.829		4.490				
1xZn	2.325(6)	0.0148(8)					-6.8(8)	34.90	0.570
3xZn annealed to 540C	2.336(7)	0.0156(10)					-7.9(9)	38.6	0.747
3xZn, 0.005xCu	2.324(6)	0.0151(9)					-7.43	36.3	0.611
1xZn	2.324(6)	0.0166(9)					7.5(8)	33.1	0.603

Table 4.2 Refined Zn K-edge EXAFS for sample converted to ZnO by annealing in air.										
	Zn-O x 4	Zn-Zn x6	Zn-O x1	Zn-Zn x6	Zn-O x9	Zn-Zn x6	Zn-O x 6	E_f / V	R	FI
r / Å	1.959(7)	3.188(31)	not refined	3.273(36)	3.778(38)	4.579(16)	4.475(73)	-6.2 (10)	36.4	0.600
$2\sigma^2$ / Å^2	.0083(13)	.0151(53)		.0179(97)	.0221(93)	.0166(41)	.0166(41)			
XRD data[55]	1.975 x3 1.983 x 1	3.208 x 6	3.222 x 1	3.249 x 6	3.806 x 9	4.566 x 6	4.576 x 6			

Table 4.3 Cu K-edge EXAFS refined parameters					
	r_{Cu-S} /Å (x4)	$2\sigma^2_{Cu-S}$ / Å^2	E_f /V	R	FI
3xZn, 0.7mg $CuCl_2$	2.264(9)	0.0193(15)	-6.5(11)	50.3	1.28
1.3xZn, 5mg $CuCl_2$	2.251(20)	0.0200(35)	-3.9(20)	76.5	3.69
3xZn, 0.01g $CuCl_2$	2.268(15)	0.0232(26)	-5.7(14)	62.7	2.31
3xAll, 0.1g $CuCl_2$	2.250(21)	0.0221(37)	-4.0(20)	69.9	3.67

E_f is a single refined parameter to reflect differences in the theoretical and experimental Fermi levels,

$FI = \Sigma [(\chi_i^T - \chi_i^E)k_i^3]$, $R = [(\int|\chi^T - \chi^E|k^3 dk) / (\int|\chi^E|k^3 dk)] \cdot 100\%$

4.5.d. Optical Microscopy

A thorough observation of the deposited films was often performed by optical microscopy. The observation gave a good idea of how the films were grown on the substrate and their morphology in general, as described above, in Section 4.3.b. On certain occasions, larger crystal structures, of a variety of shapes would be found. Two formations of greater interest in terms of their evident crystal structure are presented here.

The first one resembles a sodium chloride crystal grain of cubic structure (Figure 4.42). The grain was found on a ZnS film doped with silver. The rest of the film had a typical height and structure, but it had sparse larger features in similar dimensions to the one displayed here. The sides of the first and second largest cubes measure 88 and 60 μm respectively. It is not common to find zinc sulfide crystals with an exact cubic shape. Minerals of galena and sphalerite, macroscopically often resemble a cube with a missing edge, or a cluster made of pentagon shaped faces, or a rhomboidal wedge.[14]

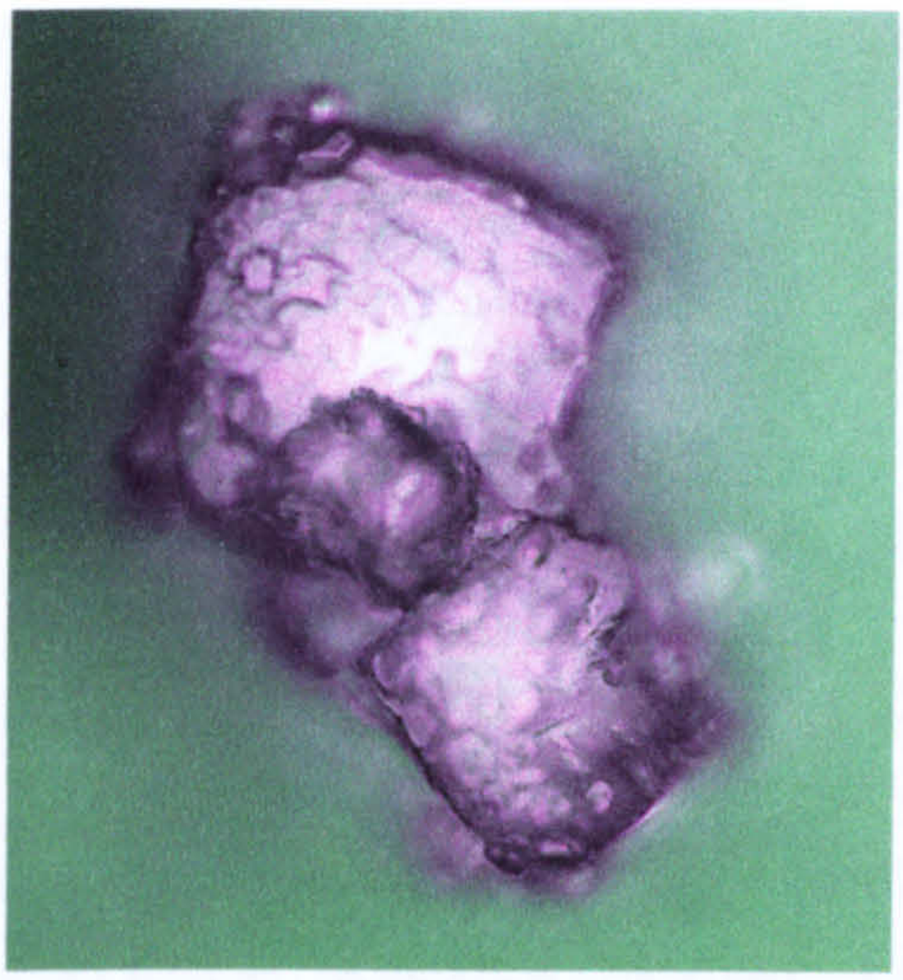

Figure 4.42 Crystal grain of cubic-like form observed on a ZnS:Ag film. The side of the larger cube at the bottom was measured at 88 μm with the microscope software.

The second feature of interest was observed on the edge of a substrate covered with a CdZnS:Ag film, prepared from a bath with a 1:1 weight ratio of the cadmium and zinc salts and a 10:1 ratio of the manganese to zinc or cadmium salts. The edge of the substrate was affected by possible evaporation of hydrochloric acid from the surface of the gloves, while it was being handled for cleaning the other side of the substrate. It is a standard process to clean one of the sides of the substrate after the bath deposition (usually the side that was less covered by the film), thus rendering the sample usable for the laser transfer procedure, where the laser beam will need to pass through the substrate before reaching the target film surface. The side of the substrate carrying the feature was here the outer surface (the one facing away from the heater), while the inner had a smaller coverage and was therefore cleaned way. The crystal features seem to be a fusion of the surrounding needle-like crystals and attribute a hexagonal perimeter (Figure 4.43). That is again not necessarily any proof of a hexagonal crystal structure, though CdS is expected to occur in its hexagonal phase, regardless of the formation conditions. Crystals in a hexagonal phase are found in a variety of shapes, that only occasionally feature hexagon shaped faces or circumference.[14]

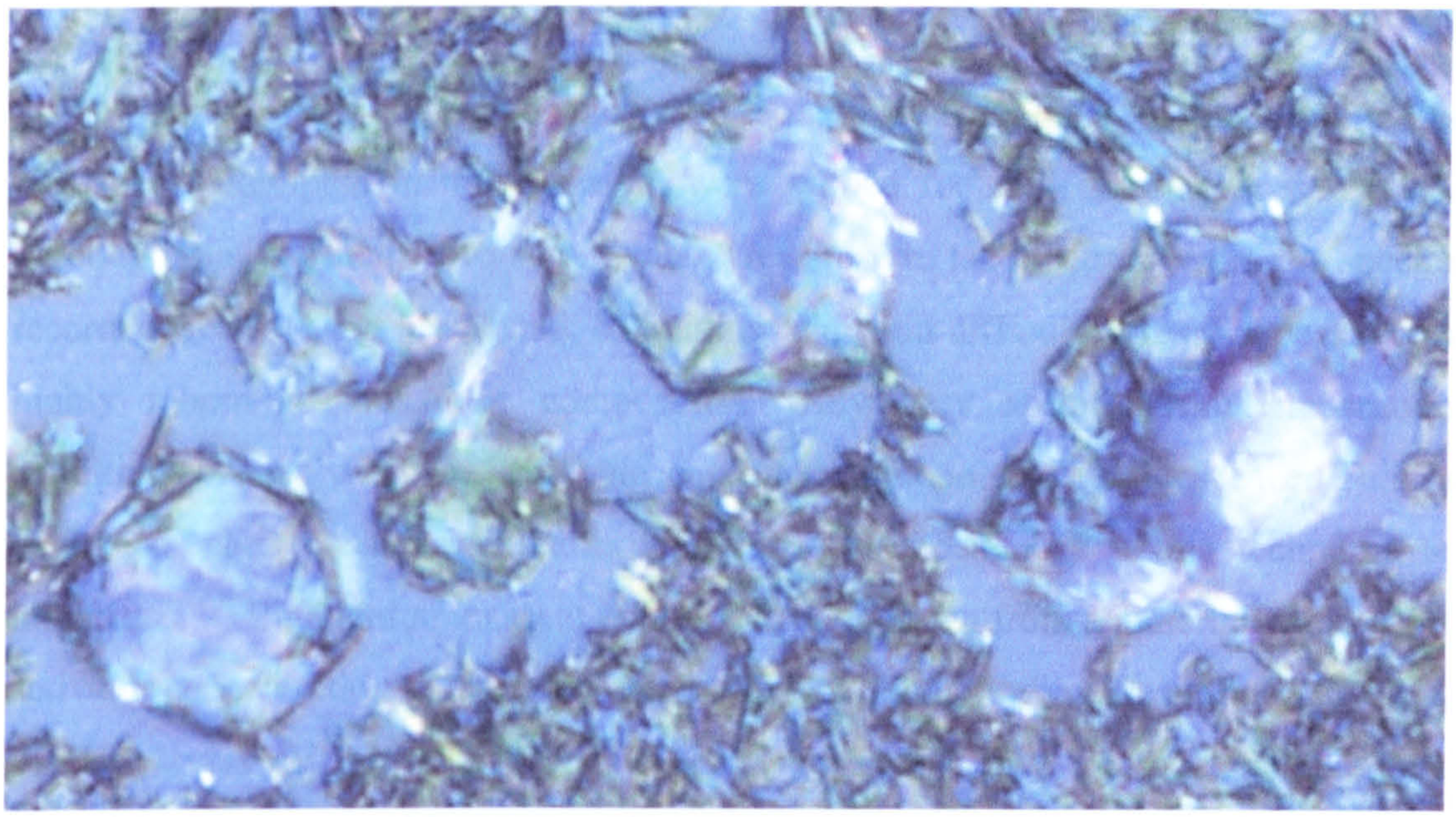

Figure 4.43 Crystallic features observed on the edge of a CdZnS:Mn sample, affected locally by HCl fumes. The crossection of the three main crystal features is approximately 10 μm and the width of the surrounding needles 0.67 μm.

4.6 Luminescent Properties

Luminescent properties of the deposited films were investigated by cathodoluminescence and photoluminescence techniques. The two techniques, as explained in sections 1.1.a and 1.1.b, are related in their principle of operation, with the difference that one uses high-energy photons and the other accelerated electrons to excite the phosphor material. The investigated luminescence properties though will not necessarily be reproduced when the material is employed in a thin film electroluminescent cell. The intense electric field applied over the thin film will not allow for successful trapping of electrons and holes, therefore, only activators that emit by impact excitation will work as efficient luminescent centres. Hence, from the three elements used for intended doping in the generated films, copper, silver and manganese, only the last one is an acceptable activator for thin film devices. Nickel and cobalt were not expected to cause any luminescence of the materials. Luminescence recorded from copper and silver doped films provided a unique insight to the properties of the deposited materials and an indication of whether they can carry such properties with them after the laser transfer process.

4.6.a. Cathodoluminescence

Samples prepared under most of the deposition regimes and conditions that have been attempted in this research, were probed for cathodoluminescence (CL). Although most of them gave some kind of response to the electron beam, the spectra recorded were of very low signal, containing wide and difficult to resolve peaks, or a highly inhomogeneous film composition. Only very specific film preparation conditions were fruitful in achieving acceptable amounts of luminescence. This is explained when considering the explicitly strong dependence of the technique to impurities.[56] Cathodoluminescent emission can be drawn from a material with potent activator concentration at limits as low as one in ten thousand; while at the same time, similar levels of unwanted impurities could sufficiently provide radiationless recombination routes. Moreover, other characteristics of the host lattice, such as defect concentration and carrier mobility, could also prove essential in allowing for luminescence inflicted by the cathode ray.

One of the first samples examined in the CL chamber was not a chemically deposited film, but pieces and ground powder of a ZnS bulk specimen, prepared by firing zinc and sulfur by previous researchers. The powder was ground by pestle and mortar to fine dust and attached to a metallic carrier by silver paste. The pieces were 1 to 2 mm in length or diameter, entrapped in folded sheet of aluminium foil. An incredibly intense blue light was emitted from both types of this sample, which at certain angles was too intense even for the human eye at direct observation (Figure 4.44). The spectrum was recorded at an angle and with the use of the smallest detector aperture available. In Figure 4.45 below, the CL emission of the powder sample is illustrated. The separate bits gave the exact same spectrum at different intensities. The main peak is at 495 nm, with a shoulder at 457 nm. Neither of the two peaks is identified as the typical emission of self activated ZnS due to sulfur vacancies, often observed around 415 to 420 nm. If one does not question the purity of the material, the only possible transitions are those involving sulfur vacancies, or zinc vacancies and interstitials.[57]

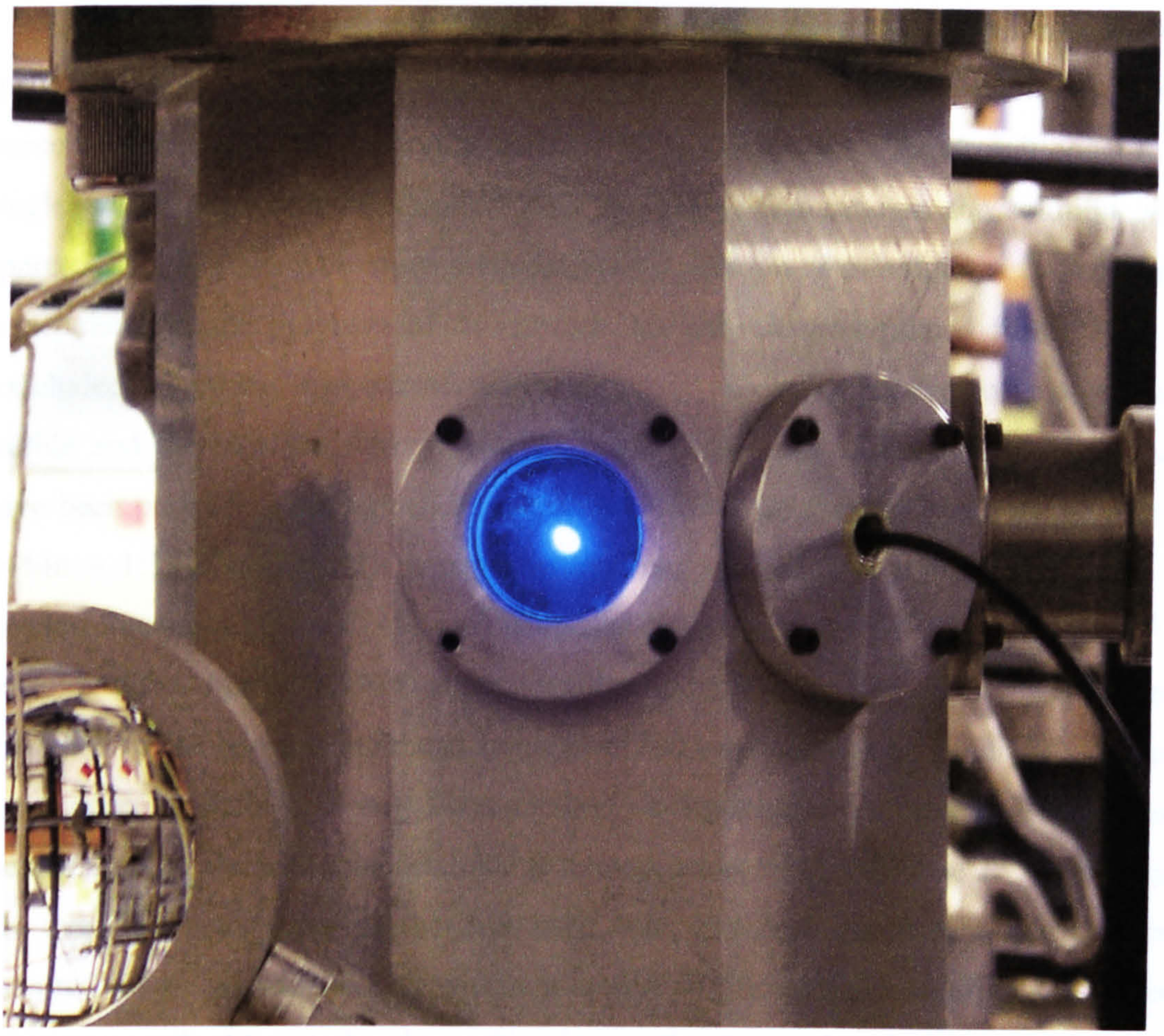

Figure 4.44 Photograph of bulk ZnS powder emitting a bright blue light under the excitation of a cathode ray.

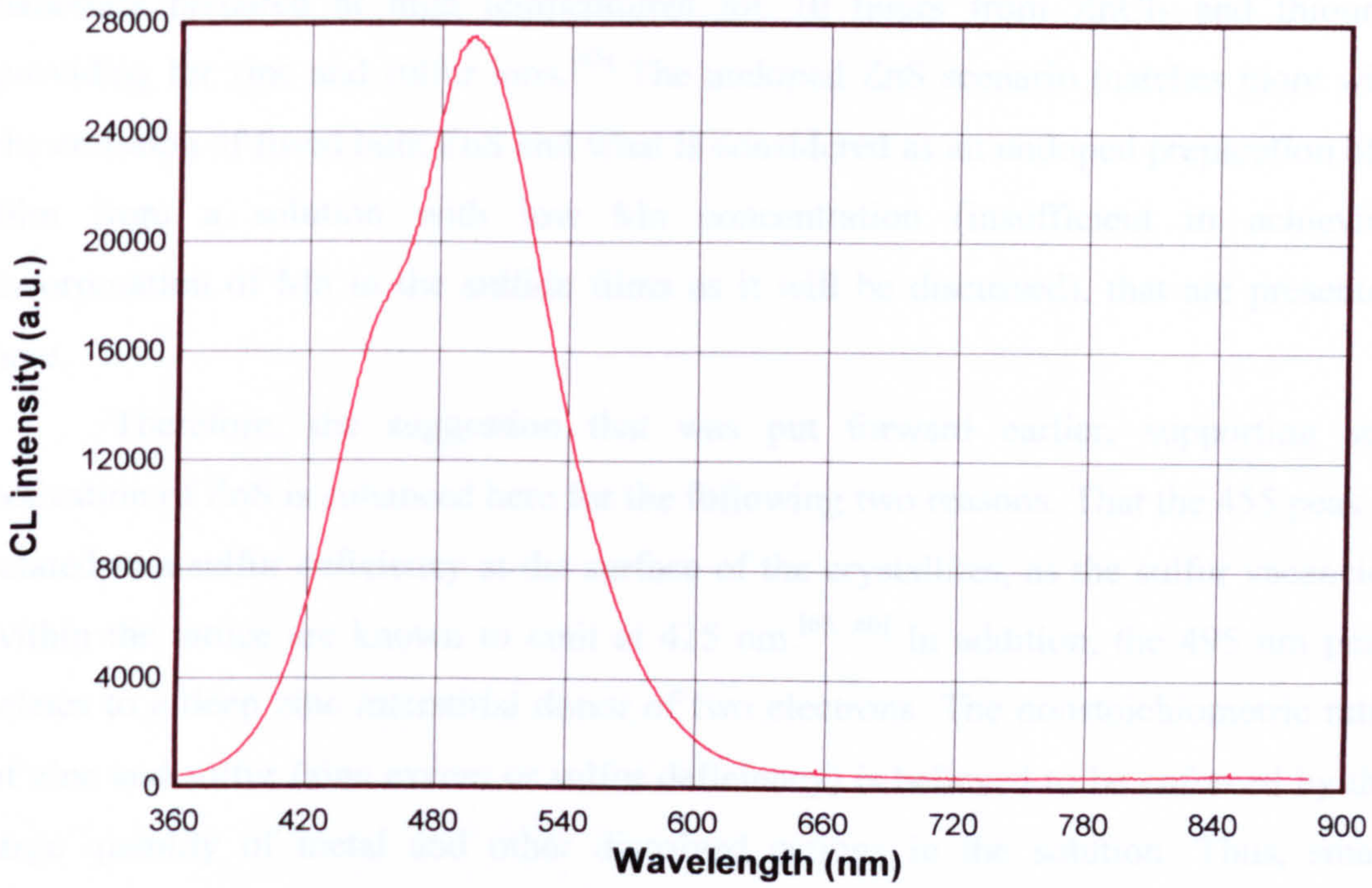

Figure 4.45 Cathodoluminescence of bulk ZnS prepared by firing.

An remarkably similar peak was also recorded as a photoluminescence spectrum of a ZnS sample (Figure 4.52) deposited in a bath containing triple concentrations of all basic reactants and a dose of manganous chloride salt equal to a single typical dose of zinc chloride (i.e. the Zn to Mn ratio in the solution was approximately 3:1). The dose of manganese salt in the solution is regarded insufficient for the purposes of its introduction into the precipitated films. This is concluded by taking into consideration the small solubility product of manganous sulfide and the fact that successful experiments achieving expected emissions that have been performed with much higher concentrations of the salt in the solution (Zn to Mn = 1:10). Remarkably, a photoluminescent peak at 2.48 eV (500 nm) and a smaller one around 2.7 eV (458 nm) have also been reported by R.D. Yang et. al.,[44] being emitted from ZnS:Mn nanocrystalline precipitates. The peaks have been attributed to the Mn d-d intraband transition (500 nm) and a temperature dependent donor acceptor pair (458 nm). Their method of deposition also involved mixing of metal chloride salts with thioacetamide at a temperature of 110 ^{o}C. The Zn to Mn ratio was even larger than the 3:1 that was used here. The peak assignment can only be accepted for heavily doped ZnS with non-activating metals that will affect the lattice parameter, as the Mn intraband transition is usually observed in the vicinity of 580 to 600 nm.[19, 39, 44, 58-64] A 500 and 450 nm peak set was reported for undoped ZnS nanorods prepared at high temperatures for 10 hours from $ZnCl_2$ and thiourea providing for zinc and sulfur ions.[45] The undoped ZnS scenario matches more with the emission of fused bulk ZnS and what is considered as an undoped preparation of a film from a solution with low Mn concentration (insufficient in achieving incorporation of Mn in the sulfide films as it will be discussed), that are presented here.

Therefore, the suggestion that was put forward earlier, supporting self activation of ZnS is enhanced here for the following two reasons. That the 455 peak is related to a sulfur deficiency at the surface of the crystallites, as the sulfur vacancies within the lattice are known to emit at 415 nm.[65, 66] In addition, the 495 nm peak relates to a deep zinc interstitial donor of two electrons. The nonstoichiometric ratio of zinc and sulfur (zinc excess or sulfur deficiency) is believed to be enforced by the large quantity of metal and other dissolved cations in the solution. Thus, small quantities of manganous chloride in the solution only act as a regulator of the precipitate stoichiometry, instead of taking part in the formation of the films.

From solutions with an increased zinc chloride concentration, compared to thioacetamide and urea, films were produced that emitted strongly at 515 nm after annealing at 700 °C under argon (Figure 4.46). The peak has been attributed to copper, coactivated by aluminium,[66] or to gold with no coactivator.[65] Copper contaminants cannot be ruled out from any of the samples that have been prepared after experiments with large copper chloride concentrations, because small remnants of copper sulfide on the heater would easily redissolve in the solution. Gold impurities are not expected to arise from any source and were not detected in any analysis technique. A small molar percentage of aluminium, approximately 0,022 %, was detected by ICPMS (Section 4.2.b), included in the other metal elements in Figure 4.6. None of the samples were expected to have Al contaminants, so its detection in one, signifies a possibility of its occurrence in others. This molar participation could be enough to coactivate copper contaminations in order to obtain a considerable amount of favourable donor to acceptor transitions. Therefore, the 515 nm emission could relate to an increased efficiency of the aluminium-copper transitions. Substitution of sulfur with chlorine could also provide possible coactivation sites, due to high amount of $ZnCl_2$ introduced to the solution (13.8 mM of $ZnCl_2$ as opposed to the suggested 5.2 mM that is used normally). The chlorine substitutes for sulfur would create an energy level at a distance to the conduction band, similar to the aluminium impurities.

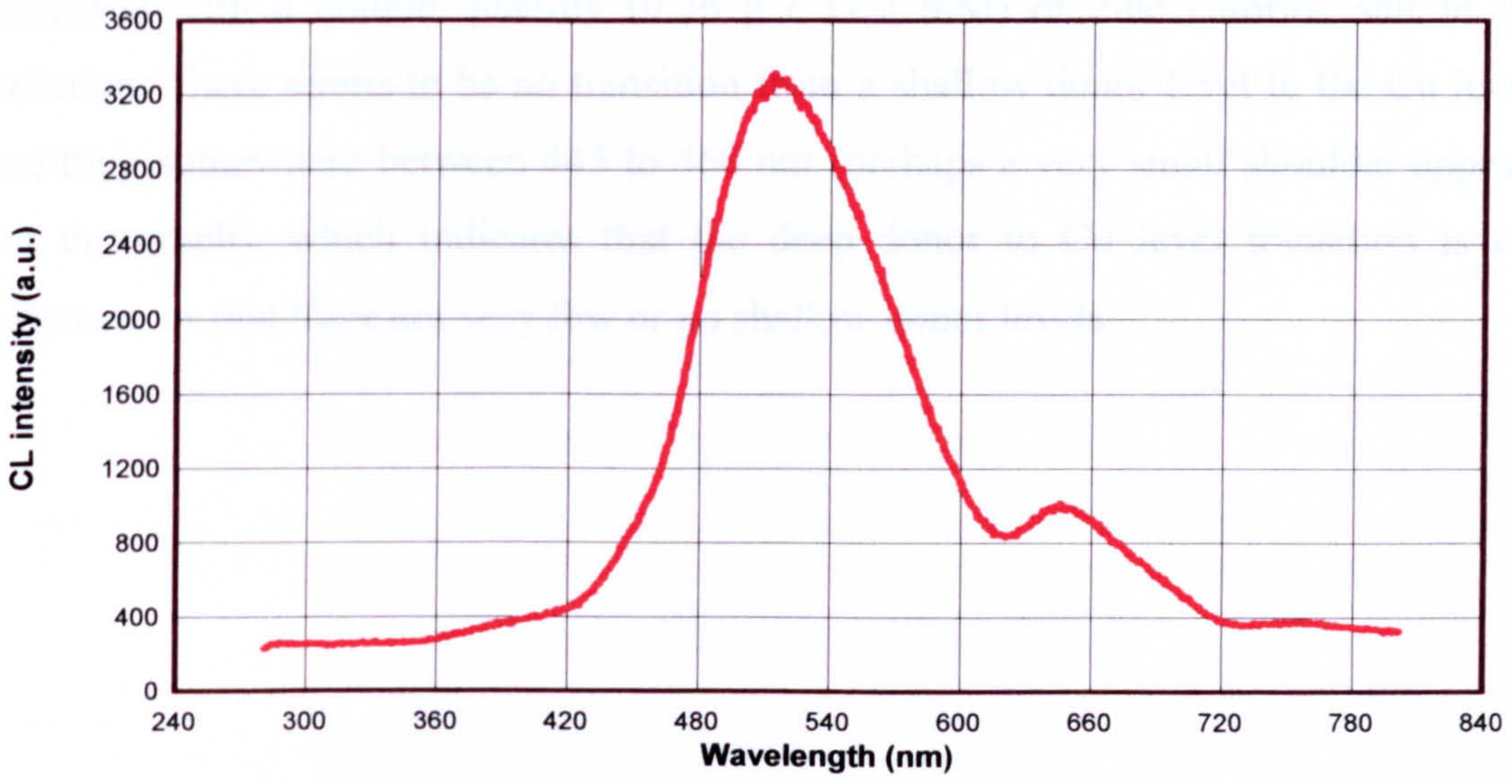

Figure 4.46 Cathodoluminescence spectra of an undoped zinc sulfide film, prepared from a bath with an excess of zinc chloride. The film was annealed at 700 °C.

The smaller peak at 645 nm in Figure 4.46 belongs to the silica substrate. It is observed in all recorded spectra of films deposited on silica slides. It differs slightly in position, between different batches of slides, ranging from 640 to 660 nm and in shape, between spectra recorded at different angles from the electron beam. In Figure 4.47, a CL spectrum of a clean silica slide stock-substrate is illustrated, featuring the characteristic 650 nm peak. The other weaker features are reflections from the electron gun filament and other ambient light entering the chamber that are often recorded in spectra of low signal and vary a lot with acquisition angle. A photoluminescence peak at 650 nm of sintered silica samples in oxygen atmosphere is reported by Ivanda et. al.,[67] also including a weaker 620 nm feature. The PL peaks are attributed to defects influenced by the oxygene atmosphere in the sintering process.

By adding copper chloride salt in the solution in very small amounts, the ZnS films were activated. By annealing the films, the familiar green emission of ZnS:Cu is obtained in the cathodoluminescence chamber. A boundary is found at 700 to 750 °C in the annealing temperatures, above which, the CL maximum of emission shifts from 540 nm to 525 nm. These are the maxima expected for transitions to a copper impurity, in a zincblende (535 nm) and a wurtzite (523 nm) crystal structure, with the difference arising from the distance between the atoms in the two lattices.[14, 68] Two representative curves are given in Figure 4.48 which have been obtained by films prepared with a double quantity (0.26 g / 11.2 mM) of zinc chloride salt in the solution. There seems to be no transition from a shallow donor level to the Cu level, emitting somewhere between 445 to 460 nm (perhaps a very small shoulder appears on the graph), which indicates that the deep donor to Cu level transition is too efficient, or that there are very few or no shallow donor levels.

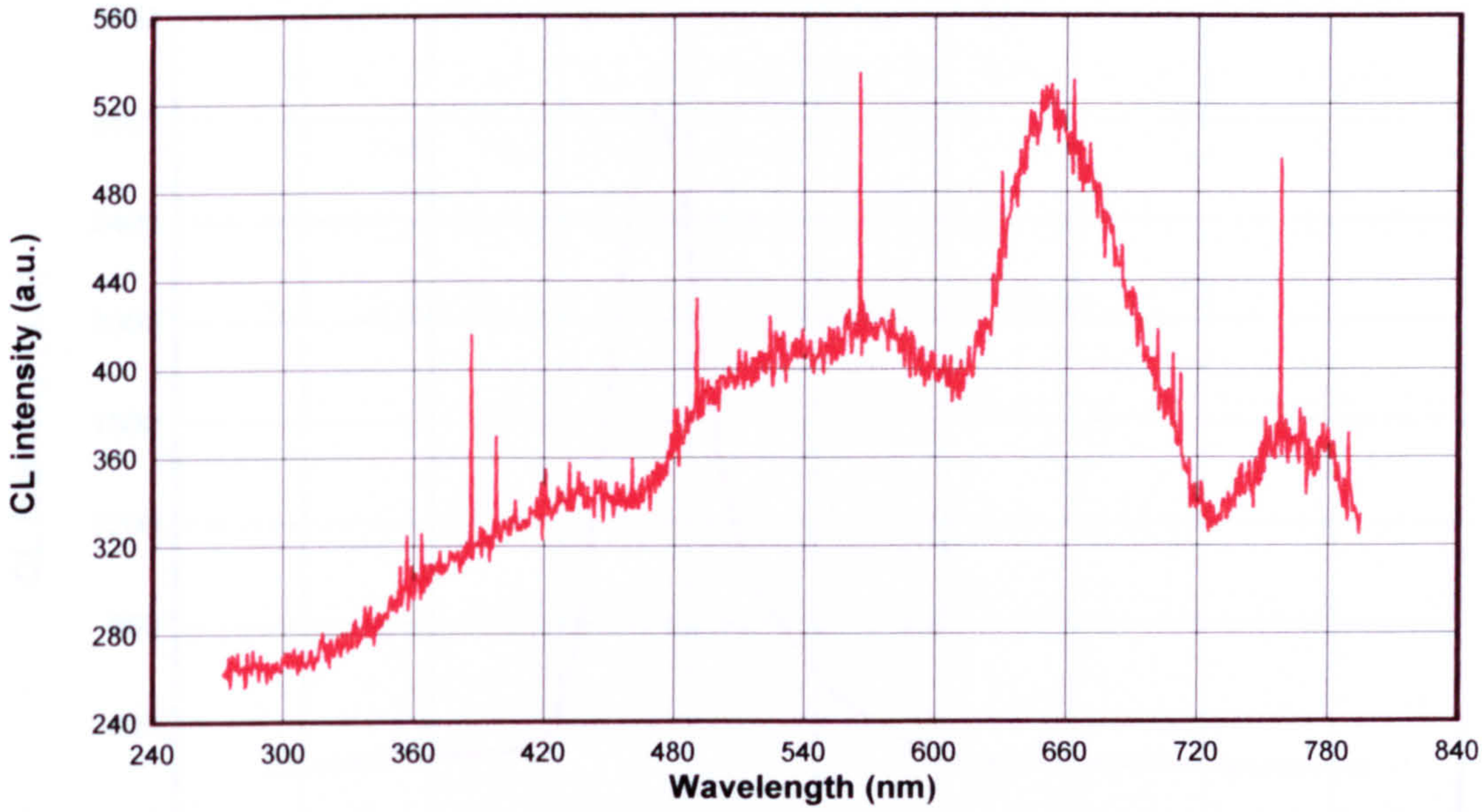

Figure 4.47 Cathodoluminescence spectrum recorded from a clean SiO_2 slide substrate.

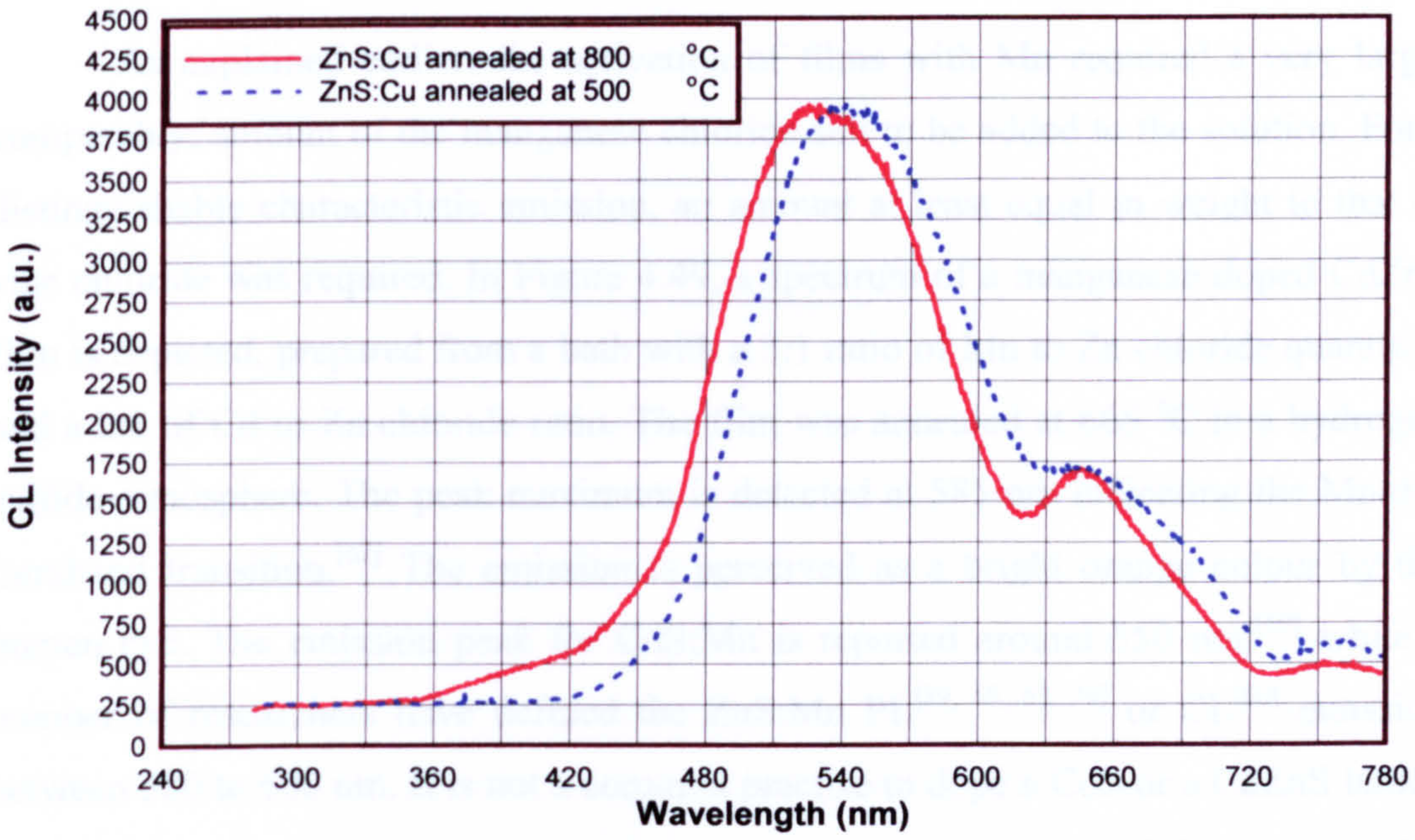

Figure 4.48 Cathodoluminescence spectra of ZnS:Cu films. Both films were prepared in baths with 0.26g (11.2 mM) $ZnCl_2$ and a very small quantity of $CuCl_2$. The films were annealed at different temperatures.

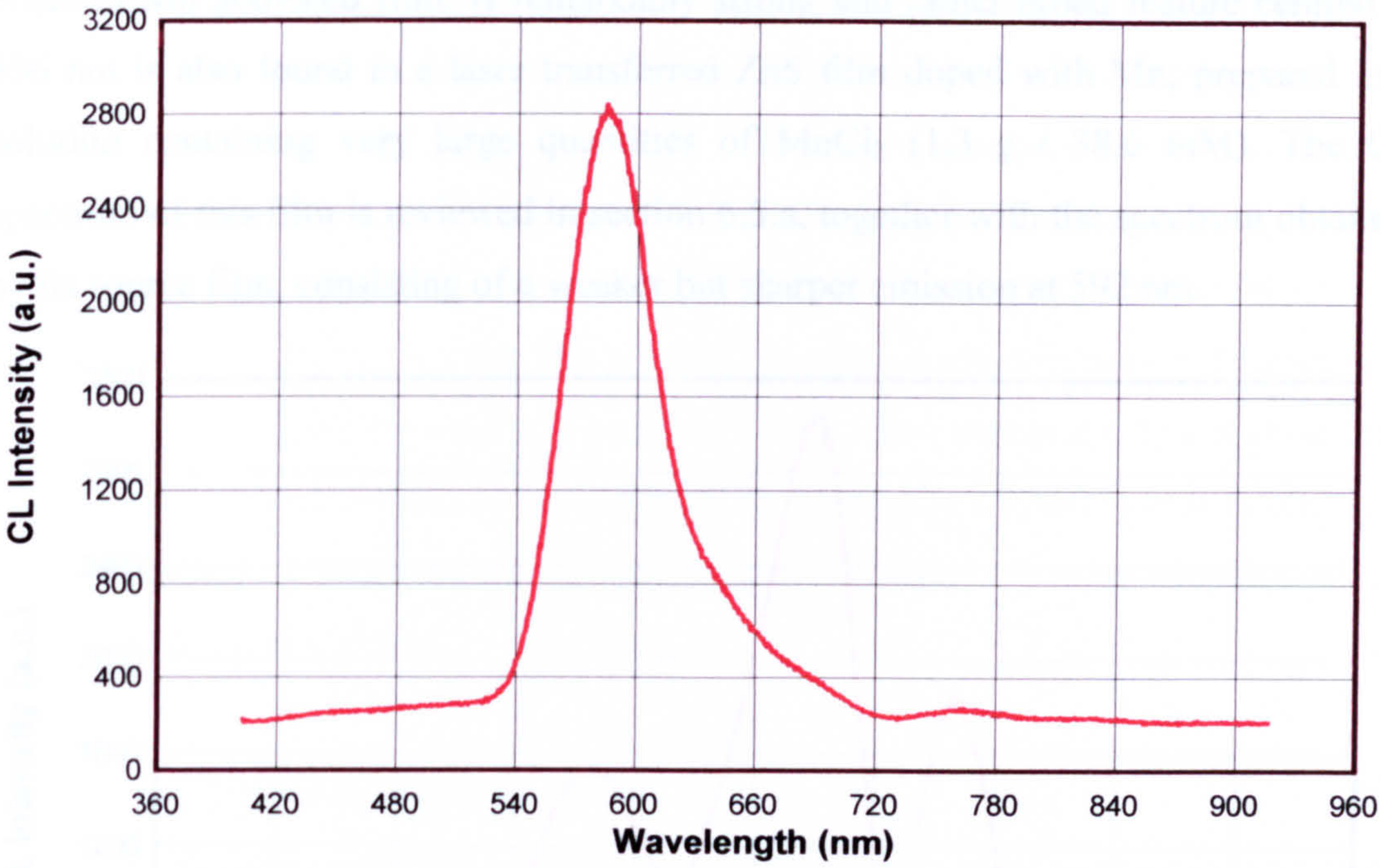

Figure 4.49 Cathodoluminescence spectrum of a CdZnS:Mn film, annealed at 665°C in a H_2S atmosphere.

As explained earlier, the activation of films with Mn required a very large, comparably, amount of the manganese chloride salt to be added to the solution. For a distinguishable characteristic emission, an amount at least equal in weight to that of zinc chloride was required. In Figure 4.49, a spectrum of a manganese doped CdZnS film is depicted, prepared from a bath with a 3:1 ratio of Mn to Zn chloride quantities and a 2:1 of Cd to Zn chloride ratio. The film was annealed at 665 °C in a hydrogen sulfide atmosphere. The peak maximum is detected at 585 nm indicating the Mn d-d intraband transition.[62] The emission is perceived as a bright orange colour by the human eye. The emission peak for CdS:Mn is reported around 550 nm,[69] while a number of researchers have defined the ZnS:Mn PL[39, 58, 63, 70] or CL[60] emission between 580 to 600 nm. It is not a common practise to dope a CdS or a CdZnS lattice with manganese, since the orange-red emission is also attained by the simpler ZnS:Mn system.

The films were prepared in an experiment attempting to achieve successful incorporation of Mn in a CdZnS lattice and to investigate the effects of annealing under a H_2S atmosphere. The large height difference between the 585 nm Mn peak and the 660 nm SiO_2 peak and the lack of any other peaks relating to a self activated lattice, indicate that the annealing process in an H_2S atmosphere has resulted in a very

efficient Mn activated film. A remarkably strong and rather broad feature centred at 596 nm is also found in a laser transferred ZnS film doped with Mn; prepared in a solution containing very large quantities of $MnCl_2$ (1.3 g / 38.6 mM). The CL spectrum of this film is reviewed in section 6.5.a, together with the spectrum obtained by its source film, consisting of a weaker but sharper emission at 592 nm.

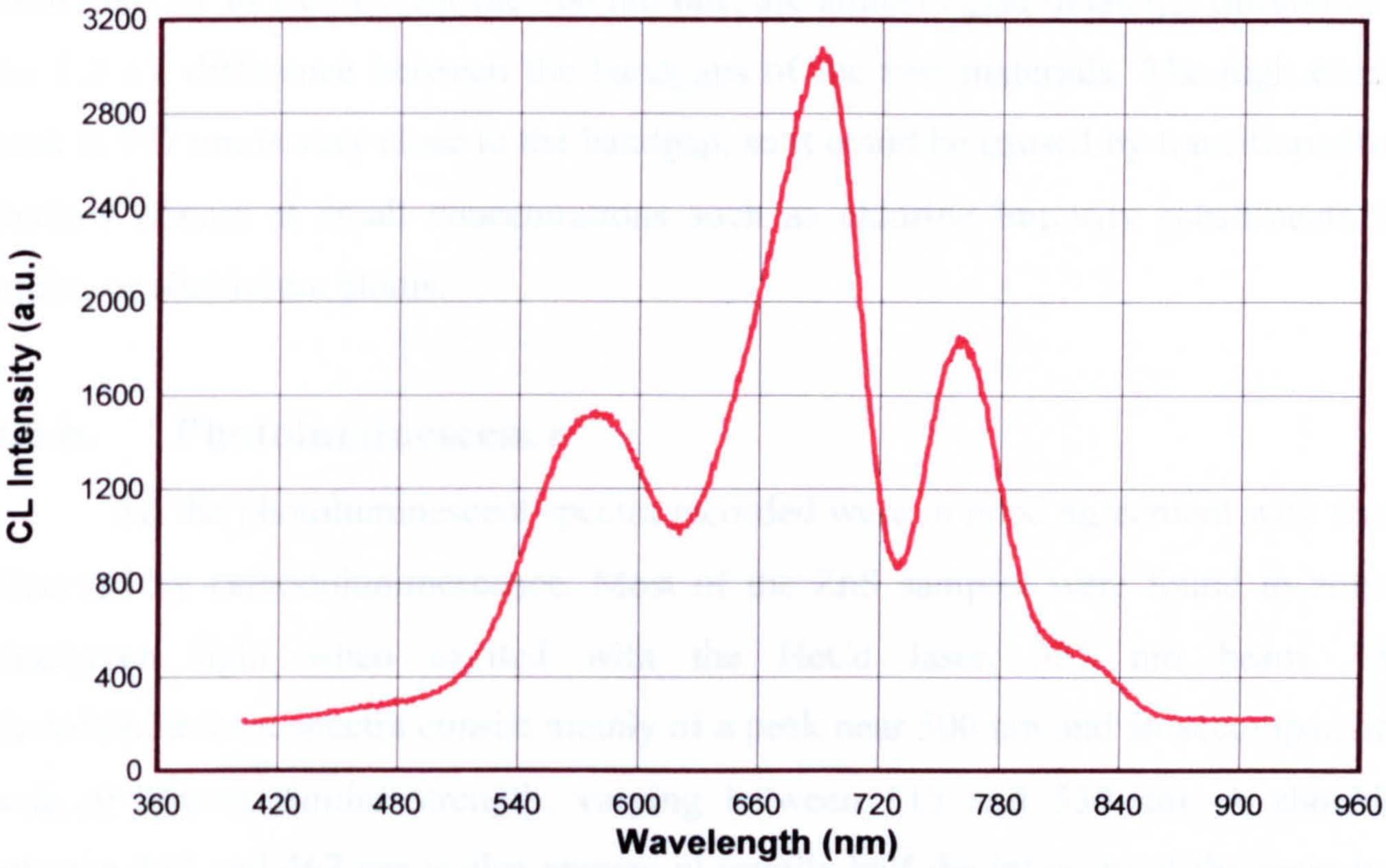

Figure 4.50 Cathodoluminescence spectrum of CdZnS:Ag. Prepared in a bath with a 2:1 cadmium to zinc chloride salt.

A CL spectrum of a silver doped CdZnS film is shown in Figure 4.50. The film was prepared with three 0.13g portions of chloride salts, two of cadmium (6.7 mM) and one of zinc (5.6 mM). There are three main peaks in the spectrum, at 577, 690 and 760 nm. According to Leverentz,[71] a 1:1 molar ratio between the two metal elements in the lattice and a 0.01% silver content would give a main emission peak around 577 nm, or a 2:1 in the favour of cadmium would be approaching the 690 range. A 2:1 weight ratio of the chloride reactants was used, but when considering the large difference in the solubility products and an indirect bandgap calculation of 2.44 eV, it becomes quite clear that the film is most likely to be composed of mainly CdS, regardless of the molarity ratio being close to 1:1. A similar diagram to that of Leverentz, given by Curie[68] predicts an emission peak that approaches 700 nm, at CdS participation in the compositions above 80%. The later scenario is more compatible with the measurements presented here. Moreover, if the assignment of

transitions to photoluminescent peaks in Figure 4.53 is considered and the change of bandwidth from 3.64 eV for ZnS to 2.44 eV recorded here for the mostly CdS film, then the two low energy peaks in Figure 4.50 can be assigned to transitions from sulfur vacancies to the valance band and from deep donor levels to silver acceptor impurities. The shifts from 2.98 eV to 1.79 eV, for the tallest peak at 690 nm and from 2.80 eV to 1.63 eV for the 760 nm one, are almost equal in energy difference to the 1.2 eV difference between the bandgaps of the two materials. The high energy peak at 577 nm is very close to the bandgap, so it could be caused by transitions from shallow donors at small concentrations such as chlorine impurity substituents for sulfur, or aluminium atoms.

4.6.b. Photoluminescence

All the photoluminescent spectra recorded were in good agreement with those observed by cathodoluminescence. Most of the ZnS samples were found to emit a blue/green light when excited with the HeCd laser, 325 nm beam. The photoluminescent spectra consist mainly of a peak near 500 nm and an accompanying peak of almost similar strength, varying between 515 and 530 nm. A shoulder between 442 and 467 nm is also present at usually half the intensity of the main two peaks. There is a huge volume of literature referring to a blue and green copper emission and several theories are put forward in terms of the corresponding transitions.[16, 68, 72-79] The scenario evolved in section 4.6.a, above, is also inherited here and is also expanded by adding the possibility of coexistent transitions from a sulfur vacancy to a copper level and from an aluminium or chlorine donor level to the copper acceptor. By simple subtraction of listed ionisation energies[80] for a number of impurities, from the bandgap, similar values are obtained for the transitions. The Al and Cl donor impurities are listed with an energy difference from the conduction band of 0.25 eV and the Cu acceptor at 0.95 eV above the valance band, which works out at approximately 460 nm for the conduction band (CB) to Cu transition and to 508 nm for the Al to Cu transition. Figure 4.51 illustrates a typical spectrum obtained from a ZnS:Cu film, with peaks at 500, 515 and 445 nm.

The spectrum recorded from a ZnS film prepared in a bath containing small amounts of manganese chloride is laid out in Figure 4.52 below. As it was mentioned earlier, it is unlikely that Mn impurities have been incorporated in the film, but it is

more possible that Cu contamination has taken place instead, from residues of previous experiments. The similarity to the CL spectrum obtained from the bulk ZnS sample could also suggest self activation, as described in Section 4.6.a. Still the small feature at 520 nm did not exist in the CL spectrum above.

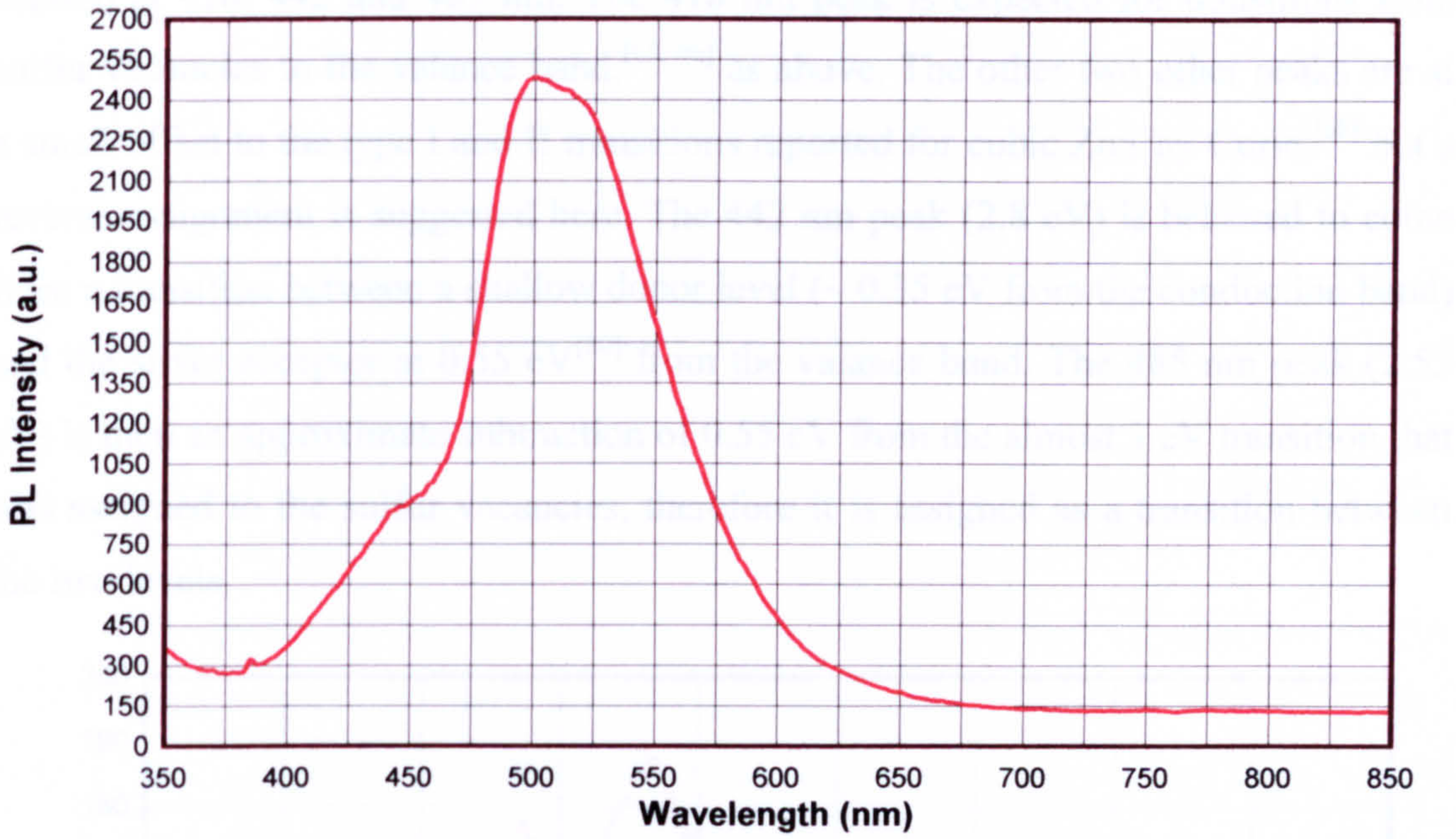

Figure 4.51 Photoluminescent spectrum of a ZnS:Cu sample prepared in a bath with an excess of zinc chloride (0.4 g / 17.3 mM).

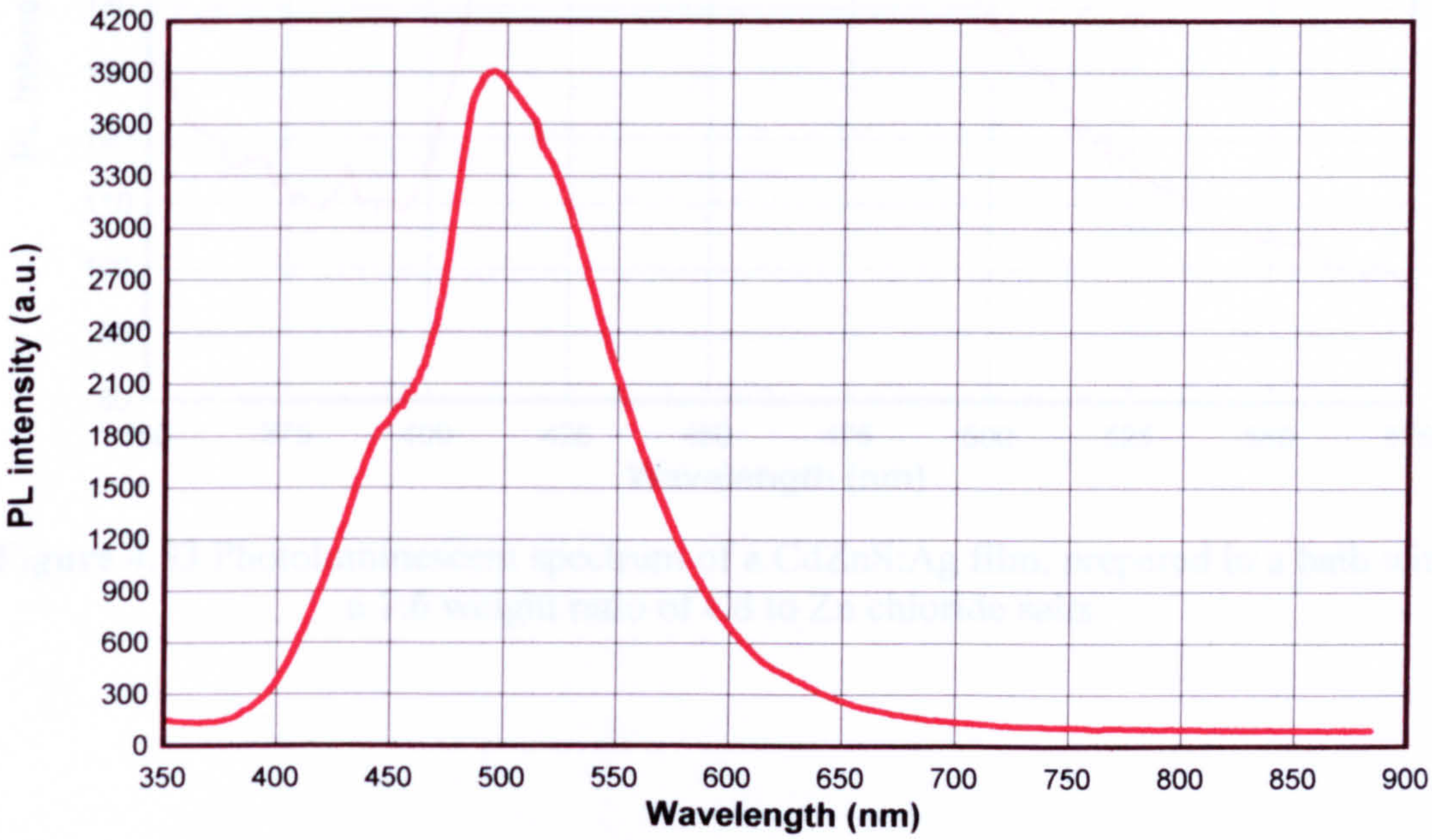

Figure 4.52 Photoluminescence spectrum of a ZnS:Mn film prepared with comparably small quantity of manganese salt (3:1 Zn to Mn weight ratio).

Finally, a weak photoluminescent emission containing three peaks was obtained from a CdZnS:Ag film (Figure 4.53). The film was prepared in a bath with an excess of zinc chloride, at 6 times the quantity of cadmium chloride. The short wavelength peaks suggest a nature closer to that of ZnS for the film. The peaks are centred at 418, 442 and 485 nm. The 418 nm peak is expected for transitions from sulfur vacancies to the valance band,[65, 66] as above. The other two other peaks are at a small offset to the type I and II transitions reported for cubic ZnS by Curie,[68] but a reverse assignment is suggested here. The 442 nm peak (2.8 eV) is believed to come from a transition between a shallow donor level (~ 0.35 eV from the conduction band) and the silver acceptor at 0.55 eV[80] from the valance band. The 485 nm peak (2.55 eV) is then an approximate subtraction of 0.55 eV from the almost 3 eV transition that was assigned to the sulfur vacancies, therefore it is assigned as a transition between the two levels.

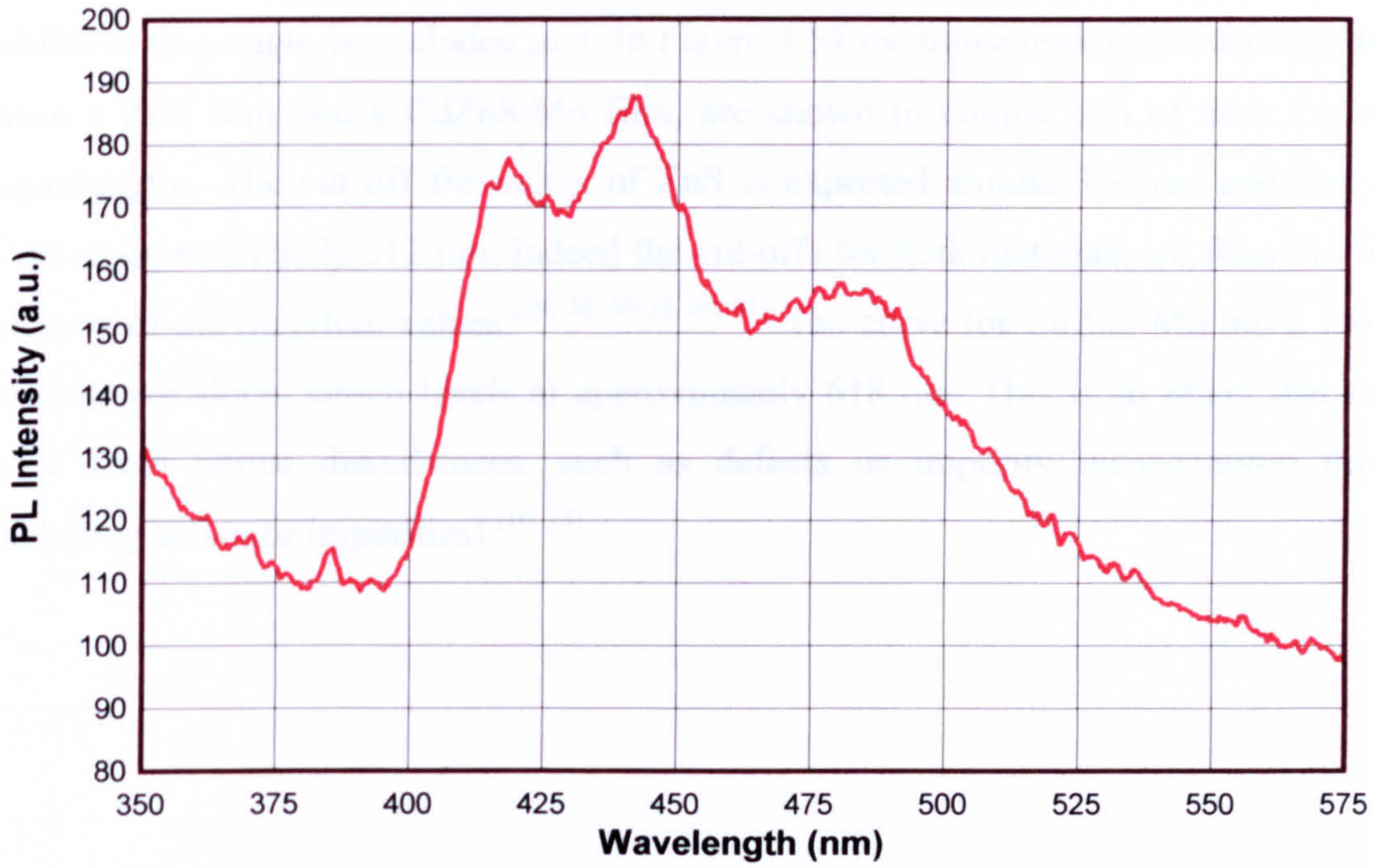

Figure 4.53 Photoluminescent spectrum of a CdZnS:Ag film, prepared in a bath with a 1:6 weight ratio of Cd to Zn chloride salts.

4.7 Analysis of Optical Properties (UV-Vis)

4.7.a. Transmission and Bandgap calculation

Transmission spectra were recorded of films deposited under conditions that produced the most stable and reproducible results. For the experimental procedure where the temperature was varied to accommodate for replenishment of solvent in large volumes, acidic solutions with pH 3.5 and 4.5 were investigated. The aim of those primary experimental procedures was to generate pure ZnS films only. Then films that were formed by the CT140 procedure, as explained in chapter 3, with or without the PID controller were also evaluated. The temperature and solution replenishment during those two types of experimental procedures were kept on the same ongoing rate. Additionally doping and generation of ternary compounds only took place at constant temperature procedures.

The spectra are characteristic of the semiconductor material and the various additives that might be included in it. In Figure 4.54 the transmission spectra recorded from a ZnS film and a CdZnS:Mn film, are shown in comparison of their cut off wavelengths. The cut off frequency of ZnS is expected around 350 nm and that of CdS at approximately 512 nm. Indeed the cut-offs for both materials are found in the vicinity of the literature values.[24, 26, 30-32, 69, 81] The curve for CdZnS:Mn has a more progressive slope, which levels at approximately 618 nm. This is an effect that can arise from lattice disturbances, such as defects or impurity incorporation (also including activator impurities).[16, 73]

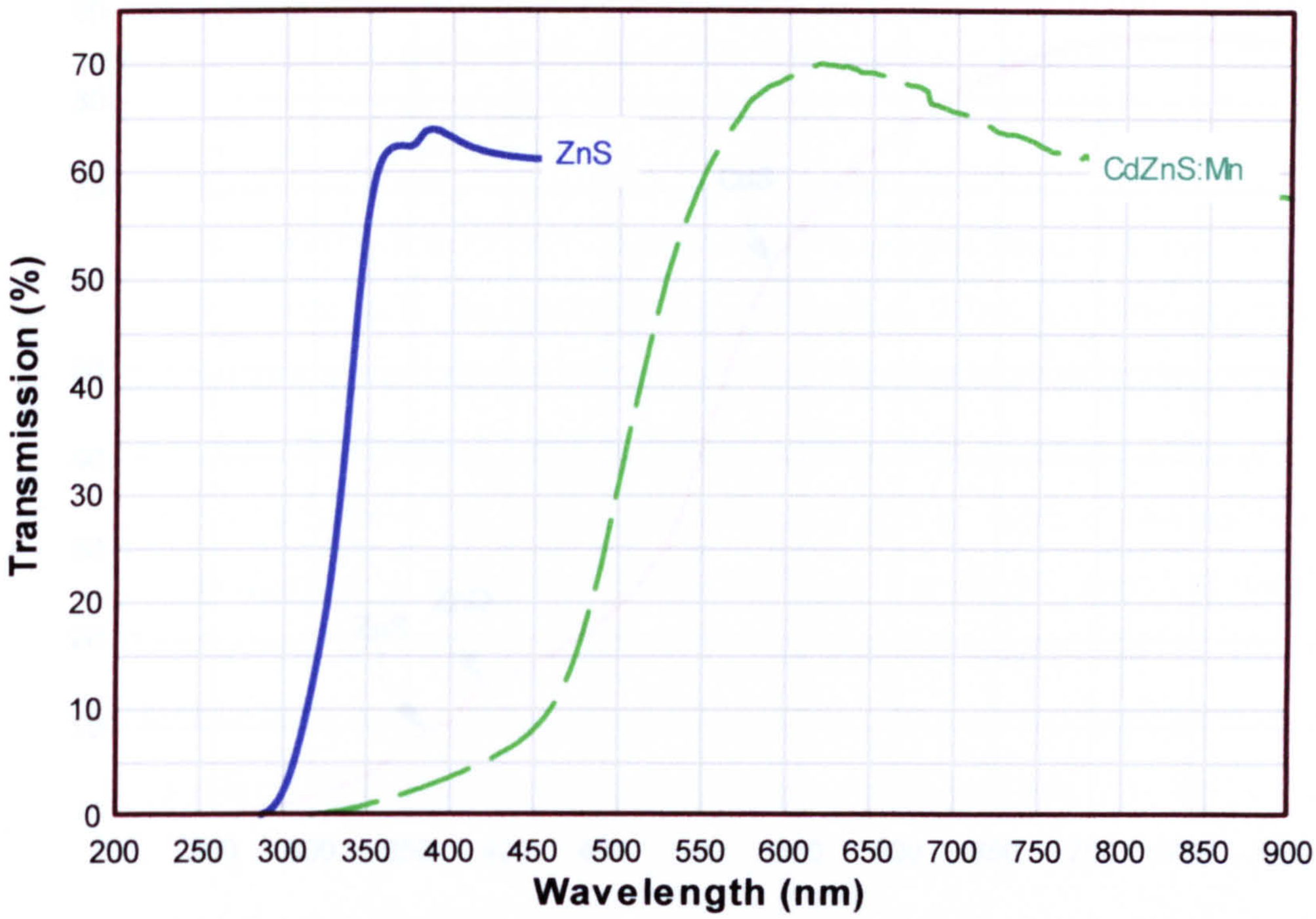

Figure 4.54 Transmission spectra of ZnS and CdZnS:Mn films.

An interesting spectrum of a CdZnS:Ag film, with double the amount of cadmium chloride reactant, against that of zinc chloride, is illustrated in Figure 4.55. The spectrum features a main, progressive, cut-off at 514 nm, corresponding to CdS and two smaller transitions at 354 and 388 nm attributed to ZnS and ZnO, [40, 82, 83] respectively. The CdS cut-off is characterised as progressive, due to the slowly changing slope of the spectrum after the 514 nm point, occurring for similar reasons as above.

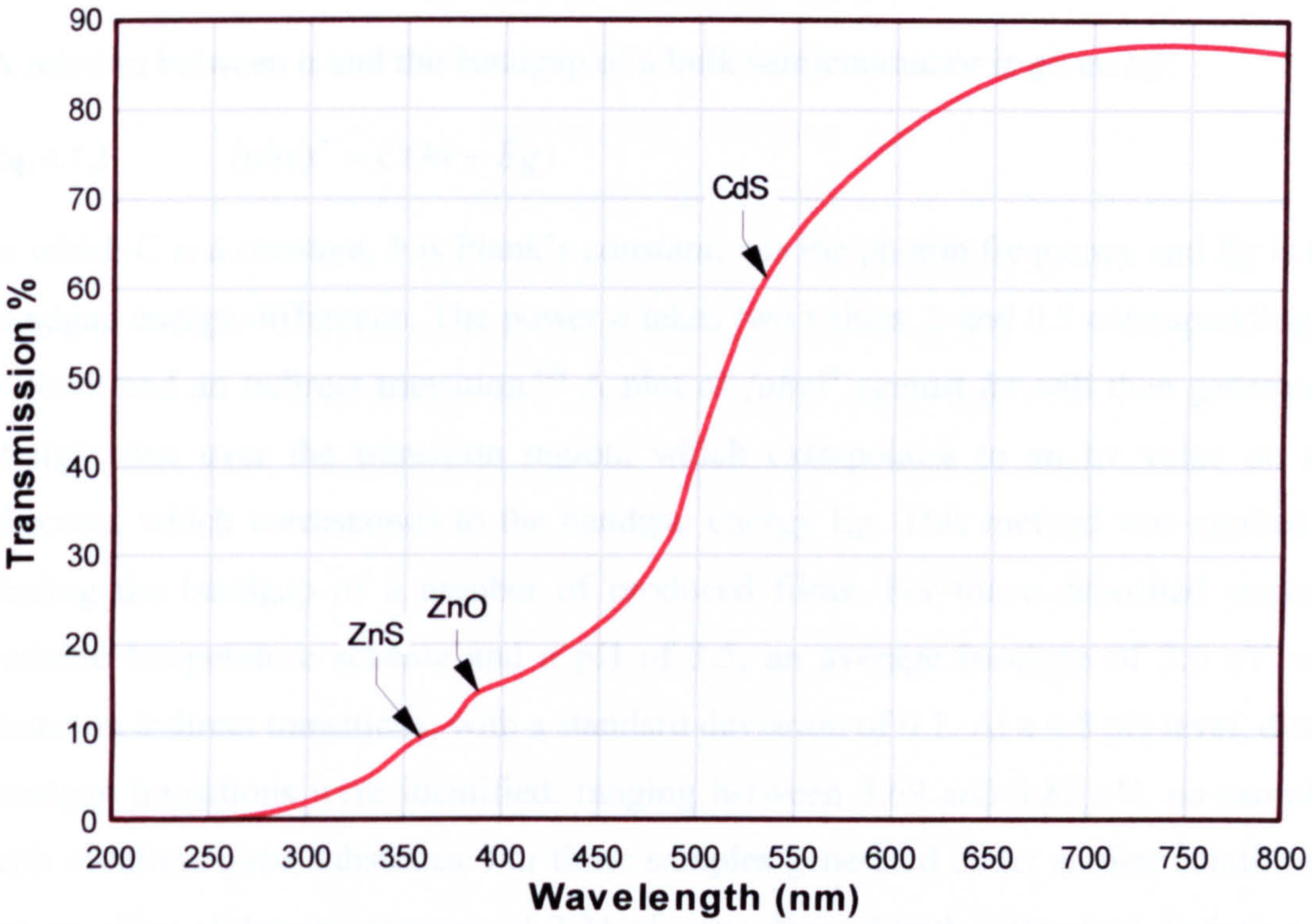

Figure 4.55 Transmission spectrum of CdZnS:Ag film made in a bath with a 2:1 ratio of cadmium to zinc chloride reactant. The cut-off absorptions for CdS, ZnO and ZnS are observable.

The transmission spectra can be exploited in deducing the optical absorption coefficient α and hence the semiconductor bandgap. It is assumed here that the reflectivity of the films induces an inflated absorption, as it was not possible to setup equipment in order to obtain a transmission and reflection spectrum of a sample simultaneously. Deduction of bandgap for similar materials from transmission spectra exclusively is not an uncommon practice.[83, 84] The derivation of the absorption coefficient from the absorption/transmission spectrum is based on the application of the Beer-Lambert equation on solids, where:

Eq. 4.7.1 $$I = I_0 e^{-\alpha t}$$

and

Eq. 4.7.2 $$T = \frac{I}{I_0}$$

I and I_0 are the transmitted and incident light intensity respectively, α is the absorption coefficient and t is the film thickness.

A relation between α and the bandgap of a bulk semiconductor is given by:

Eq. 4.7.3 $$(ahv)^n = C(hv - Eg)$$

in which C is a constant, h is Plank's constant, v is the photon frequency and Eg is the bandgap energy difference. The power n takes two values, 2 and 0.5 corresponding to a direct and an indirect transition.[2] A plot of $(ahv)^n$ against hv will then generate a straight line over the transition region, which extrapolates to an hv value on the abscissa, which corresponds to the bandgap energy Eg. This method was applied in finding the bandgap of a number of produced films. For those deposited under a variable temperature scheme and a pH of 3.5, an average bandgap of 3.6 eV was found on indirect transitions, with a standard deviation of 0.1. At a 4.5 pH level, direct bandgap transitions were identified, ranging between 3.69 and 3.82 eV, on samples with sodalime glass substrates. For those samples generated under similar conditions, but on silica slides and average of 3.31 eV was derived with a standard deviation of 0.05. This could be an indication of a tendency to grow ZnO films on silica substrates, under those conditions.

By following constant temperature (or heating) procedures, like CT140, or setting the PID controller at 92°C, ZnO formation was suppressed to normal levels, i.e. film nucleation on substrates surface. With a CT140 procedure and reactant concentrations elevated up to three times those of the typical amounts (Urea=4.5g / 0.44 M, TAA=2.25g / 0.18 M, ZnS=0.39g / 16.8 mM), the average bandgap was measured at 3.61 eV, with a standard deviation of 0.1. When extra zinc chloride was added disproportionally with the other reactants of the bath or the addition of $CuCl_2$ for the purposes of doping the film, a bandgap average of 3.65 eV and a standard deviation of 0.02 were determined. However, in the case of cadmium sulfide, the CdS transition is much more dominant. Indeed the bandgap values averaged at 2.44 eV, with a standard deviation of 0.06. This was the situation for all the samples investigated that contained CdS.

A remarkable transmission spectrum was recorded from a CdZnS:Ag sample, grown at a temperature of 92 °C, with no added acid and a 0.13 to 0.07 grams (3.3 to 1.8 mM) of $CdCl_2$ to $ZnCl_2$ reactant ratio. The sample was annealed at 730 °C, a procedure that converted the CdS transition from a moderately progressive slope, to an incredibly sharp step at 514 nm. The sample was examined many times on two

different spectrometers, to confirm the validity of the spectrum. This extremely sharp transition is most likely an indication of a highly ordered crystal lattice that has formed over the whole film through the annealing process. The curve extending below the step, over smaller wavelengths and the feature at 240 nm are characteristic of the silica substrates S5, used in this experiment, but it manifests at levels reaching almost 100 % of transmission. The sharp CdS absorption affects only 10% of the total incident light, because of the very small thickness of the initial film, found by the second reflectivity modelling method (see section 2.2) to be around 80 nm.

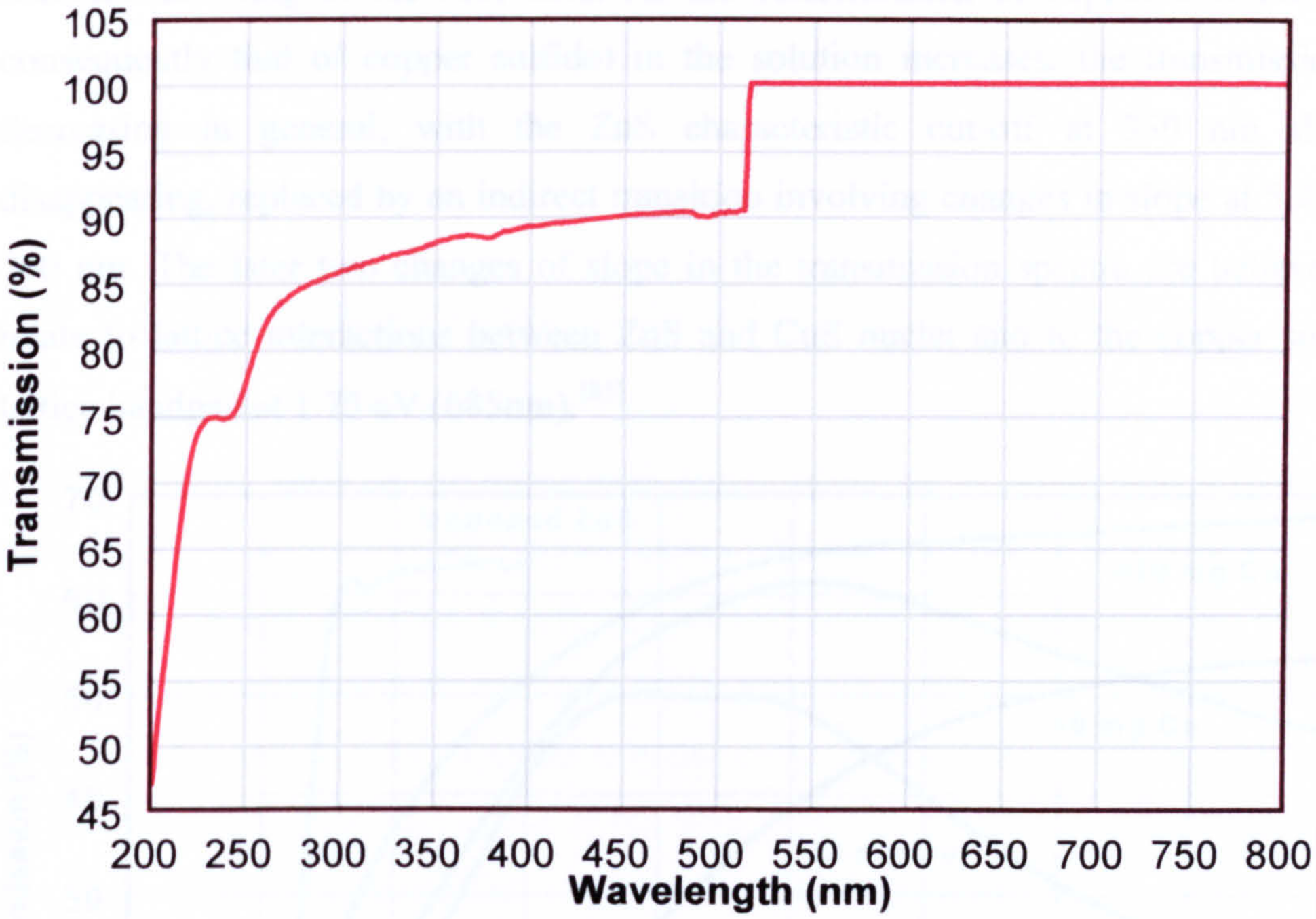

Figure 4.56 Annealed CdZnS:Ag film at 730 °C for 24 hours, presenting a step transition at 514 nm.

4.7.b. Material and doping observations

The effect of doping on the transmission of the films was investigated by performing a sequence of experiments under similar conditions and concentrations of reactants, apart from the amount of the activator salt. Such an investigation was performed for copper as an activator of ZnS films. The amount of copper chloride hydrate was varied from very small quantities, almost impossible to weigh, to 3 times the mass of zinc chloride. The number of water molecules surrounding the chlorides is different, but comparing the quantities in terms of weight is still a good means of regulating the solution.

In Figure 4.57 the transmission spectra of films generated from baths containing 390 mg, 23 mg, 10mg (13.5, 0.8, 0.3 mM, respectively) and less than 10 mg of copper II chloride hydrate are compared together with that of a ZnS film, with no added activator in the solution. For the smallest quantity of copper chloride used, a small number of thin crystallites of the hydrate were added to the solution, their weight did not come up to a measurable magnitude on the electronic weighing scale, where resolution was 10 mg. In terms of volume, or an approximate count of the similar in size crystallites, the quantity appeared to be around 5 to 10% of that included in 10mg of the substance. As the concentration of copper chloride (and consequently that of copper sulfide) in the solution increases, the transmission is decreasing in general, with the ZnS characteristic cut-off at 350 nm slowly disappearing, replaced by an indirect transition involving changes in slope at 560 and 700 nm. The later two changes of slope in the transmission spectra are believed to relate to lattice interactions between ZnS and CuS nuclei and to the copper sulfide lattice bandgap at 1.75 eV (685nm).[85]

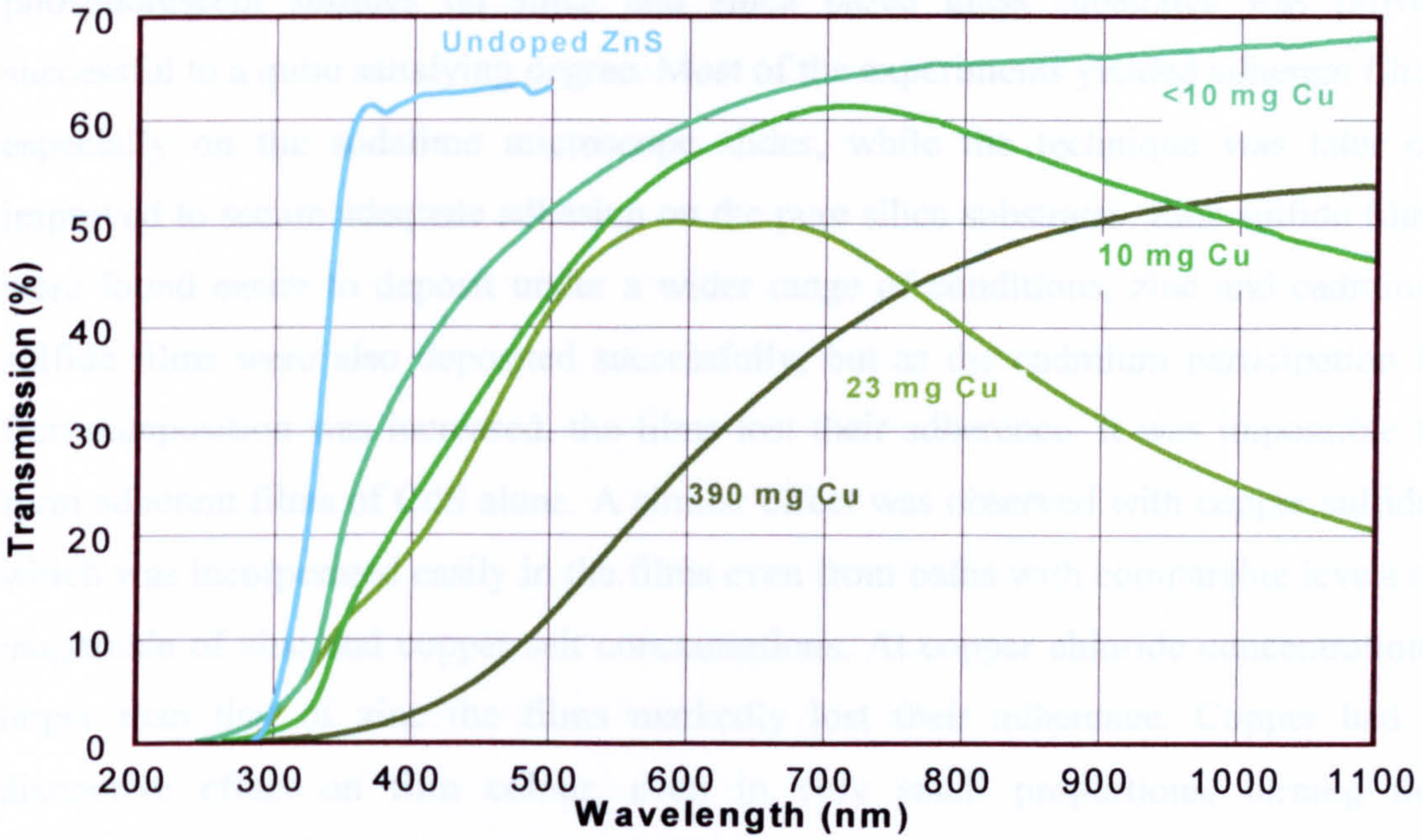

Figure 4.57 Effect of dissolved activator salt quantity in the transmission spectra of deposited films.

Due to the very small solubility of copper sulfide ($K_{sp} = 5x10^{-36}$), independent nuclei are expected to form in the solution long before any productive precipitation of ZnS. At small concentrations, it is expected to act as the most important nucleation agent of the ZnS clusters that will form the film. Therefore a large interface between

ZnS and CuS is expected to be present, as the large number of CuS nuclei will be dispersed in the resulting precipitate. At larger concentrations, like those generated by an introduction of 23 or 39 mg of the chloride salt, a large portion of the films would constitute of CuS. To a great extend, Cu is considered to have the same oxidation state to zinc, in the produced sulfide lattices, thus accommodating the possibility of counter-substitution of the two elements in the expanding nuclei. For the purposes of photoluminescence and electroluminescence, only quantities far below 1mg of copper chloride are considered acceptable, as the target concentration of copper as a metal activator substituent is 0.1 to 1 %. [16, 72, 86, 87] Moreover, it should be noted that copper I is the acceptable species in doping of ZnS lattices, since it is expected to provide an electron acceptor energy level.[68]

4.8 Conclusion on the Chemical Bath Deposition

The chemical bath method chosen as a route for depositing thin films of phosphorescent sulfides on silica and silica based glass substrates was proven successful to a quite satisfying degree. Most of the experiments yielded adherent films especially on the sodalime microscope slides, while the technique was later on improved to secure adequate adhesion on the pure silica substrates. Zinc sulfide films were found easier to deposit under a wider range of conditions, zinc and cadmium sulfide films were also deposited successfully, but as the cadmium participation in film composition was increased, the films lost their adherence. It was impossible to form adherent films of CdS alone. A similar effect was observed with copper sulfide, which was incorporated easily in the films even from baths with comparable levels of magnitude of zinc and copper salt concentrations. At copper chloride concentrations larger than that of zinc the films markedly lost their adherence. Copper had a distinctive effect on film colour, even in very small proportions, turning the clear/white ZnS films into green and dark green. Cobalt had similar effects, while cadmium introduced a yellow to deep orange tone. Nickel had much smaller effects, only achieving a grey tint at high concentrations. Silver was only ever used at very small concentrations, aiming in doping and manganese had almost no effect on film colour.

Based on adherence, film clarity and thickness, the best conditions for film growth were defined. The temperature was controlled by a PID controller. The best setting was at a target temperature of 92 °C and a voltage feed of 180 V. Otherwise the voltage setting was kept stable at 140 Volts which reached the same temperature approximately 10 minutes later than the PID controlled system and stabilised there, but showed a dependence on environmental temperature. Replenishing the water volume lost by evaporation should be done at a constant drop-rate, at 1 drop every 2 to 3 seconds. The solution pH was between 6 and 6.5, because of the chloride salts and no extra hydrochloric acid was needed, though a small reduction of pH to 5 does not bring about any significant changes in the quality of the resulting films, apart from possibly restricting the formation of a thick zinc oxide layer.[2, 4, 88]

Under these conditions, glass samples are covered by a film on both sides, but the greatest continuity in coverage and adherence is achieved on the side facing away from the heater, called the "outer side" of the sample. The samples can be held against the heater with or without space separators. The thickness of the films is between 100 and 150 nm. Standing the glass against a surface with vertical grooves as described in chapter 3, or using the 0.25 mm glass separators results in slightly thicker films around 200 nm, but provides a more stable environment for film growth under a larger variety of conditions, for example lower acidity and hotter or cooler solution (Figure 4.58). The film roughness increases around the separator contact area, or wherever the substrate touches the metallic heater surface. Small spacing between the heater and the substrate does not allow for cluster penetration and adhesion but permits ion-by-ion precipitation between the walls, of partial coverage. Larger spacing as in the case of the 1mm spacer configuration, allows for faster growth of films, but also introduces more intense roughness features, as the large number of clusters available inside the gap, is depositing in a rather disordered manner. Bubble formation between the glass and heater surfaces could be a major contributor of observed disorder at such distances, while bringing the surfaces closer to each other seems to suppress the bubble generation phenomenon.

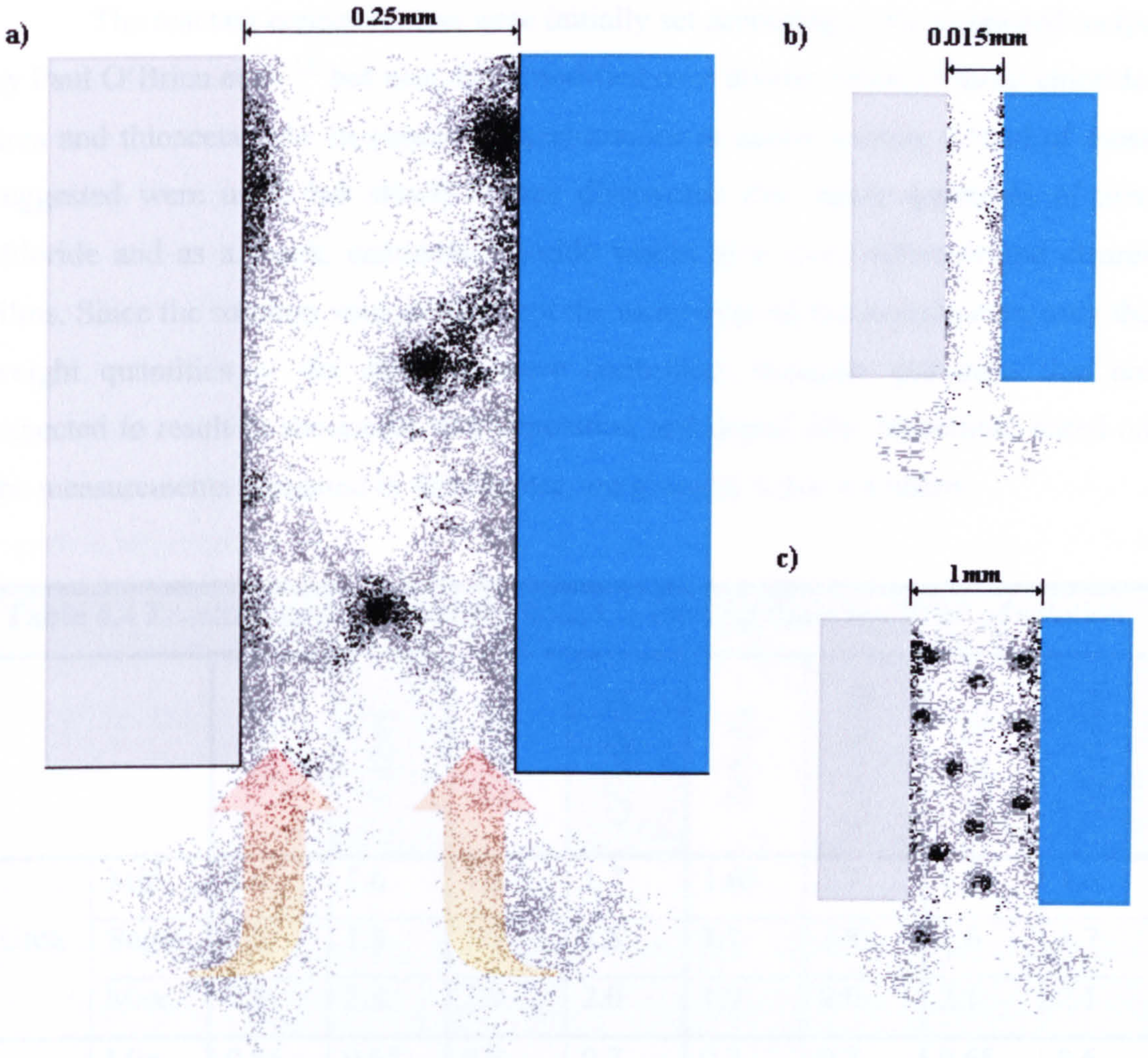

Figure 4.58 Schematic of deposition scenarios at different heater-substrate distances. At 0.25mm (a), the material, including clusters, is flowing through the gap due to convection and slowly adheres in a controllable manner. At 0.015mm (b), only ions manage to penetrate and at 1mm (c), clusters are also forming between the two surfaces and deposit irregularly.

As the chemical deposition technique was evolved and was optimised around the formation of zinc sulfide films a wider range of conditions were wielded to achieve that. It was possible to deposit zinc sulfide films in a temperature range of 72 to 98 °C and at a pH varying from 2.5 to 6.5. The time duration for which the substrates are submerged in the bath can range from approximately 50 minutes, to 100 minutes, for a constant temperature setting of 92 °C. Achieving deposition of a visible film could require an even smaller duration than 45 minutes, as long as the system's temperature could be raised faster, or by introduction of species that yield a metal sulfide of smaller K_{sp}, as in the case of doping for example. The quality of the films is expected to reduce or differ when deviating from the suggested conditions.

The reactant concentrations were initially set according to the suggested recipe by Paul O'Brien et.al. [5] but were later modified over diverse ratios of metal chloride, urea and thioacetamide. In general, concentrations at approximately a third of those suggested were used, but slowly it was discovered that larger quantities of zinc chloride and as a result, cadmium chloride would give more adherent and clearer films. Since the solution volume was kept the same over all the experiments, only the weight quantities of the reactants were controlled. Reactant quantities that are expected to result in successful film deposition and doped film deposition, based on the measurements presented in this chapter, are given in Table 4.4 below.

Table 4.4 Reactant quantities that succeeded in forming films in 170 ml of solution.

		ZnS	CdZnS	ZnS:Cu	CdZnS:Cu	ZnS:Ag	CdZnS:Ag	ZnS:Mn	CdZnS:Mn
Urea	Min.	1.4	1.6	1.5	1.7	1.65	1.7	1.5	1.6
	Sugst.	1.6	1.8	1.7	1.8	1.7	1.8	1.6	1.7
	Max.	2.3	2.3	1.9	2.0	1.9	2.0	2.1	2.1
TAA	Min.	0.55	0.65	0.7	0.7	0.7	0.7	0.65	0.6
	Sugst.	0.75	0.7	0.75	0.75	0.75	0.7	0.8	0.75
	Max.	0.8	0.85	0.8	0.85	0.8	0.85	0.85	0.85
$ZnCl_2$	Min.	0.11	0.06	0.17	0.07	0.18	0.07	0.13	0.06
	Sugst.	0.25	0.1	0.28	0.12	0.28	0.12	0.22	0.08
	Max.	0.66	0.32	0.66	0.3	0.33	0.3	0.3	0.2
$MnCl_2$	Min.	-	-	x	x	x	x	0.1	0.13
$AgCl_2$	Sugst.	-	-	0.001	0.001	0.001	0.001	0.7	0.8
$CuCl_2$	Max.	-	-	0.005	0.005	0.005	0.005	1.8	2.0
$CdCl_2$	Min.	-	0.05	-	0.1	-	0.1	-	0.08
	Sugst.	-	0.18	-	0.25	-	0.25	-	0.3
	Max.	-	0.67	-	0.7	-	0.7	-	0.6

Notes: All quantities are given in grams. The metal chlorides are in their hydrate forms as described in Chapter 3. Letter x denotes that no further investigation was performed towards that route. See Appendix 1 for quantities in Molarity.

To summarise the discussions concerning growth and structure of the films, an encompassing scenario is recited here. In sections 4.2.a, 4.3.a and 4.3.b it was argued that there is always an initial thin layer based on zinc, which adheres to the glass substrates. That is basically derived from the fact that the precipitates formed in the solution do not adhere to the substrates without the addition of any zinc chloride salt. It is quite possible that this highly adherent precursor film is zinc oxide instead of a sulfide, a condition that could be promoted by the oxygen atoms on the surface of the silicon oxide substrate. On top of this precursor layer, deposition of a ZnS or CdZnS layer is supported through two different routes (the two layers of different thickness in Figure 4.14 could be explained in this way). The inhomogeneous route gives a slow successive build of the film by atoms as ions, molecules, or embryo clusters composed of a few molecules, that are more stable against the system's entropy, when adhered on the substrate of film. Homogeneously grown clusters of spherical nature could also adhere on the developing film (Figures 4.7, 4.8, 4.9 and 4.17), either because of the compatibility of the two materials, or again an increased stability of the system. A constant feed of solution is necessary over the substrates surface, in order to achieve continuous coverage of this type. Such a constant feed was accomplished by making use of thermal convection, induced by the hot surface of the heater/substrate and the cooler surface of the container. The spheres continue to grow further, after being incorporated on the film, as long as there are more reactants left in the solution. Therefore, they can eventually mould in with the rest, thus loosing their well defined spherical shapes.

When cadmium chloride is included in the solution for obtaining CdZnS films, it is expected that the homogeneously grown clusters progress through two stages. Because of its small solubility product, CdS is expected to form first in the solution and then ZnS continues to precipitate over the initial CdS spheres. This can be observed in the colour changes of the solution, where a dark orange colour predominates, approximately 10 to 15 minutes before the white and opaque appearance of the solution takes over. As soon as the spheres acquire a ZnS sheltering nucleation site, they can begin to adhere to the ZnO/ZnS double layer that may have deposited on the substrates. If no zinc is added, the solution progresses only towards an ever darkening orange tint and no adherence is achieved. The incorporation of CdS in the zinc containing films is detected by EDX (Figure 4.3) and it affects the transmission spectra due to its lower bandgap (Figures 4.54, 4.55 and 4.56).

A similar scenario is also suggested for solutions containing copper chloride and silver chloride. Even though the concentrations of the two salts are very small, intended only for doping of the films with the two metal elements, the even greater difference of K_{sp} is believed to force the formation of CuS or AgS nuclei. These will then act as seeds for the much larger CdS or ZnS clusters. The early formation of those small nuclei is again observed in the solution as a colour change in the solution, especially in the case of copper, where a green tint is given to the solution, almost immediately after the introduction of copper chloride, provided that thioacetamide has already been dissolved in the prepared bath mixture. The scenario of separate phases existing between ZnS and CuS is also supported by the EXAFS measurements in Section 4.5.c. Mixing of all metals in the ZnS or CdS lattice is not excluded in any of the cases, as successful doping was accomplished with all three metals, Cu, Ag and Mn (EDXA Figure 4.4, ICPMS Figure 4.5 and 4.6, CL Figure 4.48 and 4.50 and PL Figure 4.51 and 4.53). For the case of manganese though, an initial formation of cluster nuclei is not expected, as the solubility of manganese sulfide in water is quite large compared with any other of the sulfides involved in these experiments. Therefore, manganese ions are expected to stay dissolved to the largest extent and only a few would eventually get trapped in the precipitates (For CL and PL of doped film see: Figure 4.49 and 4.52). Moreover, the progress of the Mn containing experiment is exactly the same as that of ZnS or CdZnS, with no extra changes in colour or clarity. A schematic of the film's structures as they would evolve within the different described scenarios of each material system is displayed in Figure 4.59 below. Finally, the cathodoluminescence and photoluminescence investigation of these activated films did yield emissions within the characteristic bands, for each activator element. The performance of the films as active layers in electroluminescent devices was never established though. Moreover, any electroluminescence activity is primarily expected from the Mn doped films, rather than any other films, since in very strong electric fields, the metastable states induced by chlorine or aluminium, or even the self activation sites, are not expected to be able to sustain exciton pairs long enough for successful radiative recombinations to occur, as discussed in Sections 1.1.b and 1.2.b.[62]

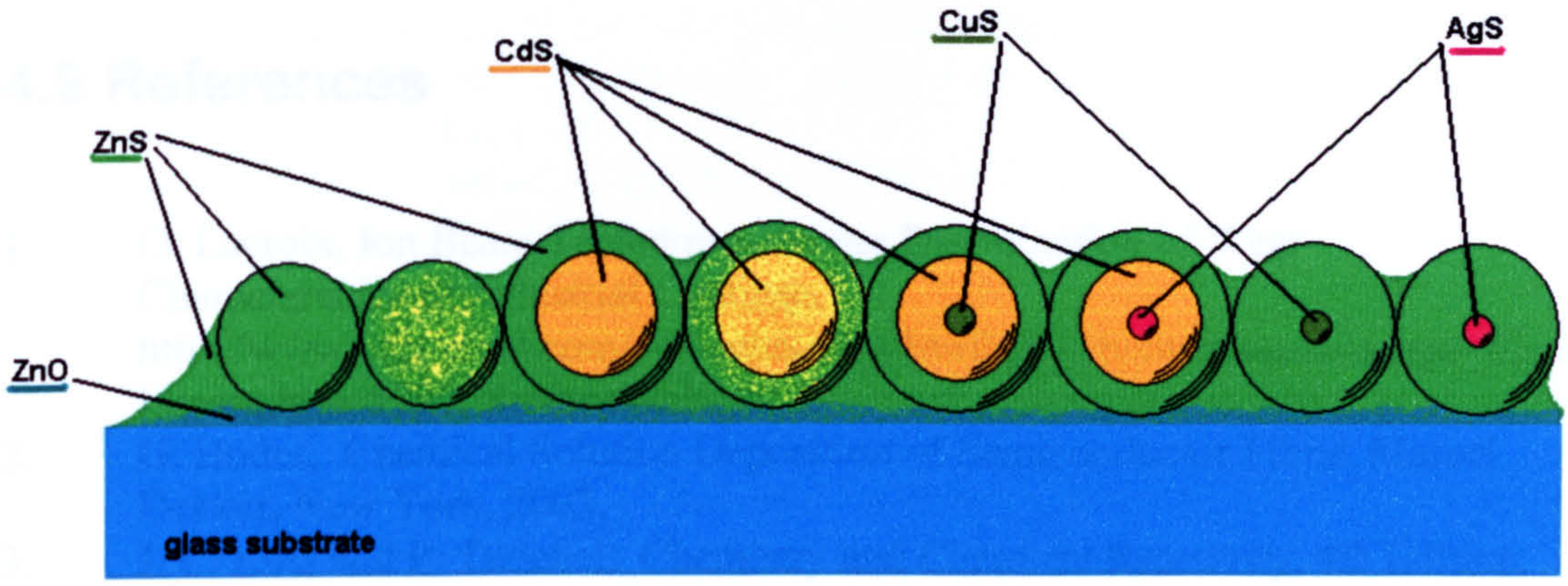

Figure 4.59 Schematic, summarising the film deposition scenarios for all attempted material systems. Each scenario is demonstrated at different lengths.

4.9 References

1. O. Lacroix, Ion Beam Techniques for the Dtermination of Wear Characteristics of Industrial Coatings, http://www.btinternet.com/~catechnology/surfaceweb/swebjournalspage_files/lacroix.htm, 1997, SurfaceWeb.
2. G. Hodes, Chemical Solution Deposition of Semiconductor Films, Marcel Dekker, New York, 2003.
3. J. C. Kotz and P. Treichel, Chemistry and Chemical Reactivity, 4th Edition, Saunders Colledge Publishing, 1999.
4. P. O'Brien and J. McAleese, Developing an Understanding of the Processes Controlling the Chemical Bath Deposition of ZnS and CdS, J. Mater. Chem., 1998, **8**, p 2309.
5. P. O'Brien, D. J. Otway and D. S. Boyle, The importance of Ternary Complexes in Defining Basic Conditions for the Deposition of ZnS by Aqueous Chemical Bath Deposition, Thin Solid Films, 2000, **361-362**, p 17.
6. T. Ren, Z. Lei, G. Luan, G. Jia, J. Zhang, R. Yu and C. Li, Fabrication of CdS-ZnS Layered Thin Films by Hydrothermal Seeded Growth Method, Thin Solid Films, 2006, p 99.
7. H. H. Willard, L. L. Merritt, J. A. Dean and F. A. Settle, X-Ray Methods, in Instrumental Methods of Analysis, 1988, Wadsworth Publishing Company, p. 370.
8. S. J. Hill, Sheffield Analytical Chemistry: Inductively Coupled Plasma Spectrometry and its Applications, Sheffield Academic Press, Sheffield, 1999.
9. A. Montaser, Inductively Coupled Plasma Mass Spectrometry, John Wiley, New York, 1998.
10. H. H. Willard, L. L. Merritt, J. A. Dean and F. A. Settle, Atomic Emission Spectroscopy with Plasma and Electrical Discharge Sources, in Instrumental Methods of Analysis, 1988, Wadsworth Publishing Company, p. 197.
11. H. Xi, X. Qian, J. Yin, L. Bian, R. He and Z. Zhu, Photoluminescence of ZnS-PVK Nanocomposites Confined in Ethylenediamine Modified MCM-41 Mater. Lett., 2003, **57**, p 2657.
12. T. Y. Zhou, X. Yuana, J.-M. Hongc and X.-Q. Xina, Room-Temperature Solid-State Reaction to Nanowires of Zinc Sulfide, Mater. Lett., 2006, **60**, p 168.
13. M. Aven and J. S. Prener, Physics and Chemistry of II-VI Compounds, North-Holland Publishing CO., Amsterdam, 1967.
14. M. Farnsworth, Zinc Chemicals, Zinc Development Association, London, 1973.
15. R. S. Becker, Theory and Interpretation of Fluorescence and Phosphorescence, Wiley Interscience, 1969.
16. W. V. Gool, Fluorescence Centres in ZnS, Philips Research Reports Supplements, University of Amsterdam, Amsterdam, 1961.
17. A. N. Krasnov, J. P. Bender and W. Y. Kima, Increased Luminance of ZnS/Mn Thin-Film Electroluminescent Displays due to Ag Co-Doping, Thin Solid Films, 2004, **467**, p 247.

18. H. Yang, C. Huang, X. Su and A. Tang, Microwave-Assisted Synthesis and Luminescent Properties of Pure and Doped ZnS Nanoparticles, J. Alloys Compd., 2005, **402**, p 274.
19. J. Benoit, P. Benalloul, A. Geoffroy, N. Balbo, C. Barthou, J. P. Denis and B. Blanzat, Study of Highly Concentrated ZnS : Mn ACTFEL Devices, Phys. Status Solidi A, 1984, **83**, p 709.
20. J. Benoit, P. Benaloul, C. Barthou, S. Casette and J. C. Soret, De-Excitation Processes and Efficiency in ALE ZnS : Mn Thin Film Electrolumninescent Devices, Phys. Status Solidi A, 1990, **122**, p 427.
21. H. Xian, P. Benalloul, C. Barthou and J. Benoit, Quantitative Analyses and Crystallographic Studies of ZnS:Mn Thin Films Prepared by R.F. Magnetron Reactive Sputtering, Thin Solid Films, 1994, **248**, p 193.
22. Goldberg and J. W. Nickerson, D.C. Electroluminescence in Thin Films of ZnS : P, J. Appl. Phys., 1963, **34**, p 1601.
23. S. Zhang, H. Kinto, T. Yatabe and S. Iida, Nitrogen and Phosphorus Doping in ZnS Layers Grown by Vapor Phase Epitaxy on GaAs Substrates, J. Cryst. Growth, 1990, **96**, p 382.
24. J. M. Doña and J. Herrero, Process and Film Characterisation of Chemical-Bath-Deposition ZnS Thin Films, J. Electrochem. Soc., 1994, **141**, p 205.
25. M. Kostoglou, N. Andritsos and A. J. Karabelas, Incipient CdS Thin Film Formation, J. Colloid Interface Sci., 2003, **263**, p 177.
26. X. Liu, J. Cui, L. Zhang, W. Yu, F. Guo and Y. Qian, A Solvothermal Route to Semiconductor ZnS Micrometer Hollow Spheres with Strong Photoluminescence Properties, Mater. Lett., 2006, **60**, p 2465.
27. L. Wang, L. Chen, T. Luo and Y. Qian, A Hydrothermal Method to Prepare the Spherical ZnS and Flower-Like CdS Microcrystallites, Mater. Lett., 2006, p 3627.
28. H. Deng, C. Chen, Q. Peng and Y. Li, Formation of Transition-Metal Sulfide Microspheres or Microtubes, Mater. Chem. Phys., 2006, **100**, p 224.
29. H. J. Lee and S. I. Lee, Deposition and Optical Properties of Nanocrystalline ZnS Thin Films by a Chemical Method, Curr. Appl. Phys., 2007, **7**, p193.
30. R. O. Borges, D. Lincot and J. Vedel, Chemical Bath Deposition of Zinc Sulfide Thin Films, 12-16 October, 11th E.C. Photovoltaic Solar Energy Conference, 862.
31. D. S. Boyle, P. O'Brien, D. J. Otway and O. Robbe, Novel Approach to the Deposition of CdS by Chemical Bath Deposition: the Deposition of Crystalline Thin Films of CdS from Acidic Baths, J. Mater. Chem., 1999, **9**, p 725.
32. J. Cheng, D. Fan, H. Wang, B. Liu, Y. Zhang and H. Yan, Chemical Bath Deposition of Crystalline ZnS Thin Films, Semicond. Sci. Technol., 2003, **18**, p 676.
33. X. Liu, X. Cai, J. Qiao, J. Mao and N. Jiang, The Design of ZnS/Ag/ZnS Transparent Conductive Multilayer Films, Thin Solid Films, 2003, **441**, p 200.
34. N. I. Kovtyukhova, E. V. Buzanevab, C. C. Waraksac and T. E. Malloukc, Ultrathin Nanoparticle ZnS and ZnS: Mn Films: Surface Sol–gel Synthesis, Morphology, Photophysical Properties, Mater. Sci. Eng., B, 2000, **69-70**, p 411.
35. R. M. A. Azzam and N. M. Bashara, Ellipsometry and Polarized Light, Elsevier Science Publications Co. , Amsterdam, 1987.

36. H. G. Tompkins and E. A. Irene, Handbook of Ellipsometry William Andrews Publications, Norwich, NY, 2005.
37. H. G. Tompkins, A User's Guide to Ellipsometry, 1st Edition, Academic Press Inc., London, 1993.
38. L. Q. Burtrand, I. Lee, J. M. Kim, J. E. Jang and J. Y. Choe, Synthesis and Characterisation of ZnS:Cu,Al Phosphor Prepared by a Chemical Solution Method, J. Lumin., 2003, **104**, p 261.
39. W. Chen, G. Li, J. O. Malm, Y. Huang, R. Wallenberg, H. Han, Z. Wang and J. O. Bovin, Pressure Dependence of Mn^{2+} Fluorescence in ZnS : Mn^{2+} Nanoparticles, J. Lumin., 2000, **91**, p 139.
40. D. Bao, H. Gu and A. Kuang, Sol-gel-Derived C-Axis Oriented ZnO Thin Films, Thin Solid Films, 1998, **312**, p 37.
41. X. M. Wen, P. Xu and P. B. Lukins, Characterisation of Enhanced Emission from Excimer Laser Treated ZnO Ceramics Using One- and Two-Photon Luminescence Spectroscopy and Microscopy, J. Lumin., 2004, **106**, p 1.
42. Y. Nakanishi, A. Miyake, H. Kominami, T. Aoki, Y. Hatanaka and G. Shimaoka, Preparation of ZnO Thin Films for High Resolution Field Emission Display by Electron Beam Evaporation, Appl. Surf. Sci., 1999, **142**, p 233.
43. E. J. Ibanga, C. L. Luyer and J. Mugnier, Zinc Oxide Waveguide Produced by Thermal Oxidation of Chemical Bath Deposited of Zinc Sulphide Thin Films, Mater. Chem. Phys., 2003, **80**, p 490.
44. R. D. Yang, S. Tripathy, F. E. H. Tay, L. M. Gan and S. J. Chua, Photoluminescence and Micro-Raman Scattering in Mn-Doped ZnS Nanocrystalline, J. Vac. Sci. Technol., 2003, **B23**, p 984.
45. Q. T. Zhao, L. S. Hou, R. A. Huang and S. P. Gu, Optical Properties and Structure Analysis of Zin Sulfide Nanorods, Chin. Phys. Lett., 2003, **20**, p 1496.
46. C. Lan, K. Hong, W. Wang and G. Wang, Synthesis of ZnS Nanorods by Annealing Precursor ZnS Nanoparticles in NaCl Flux, Solid State Commun., 2003, **125**, p 455.
47. C. Cheng, G. Xu, H. Zhang, J. Cao, P. Jiao and X. Wang, Low-Temperature Synthesis and Optical Properties of Wurtzite ZnS Nanowires, Mater. Lett., 2006, p 3561.
48. B. Gilbert, B. H. Frazer, H. Zhang, F. Huang, J. F. Banfield, D. Haskel, J. C. Lang, G. Srajer and G. De-Stasio, X-ray Absorption Spectroscopy of the Cubic and Hexagonal Polytypes of Zinc Sulfide, Phys. Rev B, 2002, **66**, p 245205-1.
49. B. Gilbert, H. Zhang, F. Huang, J. F. Banfield, D. Haskel, J. C. Lang, G. Srajer, A. Jurgensen and G. A. Waychunas, Analysis and Simulation of a Nanoparticle Structures Observed in a Surface-Driven Transition, J. Chem. Phys., 2004, **120**, p 11785.
50. H. K. Henisch, Electroluminescence, Pergamon Press, Oxford, 1962.
51. E. A. Jumpertz, Ueber die Elekronendichteverteilung in der. Zinkblende, Z. Elektrochem., 1955, **59**, p 419.
52. S. Lindroos, Y. Charreire, T. Kannianinen, M. Leskelä and S. Benazeth, Zn K-edge EXAFS Study of SILAR-Grown Zinc Sulfide Thin Films, J. Mater. Sci., 1997, **7**, p 741.
53. R. A. D. Pattrick, J. F. W. Mosselmans and J. M. Charnock, An X-ray Absorption Study of Doped Sphalerites, Eur. J. Miner., 1998, **10**, p 239.

54. R. A. D. Patrick, J. F. W. Mosselmans, J. M. Charnock, K. E. R. England and G. R. Helz, The Structure of Amorphous Copper Sulfide Precipitates: An X-ray Absorption Study, Geochim. Cosmochim. Acta, 1997, **61**, p 2023.
55. H. Sawada, R. P. Wang and A. W. Sleight, An Electron Density Residual Study of Zinc Oxide, J. Solid State Chem., 1996, **122**, p 148.
56. L. Ozawa, Cathodoluminescence: Theory and Applications, John Wiley & Sons Inc, 1990.
57. J. S. Prener and F. E. Williams, Self-Activation and Self-Coactivation in Zinc Sulfide Phosphors, J. Chem. Phys., 1956, **25**, p 361.
58. R. N. Bhargava, Doped Nanocrystallin Materials - Physics and Applications, J. Lumin., 1996, **70**, p 85.
59. E. Chimczak and M. Z. Bertrandt, Kinetic Properties and Energy Transfer in the Electroluminescence of Thin Film Cells Based on ZnS:Mn, Thin Solid Films, 1988, **161**, p 59.
60. M. Frackowiak, E. Chimczak, M. Kozielski, J.Kruszyna and A. Kuleczka, Luminescent Thin ZnS : Mn Films, J. Lumin., 1975, **14**, p 243.
61. R. Mach and G. O. Muller, Phys. Status Solidi A, 1982, **69**, p 11.
62. P. D. Rack and P. H. Holloway, The Structure, Device Physics and Material Properties of Thin Film Electroluminescent Displays, Mater. Sci. Eng., 1998, **R21**, p 171-219.
63. H. Yang, J. Zhao, L. Song, L. Shen, Z. Wang, L. Wang and D. Zhang, Photoluminescenct Properties of ZnS:Mn Nanocrystals Prepared in Inhomogeneous System, Mater. Lett., 2003, **57**, p 2287.
64. J. Yu, H. Liu, Y. Wang and W. Jia, Hot Luminescence of Mn^{+2} in ZnS Nanocrystals, J. Lumin., 1998, **79**, p 191.
65. J. Hu, G. Wang, C. Guo, D. Li, L. Zhang and J. Zhao, Au-Catalyst Growth and Photoluminescence of Zinc-Blende and Wurtzite ZnS Nanobelts via Chemical Vapor Deposition, J. Lumin., 2007, 122-123, p 172.
66. K. Manzoor, V. Aditya, S. R. Vadera, N. Kumar and T. R. N. Kutty, Self-Assembly of Doped Semiconductor Nanocrystals Leading to Formation of Highly Luminescent Nanorods, Appl. Surf. Sci., 2006, **252**, p 3968.
67. M. Ivanda, R. Clasen, M. Hornfeck and W. Kiefer, Raman Spectroscopy on SiO_2 Glasses Sintered from Nanosized Particles, J. Non-Cryst. Solids, 2003, **322**, p 46.
68. D. Curie, Luminescence in Crystals, Methuen & Co. Ltd., Wiley scientific, London, 1963.
69. Q. Wang, Z. Xu, L. Yue and W. Chen, Characteristics and Optical Properties of Cd1−xMnxS Nanorods Prepared Through Hydrothermal Route, Opt. Mater., 2004, **27**, p 453.
70. H. E. Ruda, Electronic Materials: Widegap II-VI Compunds for Opto-electronic Applications, Chapman & Hall, London, 1992.
71. Leverentz, An Introduction to Luminescence of Solids, John Wiley, New York, 1943.
72. A. A. Bol, J. Ferwerda, J. A. Bergwerff and A. Meijerink, Luminescence of Nanocrystalline $ZnS:Cu^{2+}$, J. Lumin., 2002, **99**, p 325.
73. G. F. J. Garlick, Luminescent Materials, Oxford University Press, London, 1949.
74. V. Khomchenko, L. Fedorenko, N. Yusupov, V. Rodionov, Y. Bacherikov, G. Svechnikov, L. Zavyalova, N. Roshchina, P. Lytvyn and M. Mukhlio, Laser

Processing and Characterization of ZnS:Cu Thin Films, Appl. Surf. Sci., 2005, **247**, p 434.
75. D. Kim, K.-D. Min, J. Lee, J. H. Park and J. H. Chun, Influences of Surface Capping on Particle Size and Optical Characteristics of ZnS:Cu Nanocrystals, Mater. Sci. Eng., B, 2006, **131**, p 13.
76. W. Q. Peng, G. W. Cong, S. C. Qu and Z. G. Wang, Synthesis and Photoluminescence of ZnS:Cu Nanoparticles, Opt. Mater., 2006,**2-3**, p313.
77. L. Qi, B. I. Lee, J. M. Kimb, J. E. Jang and J. Y. Choe, Synthesis and Characterization of ZnS:Cu,Al Phosphor Prepared by a Chemical Solution Method, J. Lumin., 2003, **104**, p 261.
78. G. Sharma, S. D. Han, J. D. Kim, S. P. Khatkar and Y. W. Rhee, Electroluminescent Efficiency of Alternating Current Thick Film Devices Using ZnS:Cu,Cl Phosphor, Mater. Sci. Eng., B, 2006, **131**, p 271.
79. S. J. Xu, S. J. Chua, B. Liu, L. M. Gan, C. H. Chew and G. Q. Xu, Appl. Phys. Lett., 1998, **73**, p 473.
80. R. H. Bube, Photoconductivity in Solids, John Wiley, New York, 1960.
81. L. Wenyi, C. Xuna, C. Qiulonga and Z. Zhibinb, Influence of Growth Process on the Structural, Pptical and Electrical Properties of CBD-CdS Films, Mater. Lett., 2005, **59**, p 1.
82. M. Fahoume, O. Maghfoul, M. Aggour, B. Hartiti, F. Chraïbi and A. Ennaoui, Growth and Characterization of ZnO Thin Films Prepared by Electrodeposition Technique, Sol. Energy Mater., 2006, **90**, p 1437.
83. F. D. Paraguay, W. L. Estrada, D. R. N. Acosta, E. Andrade and M. Miki-Yoshida, Growth, Structure and Optical Characterisation of High Quality ZnO Thin Films Obtained by Spray Pyrolysis, Thin Solid Films, 1999, **350**, p 192.
84. I. O. Oladeji and L. Chow, A Study of the Effects of Ammonium Salts on Chemical Bath Deposited Zinc Sulfide Thin Films, Thin Solid Films, 1998, **339**, p 148.
85. L. Reijnen, B. Meester, A. Goossens and J. Schoonman, Nanoporous TiO2/Cu1.8S Heterojunctions for Solar Energy Conversion, Mater. Sci. Eng., C, 2002, **19**, p 311.
86. S. H. Chen, A. P. Greeff and H. C. Swart, A Comparative Study Between the Simulated and Measured Cathodoluminescence Generated in ZnS:Cu, Al, Au Phosphor Powder, J. Lumin., 2005, **113**, p 191.
87. W. Sang, Y. Qian, J. Min, D. Li, L. Wang, W. Shi and L. Yinfeng, Microstructural and Optical Properties of ZnS:Cu Nanocrystals Prepared by an Ion Complex Transformation Method, Solid State Commun., 2002, **121**, p 475.
88. S. Gorer and G. Hodes, Quantum Size Effects in the Study of Chemical Solution Deposition Mechanisms of Semiconductor Films, J. Phys. Chem., 1994, **98**, p 5338.

Chapter 5.

Laser transfer of chemically deposited films

Chapter 5. Laser transfer of chemically deposited films

5.1 Introduction to laser induced forward transfer

A selection of the successfully deposited films by the chemical bath deposition method is passed on to the laser induced forward transfer (LIFT) process. These films were deposited on silica substrates called source substrates and had a clear smooth character. They had to uniformly cover one side of the substrate only. It was mostly the films produced from optimised chemical depositions, of ZnS or CdZnS films, that were employed in the LIFT process. A large number of chemical depositions were performed in order to provide candidate samples for the LIFT step of the overall research.

The LIFT process step was chosen and combined with films deposited in a chemical bath, because of its advantage of transferring and redepositing an intact film on a new substrate. Employing the LIFT process for deposition of thin films on a new substrate allows for careful control of the alteration induced upon the transferred material by the laser beam. The films can be transferred with a relatively small energy flux, thus giving the potential for partial modification of the properties of the film during the transfer or for complete maintenance of the initial properties. Other advantages are the deposition on a preformed multilayer system on the target substrate, often necessary for the fabrication of electroluminescent cells and the writing of well-defined shapes in micrometer scale of active luminescent materials on small scale devices.

5.2 Laser Induced Forward Transfer in Theory

The laser induced forward transfer is a technique where a thin film is transferred from its current substrate to a new substrate positioned against it. A focussed laser beam is used to transfer the energy needed to transfer the film across. A distance of a few microns to almost a millimetre is introduced between the two substrate surfaces, though direct contact has also been used.[1] The laser beam passes through the substrate that initially holds the film, launching the irradiated portion of the film forward, thus the name of the process is derived. The method is also referred to as a direct writing method of thin film patterns.[2] The film is typically transferred by a single laser pulse, hence the stage holding the two substrates can be translated in

two dimensions, with a new pulse applied after each translation, in order to achieve the formation of a desired pattern.

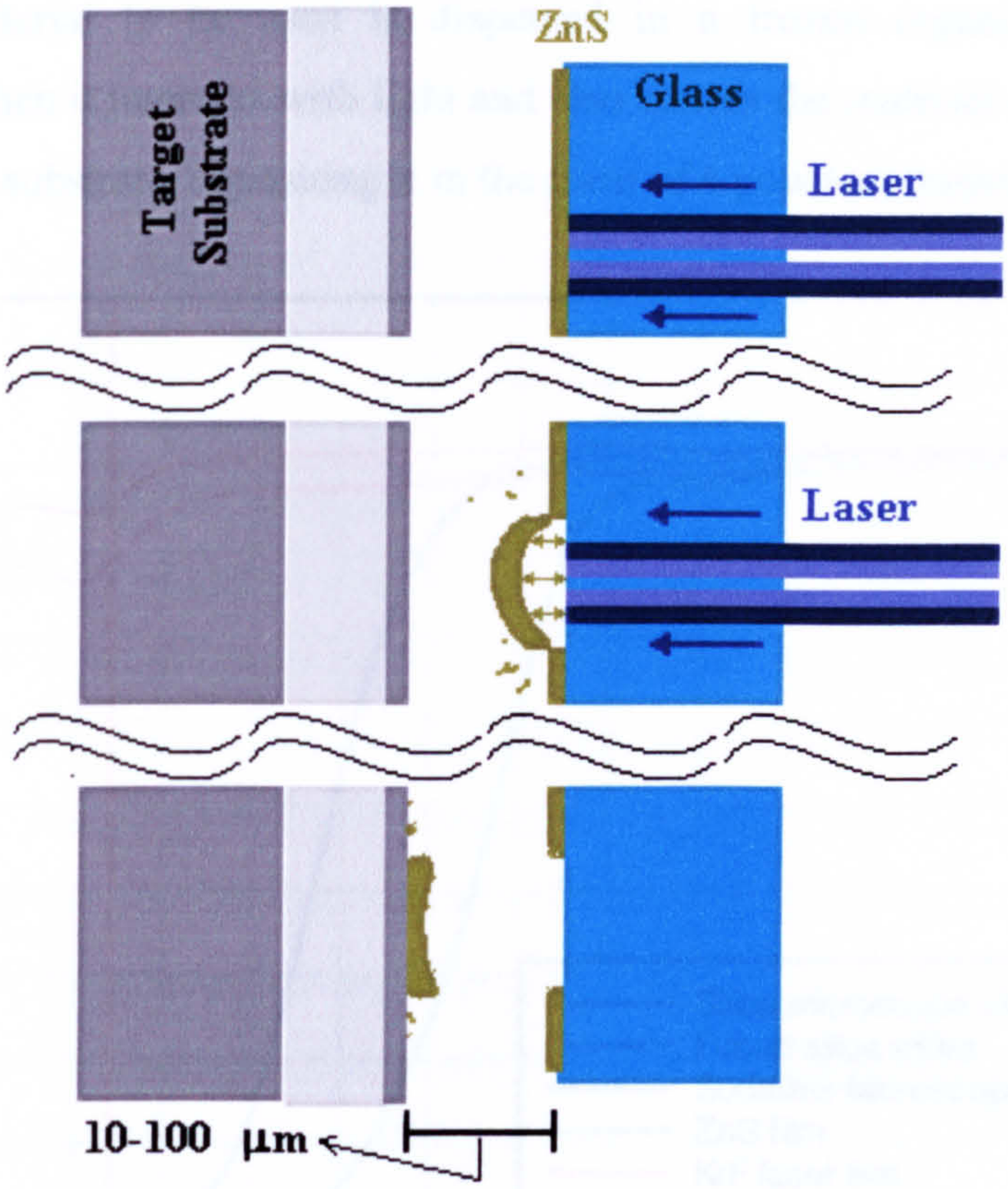

Figure 5.1 Laser induced forward transfer illustrated in 3 steps.

The three main steps of the process are depicted in Figure 5.1. The initial (source) substrate, where the film was deposited by the chemical bath method here or other methods, for example RF sputtering, has to be transparent to the laser beam. The beam is absorbed when it reaches the interface between the source substrate and the film to be transferred. Sodalime glass, which is often used as a typical window glass, strongly absorbs light with wavelength lower than 320 nm. Pure silica glasses have a wide bandgap, allowing for sufficient transmission of light below 200 nm, for UV grade silica glasses such as Suprasil, it can reach down to 160 nm. A silica glass substrate will therefore allow for transmission of the KrF Excimer laser wavelength at 248 nm, while a typical sodalime glass is not suitable for this purpose. At the same time, most of the semiconducting materials[3] even those that are considered of a relatively wide bandgap,[4] will absorb almost 100 % of the 248 nm radiation. The method is often applied to conducting metal films which may or may not present a

large reflectivity over the visible range of the spectrum, but are easily processed by a high photon energy beam.[1, 5-7] Another technique that aids the absorption of laser light by the source films is the matrix assisted pulsed laser evaporation (MAPLE) where the material to be used is dispersed in a frozen organic chemical that decomposes when it interacts with light and also carries the material of interest across to the opposite substrate, depositing it in the form of a powder composed film.[2]

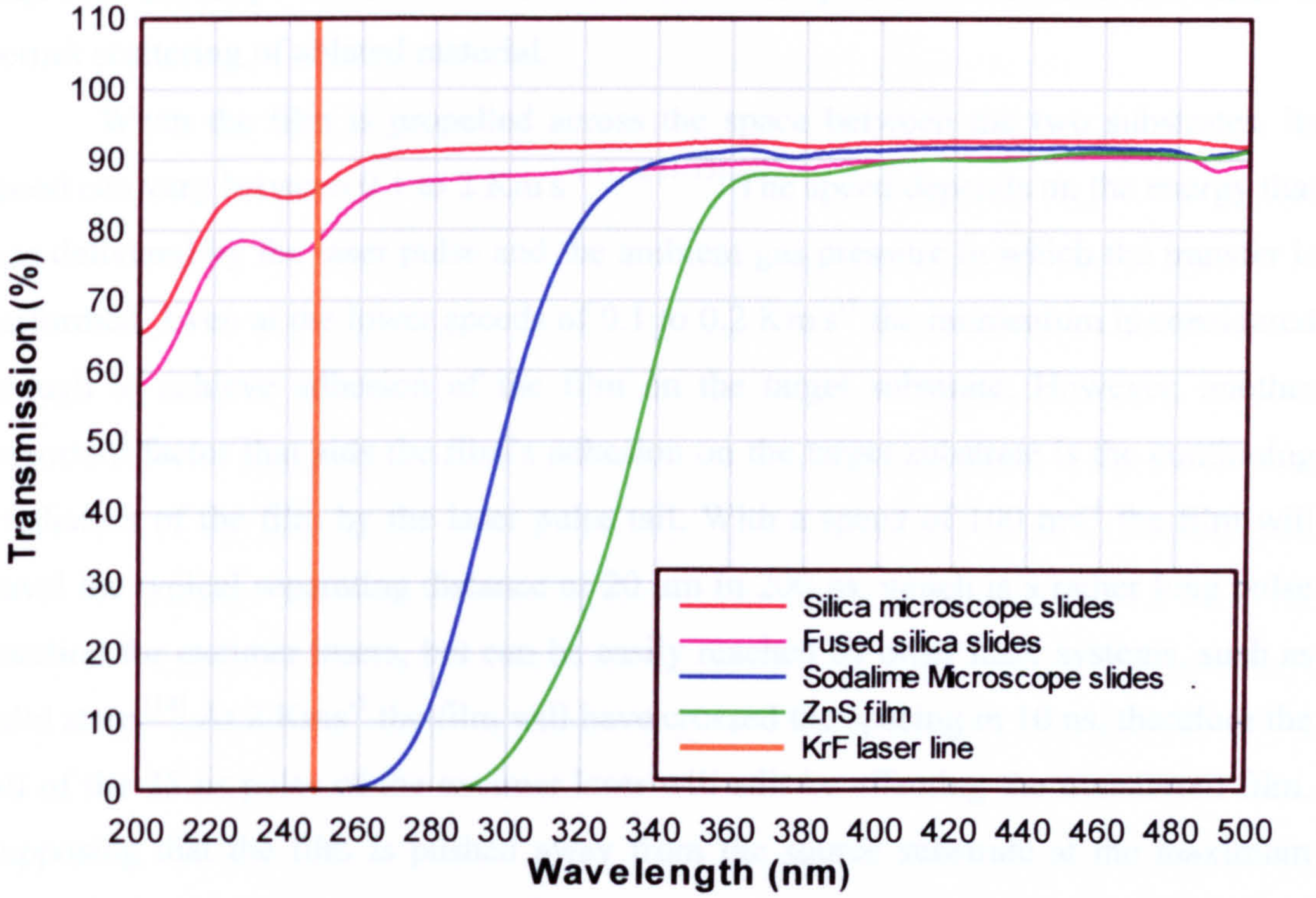

Figure 5.2 Comparison of transmission spectra between clear silica, sodalime glass and film covered substrates.

Therefore, light is being absorbed by the material to be transferred, at the interface of the film and the source substrate. According to the Beer-Lambert law, the intensity of light transmitting through a material is decaying as an inverse exponent. In a highly absorbing material, this decay will be very sharp. Thus, most of the light that reaches the film is absorbed in the first few nanometers of the film's width.[8, 9] A thin layer of the material attached to the substrate's surface will pass on to a plasma state, where molecules of high kinetic energy and free electrons will create a high pressure between the still solid part of the film and the substrate. The force raised by the expanding plasma will act upon the thinner and loosely bound film than the hard crystalline substrate. It only has to overcome the shearing force at the boundaries of the irradiated area of the film with the non-irradiated, in order to free the film under

the focussed beam from the rest of the source film/substrate system. The high pressure is more than enough to propel the detached part of the film, across to the new substrate's surface.[1, 10] The film can be propelled over a distance ranging from a few micrometers[5, 10, 11] to 1 mm,[4, 6] but in general a source-target substrate separation smaller than 50 μm is suggested, while transfers of metallic films in absolute contact have also been reported.[1] The small distance over which the transfer is performed, improves the shape definition of the transferred film portion, as there is less space to permit scattering of ablated material.

When the film is propelled across the space between the two substrates, its speed can vary between 0.1 to 2 $Km{\cdot}s^{-1}$.[1, 6, 11-13] The speed depends on the energy that was delivered by the laser pulse and the ambient gas pressure in which the transfer is performed. Even at the lower speeds of 0.1 to 0.2 $Km{\cdot}s^{-1}$ the momentum is considered enough to achieve adhesion of the film on the target substrate. However, another important factor that aids the film's adhesion on the target substrate is the continuing irradiation of the film by the laser pulse tail. With a speed of 100 ms^{-1} the film will travel the typical separating distance of 20 μm in 200 ns, which is a rather long pulse duration for excimer lasers, but can be easily reached by other laser systems, such as solid state.[14] At 2 Kms^{-1} the film will have crossed the spacing in 10 ns, therefore the tail of the 25 ns pulse of the excimer laser will still be affecting the transferred film. Supposing that the film is pushed away from the source substrate at the maximum energy point of the pulse, the tail of the pulse will keep on irradiating the transferring film for 10 to 15 ns more. Hence the transferring film that leaves the source substrate in a mostly solid phase, can pass on to the liquid phase, or can change structural characteristics during the transfer.[15, 16] Conversely, researchers using femtosecond or picosecond laser pulses for achieving LIFT consider the lack of interaction between the laser beam and the transferring film after its detachment, to be beneficiary for the whole process.[5, 10, 11] Finally, Yamada et al.[1] suggests direct contact between the film covered source and accepting target substrates, in order to achieve ideal shape definition. In this case, they believe that the propelling plume is trapped between the source substrate and the transferred film, but an inexistent separation suggests that the film will also adhere to the new surface both because of the applied pressure and the laser heating.

Review of laser based processing of inorganic luminescent materials

Laser processing of ZnO and ZnS has been performed as means of annealing deposited films, or improving their morphology in terms of roughness. Wen et al.[17] reports modification of ZnO structure when irradiated with XeCl excimer laser radiation at 308 nm. Energy densities between 0.35 to 0.6 Jcm^{-2} have changed the structure of the compressed disc surface, fusing the apparent granules composing the original material. A blackening of the material's appearance was observed, with a large improvement on the two-photon luminescence characteristics of the discs. Irradiation of the blackened material with smaller energy densities of 0.15 to 0.25 Jcm^{-2} returned the material back to its original white colour and to a similar luminescence performance. The process of improving and reducing the luminescence performance of the material's surface is attributed to an increase or decrease, respectively, of oxygen vacancies close to surface. Energy densities above 0.36 Jcm^{-2} will achieve a surface temperature above the melting point, which is expected to eject a number of oxygen atoms. It is then proposed that the low energy densities will achieve a certain amount of reoxidation (absorption of oxygen species) of the material's surface. However, the recovery of the original colour may be an indication of re-granulation of the molten surface. Ablation is reported with laser fluence above 0.8 Jcm^{-2}.

Khomchenko et al. [18] also reports blackening of ZnS films with irradiation by pulsed nitrogen laser at 337 nm. Small fluence levels of 0.115 Jcm^{-2}, over the 5 ns pulses, were found to reduce the surface roughness of the films from 55 nm to 27 nm, rms. However, the granule size, in the vertical direction, is reported to decrease here after irradiation, from 600 to 100 nm, due to abrupt temperature gradients observed both in space (depth-wise) and time (from the short 5 ns pulses and also observed with 20 ns pulses of a KrF laser[19]). Material loss due to ablation is also reported at the same energy densities and is found at a double rate, in comparison with results obtained by KrF irradiation,[19] because of the absorption coefficient difference between the two wavelengths. The different behaviour in terms of cracking and ablating, between ZnO and ZnS, when irradiated with low fluence beam can be attributed to the direct sublimation point of ZnS at almost half the melting point temperature of ZnO, 1185 against 1975 °C respectively. Mastio et al.[20] reports an increased photoluminescence intensity of KrF laser treated ZnS:Mn films by 67% and

19%, compared to thermally annealed equivalents at 500 °C and 700 °C respectively. The processing is again performed with energy densities between 0.1 and 0.2 Jcm^{-2}, on RF sputtered films, which also achieves improved electroluminescent characteristics in a somewhat smaller degree though.

Similar energy density was used by Ozerov et al.[21] to anneal ZnO films. A KrF laser was used to provide 30 successive pulses at fluence settings of 0.075, 0.094 and 0.14 Jcm^{-2} resulting in increasing PL intensity of the annealed films as the energy density was also increased. The films were deposited by pulsed laser ablation deposition with the same laser, at an optimum fluence of 3.5 Jcm^{-2}. The high fluence setting employed here is again a result of the high melting and consequently boiling point of the zinc oxide compared with the sulfide.

Pulsed laser ablation deposition of a similar in nature material also used in construction of electroluminescent devices, SrS, is discussed by Piqué et al.[22] A KrF laser beam was focussed on SrS targets doped with Eu-Sm, Ce-Sm or Cu-Ge, at a fluence between 1 and 2 Jcm^{-2}. A deposition rate of 2.5 $Ås^{-1}$ was obtained with a 5 Hz laser pulse repetition rate (i.e. roughly 0.5 Å per pulse). Depositions of 0.05 to 2.0 μm films were achieved on MgO substrates heated at 600 to 850 °C, in Ar and H_2S gas mixture in sub-atmospheric pressure. They were very smooth films with excellent crystallinity examined by X-Ray diffractograms. A fluence of 1.6 Jcm^{-2} is also suggested by Fitz-Gerald et al.[23] for pulsed laser ablation deposition of SrS films with a KrF laser, while a tellurium overlayer required for doping purposes in their research was deposited by 1 Jcm^{-2}.

Review of Laser Induced Forward Transfer Literature

The first reported use of single pulse laser induced forward transfer technique, is widely accepted to be that by Bohandy et al.[24] who used an ArF laser to transfer metal films (copper) from a transparent source substrate to a silicon target. The method was referred to as a direct writing technique of metal features. In a later publication with others[13] they have modelled the effect of the laser beam on the metal film before its detachment, using a one-dimensional thermal diffusion equation. Their modelling clarified that a thin layer of film facing directly the impinging laser radiation reaches its boiling point before the rest of the film melts as it was already

explained above, a notion that is also supported by Baseman, Froberg and others in two publications.[8, 9] regarding transferred gold films by a KrF laser.

Since then, the technique was attuned to achieve transfer of oxide films (apart from its already known application on metals)[11, 25]. Combined with the technique of matrix assisted pulsed laser evaporation (MAPLE) by Piqué et al.[2] the LIFT process acquires wide capabilities on deposition of more complex materials such as $BaTiO_3$, $SrTiO_3$, $Y_3Fe_5O_{12}$ and also Au and Ag metal films in repeated passes. Patterns of thickness rising up to 25 μm have been grown with some of the complex oxides involved in their experiments, while the metal bands also attributed thickness magnitudes of up to 15 μm. The materials were deposited in patterns forming capacitors, inductors and chemoresistors in the micron scale, with proven operational characteristics. Laser fluences of 0.5 to 3 Jcm^{-2} were used for the depositions, depending on the type and volume of the material to be transferred and also on the film characteristics and surface finishing desired.

Another remarkable use of the LIFT technique is that by Bähnisch et al.[5] who deposited 1 μm thick films of AuSn for wire soldering applications in the micron scale, by using a Ti:sapphire laser at 775 nm with 0.1 to 8 ps pulse lengths. Energy densities between 1 to 6 Jcm^{-2} were applied for successful transfers of the films, attributing an initial thickness of 0.76 or 1.8 μm. Finally, Tóth and Szörényi[3] demonstrated how fused compound films could be created by single pulse irradiation and transferring of stacked layers of germanium and selenium. The thickness of the source films was 74 nm of selenium and 30 nm of germanium initially created by vacuum evaporation. A q-switched ruby laser giving 20 ns pulses, at 694 nm, was used for the transfer, with the applied fluence changed from around 0.04 Jcm^{-2} to 1.2 Jcm^{-2}. A control over the ratio between the two materials is accomplished, on both the transferred and remaining layers, by adjusting the laser fluence. Findings of modelling based on thermal and optical characteristics of the two layers are contrasted against the experimental values and are found in good agreement, thus making it a promising technique for application in layers of other materials too. Here, melting of the films is a result of the small thickness of the two layers and the use of the low wavelength and long pulse length of the laser, compared to ps or fs pulse lengths of the other red or near infrared lasers used in LIFT processes.

5.3 Experimental

5.3.a. The laser

As it was already explained above, a KrF laser seems like an ideal laser beam generation device for performing the LIFT process on the ZnS or CdZnS films. The two main reasons for this are the very small absorption depth of its short wavelength and the low transmission of the beam through these semiconductor materials. A Questek series 2000 laser head was used for this purpose, filled with a Kr/F_2 gas mixture, at the manufacturer recommended partial pressures of 150 mbar for Kr, 140 mbar for F_2 (The F_2 gas is added as a mixture of 5% F_2 in He gas) and 2400 mbar for He, used as buffer. The purity of the gases used is 98%, technical grade, for F_2 (before it is introduced to the 5% mixture), 99.995%, research grade, for Kr and 99.9995%, research grade, for the He buffer. Figure 5.3 shows a schematic of the laser system with its gas and cooling water connections and an external gas-processing unit, whose operation is optional. A new gas mixture gave an approximate maximum output of 350 mJ per pulse. As the gas mixture degraded, it was occasionally needed to circulate it through a gas processor unit. The mixture is also filtered by a Wafergard II, F-6, inline gas filter by Millipore. The gas processor unit available was a liquid nitrogen cooled GP2000 by Oxford Lasers. The laser pulse output energy was controlled by setting an 8 bit digital number at the unit's control panel corresponding to an equivalent discharge voltage between the electrodes. This method provided a stable pulse shape, while the energy of each pulse, was monitored separately and recorded for each pulse applied on a sample to achieve film transfer or processing. The pulse repetition rate was thus kept at very low levels, around 0.3 to 0.1 Hz, allowing for time to record the energy of the last ejected pulse.

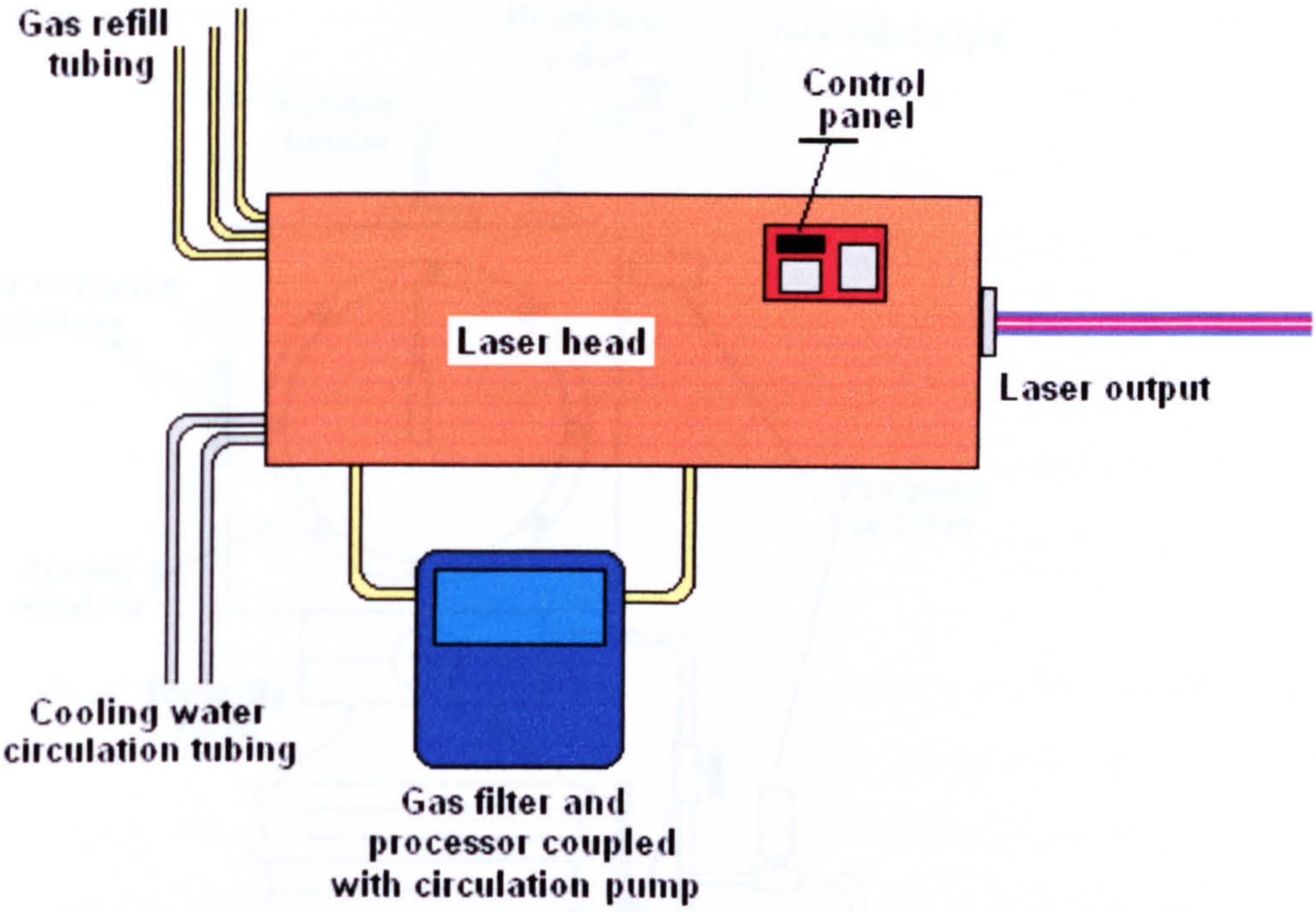

Figure 5.3 Schematic of excimer laser system, with external gas processor unit.

5.3.b. The chamber

In order to avoid oxidation of the films during laser induced transferring and also to minimise any resistance posed by atmospheric pressure while the film portions are detached from the source substrate, the process needed to be performed in subatmospheric pressures and ideally in an inert atmosphere. The samples were therefore placed on a holder, which suspended them inside a vacuum chamber. Windows transmitting in the UV allowed the laser beam to reach the samples. The vacuum chamber was a steel cube, with small transmitting windows at the entrance and two large observation and access windows on the sides. All other windows apart from the beam entrance window were made of no UV transmitting glass, hence preventing as much as possible radiation to escape the chamber. The holder's position was controlled by a shaft, extending out of the chamber, through a solenoid valve that provided the necessary sealing.

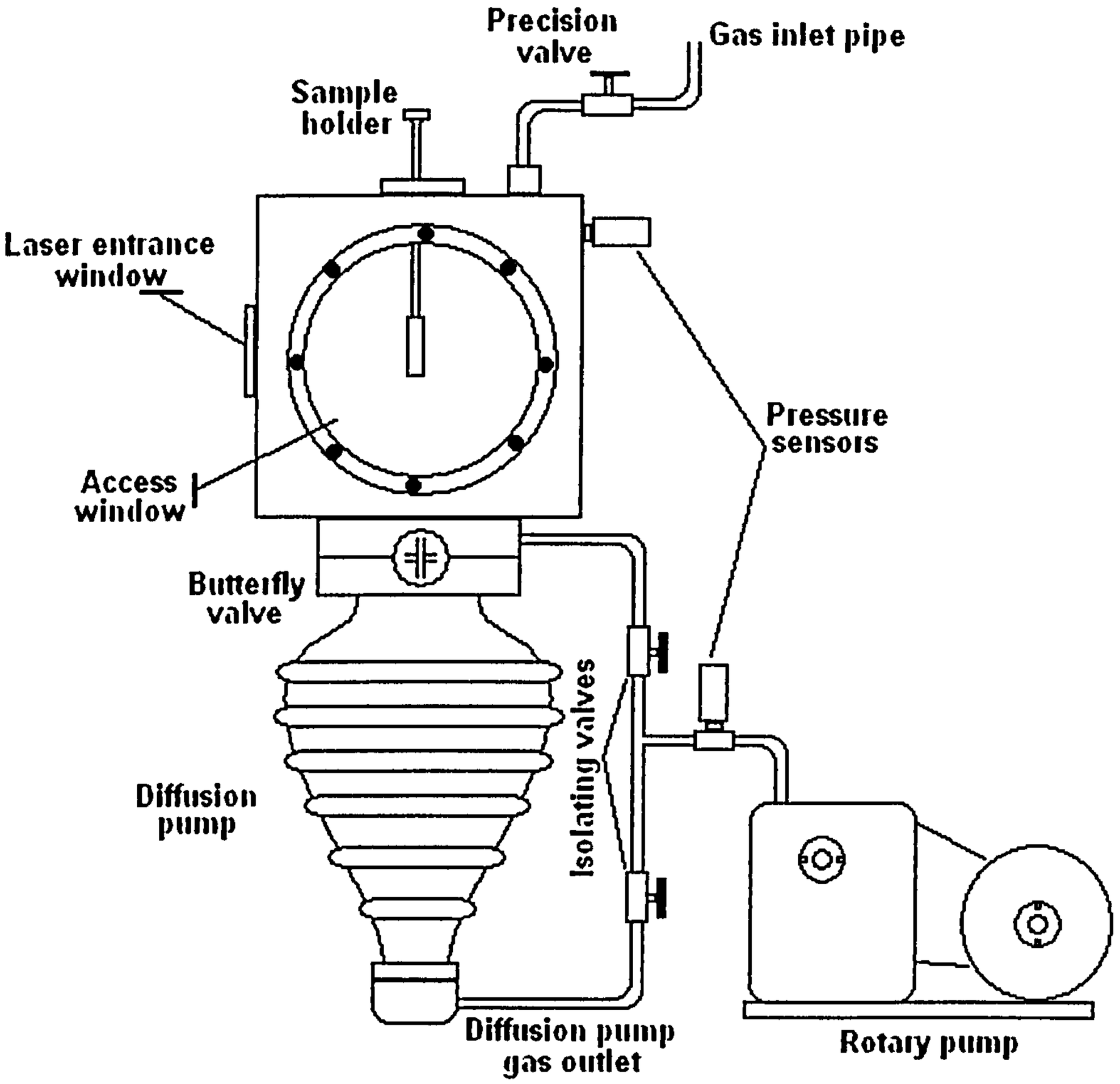

Figure 5.4 Schematic of vacuum chamber for the transferring process, with its dual pumping system.

The gas is pumped out using either a rotary pump alone, or a combination of a diffusion and a rotary pump. The pumps are connected to the bottom of the chamber by a three-valve isolation pipe network. The valves are used to isolate each of the pumps from the chamber or from each other. When the nitrogen-cooled diffusion pump is set in operation, the chamber is initially pumped out using the rotary pump, at a pressure of 10^{-1} to 10^{-2} bar and then a butterfly valve brings the diffusion pump into the system. The rotary pump is attached to the exhaust of the diffusion pump, as support, when the later is put in use. A pressure gauge indicates the pressure in the chamber and at the inlet of the rotary pump, helping to keep track of the correct flow of gas. The exhaust of the rotary pump is taken away into a fume processing and extractor unit.

For the first few sets of experiments, designed to determine some boundaries of the transferring conditions, the atmospheric air inside the chamber was pumped out

and the experiments were conducted in a low pressure of atmospheric air. The pressure was stabilised through a precision valve at the top of the chamber. When a inert gas was later on required, the chamber was pumped out and then flushed with argon, reaching almost an atmospheric pressure again. Nitrogen was only used in two experiments, but argon was considered a better choice, because of its inherent and undisputed inertness. The new inert atmosphere was again brought down to the necessary pressure, usually in the vicinity of 10^{-3} to 10^{-5} mbar. The inert gas was slowly fed in the chamber through the precision valve, in order to stabilise the pressure at the desired level.

A single experiment involving film transferring under a H_2S atmosphere was also set up. The chamber was again flushed with argon like before and when the argon gas was pumped out, the hydrogen sulfide gas was let in through another precision valve, raising the pressure only by one order of magnitude, to achieve dominating population of the desired molecule species. This process was meant to avoid the use of large amounts of highly toxic gas, as the chamber volume was approximately 8 litres. The chamber was again flushed out twice after the experiment, with argon and atmospheric air.

5.3.c. The sample holders

As explained above, the source and target substrates have to be held against each other at the image point of the focussed beam. Therefore, a sample holder was constructed to suspend the two substrates inside the chamber. The simplest system of introducing a set separation between the two substrates is by introducing a spacer in between, instead of holding each substrate separately. The substrates and the spacers are tightened on the sample holder in a sandwich configuration. The size of the spacer was decided based on the literature review. Most of the researchers that have experimented with a varying distance of the substrates in the LIFT process have concluded towards an optimum magnitude of 10 to 75 μm. Two bands of aluminium foil were used on the two longer sides of the glass microscope slides as spacers. The thickness of the aluminium foil, measured by an electronic micrometer at various point, was found to be 15 μm. The measurement was repeated under a microscope, after the substrate-spacer-substrate sandwich had been assembled on the holder, at randomly selected experiments and the distance between the substrates was again

found to be 15 μm. This distance gave very good results from the beginning and was kept in all the experiments. Double spacers were introduced in one experiment, but the definition of the transferred films diminished significantly, with a large amount of debris deposited out of the irradiated area boundaries at a fluence setting of 1.1 Jcm^{-2}. Hence, no other spacer configuration was ever attempted, but a lesser distance might have also returned some good results, based on the impression acquired by the literature.

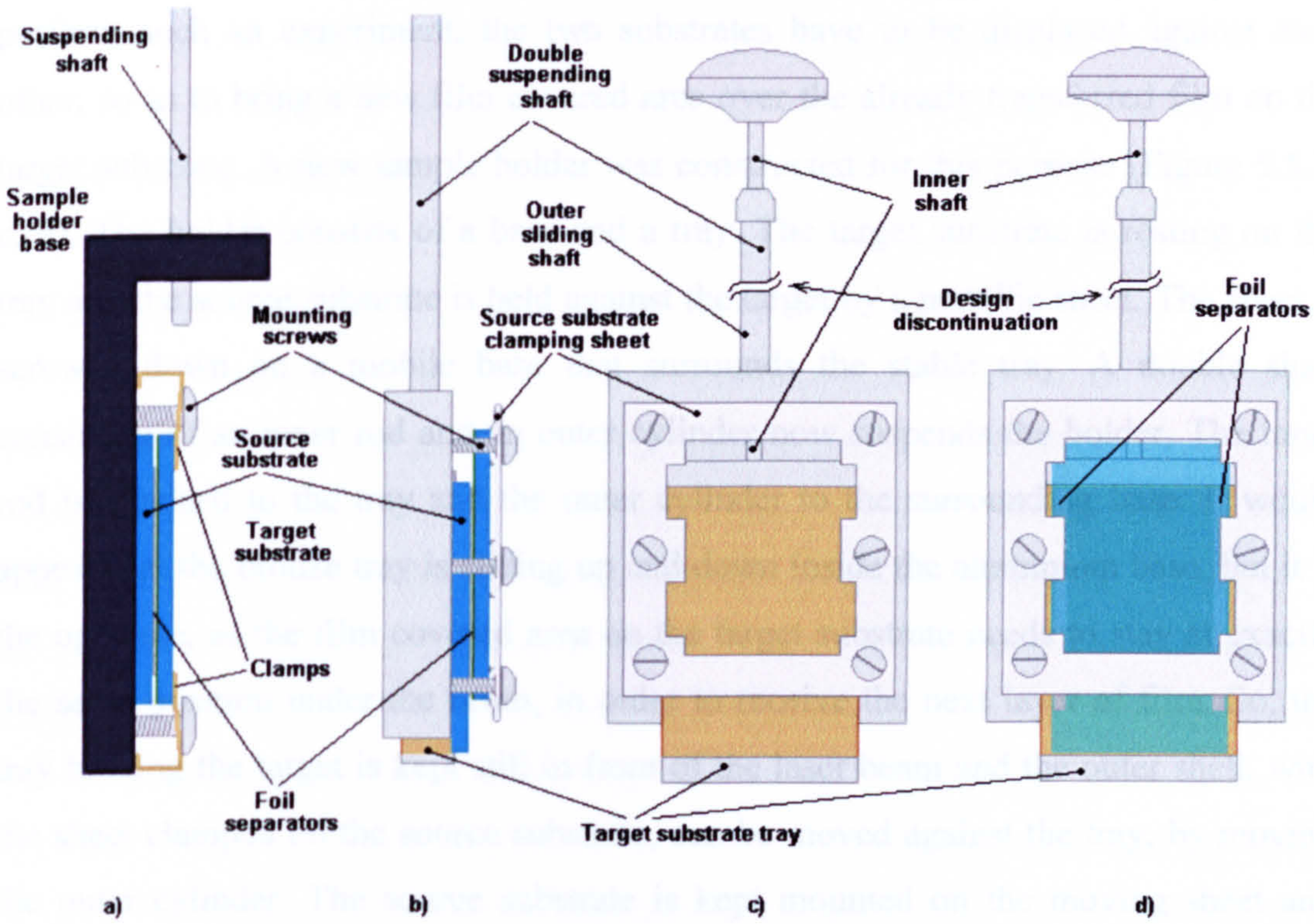

Figure 5.5 Schematic of sample holders. a) Side view of simple holder for single layer transfers, b) side view of multiple layer transferring holder with sliding tray, c) Front view of holder for multiple layer transfers without the mounted samples and d) with the mounted substrates and the spacers at an offset to each other.

The first sample holder that was constructed (Figure 5.5.a) had a metallic base suspended by a shaft, moving through a solenoid valve. Two small screws are used to tighten the substrate-separator-substrate assembly against the holder base, by the use of two bronze clamps. The target substrate is placed at the bottom, resting against the holder's base and the source is on the outer side, being pressed down by the clamps, which is also exposing it to the laser beam. The clamps have a width of approximately 0.6 cm and are covering an area less than 0.4 cm^{-2} of the substrate's surface, therefore,

exposing as much as possible of it to the laser beam. The whole holder-samples assembly can be moved up and down during the experiment, using the shaft. The left to right motion is controlled by moving the whole vacuum chamber onto metallic sliding trails. Thus, this holder gives the ability to focus the beam on an area of choice defined by two dimensions.

It was considered interesting to investigate the possibility of transferring multiple layers of film on top of each other, hence creating thicker films and achieving a degree of greater control over the thickness of the transferred films. To perform such an experiment, the two substrates have to be displaced against each other, so as to bring a new film covered area over the already transferred film on the target substrate. A new sample holder was constructed for this purpose (Figure 5.5.b, c, d). The holder consists of a base and a tray. The target substrate is resting on the tray and the source substrate is held against the target by a metallic sheet. The sheet is screwed down on a mobile base that surrounds the stable tray. A double shaft consisting of an inner rod and an outer cylinder now suspends the holder. The inner rod is attached to the tray and the outer cylinder to the surrounding base. It would appear that the bronze tray is sliding up and down inside the aluminium base, but it is the opposite, as the film covered area on the target substrate needs to stay at exactly the same position under the beam, in order to receive the next layer of film. So, the tray holding the target is kept still in front of the laser beam and the outer shell, with the sheet clamped on the source substrate, can be moved against the tray, by moving the outer cylinder. The source substrate is kept mounted on the moving sheet and shell, by friction points from the sheets inward extensions. These extensions are touching only the sides of the source substrate, thus exposing the rest of the surface to the laser beam.

The whole assembly can also be moved simultaneously up and down, by sliding the double suspending shaft through the solenoid valve. Motion in the horizontal dimension is again achieved by sliding the chamber on trails like before. So, this second, advanced sample holder, can give the ability to displace the substrate assembly in two dimensions against the focussed laser beam and also to displace the source substrate with respect to a firm target substrate. Still, the first, simpler holder was used if only single layer transfers were needed, due to the simplicity it provides on mounting the samples. Precise movements of the holders against the beam were achieved by markings on the suspending shafts, out of the chamber and on the

chamber table. Similar markings were designed on the double shaft in order to allow for easier control of the sample displacement against each other. Finally, the access windows and the laser entrance windows allowed for observation of the correct positioning of the samples, while the use of the focussing lens to magnify the target area to the observers eye was also very useful when performing multiple film transfers, as long as the laser head beam shutter was securely closed.

5.3.d. The optical system

A very simple optical system was constructed on the beam path, to control and deliver the desired laser energy to the samples. The simplest version of the optical system consists of the mask, a focussing lens and the sample assembly, arrayed in this order, away from the laser head. The mask is used to give a shape to the laser beam ejected from the laser head aperture. It is a metal plate with a rectangular opening of 10 mm by 5 mm in dimensions, which is positioned right at the centre of the beam, allowing the stronger and more uniform part of the beam profile to pass through. The focussing lens is a UV transmitting lens, as the laser beam is at 248 nm and the losses should be minimised in the optical system. In designing the optical system, it is assumed that the object to be imaged onto the sample is the mask. The lens was at a distance of 2 meters from the mask and had a focal length of 19 cm. By manipulating the imaging equation (Equation 5.1) for thin lenses,[26] the image distance can be calculated by reorganising it (Equation 5.2). The calculated value for the image distance was 20.994 cm, while an experimental investigation of the image point gave a result of 20.7 cm from the lens.

$$\frac{Obj.Dist.}{I.Dist.} = \frac{focalLen.}{I.Dist. - focalLen.} \quad (5.1)$$

$$I.Dist. = \frac{Obj.Dist. \times focalLen.}{Obj.Dist. - focalLen.} \quad (5.2)$$

This experiment was performed by moving the sample in steps of 1mm on the beam path, until the best image quality was obtained. A wire was also attached across the mask aperture, at an angle to the sides of its rectangular sides, thus creating a shape with sharper features than the rectangle, while usually, a well defined image of the wire can be sufficient for defining the image point.

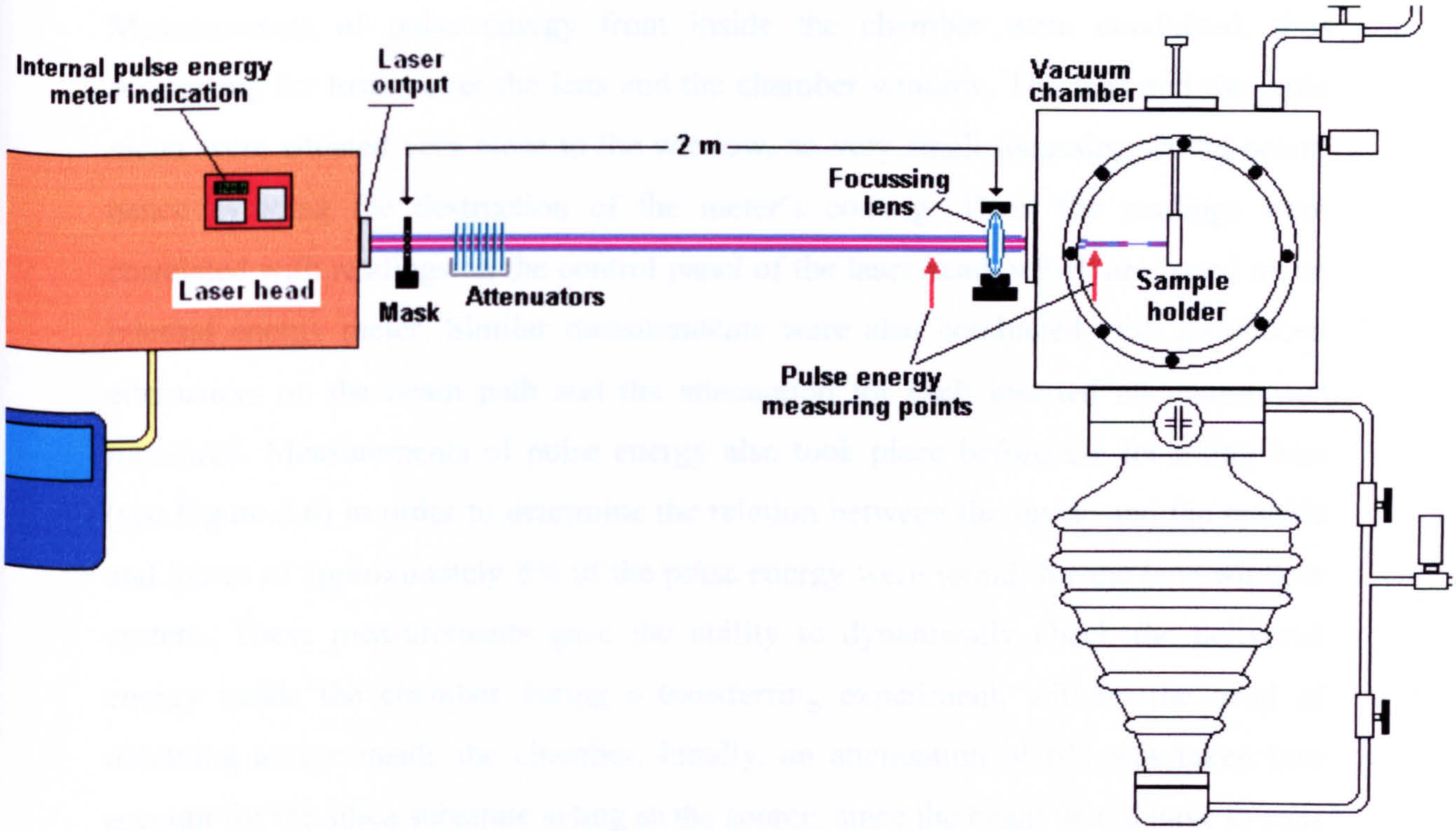

Figure 5.6 Optical system setup, delivering the laser beam pulse from the laser head to the sample assembly inside the vacuum chamber. The red arrows indicate the points where a pulse energy meter was inserted, intercepting the beam, in order to measure the energy delivered to the samples.

Of course the system becomes slightly more complex because of the need of keeping the samples in vacuum when they are being processed by the laser radiation. That introduces a UV transmitting window, which introduces some very small amount of absorbance and possible refraction, since it lies after the focussing lens. Moreover, the preferred method of attenuating the beam is by the use of power attenuating slides, as they leave the pulse shape and beam profile unaltered and this of course assumes that they have optically flat surfaces and uniform refractive index. Silica microscope slides were used for this purpose, right after the mask. Their absorbance at 248 nm was 12 %, higher than that of the UV grade silica used for the lens and the chamber window. A stack of 15 or 20 was needed to be used at certain experiments, in order to lower the energy of the laser pulse to low levels. The final optical system setup is shown in the schematic of Figure 5.6, including the laser head and the vacuum chamber enclosed samples.

The fluence delivered to the film on the source sample was calculated based on the energy of the pulse reaching the film and the irradiated area. So, the energy that reached the source sample film had to be known for each pulse applied to the sample.

Measurements of pulse energy from inside the chamber were conducted, thus accounting for losses over the lens and the chamber window. The lens and the joule meter were situated very close to the window, so very small focussing would occur, hence avoiding the destruction of the meter's coating. Then, the readings were correlated with readings on the control panel of the laser head, which are based on an internal energy meter. Similar measurements were also conducted with introduced attenuators on the beam path and the attenuation for each inserted attenuator was measured. Measurements of pulse energy also took place before the focussing lens (see Figure 5.6) in order to determine the relation between the inside and the outside and losses of approximately 8% of the pulse energy were found, for the lens-window system. These measurements gave the ability to dynamically check the delivered energy inside the chamber during a transferring experiment, without the need of obtaining access inside the chamber. Finally, an attenuation of 6% was taken into account for the silica substrate acting as the source, since the beam would have to pass through it before reaching the film. Only half of the absorption at 248 nm, of such a silica slide is taken into account for this calculation, as the reflections from the film-covered surface should not be evaluated. All these parameters had to be considered; as the laser pulse fluence delivered on a film at a laser induced forward transfer process is one of the most defining properties of the process and it is what most researchers will seek to compare their own results of similar experiments with.

5.4 References

1. H. Yamada, T. Sano, T. Nakayama and I. Miyamoto, Optimisation of Laser Induced Forward Transfer Process of Metal Thin Films, Appl. Surf. Sci., 2002, **197-198**, p 411.
2. A. Piqué, D. B. Chrisey, R. C. Y. Auyeung, J. Fitz-Gerald, H. D. Wu, R. A. McGill, S. Lakeou, P. K. Wu, V. Nguyen and M. Duignan, A Novel Laser Transfer Process for Direct Writing of Electronic and Sensor Materials, Appl. Phys. A, 1999, **69 [Suppl.]**, p S279.
3. Z. Tóth and T. Szörényi, Pulsed Laser Processing of Ge/Se Thin Film Structures, Appl. Phys. A, 1991, **52**, p 273.
4. I. Zergioti, S. Mailis, N. A. Vainos, P. Papakonstantinou, C. Kalpouzos, C. P. Grigoropoulos and C. Fotakis, Microdeposition of Metal and Oxide Structures Using Ultrashort Laser Pulses, Appl. Phys. A, 1998, **66**, p 579.
5. R. Bähnisch, W. Groß and A. Menschig, Single-Shot, High Repetition Rate Metallic Pattern Transfer, Microelectron. Eng., 2000, **50**, p 541.
6. Y. Nakata and T. Okada, Time-Resolved Microscopic Imaging of the Laser-Induced Forward Transfer Process, Appl. Phys. A, 1999, **69 [Suppl.]**, p 275.
7. I. Zergioti, S. Mailis, N. A. Vainos, C. Fotakis, S. Chen and C. P. Grigoropoulos, Microdeposition of Metals by Femptosecod Excimer Laser, Appl. Surf. Sci., 1998, **127-129**, p 601.
8. R. J. Baseman and N. M. Froberg, Time-Resolved Transmission of Thin Gold Films During Laser Blow-off, Appl. Phys. Lett., 1989, **55**, p 1841.
9. R. J. Baseman, N. M. Froberg, J. C. Andreshak and Z. Schlesinger, Minimum Fluence for Laser Blow-off of Thin Gold Films at 248 and 532 nm, Appl. Phys. Lett., 1990, **56**, p 1412.
10. B. Tan, K. Venkatakrishnan and K. G. Tok, Selective Surface Texturing Using Femptosecond Pulsed Laser Induced Forward Transfer, Appl. Surf. Sci., 2003, **207**, p 365.
11. I. Zergioti, D. G. Papazoglou, A. Karaiskou, N. A. Vainos and C. Fotakis, Laser Microprinting of InO_x Active Optical Structures and Time Resolved Imaging of the Transfer Process, Appl. Surf. Sci., 2002, **197-198**, p 868.
12. I. Y. S. Lee, W. A. Tolbert, D. D. Dlott, M. M. Doxtader, D. M. Foley, D. R. Arnold and E. W. Ellis, Dynamics of Laser Ablation Transfer Imaging Investigated by Ultrafast Microscopy, J. Imag. Sci. Tech., 1992, **36**, p 180.
13. F. J. Adrian, J. Bohandy, B. F. Kim, A. N. Jette and P. Thompson, A Study of the Mechanism of Metal Deposition by the Laser-Induced Forward Transfer Process, J. Vac. Sci. Technol., 1987, **B5**, p 1490.
14. W. T. Silfvast, Laser Fundamentals, 2nd Edition, Cambridge University Press, Cambridge, 2004.
15. H. W. Bergman and H. Junge, Präzise Optische Bearbeitung von Festkörpern, 5 Edition, VDI Verlag, Düsseldorf, 1996.
16. V. Schultze and M. Wagner, Blow-off of Aluminium Films, Appl. Phys., 1991, **A53**, p 241.
17. X. M. Wen, P. Xu and P. B. Lukins, Characterisation of Enhanced Emission from Excimer Laser Treated ZnO Ceramics Using One- and Two-Photon Luminescence Spectroscopy and Microscopy, J. Lumin., 2004, **106**, p 1.
18. V. Khomchenko, L. Fedorenko, N. Yusupov, V. Rodionov, Y. Bacherikov, G. Svechnikov, L. Zavyalova, N. Roshchina, P. Lytvyn and M. Mukhlio, Laser

Processing and Sharacterization of ZnS:Cu Thin Films, Appl. Surf. Sci., 2005, **247**, p 434.
19. E. A. Mastio, E. Fogarassy, W. M. Cranton and C. B. Thomas, Ablation Study on Pulsed KrF Laser Annealed Electroluminescent ZnS:Mn/Y2O3 Multilayers Deposited on Si, Appl. Surf. Sci., 2000, **154-155**, p 35.
20. E. A. Mastio, C. B. Thomas, W. M. Cranton and E. Fogarassy, The Effects of Multiple KrF Laser Irradiations on the Electroluminescence and Photoluminescence of RF-Sputtered ZnS:Mn-Based Electroluminescent Thin Film Devices, Appl. Surf. Sci., 2000, **157**, p 74.
21. I. Ozerov, D. Nelson, A. V. Bulgakov, W. Marine and M. Sentis, Synthesis and Laser Processing of ZnO Nanocrystalline Thin Films, Appl. Surf. Sci., 2003, **212-213**, p 349.
22. A. Piqué, R. C. Y. Auyeung, S. B. Qadri, H. Kim, B. L. Justus and A. L. Huston, Growth of Epitaxial Doped Strondium Sulfide Thin Films by Pulsed Laser Deposition, Thin Solid Films, 2000, **377-378**, p 803.
23. J. M. Fitz-Gerald, J. Hoekstra, J. D. Fowlkes and P. D. Rack, Pulsed-Laser-Deposited Ultraviolet Emitting SrS:Te Thin Films, Applied Physics Letters, 2003, **80**, p 20.
24. J. Bohandy, B. F. Kim and F. J. Adrian, Metal Deposition from a Supported Metal Film Using an Excimer Laser, J. Appl. Phys., 1986, **60**, p 1538.
25. K. Kordás, A. E. Pap and S. Leppävuori, Laser-Enhanced Selective TiO2 Deposition on Si, Surf. Coat. Technol., 2003, **176**, p 84.
26. E. Hecht, Optics, 4th Edition, Addison Wesley Longman, Inc., New York, 2002.

Chapter 6.

Analysis of transferred films

Chapter 6. Analysis of transferred films

6.1 Introduction

After transferring the film to a new substrate by the LIFT process, it becomes interesting to investigate both the transferred film and the ablation site on the source substrate. An understanding of the progress of laser transferring can be developed, based on this investigation. Comparisons between the precursor chemically deposited (at the source sample) and the laser transferred (at the target sample) films give a good idea of the transformations that take place during the transfer. And finally, it is interesting to define the most ideal conditions for laser transferring of II-VI materials. However, the ideal conditions are closely related to the results of the chemical deposition process, thus the suggested transferring conditions must be coordinated with those of the successful chemical depositions.

The main difference between analysing the as deposited (by the chemical bath method) films and the transferred films is the available area of investigation. The transferred film sites usually cover an area of 2 mm^{-2}, which has often proved difficult to target with an analysis tool, or to obtain an analysis signal integrated over the selected site area only, without including the surrounding substrate surface. Generating wide-area transfers did improve targeting and signal collection, but not in all cases. The other difference is the film thickness. Since some of the mass of the transferred film is lost in ablation during the transfer, or is being scattered outside the limits of the imaged beam, the resulting film thickness on the target substrate is always smaller than that of the source. Hence, some of the analysis methods that require a greater volume of material for the analysis could not be used with every transfer that was attempted. This had a greater impact on the cathodoluminescence and photoluminescence investigations, where a greater volume of deposited film is always beneficial and a large variety of sample preparation conditions had to be examined. Multiple layer transferring did help in that context, especially for the case of the Raman scattering technique, where it proved very fruitful compared to the technique's application on the chemically deposited films.

This chapter lays out the most important findings concerning the laser induced forward transferring of the chemically deposited zinc sulfide and cadmium sulfide films. The films are examined in a similar manner to that of the as deposited films in

chapter 4, with the techniques split in groups of composition, surface morphology, crystal structure and luminescence. The differences and similarities between the transferred and precursor films are pointed out in each investigation method and suggestions are put forward, on achieving successful transfers of the material, with the best film structure and definition initially and luminescence efficiency later.

6.2 Composition

6.2.a. Raman Microscopy

Here, Raman microscopy is classified as a composition analysis technique, as it is exploited in such a way as to discriminate between CdS and ZnS. A small piece taken from bulk, fired ZnS was analysed by Raman microscopy in section 4.5.b where a peak at 350 cm^{-1} was detected. The peak is attributed to the longitudinal optical vibration mode of the expected cubic phase[1, 2] of that sample (Figure 4.33). As it was already explained, it was impossible to obtain any meaningful data from the chemically deposited films, but it was feasible to do so from the thick films generated by multiple transferred layers. It was found that films formed by laser deposition of 5 successive layers can reach a thickness of approximately 1 μm (see Section 6.3.b). Hence, at least half of the height of the focal probing cylinder of the instrument can be occupied by material of interest. Two samples were investigated, following this route. One was a transfer from a ZnS sample prepared in a bath with doubled the quantity of zinc chloride. The other was a CdZnS:Mn with equal quantities of cadmium and zinc chloride salts at 0.13 g (5.6 mM of $ZnCl_2$ and 3.3 mM of $CdCl_2$) and 1.3 g of manganese chloride (38.6 mM).

The Raman shift recorded for the ZnS sample features a rather strong peak at 347 cm^{-1}(Figure 6.1), very close to the expected 350 cm^{-1} for cubic ZnS,[3-6] and to the peak observed for the bulk ZnS sample prepared by firing. Apart from the slight shift of the peak to a lower wavenumber, its bandwidth (FWHM) is also rather expanded, reaching 20 cm^{-1}. Both Osada et al.[4] and Yang et al.[5] assign the shift to lower wavenumber and the expansion of the peak's FWHM to small crystallites and a possible blend between the cubic and hexagonal forms of ZnS. A study on the dependence of these two features in the Raman spectrum of ZnS on its acquisition temperature, examining temperatures between almost 5 and 300 degrees Kelvin, by

Moon Yu et al.,[6] indicates that acquisition at room temperature would inflict similar effects on the peak position and FWHM, to the ones observed in this research. Either explanation can be applied here, as the experiment was conducted at room temperature and the laser deposition of multiple layers could have produced grained and mixed phase crystallisation, due to sudden cooling on the instant of contact with the target surface.

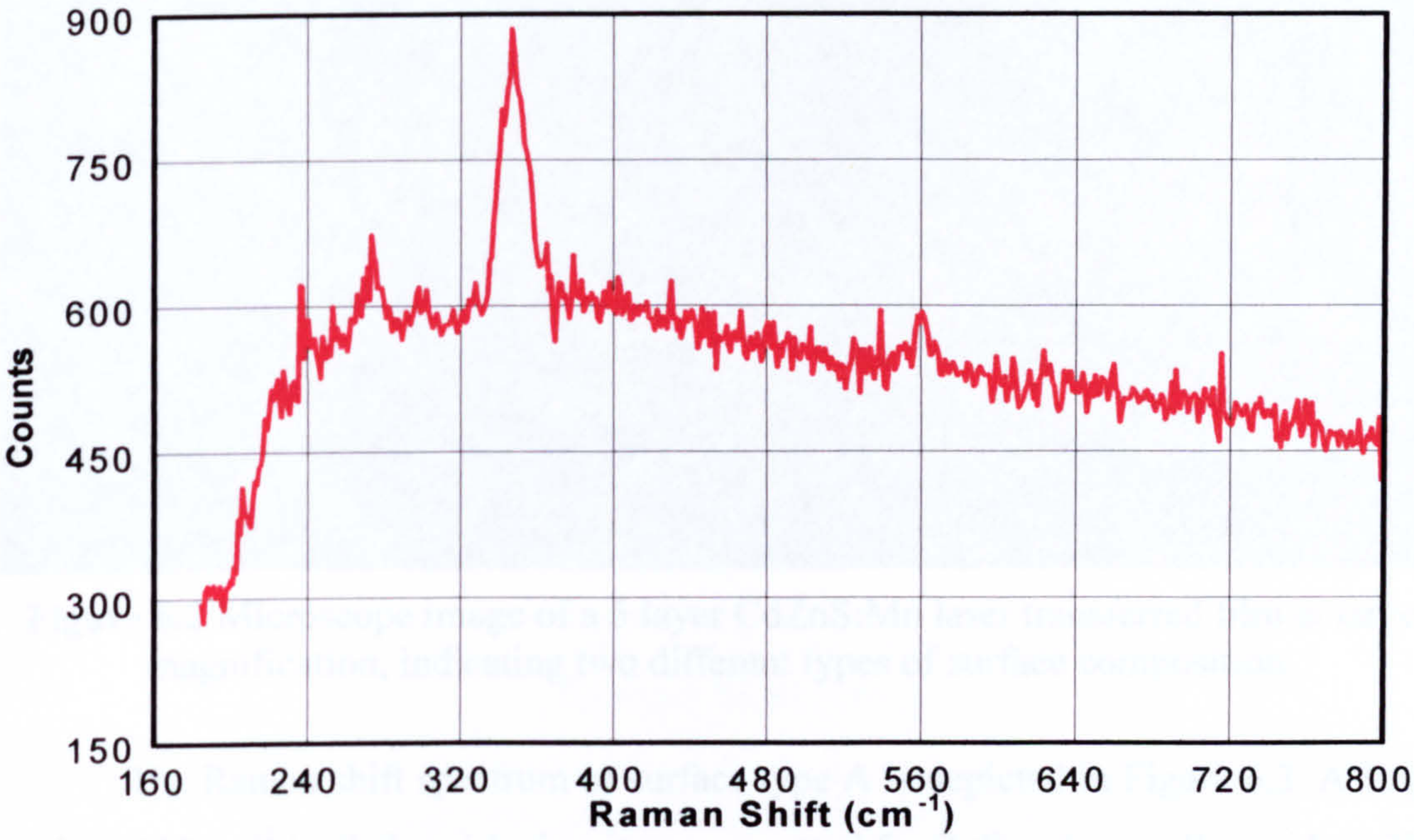

Figure 6.1 Raman spectrum of 6 successive layers of laser transferred ZnS by 0.85 Jcm^{-2} per pulse.

Two different spectra were recorded from the CdZnS sample. As microscopic imaging was available for targeting the area of interest, two areas of different colour were chosen for each spectrum. The two colours appeared alternating between them all over the transferred film in a rather random pattern. Figure 6.2 shows a filtered microscope image of the transferred film site, which helps identify that nature of the surface that gives the two different colours in lower magnifications. The larger pieces of lower roughness appear bright yellow or green (surface type A), while the high roughness areas appear dark brown (surface type B) under the Renishaw microscope.

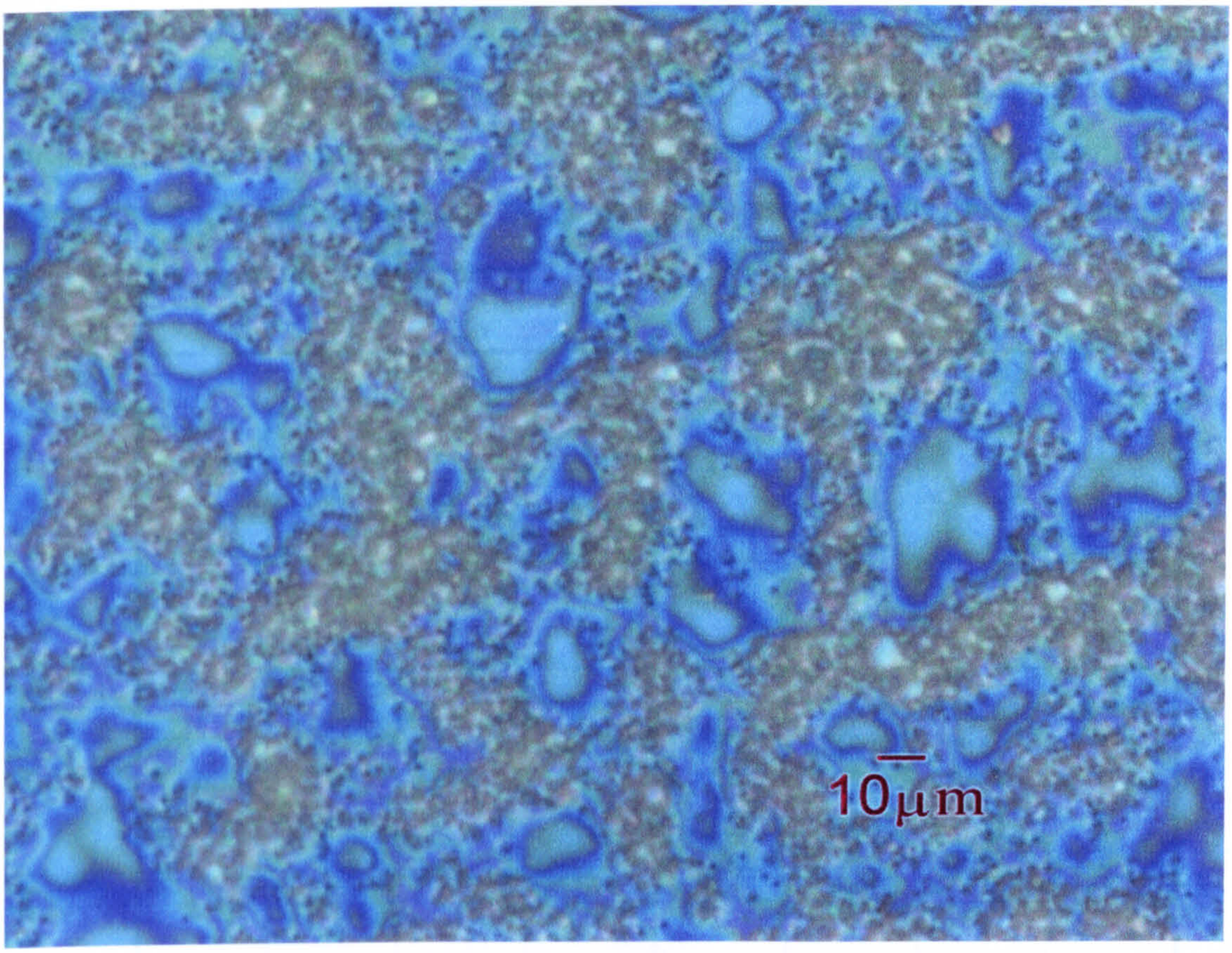

Figure 6.2 Microscope image of a 5 layer CdZnS:Mn laser transferred film at large magnification, indicating two different types of surface composition.

The Raman shift spectrum of surface type A is depicted in Figure 6.3. A large peak at 349 cm^{-1} is distinguished as it was expected for ZnS and a smaller peak at 295 cm^{-1}. Peaks at around 300 cm^{-1} are usually attributed to CdS,[7-9] though Osada et al.[4] relate it with the hexagonal phase of ZnS, but Cheng et al. claim that the transverse optical (TO) mode of the hexagonal ZnS form appears at 284 cm^{-1}.[10] Since the film under inspection consists of both zinc and cadmium sulfide, it is normal to expect a peak for CdS. On the other hand, one would expect the CdS related peak to be of at least the same size of the ZnS one and if we consider the solubility product difference of the two materials, a much larger one should be observed at 300 cm^{-1}. Here it is assumed that a larger participation of one or the other material would scatter a greater amount light corresponding to its lattice structure and also that there is a phase separation between the two materials.

A smaller sharper peak can also be seen at 269 cm^{-1} and an even smaller and wider peak at around 220 cm^{-1}. A peak at 270 cm^{-1} is attributed by the literature, to the TO mode of CdS with an accompanying surface phonon shoulder at 260 cm^{-1},[11] or to the TO mode of cubic ZnS[5]. The 220 cm^{-1} peak is attributed to the Mn

impurities by Yang et al.,[5] but it is also observed by other researchers to arise from undoped lattices,[4, 6, 10] and also a peak from small concentration of species (suitable for luminescent semiconductor doping), is not expected. Nonetheless, it is still hard to argue that these two peaks are not noise generated features that coincide with observations from other researchers.

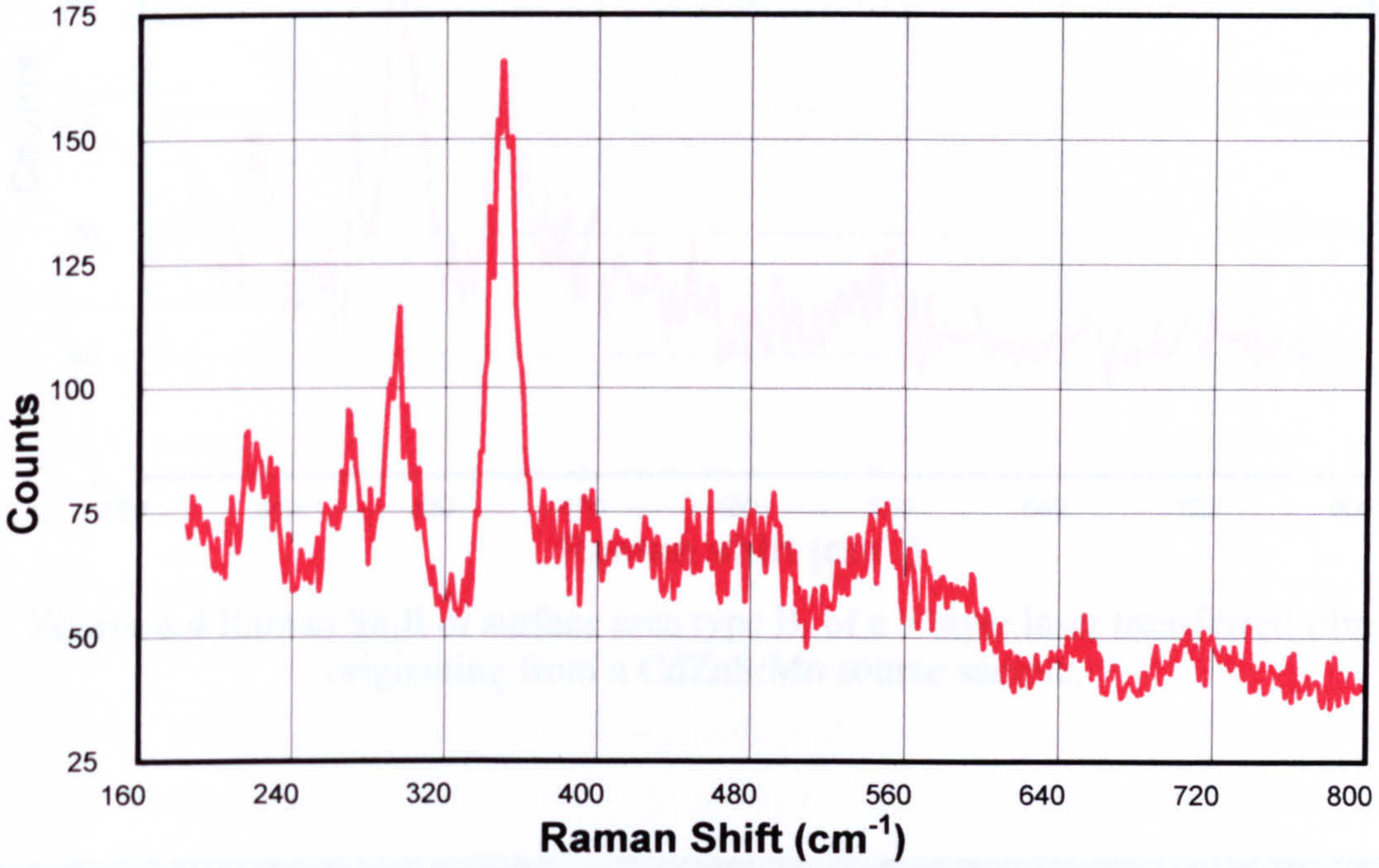

Figure 6.3 Raman shift spectrum of surface area type A, of a 5 layer laser transferred film, originating from a CdZnS:Mn source sample.

Taking a spectrum from surface type B, the opposite situation is revealing. A peak at 295 cm^{-1} appears much larger than the now wider peak at 349 cm^{-1} (see Figure 6.4). The smaller peaks at 220 and 270 are again present but still do not discern much from noise. The different appearance under the microscope and balance of the Raman peaks in the spectra of the two types of surface suggest that there is a phase separation between CdS and ZnS, at least after a multiple transfer has taken place. The separation is rather random in this case as it is observed in Figure 6.2, but the participation of each phase in terms of area covered in this microscope image is approximately 50%, which is not anticipated even with equal weight quantities of the two metal chloride salts. However, the gradual colour change in Figure 6.5 illustrates that the distribution of material changes between different areas. Yet there was no observed pattern governing the accumulation of each material over certain areas of the transferred film site, as these areas could be found in the centre, edge or randomly orientated at the boundaries of the multilayered transfer.

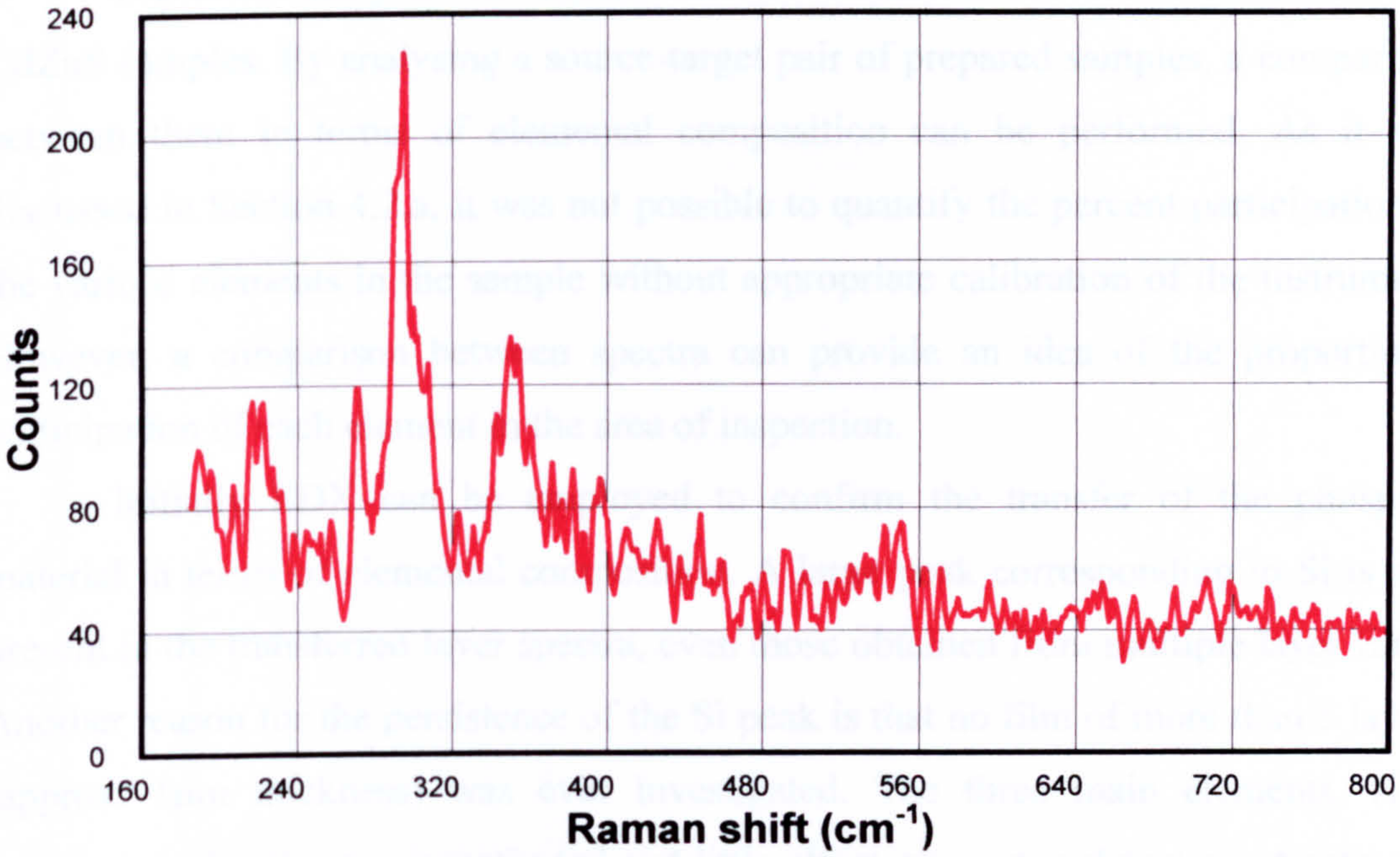

Figure 6.4 Raman Shift of surface area type B, of a 5 layer laser transferred film, originating from a CdZnS:Mn source sample.

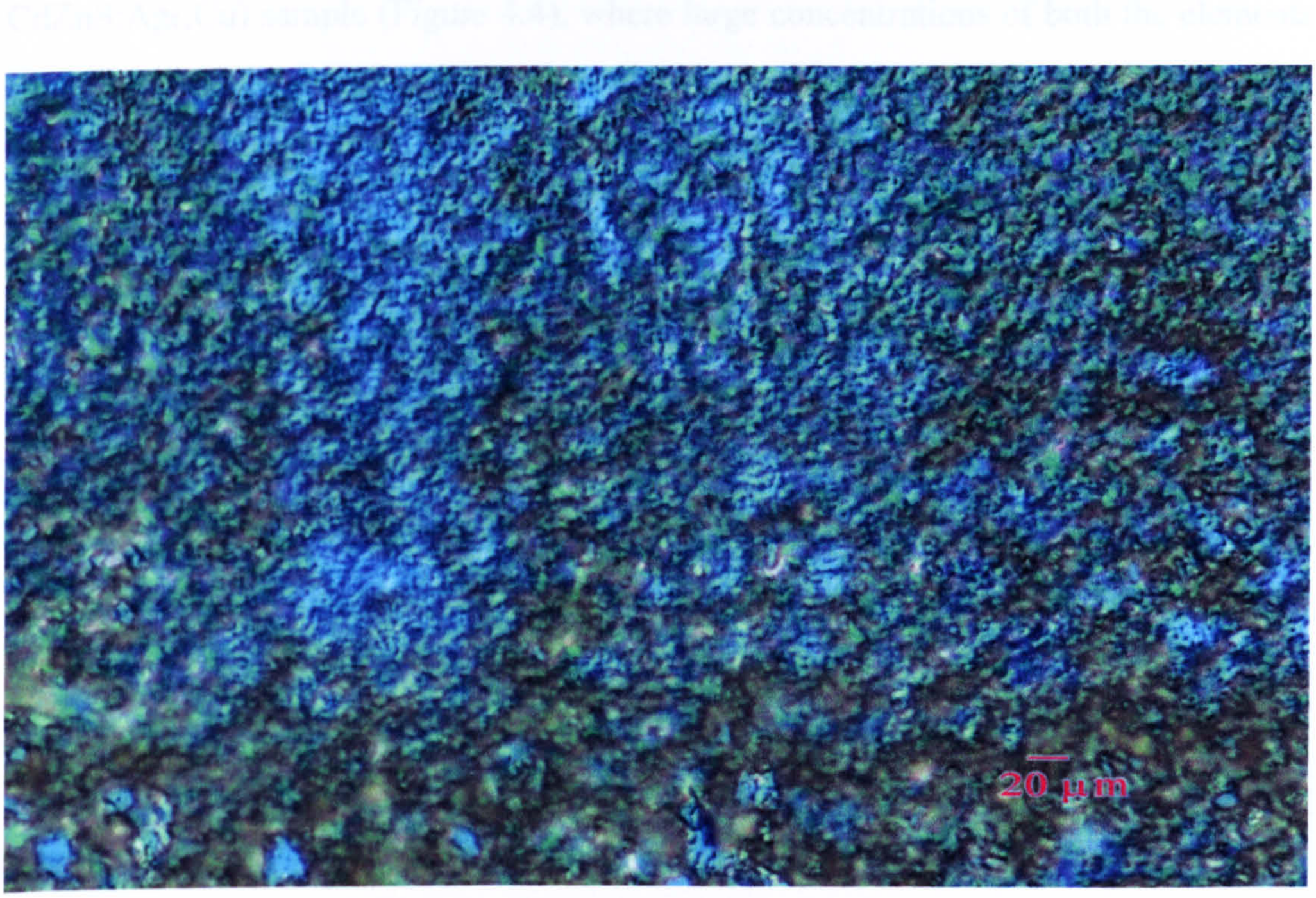

Figure 6.5 Microscope image of a 5 layered CdZnS:Mn laser transferred film, indicating the difference in area distribution of the two types of surface composition (material phase).

6.2.b. EDX of Transferred films

Elemental analysis was carried out on the transferred films of both ZnS and CdZnS samples. By analysing a source-target pair of prepared samples, a comparison between them in terms of elemental composition can be performed. As it was discussed in Section 4.2.a, it was not possible to quantify the percent participation of the various elements in the sample without appropriate calibration of the instrument. However, a comparison between spectra can provide an idea of the proportional participation of each element in the area of inspection.

Initially EDX can be employed to confirm the transfer of the phosphor material in terms of elemental composition. A large peak corresponding to Si is still present in the transferred layer spectra, even those obtained from multiple layer films. Another reason for the persistence of the Si peak is that no film of more than 5 layers (approx. 1μm thickness) was ever investigated. The three main elements, zinc, cadmium and sulfur are investigated and little effort was put in detection of activator species as their concentrations were usually at the lowest limits of detection. Activator impurities were only detected on thin films left back on the ablation sites of a CdZnS:Ag(,Cu) sample (Figure 4.4), where large concentrations of both the elements were involved in the chemical preparation bath. The very small concentrations of activator species required for electroluminescence should normally lie below the detection threshold of the OX200 EDX instrument, here roughly taken as 1%.

The spectra of a triple layer transfer of a ZnS film and its source are compared in Figure 6.6. The height ratios of the sulfur K_a and zinc L_{a1} peaks were calculated at 1.97 for the source film and 2.45 for the target film. This is taken as an indication of zinc being left behind, or being lost in the transfer. The scenario of an amount of zinc atoms being left behind after the transfer, fits well with the growth scenario analysed in section 4.8 according to which an initial layer of ZnO is deposited first on the glass substrates before the ZnS or the CdZnS main film forms. The scenario is also consistent with what is observed by optical microscopy in Figure 6.9, where depending on the laser pulse energy, a layer of different thickness is left behind on the source sample. This layer is expected to be richer in Zn than the overall as deposited film. A distinctive peak at 3.6 keV appears in the target spectrum, which belongs to the calcium atoms incorporated in the window glass microscope slide substrate that was used in this experiment.

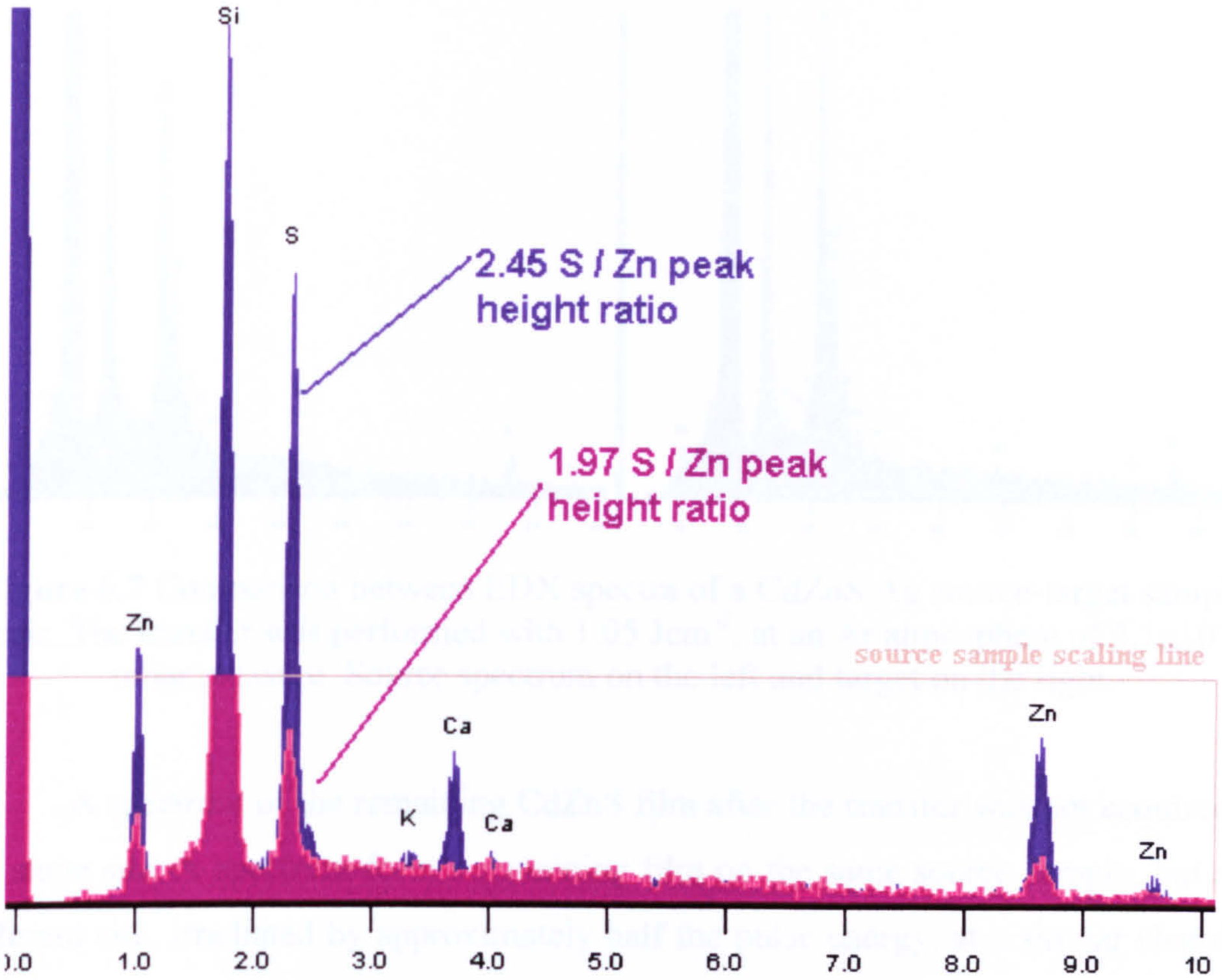

Figure 6.6 Comparison of EDX spectra acquired from a source-target sample pair, indicating calculated S/Zn corresponding peak height ratios. The source spectrum is indicated with purple and the target with blue.

Another comparison between EDX spectra of a transferred film and its chemically deposited origin, further supports the homogeneous formation of CdZnS clusters and their conditional deposition on a precursor ZnO/ZnS layer. In Figure 6.7, the three peaks corresponding to the cadmium L_{a1}, L_{b1} and L_{b2} lines, are observed at a greater height in the target sample spectrum, than in the source. The sulfur peak is again used here as a means of comparison between the spectra. Moreover, the Zn peak at approximately 1 keV is again weaker for the target sample. It is not expected that the entire CdZnS layer is transferred across to the new substrate by the LIFT process. Whether it is only composed of clusters, or of a combination of homogeneously and inhomogeneously grown material, a part of it is expected to be left behind with the Zn rich film, especially at lower pulse energies.

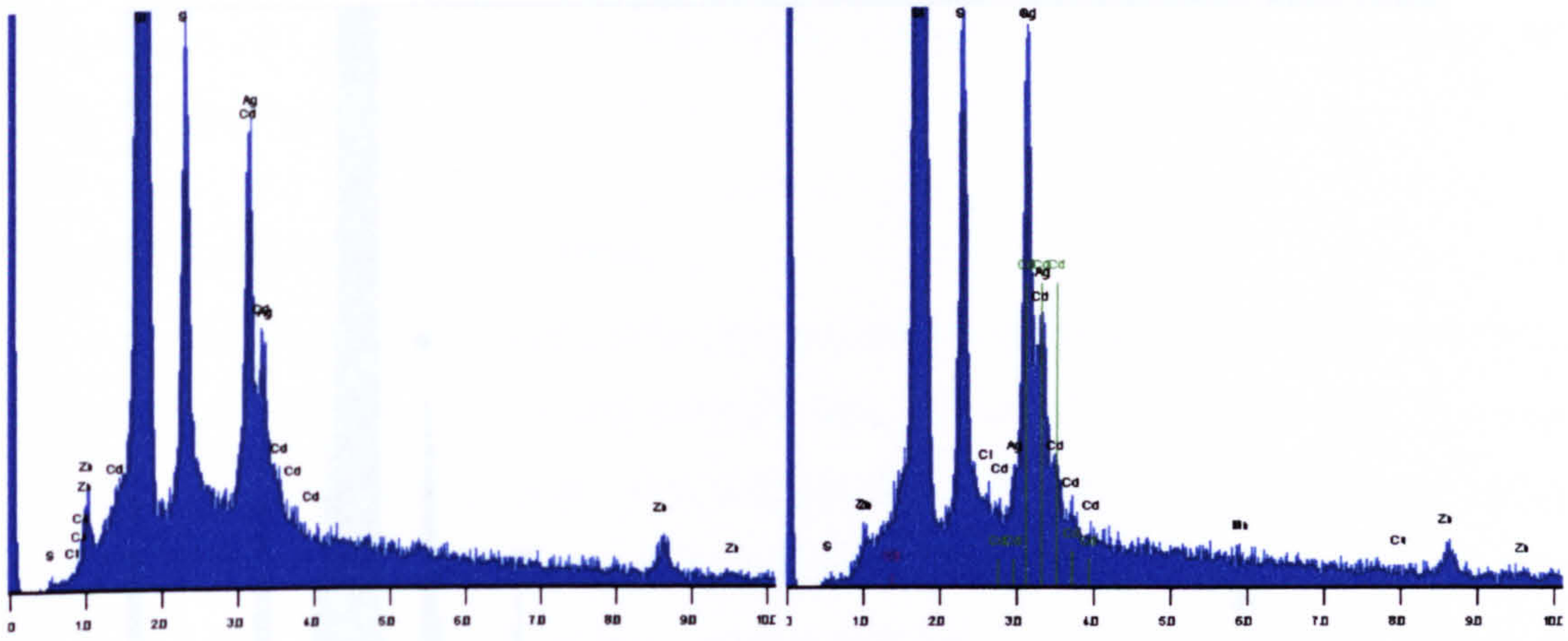

Figure 6.7 Comparison between EDX spectra of a CdZnS:Ag source-target sample pair. The transfer was performed with 1.05 Jcm^{-2}, at an Ar atmosphere of $3.1x10^{-2}$ mbar pressure. Source spectrum on the left and target on the right.

A spectrum of the remaining CdZnS film after the transfer was not acquired at the same site. A spectrum from a remaining film on the same source sample, but at a different site, irradiated by approximately half the pulse energy, at a similar chamber pressure, strongly agrees with the chemical deposition scenario discussed above for the CdZnS samples (Figure 6.8). Here the Zn peak at 1 keV is much larger than the sulfur peak, while the cadmium triplet is barely visible. A much stronger peak is found at 2.95 keV, close to the silver L_{a1} line and also a weak but distinguishable peak at 8 keV, which is attributed to the copper K_a transition. Copper is again expected to be incorporated as a contaminant from a previous bath, very concentrated in copper chloride salt. Combining this observation, concerning strong peaks of Cu and Ag in Figure 6.8 and the fact that the chemical deposition of films progressed much faster with addition of metals which would give sulfides of very low solubility product, such as Ag and Cu, shows that doping with such elements in the bath, aids both the homogeneous and inhomogeneous growth of films. It appears that apart from nucleating clusters, silver and copper sulfides have the ability to initiate or promote film formation on the glass substrates.

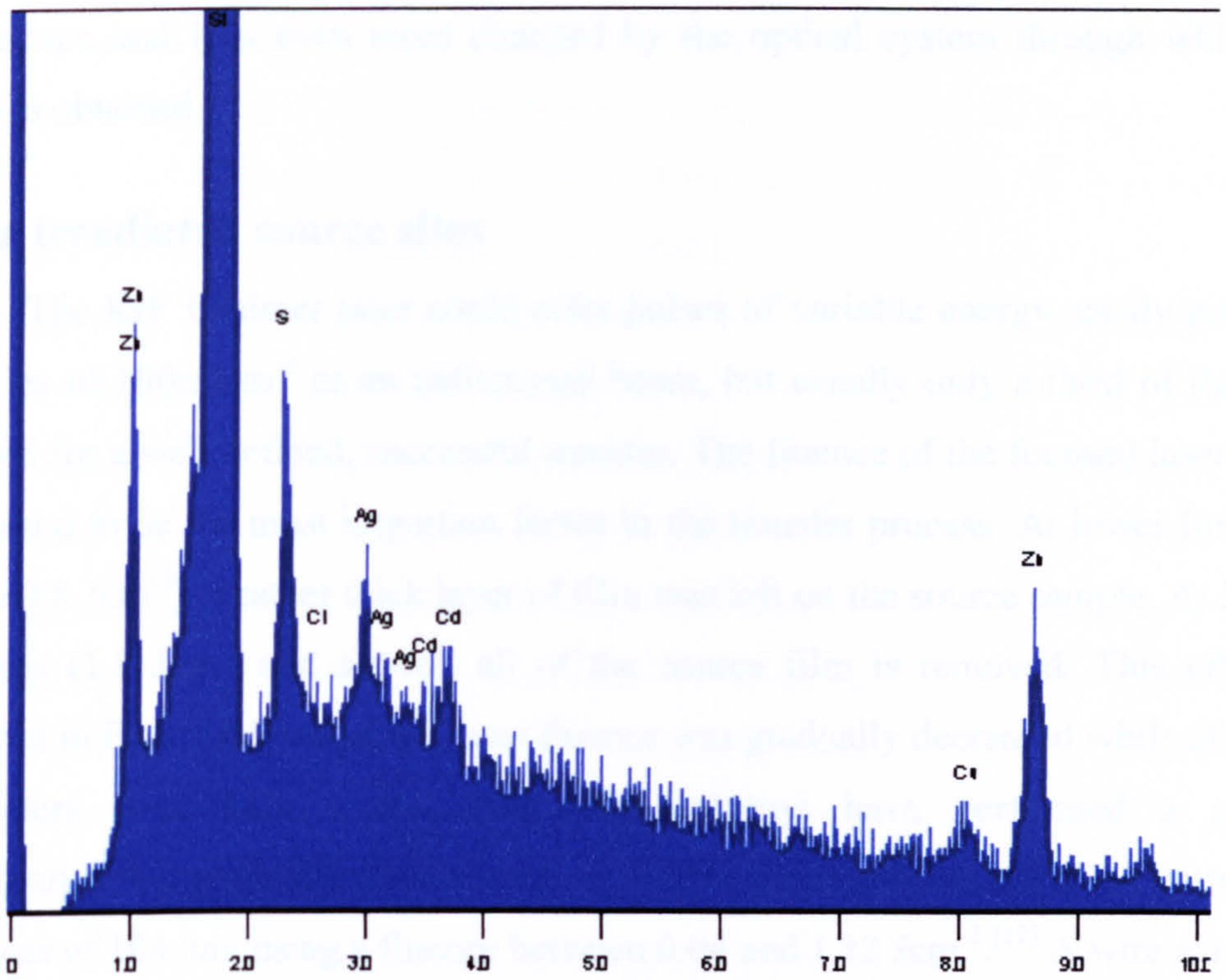

Figure 6.8 An EDX spectrum of a remaining layer of CdZnS:Ag film at the source sample, after the LIFT process. Site was irradiated with 0.6 Jcm^{-2}, at an Ar atmosphere of $2.5x10^{-5}$ bar pressure.

6.3 Surface Morphology

6.3.a. Optical Microscopy

Almost every laser transfer performed was examined under the optical microscope. Images of both the transferred film and the origin sites were obtained at different magnifications. Observations based upon the images are used to determine the best transfer conditions, such as fluence and chamber pressure and the effects of varying these conditions on the quality of the transferred film and efficiency of the process. In this section, the observations are separated into those concerning the sites irradiated at the source sample and the sites covered by transferred film at the target samples. Observation of the source sites aids in forming a better understanding of the transfer process, while images of the transferred film portions are a direct representation of the resulting film. There is almost no difference between ZnS and CdZnS films, either doped or undoped, apart from possibly the colour of the film, but that changes between areas of different consistency, when observed under a

microscope and it is even more changed by the optical system through which the image is obtained.

Laser irradiated source sites

The KrF Excimer laser could offer pulses of variable energy, easily reaching fluencies of 100mJcm^{-2} as an unfocussed beam, but usually only a third of that was required for a well defined, successful transfer. The fluence of the focused laser beam was found to be the most important factor in the transfer process. At lower fluencies (0.4 to 0.8 Jcm^{-2}), a rather thick layer of film was left on the source sample. At higher fluencies (1.8 Jcm^{-2} and above), all of the source film is removed. This effect is observed in Figure 6.9 where the laser fluence was gradually decreased while all other parameters were kept stable. Tòth and Szörènyi have performed a similar investigation of gradually transferring a double layer of Se and Ge, with total thickness of 104 nm, using a fluence between 0.04 and 1.12 Jcm^{-2}.[12] A wire was used across the rectangular aperture in order to determine the imaging quality of the optical setup and therefore a white line of material is distinguished on the irradiated sites. Changing the chamber pressure was found to affect the amount of film left behind, but to a much smaller extent than fluence did. Higher pressures would force greater temperatures to be reached close to the source substrate before the film's detachment. The chamber pressure would need to be varied by many orders of magnitude in order to achieve such definitive effects as in the figure below.

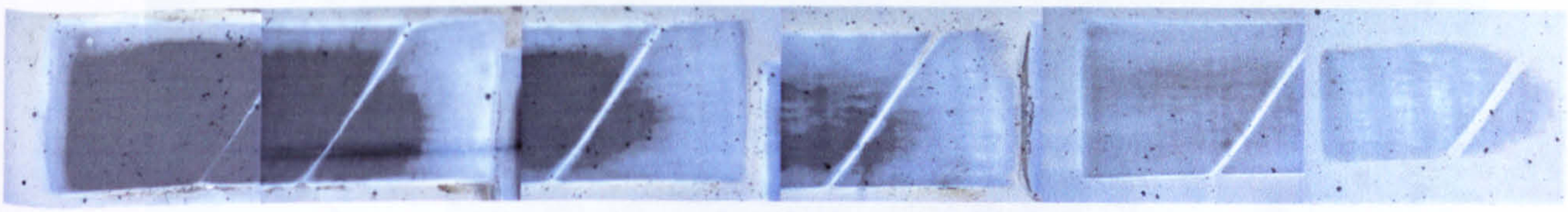

Figure 6.9 Irradiated areas at a source sample, where a beam of varying fluence was used. The chamber pressure was 3 x10^{-4} mbar. From left to right the focussed laser pulse fluence was, 1.8, 1.6, 1.3, 1.1, 0.8, 0.4 Jcm^{-2}. The darker/grey areas are the glass substrate and the lighter or brown areas are covered by film of some type.

Another aspect of the transfer process, which is significantly affected by the laser light fluence, is the definition of the imaged aperture shape. The best definitions of the aperture shape are found at rather low impinging fluencies of 0.5 to 0.6 Jcm^{-2}, where the source site is fully covered with a thin layer of material that is left behind.

At higher energies, the definition at the edges starts reducing and the sides of the rectangular pulse shape are transformed into curves. The material under the area screened by the wire on the aperture is also affected, until most of it clears as the fluence of the focussed beam approaches 1.7 Jcm^{-2}.

Another factor defining the quality of a transfer is the amount of debris deposited around the site, almost equally on the source and the target. At approximately 1 Jcm^{-2} a small amount of debris starts to appear along the sides of the pulse shape. It does not seem to cause great distortion to the shape of a single shot transferred film, but it may affect adjacent transfers and it starts forming into a film when multiple transfers are performed over the same area. At higher fluencies the effects becomes quite visible and often results in most of the source film being converted into side-deposited debris. An example is given in Figure 6.10. where the sides of two source irradiated areas are shown (laser fluence at 1.9 and 2.2 Jcm^{-2}), with debris scattered from each transfer almost over the same area.

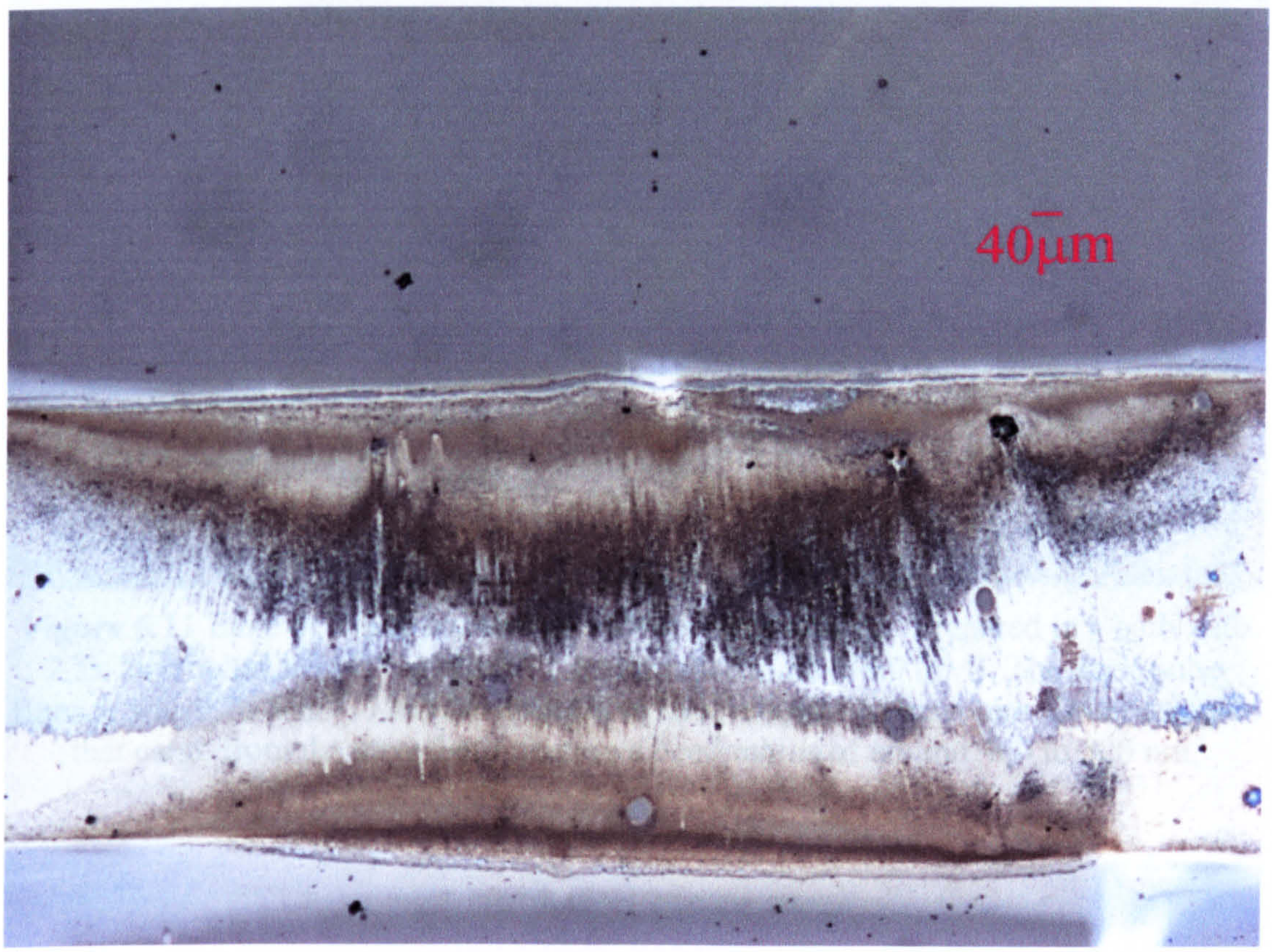

Figure 6.10 The edges of two source sites, irradiated with a beam of 1.9 Jcm^{-2} (lower) and 2.2 Jcm^{-2} (upper) at a chamber pressure of $1.1x10^{-5}$ mbar. A large volume of the irradiated film is laid down as debris on both target and source substrates.

It was interesting to find out, using high magnification, that the edge of the irradiated site is more clearly defined when the source film has a beadlike structure. The film in Figure 6.11 has an approximate bead size of 400 to 500 nm, which was measured on films prepared in the same chemical bath (with 14.2 mM $ZnCl_2$ and 88.0 mM TAA). It has been irradiated with 0.75 Jcm^{-2} which managed to detach the film completely from the source substrate (blue area). Moreover, it seems that performing the LIFT process on films with beadlike structures minimises the amount of debris scattered next to the site edges. There is also no thin layer of the film left behind. When lower energy is used on a film of similar beadlike structure, a very thin layer is left behind. Such is the case for the site depicted in Figure 6.12, which was irradiated by 0.4 Jcm^{-2}, where a light brown film is distinguished in the centre of the missing film area.

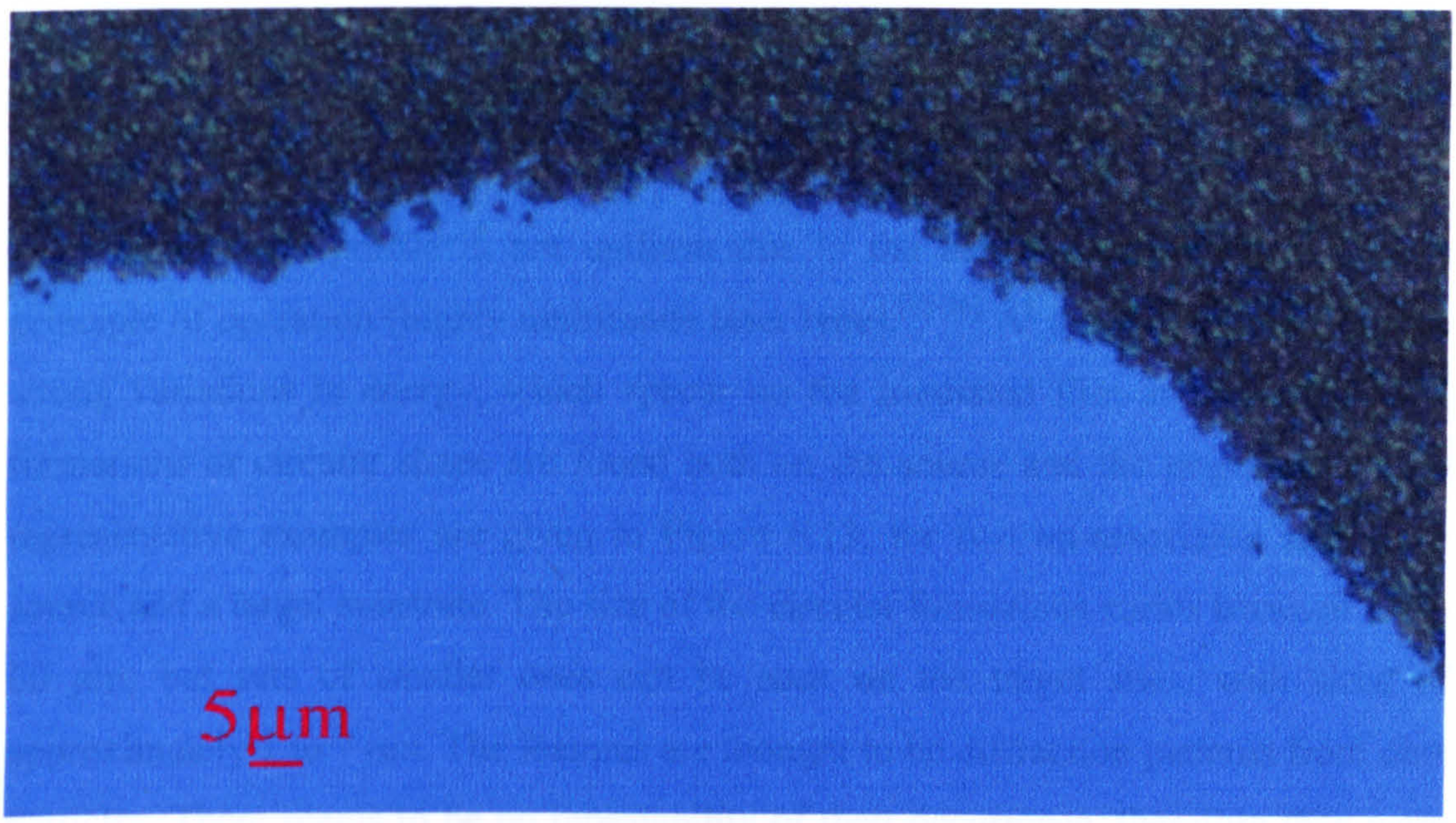

Figure 6.11 Edge of irradiated area at a source ZnS sample. Prepared in a bath with 2.5x zinc chloride (14.2 mM) and 1.5x thioacetamide (88.0 mM). The laser pulse fluence was 0.75 Jcm^{-2}. The film appears to have a bead-like structure. Other samples that came from the same bath, feature a bead radius of around 400 to 500 nm.

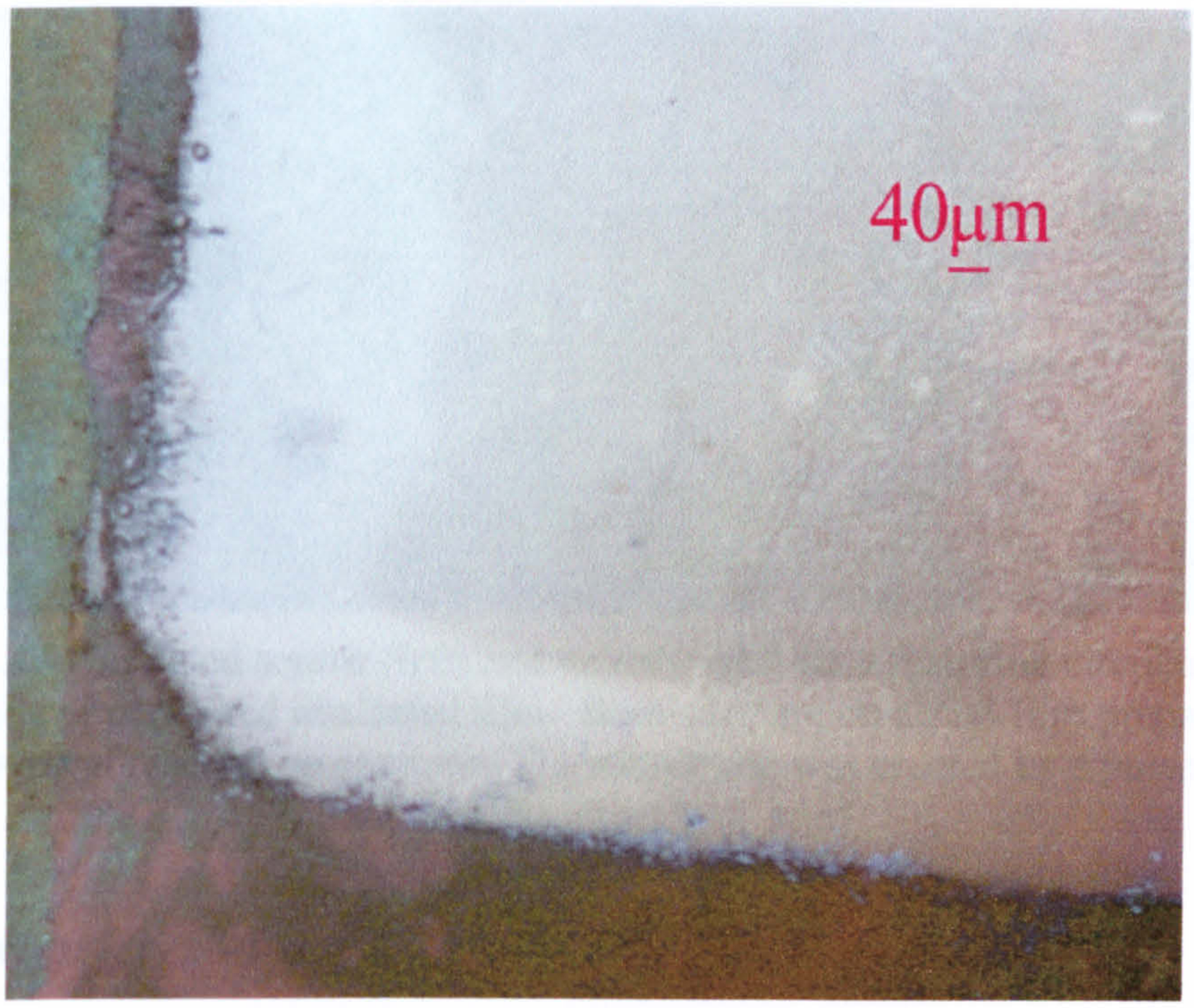

Figure 6.12 Source irradiated area of a CdZnS film, prepared with 0.25 g (8.2 mM) of metal chloride salts. It is expected to have a beadlike structure of a bead radius around 400 to 500 nm, by SEM examination of other source samples of the same bath.

The beam profile is not uniform due to the nature of the excimer laser's principle of operation (highly multimode laser type).[13-16] At the same time, there are strong variations in energy, which appear on the irradiated film area. Such typical formations or circular shape are found both on the source and the target sites. Two representative examples are given in Figure 6.13, for two un-associated sites on a source and a target substrate. The size of the circular formations varies between 15 to 60 μm, but sets of smaller ones can be seen on the target sites, with sizes of approximately 1 to 7 μm. The features are thought to be diffraction patterns from dust particles. There seems to be no repeatability of their occurrence, therefore they were either adhered on the side of the source glass that directly faced the laser, or floating dust particles in the beam path. These patterns are discussed here only for clarification purposes and are not taken in any further consideration in the analysis of results.

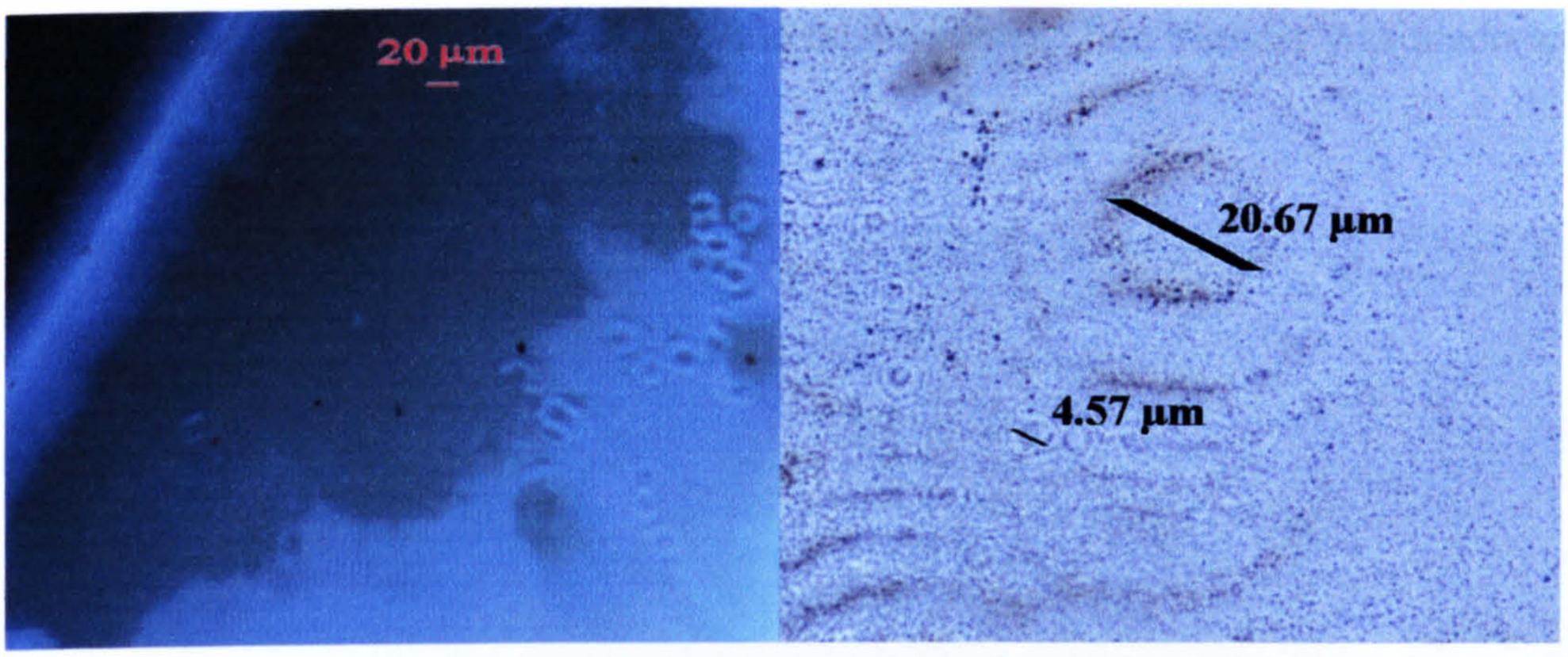

Figure 6.13 Unrelated source (left) and target (right) sites featuring circular patterns of missing or deposited irradiated film. Both sites are on a ZnS film prepared in a bath of typical reactant proportions. The source site was created by a pulse of 1.18 Jcm^{-2} and the target 1.84 Jcm^{-2}.

Laser Transferred films

Transfers on new substrates were accomplished with all types of chemically deposited films. Generally when the LIFT process is applied, it is expected for the material to reach its melting point in order to adhere to the new substrate. Adherence of the transferred films was achieved under most conditions, but the material might have never passed completely into the liquid phase. Zinc sulfide and cadmium sulfide are known to sublime at temperatures around 1180 and 980 °C respectively, in atmospheric pressure.[1, 17-19] Melting can be achieved in ZnS at 3.5 bar and in CdS at 100 bar but at almost double the quoted sublimation temperatures. The experiments are performed in a vacuum chamber set typically at pressures of the scale of 10^{-5} bar, but the distance between the two substrates is only 15 μm, moreover, the transfer takes place in a few nanosecods. These three facts make it difficult to determine whether the films would theoretically pass into a liquid phase at some point in the transfer process. Thus, the surface formations of the transferred films are contemplated with regard to the adhesion process.

It is more interesting to observe a transferred film at places with a distinguishable level difference between the film and substrate surfaces, for example a well-defined edge, or a contained area of detached film. A rather well defined edge is depicted in Figure 6.14 where the whiter part is covered by transferred ZnS film. The surface of the glass after the edge of the film is partially covered by white material. It has been carried and deposited there by the expanding gas that propelled the transferred film. Marks from the motion of gases expanding outwards can be seen

over the transferred film, on its edges and beyond them. The transfer was made with a fluence of 0.87 Jcm^{-2}.

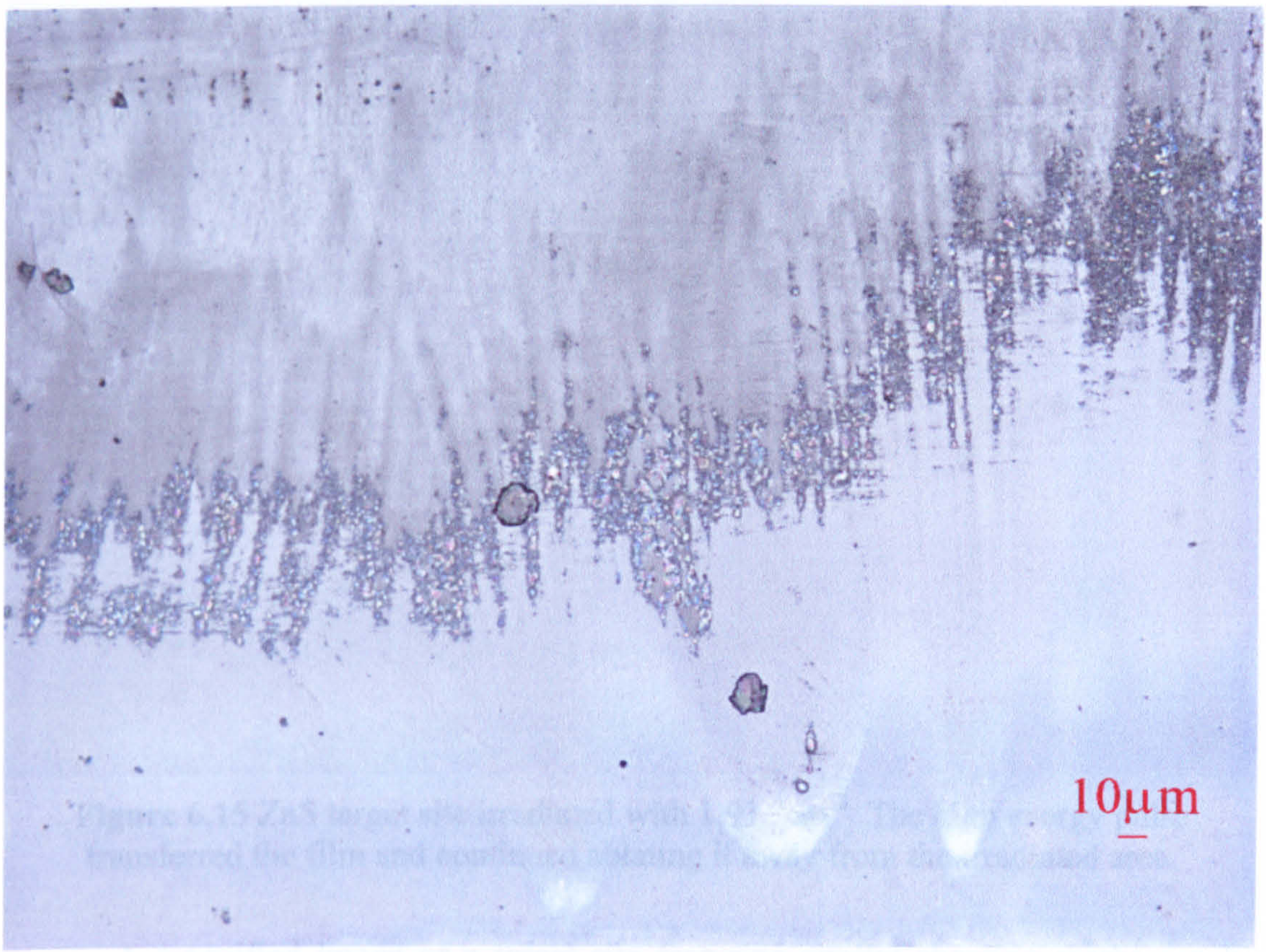

Figure 6.14 Transferred ZnS film edge, with a fluence of 0.87 Jcm^{-2} at a chamber pressure of $1.7x10^{-2}$ mbar.

At higher fluences, the transferred material continues to ablate even after its attachment to the target substrate. Scrape marks from the motion of the gases are becoming much more intense and above 1.3 Jcm^{-2} the film on the target substrate is gradually being depleted, revealing again the substrate underneath it. In Figure 6.15 an attempt has been made to transfer a ZnS film with a high fluence of 1.91 Jcm^{-2}. The centre of the irradiated site is emptied from the attached film. White film is seen close to the edges and also a large amount of it is deposited out of the site's boundaries.

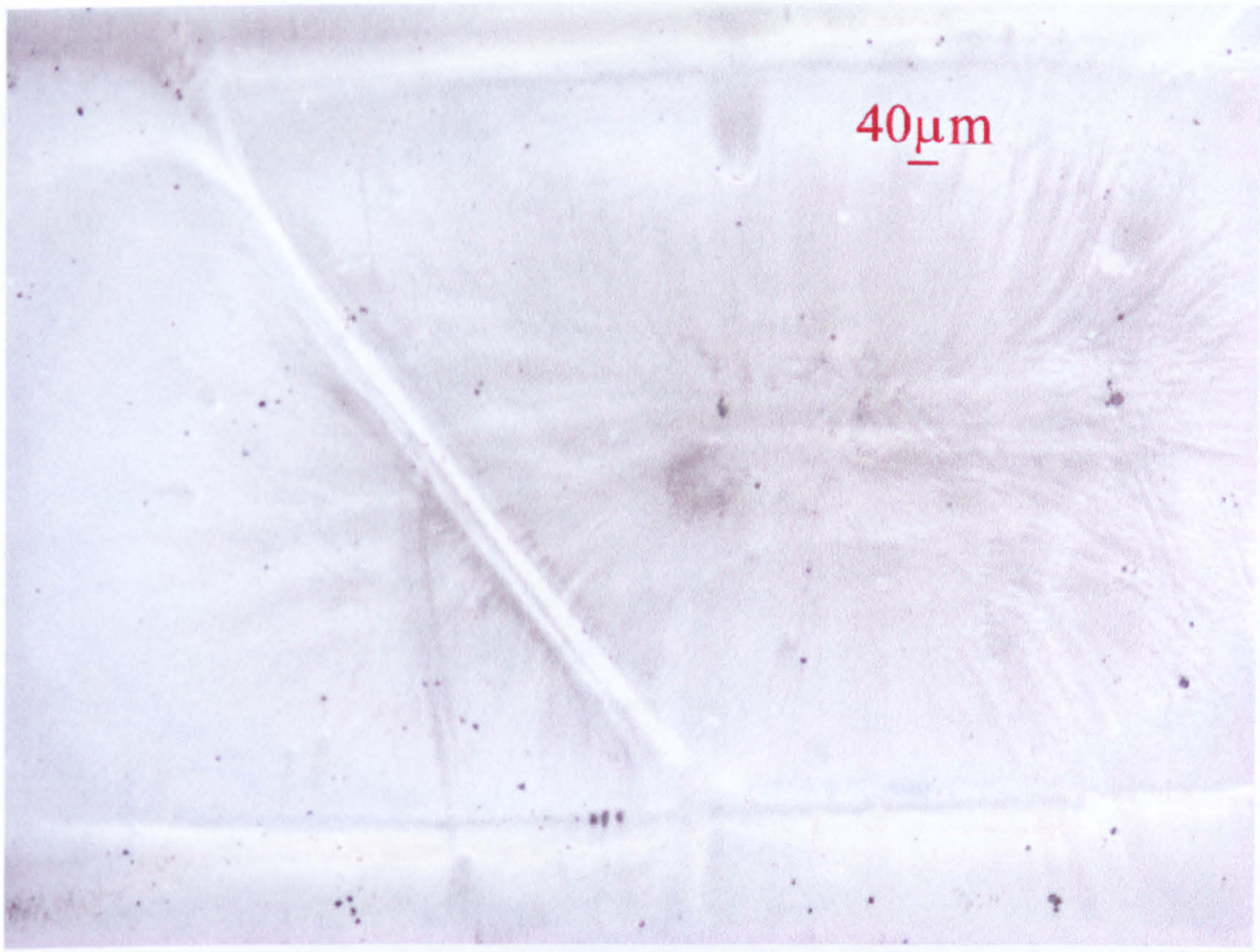

Figure 6.15 ZnS target site irradiated with 1.91 Jcm^{-2}. The high energy pulse transferred the film and continued ablating it away from the irradiated area.

A magnified image of a target site featuring similar shearing marks can be seen in Figure 6.16. The image is centred on a tall white obstacle (film mountain) opposing the expanding motion of gasses and ablated material. The obstacle is a big volume of material that was transferred and adhered well on the new substrate. Because of its volume it persists to the vaporisation of mass induced by the excess of laser radiation. Such large volumes of transferred material are moderately frequent, but create noticeable effects on high pulse energy transfers. The empty (darker) area behind the obstacle indicates that a greater amount of material should have been removed from the target substrate's surface. So the whiter areas around the obstacle have been recovered by material transferred that was brought there from the centre of the irradiated site and recrystallised, before it had the chance of passing the site's edges.

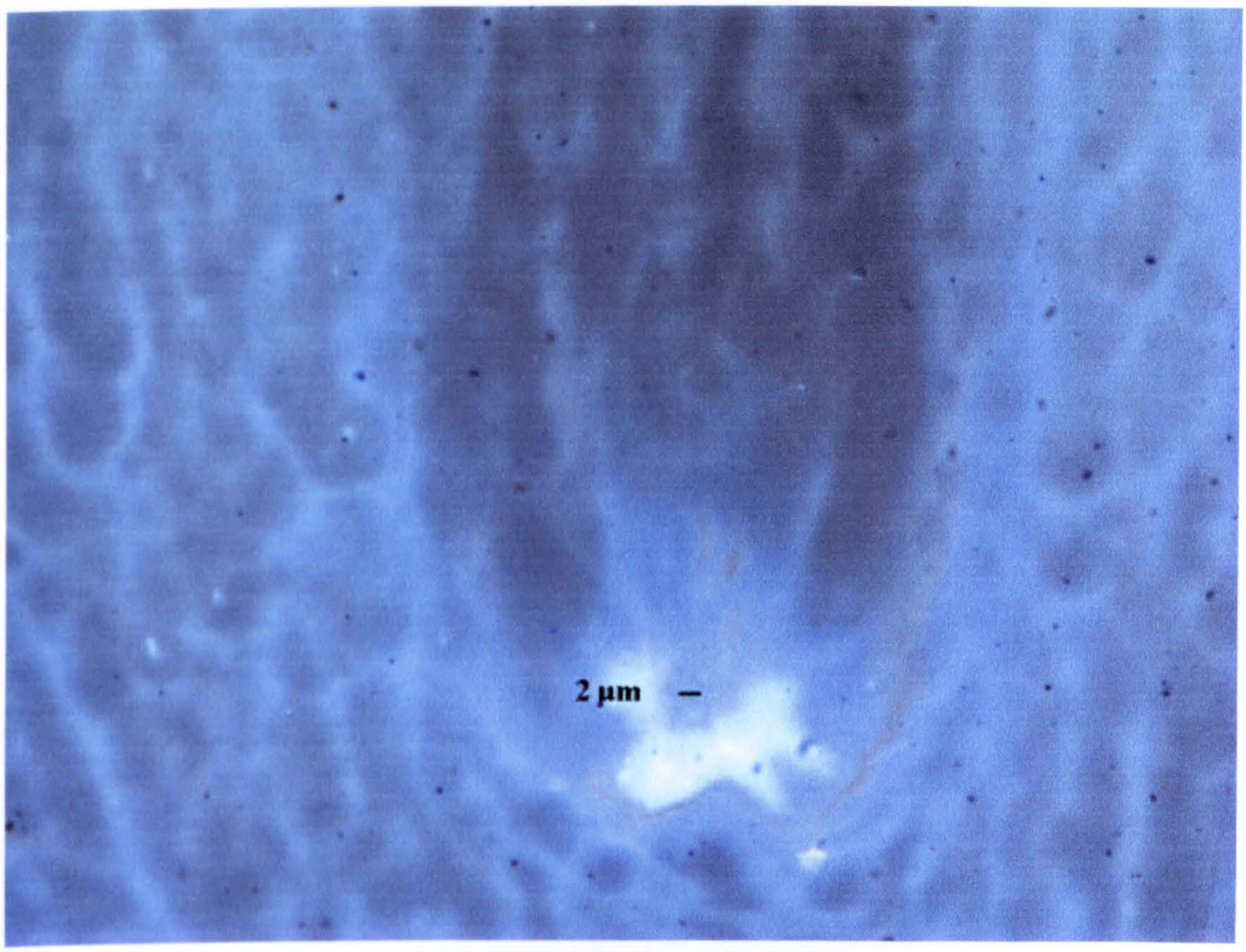

Figure 6.16 High magnification image of a large deposited volume (obstacle) at a ZnS target site. The transfer was performed with 2.07 Jcm^{-2}.

Lower pulse energies that achieve transferring of films produce more intact and well-defined layers on the target sites. An example is given in Figure 6.17 where the film seems to have been transferred as a whole on a silicon wafer target. The wafers are expected to form a thin layer of oxide on their surface, when they are kept in atmospheric air. Therefore, the properties of the material at least at a surface level are not much different from those of the silica glass slides. The film here seems to have been transferred as a whole, presenting slight cracks on the surface. The edge has a layered structure that is perhaps indicative of compression of the film during its attachment to the new substrate. The fluence of the laser pulse was 0.6 Jcm^{-2} and at these low energy transfers, there is hardly any material deposited outside the boundaries of the irradiated area. This fact enhances the definition of the transferred film shapes and defines the most suitable conditions for direct writing of such films.

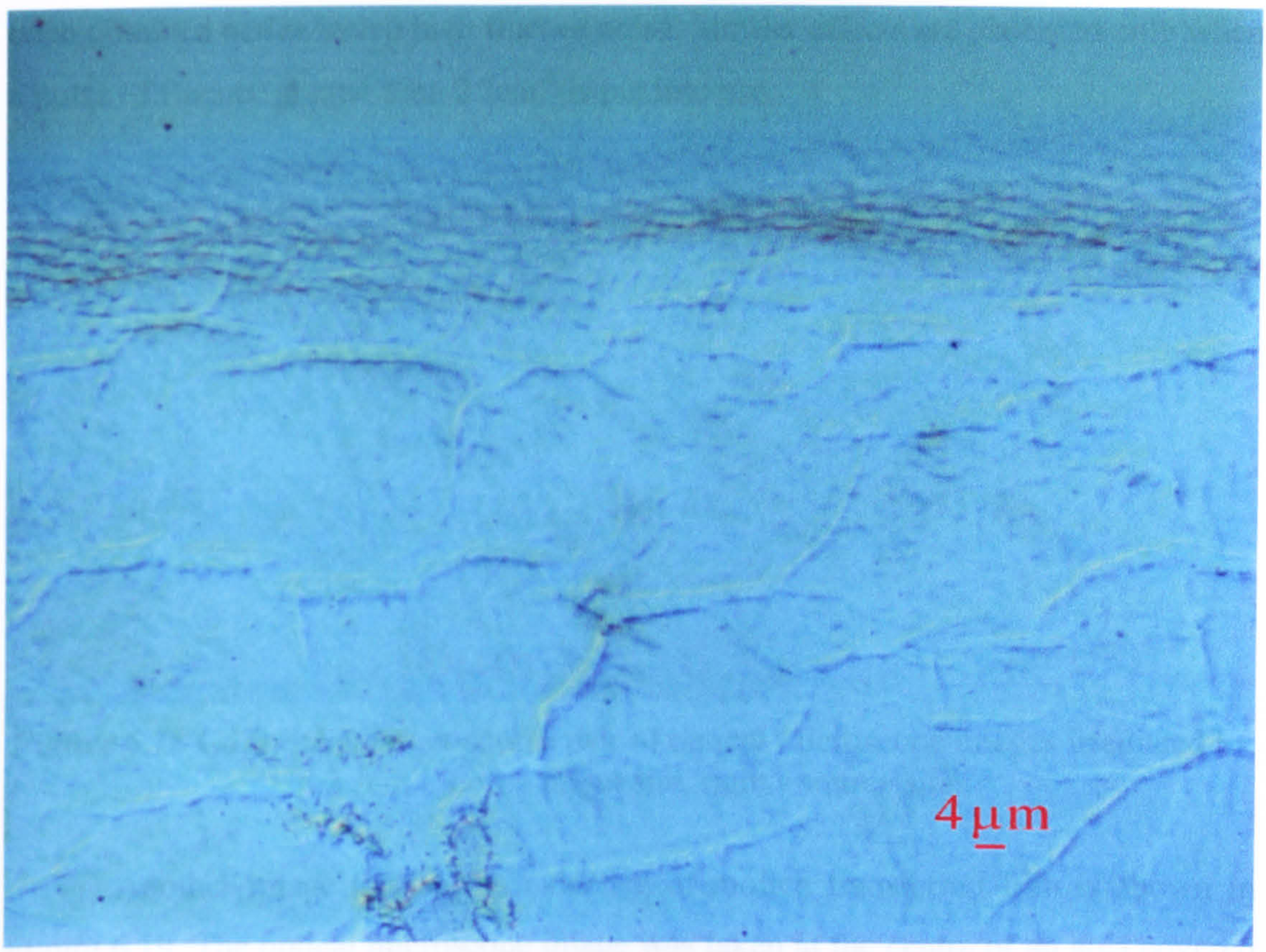

Figure 6.17 Well defined transferred film edge on a silicon wafer target substrate, irradiated with 0.6 Jcm^{-2} at a chamber pressure of $2.5x10^{-2}$ mbar.

No clear evidence of a melting film has been presented so far that are based in optical microscopy. Proof of melting film on source and target samples was found on high fluence transfers. In Figure 6.18 a source-target image pair, irradiated with 2.2 Jcm^{-2} at a $3x10^{-2}$ mbar argon pressure, is illustrated, where recrystallised drifted drops of the material are dominating both the images. The drops originate from whiter areas of film, where its thickness is greater and move away from the centre of the irradiated area. It appears that the film partially reaches its melting point and it is carried away in the form of droplets, by the expanding gasses. The film is composed of CdZnS:Ag, formed in a bath with a 2:1 ratio of Cd and Zn chloride salts. The high energy delivered to the film by the laser pulse was able to melt the transferred film and the layer left behind. As the layer left on the source substrate is expected to be ZnO, which has a melting point close to 2000 ^{o}C and the two sulfides have a melting point at slightly lower temperatures under high pressure, it could be assumed that both layers have reached such temperatures, At the same time, a high pressure was built between the two substrates, because of the high rate of gas production due to ablation. Therefore, the right conditions for melting of all three types of materials could have

been obtained under such a high fluence pulse. Similar effects are observed only when a pulse of fluence greater than 2 Jcm^{-2} is put into use.

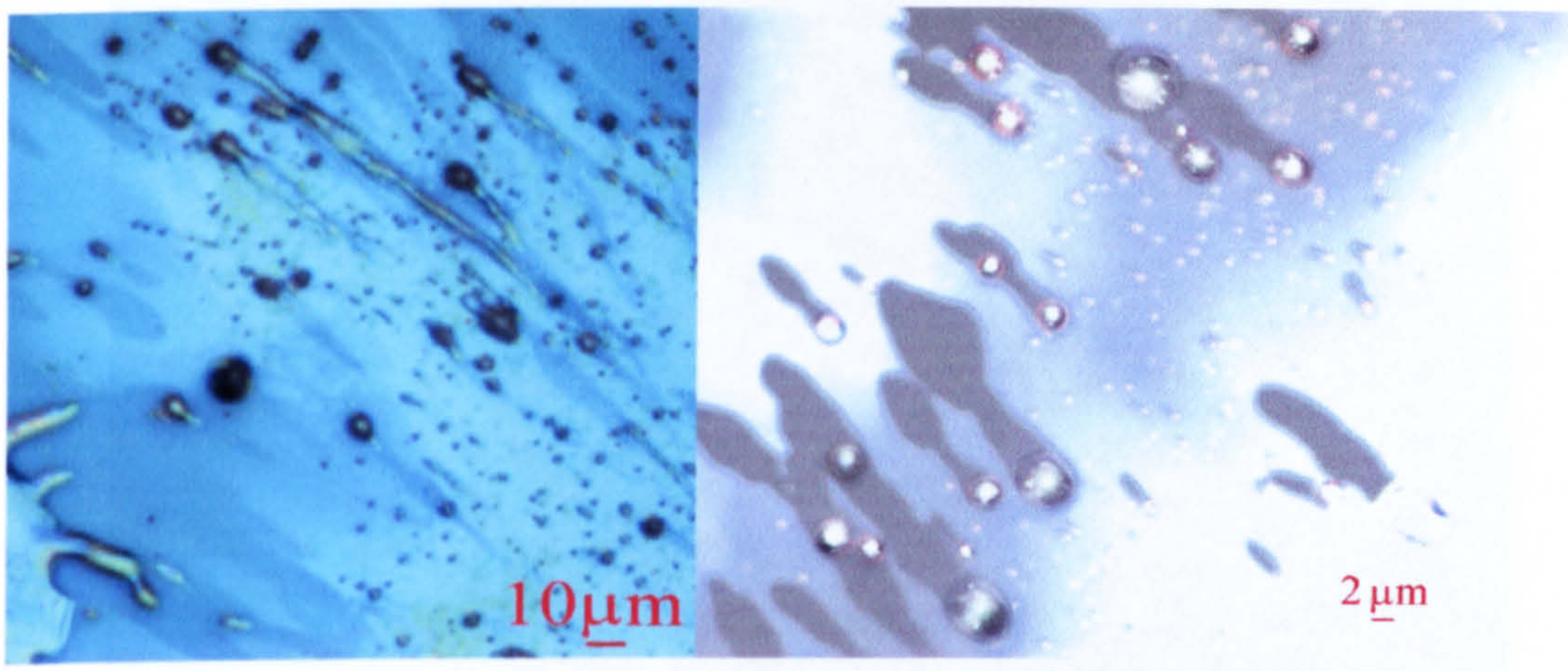

Figure 6.18 CdZnS:Ag, target-source pair of optical microscope images irradiated by 2.2 Jcm^{-2}. Left – target site, right - source site.

Another image that shows evidence of molten transferred film is shown in Figure 6.19. The optical microscope image was taken at the centre of an area covered by nine transferred layers. The transfers were performed in a chamber pressure of $3.4x10^{-2}$ mbar with a fluence of 0.76 Jcm^{-2}. The source is a CdZnS:Mn sample. There is an interchange of colours and shapes, indicating that the successive depositions of film layers, eventually moulded together. The various colours most likely correspond to different composition of the material, as analysed in section 6.2.a. The phenomenon of moulded successive layers of CdZnS or ZnS transferred even with low energy pulses is common and becomes more intense as the number of successive deposited films is increased.

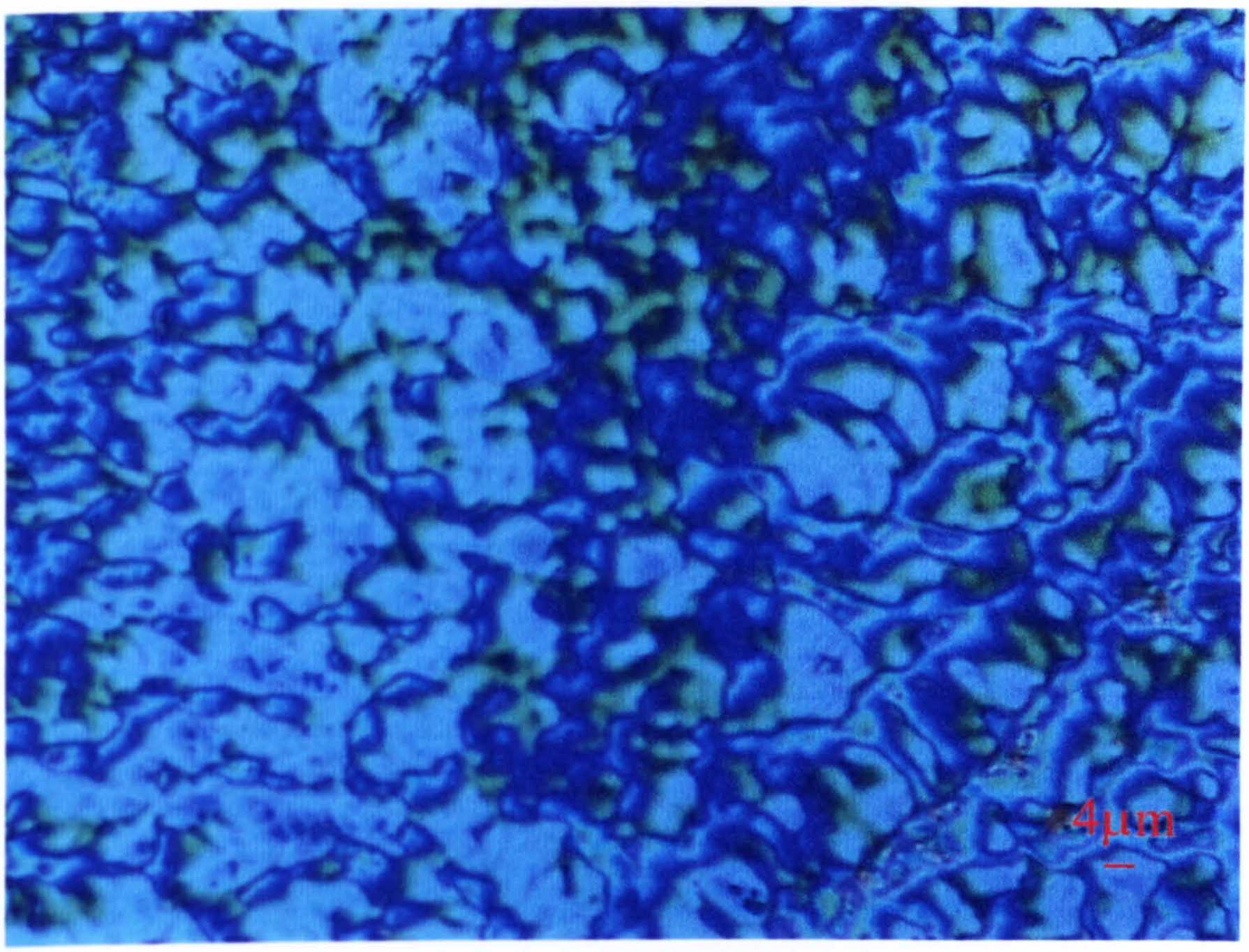

Figure 6.19 Centre of area covered by 9 successive layers of CdZnS:Mn, transferred by 0.76 Jcm^{-2} in an argon atmosphere at $3.4x10^{-2}$ mbar.

The idea of depositing multiple layers of film on the same target area originated from an observation on two overlapping transfers (Figure 6.20). The transfers were performed with quite high fluencies, 2.5 Jcm^{-2} for the first deposited film and 2.2 Jcm^{-2} for the second. Due to the high energy of the laser pulses, a large amount of transferred material was ablated from the target too, therefore leaving only a very thin white layer on the site. The narrow line that was shielded by the wire on the imaged mask retained a greater volume of transferred material that was digressively deposited there. The line was not irradiated by the laser light, therefore it maintained any material that it received. The part of the shielded line of the underlying layer that was overlapped by the new layer, was partially ablated. Though it was deformed and faded by the partial ablation, it seems to have integrated well with the new layer, adding to its thickness over the area that it resided. Therefore, it was speculated that successive pulses over the same target area at lower fluencies, would be able to deposit more and more layers of film. The process would be able to deposit films of greater thickness than that of the source sample. Moreover, the target multilayered film would consist of material fused together, instead of separate films.

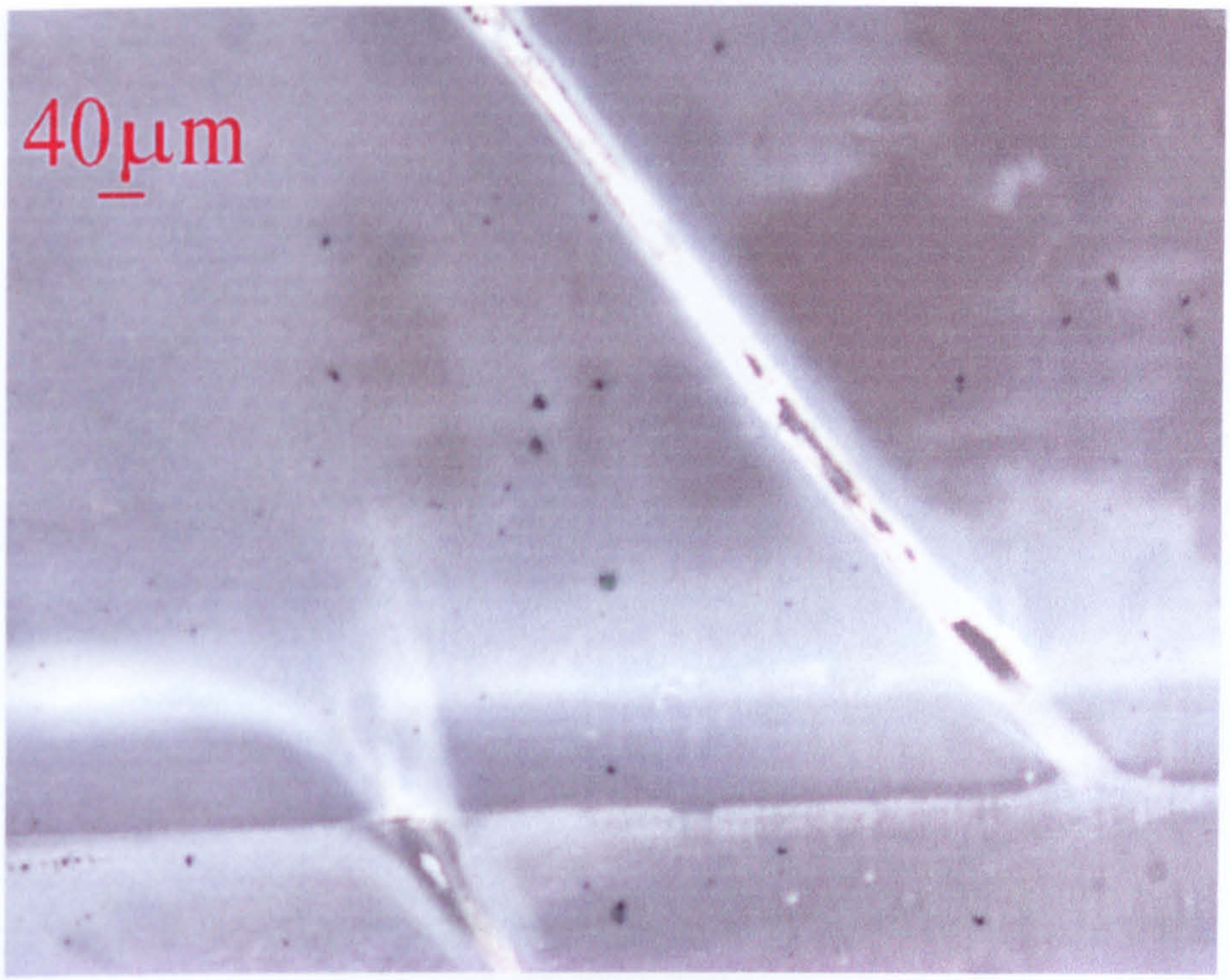

Figure 6.20 Overlapping edges of two transfers of ZnS film. The lower one was deposited first with a pulse fluence of 2.5 Jcm^{-2} and the upper one second with a fluence of 2.2 Jcm^{-2}.

Indeed, an attempt to deposit 6 overlapping layers of material proved successful. In Figure 6.21, an image of 6 ZnS film layers, where parts of them occupy the same area on the target substrate, is illustrated. The target substrate has been shifted along as a new non-irradiated area of the source substrate was being positioned over the site. The edges of each transferred rectangle layer are clearly defined even underneath the other layers. Each layer transforms the appearance of the surface over which it has been deposited. As the thickness of the film increases, the colour turns to dark blue and then yellow spots and regions start to appear. Low fluence laser pulses were used for the transfers, around 0.63 Jcm^{-2} and the source film was deposited with an increased thickness, from a bath with a double concentration of thioacetamide (112.7 mM) and a rahter large concentration of zinc chloride (14.2 mM). The image proves that overlapping of layers is possible, while at the same time, ablation of the precursor layers is avoided to a significant degree. The already examined site, illustrated in Figure 6.19 gives an idea of the progress of the resulting film after a greater number of non-displaced successive transfers.

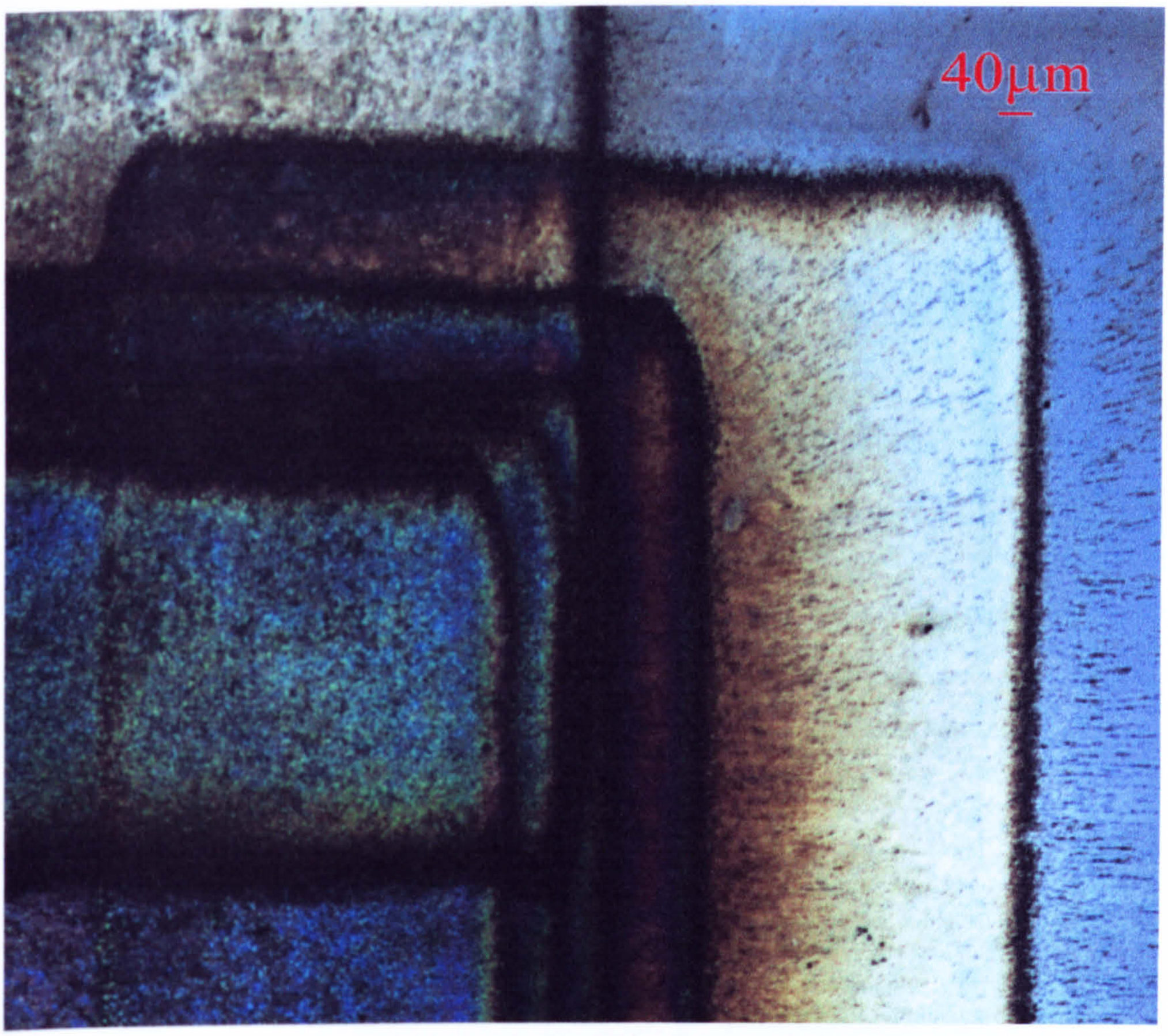

Figure 6.21 Six overlapping transferred layers of ZnS film. The lowest one extends more to the right, two more are over its left part, then one transversed upwards and two more again being displaced left. The transfers were made with a fluence of 0.63 Jcm^{-2} in an argon atmosphere at a pressure of $4.2x10^{-2}$ mbar.

Non-displaced transfers, where the edges of each layer match almost exactly with those of the others, are obviously desired for application purposes, instead of the displaced overlapping layers. Exact matched multilayered transferred films have been produced with a various numbers of successive layers. The technique has also been used before for example in generating LIFT deposited films of increased thickness of Ag for construction of electronic components.[20] A good example is depicted in the microscope image in Figure 6.22 where a length of 8 successive layers that have been deposited on exactly the same site. The material from all 8 transfers seems to have fused together and the definition of the final film edges is quite precise. The transfers were performed with a fluence of 1.0 Jcm^{-2}. A certain amount of material has been ablated and deposited outside of the site's boundaries, but the height difference

between the two films is quite large here. Smaller fluences, can be used for less ablation of material.

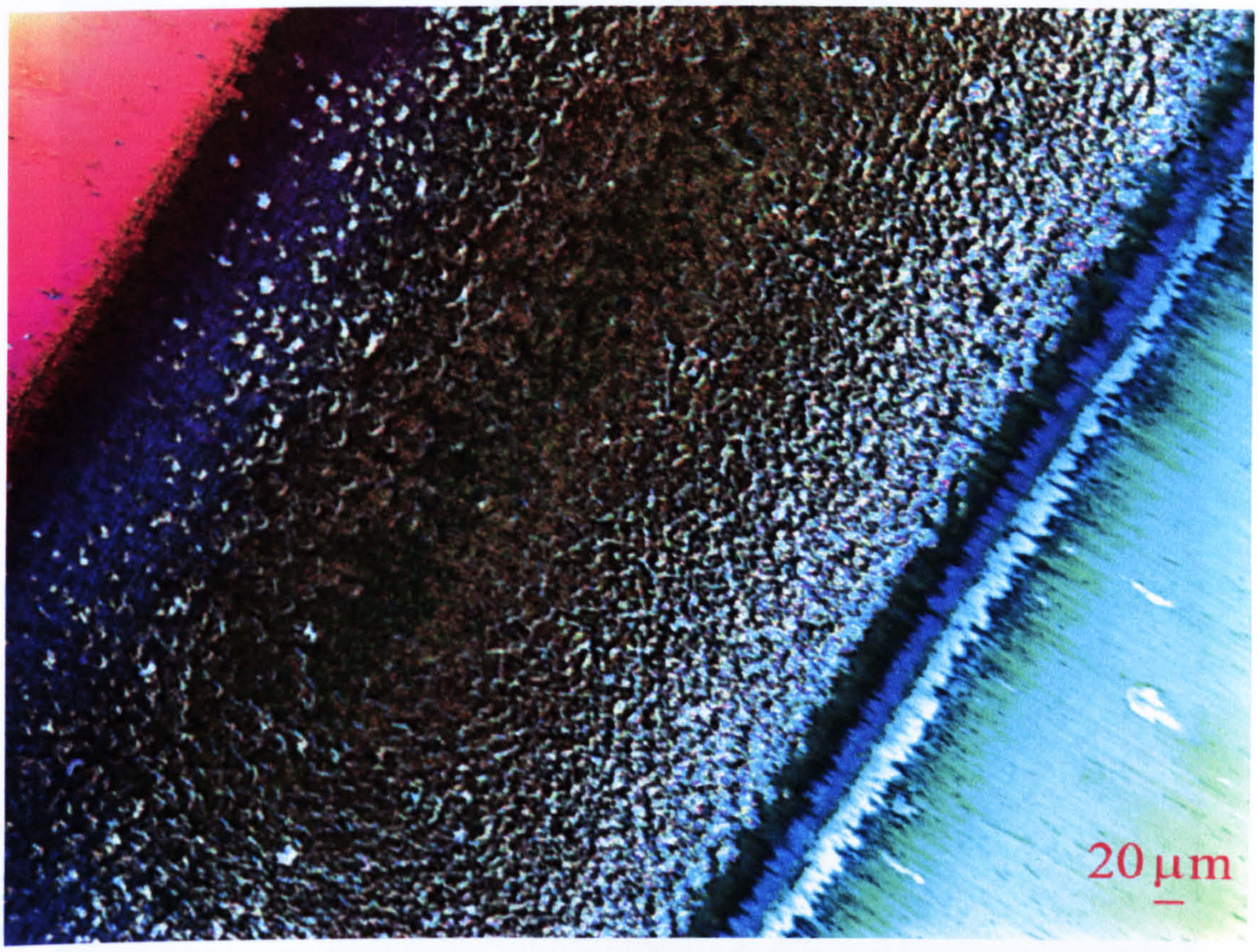

Figure 6.22 Eight successively transferred layers over the exact same area on the target sample. All the transfers were perfomed by 1.0 Jcm^{-2}, in an argon atmosphere of pressure $3.4x10^{-2}$ mbar. The source film was a CdZnS:Cu sample. The films lie almost diagonally to the picture (in dark blue/brown colour). The light blue lower light edge and the pink upper left edges are debris covered substrate. The image was taken with a colour shading filter giving a colour defined 3 dimensional feeling.

At very low fluence regimes, beadlike layer structures were observed on the target substrates. The beads are probably ablated material, recrystallising when it meets the target surface. The phenomenon is observed at laser pulse fluences below 0.4 Jcm^{-2}. An example is given in Figure 6.23 where a beadlike layer was formed by use of a fluence of 0.21 Jcm^{-2}. The lack of transferred volume of material at low fluences could be the reason that beadlike or possibly hemispheric droplets are forming on the target, as a flat film made from the same amount of material would have a larger surface than the beads or hemispheres and thus a greater surface tension would build up. This however does not explain the layer structure in Figure 6.23, which contains a great density of those particles. Another explanation for this is that low fluences are only able to transfer loose particles (mostly found as spheres on the

source substrate) and unless a large enough number of them is transferred, they would not be enough to mould into a film.

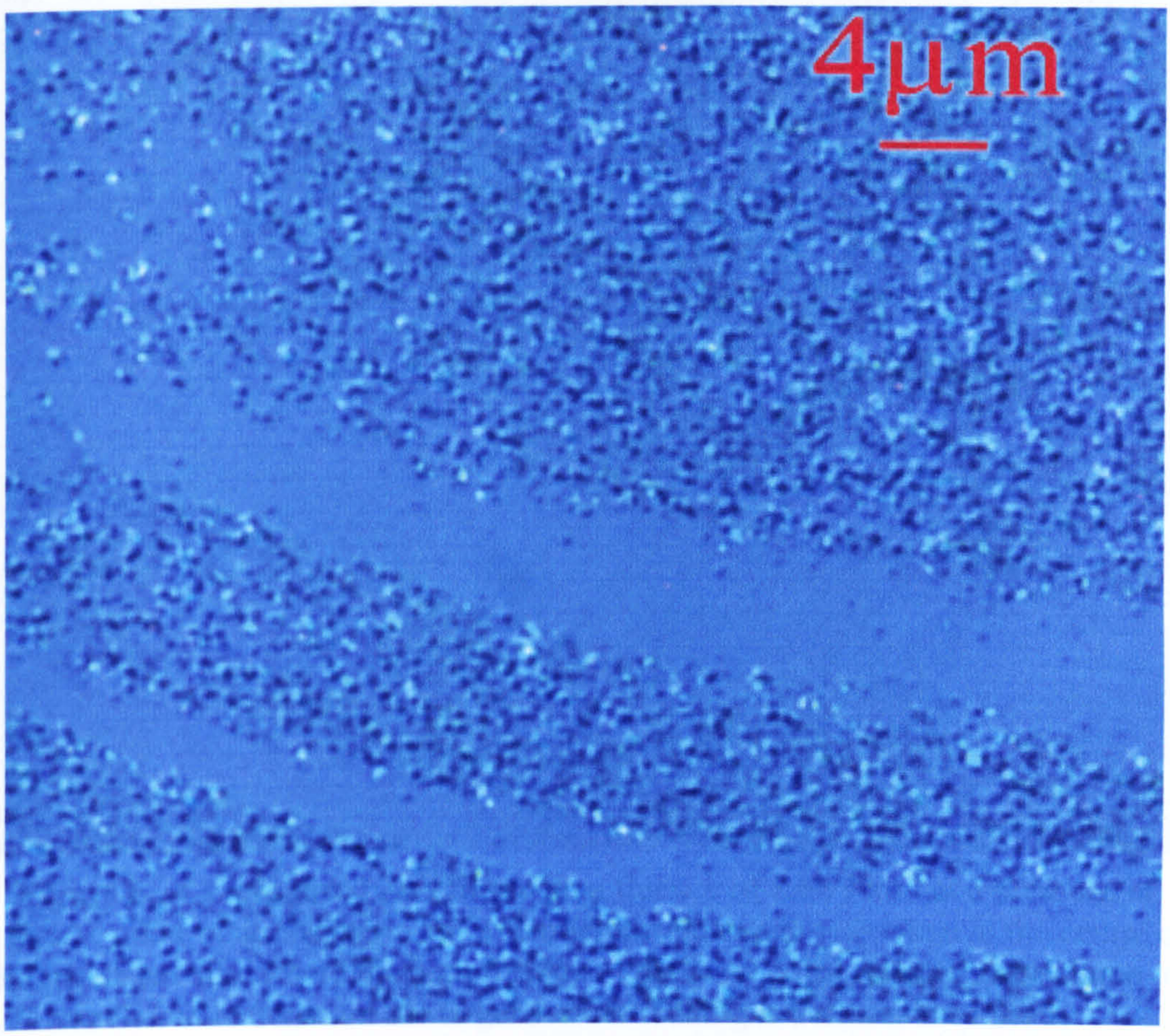

Figure 6.23 A scratch on a low fluence transferred ZnS:Cu layer composed of beads. The chamber pressure was 4.4×10^{-2} mbar of atmospheric air and a fluence of 0.21 Jcm^{-2} was used for the transfer.

Still, the low volume / high surface tension explanation can be applied in cases of rather high fluence, where material is being ablated from the target in such a degree that very small volumes can remain over rather large surfaces. If the material passes to its liquid form, it forms droplets. An example is illustrated in Figure 6.24, with bead-like particles of diameter between 150 to 800 nm that have formed only in areas which are not covered by the lighter in colour material. There the volume of material that remained could not sustain its film like form and thus produced beads in a small density this time. The transfer was made with a fluence of 1.68 Jcm^{-2}.

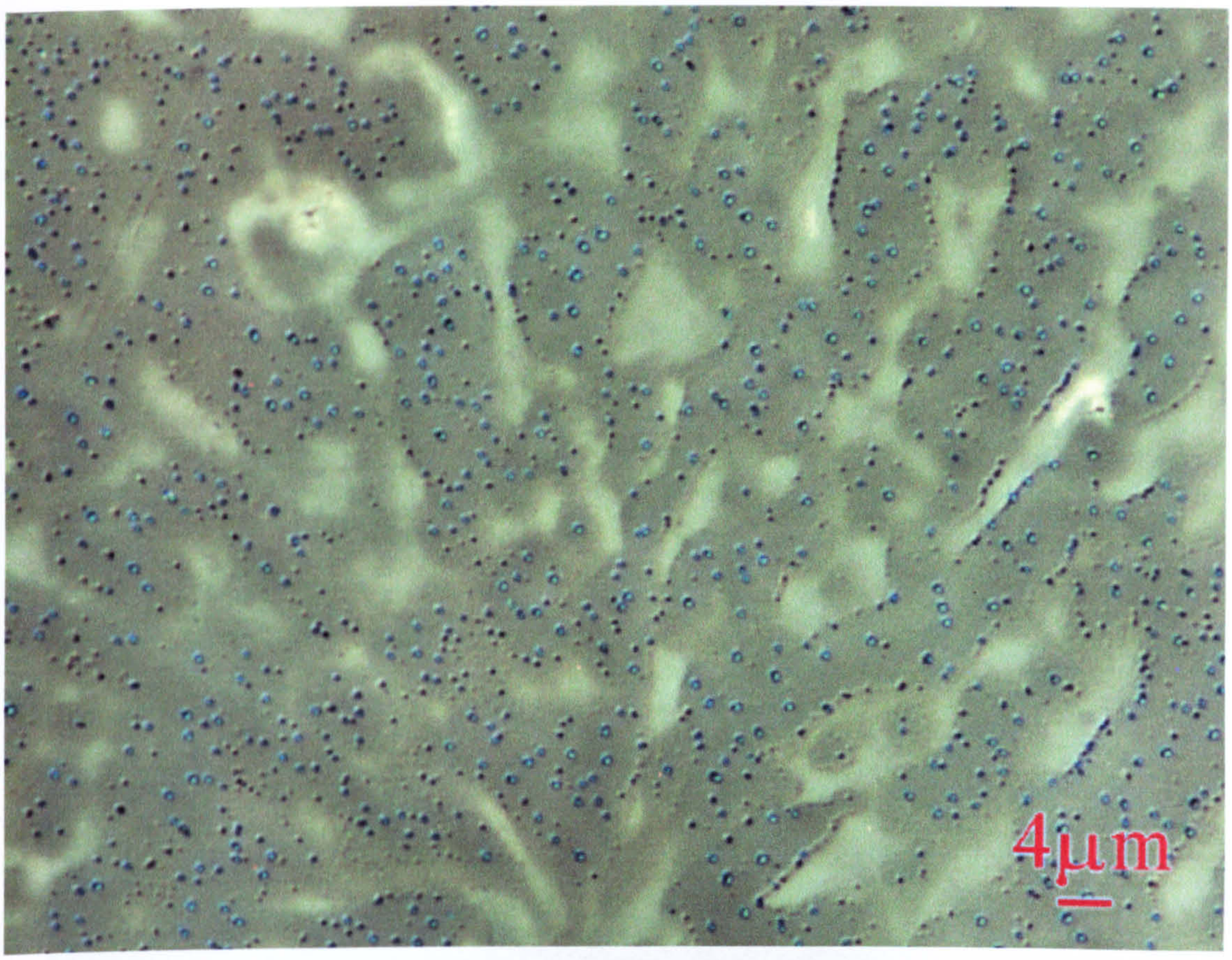

Figure 6.24 Transferred ZnS film with a fluence of 1.68 Jcm^{-2} at a pressure of $1.6x10^{-2}$ mbar of atmospheric air. The microscope image was taken at the centre of the irradiated site, where the high fluence of the laser pulse reduced the volume of adhered material on the target surface leading in formation of beads.

Attempting a large number of successive layer transfers at fluencies higher than 1 Jcm^{-2} can cause destruction and dislocation of the deposited layers. The site depicted in Figure 6.25 is a good example of thirteen successive pulses. The white areas are missing film. The areas where film was detached are characterised by features similar to those in the lower set of two pictures, where flakes of the film are reaching up to 8 or 10 µm. It should be noted here that the distance between the two substrates is only 15 µm. The transfers were performed with a fluence of 1.4 Jcm^{-2} at a chamber pressure of $3.4x10^{-2}$ mbar. Back ablation of the attached layers by the high-energy pulses seems to have bridged the target and source films together, which led to detachment of certain areas. The bridging pieces of film have formed lifted flakes when the source-target pair was displaced against each other. Multiple transfers performed at fluencies under 1 Jcm^{-2} did not cause detachment of the transferred films, even at a number of 20 successively deposited layers.

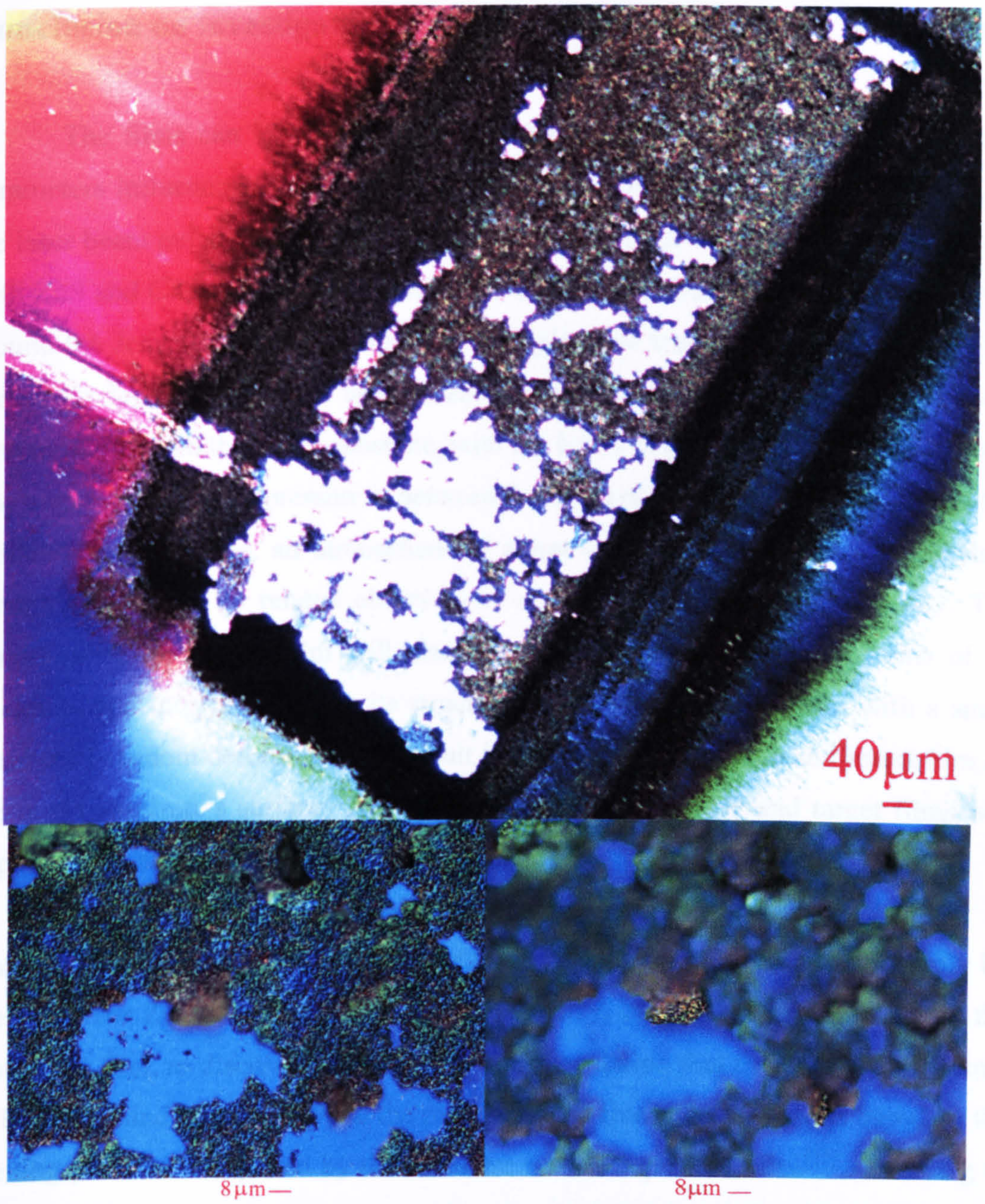

Figure 6.25 Detachment of transferred film composed of 13 successive layers. Laser pulse fluence used was 1.4 Jcm^{-2}, in a chamber with gas pressure of argon atmosphere at $3.4x10^{-2}$ mbar. The upper picture depicts the site as a whole, while the lower two are magnified images of the centre of the site, focused at the bottom of the detached flakes (left) and the top (right). The light blue areas in the bottom two pictures are the exposed substrate.

Conclusion on investigation of transferred film by optical microscopy

The films can be transferred successfully on the target substrates. The two parameters influencing the quality of the resulting film are the maximum fluence of the laser beam pulse and the chamber pressure. The suggested fluence for transfers of both ZnS and CdZnS films are between 0.5 and 1 Jcm^{-2}. More specifically, a fluence around 0.6 Jcm^{-2} is ideal for performing multiple layer transfers and 0.6 to 0.8 Jcm^{-2} for single layer transfers. A laser fluence lower than 0.4 Jcm^{-2} can achieve bead structured films on the target substrate, with the beads being unattached to each other. The suggested chamber pressure is between 2 and 6 $x10^{-2}$ mbar. For protecting against oxidation of the films, an atmosphere of argon or other neutral gas is suggested, though there were no related observations noted through optical microscopy. The condition of the source film will also play a role in transferring, in terms of its thickness and most importantly its structure. A continuous, intact film with a small number of random deformities will result in an equally continuous and intact film on the target substrate's surface. The distance between the source and target films was kept constant at 15 μm, which gave good results.

The laser irradiated areas are often found with a remaining thin layer of material still covering the substrate. The layer is believed to be composed mostly by the precursor ZnO layer grown during the chemical bath, granting adherence to the rest of the film, as discussed in chapter 4. The speculation that the ZnO layer is likely to be left behind especially when the recommended fluencies are used is based on the melting point values quoted by the literature for the deposited salts.[21] According to those, ZnS and CdZnS will pass to the gas phase, while ZnO is still solid, thus generating propelling gasses between the two layers of material, hence achieving transferring of the upper part of the film only. The film can be fully removed when the laser fluence is increased above 1.7 Jcm^{-2} but the resulting transferred layer may loose its continuity, while a lot of material will be translated outside the irradiated site's boundaries.

The transferred films can result in uniformly layered material within the desired boundaries set by focussing the laser beam, or in a number of other configurations, mainly featuring bead formation, surface waves due to high gas pressure currents, arising from the ablated material and several forms of coherent light

interference (mainly circles and far field interference). At high fluencies, above 1 Jcm^{-2} the material is often transferred before the end of the laser pulse duration, thus the remaining delivered energy is often found to be affecting the deposited film and reducing its volume. The transferred volume does not need to pass to a liquid phase in order to adhere on silicon oxide and silicon wafer substrates.[22-28] Adherent films of material that have either retained their structure to a great extent or were deposited in a completely deformed state, were found. Evidence of melting was also present, especially at high fluences approaching 2 Jcm^{-2}.[25]

Multiple layers of film have been successively transferred on the same area of a target substrate. Depositions of up to 20 successive layers have been observed by optical microscopy. The successive films are found to adhere and even fuse into one thicker film. Here the energy (fluence) of the laser pulse becomes very important in defining the number of the possible transfers, as little energy (fluence regimes of 0.2 to 0.3 Jcm^{-2}) may not achieve fusion of the film formed on the target and too much (regimes above 1.8 Jcm^{-2}) will re-ablate the previous films or will gradually destroy the deposition. The thickness of the multiple-layer, transferred film grows with the increasing number of successive transfers. A typical number of layers that can be transferred successfully is five, while the laser fluence should be reduced towards 0.5 to 0.6 Jcm^{-2} when a greater number is required.

6.3.b. SEM

Images of target and source sites, in great magnification and with a three dimensional perception were obtained by Scanning Electron Microscopy. They are used here to complement the observations performed by optical microscopy. Regardless of the better quality of the images against those of optical microscopy, only a small number of SEM pictures was available due to the complexity of the technique compared with the straight forward optical microscopy and thus only certain samples of high interest were examined, mainly as supportive evidence.

The surface morphology of the transferred sites can be compared in two different fluence schemes. In Figure 6.26 the surfaces of two transferred films can be seen. One was transferred at 0.89 Jcm^{-2} and shows evidence of a reformed and molten material that has settled on the new substrate with a rather smooth surface. The other

is a transfer at 0.56 Jcm^{-2}, where the material is more crudely deposited, keeping a lot of the characteristics of the original film and not flowing into a uniform film. This correlates with the observations put forward in the previous section, as to how much fluence should be used, where a fluence of 1 Jcm^{-2} would cause melting of the transferred film. On the other hand, a fluence of around 0.5 Jcm^{-2}, transfers a well defined film, but sometimes only a portion of it and the film does not seem to be fusing into a more uniformly flat surface.

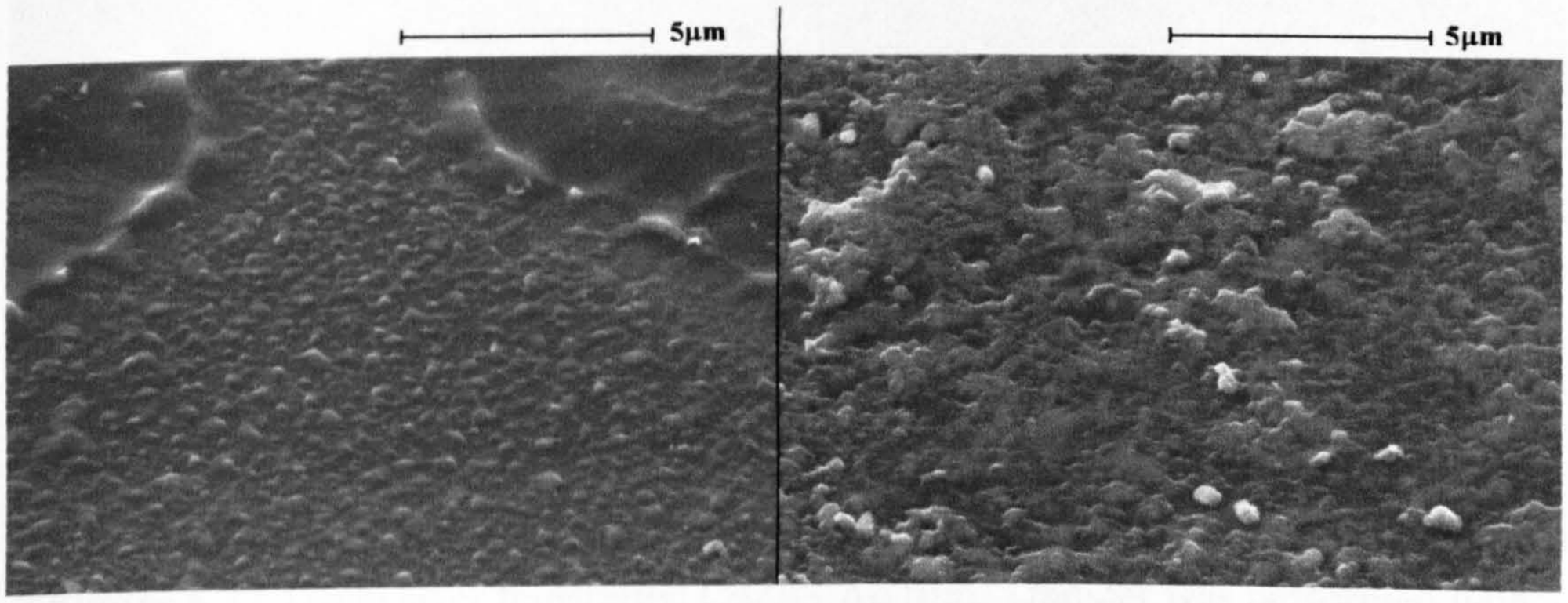

Figure 6.26 Two target sites of CdZnS:Ag samples. Single shots of 0.89 Jcm^{-2} (left) and 0.56 Jcm^{-2} (right) were used for the transfer in an argon environment with pressure of approximately $4x10^{-2}$ mbar.

Another type of transferred film with interesting surface formations is that of a multiple layer transfer at a rather moderate fluence. In Figure 6.27 a triple layer transferred film with a fluence of 0.72 Jcm^{-2} in an argon atmosphere of $2.5x10^{-2}$ mbar, is shown. The film appears in a frozen-boiling state. It is quite flat, apart from round droplet formations pointing upwards and empty holes that indicate ablation of the film. The flat moulded surface shows that the layers must have reached some sort of melting point at least at the surface. The observation put forward here, concerning the ablation of film at 0.72 Jcm^{-2}, combined with those in the previous section, suggest that a fluence in this vicinity is almost at the maximum acceptable setting. Above that, a good amount of transferred volume will be ablated and lost instead of depositing on the target substrate.

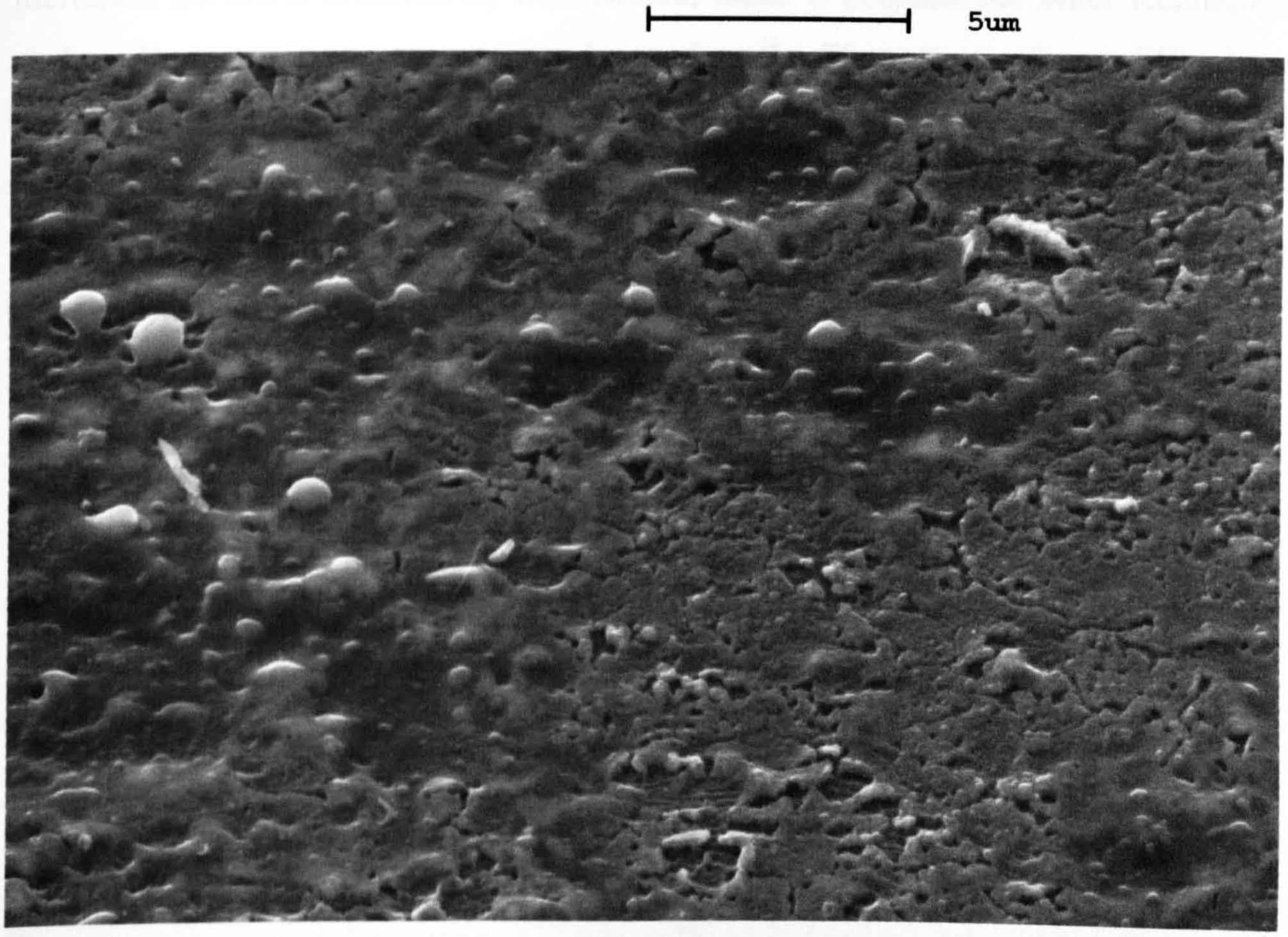

Figure 6.27 Triple layer transferred CdZnS:Ag film. Transfer was performed with 0.72 Jcm^{-2} at a an argon atmosphere pressure of $2.5x10^{-2}$ mbar.

A silicon wafer target substrate holding multiple layer transfers was cut. The cut was passing through the middle of a 5-layer site transferred at 0.49 Jcm^{-2}. An SEM image was taken looking directly at the side of the cut, where the interface between the deposited film and the substrate was incredibly clear (Figure 6.28). The film had lifted slightly away from the surface of the substrate due to the detachment motion of the two pieces of substrate. The five-layer film thickness can be measured, taking into account the observation angle of 70 degrees and it is found to be 800 nm. The thickness of the source film was 186 nm with a roughness layer of 40 nm, measured by the reflectivity fitting method 1 (Runge-Kutta algorithm). Therefore, approximately 50 nm of each film transfer were lost in the process, with each pulse depositing about 160 nm of material. The surface of the film is quite smooth and it has obviously fused into one layer instead of five. This image is the most undisputed proof that multiple transfers on the same site are possible, with each new pulse adding to the already deposited volume. May it also be pointed out that it is evidence of successfull multiple layer deposition of II-VI materials by a laser induced forward transfer method, that has never been demonstrated by others before. Moreover, the

increased thickness achieved by this method, made it possible for other techniques such as Raman microspectroscopy to be used on the films. It was found difficult to obtain similar images of the rest of the transferred sites lying on the cut, as it had produced a large amount of debris on the edge, making it impossible to distinguish the film from the substrate. Perhaps a more precise cut with a polishing step would provide a better sample for such observations.

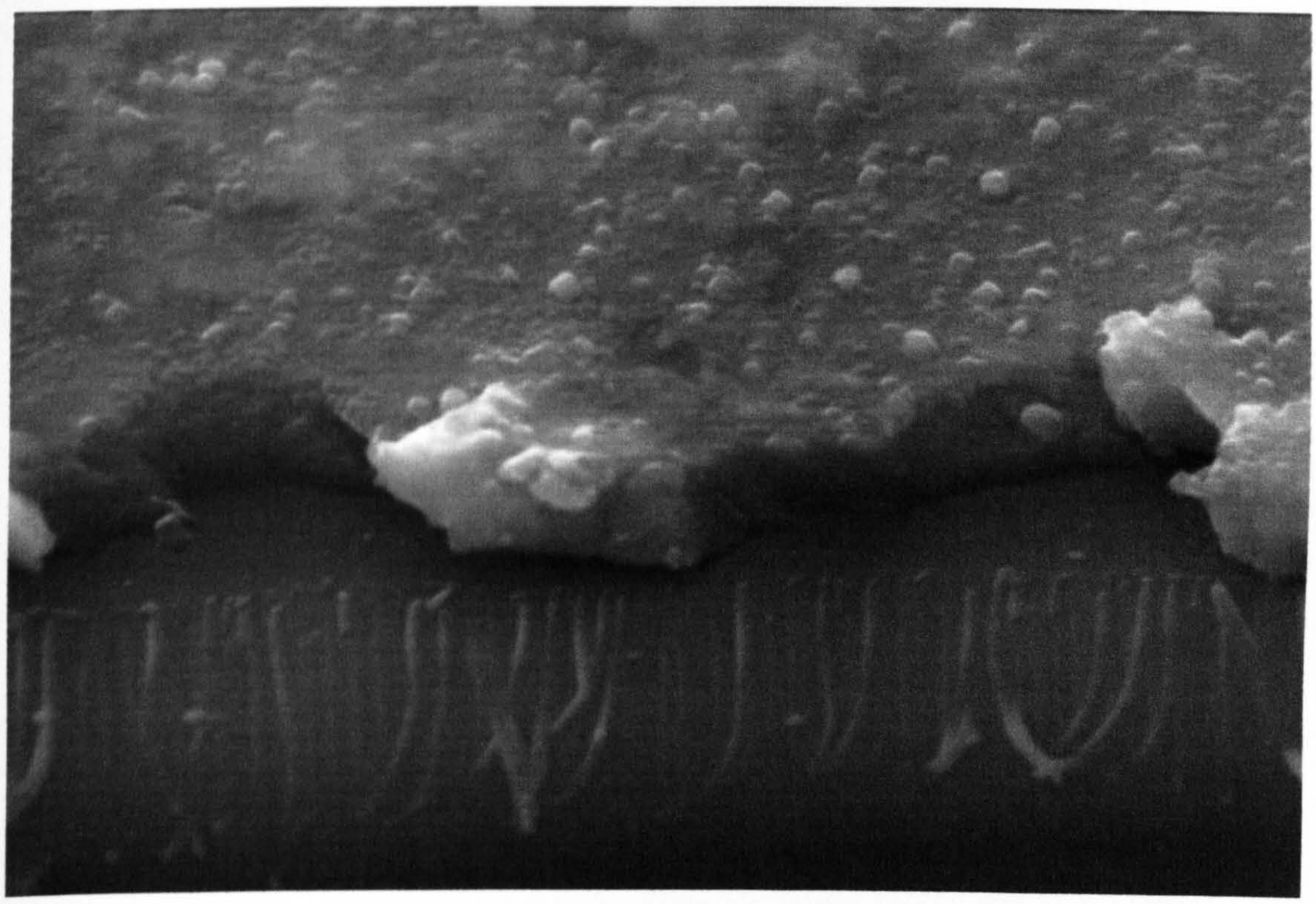

Figure 6.28 Five successive film transfers over the same site. The source was a CdZnS:Ag film. The fluence used for the transfers was 0.49 Jcm^{-2} and the chamber atmosphere was argon at a pressure of $2.5x10^{-2}$ mbar.

Another achievement of the laser transfer process that is examined here is the successful transfer of source film with a distinct bead-like structure in a resulting film with quite similar characteristics. Formation of bead structured chemically deposited films was discussed in chapter four (with images laid out in 4.3.a and 4.3.b). A source-target pair of bead structured films is presented in Figure 6.29. A non-irradiated part of the film is shown in part (a) of the illustrated images and the transferred film in part (b). The source is composed of very distinct spheres. It is a CdZnS:Ag film deposited with 0.10 g (4.3 mM) of $ZnCl_2$ and 0.15 g (3.9 mM) of $CdCl.2.5H_2O$ salts. It is very interesting that the transferred film has more or less

retained the structure. The spheres are distorted and fused in a more unified film. The transfer was performed with a single shot of 1.7 Jcm^{-2}. The fluence was quite high and often results in loss of a great amount of film and melting as discussed above. Perhaps the spherical structure of the particles proved enhanced resistivity to ablation by high fluence irradiation. At the same time, it is noted that the average sphere diameter is different in the two films.

The images are not from exactly the same area, but the source film was found to have a rather uniform structure with beads of approximately the same size distribution, being at an average of 250 nm. The target formed beads have a size average distribution of 450 nm. The increase in diameter of the beads could denote that the film indeed has passed to the liquid phase, but the ratio between the two substances, CdS and ZnS, could be accommodating the formation of spherical particles, instead of a flat film, with a possible phase separation of the two substances, as described in section 4.8, in which the central part of the spheres is composed of CdS and the outer of ZnS. The theory is based on the slightly different melting points of the two materials, which is causing phase separation and various surface effects, resulting in formation of spheres. The effect has similar results to those observed in the chemical bath process due to the difference in the solubility product of the two materials but here it is governed more by the melting points difference.

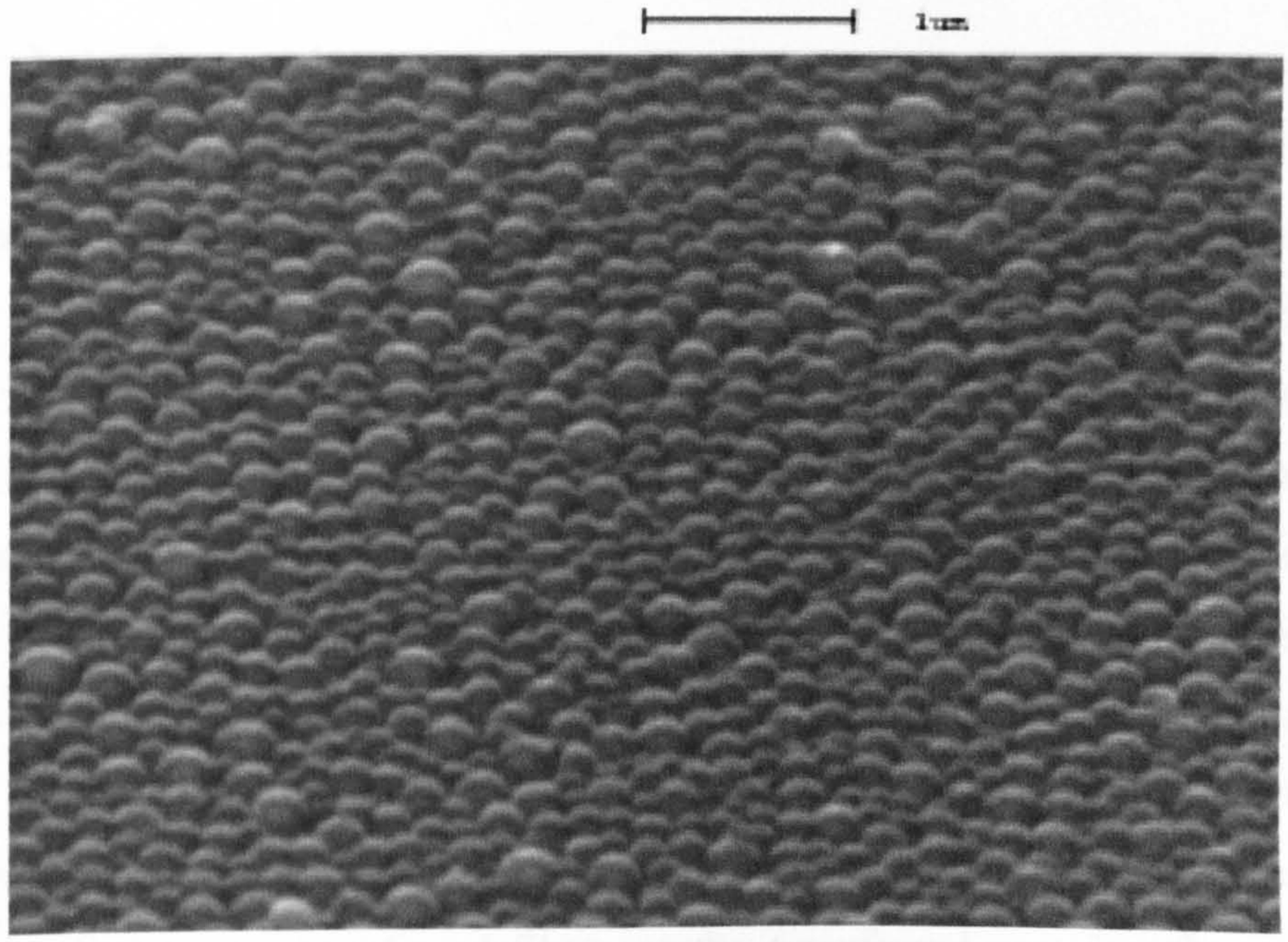

a)

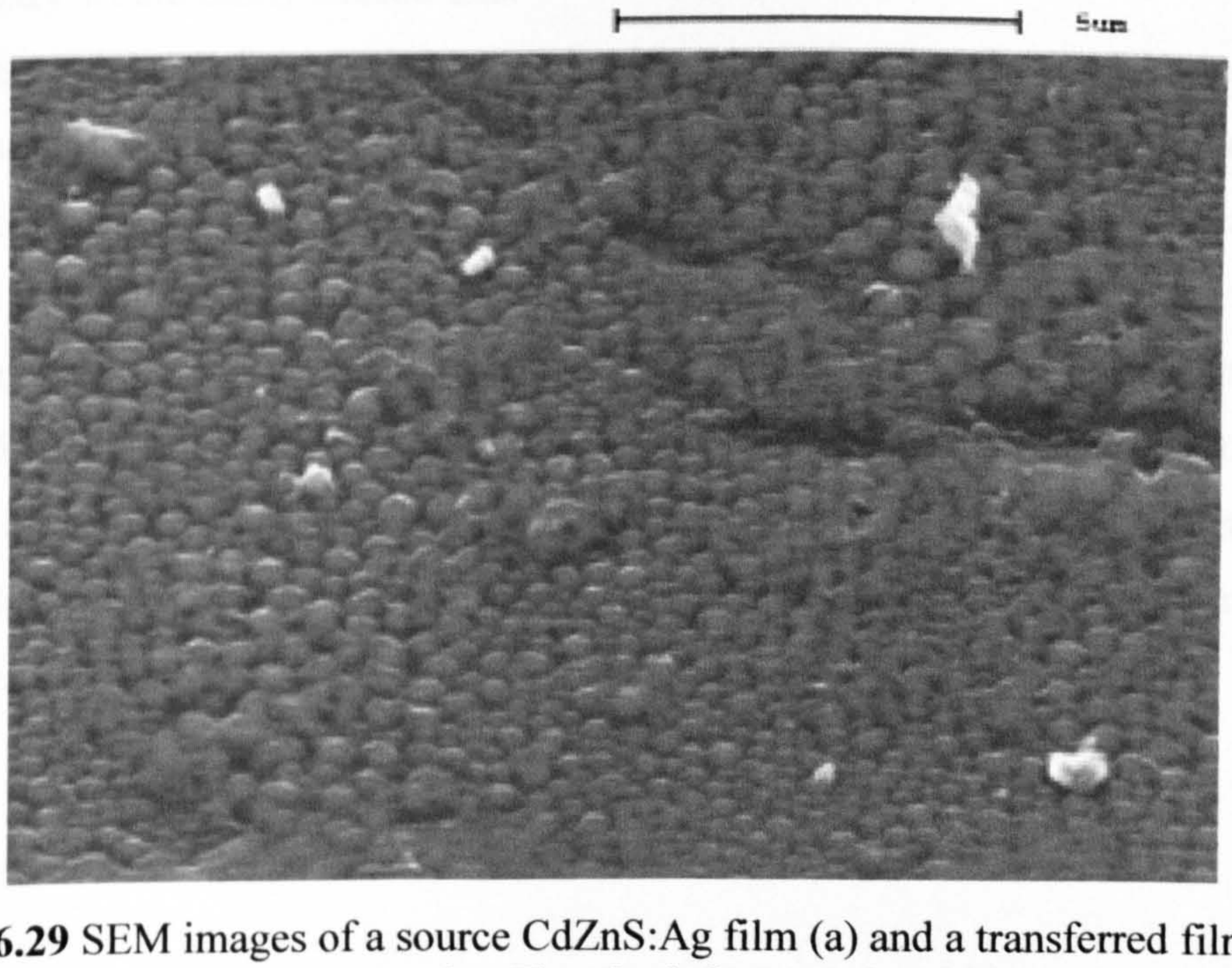

b)

Figure 6.29 SEM images of a source CdZnS:Ag film (a) and a transferred film (b) originating from the same sample. They both feature a bead-like structure with average bead diameters of 250 and 450 nm respectively. The transfer was performed with a fluence of 1.7 Jcm^{-2}, in an argon atmosphere at a pressure of $4x10^{-2}$ mbar.

6.3.c. Interferometry

The surface profiles obtained by interferometry can be considered as optical microscope images coupled with topographic data for each pixel. Therefore, the technique is mainly used to reveal height information for the various features found on the surface of the samples and thus aiding in characterising them and determining their origin. The 3D profile images acquired by interferometry here will often appear rather rough, with a large density of sharp spiked features, as the height (z dimension) of the profile is significantly expanded with respect to the other two dimensions of the profile. When investigating transferred films it is very interesting to determine their thickness, or sometimes the variation of thickness over the transferred film area. The techniques used for finding the thickness of the chemically deposited films cannot easily be applied to the transferred films, as the transferred area is often 2 square millimetres or less, therefore the probing beam of light in ellipsometry or reflectometry would easily exceed this.

The height difference between the lowest detected point and the average height in a surface profile scan could give an indication of the film height, assuming that the lowest point corresponds to the flat substrate surface. Two transferred film sites from the same CdZnS:Cu source sample were analysed with the WYKO surface profiler and are displayed in Figure 6.30 and Figure 6.31. The surface scans were performed in the middle of the transferred sites and thus it is not certain that the lowest point actually corresponds to an uncovered target substrate area. Nonetheless, a height difference between extreme points can be measured at 114 and 75 nm in the two images.

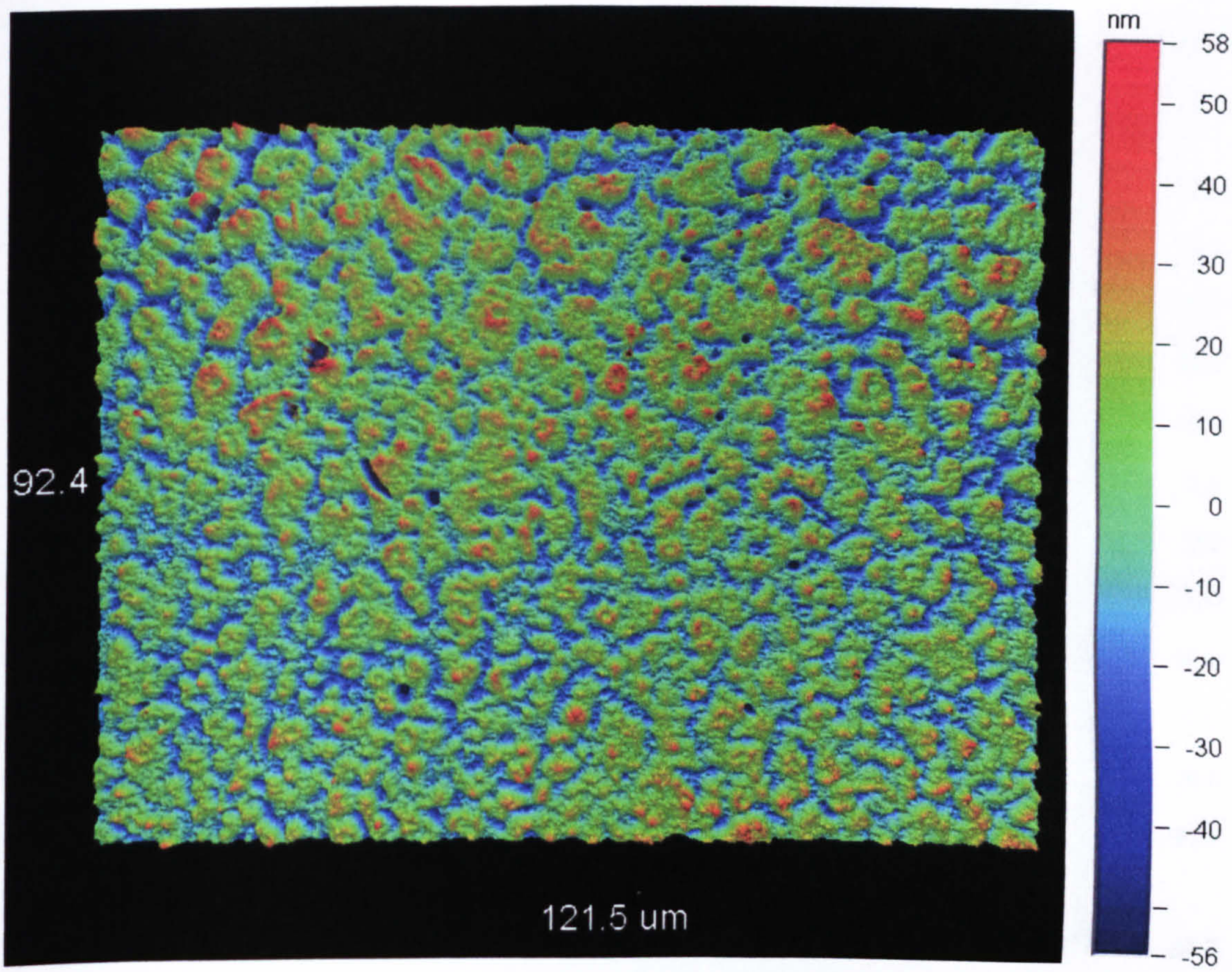

Figure 6.30 Surface profile of a transferred CdZnS:Cu film, with 0.51 Jcm^{-2} beam fluence in an atmosphere of $3.6x10^{-2}$ mbar of Ar.

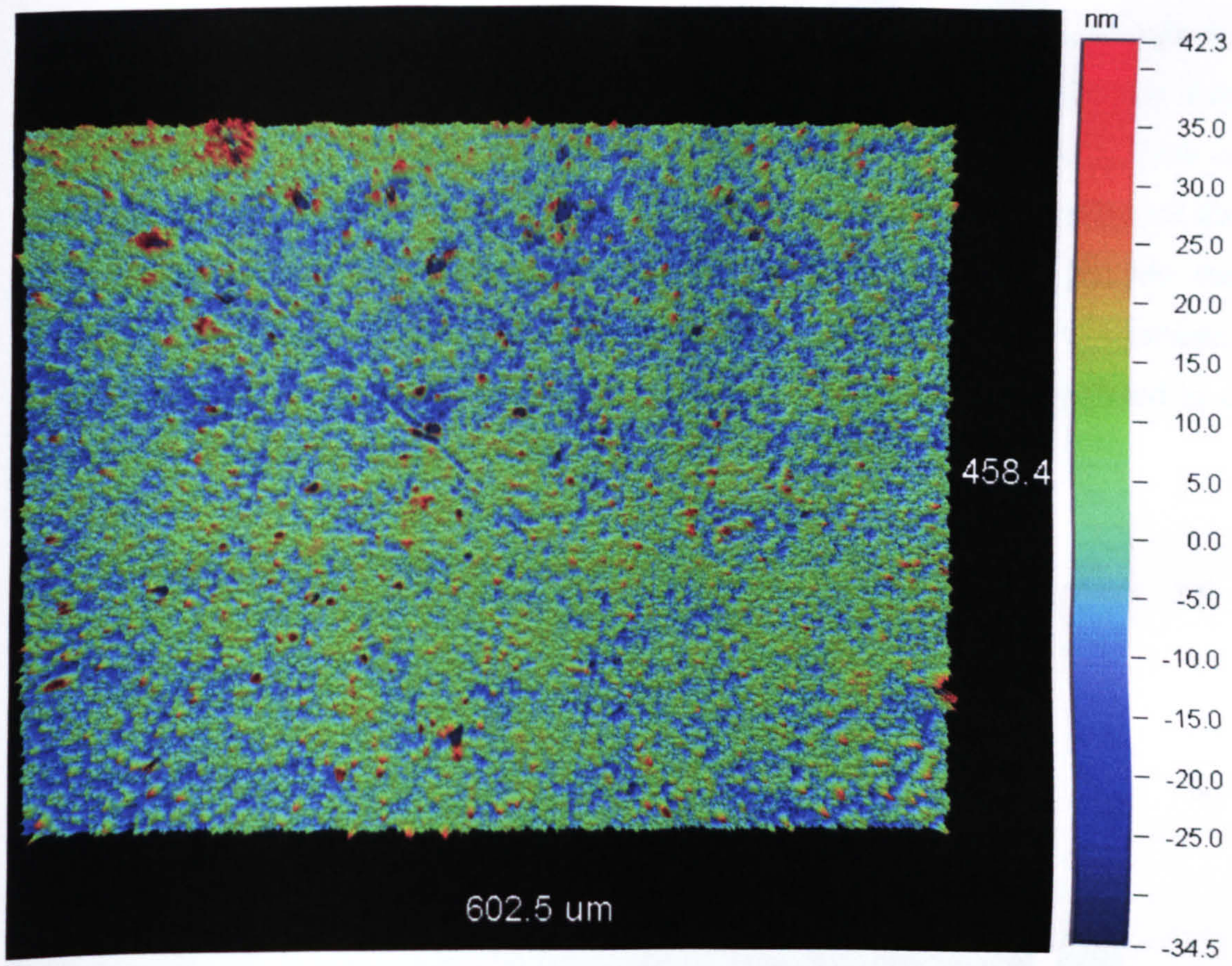

Figure 6.31 Surface profile of another transferred CdZnS:Cu film, with 0.51 Jcm^{-2} beam fluence at $3.6x10^{-2}$ mbar of Ar.

The measurement of transferred film thickness would be far more reliable if the investigated area was at an edge of the film, thus, the height of the surface beyond the edge would be attributed to the top of the target substrate. Such a profile is given in Figure 6.32. Unfortunately, in this image, the thickness (height) of the laser-transferred film is misconceived by the instrument. Clearly, the film covered area would be expected to be at a higher level than the substrate surface, but the opposite is found. The fluence used for the transfer was 0.92 Jcm^{-2}, which, based on the observations that were put forward in sections 6.3.b and 6.3.a, would not have been enough to ablate both the transferred film and part of the target substrate's surface. As it is explained in section 2.4 and also in the instrument's reference manual[29] the measurement is strongly influenced by the refractive index of the materials being measured. There is a difference of approximately one unit between the refractive index of silica and those of zinc sulfide and cadmium sulfide.[30] Hence, there is a large possibility of erroneous readings of film thickness being taken for the areas that are completely covered by film, when compared to the exposed silica surface. In areas

where there is a frequent change between transferred material droplet surfaces and the silica substrate surface, larger height differences are observed between the two materials, though it is uncertain whether the correct heights are attributed to each of them. Areas with frequent changes of exposed material are next to the edge of the film, where droplets of the transferred material have been scattered outside the irradiated area boundaries and close to the centre of the irradiated area. For example, the right side of the image on Figure 6.32 which seems to have been re-ablated to a great extent, thus exposing some of the underlying silica substrate.

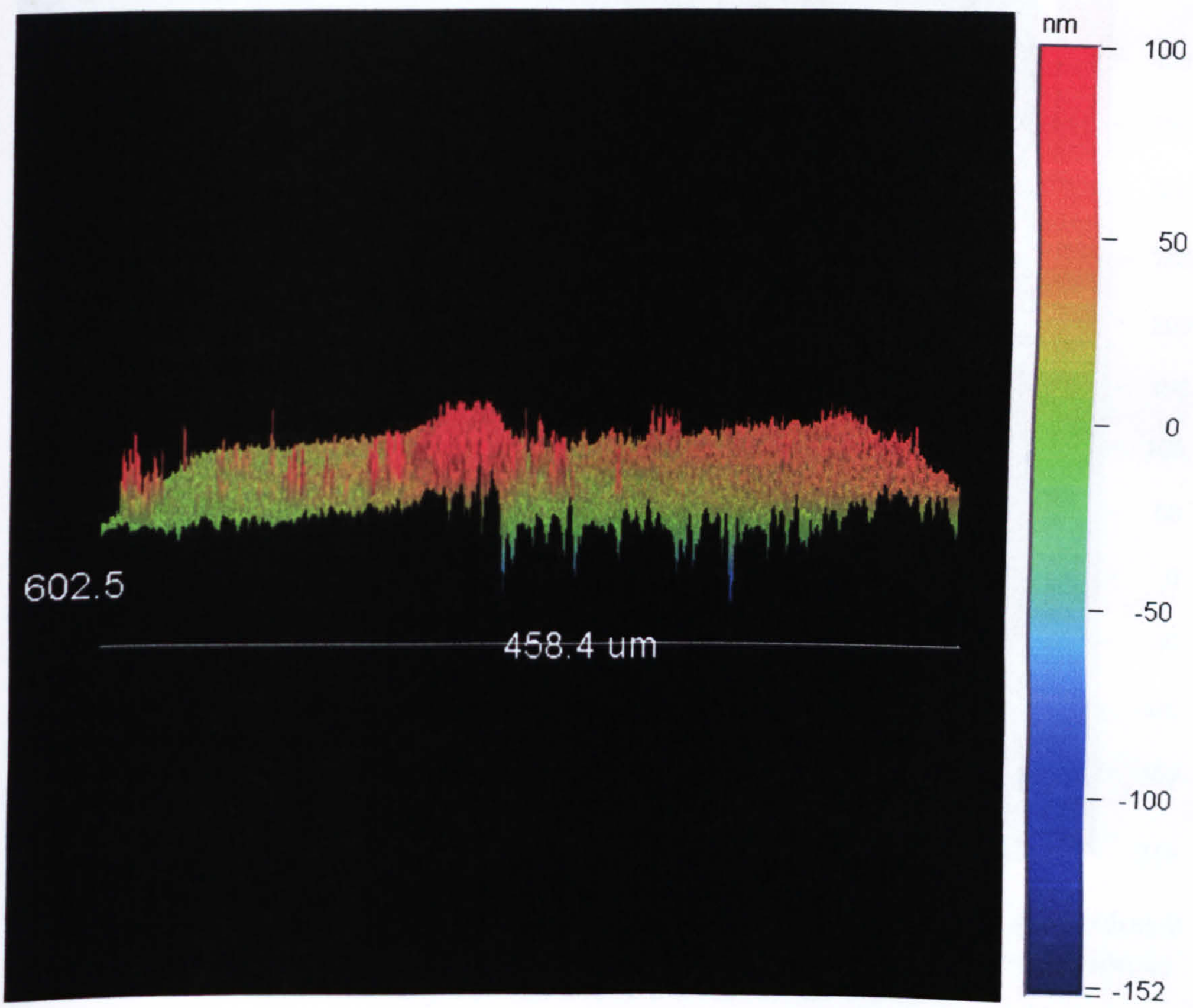

Figure 6.32 Surface profile of a CdZnS:Ag transferred film edge, at 0.85 Jcm^{-2} in an argon atmosphere of $4.0x10^{-2}$ mbar. The film covered area is on the right of the image.

In order to verify whether a false reading of film thickness was taken from the data above and also to get a better idea of the perception of the instrument's analysis software of materials with different refractive index, an area containing an artificial scratch was examined. Normally, it is expected that the pixels over the artificial

scratch on the film would carry a height value lower than that of those over the film. However, as can be seen in Figure 6.33 and Figure 6.34 the line along the scratch trench is represented as an elevated area with respect to the rest of the image that is still covered by film. Even if it is supposed that the film was mechanically lifted at the sides of the scratch, the middle of it is still attributed with a green colour, corresponding to about 100-150 nm elevation (Figure 6.33).

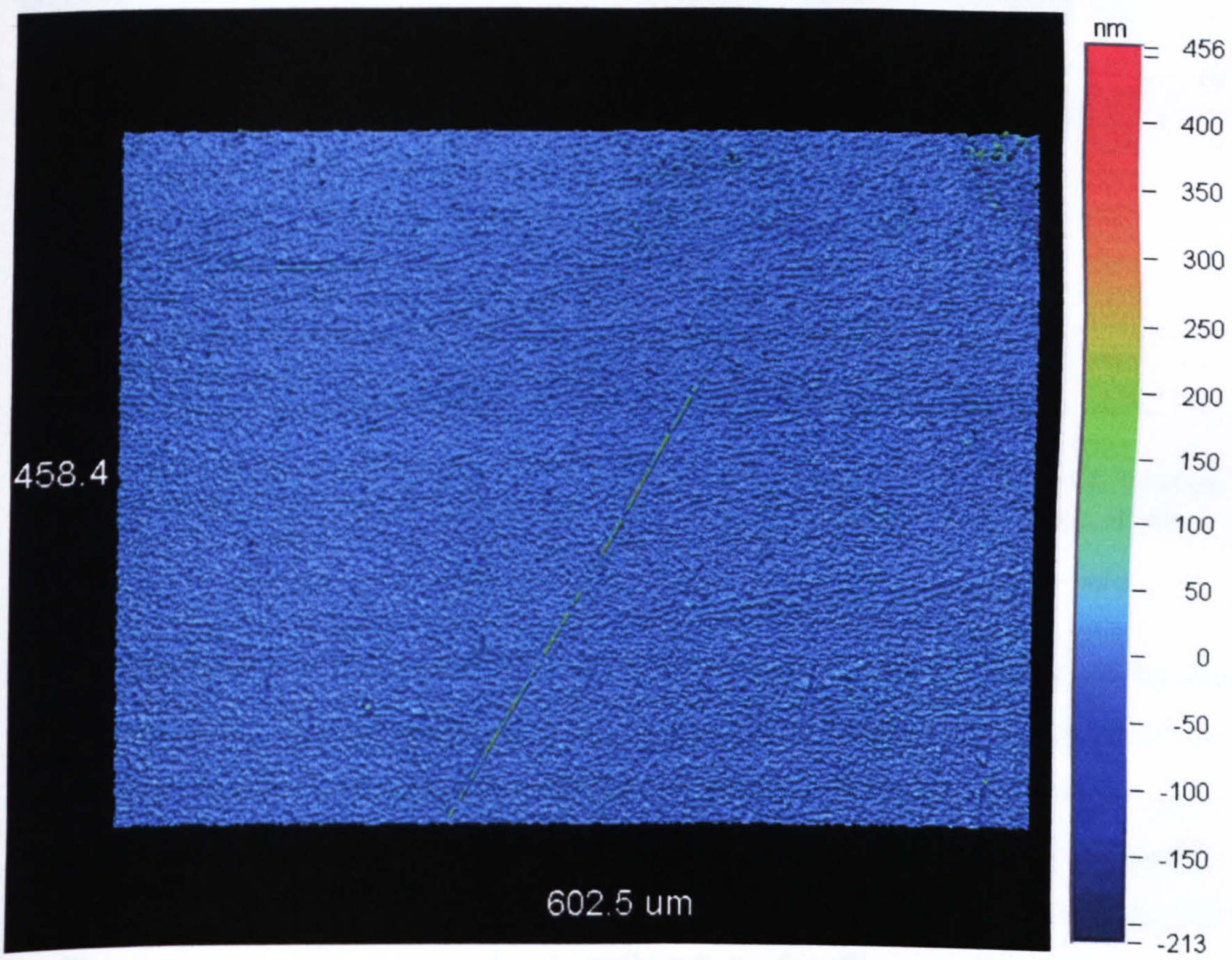

Figure 6.33 Surface profile of a ZnS:Cu film prepared with an excess of zinc chloride salt. The surface carries a scratch coded with a green colour, indicating elevation of approximately 100 nm above the rest of the surface.

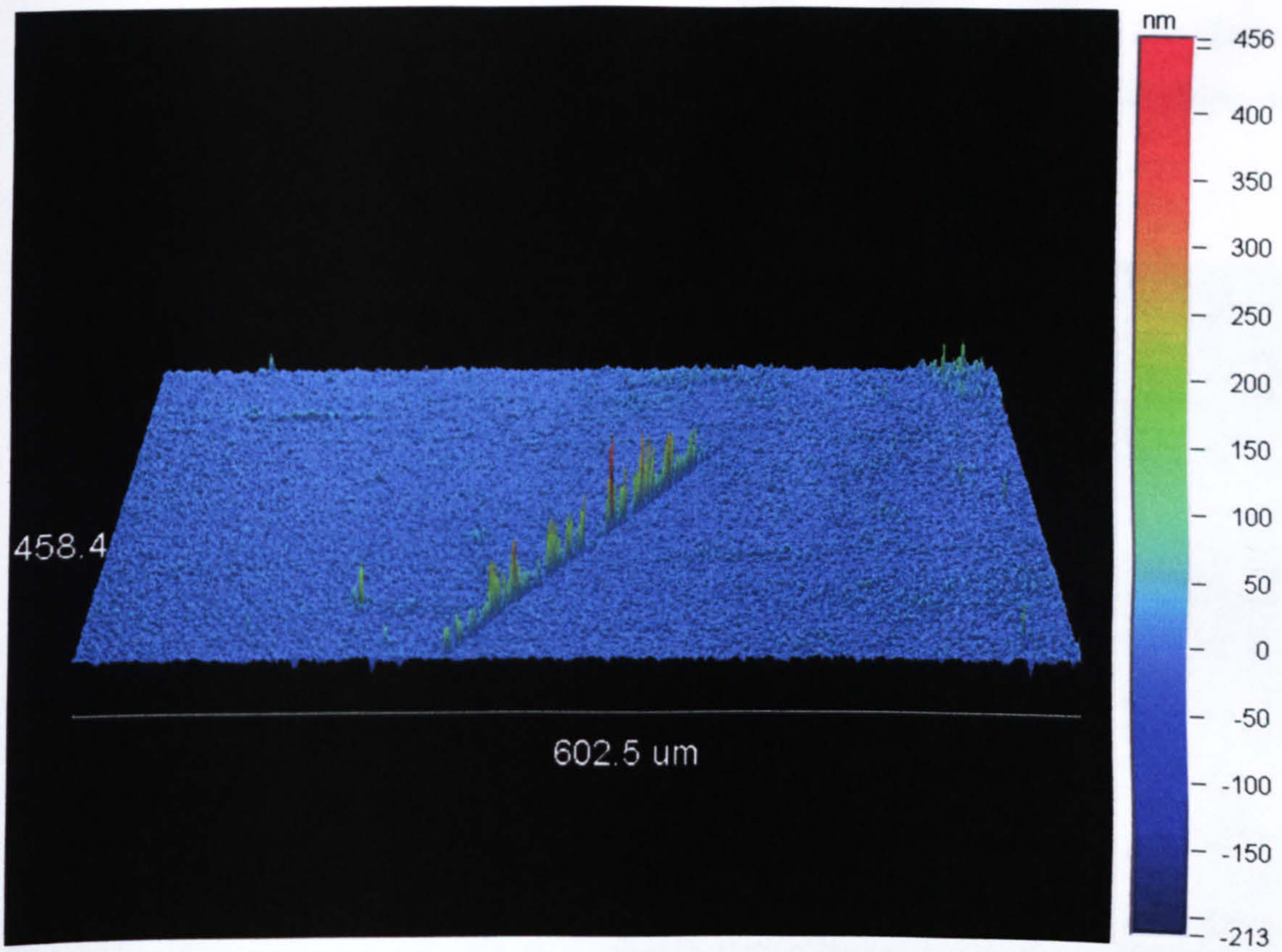

Figure 6.34 Surface profile of a ZnS:Cu film (as above), prepared with an excess of zinc chloride salt. The profile is tilted in 3D mode revealing the perception of elevation at the scratch.

Looking at a transferred film site with a wide scratch on it caused by the movement of the metallic holder over the target sample a similar effect is observed. The area of the scratch has a rather flat profile being at the same level as the glass substrate surface surrounding the transferred film (Figure 6.35.a). The area covered by the film carries a large density of alternating elevation spots, appearing in the 3D profile as spikes. The average level attributed to the film covered area by the instrument is below that of the glass surface, especially close to the centre of the pulse. Ablation of the film and the glass substrate is ruled out in this case, not only because of a low laser beam fluence of 0.68 Jcm^{-2}, but also because the scratch is imaged above the deformed profile covered by the film. In the case that the scratch had affected the glass, it would also appear at a lower level compared with the substrate's surface, instead of bridging the two sides of the transferred site. As the magnification is getting larger (Figure 6.35.b, c and d), the average height of the film covered area is perceived to occur at higher levels, which finally exceeds that of the flat scratch. Figure 6.35.d is of a slight discontinuation of the scratch and here the film

covered area is clearly above the substrate's surface at the scratch. Still the few deeper (dark blue coloured) points indicate that the perception of height is still false, in comparison with the silica surface.

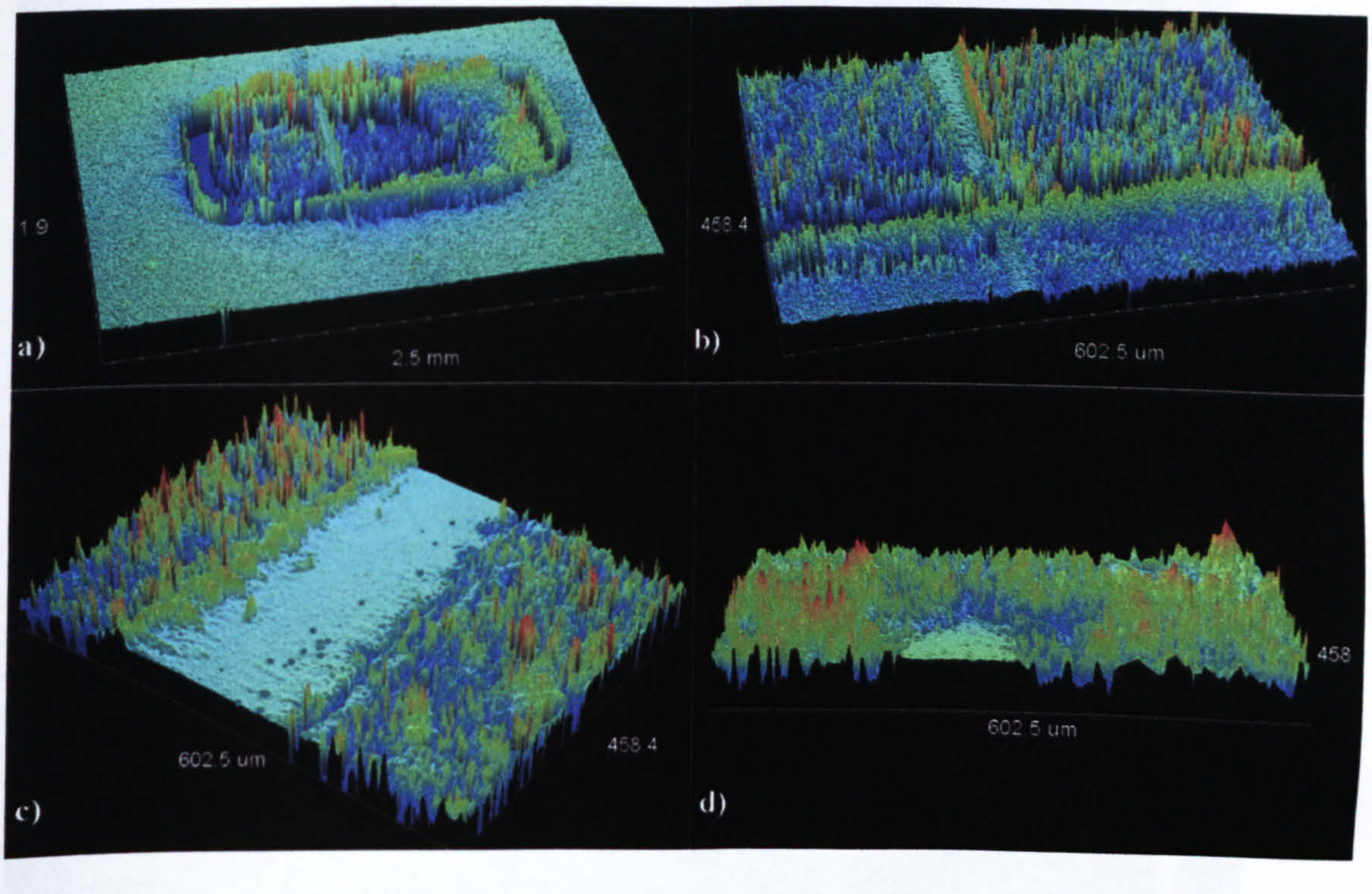

Figure 6.35 Surface profile of a transferred CdZnS:Ag film site at increasing magnification from a) to d). The site features a wide scratch at the same level of the target substrate surface. As the magnification increases, the film covered area elevates above the substrate's surface level.

To avoid the problems that accompany refractive index mismatch of the two materials taking part in the profiled area, the carbon coated samples used for SEM, were employed. Due to the thin layer of carbon applied over both the film and the substrate, the two types of surface now have the same refractive index, while the surface morphology remains the same, as the layer is usually homogeneous with a thickness of a few nanometers. The height difference between the five-layer transferred film in Figure 6.28 and its silicon wafer substrate, is measured by the 2D analysis module of the instrument and roughly by comparing the colour coding of the profile image shown in Figure 6.36. Linear level averages are taken from the surroundings of the measurement point, aiding a more objective area level comparison. The 5-layer film height was found between 600 to 800 nm, in agreement with the thickness measured on the SEM image of 800 nm (Figure 6.28). So, profiling of a surface with uniform refractive index, by interferomentry, thus including film

coated surfaces, can be quite reliable, in contrast with surfaces composed of two or more different materials. Unfortunately no other sites on a carbon coated sample were found to accommodate undisputed film thickness measurements.

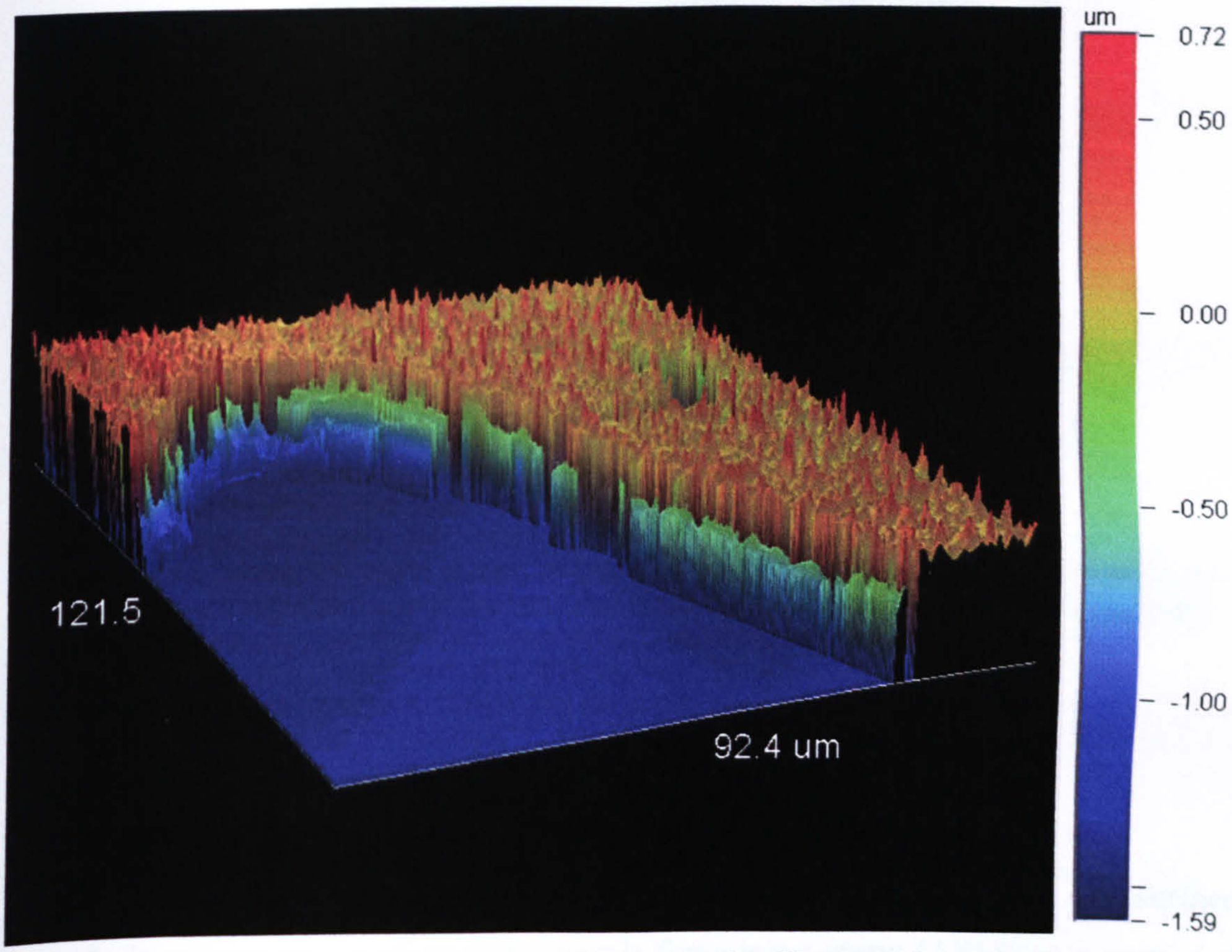

Figure 6.36 Surface profile at the broken edge of a silicon wafer sample carrying a five layer CdZnS:Ag film. The fluence used for the transfers was 0.49 Jcm^{-2} and the chamber atmosphere was argon at a pressure of $2.5x10^{-2}$ mbar. The step between the red spot tops and the green is the thickness of the film.

In a similar way, a trench found on an uncoated ZnS:Cu source film was interpreted correctly as a depression (Figure 6.37). The trench was not artificially induced on the film. It appears to be a discontinuity on the growth or attachment of the ZnS film composing particles. The level difference between the light blue area of the trench and the green areas characterising the ZnS film is approximately 135 nm. This is also the expected film thickness for the sample, according to the chemically deposited film thickness investigation presented in section 4.4. However, the light blue areas do not correspond to the source substrate's surface, but rather to the expected ZnO thin prelayer allowing for further growth of ZnS on the silica surface. The refractive indices of ZnS and ZnO fall much closer than that of SiO_2 and even more, the ZnO layer could already be carrying a thin inhomogenously grown ZnS

layer on it, which would secure the matching of refractive index between the two areas.

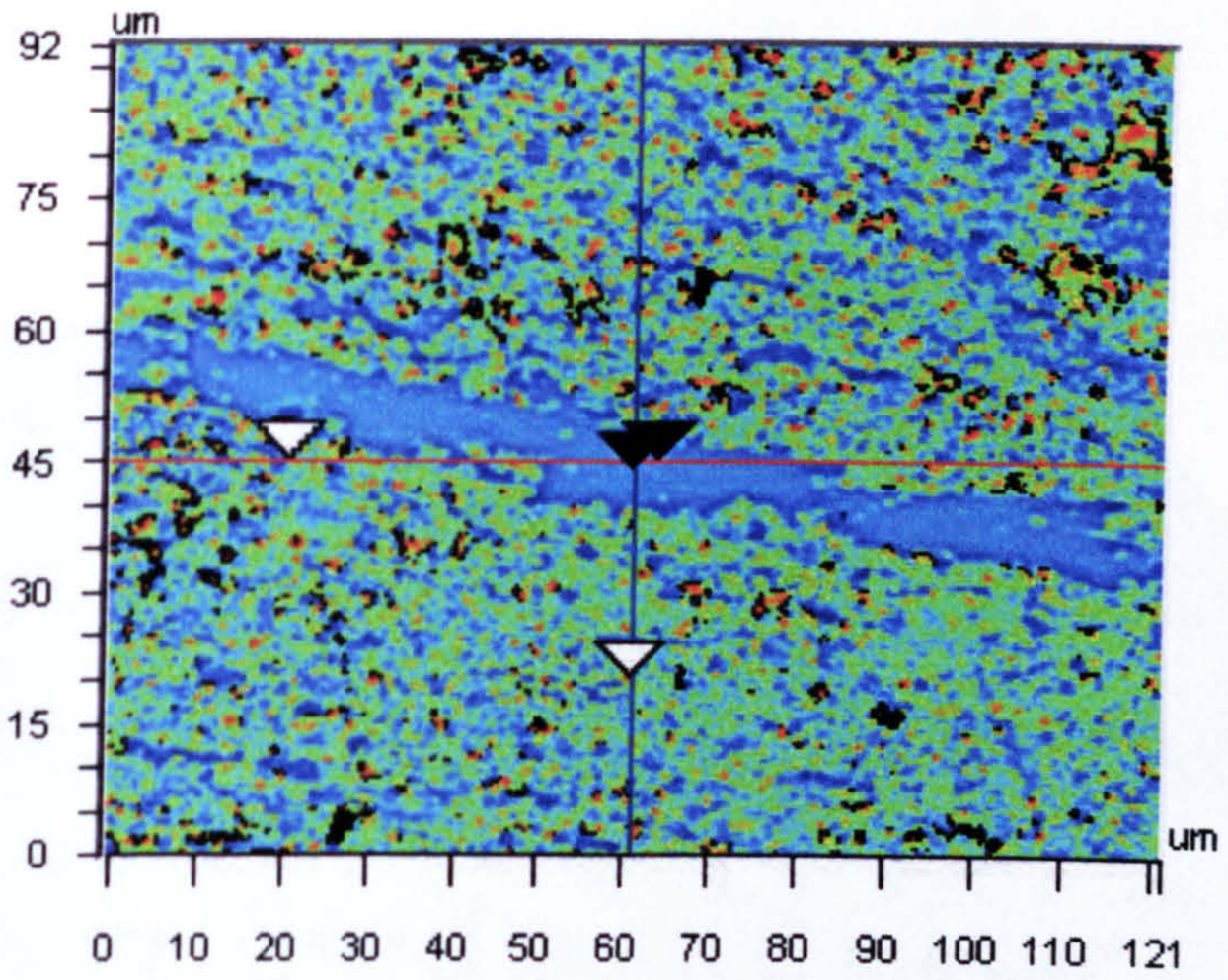

Figure 6.37 Surface profile of a ZnS:Cu source sample prepared in an excess of zinc chloride salt. The surface features a ZnS film growth discontinuity upon the ZnO prelayer.

6.3.d. AFM

An investigation of source and transferred films in terms of surface morphology, was also performed by atomic force microscopy (AFM) on a restricted number of source and target samples. Unlike interferometry, which gave very good resolution only in measuring the height of the various surface features, atomic force microscopy can obtain topographic surface scans with good resolution in all dimensions. Unfortunately, the equipment did not allow for accurate targeting on the investigated areas. Therefore it is quite questionable how much each scan represents the sample or transfer site under examination.

Nonetheless, the scans obtained from the chemically deposited films reveal a surface morphology that is very similar to that observed in the SEM images. The films are composed of a number of fused particles with an approximate diameter of 150 to 300 nm (Figure 6.38). The surface resembles a single layer of beads where all are grown to a certain height as discussed in section 4.3.a. Therefore, the surface appears quite flat except from shallow depressions defining the round particles. The diameters of the fused beads seem to be close to the values mainly obtained from the SEM images.

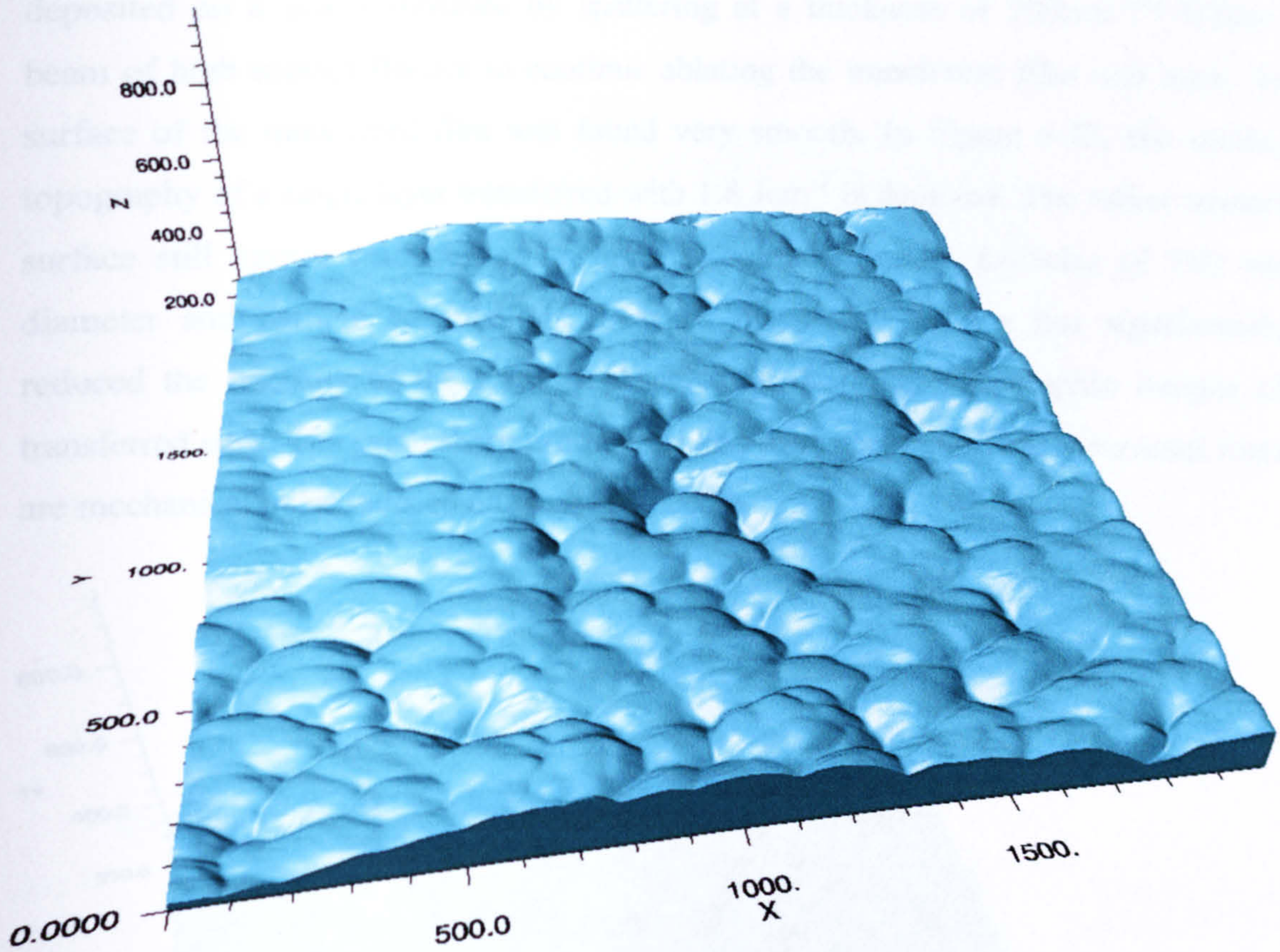

Figure 6.38 AFM surface topography of a chemically deposited CdZnS:Mn film. Units are in nm.

The size of particles, or round surface impressions that are observed on the target samples varies from approximately 100 nm (Figure 6.39), to similar levels with those of the source samples (Figure 6.40). Pique et. al. have presented AFM images of KrF laser transferred SrS films, using a fluence between 1 and 2 Jcm^{-2}. These had particles of similar size to those in this study. However, their films did not originate from chemically deposited films and there is no indication of structure of their equivalent source films.[31] In comparison between our source and target samples, the beads seem more disordered here, thus making the surface rougher than what is observed in the source film topographic image. However, the source and target sites investigated by AFM are fairly unrelated, therefore different surface structures are expected. At some of the investigated transferred film areas, larger features are found on the surface, reaching sizes above 500 nm. They appear to be coagulations of the smaller 100 to 200 nm particles (Figure 6.41). Similar formations are observed in

laser induced forward transferred gold films by a fluence of 0.2Jcm^{-2}, initially deposited on a quartz substrate by spattering at a thickness of 200nm.[24] When a beam of high enough fluence to continue ablating the transferred film was used, the surface of the transferred film was found very smooth. In Figure 6.42, the surface topography of a single layer transferred with 1.8 Jcm^{-2} is depicted. The rather smooth surface still carries evidence of its original composition by particles of 100 nm diameter and particle coagulations. Loss of mass and melting has significantly reduced the intensity of the features observed in the other topographic images of transferred sites. The small sharp protrusions and their accompanying horizontal lines are mechanical noise induced on the AFM needle.

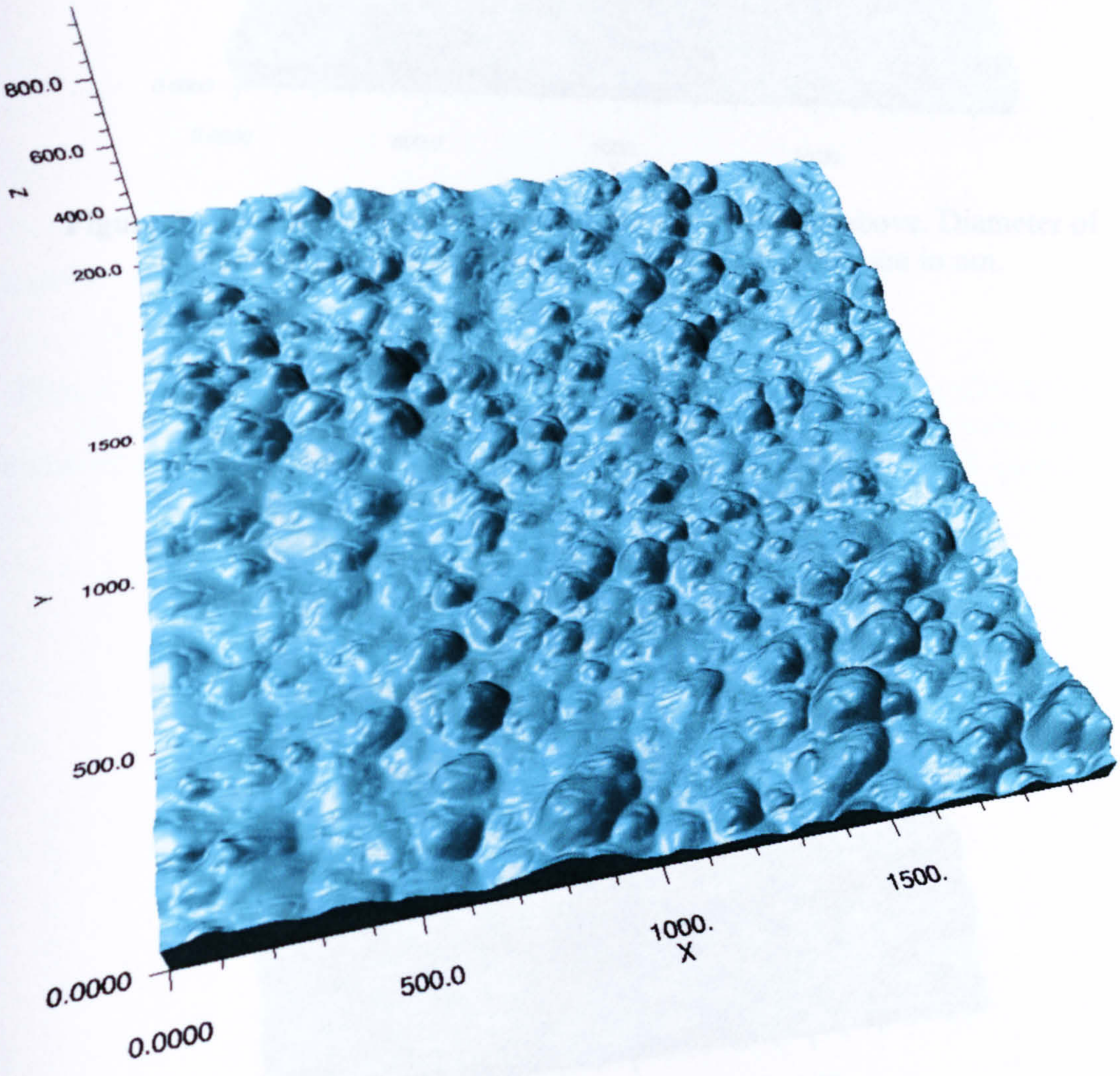

Figure 6.39 AFM topographic image of a CdZnS:Cu transferred film, with a fluence of 0.48 Jcm^{-2} in an argon atmosphere of 3.6x10^{-2} mbar. Diameter of component particles is between 100 to 200 nm. Units are in nm.

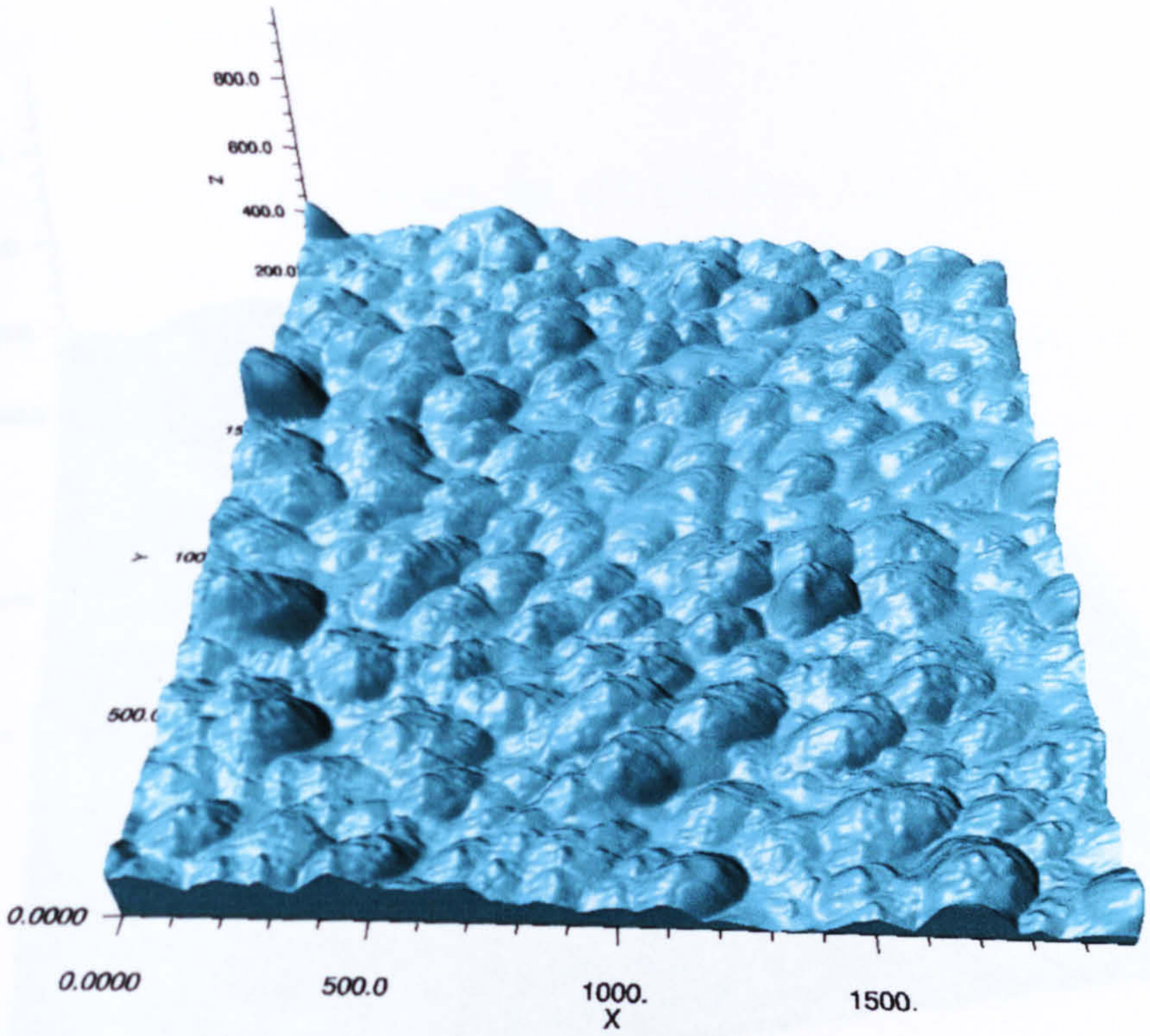

Figure 6.40 AFM topographic image of the site described above. Diameter of component particles is between 150 to 300 nm. Units are in nm.

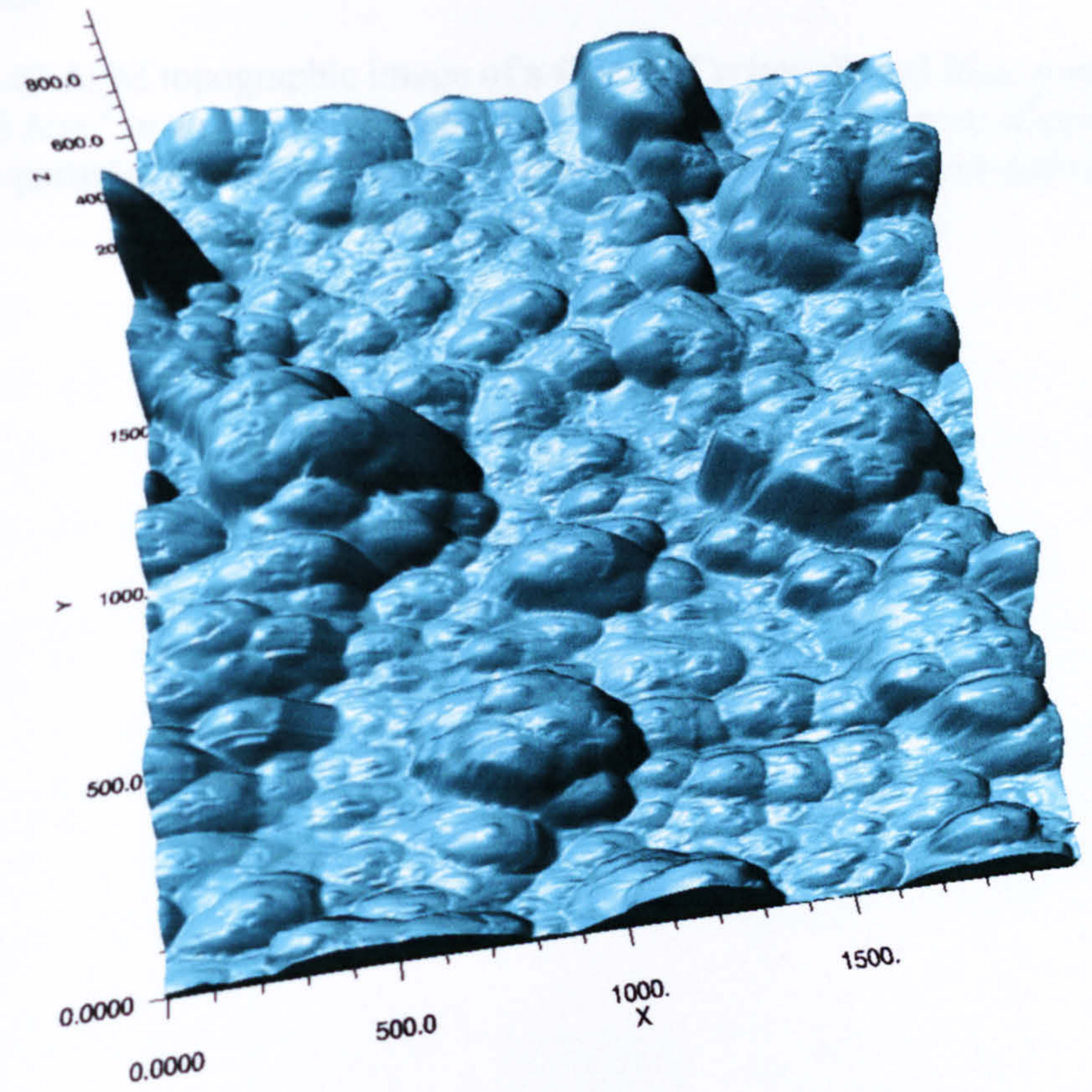

Figure 6.41 AFM topographic image of the site described above. Particle coagulants of size greater than 600 nm are distinguished. Units are in nm.

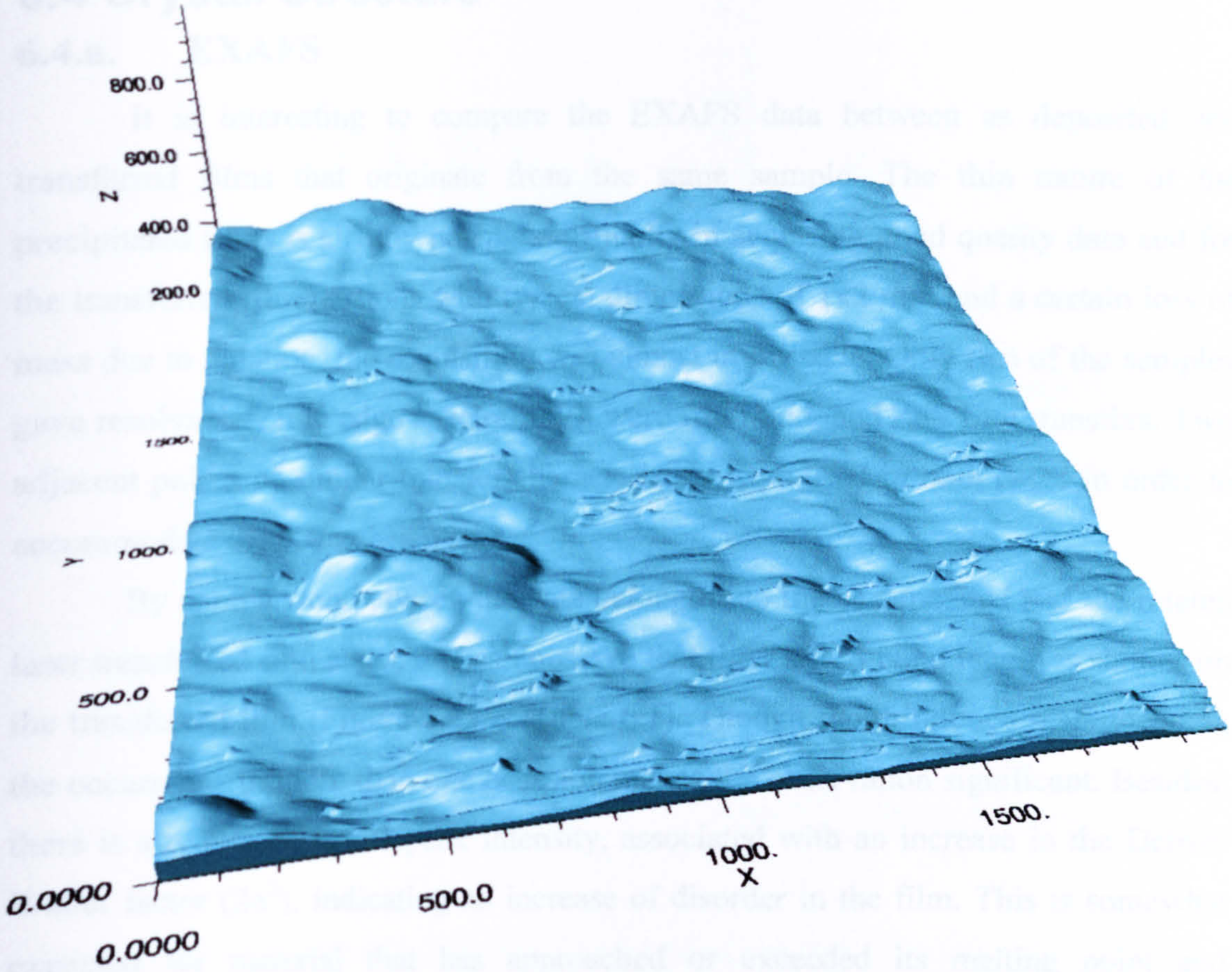

Figure 6.42 AFM topographic image of a CdZnS:Cu transferred film, with a fluence of 1.8 Jcm^{-2} in an argon atmosphere of 3.6x10^{-2} mbar. Evidence of precursor composite particles is present, indicating diameters of 100 to 200 nm and coagulations reaching up to 500 nm in size. Units are in nm.

6.4 Crystal Structure

6.4.a. EXAFS

It is interesting to compare the EXAFS data between as deposited and transferred films that originate from the same sample. The thin nature of the precipitated films is already posing a difficulty in acquiring good quality data and for the transferred film portions with typical dimensions of 1x2 mm and a certain loss of mass due to ablation, the acquisition was almost impossible. Only two of the samples gave resolvable Zn K-edge spectra. Both were from undoped ZnS film transfers. Two adjacent pulses of similar transfer characteristics were used in both cases in order to accommodate the X-ray beam spot.

By comparison between the data belonging to the as deposited and the related laser transferred film areas, one can observe that the Zn to S bond length is shorter on the transferred film (Figure 6.43 & Table 6.1). Though the difference is quite small, the occurrence in more than one occasion makes the observation significant. Besides, there is a reduction in the peak intensity, associated with an increase in the Debye-Waller factor ($2\sigma^2$), indicating an increase of disorder in the film. This is somewhat expected for material that has approached or exceeded its melting point and recrystallised on a new surface in a maximum of a few hundred nanoseconds. It also agrees with the speculation in Section 6.2.b concerning the loss of sulfur during the transfer, based on a comparison of EDX spectra (Figure 6.6). On the other hand, a comparison between SEM micrographs of the source and target samples in section 6.3.b proves that the morphology of the as deposited film can be retained to a certain degree, even after the transfer, though the sample examined by EXAFS was irradiated with a much higher fluence for that type of transfer.

Table 6.1 Zn K-edge EXAFS refined parameters for source-target sample pairs

	$r_{Zn\text{-}S}$ /Å (x4)	$2\sigma^2_{Zn\text{-}S}$ / Å^2	E_f /V	R	FI
3xZn, source, annealed at 540 °C	2.336(7)	0.0156(10)	-7.9(9)	38.6	0.747
3xZn, Irradiated with 1 Jcm^{-2}, annealed at 540 °C	2.328(14)	0.0163(21)	-8.0(17)	45.5	1.73
1xZn source	2.324(6)	0.0166(9)	7.5(8)	33.1	0.603
1xZn, Irradiated with 1.3 Jcm^{-2}	2.302(11)	0.0215(17)	-3.9(13)	47.3	1.32

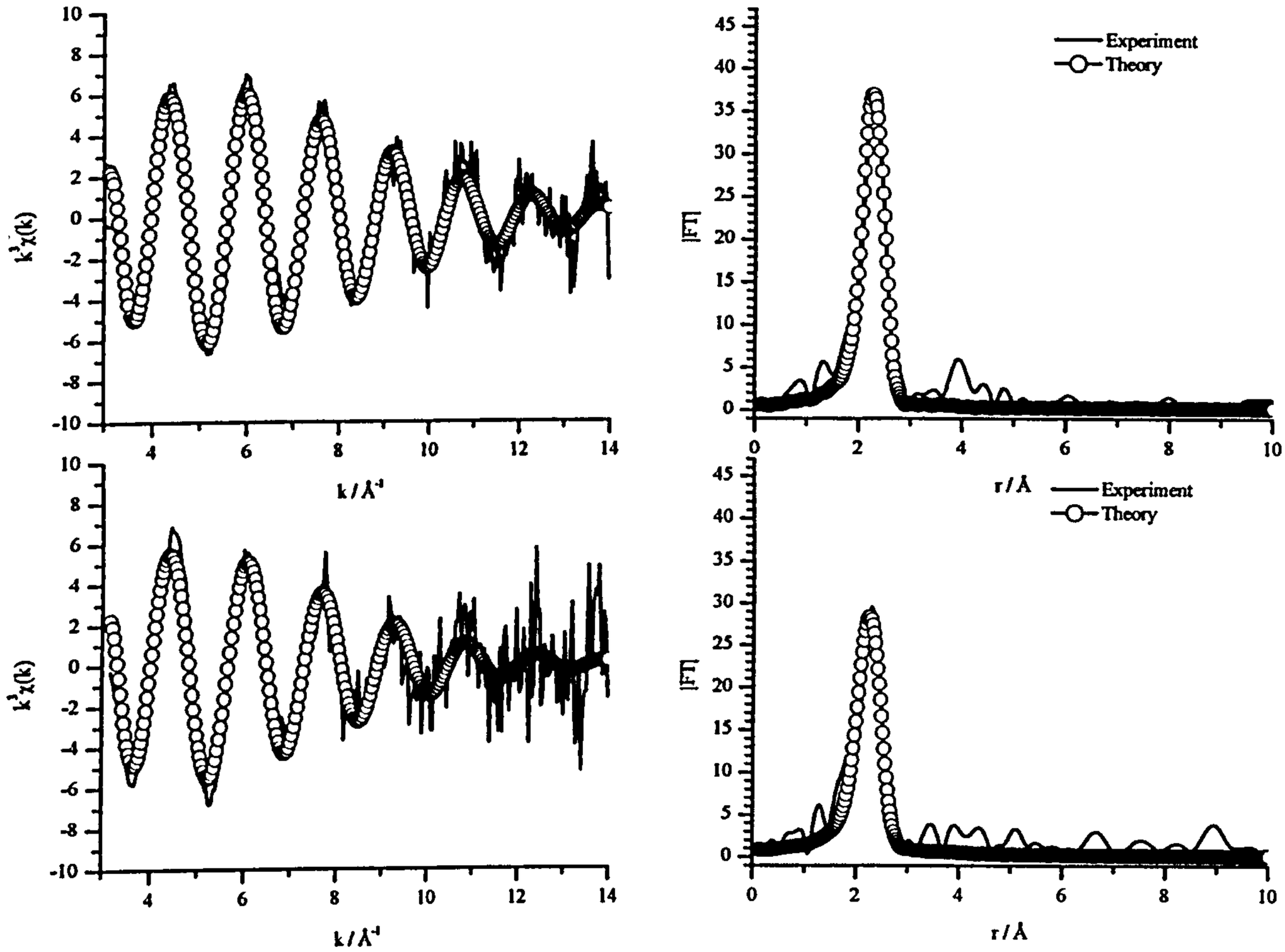

Figure 6.43 Zn K-edge EXAFS and FTs for a ZnS, source (top) and target (bottom) sample pair, irradiated with 1.3 Jcm^{-2} in a chamber pressure of $1.3x10^{-5}$ mbar of atmospheric air.

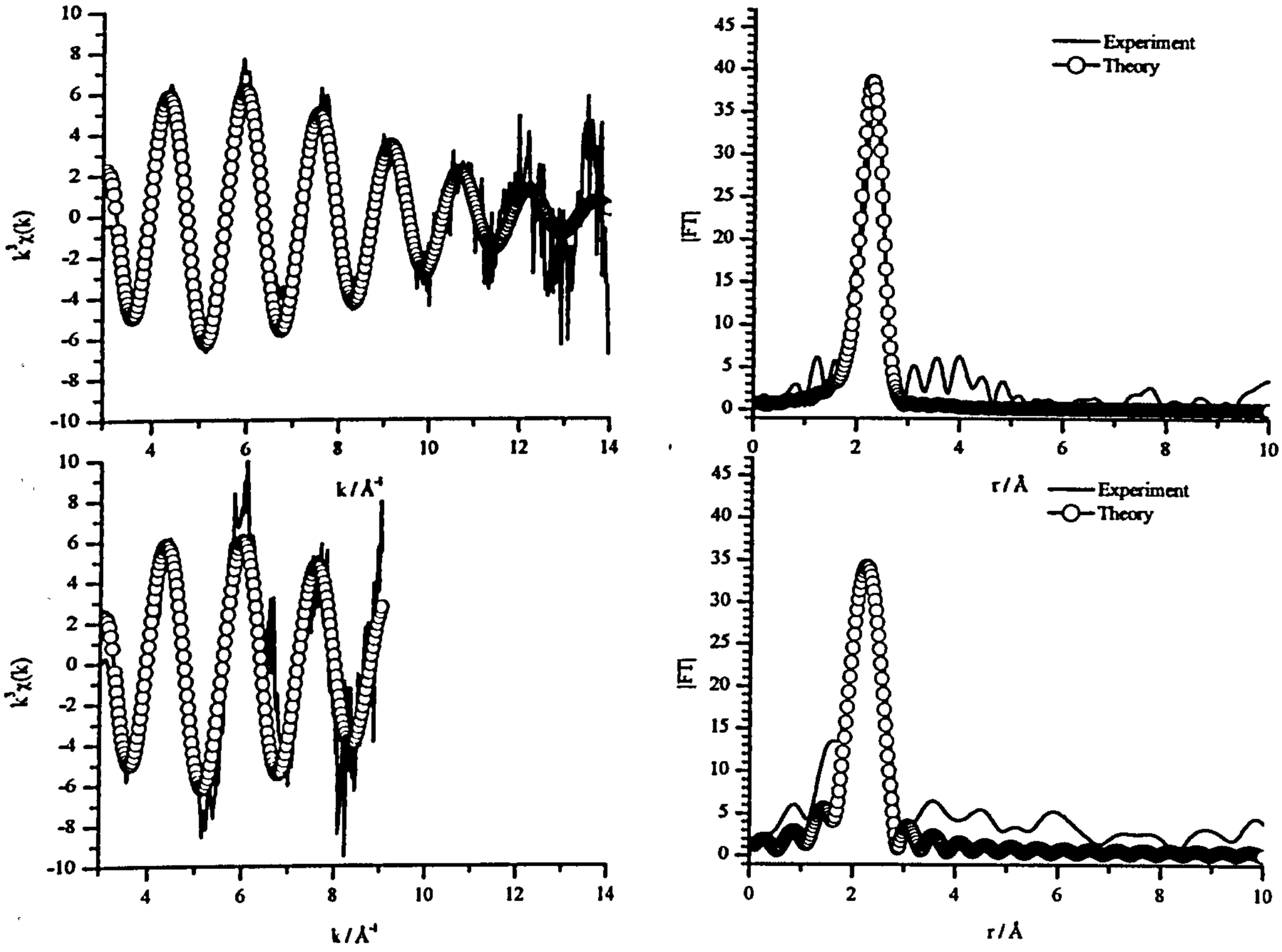

Figure 6.44 Zn K-edge EXAFS and FTs for a ZnS(3:1 ratio of metal chloride to TAA concentration), source (top) and target (bottom) sample pair, irradiated with 1 Jcm^{-2} in argon at a pressure of $4.0x10^{-5}$ mbar. The data towards the end of the target associated spectrum (bottom-left) is missing, possibly due to a small malfunction in the acquisition and processing electronics, or extensive noise. Yet, useful information have been deduced.

6.5 Luminescence

6.5.a. Cathodoluminescence

The majority of the transferred sites did not emit any significant luminescence under the cathode ray and most of them did not show any form of reaction to it. The cathode ray guiding system and the multiple point light probe coupled with it did allow to a great extent for area selective focussing on the samples under investigation. Also, large-area transfers and multiple pulse depositions were attempted in order to increase the luminescence yield, but unfortunately, with no significant improvement. Only a selection of sites and samples, grown and transferred under certain conditions described below, gave weak, or sometimes, strong cathodoluminescent (CL) spectra that related to its source film characteristics. Investigation of the same samples by photoluminescence was slightly more fruitful with most of the sites, giving at least some amount of detectable light.

The undoped zinc sulfide transferred sites were not emitting strongly enough under the cathode ray, in order to allow for observation. Transferred sites of undoped zinc sulfide that have been annealed at 700 °C, were found to emit weakly at similar wavelengths as the undoped ZnS source samples and the bulk samples of fired zinc sulfide. The CL emission spectrum of such a site is depicted in Figure 6.45 featuring a main peak at 505 nm and a shoulder at 455 nm. In section 4.6.a the 455 shoulder was related to surface sulfur deficiencies. The 505 nm peak is between the 495 nm, attributed to zinc interstitials and the 515 nm one, occurring in similarly annealed samples, which was associated with copper impurities interacting with either chlorine substitutions, or unintentionally incorporated aluminium impurities. Unlike the source sample spectra of this type that have already been analysed in section 4.6.a, the initial film of this sample was not prepared in a bath with an excess of zinc. The flat emission band from 620 to 700 nm and the small peak at 762 nm are the SiO_2 substrate emission, combined with reflected light from the filament.

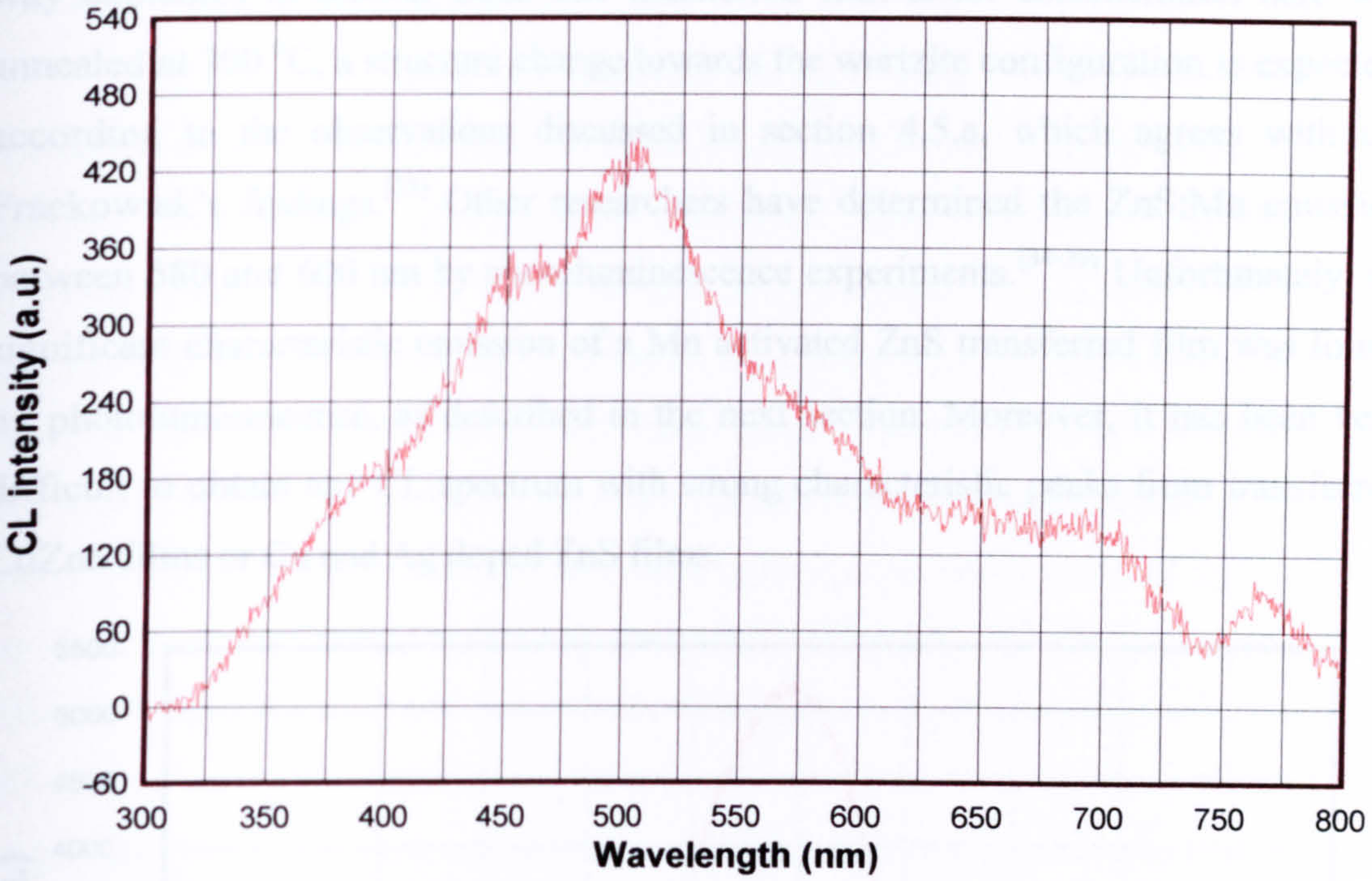

Figure 6.45 CL spectrum of transferred, undoped ZnS film, annealed at 700 °C. A laser fluence of 0.52 Jcm^{-2} was used for the transfer, at a pressure of $1x10^{-4}$ mbar, air.

The strongest cathodoluminescence emission obtained from a transferred film belongs to a manganese-activated ZnS film (Figure 6.46). The film was prepared in a bath with double quantity of zinc chloride salt and a 5:1 ratio of Mn to Zn salts, therefore securing coprecipitation of the high K_{sp} Mn species with the zinc sulfide films. The transfer was carried out using a laser fluence of 0.63 Jcm^{-2} at a chamber pressure of $2.8x10^{-2}$ mbar, flushed with argon. It is noteworthy that most of the transferred sites that emit under the cathode ray, were transferred with a rather low fluence, between 0.5 and 0.7 Jcm^{-2}. Moreover, annealing the target samples at 650 to 700 °C is found to significantly increase the emission intensity.

The main emission peak in the CL spectrum of Figure 6.46 is centred at 596 nm, being very close to the generally accepted 585 nm emission of the 3d-3d Mn transition. The emission peak of its source target is sharper, but of lower intensity, presenting a maximum at 592 nm. Dinsmore et al. also report a CL peak in the spectrum of ZnS:Mn nanoparticles, centred at 600 nm.[32] Furthermore, Frackowiak et al., find well resolved CL peaks on the spectra of ZnS:Mn, ranging from 575 nm to 608 nm, with the most intense one at 585 nm for a zincblence structure and at 590 to 599 for wurtzite structures.[33] As the 3d orbitals are unshielded from the environment,[34] the transition energy can be affected by the lattice parameter in the

way explained in section 4.6.a. The transferred film under consideration here was annealed at 700 °C, a structure change towards the wurtzite configuration is expected, according to the observations discussed in section 4.5.a, which agrees with the Frackowiak's findings.[33] Other researchers have determined the ZnS:Mn emission between 580 and 600 nm by photoluminescence experiments.[34-39] Unfortunately, no significant characteristic emission of a Mn activated ZnS transferred film was found by photoluminescence, as described in the next section. Moreover, it has been very difficult to obtain any CL spectrum with strong characteristic peaks from transferred CdZnS films or Cu and Ag doped ZnS films.

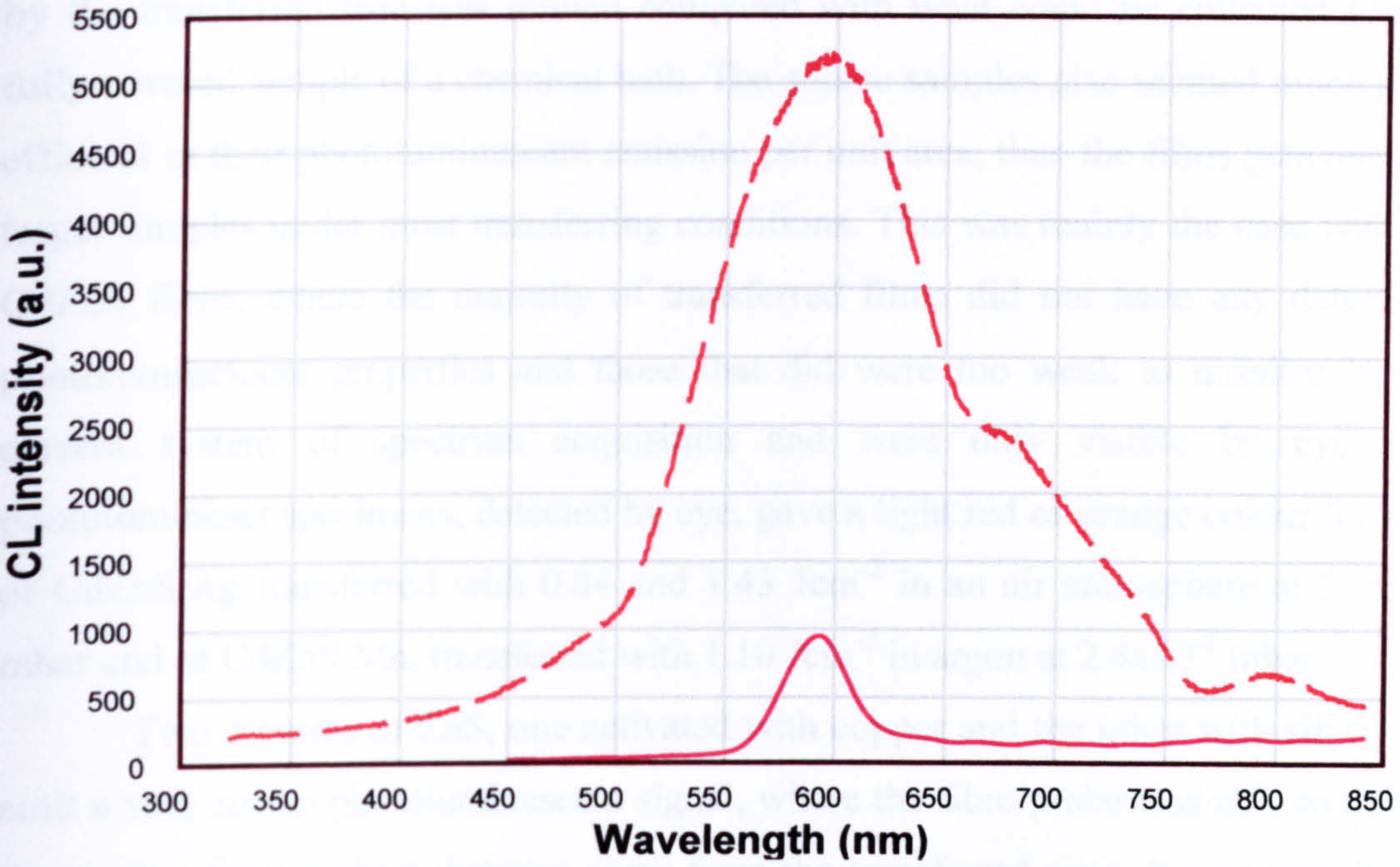

Figure 6.46 CL spectrum of a transferred ZnS:Mn film (dashed line) and its source (full line). The sample was prepared in a bath with 0.26 g (11.2 mM) of zinc chloride salt and 1.3 g (38.6 mM) of manganous chloride hydrate salt. The transfer was performed with 0.63 Jcm^{-2} laser fluence, at $2.8x10^{-2}$ mbar of argon. The target sample was then annealed at 700 °C for 26 hours.

6.5.b. Photoluminescence

The transferred films were generally not very reactive to the photoluminescent excitation beam of the He-Cd laser (tuned at 325 nm), though a larger number of them emitted faintly with the photonic excitation than with the cathodic. The photoluminescent emission was collected by a polymer optical fibre that did not include any focussing optics at its entrance. As a result the fibre had to approach very close to the surface of the transferred films, most of which were of a similar size to the diameter of the fibre. Thus, part of the transferred film was shaded by the probing fibre. Even when large area transfers were investigated, the amount of light emitted by the transferred film was limited compared with what could be collected from a fully covered sample of a chemical bath. The source samples also seemed much more efficient in their photoluminescent emission per unit area, than the films generated on target samples under most transferring conditions. This was mainly the case with the CdZnS films, where the majority of transferred films did not have any detectable photoluminescent properties and those that did were too weak to monitor by the current system of spectrum acquisition and were only visible by eye. The photoluminesct specimens, detected by eye, gave a light red or orange colour for sites of CdZnS:Ag transferred with 0.84 and 1.43 Jcm^{-2} in an air atmosphere at $3.7x10^{-2}$ mbar and of CdZnS:Mn, transferred with 1.10 Jcm^{-2} in argon at $2.4x10^{-2}$ mbar.

Two samples of ZnS, one activated with copper and the other with silver, did emit a very strong photoluminescent signal, where the fibre probe was able to collect the spectra from a short distance away from the transferred sites. It was possible to analyse the spectra and relate them to those obtained by equivalent source films. In the ZnS:Cu transferred films (Figure 6.47), the characteristic 495 to 520 or 530 nm features of copper activated zinc sulfide appear.[40, 41] As above, the 495 to 530 nm set of peaks is related to a transition from the Cl, or Al substituents, to the copper activator level.[42-45] A shoulder at 460 to 470 nm arising from conduction band to Cu level transitions,[46, 47] is absent in these data. The source sample was created in a bath with an excess of zinc chloride salt (triple quantity). The recipe gave samples with equally efficient photoluminescence as their source substrates. The spectrum collected at a liquid nitrogen temperature (broken blue line) was of lower intensity than that in room temperature, because the probing optical fibre had to be positioned closer to the sample in order to achieve better targeting of the correct transfer site. Therefore, less

excitation light from the laser source was reaching the site directly. The site that gave the strongest emission was the one transferred with the lowest fluence setting on the sample. The fluence used was 1.31 Jcm^{-2}, while the rest of the sites had been obtained with higher fluence settings, reaching up to 2.7 Jcm^{-2}. A rather typical chamber pressure of atmospheric air was used, at $4.6x10^{-2}$ mbar. Ideally, a lower energy regime should have been used, as will be discussed in the next section and the results of this transferring attempt showed a degree of success in terms of photoluminescence, only because of the high efficiency of the equivalent source samples.

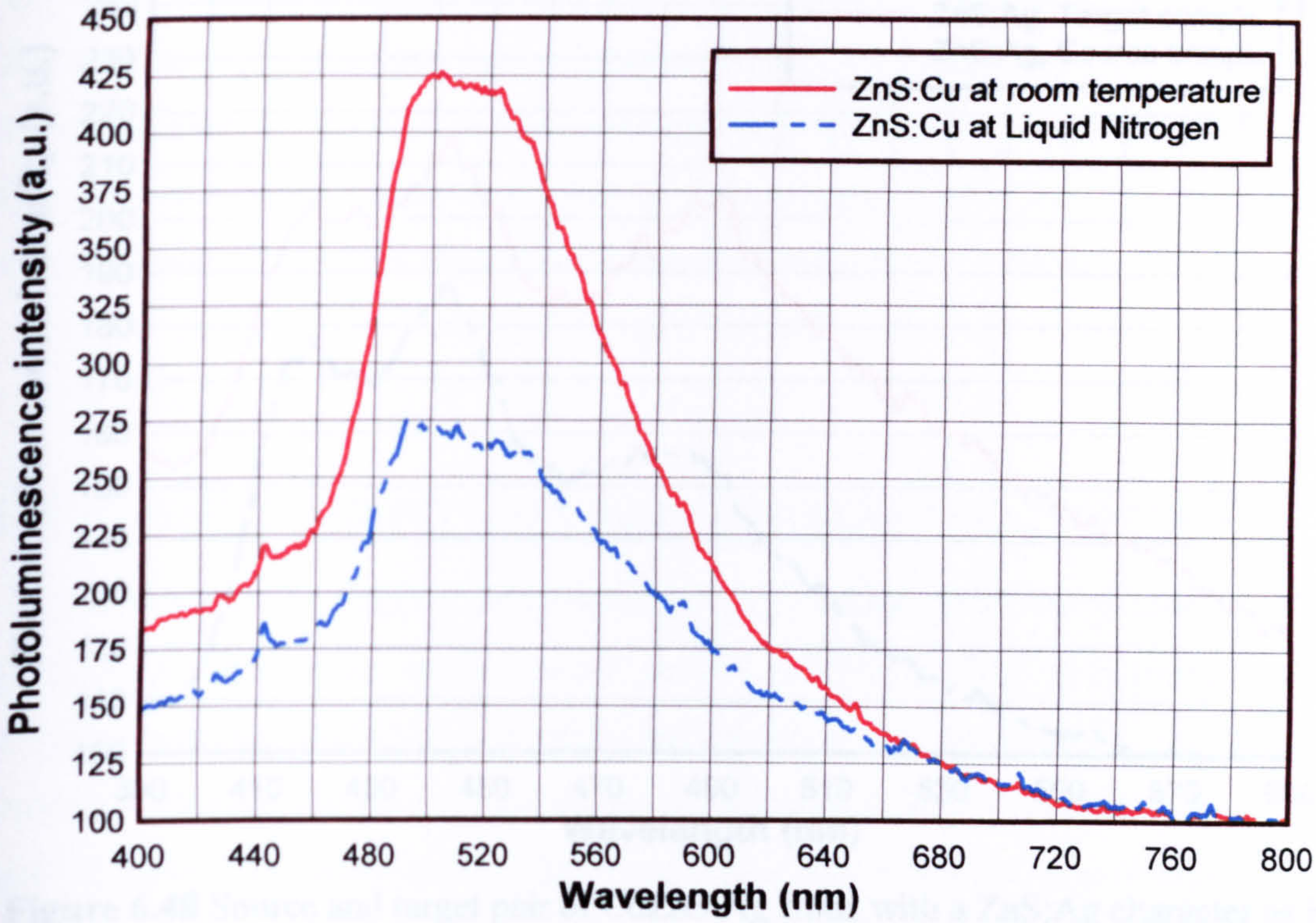

Figure 6.47 Transferred ZnS:Cu film spectra, obtained at room temperature and liquid nitrogen temperature. The transfer was performed with a fluence of 1.41 Jcm^{-2} at an atmospheric gas pressure of $4.6x10^{-2}$ mbar. The source sample was prepared in an excess of zinc chloride salt.

A source-target pair of CdZnS:Ag films was examined in terms of photoluminescence. Their spectra are shown in Figure 6.48, where the target spectrum is unexpectedly higher in intensity than the source, which is because of the different angles in which the emission was collected. Here the transfer was made with a lower fluence than the ZnS:Cu sample above, reaching approximately half its magnitude, 0.66 Jcm^{-2}, at an argon gas pressure of $2.5x10^{-2}$ mbar. The same three peaks are recognised in both the source and the target film spectra. Again the peak assignment

of the source sample is obviously identical here, with transitions giving the 418 nm peak from sulfur vacancies to the valance band,[48, 49] the 442 nm peak between a coactivating donor level and the silver acceptor level,[40] and the 485 peak, between the sulfur vacancies and the silver level again.[46] Hence, the existence of chlorine, aluminium or possible zinc interstitial atoms is rather beneficial for the luminescence properties of the films, as they seem to provide an efficient route of radiative de-excitation of the phosphor material.

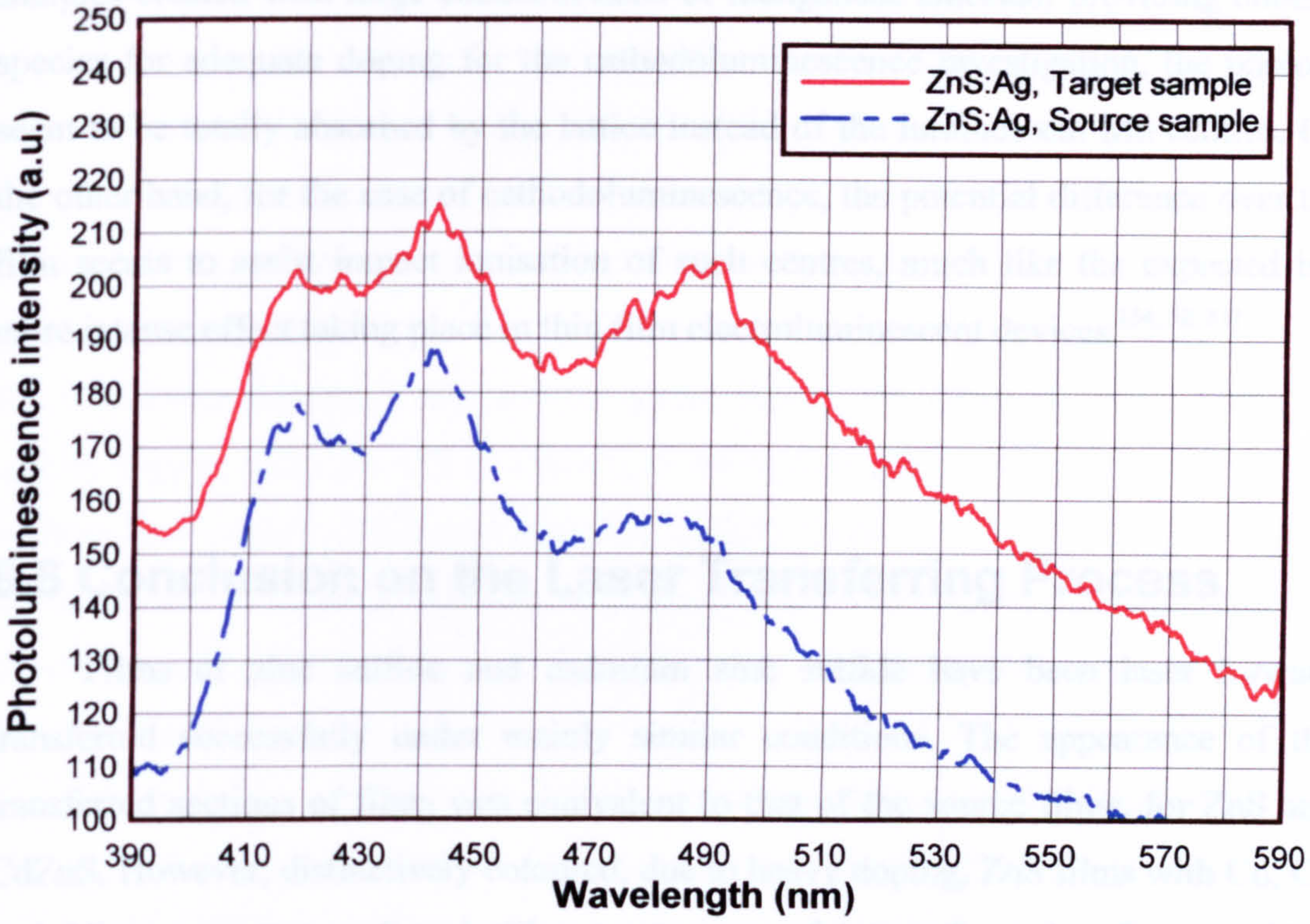

Figure 6.48 Source and target pair of CdZnS:Ag films with a ZnS:Ag character as it was chemically prepared in a great excess of zinc salt. The transfer was performed with 0.66 Jcm^{-2}, at an argon atmosphere pressure of $2.5x10^{-2}$ mbar.

It is thus found that the source samples that gave a strong photoluminescence emission, are the ones that can give the more efficient, in terms of photoluminescence, transferred films. The key element in the chemical preparation of these source films seems to be the excessive concentration of zinc chloride in the bath. The combined success of the recipe in achieving adherent clear films suggests that the use of double quantity of zinc chloride salt, at least 0.26 g (11.2 mM), together with 0.75 g (58.7 mM) of thioacetamide and 1.6 g (0.17 M) of urea. As it was also observed in sections 6.3.a, 6.2.b and 6.5.a, use of low fluence, between 0.5 and 1 Jcm^{-2} achieves transfer of a rather intact film, with similar characteristics to those of the source film, thus, also

inheriting its luminescent capabilities. Small doping of Cu or Ag aids the luminescence of both the source and the transferred films. Still, a degree of activation, independent of intentionally introduced dopants, occurs by the chemical deposition process. In fact, the efficiency of transitions related to the unintentional activation levels is high enough to absorb most of the UV photons in the case of photoluminescence, as it can be observed in the photoluminescent spectra, therefore quenching the expected Mn related emission in the manganese doped films. Even at samples created with large concentrations of manganese chloride, providing enough species for adequate doping for the cathodoluminescence investigation, the photons seem to be totally absorbed by the lattice instead of the luminescent Mn centres. On the other hand, for the case of cathodoluminescence, the potential difference over the film seems to assist impact ionisation of such centres, much like the expected but more intense effect taking place in thin film electroluminescent devices.[34, 50, 51]

6.6 Conclusion on the Laser Transferring Process

Films of zinc sulfide and cadmium zinc sulfide have been laser forward transferred successfully under mainly similar conditions. The appearance of the transferred sections of films was equivalent to that of the source films, for ZnS and CdZnS. However, distinctively coloured, due to heavy doping, ZnS films with Cu, Co and Ni were not transferred. The most successful transfers also featured high reflectivity. It was possible to deposit successfully multiple layers of each type of film over the same area, thus increasing the film thickness.

One of the first concerns after the laser transferring process is whether the transferred film has remained the same in composition as its source. Raman investigation of thick films generated by multiple layer transferring in section 6.2.a identified the main emission peak that was also found in bulk cubic ZnS in section 4.5.b, for a transferred film from a ZnS source sample. The method has also identified peaks corresponding to CdS according to other researchers and to ZnS on the same transferred site originating from a CdZnS chemically deposited film. Unfortunately, it was not possible to compare Raman spectra directly between source and target samples, as the source samples contained only very thin films, not suitable for such an

investigation. However, the spectra themselves were interpreted to represent blending of the hexagonal and cubic forms in the zinc sulfide samples and increased fragmentation of the crystallites. Lateral phase separation between the CdS and ZnS phases of the CdZnS films was observed to take place at least on the multiple layer transferred films. An increased disorder in the transferred films is also found by EXAFS, accompanied by a slight shrinking of the Zn-S bonds on the target ZnS films. Moreover, EDX analysis of the transferred sites detected zinc, sulfur and cadmium as the main elemental components of the films. There was a reduction of the Zn peak intensity, in contrast with that of sulfur, on the transferred films compared with their source films and an increase in the intensity of the Cd associated peaks.

It is also interesting to discuss the assumed progress of the transfer process. As most of the laser beam energy at 248 nm transmits through the silica glass medium, acting as a carrying substrate for the film of interest, it reaches the interface between the chemically deposited film and the glass. There it is absorbed by the film, to a certain degree, either by ZnS or CdZnS, as the wavelength is well above the bandgap of both zinc sulfide (3.64) and cadmium sulfide (2.44). As the absorbed energy is converted into heat, the material at the heated interface will vaporise. These gases will be the ones to propel the rest of the film away from the source substrate surface, towards that of the target.

However, the scenario appears to be somewhat more complex than that, as it is proven by the various observations set out above. In chapter 4 it was pointed out that a very thin ZnO layer is needed to grow first on the substrate, during chemical deposition which will then aid the adherence and growth of the film's main volume consisting of either ZnS or CdZnS. Therefore, the light would absorb differently on the oxide and the sulfide and here is essentially another interface between the two types of deposited materials. Most importantly, the build up of heat will have different effects on the sulfide than on the oxide. ZnO has a melting point at 1975 ^{o}C, while ZnS sublimes at 1185 ^{o}C (possibly through partial decomposition) and CdS at an even lower temperature of 980 ^{o}C. Consequently, as the sulfide passes to the gas phase on the sulfide/oxide interface, the thin ZnO layer may still be in the solid phase. A gradient of approximately 1000 ^{o}C is required over a space of a few tenths of nanometres, equivalent to the thickness of the ZnO layer, in order to obtain melting of ZnO and sublimation of the ZnS or CdZnS simultaneously, which is unlikely even at the very short timescales of thermal build up, whereas transmission through the ZnO

layer and optical absorption by the sulfide has to be considered. Hence, the gases formed on the sulfide/oxide interface would propel only the sulfide layer away from the ZnO and source sample. This is supported by observations in sections 6.2.b, 6.3.a and 6.3.c.

The full film is removed at high fluence regimes, above 1.7 Jcm^{-2} where a large amount of material is scattered outside the boundaries of the imaged laser beam. The scattered material increases as the chamber pressure drops. At such high fluence, the temperature is obviously reaching stages where the ZnO layer is also passing to the gas phase, or is pushed away in its liquid form, by the high pressure of the gasses formed by the sulfide layer. The edge definition of the transferred film section on the target substrate becomes highly disturbed under these conditions. At very high fluence, above 2.2 Jcm^{-2}, the transferred film is ablated away from the target surface, as well as the source.

At low fluences, that are not able to transfer the irradiated film area, particles of the source film can still be detached and transferred on the target. This phenomenon is observed with fluence settings below 0.4 Jcm^{-2}. Here the existence of feebly attached particles is assumed on the source sample. With only small amounts of energy delivered by the beam, the film does not reach its sublimation point homogeneously over all of the irradiated area, therefore the loose particles will detach first from the film, while the rest will remain adhered on the source. In addition, the connection points of such particles to the rest of the film often form lattice mismatches, which absorb a greater amount of energy compared to the continuous lattice and thus locally, greater temperatures are raised. These connections could provide the propelling gas generating areas for the transfer of individual particles. Thermal modelling of the laser irradiated source films would enlighten further the speculations set out here, describing the transferring process.

Multiple layers of both film types can be deposited on the same area of the target substrate. The edge definition is of the same quality as the single layer transfers, up to 5 successive layers. It remains acceptable up to around 8 to 10 layers, depending on the transferring conditions and the thickness of the source film. That is, at low fluence, close to 0.5 Jcm^{-2} and with a thin source film, more layers can be deposited on each other, with less disturbance induced on the surface and edge definition of the resulting film. The layers appear to integrate well with each other, even at a low fluence. When the number of layers, or the laser fluence increases, melting effects are

observed on the surface of the transferred film, under which the surface is slowly smoothed out and any sharp characteristics, occasionally originating from the source film, are gradually removed. When the number of successive laser deposited layers over the same area increases above 15, the film becomes quite thick and may start loosing its volume by further irradiations, or detach and translate.

Luminescence

It was very difficult to obtain luminescence spectra from the transferred film sites. Most of them did not fluoresce under UV or cathodic excitation. Only the most efficient source films, in terms of their luminescent properties, gave target sites with a significant emission under excitation, especially in the photoluminescence experiments. The increased disorder detected in the EXAFS investigation and the small crystallite composition associated with the Raman spectra, seem to be a result of the transferring process. In combination with high concentration of unwanted impurities, found in the source films by ICPMS and sometimes by the less sensitive EDX, these characteristics of the transferred films are expected to quench the excitation of luminescent centres or the radiative transitions associated with the intended dopant. For the PL experiments, transitions are taking place in the crystallite interfaces and non-radiatively between unwanted impurity levels. For CL, the electrons are absorbed at interfaces, or opposed by mismatches in activating the luminescent centres. An increased concentration of the metal chloride salts in the preparation bath and especially of zinc chloride, seems to reduce faults, or induce a form of continuity to the crystal, that aids radiative transitions in both cases.

Since the films are investigated as prospective electroluminescent films, efficient emissions like that of Mn in the ZnS lattice, under cathodic excitation were pursued. An annealing step applied to the target substrate, at 650 °C proved very successful in achieving adequately cathodoluminescent transfer sites. A similar method can be followed with activators such as Tb, situated in a similar geometry to Mn,[34] and possibly with other lanthanides, such as Ce, Eu and Sm. It is therefore proven that addition of extra $ZnCl_2$ in the chemical bath, is beneficial for all stages of producing and transferring ZnS and CdZnS films. Quantities of 0.2 to 0.5 g (8.6 to 21.6 mM) are recommended with all other possible mixtures of metal chlorides.

Recommended LIFT conditions and film characteristics

For electroluminescent films, ZnS source films are the most recommended, followed by CdZnS, which are less efficient due to the phase separation detected by Raman microscopy. The films should be grown in a stable temperature bath at 92 °C, on the outer side of the silica sample, with concentration defining quantities of 0.32g (13.8 mM), 0.74g (57.9 mM) and 1.7g (0.17 mM) for zinc chloride, thioacetamide and urea respectively. The manganese chloride mass in the bath should reach the levels of 1 to 1.5 g (29.7 - 44.6 mM), in order to achieve adequate doping. It would be interesting to attempt a similar deposition with a similar quantity of terbium chloride. For cadmium dominated films, a quantity of 0.25g (6.4 mM) of $CdCl_2$ against that of 0.1g (4.4 mM) for zinc chloride, can result in a film with good luminescent characteristics and a mainly cadmium sulfide character, with the characteristics retained to a great extent in the transferred film. A transfer fluence between 0.6 and 0.7 Jcm^{-2} is suggested for single layer transfers and a 0.5 to 0.6 Jcm^{-2} for multiple layer transfers. Low fluence regimes (0.4 to 0.8 Jcm^{-2}) are suggested for CdZnS films, while higher can be used for ZnS only (up to 1.2 Jcm^{-2}). A chamber pressure of $4x10^{-2}$ mbar, with an argon flushed chamber, appears to provide the best environment for well defined transferred sites, protecting against oxidation at the same time. To generalise the fluence and chamber pressure boundaries for similar in thickness films of the II-VI group, apart from the oxides, the recommended fluence at 248 nm is between 0.5 and 1.1 Jcm^{-2} and the chamber pressure can generally vary between $1x10^{-2}$ to $1x10^{-1}$ mbar. For transferring oxides, a higher fluence of 1.3 to 1.6 Jcm^{-2} will be needed. An annealing step at 630 to 650 °C for 8 or 10 hours will significantly improve the transferred film's luminesce performance. The annealing step can either be performed in a flowing argon atmosphere or an H_2S atmosphere, which will improve the balance of ion constituents in the lattice, aiding more the cases of luminescent centre based materials, as the case of ZnS:Mn.

6.7 References

1. M. Farnsworth, Zinc Chemicals, Zinc Development Association, London, 1973.
2. T. P. Tang, M. R. Yang and K. S. Chen, Effect of LiCl Flux on the Red ZnS:Sm Phosphors Fired in Reductive Atmosphere, Ceram. Intern., 2000, **26**, p 341.
3. C. Lan, K. Hong, W. Wang and G. Wang, Synthesis of ZnS Nanorods by Annealing Precursor ZnS Nanoparticles in NaCl Flux, Solid State Commun., 2003, **125**, p 455.
4. M. Osada, M. Kakihana, R. Adachi, T. Ichihara and N. Kijima, Near-Infrared Raman Spectroscopy as a Unique Tool for Characterisation of Visible Luminescent ZnS Phosphor, J. Ceram. Soc. Jpn., 2002, **110**, p 225.
5. R. D. Yang, S. Tripathy, F. E. H. Tay, L. M. Gan and S. J. Chua, Photoluminescence and Micro-Raman Scattering in Mn-Doped ZnS Nanocrystalline, J. Vac. Sci. Technol., 2003, **B23**, p 984.
6. Y. M. Yu, S. Nam, B. O, K.-S. Lee, Y. D. Cho, M.-Y. Yoon and P. Y. Yu, Resonant Raman Scattering in ZnS Epilayers, Mater. Chem. Phys., 2003, **78**, p 149.
7. J. Lee, Raman Scattering and Photoluminescence Analysis of B-doped CdS Thin Films, Thin Solid Films, 2004, **451-452**, p 170.
8. G. Perna, V. Capozzi, M. Ambrico, V. Augelli, T. Ligonzo, A. Minafra, L. Schiavulli and M. Pallara, Structural and Optical Characterization of Undoped and Indium-Doped CdS Films Grown by Pulsed Laser Deposition, Thin Solid Films, 2004, **453-454**, p 187.
9. O. Z. Angel, F. L. C. Alvarado, J. A. López, A. E. Esquivel, G. C. Puente, R. L. Morales and G. T. Delgado, Raman Studies in CdS Thin Films in the Evolution from Cubic to Hexagonal Phase, Sol. State Comms., 1997, **104**, p 161.
10. C. Cheng, G. Xu, H. Zhang, J. Cao, P. Jiao and X. Wang, Low-Temperature Synthesis and Optical Properties of Wurtzite ZnS Nanowires, Mater. Lett., 2006, p 3561.
11. A. Mlayah, A. M. Brugman, R. Carles, J. B. Renucci, M. Y. Valakh and A. V. Pogorelov, Surface Phonons and Alloying Effects in (CdS)x(CdSe)1−x Nanospheres, Sol. State Comms., 1994, **90**, p 567.
12. Z. Tòth and T. Szörènyi, Pulsed Laser Processing of Ge/Se Thin Film Structures, Appl. Phys. A, 1991, **52**, p 273.
13. D. Basting and G. Marowsky, Excimer Laser Technology, Springer/Praxis, 2005.
14. C. A. Brau, Excimer Lasers, 2nd enlarged Edition, Springer-Verlag, 1984.
15. A. E. Siegman, Lasers, Oxford University Press, 1986.
16. W. T. Silfvast, Laser Fundamentals, 2nd Edition, Cambridge University Press, Cambridge, 2004.
17. M. Aven and J. S. Prener, Physics and Chemistry of II-VI Compounds, North-Holland Publishing CO., Amsterdam, 1967.
18. A. Goldsmith, H. J. Hirschhorn and T. E. Waterman, Handbook of Thermophysical Properties of Solid Materials, Revised Edition Vol. 2 & 5, Pergamon Press, Oxford, 1961.

19. G. Hodes, Chemical Solution Deposition of Semiconductor Films, Marcel Dekker, New York, 2003.
20. A. Piqué, D. B. Chrisey, R. C. Y. Auyeung, J. Fitz-Gerald, H. D. Wu, R. A. McGill, S. Lakeou, P. K. Wu, V. Nguyen and M. Duignan, A Novel Laser Transfer Process for Direct Writing of Electronic and Sensor Materials, Appl. Phys. A, 1999, **69 [Suppl.]**, p S279.
21. H. J. Hirschhorn and T. E. Waterman, Handbook of Thermophysical Properties of Solid Materials, Vol. 1-5, Pergamon Press, Oxford, 1961.
22. I. Zergioti, S. Mailis, N. A. Vainos, C. Fotakis, S. Chen and C. P. Grigoropoulos, Microdeposition of Metals by Femptosecod Excimer Laser, Appl. Surf. Sci., 1998, **127-129**, p 601.
23. I. Zergioti, S. Mailis, N. A. Vainos, P. Papakonstantinou, C. Kalpouzos, C. P. Grigoropoulos and C. Fotakis, Microdeposition of Metal and Oxide Structures Using Ultrashort Laser Pulses, Appl. Phys. A, 1998, **66**, p 579.
24. B. Tan, K. Venkatakrishnan and K. G. Tok, Selective Surface Texturing Using Femptosecond Pulsed Laser Induced Forward Transfer, Appl. Surf. Sci., 2002, **207**, p 365.
25. X. Liu, D. Du and G. Mourou, Laser Ablation and Micromachining with Ultrashort Laser Pulses, IEEE J. Quantum Electron., 1997, **33**, p 1706.
26. D. B. Chrisey, A. Pique, J. Fitz-Gerald, R. C. Y. Auyeung, R. A. McGill, H. D. Wu and M. Duignan, New Approach to Laser Direct Writing Active and Passive Mesoscopic Circuit Elements, Appl. Surf. Sci., 2000, **154-155**, p 593.
27. A. B. Bullock and P. R. Botton, Laser Induced Back Ablation of Aluminium Thin Film Using Picosecond Laser Pulses, J. Appl. Phys., 1999, **85**, p 460.
28. R. Bähnisch, W. Groß and A. Menschig, Single-Shot, High Repetition Rate Metallic Pattern Transfer, Microelectron. Eng., 2000, **50**, p 541.
29. C. Lamb and M. Zecchino, WYKO Surface Profilers Technical Reference Manual, Veeco Metrology Group, 2.2.1 Edition, Tuscon, Arizona, 1999.
30. L. Ward, The Adam Hilger Series on Optics and Optoelectronics: The Optical Constants of Bulk Materials and Films, Adam Hilger, Bristol, 1988.
31. A. Piqué, R. C. Y. Auyeung, S. B. Qadri, H. Kim, B. L. Justus and A. L. Huston, Growth of Epitaxial Doped Strondium Sulfide Thin Films by Pulsed Laser Deposition, Thin Solid Films, 2000, **377-378**, p 803.
32. A. D. Dinsmore, D. S. Hsu, S.B.Qadri, J. O. Cross, T. A. Kennedy, H. F. Gray and B. R. Ranta, Structure and Luminescence of Annealed Nanoparticles of ZnS:Mn, J. Appl. Phys., 2000, **88**, p 4985.
33. M. Frackowiak, E. Chimczak, M. Kozielski, J.Kruszyna and A. Kuleczka, Luminescent Thin ZnS : Mn Films, J. Lumin., 1975, **14**, p 243.
34. P. D. Rack and P. H. Holloway, The Structure, Device Physics and Material Properties of Thin Film Electroluminescent Displays, Mater. Sci. Eng., 1998, **R21**, p 171-219.
35. J. Benoit, P. Benalloul, A. Geoffroy, N. Balbo, C. Barthou, J. P. Denis and B. Blanzat, Study of Highly Concentrated ZnS : Mn ACTFEL Devices, Phys. Status Solidi A, 1984, **83**, p 709.
36. R. N. Bhargava, Doped Nanocrystallin Materials - Physics and Applications, J. Lumin., 1996, **70**, p 85.
37. W. Chen, G. Li, J.-O. Malm, Y. Huang, R. Wallenberg, H. Han, Z. Wang and J.-O. Bovin, Pressure Dependence of Mn^{2+} Fluorescence in ZnS : Mn^{2+} Nanoparticles, J. Lumin., 2000, **91**, p 139.

38. E. Chimczak and M. Z. Bertrandt, Kinetic Properties and Energy Transfer in the Electroluminescence of Thin Film Cells Based on ZnS:Mn, Thin Solid Films, 1988, **161**, p 59.
39. H. Yang, J. Zhao, L. Song, L. Shen, Z. Wang, L. Wang and D. Zhang, Photoluminescenct Properties of ZnS:Mn Nanocrystals Prepared in Inhomogeneous System, Mater. Lett., 2003, **57**, p 2287.
40. R. H. Bube, Photoconductivity in Solids, John Wiley, New York, 1960.
41. W. V. Gool, Fluorescence Centres in ZnS, Philips Research Reports Supplements, University of Amsterdam, Amsterdam, 1961.
42. A. A. Bol, J. Ferwerda, J. A. Bergwerff and A. Meijerink, Luminescence of Nanocrystalline ZnS:Cu^{2+}, J. Lumin., 2002, **99**, p 325.
43. V. Khomchenko, L. Fedorenko, N. Yusupov, V. Rodionov, Y. Bacherikov, G. Svechnikov, L. Zavyalova, N. Roshchina, P. Lytvyn and M. Mukhlio, Laser Processing and Characterization of ZnS:Cu Thin Films, Appl. Surf. Sci., 2005, **247**, p 434.
44. L. Qi, B. I. Lee, J. M. Kimb, J. E. Jang and J. Y. Choe, Synthesis and Characterization of ZnS:Cu,Al Phosphor Prepared by a Chemical Solution Method J. Lumin., 2003, **104**, p 261.
45. G. Sharma, S. D. Han, J. D. Kim, S. P. Khatkar and Y. W. Rhee, Electroluminescent Efficiency of Alternating Current Thick Film Devices Using ZnS:Cu,Cl Phosphor, Mater. Sci. Eng., B, 2006, **131**, p 271.
46. D. Curie, Luminescence in Crystals, Methuen & Co. Ltd., Wiley scientific, London, 1963.
47. G. F. J. Garlick, Luminescent Materials, Oxford University Press, London, 1949.
48. J. Hu, G. Wang, C. Guo, D. Li, L. Zhang and a. J. Zhao, Au-Catalyst Growth and Photoluminescence of Zinc-Blende and Wurtzite ZnS Nanobelts via Chemical Vapor Deposition, J. Lumin., 2007,**122-123**, p 172.
49. K. Manzoor, V. Aditya, S. R. Vadera, N. Kumar and T. R. N. Kutty, Self-Assembly of Doped Semiconductor Nanocrystals Leading to Formation of Highly Luminescent Nanorods, Appl. Surf. Sci., 2006, **252**, p 3968.
50. H. K. Henisch, Electroluminescence, Pergamon Press, Oxford, 1962.
51. S. Matsumoto, I. Ohta, T. Kamegaya, M. Tamura, T. Beppu and H. Morita, Electronic Display Devices, English Edition, John Wiley & Sons, Tokyo, 1984.

Chapter 7.

Concluding remarks

Chapter 7. Concluding remarks

This three-year course of experimentation and concentrated study on electroluminescent materials required experience in the use of high power lasers for materials processing and more specifically the laser induced forward transfer technique. The chemical bath deposition involved the use of highly hazardous solid, liquid and gas chemicals and necessitated a great deal of care. The theoretical study of luminescence offered a good insight to the science of light emission and more specifically that of inorganic phosphors and light emitting semiconductors. In addition, a detailed understanding of the technology of display devices was built, gaining the ability to assess the positive and negative aspects of each type of device that exists in the market today and the trades of constructing such devices. Furthermore, a large number of analysis techniques were utilised for the characterisation of the prepared films. The techniques range from spectroscopy to various types of microscopy and from restricted surface probing to bulk materials interrogation. Moreover, the experiments often dealt with ionising beams and radiation, with the most significant in this domain being the ones at the synchrotron radiation source facilities of Daresbury laboratories, where the EXAFS measurements were performed.

In this small chapter a summary of the work described in the above chapters, is given, starting with what was achieved with the experimental investigation in terms of precipitation and laser processing. Then a few suggestions for improvement and further work that can be performed to complement the outcome of this research are laid out. Finally, a short paragraph assessing the performance of the investigated processes in the industry is set out, defining the main limitations and how they can be surpassed.

7.1 Research achievements

Here is a summary of the key accomplishments of this research. Some of them arise from the objectives set at the beginning of the research and stated in section 1.4. Others were essential for the progress of this work and yet significant to science. The presentation form of bulletpoints, chosen here to outline these achievements is very

definite. However, many more outcomes of this work would draw the individual reader's interest when examining the volume of this text.

- Optimisation of the chemical bath deposition method for precipitation of well adherent ZnS and ZnCdS films on SiO_2.
- Good control of the precipitation process, especially in terms of film thickness.
- Novel method of defining and quantifying surface roughness of layers composed by adjacent spherical objects.
- Definition of a new roughness factor based on the air/material ratio.
- Laser induced forward transfer of luminescent ZnS and ZnCdS films on Si and SiO_2 substrates.
- Multiple layer deposition of ZnS and ZnCdS films via the LIFT process for the first time.
- Optimisation of both processes and their combination, for the deposition of II-VI luminescent films on selected areas.

7.2 Film Precipitation

The present work began with outlining the known properties, physicochemical characteristics and the typical, as much as the possible future, applications of the inorganic electroluminescent phosphors. It has then moved on to describe the main routes of obtaining light emission from such materials and the structural and compositional characteristics that will affect their luminescence efficiency. A relation between their general luminescence and more specific electroluminescence capabilities was also established in theoretical terms. A more in-depth examination of the traits of group II sulfides and oxides is then laid out, leading to chemical preparation methods and laser processing of II-VI phosphor films.

The chemical preparation of doped and undoped ZnS and CdZnS was investigated in the form of a film precipitating bath. The best conditions of film precipitation where determined to be 92 ^{o}C solution temperature, stabilised by a PID controller, 5.5 to 6.5 pH induced by the metal chloride reactants and solution circulation over the surface of the substrate by convection. The best reactant

concentrations were 7.22 to 15.53 mM (2.4 to 3.6 g) of metal chlorides, 56.36 mM (0.72 g) of thioacetamide and 167.71 mM (1.7 g) of urea. These conditions achieve a two layer modelled film with a first layer thickness of 150 to 160 nm and a second layer thickness of 20 nm, carrying the roughness features. In total, the films present a thickness of 170 nm with approximately 10 nm variations. The conditions can be modified to effect film thickness, achieving a range between 70 to 430 nm.

The precipitation of the films is a combination of homogeneous and inhomogeneous nucleation and progressive growth process. Inhomogeneous nucleation allows for the formation of the film on the glass substrates. It was found that it begins with the formation of a very thin ZnO layer on the SiO_2 (or SiO_2 based) surface, which acts as the basis for ZnS and CdZnS film growth or particle adhesion. The ready made particles are inhomogeneously nucleated around embryo nuclei comprising of the sulfide material with the lowest solubility product (which is silver sulfide or copper sulfide when doping, or cadmium sulfide when preparing undoped ternary compounds). The particles have a fairly spherical shape and continue to grow even after their adhesion on the precursor film. Yet, the spherical shapes are still observed in the final form of the films under the electron microscope and very roughly under the optical microscope. Due to the nature of this process, there is a substantial phase separation between the sulfide species precipitated in this method. Moreover, complete lack of zinc chloride in the reaction vessel was found not to generate adherent films, as the precursor oxide film forms only for zinc at neutral or slightly acidic environments. Consequently, an increase of low K_{sp} material's concentration in the solution would impair film adherence on the glass substrates.

The size of the sphere and consequently the thickness of the film, is controlled by adjusting the precipitation conditions. An increase in the temperature is believed to eliminate the small unstable embryos and thus allows only for further and faster growth of the largest spheres. A similar effect was observed when lowering the pH, down to almost 2. Reversing any of the two conditions would promote the formation of a large number of nuclei, with a diversity of shapes and sizes and reduce the amounts of homogeneously grown particles that participate in film formation. Therefore, larger pH values or lower temperatures can produce thinner films. The reaction temperature was also found to be a key factor defining the speed of precipitant formation (speed of reaction) in an analogous manner. Incorporation of

metals that would give very sulfides with very low solubility products also increased the progress rate of the chemical bath deposition procedure.

7.2.a. Luminescence

Strong luminescence was obtained only from copper doped ZnS and manganese doped CdZnS, which was annealed at approximately 650 °C in a H_2S atmosphere. However, luminescent peaks, in accordance with existing literature,[1-3] were detected during cathodoluminescence and photoluminescence experiments that were attributed to activation of luminescent centres or donor-acceptor level transitions, for all the investigated activators, as illustrated in Figure 7.1. ZnS films demonstrate a degree of self activation and spectrum differentiation depending on the annealing step and hence the acquired cubic or hexagonal form. The aluminium impurities detected by trace element analysis and the chlorine atoms incorporated from the solution, have a strong significance, acting as co-activators. Manganese is only incorporated in ZnS. Owing to the phase separation in the homogeneously formed cluster spheres, for CdZnS precipitations, a peak at 585 nm, being characteristic of a ZnS:Mn system, is detected. In films annealed at temperatures close to 700 °C, the ZnS lattice experiences a phase transformation from the cubic to the hexagonal form. As a result, the Zn-S bond length increases and the d orbital splitting decreases, due to the weakening of the ion induced electric field. Thus, the luminescence peak shifts to a higher wavelength, around 600 nm.

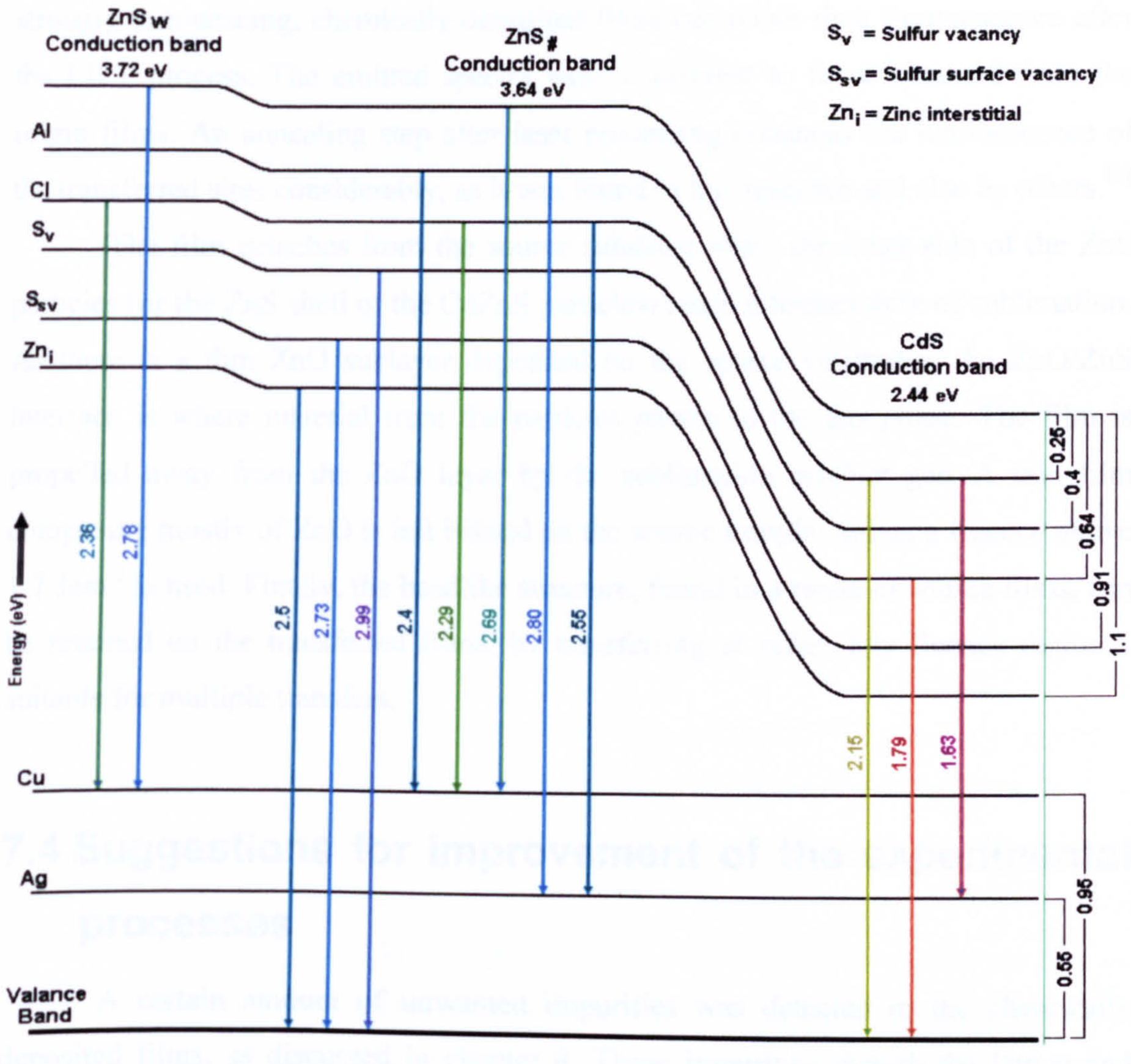

Figure 7.1 Light emitting transitions (represented by coloured arrows) observed in the prepared ZnS and CdZnS films, by cathodoluminescence and photoluminescence. The films were undoped or doped with donor or acceptor impurities, as opposed to luminescent centres.

7.3 Laser Transfer

The chemically prepared films were successfully transferred on silica based glass substrates, or silicon wafers, using a KrF, excimer laser at 248 nm. The ideal transferring conditions are a fluence of 0.6 to 0.7 Jcm^{-2}, in an argon atmosphere at a pressure of 4 $x10^{-2}$ mbar, travelling a distance of 15 μm. It was possible to achieve multiple layer transfers on the same area, thus increasing the film's thickness. The maximum number of films laid successfully on the same site reaches up to 15. A slightly lower fluence is required for multiple layer transfers, at 0.5 to 0.6 Jcm^{-2}. Only

strongly luminescing, chemically deposited films can retain their luminescence after the LIFT process. The emitted spectra were equivalent to those obtained from the origin films. An annealing step after laser processing enhances the luminescence of the transferred sites considerably, as it was found in this research and also by others.[4]

The film detaches from the source substrate when the inner side of the ZnS particles (or the ZnS shell of the CdZnS particles) reach a temperature of sublimation. As there is a thin ZnO sublayer deposited on the source substrates, the ZnO/ZnS interface is where material from the particles passes to the gas phase. The film is propelled away from the ZnO layer by the sublimation product gas. A thin film composing mostly of ZnO is left behind on the source sample, unless a fluence above 1.7 Jcm^{-2} is used. Finally, the beadlike structure, found in a range of source films, can be retained on the transferred films, by transferring at rather low fluence regimes, suitable for multiple transfers.

7.4 Suggestions for improvement of the experimental processes

A certain amount of unwanted impurities was detected in the chemically deposited films, as discussed in chapter 4. These impurities disturb the lattice and reduce its efficiency as a luminescent material. Therefore, it would be very beneficial if their concentration in the films could be more tightly controlled. The bath solution is contaminated via two main routes. One is by receiving floating particles from the surrounding air in the laboratories, through the exposed surface of the solution. The other is by slow dissolution of the stainless steel heater and the various metals contained in its alloy, in the solution, by the hydrochloric acid. An inert, closed vessel, made from heat resistant (borosilicate) glass, would solve both of these problems. The heat can be transferred to the solution from an external source. It would also be interesting to investigate microwave heating of a bath carried out in such a vessel. In terms of laser processing, good control of the laser output power will aid the experimental process, while it would be essential in an industrial application of such a technique.

7.5 Scope of future research

Time is always restricting and no limit can be set to define a complete research. Therefore, there will always be some more interesting aspects to investigate on a subject, to complement what is already known. Following the suggestions that were brought forward above, for improving the purity of the films, it would be interesting to see how much can the luminescence of the materials can be improved, in parallel to the purity. Another step that can be taken to ameliorate the quality of the films is by attempting to supply the sulfur ions in the solution, by dissolving hydrogen sulfide in the solution, directly from its gas phase. This is one of the classic methods of forming ZnS precipitate in a solution.[5]

The beadlike formation is agreeably a very interesting aspect of the films,[6] and it should be investigated further, in an effort to expand the applications of such films.[7, 8] The phase separation between materials of low and high solubility products was a theoretical scenario that explains a great number of observations in this research. However, such a phase separation can be observed by means of a transmission electron microscope[9-11] which depicts low and high density of materials at a different contrast. Thus the Cd atoms in the CdS cores, being heavier than the Zn atoms in the shell would appear at a different shade on the microscope image. It is suggested that the beads are deposited on the matrix used to insert the sample in front of the electron beam, by the LIFT process at a low fluence (0.5 Jcm^{-2}). Though the beadlike structure was retained with a low fluence regime, it has not been attempted to perform a multiple layer transfer of a source film, featuring well defined beads, hence resulting in a film with multiple layers of beads. Decreasing the fluence of the laser beam at 0.3 to 0.4 Jcm^{-2} after the transfer of the first layer or by 0.2 to 0.3 after each successive layer, when using an initial fluence of 1.2 Jcm^{-2}, would help to keep intact the structure of the previous layers. Finally a more systematic observation of all the deposited and laser processed samples by the SEM and EDX techniques, is suggested, as they were both found to demystify a number of results and give the ability to ascribe elemental composition to film areas and features in the micron scale.

7.6 Viability of the developed film preparation methods, applications and limitations

As it was mentioned in the first chapter, the development of such materials is aimd mostly at thin film electroluminescent display device applications. Any possibility of achieving quantum confinement effects would possibly extend the application to the field of light emitting diodes. At this stage, the experiments have only proved the feasibility of chemical deposition of II-VI doped or undoped films in a solution of comparably neutral pH and the ability to perform the LIFT process on them for redeposition onto a new substrate. Though higher purity films of greater luminescence will be needed for constructing a thin film display device, utilisation of the LIFT process for redeposition can easily be suggested for direct writing of phosphor films on a display matrix. By raising the purity of the chemically prepared films to a good standard, the process is very economic and would be significantly valuable for mass prroduction of II-VI inorganic phosphor films. The requirements for chemical bath deposition are minimal, such as water boiling temperature heaters, glass vessels and possible steering. Precipitation on very large surfaces of glass is possible in well controlled temperature and solution convex conditions. Moreover, the substrates participating in the chemical bath as precursors to the LIFT process can be easily cleaned by hydrochloric acid and reused in the bath.

7.7 Closing remarks

The technology of thin films has allowed for fast progress in the field of light emitting display devices and the market has grown demanding around it for better characteristics and quality of such devices. Improving the materials is perhaps the most groundbreaking step that can be taken under such circumstances. In this research it was attempted to combine a material fabrication method and a processing one. Each offering its unique attributes to this type of science. A chemical bath deposition of inorganic salts was employed for the fabrication of thin precursor films, which is a rather economic method of producing semiconductor materials, while its applications stretch out to one of the most advanced sections of the semiconductors field, that of quantum confinement. At the same time, laser redeposition of the precursor films is a materials processing method combining high precision efficiency and effectiveness.

Phosphorescent and luminescent ZnS and CdZnS films were prepared and transferred successfully to a new substrate by the laser direct writing process. However, the luminescence and quality of the films is yet to be improved before applying this mixture of materials science in the industry. Nonetheless, a few further steps were taken in the science of phosphor processing, with the most innovating one being laser induced forward transfer of II-VI films. A better understanding of film formation in a chemical bath and its detachment by laser radiation was also established. Thus, it is in good hope that the observations of this research will be valuable for future researchers of II-VI materials.

7.8 References

1. R. H. Bube, Photoconductivity in Solids, John Wiley, New York, 1960.
2. G. F. J. Garlick, Luminescent Materials, Oxford University Press, London, 1949.
3. W. V. Gool, Fluorescence Centres in ZnS, Philips Research Reports Supplements, University of Amsterdam, Amsterdam, 1961.
4. T. Sugimoto, S. Wu, H. Itoh and T. Kojima, Well-Defined Fluorescent Particles of ZnS:Cu -- 1. Preparation and Effects of Annealing J. Colloid Interface Sci., 2003, **257**, p 47.
5. M. Farnsworth, Zinc Chemicals, Zinc Development Association, London, 1973.
6. G. Hodes, Chemical Solution Deposition of Semiconductor Films, Marcel Dekker, New York, 2003.
7. D. Bimberg, M. Grundmann and N. N. Ledentsov, Quantum Dot Heterostructures, John Wiley and Sons, Ltd., Sussex, 1999.
8. L. Cao, S. Huang, S. Lü and J. Lin, Effect of Layer Thickness on the Properties of ZnS/CdSZnS Quantum Dot Qunatum Well, J. Colloid Interface Sci., 2005, **284**, p 516.
9. M. A. Correa-Duarte, M. Giersig and L. M. Liz-Marán, Stabilization of CdS Semiconductor Nanoparticles Against Photodegradation by Silica Coating Procedure, Chem. Phys. Lett., 1998, **286**, p 497.
10. L. M. Liz-Marán and P. Mulvaney, Nanostructuring Metals and Semiconductors with Silica. From Nanolayers to Crystals, Recent Research Devel. Phys. Chem., 1998, **2**, p 1.
11. T. Ung, L. M. Liz-Marán and P. Mulvaney, Controlled Method for Silica Coating of Silver Colloids Influence of Coating on the Rate of Chemical Reactions, Langmuir, 1998, **14**, p 3740.

Appendix

Appendix 1. Table of successful reactant quantities mixtures specified in Molarities

Molarity equivalent of table 4.4 Reactant quantities that succeeded in forming films in 170 ml of solution.

		ZnS	CdZnS	ZnS:Cu	CdZnS:Cu	ZnS:Ag	CdZnS:Ag	ZnS:Mn	CdZnS:Mn
Urea	Min.	0.137113	0.156701	0.146907	0.166495	0.161598	0.166495	0.146907	0.156701
	Sugst.	0.156701	0.176288	0.166495	0.176288	0.166495	0.176288	0.156701	0.166495
	Max.	0.225257	0.225257	0.186082	0.195876	0.186082	0.195876	0.20567	0.20567
TAA	Min.	0.043057	0.050885	0.0548	0.0548	0.0548	0.0548	0.050885	0.046971
	Sugst.	0.058714	0.0548	0.058714	0.058714	0.058714	0.0548	0.062628	0.058714
	Max.	0.062628	0.066542	0.062628	0.066542	0.062628	0.066542	0.066542	0.066542
$ZnCl_2$	Min.	0.004748	0.00259	0.007337	0.003021	0.007769	0.003021	0.005611	0.00259
	Sugst.	0.01079	0.004316	0.012085	0.005179	0.012085	0.005179	0.009495	0.003453
	Max.	0.028486	0.013811	0.028486	0.012948	0.014243	0.012948	0.012948	0.008632
$MnCl_2$	Min.	-	-	x	x	x	x	0.002972	0.003864
$AgCl_2$	Sugst.	-	-	0.000035	0.000035	0.000033	0.000033	0.020806	0.023779
$CuCl_2$	Max.	-	-	0.000173	0.000173	0.000165	0.000165	0.053502	0.059447
$CdCl_2$	Min.	-	0.001288	-	0.002576	-	0.002576	-	0.002061
	Sugst.	-	0.004637	-	0.00644	-	0.00644	-	0.007728
	Max.	-	0.017259	-	0.018032	-	0.018032	-	0.015456

Notes: All quantities are given in moles per litre. The metal chlorides are <u>not</u> in their hydrate forms as described in Chapter 3. Letter x denotes that no further investigation was performed towards that route.